Thomas Brabec
Editor

SPRINGER SERIES IN OPTICAL SCIENCES 134

Strong Field Laser Physics

Springer Series in

OPTICAL SCIENCES 134

Founded by H.K.V. Lotsch

Springer Series in
OPTICAL SCIENCES

The Springer Series in Optical Sciences, under the leadership of Editor-in-Chief *William T. Rhodes*, Georgia Institute of Technology, USA, provides an expanding selection of research monographs in all major areas of optics: lasers and quantum optics, ultrafast phenomena, optical spectroscopy techniques, optoelectronics, quantum information, information optics, applied laser technology, industrial applications, and other topics of contemporary interest.
With this broad coverage of topics, the series is of use to all research scientists and engineers who need up-to-date reference books.
The editors encourage prospective authors to correspond with them in advance of submitting a manuscript. Submission of manuscripts should be made to the Editor-in-Chief or one of the Editors. See also www.springer.com/series/624

Thomas Brabec
Editor

Strong Field Laser Physics

Springer

Editor
Thomas Brabec
Department of Physics
University of Ottawa
Ottawa, ON
Canada
brabec@uOttawa.ca

ISSN: 0342-4111 e-ISSN: 1556-1534
ISBN: 978-0-387-40077-8 e-ISBN: 978-0-387-34755-4
DOI: 10.1007/978-0-387-34755-4

Library of Congress Control Number: 2008931586

Printed on acid-free paper

springer.com

Contents

Contributors

Carlo Altucci
CNISM and Dipartimento di Scienze Fisiche, Università di Napoli "Federico II", Napoli, Italy, phone: (+39 081) 676289, altucci@na.infn.it

Sarah Baker
Blackett Laboratory, Imperial College, Prince Consort Road, London SW7 2BZ, UK, phone: (+44 20) 75947864, sarah.baker@imperial.ac.uk

V. R. Bhardwaj
Physics Department, University of Ottawa, 150 Louis Pasteur, Ottawa K1N 6N5, ON, Canada, phone: (613) 5625899 6759, ravi.bhardwaj@uottawa.ca

Thomas Bornath
Physics Department, Institut für Physik, Universität Rostock, Rostock 18051, Germany, phone: (+49 381) 4986915, thomas.bornath@uni-rostock.de

Thomas Brabec
Physics Department, University of Ottawa, Ottawa K1N 6N5, ON, Canada, phone: (613) 5625800 6756, brabec@uottawa.ca

Gilles Chériaux
Laboratoire d'Optique Appliquée, Ecole Nationale supérieure de Techniques Avancées, École Polytechnique, CNRS UMR 7639, Chemin de la Hunière, 91761 Palaiseau Cedex, France, phone: (+33 1) 69319891, gilles.cheriaux@ensta.fr

Ciprian C. Chirila
Institute of Physics, University of Kassel, Heinrich-Plett-Str. 40, 34132 Kassel 34132, Germany, phone: (+49 561) 8044574, chirila@physik.uni-kassel.de

Ivan Christov
Physics Department, Sofia University, 5 James Bourchier Street, 1164 Sofia, Bulgaria, phone: (+35 92) 8161741, ipc@phys.uni-sofia.bg

Paul B. Corkum
Steacie Institute for Molecular Sciences, National Research Council,
100 Sussex Drive, Ottawa K1A 0R6, ON, Canada, phone: (613) 9937390,
Paul.Corkum@nrc-cnrc.gc.ca, paul.corkum@nrc.ca

Steven T. Cundiff
JILA, National Institute of Standards and Technology and University of Colorado, Boulder 80309-0440, CO, USA, phone: (303) 4927858, cundiffs@jila.colorado.edu

Sandro De Silvestri
Department of Physics, National Laboratory for Ultrafast and Ultraintense Optical Science – CNR–INFM, Politecnico, Milano, Italy, phone: (+39 02) 2399 x 6151, sandro.desilvestri@fisi.polimi.it

Clemens Dietrich
University of Duisburg-Essen, Institute of Experimental Physics, Lotharstr. 1, 47048, Duisburg, Germany

Patrick W. Dooley
Department of Physics and Astronomy, McMaster University, Hamilton, L8S 4M1, ON, Canada, patrickdooley@rogers.com

Farhad M. H. Faisal
Fakultät für Physik, Universität Bielefeld, D-33615 Bielefeld, Germany, phone: (+49521) 106 5320, ffaisal@physik.uni-bielefeld.de

Josef Feldhaus
Hamburger Synchrotronstahlungslabor HASYLAB, Deutsches Elektronen-Synchrotron DESY, Notkestrasse 85, 22603 Hamburg, Germany,
phone: (+49 40) 8998 3901, josef.feldhaus@desy.de

Takao Fuji
RIKEN, Chemical dynamics laboratory, Hirosawa 2-1, Wako, Saitama 351 0198 Japan, phone: (+81 48) 4671434, takaofuji@riken.jp

Hideaki Habara
Central Laser Facility, Rutherford Appleton Laboratory, Chilton, Didcot, Oxfordshire, OX11 0QX, UK

Misha Yu. Ivanov
Steacie Institute for Molecular Sciences, National Research Council,
100 Sussex Drive, Ottawa K1A 0R6, ON, Canada, phone: (613) 9939973,
Misha.Ivanov@nrc-cnrc.gc.ca

Karol A. Janulewicz
Max-Born-Institute Berlin, Berlin, Germany, phone: (+49 30) 6392 1311,
janulewi@mbi-berlin.de

Vladimir Krainov
Moscow Institute of Physics and Technology, 141700 Dolgoprudny, Moscow Region, Russia, krainov@online.ru

Ferenc Krausz
Max Planck Institute for Quantum Optics, D-85748 Garching, Germany; Chair of Experimental Physics, Ludwig Maximilians University, Munich, Germany, phone: (+49 89) 32905 602, ferenc.krausz@mpq.mpg.de

Francois Légaré
Steacie Institute for Molecular Sciences, National Research Council, 100 Sussex Drive, Ottawa K1A 0R6, ON, Canada, legare@emt.inrs.ca

Mandred Lein
Institute of Physics, University of Kassel, Heinrich-Plett-Str. 40, 34132 Kassel, Germany, phone: (+49 561) 8044407, lein@physik.uni-kassel.de

Matthias Lenzner
Department of Physics, City College of CUNY, Convent Ave & 138th Street, New York 10031, NY, USA, phone: (212) 650-6824, mlenzner@sci.ccny.cuny.edu

Maciej Lewenstein
Institute of Photonic Sciences, Parc Mediterrani de la Tecnologia, Av. del Canal Olímpic s/n, 08860 Castelldefels, Barcelona, Spain, phone: (+34 93) 5534072, maciej.lewenstein@icfo.es

Igor. V. Litvinyuk
Physics Department, Kansas State University, Manhattan 66506-2601, KS, USA, phone: (785) 532-1615, ivl@phys.ksu.edu

Anne L'Huillier
Atomic Physics, Lund Institute of Technology, P.O. Box 118, SE-221 00 Lund, Sweden, phone: (+46 46) 222 76 61, anne.lhuillier@fysik.lth.se

Alfred Maquet
Université Pierre et Marie Curie, Laboratoire de Chimie Physique—Matière et Rayonnement, 11, rue Pierre et Marie Curie, 75231 Paris Cedex 05, France, phone: (+33 1) 44276633, alfred@maquet@upmc.fr

Jon P. Marangos
Blackett Laboratory, Imperial College, Prince Consort Road, London SW7 2BZ, UK, phone: (+44 20) 75947857, j.marangos@imperial.ac.uk

Adrian Melissinos
Department of Physics and Astronomy, University of Rochester, Rochester 14627, NY, USA, phone: (585) 275-2707, meliss@pas.rochester.edu

Harm G. Muller
FOM Institute for Atomic and Molecular Physics, Kruislaan 407, Amsterdam, The Netherlands, phone: (+31 20) 6081234, h.g.muller@amolf.nl

Peter Nickles
Max Born Institute, Berlin, Germany; Advanced Photonics Research Institute at the Gwangju Institute of Science and Technology, Gwangju, Republic of Korea, Germany, phone: (+49 30) 6392 1310, nickles@mbi-berlin.de

Hiromichi Niikura
Steacie Institute for Molecular Sciences, National Research Council of Canada, 100 Sussex Drive, Ottawa K1A 0R6, ON, Canada, phone: (613) 9900143, Hiromichi.Niikura@nrc-cnrc.gc.ca

Mauro Nisoli
Department of Physics, National Laboratory for Ultrafast and Ultraintense Optical Science – CNR–INFM, Politecnico di Milano, Milano, Italy, phone: (+ 39 02) 2399 x 6167, mauro.nisoli@fisi.polimi.it

Peter Norreys
Central Laser Facility, Rutherford Appleton Laboratory, Chilton, Didcot, Oxfordshire, OX11 0QX, UK, phone: (+44 1235) 445300, P.A.Norreys@rl.ac.uk

Enrico Priori
Department of Physics, Politecnico, Milano, Italy, phone: (+39 02) 2399 x 6194, priori@elet.polimi.it

Alexander Pukhov
Institut für Theoretische Physik I, Heinrich-Heine-Universität Düsseldorf, 40225 Düsseldorf, Germany, phone: (+49 211) 8113122, pukhov@tpl.uni-duesseldorf.de

Lora Ramunno
Physics Department, University of Ottawa, Ottawa K1N 6N5, ON, Canada, phone: (613) 5625800 6790, lora.ramunno@uottawa.ca

David M. Rayner
Steacie Institute for Molecular Sciences, National Research Council, 100 Sussex Drive, Ottawa K1A 0R6, ON, Canada, phone: (613) 9937028, David.Rayner@nrc-cnrc.gc.ca

Heidi Reinholz
Physics Department, Institut für Physik, Universität Rostock, Rostock 18051, Germany, phone: (+49 381) 4986945, heidi.reinholz@uni-rostock.de

Joseph S. Robinson
Blackett Laboratory, Imperial College, Prince Consort Road, London SW7 2BZ UK, phone: (+44 20) 75947864, joseph.robinson@imperial.ac.uk

Ian N. Ross
CLRC Rutherford Appleton Laboratory, Chilton, Didcot, Oxon OX11 0QX, UK, phone: (+44 1235) 445347, I.N.Ross@rl.ac.uk

Antoine Rousse
Laboratoire d'Optique Appliquée, ENSTA, CNRS UMR7639, Ecole Polytechnique, Chemin de la Hunière, 91761 Palaiseau, France, phone: +33 (0)1 6931 9901, rousse@enstay.ensta.fr, antoine.rousse@ensta.fr

Wolfgang Rudolph
Department of Physics and Astronomy, University of New Mexico, 800 Yale Blvd. NE, Albuquerque, NM, USA, phone: (505) 2772081, wrudolph@unm.edu

Pascal Salières
CEA-Saclay, IRAMIS/SPAM, 91191 Gif-sur-Yvette, France, phone: (+33 1) 69086339, pascal.salieres@cea.fr

Wolfgang Sandner
Max-Born-Institute Berlin, Berlin, Germany, phone: (+49 30) 6392 1300, sandner@mbi-berlin.de

Giuseppe Sansone
Department of Physics, Politecnico, Milano, Italy, phone: (+39 02) 2399 x 6194, giuseppe.sansone@polimi.it

Kenneth J. Schafer
Department of physics and astronomy, Louisiana State University, Baton Rouge 70803-4001, LA, USA, phone: (504) 388-0466, schafer@rouge.phys.lsu.edu

Armin Scrinzi
Institute for Photonics, Vienna University of Technology, Gusshausstr. 27, A-1040 Vienna, Austria, phone: (+43 1) 58801 38733, ascrinzi@pop.tuwien.ac.at

Ravi Singhal
Department of Physics & Astronomy, University of Glasgow, Kelvin Building, Room 515a, Glasgow, G12 8QQ, Scotland, UK, phone: (+44 141) 330 6433, r.singhal@physics.gla.ac.uk

Bernd Sonntag
Institut fur Experimentalphysik, Universitat Hamburg, Luruper Chaussee 149, 22761 Hamburg, Germany, phone: (+49 40) 8998 3703, bernd.sonntag@desy.de

Salvatore Stagira
Department of Physics, Politecnico, Milano, Italy, phone: (+39 02) 2399 x 6167, stagira@polimi.it

Orazio Svelto
Department of Physics, Politecnico, Milano, Italy, phone: (+39 02) 2399 x 6108, orazio.svelto@fisi.polimi.it

Richard Taieb
Université Pierre et Marie Curie, Laboratoire de Chimie Physique—Matière et Rayonnement, 11, rue Pierre et Marie Curie, 75231 Paris Cedex 05, France, richard.taieb@upmc.fr

Kim Ta Phouc
Laboratoire d'Optique Appliquée, ENSTA, CNRS UMR7639, Ecole Polytechnique, Chemin de la Hunière, 91761 Palaiseau, France, phone: +33 (0)1 6931 9989, kim.ta-phuoc@ensta.fr

Alexander Tarasevitch
University of Duisburg-Essen, Institute of Experimental Physics, Lotharstr. 1, 47048 Duisburg, Germany, phone: (+49 203) 379 4567, alexander.tarasevitch@uni-due.de

John W. G. Tisch
Blackett Laboratory, Imperial College, Prince Consort Road, London SW7 2BZ UK, phone: (+44 20) 7594710, john.tisch@ic.ac.uk

Ricardo Torres
Blackett Laboratory, Imperial College, Prince Consort Road, London SW7 2BZ UK, phone: (+44 20) 75947520, r.torres@imperial.ac.uk

Joachim Ullrich
Max-Planck-Institut für Kernphysik, Saupfercheckweg 1, D-69117 Heidelberg, Germany, phone: (+49 6221) 516696, joachim.ullrich@mpi-hd.mpg.de

Ricardo Velotta
CNISM and Dipartimento di Scienze Fisiche, Università di Napoli "Federico II", Napoli, Italy, phone: (+39 081) 676148, velotta@na.infn.it

Valarie Veniard
Université Pierre et Marie Curie, Laboratoire de Chimie Physique—Matière et Rayonnement, 11, rue Pierre et Marie Curie, 75231 Paris Cedex 05, France, Valerie.Veniard@polytechnic.fr

David Villeneuve
Steacie Institute for Molecular Sciences, National Research Council, 100 Sussex Drive, Ottawa, K1A 0R6 ON, Canada, phone: (613) 9939975, David.Villeneuve@nrc-cnrc.gc.ca, david.villeneuve@nrc.ca

Alexander Voitkiv
Max-Planck-Institut für Kernphysik, Saupfercheckweg 1, D-69117 Heidelberg, Germany, phone: (+49 6221) 516609, alexander.voitkiv@mpi-hd.mpg.de

Dietrich von der Linde
University of Duisburg-Essen, Institute of Experimental Physics, Lotharstr. 1, 47048 Duisburg, Germany, phone: (+49 203) 379 4531, dietrich.von-der-linde@uni-due.de

Part I
High-Intensity Laser Sources

High-Energy Pulse Compression Techniques

Sandro De Silvestri, Mauro Nisoli, Giuseppe Sansone, Salvatore Stagira, Caterina Vozzi, and Orazio Svelto

1 Introduction

The development of femtosecond laser sources has opened the way to the investigation of ultrafast processes in many fields of science. An important milestone in the generation of femtosecond pulses was posed in 1981, with the development of the colliding pulse mode-locked (CPM) dye laser [1]. Pulses as short as 27 fs were generated in 1984 using a prism-controlled CPM laser [2]. With the first demonstration of Kerr-lens mode-locking in a Ti:sapphire oscillator in 1991 [3], performances of femtosecond sources were boosted to unprecedented levels: pulses as short as 7.5 fs have been directly generated by a Ti:sapphire oscillator controlling the intracavity dispersion by using chirped mirrors [4]; in 1999, sub-6-fs pulses were generated by using intracavity prism pairs in combination with double-chirped mirrors [5] and with the additional use of broadband semiconductor saturable absorber mirror [6]. In the meanwhile, owing to the introduction of the chirped-pulse amplification technique (CPA) [7], amplification of ultrashort pulses to extremely high power levels became accessible. Pulses as short as 20 fs have become available with terawatt peak powers at repetition rates of 10–50 Hz [8,9,10] and with multigigawatt peak power at kilohertz rates [11,12].

Generation of ultrashort pulses can also be achieved by extracavity compression techniques. In 1981, Nakatsuka and coworkers [13] introduced an optical compression technique based on the interplay between self-phase modulation (SPM) and group velocity dispersion (GVD) occurring in the propagation of short light pulses in single-mode optical fibers. Nonlinear propagation induces spectral broadening and chirping of the laser pulses; subsequent propagation in an appropriate optical dispersive delay line provides compression of the chirped pulse. The increased spectral bandwidth of the output pulse leads to the generation of a compressed pulse shorter in duration than the input one. Using this

M. Nisoli
National Laboratory for Ultrafast and Ultraintense Optical Science – CNR–INFM, Department of Physics, Politecnico di Milano, Milano, Italy
e-mail: mauro.nisoli@fisi.polimi.it

T. Brabec (ed.), *Strong Field Laser Physics*,
DOI: 10.1007/978-0-387-34755-4_1,

technique, pulses as short as 6 fs at 620 nm were obtained in 1987 from 50-fs pulses generated by a CPM dye laser [14]. In 1997, 13-fs pulses from a cavity-dumped Ti:sapphire laser were compressed to 4.6 fs with the same technique using a prism chirped-mirror Gires–Tournois interferometer compressor [15,16]. However, owing to the low-intensity threshold for optical damaging, the use of single-mode optical fibers limits the pulse energy to a few nanojoules. In 1996, a novel technique [17], based on spectral broadening in a hollow fiber filled with noble gases, extended pulse compression to high-energy pulses (mJ range). This technique presents the advantages of a guiding element with a large diameter mode and of a fast nonlinear medium with high damage threshold. The capabilities of the hollow fiber technique were demonstrated with 20-fs seed pulses from a Ti:sapphire system [11] and a high-throughput broadband prism chirped-mirror dispersive delay line, leading to the generation of multigigawatt 4.5-fs pulses [18,19]. A prerequisite for achieving this result was the control of group-delay dispersion (GDD) in the compressor stage over an ultrabroadband (650–950 nm) spectral range. Advances in the design of chirped multilayer coatings [20,21] led to the demonstration of chirped mirrors providing adequate dispersion control over the above-mentioned spectral range without the need for prisms. These mirrors have opened the way to scaling sub-10-fs hollow fiber-based compressors to substantially higher pulse energies than previously possible. Pulses as short as 5 fs with peak power up to 0.11 TW were generated at 1 kHz repetition rate [22].

Owing to the strong importance of dispersion control in femtosecond technology, much effort has been spent in the last few years looking for alternative solutions to this problem. A promising tool has been individuated in adaptive optical elements. This approach was initially applied to CPA laser systems in order to optimize pulse compression after amplification. Correction for high-order dispersion terms has been achieved using liquid-crystal spatial light modulators [23] or deformable mirrors [24,25] combined with gratings; acousto-optic programmable dispersive filters were also successfully employed [26]. Adaptive optics have been used in conjunction with chirped mirrors for the compression of ultrashort pulses generated by an optical parametric amplifier [27]. In 2003, pulses as short as 3.8 fs have been generated by adaptive compression of a supercontinuum produced in two gas-filled hollow fibers [28,29]. The minimum pulse duration obtained so far using the hollow fiber compression technique and a feedback phase compensation system is 2.8 fs [30].

This chapter focuses on the discussion of the standard hollow fiber compression technique, which is a widespread tool for the generation of high-energy ultrashort pulses in the mJ range. Thanks to this technique, peak powers in the sub-TW level are nowadays accessible with pulse duration in the sub-10-fs regime, thus allowing the investigation of laser-matter interaction in the novel field of ultrafast, extreme nonlinear optics. The chapter is organized as follows: in Section 2, the hollow fiber compression technique is described; a numerical model for nonlinear pulse propagation is presented and some guidelines for scaling this technique are discussed; in Section 3, experimental results on

high-energy pulse compression are presented; application and perspectives of the compression technique are then introduced in Section 4.

2 Hollow Fiber Compression Technique

In this section, the hollow fiber compression technique is described in detail. The technique is based on the propagation of laser pulses in dielectric capillaries filled with noble gas. Owing to nonlinear effects occurring during propagation, the pulses undergo spectral broadening; optical compression is then achieved by a dispersive delay line. It must be clarified at this point that spectral broadening could be easily obtained also by focusing the intense femtosecond pulses directly in a bulk medium. Nevertheless, the lack of spatial uniformity in the laser beam profile would lead to a not uniform self-phase modulation; in order to have an optimal compression of the pulse, beam clipping would then be required before the compression stage [31]. On the contrary, the use of a guiding structure allows one to obtain uniform spectrally broadened pulses. In the following, we will discuss the properties of hollow fiber propagation modes and we will present a numerical model for nonlinear propagation of ultrashort pulses in a gas-filled capillary.

2.1 Propagation Modes in Hollow Fibers

Light propagation in a hollow waveguide is a well-studied topic [32], which was developed when long-distance communication in standard optical fibers was still inaccessible. Electromagnetic radiation propagates in hollow fibers by grazing incidence reflections; only leaky modes are supported because of power losses through the fiber walls. Three kinds of propagation modes can be excited: transverse circular electric (TE_{0m}) modes, in which the electric field lines are transverse concentric circles centered on the propagation axis; transverse circular magnetic (TM_{0m}) modes, with the electric field directed radially; hybrid modes (EH_{pm}, with $p \geq 1$). In EH_{pm} modes all field components are present, but axial components are so small that such modes can be thought as transverse. For fiber diameters sufficiently larger than the optical wavelength, EH_{1m} modes appear linearly polarized and can be efficiently coupled to a laser beam. The radial intensity profile of EH_{1m} modes is given by $I_c(r) = I_{c0}J_0^2(u_m r/a)$, where I_{c0} is the peak intensity, J_0 is the zero-order Bessel function, a is the capillary radius and u_m is the m th zero of $J_0(r)$. The complex propagation constant $\beta(\omega)$ of the EH_{1m} mode is given by [32]

$$\beta(\omega) = \frac{\omega\eta(\omega)}{c}\left[1 - \frac{1}{2}\left(\frac{u_m c}{\omega\eta(\omega)a}\right)^2\right] + \frac{i}{a^3}\left(\frac{u_m c}{\omega\eta(\omega)}\right)^2 \frac{\nu^2(\omega)+1}{\sqrt{\nu^2(\omega)-1}}, \qquad (1)$$

where ω is the laser frequency, $\eta(\omega)$ is the refractive index of the gas and $\nu(\omega)$ is the ratio between the refractive indexes of the external (fused silica) and internal (gas) media. The refractive index $\eta(\omega)$ can be calculated at standard conditions (gas pressure $p = 1$ atm, temperature $T_0 = 273.15$ K) by tabulated dispersion relations [33]; the actual refractive index can then be easily determined in the operating conditions used for pulse compression [34].

When the laser beam is injected into the capillary, many modes can be excited. Nevertheless single-mode operation is generally required for pulse compression; thus mode discrimination must be actuated. This goal can be easily achieved by optimal coupling between the input laser beam and the fundamental fiber mode EH_{11}. Assuming a Gaussian linearly polarized input beam with an intensity profile $I_l(r) = I_{l0}\exp(-2r^2/r_l^2)$, it is possible to determine the equation for the coupling efficiency between the input beam and the capillary modes. Numerical calculations show that for an optimum value of $r_l/a = 0.65$, the coupling efficiency of the EH_{11} mode with the laser beam is $\sim$98 %, while higher-order modes show a value lower than 0.5%. It is worth pointing out that even if higher-order modes were excited, mode discrimination would be achieved anyway, owing to the higher loss rate of EH_{1m} with respect to fundamental mode. This is clearly shown in Fig. 1, where the transmission of the fundamental mode through a 70-μm-radius hollow fiber is compared to that of the next hybrid mode EH_{12}; after a 60-cm propagation, the EH_{11} mode has a transmission higher than 60%, while EH_{12} has a transmission lower than 10%.

Mode discrimination in the capillary allows one to perform a spatial filtering of the input beam. This characteristic is depicted in Fig. 2, where the measured beam diameter at the output of the hollow fiber is compared to numerical calculation performed assuming a free-space propagation of a beam with an initial shape equal to that of the EH_{11} mode of the fiber. The good agreement between experimental and theoretical results is the demonstration that the hollow fiber delivers a diffraction-limited beam at the output.

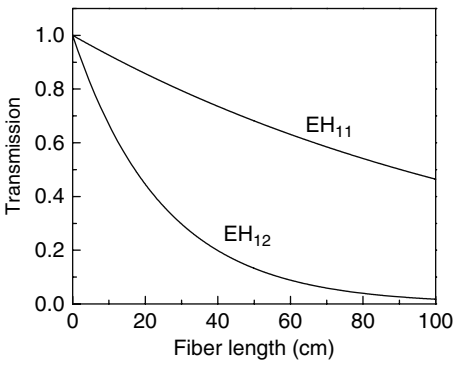

Fig. 1 Transmission of EH_{11} and EH_{12} modes for a 70-μm-radius hollow fiber vs propagation length along the fiber

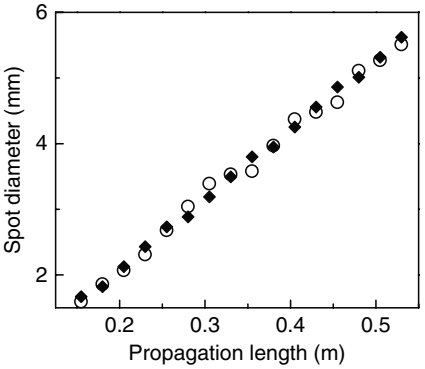

Fig. 2 *Solid diamonds*: calculated full width at half maximum (FWHM) of the beam at the output of a hollow fiber (radius $a = 70$ μm) as a function of propagation distance; *open circles*: measured values

2.2 Nonlinear Pulse Propagation in Hollow Fibers

The propagation of ultrashort pulses in nonlinear media is often treated considering the evolution of the pulse envelope alone. Such approach is valid down to single-cycle optical pulses [35], provided the slowly evolving wave approximation (SEWA) is applicable. The SEWA has two requirements: (a) the pulse envelope undergoes "small" changes during propagation and (b) the carrier-envelope phase does not change significantly on a distance equal to a wavelength. Both these conditions are met if nonlinear propagation in noble gases is considered. In the following, we will consider a numerical model for nonlinear propagation in the framework of the SEWA. Let us consider a linearly polarized input pulse, whose electric field in the hollow fiber is given in the spectral domain by

$$\widetilde{E}_c(r, z, \omega) = F(r/a)\widetilde{A}(z, \omega)e^{i\beta(\omega)z}, \tag{2}$$

where z is the propagation coordinate along the capillary axis; r is the radial distance from the capillary axis; $F(r/a)$ is the modal field distribution along the section, which is supposed to be independent of the laser frequency; $\beta(\omega)$ is the propagation constant of the capillary mode excited by the laser input beam. Assuming ω_0 to be the central laser frequency, the complex pulse envelope $A(z, t)$ can be calculated in time domain by inverse Fourier transforming of $\widetilde{A}(z, \omega + \omega_0)$; this procedure corresponds in the temporal domain to the extraction of the pulse envelope from the electric field waveform by elimination of the optical carrier at the laser frequency.

In order to write the nonlinear propagation equation in a more convenient form, a moving reference frame is usually introduced, with the new coordinates $T = t - z/v_g$ and $Z = z$, where $1/v_g = Re\left[(\partial\beta/\partial\omega)_{\omega_0}\right]$. In this new frame, the propagation equation for the pulse envelope is [35,36]

$$\frac{\partial A}{\partial Z} = i\hat{\mathcal{D}}A + i\gamma\left(1 + \frac{i}{\omega_0}\frac{\partial}{\partial T}\right)A|A|^2, \tag{3}$$

where $\hat{\mathcal{D}}$ is a differential operator accounting for radiation losses and dispersion that will be analyzed in the following and $\gamma = \omega_0\eta_2/(cS_{eff})$ is a coefficient accounting for nonlinear third-order effects during the propagation. This parameter is a function of the nonlinear refractive index coefficient η_2 (where the overall refractive index is $\bar{\eta} = \eta + \eta_2|A|^2$) and of the effective area of the waveguide, which is given by $S_{eff} = 0.48\ \pi a^2$ for a hollow fiber. The gas nonlinear coefficient η_2 is proportional to the gas pressure p according to the relation $\eta_2 = p\psi_2$, where ψ_2 is the nonlinear refractive index per unit pressure, which can be determined from tabulated values reported in literature [34]. It is worth pointing out that the second term on the right hand side of (3) takes into account two nonlinear phenomena: self-phase modulation and self-steepening. The first is responsible for spectral broadening of the injected pulse; the second accounts for envelope deformation owing to the different value of group velocity at the pulse peak (where the refractive index is higher and the velocity is lower) with respect to the wings of the pulse. This effect produces a pulse trailing edge steeper than the leading one, thus corresponding to an asymmetric pulse spectrum, more extended on the blue side.

One of the most used solving procedure for Eq. (3) is the so-called split-step Fourier method. Let us reconsider the propagation equation in the form

$$\frac{\partial A}{\partial Z} = i(\hat{\mathcal{D}} + \hat{\mathcal{N}})A, \tag{4}$$

where $\hat{\mathcal{N}}$ is the nonlinear operator acting on A. Let us consider the propagation length divided in small slices of thickness $h \sim 1 - 10\mu m$, so that operators $\hat{\mathcal{N}}$ and $\hat{\mathcal{D}}$ can be considered uniform over the slice. Let us also assume that the two operators commute in the slice. On the basis of this assumption, the propagation of the optical field along the slice can be expressed as [36]

$$A(Z + h, T) = \exp(ih\hat{\mathcal{N}})[\exp(ih\hat{\mathcal{D}})A(Z, T)]. \tag{5}$$

The operator $\exp(ih\hat{\mathcal{D}})$ in Eq. (5) can be easily evaluated in the spectral domain; using $\Im$ to represent Fourier transform, it can be expressed as

$$\exp(ih\hat{\mathcal{D}})A(Z, T) = \Im^{-1}\{\exp[ih\hat{\mathcal{D}}(\omega)]\Im[A(Z, T)]\}, \tag{6}$$

where

$$\hat{\mathcal{D}}(\omega) = \beta(\omega + \omega_0) - Re[\beta(\omega_0)] - \frac{\omega}{v_g}. \tag{7}$$

The nonlinear operator can be simply written as

$$\exp(ih\hat{\mathcal{N}}) = \exp\left[\frac{ih}{A}\gamma\left(1 + \frac{i}{\omega_0}\frac{\partial}{\partial T}\right)A|A|^2\right]. \tag{8}$$

With the help of Eqs. (5), (6), (7), (8), the input pulse envelope can be propagated through the hollow fiber in a finite number of steps. Improved versions of Eq. (5) can be used in order to increase the accuracy of the calculation [36]. It must be pointed out that Eq. (7) takes into account the overall dispersion occurring in the hollow fiber: the expression for $\beta(\omega)$ reported in Eq. (1) considers both the dispersion of the noble gas and that of the guiding structure.

2.3 General Considerations on the Compression Technique

Equation (3) can be generalized to a wider class of nonlinear effects, such as noninstantaneous response of the nonlinear medium or Raman effect [36]. Both these phenomena can take place in molecular gases such as N_2 and H_2. The noninstantaneous response is related to the alignment of the molecules along the field direction; its signature is the red shift of the broadened spectrum with respect to the initial center frequency of the pulse [19]. High-energy pulse compression techniques based on Raman effect have also been recently proposed [37,38], but their implementation is less trivial with respect to standard techniques.

In order to avoid retarded response of the nonlinearity or Raman effect, noble gases are usually employed in the hollow fiber compression. A further reason for this choice is the high damage threshold. The appearance of excessive gas ionization at high intensities must be avoided because it can be a source of unwanted nonlinear behaviors of the pulse; moreover, ionization at the capillary entrance can be detrimental for an optimal coupling with the laser beam. As a consequence, ionization imposes an upper limit to the input peak intensity of the pulse; for an assigned input pulse energy, this restriction corresponds to having a fiber radius larger than a certain value a_{min}. In order to determine the minimum radius, we assume that the variation of the refractive index induced by the Kerr effect, $\Delta n = \psi_2 pI$, is much larger than the change of the refractive index induced by gas ionization, $\Delta n_{\mathrm{p}} = \omega_{\mathrm{p}}^2/2\omega_0^2$, where $\omega_p = \sqrt{e^2\rho_e/(m_e\epsilon_0)}$ is the plasma frequency, e and m_e are the electron charge and mass, ρ_e is the free-electron density in the gas, which can be calculated using the Ammosov–Delone–Krainov (ADK) theory [39]. Figure 3 shows the calculated minimum fiber radius as a function of the input pulse energy, calculated for various pulse durations, assuming $\Delta n \geq 10^3\ \Delta n_p$ and a fiber filled with helium. From numerical calculations, it turns out that the dependence of the minimum radius, a_{min}, on the energy, ε_0, and duration, T_0, of the input pulse can be well fitted by the following simple expression [40]:

$$a_{\mathrm{min}} = A\ T_0^{-\alpha}\ \varepsilon_0^{\beta}, \tag{9}$$

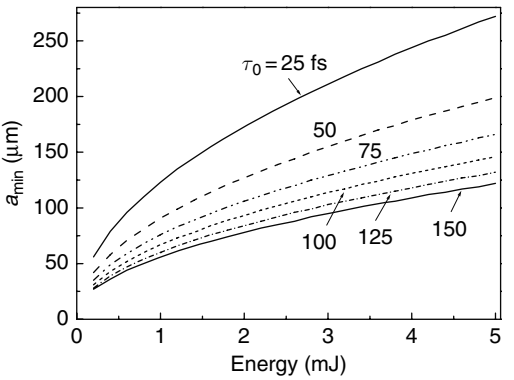

Fig. 3 Minimum fiber radius , a_{min}, as a function of the input pulse energy, calculated for various pulse durations, assuming $\Delta n \geq 10^3\ \Delta n_p$ in a helium-filled hollow fiber. τ_0 is the full-width at half maximum pulse duration, $\tau_0 = 1.665\ T_0$

where $\alpha \simeq 0.45$, $\beta \simeq 0.51$ and A is a constant, which depends on the gas. The numerical values of the constant A for various noble gases (in SI units) are the followings: $A_{\mathrm{He}} \simeq 2.62 \times 10^{-9}$ $\mathrm{ms}^{\alpha}\mathrm{J}^{-\beta}$, $A_{\mathrm{Ne}} \simeq 1.14\ A_{\mathrm{He}}$, $A_{Ar} \simeq 1.79\ A_{\mathrm{He}}$, $A_{\mathrm{Kr}} \simeq 2.08\ A_{\mathrm{He}}$.

Once the fiber radius has been chosen, there are two other free parameters in order to achieve the desired spectral broadening: the fiber length and the gas pressure. The fiber length is limited by propagation losses and by distortion of the temporal pulse shape. We will assume that the maximum fiber length is $\ell = 1$ m. In order to have a weak coupling from the fundamental transverse mode of the fiber to higher-order modes [41], the maximum pulse peak power is limited by the critical power for self-focusing, $P_{\mathrm{cr}} = \lambda_0^2/(2\psi_2 p)$ [42]. Assuming that $P_0/P_{\mathrm{cr}} < 0.3$, the maximum gas pressure turns out to be given by the following expression:

$$p_{\max} = 0.15 \frac{\lambda_0^2}{\psi_2 P_0}. \tag{10}$$

These scaling criteria must be considered as general guidelines that should be followed in the design of the compression setup; the degrees of freedom in the choice of fiber characteristics, gas type and pressure are sufficient to adapt the technique to a large variety of laser sources and desired compression performances.

3 Experimental Results

Using the hollow fiber technique, it is possible to generate few-cycle pulses with peak power of the order of 0.1 TW [22]. Input pulses of 20 fs with an energy of 1 mJ were coupled into a 60-cm-long, 500-μm diameter hollow fiber, filled with argon. After recollimation by a silver mirror the beam is directed toward the dispersive delay line. At the millijoule level, a prism chirped-mirror compressor

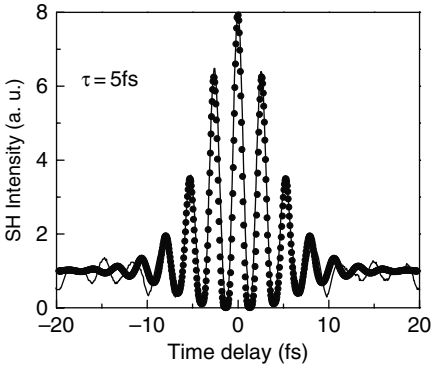

Fig. 4 Measured (*solid*) and calculated (*dots*) interferometric autocorrelation trace of the compressed pulse with 0.11 TW peak power; evaluation of pulse duration is also displayed

cannot be employed because of self-focusing in the prisms. In this case, only ultrabroadband chirped dielectric mirrors were used, which introduce an appropriate group-delay dispersion over a spectral range as broad as 150 THz (650–950 nm), and exhibit a high reflectivity over the wavelength range of 600–1000 nm. The overall transmissivity of the compressor, including the recollimating and steering optics, is $\sim 80\%$. By best compression we measured the interferometric autocorrelation trace of Fig. 4, which corresponds to a pulse duration of 5 fs. Pulse energy after compression was 0.55 mJ, which corresponds to a peak intensity of 0.11 TW.

3.1 Sub-4-fs Regime

The compression of pulses down to the sub-4-fs regime requires the development of ultrabroadband dispersive delay lines for dispersion compensation. In 2002, a novel spectral broadening technique was introduced, based on hollow fiber cascading, which allows the generation of a supercontinuum extending over a bandwidth exceeding 510 THz with excellent spatial beam quality [29]. Pulses of 25 fs were coupled into an argon-filled (gas pressure 0.2 bar) hollow fiber (0.25-mm radius). Gas pressure was chosen in order to obtain pulses with duration of about 10 fs after compression using broadband chirped mirrors. Such pulses were then injected into a second argon-filled hollow fiber (0.15-mm radius). The output beam presents excellent spatial characteristics (single-mode operation) and it is diffraction limited. The pulse spectrum at the output of the second fiber extends from $\sim$400 nm to $>$1000 nm. The possibility to take advantage of such ultrabroadband spectrum is strictly related to the development of dispersive delay lines capable of controlling the frequency-dependent group delay over large bandwidths. In 2003, ultrabroadband dispersion compensation was achieved using a liquid-crystal spatial light modulator (SLM). The beam at the output of the hollow fiber cascading was collimated and sent into a pulse shaper consisting of a 640-pixel liquid-crystal SLM, two 300-line/mm grating

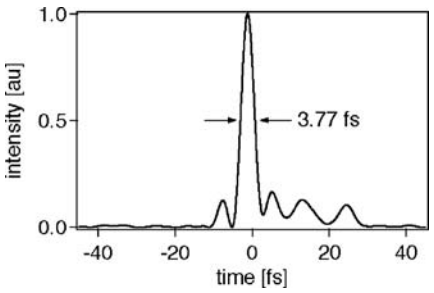

Fig. 5 Temporal pulse profile reconstructed from a SPIDER measurement. Pulse duration FWHM is 3.77 fs

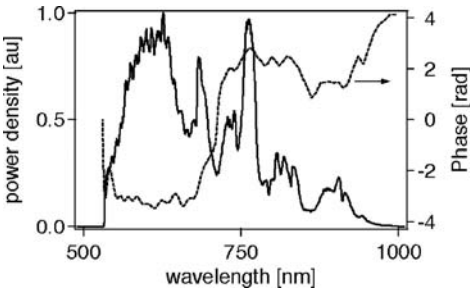

Fig. 6 *Solid curve*, experimentally measured fundamental spectrum obtained after the pulse shaper. The *dashed curve* depicts the reconstructed spectral phase of the pulse

and two 300-mm focal-length spherical mirrors (4-*f* setup). Pulse characterization was performed using the spectral phase interferometry for direct electric field reconstruction (SPIDER) technique [43]. The measured spectral phase was used to compress the pulse iteratively: compression was started with an initially flat phase written on the liquid-crystal mask. Then, the measured spectral phase was inverted and added to the phase applied to the SLM. Typically, five iterations were necessary to yield the shortest pulse. Figure 5 shows the measured temporal profile of the shortest pulse. The full width at half maximum (FWHM) is measured to be 3.77 fs [28]. The spectrum, shown in Fig. 6, spans a bandwidth of about 270 THz.

4 Applications and Perspectives

The hollow fiber compression technique allows one to generate high-intensity few-optical-cycle pulses. One can concentrate high-energy densities in a very small volume by just focusing such pulses down to the diffraction limit, thus opening the way to the tracing, with unprecedented temporal resolution, of light–matter interaction in the extreme nonlinear regime. Amongst the numerous applications of this technique, the production of high-order harmonics focusing intense and ultrashort laser pulses in noble gases has attracted a very

strong interest. It has been demonstrated that sub-10-fs pulses can drive the emission of coherent radiation down to the soft X-ray region of the electromagnetic spectrum [44]. Many applications of this radiation to biology, solid-state physics and nonlinear optics can be envisaged. Fluorescence by K-shell vacancies has been induced in light elements by harmonic pulses [45]. Besides the excellent temporal properties of compressed pulses, the hollow fiber technique delivers diffraction-limited beams with good spatial properties. The intensity profile of the output beam has a strong relevance for the harmonic emission yield; improved performances in harmonic generation were demonstrated using pulses emerging from the capillary with respect to free-propagating laser pulses [46].

The development of novel cross-correlation techniques [47] has made possible to measure XUV pulse duration down to the sub-fs range and the generation of attosecond pulses by harmonic emission was demonstrated [48], thus boosting the ultrafast laser technology beyond the femtosecond barrier. It is worth pointing out that the generation of isolated attosecond pulses requires the use of 5-fs (or shorter) driving pulses with high peak power [49]. Therefore, the introduction of the hollow fiber compression technique has proven to be essential in the rapidly evolving field of attophysics. In this contest, a key parameter of the light pulse electric field, which significantly influences the strong-field interaction, is the phase of the carrier frequency with respect to the envelope (the so-called carrier-envelope phase, CEP).

The first experimental evidence of the CEP role of few-cycle pulses has been obtained in strong-field photoionization [50]. For few-cycle pulses, depending on the CEP, the generation of photoelectrons violates inversion symmetry [51]. The CEP is expected to cause an anticorrelation in the number of electrons escaping in opposite sides orthogonally to the propagation direction of the laser beam. In the experiment, two electron detectors were placed in opposite directions with respect to the laser focus. For each laser pulse, the number of electrons detected with both detectors was recorded. A clear anticorrelation was measured using 6-fs pulses with random CEP. It is worth mentioning that CEP effects completely disappear for light pulse duration exceeding 8 fs. Much stronger CEP effects have been measured in high-order harmonic generation [52,53].

Perspectives in the use of the hollow fiber technique are related to its energy scalability. The technique can be easily employed up to mJ-level laser pulses; the upgrade toward higher energies (tens of mJ) is hindered by fiber damage and gas ionization, thus appearing to be problematic. It must be mentioned that a careful control of laser beam profile should be performed, in order to keep a good coupling with the capillary and avoid damage of the fiber entrance; light noble gases (helium or neon) should also be used, in order to increase the optical damage threshold. As a matter of fact, novel compression techniques for very high pulse energies, based on nonlinear laser–plasma interaction, have been proposed [54], but are still far from routinely operation.

5 Conclusions

Compression of high-energy pulses down to the sub-10-fs regime is nowadays a well-established technology, essentially based on the hollow fiber technique. Thanks to this tool, significant steps forward have been performed in nonlinear optics and ultrafast physics, in particular in the field of attosecond pulses. Numerous applications can be already envisaged and the apport of ultrafast technology to scientific production seems far to be completed.

References

1. R. L. Fork, B. I. Green, C. V. Shank: Appl. Phys. Lett. **38**, 671 (1981)
2. J. A. Valdmanis, R. L. Fork, J. P. Gordon: Opt. Lett. **10**, 131 (1985)
3. D. E. Spence, P. N. Kean, W. Sibbett: Opt. Lett. **16**, 42 (1991)
4. L. Xu, Ch. Spielmann, F. Krausz, R. Szipöcs: Opt. Lett. **21**, 1259 (1996)
5. U. Morgner, F. X. Kärtner, S. H. Cho, Y. Chen, H. A. Haus, J. G. Fujimoto, E. P. Ippen, V. Scheuer, G. Angelow, T. Tschudi: Opt. Lett. **24**, 411 (1999)
6. D. H. Sutter, G. Steinmeyer, L. Gallmann, N. Matuschek, F. Morier-Genoud, U. Keller, V. Scheuer, G. Angelow, T. Tschudi: Opt. Lett. **24**, 631 (1999)
7. D. Strickland, G. Mourou: Opt. Commun. **56**, 219 (1985)
8. J. Zhou, C. P. Huang, M. M. Murnane, H. C. Kapteyn: Opt. Lett. **20**, 64 (1995)
9. C. P. J. Barty, T. Guo, C. Le Blanc, F. Raksi, C. Rose Petruck, J. Squier, K. R. Wilson, V. V. Yakovlev, K. Yamakawa: Opt. Lett. **21**, 668 (1996)
10. J. P. Chambaret, C. Le Blanc, G. Chriaux, P. Curley, G. Darpentigny, P. Rousseau, G. Hamoniaux, A. Antonetti, F. Salin: Opt. Lett. **21**, 1921 (1996)
11. M. Lenzner, Ch. Spielmann, E. Wintner, F. Krausz, A. J. Schmidt: Opt. Lett. **20**, 1397 (1995)
12. S. Backus, J. Peatross, C. P. Huang, M. M. Murnane, H. C. Kapteyn: Opt. Lett. **20**, 2000 (1995)
13. H. Nakatsuka, D. Grischkowsky, A. C. Balant: Phys. Rev. Lett. **47**, 910 (1981)
14. R. L. Fork, C. H. Brito Cruz, P. Becker, C. V. Shank: Opt. Lett. **12**, 483 (1987)
15. A. Baltuška, Z. Wei, M. S. Pshenichnikov, D. A. Wiersma: Opt. Lett. **22**, 102 (1997)
16. A. Baltuška, Z. Wei, R. Szipöcs, M. S. Pshenichnikov, D. A. Wiersma: Appl. Phys. B **65**, 175 (1997)
17. M. Nisoli, S. De Silvestri, O. Svelto: Appl. Phys. Lett. **68**, 2793 (1996)
18. M. Nisoli, S. De Silvestri, O. Svelto, R. Szipöcs, K. Ferencz, Ch. Spielmann, S. Sartania, F. Krausz: Opt. Lett. **22**, 522 (1997)
19. M. Nisoli, S. Stagira, S. De Silvestri, O. Svelto, S. Sartania, Z. Cheng, M. Lenzner, Ch. Spielmann, F. Krausz: Appl. Phys. B **65**, 189 (1997)
20. G. Tempea, V. Yakovlev, B. Bacovic, F. Krausz, K. Ferencz : J. Opt. Soc. Am. B **18**, 1747 (2001)
21. N. Matuschek, L. Gallmann, D.H. Sutter, G. Steinmeyer, U. Keller: Appl. Phys. B **71**, 509 (2000)
22. G. Cerullo, S. De Silvestri, M. Nisoli, S. Sartania, S. Stagira, O. Svelto: IEEE J. Select. Top. Quantum Elect. **6**, 948 (2000)
23. D. Yelin, D. Meshulach, Y. Silberberg: Opt. Lett. **22**, 1793 (1997)
24. E. Zeek, K. Maginnis, S. Backus, U. Russek, M. Murnane, G. Mourou, H. Kapteyn: Opt. Lett. **24**, 493 (1999)
25. G. Cheriaux, O. Albert, V. Wänman, J. P. Chambaret, C. Felix, G. Mourou: Opt. Lett. **26**, 169 (2001)

26. F. Verluise, V. Laude, Z. Cheng, Ch. Spielmann, P. Tournois: Opt. Lett. **25**, 575 (2000)
27. M. R. Armstrong, P. Plachta, E. A. Ponomarev, R. J. D. Miller: Opt. Lett. **26**, 1152 (2001)
28. B. Schenkel, J. Biegert, U. Keller, C. Vozzi, M. Nisoli, G. Sansone, S. Stagira, S. De Silvestri, O. Svelto: Opt. Lett. **28**, 1987 (2003)
29. M. Nisoli, G. Sansone, S. Stagira, C. Vozzi, S. De Silvestri, O. Svelto: Appl. Phys. B **75**, 601 (2002)
30. K. Yamane, T. Kito, R. Morita, M. Yamashita: 2.8-fs clean transform-limited optical-pulse generation and characterization. In *Ultrafast Phenomena XIV* ed by T. Kobayashi, T. Okada, T. Kobayashi, K. A. Nelson, S. De Silvestri (Springer, Berlin Heidelberg 2005) pp 13–15
31. C. Rolland, P. B. Corkum : J. Opt. Soc. Am. B **5**, 641 (1988)
32. E. A. J. Marcatili, R. A. Schmeltzer: Bell Syst. Tech. J. **43**, 1783 (1964)
33. A. Dalgarno, A. E. Kingston: Proc. R. Soc. London Ser. A **259**, 424 (1966)
34. H. J. Lehmeier, W. Leupacher, A. Penzkofer: Opt. Commun. **56**, 67 (1985)
35. T. Brabec, F. Krausz: Phys. Rev. Lett. **78**, 3282 (1997)
36. G. P. Agrawal: *Nonlinear Fiber Optics*. (Academic Press, San Diego 1995)
37. M. Wittmann, A. Nazarkin, G. Korn: Opt. Lett. **26**, 298 (2001)
38. V. P. Kalosha, J. Herrmann: Opt. Lett. **26**, 456 (2001)
39. M. Ammosov, N. Delone, V. Krainov: Sov. Phys. JETP **64**, 1191 (1986)
40. C. Vozzi, M. Nisoli, G. Sansone, S. Stagira, S. De Silvestri: Appl. Phys. B **80**, 285 (2005)
41. G. Tempea, T. Brabec: Opt. Lett. **23**, 762 (1998)
42. N. Milosevic, G. Tempea, T. Brabec: Opt. Lett. **25**, 672 (2000)
43. C. Iaconis, I. A. Walmsley: IEEE J. Quantum Electron. **35**, 501 (1999)
44. Ch. Spielmann, N. H. Burnett, S. Sartania, R. Koppitsch, M. Schnürer, C. Kan, M. Lenzner, P. Wobrauschek, F. Krausz: Science **278**, 661 (1997)
45. M. Schnürer, Ch. Streli, P. Wobrauschek, M. Hentschel, R. Kienberger, Ch. Spielmann, F. Krausz: Phys. Rev. Lett. **85**, 3392 (2000)
46. M. Nisoli, E. Priori, G. Sansone, S. Stagira, G. Cerullo, S. De Silvestri, C. Altucci, R. Bruzzese, C. de Lisio, P. Villoresi, L. Poletto, M. Pascolini, G. Tondello: Phys. Rev. Lett. **88**, 33902 (2002)
47. A. Scrinzi, M. Geissler, T. Brabec: Phys. Rev. Lett. **86**, 412 (2001)
48. M. Hentschel, R. Kienberger, Ch. Spielmann, G. A. Reider, N. Milosevic, T. Brabec, P. Corkum, U. Heinzmann, M. Drescher, F. Krausz: Nature **414**, 509 (2001)
49. R. Kienberger, E. Goulielmakis, M. Uiberacker, A. Baltuška, V. Yakovlev, F. Bammer, A. Scrinzi, Th. Westerwalbesloh, U. Kleineberg, U. Heinzmann, M. Drescher, F. Krausz: Nature **427**, 817 (2004)
50. G. G. Paulus, F. Grasbon, P. Villoresi, H. Walther, M. Nisoli, S. Stagira, S. De Silvestri: Nature **414**, 182 (2001)
51. P. Dietrich, F. Krausz, P. B. Corkum: Opt. Lett. **25**, 16 (2000)
52. A. Baltuška, Th. Udem, M. Uiberacker, M. Hentschel, E. Goulielmakis, Ch. Gohle, R. Holzwarth, V. S. Yakovlev, A. Scrinzi, T. W. Hänsch, F. Krausz, Nature **421**, 611 (2003)
53. M. Nisoli, G. Sansone, S. Stagira, S. De Silvestri, C. Vozzi, M. Pascolini, L. Poletto, P. Villoresi, G. Tondello, Phys. Rev. Lett. **91**, 213905 (2003)
54. V. M. Malkin, G. Shvets, N. J. Fisch: Phys. Rev. Lett. **82**, 4448 (1999)

Ultrafast Laser Amplifier Systems

Gilles Chériaux

1 Introduction

Since the beginning of the 1990s the generation of high-intense laser pulses has known an unprecedented evolution, thanks to the conjunction of the possibility of the chirped pulse technique and the availability of spectrally broadband laser media. Lasers capable of producing petawatt pulses can now be built on few optical tables in a small laboratory. We review the generation and the amplification of ultrashort pulses by the chirped pulse amplification technique.

The application of the chirped pulse amplification (CPA) technique [1] to solid state lasers has made possible the generation of energetic few optical cycles pulses. Nowadays, nearly all high peak-power, ultrafast laser systems make use of the CPA technique, followed by optical pulse compression, as illustrated in Fig. 1.

The application of CPA to lasers originated with the work of Mourou and his co-workers [2,3]. This is a scheme to increase the energy of a short pulse, while avoiding non-linear effects and optical damages that could occur with very high peak power in the laser amplification process itself. This is done by lengthening the duration of the pulse being amplified by applying a chirp to the spectral components. This chirp is obtained in such a way that it is reversible, using the technique of optical pulse compression, developed by Treacy and Martinez [4,5,6,7,8]. By lengthening the pulse in time, energy can be efficiently extracted from the laser gain medium, while keeping the intensity below the level of non-linear effect. CPA is particularly useful for efficient utilisation of solid-state laser media with high stored energy density ($1–10\,J/cm^2$), where full energy extraction in a short pulse would lead to intensities above the damage threshold of the amplifier materials. The CPA scheme works as follows. Ultrashort pulses are generated at low pulse energy

G. Chériaux
Laboratoire d'Optique Appliquée, Ecole Nationale supérieure de Techniques Avancées, École Polytechnique, CNRS UMR 7639, Chemin de la Hunière, 91761 Palaiseau Cedex, France
e-mail: gilles.cheriaux@ensta.fr

T. Brabec (ed.), *Strong Field Laser Physics*,
DOI: 10.1007/978-0-387-34755-4_2,

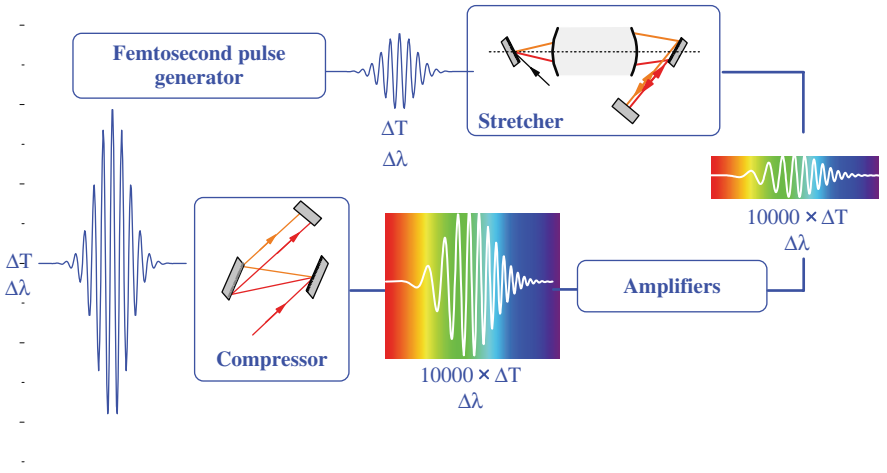

Fig. 1 Schematic diagram of a chirped pulse amplification–based laser system

through the use of an ultrashort-pulse mode-locked laser (oscillator). This mode-locked laser typically generates light pulses at a high repetition rate ($\sim 10^8$ Hz) with pulse energy in the range of few nanojoules (10^{-9} J), and with pulse duration in the range of hundreds to only few femtoseconds depending on the laser gain medium. These femtosecond pulses are then chirped using an optical stretcher consisting of a set of optical components generating a time delay between the different wavelengths of the initial short pulse. The pulse is stretched in order to reach tens of picoseond to nanosecond depending on the final energy reached. One or more stages of laser amplification are used to increase the energy of the pulse by several orders of magnitude. After optical amplification, a grating pair (optical compressor) is then used to "recompress" the pulse back to femtosecond duration. To achieve this recompression back to near the original input pulse duration without temporal distortions, proper optical design of the laser system is very important and especially the pulse stretcher.

In the following sections, we discuss in detail the various components of high-power ultrafast laser systems.

2 Ultrashort-Pulse Laser Oscillators

The CPA scheme separates the ultrashort-pulse generation process from the amplification process. The demonstration of the self-mode-locked Ti:sapphire laser by Sibbet and his group in 1990 [9] made possible the generation of very short pulses in a quite simple optical layout. Titanium-doped sapphire is a solid-state laser material with extremely desirable properties: a gain bandwidth

spanning the wavelength region from almost 600 to 1100 nm, very high thermal conductivity, and an energy storage density approaching 1 J/cm^2. This last property, although desirable for high-energy amplification, was thought to prohibit the use of Ti:sapphire in femtosecond mode-locked lasers. Existing passively mode-locked dye lasers relied on the low-energy storage density of the laser dye to facilitate the mode-locking process and thus passive mode-locking is not feasible using most solid-state gain media. However, the self-mode-locked Ti:sapphire laser relies on a different mechanism to facilitate short-pulse generation; the Kerr non-linearity of the laser crystal. Since this non-linearity is instantaneous and independent of the energy storage density of the laser medium, it made possible an entirely new class of reliable, high average power, ultrashort-pulse (~6 fs) lasers [10,11,12,13,14,15,16]. The basic cavity configuration is quite simple, as shown in Fig. 2.

The energy source for the laser is a continuous wave (cw) laser – typically an argon-ion laser or a cw diode-pumped frequency-doubled Nd:YVO4 lasers. The cw light is focused into the Ti:sapphire crystal, collinear with the mode of the laser cavity itself. The only other cavity components are an end mirror and an output coupler, together with a set of optical components (prisms pair or negatively chirped mirrors) to compensate for group velocity dispersion of the Ti:sapphire crystal. Mode-locking in this laser is achieved through the action of the Kerr lens induced in the laser crystal itself. If the laser is operating in a pulsed mode, the focused intensity inside the Ti:sapphire crystal exceeds 10^{11} W/cm^2 sufficient to induce a strong non-linear lens which quite significantly focuses the pulse. If this occurs in a laser cavity which is adjusted for optimum efficiency without this lens, this self-focusing will simply contribute to loss within the laser cavity. However, modest displacement of one mirror away from the optimum cw position by only 0.5–1 mm can result in a decrease in loss in the laser cavity when Kerr lensing is present. Thus, the Kerr lensing couples the spatial and temporal modes of the oscillator, resulting in two distinct spatial and temporal modes of operation, i.e. the cw and pulsed one. The laser can be simply aligned to be stable in either mode.

The most significant advance in Ti:sapphire oscillator design since its original demonstration has been a dramatic reduction in achievable pulse duration. This was accomplished by reducing overall dispersion in the laser by using physically shorter Ti:sapphire crystals and optimum prism materials or mirrors [17,18,19,20,21]. It is now routine to generate pulse duration of 6 fs directly from such a laser at a repetition rate of ~80 MHz, with pulse energy of

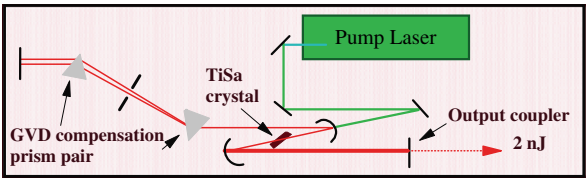

Fig. 2 Schematic diagram of a Kerr-lens mode-locked oscillator

approximately 5 nJ, and with excellent stability. Such a laser is an ideal front-end source for a high-power, ultrafast amplifier system.

3 Pulse Stretching and Recompression

Before injection into the amplifier, the short pulse (10 fs–1 ps) is stretched in time by introducing a frequency chirp onto the pulse, which increases the duration by a factor of 10^3–10^4. The duration of the stretched pulse is determined by the need to avoid damage to the optics and to avoid non-linear distortion to the spatial and temporal profile of the beam. A frequency-chirped pulse can be obtained simply by propagating a short pulse through optical material, such as a fibre. In the fibre, self-phase modulation (SPM) can broaden the bandwidth of the pulse; however, the distortion due to high-order phase terms introduced by fibres makes it difficult to use this design for femtosecond pulses.

To obtain even greater stretching factors, a grating pair arrangement can be used which separates the spectrum of a short pulse in such a way that different colours follow different paths through the optical system. Martinez realised that by placing a telescope between a grating pair, as shown in Fig. 3a, the dispersion is controlled by the effective distance between the second grating and the image of the first grating [7]. When this distance is optically made to be negative, the arrangement has exactly the opposite dispersion of a grating compressor [4], shown in Fig. 3b if one does not take into account the aberrations of the telescope. This forms the basis for a perfectly matched stretcher/compressor pair.

To avoid the wavelength-dependent walk-off (spatial chirp), a pair of mirrors are used in a roof geometry to direct the output above and parallel to the input beam. The parallelism of the grating faces and grooves must be carefully aligned to avoid spatial chirp on the output beam. For good output beam quality and focusing, the grating surfaces must also have high optical flatness ($\lambda/4$–$\lambda/10$). In fact, neglecting aberrations in the telescope used to project the image of the first grating, the stretcher phase function is exactly the opposite sign of the compressor.

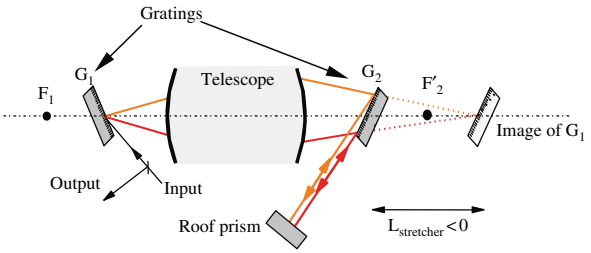

Fig. 3a Femtosecond pulse stretcher

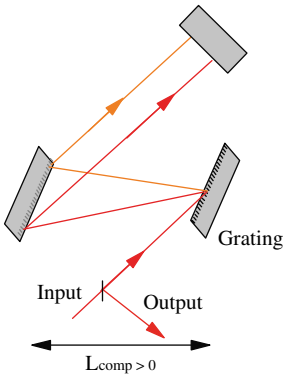

Fig. 3b Femtosecond pulse compressor

For the particular case of an aberration free optical stretcher, the second derivative of the spectral phase is given by

$$\left(\frac{\mathrm{d}^2\phi_s}{\mathrm{d}\omega^2}\right)_{\omega_0} = \frac{L_s\lambda^3}{\pi c^2 d^2 \cos^2\theta} = \phi^{(2)}{}_s(\omega_0)$$

where L_s is the distance between the two gratings at the central wavelength, λ is the central wavelength, d is the grating grooves spacing and θ is the diffracted angle.

With this expression the stretched pulse duration is given by

$$\Delta T = \Delta T_0 \sqrt{1 + \frac{16(\ln 2)^2 \phi^{(2)}{}_s{}^2}{\Delta T_0^4}}$$

or if one considers that $\phi^{(2)}$ is large

$$\Delta T = \frac{\phi^{(2)} 4 \ln 2}{\Delta T_0}$$

In the real case, the telescope can introduce some geometrical or chromatic aberrations leading to spectral or temporal phase distortions. These alter the temporal shape of the pulse after the recompression. The duration is lengthened and some wings, containing a non-negligible part of the total energy, appear. In order to obtain a very low-level pedestal pulse, an aberration-free stretcher configuration has to be used. That means that the stretcher telescope has to be aberration free since it directly translates into spectral phase distortions, which produce poor recompression and a low dynamic range onto the temporal pulse profile. Thus, the design of the telescope has to be carefully investigated. A solution that is now widely used is an all-reflective stretcher design [22] based on an aberration-free Öffner triplet (see Fig. 4). The telescope is composed of a concave and a convex mirror whose focal length is half of the concave one.

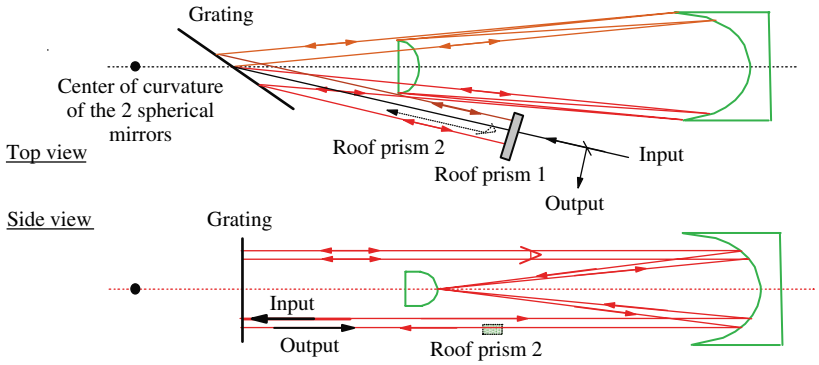

Fig. 4 Set-up of the Öffner triplet-based stretcher

These mirrors are in a concentric geometry. Such an optical system allows large stretching factor and the short pulse is recompressed to its Fourier limit.

Other schemes of pulse stretcher are used and especially when the stretched pulse duration is in the range of 10 ps the pulse stretcher can be a set of bulk material with chirped mirrors to compensate for third-order phase distortions. This kind of optical scheme has the advantage of being insensitive to the beam pointing. The recompression is therefore accomplished with a prisms pair. This solution has also the advantage of the very low loss throughput of the compressor. The main drawback of this scheme is the relatively low stretched pulse duration that can be obtained, which means that it is not usable for multiterawatt or PW laser systems [23,24,25].

4 Amplification

Since the late 1980s (following the availability of ultrashort-pulse solid-state laser sources at the appropriate wavelengths), most high-power ultrafast lasers have used solid-state amplifier media, including titanium-doped sapphire, Nd:glass, alexandrite, Cr:LiSAF and others [26]. These materials have the combined advantages of relatively long upper level lifetimes, high saturation fluences (from 1 J cm^{-2} to few tens of J cm^{-2}), broad bandwidths and high damage thresholds. To date, most high-power ultrafast lasers have used either frequency-doubled YAG and glass lasers or flashlamps as pump sources for these amplifiers. Of all potential amplifier media, titanium-doped sapphire has seen the most widespread use in the past 15 years. It has several very desirable characteristics, which make it ideal as amplifier material, including a very high damage threshold($\sim$8–10 J cm^{-2}), a high saturation fluence ($\sim$1 J cm^2) and a high thermal conductivity ($\sim$46 W/mK at 300 K). Moreover, it has a broad gain bandwidth ($\sim$200 nm), and thus can support an extremely short pulse. Finally, it has a broad

absorption bandwidth with a maximum at 500 nm (σ_{abs} at peak $\sim 6.5 \times 10^{-20}$ cm^2), making it ideal for frequency-doubled Nd:YAG or Nd:YLF pump lasers.

Since few years, optical parametric chirped pulse amplification (OPCPA) technique is developing. This technique has several advantages such as the very large spectral gain bandwidth and absence of thermal effect in the amplifiers. This technique is fully discussed in a following chapter of Ross.

In order to calculate the amplified energy in the configuration of different amplifiers configuration, the Frantz and Nodvik model can be applied to CPA. It is therefore a modified model that takes into account the chirp of the seed pulse. This model is well described in different literature [27,28].

We will now describe the different types of amplifiers that allow the increase in pulse energy.

Most high-power ultrafast laser systems use a high-gain preamplifier stage, placed just after the pulse stretcher, which is designed to increase the energy of the nJ pulses from the laser oscillator to the 1–10 mJ level [24,25, 29,30,31,32,33,34,35]. The majority of the gain of the amplifier system ($\sim 10^7$ net) occurs in this stage. The preamplifier is then followed by several power amplifiers designed to efficiently extract the stored energy and to increase the output pulse power to the multiterawatt or even petawatt level. There are two basic preamplifier designs, regenerative and multipass. These are illustrated in Figs. 5a and 5b.

Regenerative amplifiers are very similar to a laser cavity. The low-energy chirped pulse is injected into the cavity using a time-gated polarisation device such as a Pockels cell and thin film polariser. The pulse then makes $\sim$20 round-trips through a relatively low-gain medium, at which point the high-energy pulse is switched out by a second time-gated polarisation rotation. A low-gain configuration is typically used in the regenerative cavity to prevent amplified spontaneous emission (ASE) build-up. With high gain, ASE can build up quite rapidly in a regenerative configuration and deplete the gain before the short pulse can extract it. The beam's overlap between the pump and signal pulse is usually quite good in such an amplifier, which results in extraction efficiencies of up to 15%. Regenerative amplifiers are typically used as front ends for commercially available intense laser systems. This amplifier scheme tends to limit the pulse duration to 30 fs because of the relatively long optical path lengths associated with the multiple passes in the regenerative cavity together with the presence of high-index materials due to the Pockels cells and polarisers. This adds high-order dispersion, making the recompression more difficult for very short pulses. Nevertheless, regenerative amplifiers have also been used to generate 20 fs pulses [36,37] by the use of etalon or Fabry–Perot in the regenerative cavity in order to flatten the gain. Nevertheless such a technique introduces spectral modulations that lead to satellite pulses after recompression. This effect is prejudicial for laser–matter interaction at very high intensity. This contrast issue will be detailed thereafter.

A multipass preamplifier configuration (Fig. 5b) differs from the regenerative amplifier in that, as its name suggests, the beam passes through the gain

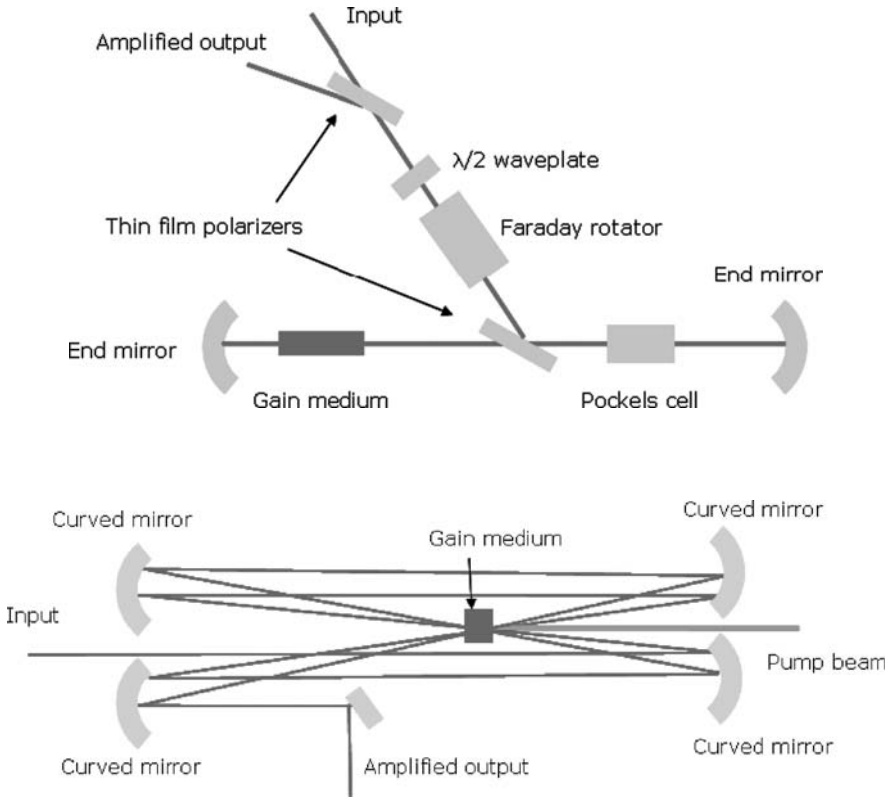

Fig. 5 (a) Regenerative amplifier layout, (b) Multipass amplifier layout

medium multiple times without the use of a cavity. The particular geometry for accomplishing this can differ from system to system [30,31,38,39]. In a multipass amplifier, since the optical path is not a resonator, ASE can be suppressed to a greater degree than with a regenerative amplifier. Thus, multipass amplifiers typically have higher gain per pass (7–10) compared with regenerative amplifiers, and fewer passes through the gain medium are needed. As a result, there is less high-order phase accumulation in multipass systems, and shorter pulses are easier to obtain upon recompression. Moreover, non-linear phase accumulation due to the B integral is also less in multipass amplifiers. Multipass preamplifiers are not as efficient as regenerative, since the pump – signal overlap must change on successive passes through the gain medium in order to extract the beam (by separating it spatially). However, multipass preamplifier efficiencies can reach $\sim$10%. Multipass amplifiers are also used not only as preamplifier but also as power amplifiers. With a set of multiple amplifiers (e.g. regenerative or multipass as preamplifier and multipass as power amplifiers), a laser system based on the titanium-doped sapphire crystal can provide

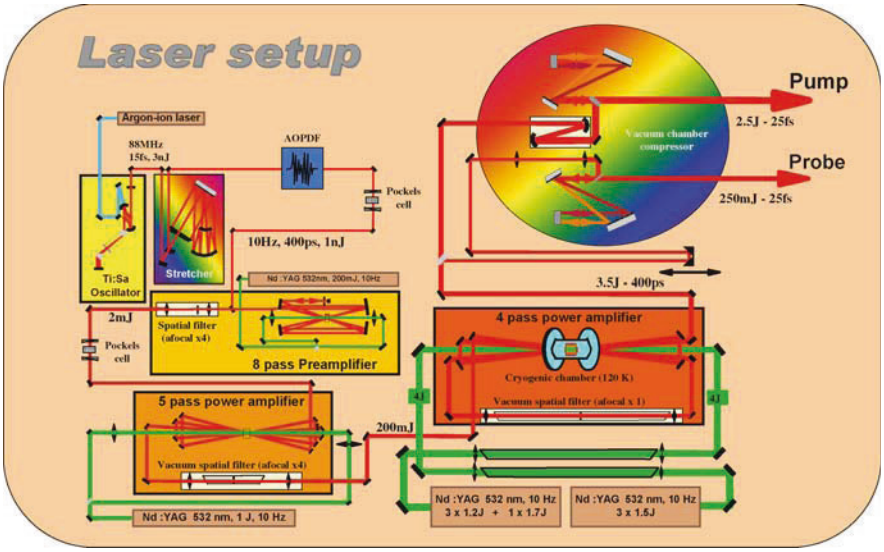

Fig. 6 Layout of a 10 Hz, 100 TW laser system [40]

pulses with a duration of 25–30 fs with energy in excess of several joules at a repetition rate of 10 Hz [40] or tens of joules at a repetition rate of a fraction of hertz [41].

The layout of a 10 Hz intense laser system is depicted in Fig. 6.

5 Limitations in Intense Laser Systems

The generation of multiterawatt or even petawatt peak power pulses is now obtained in many places, but many effects can affect the system output characteristics. The different limitations are discussed.

5.1 Thermal Effects

Although Ti:sapphire has extremely high thermal conductivity, significant attention must still be devoted to reducing thermal distortion effects associated with the fact that tens of watts of average power are deposited in the laser amplifier to obtain sufficient gain per pass. These include thermal lensing, birefringence and stress. A flat top pumping profile results in a parabolic thermal gradient and index of refraction variation across the beam, which acts as a lens whose focal length varies with pump energy. Local thermal expansion stress and bowing of the crystal surface add to the lensing effect, as well as to thermally induced birefringence. In multipass or regenerative amplifier systems, thermal lensing accumulates from successive passes through the amplifier, causing a rapid

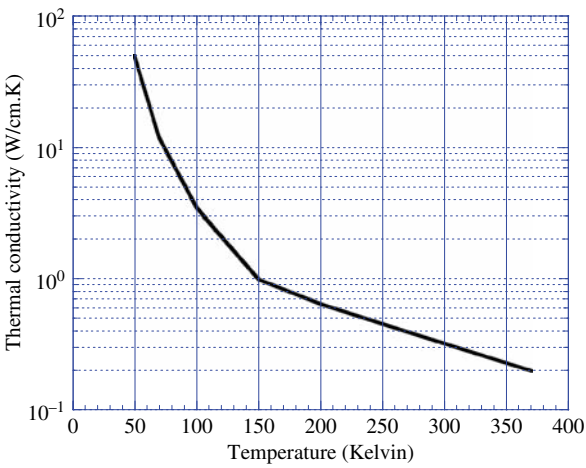

Fig. 7 Thermal conductivity of the sapphire as a function of the temperature

change in amplified beam size that can lead to optical damages. In regenerative amplifiers, the cavity can be designed to compensate for the thermal lens in a manner similar to that in laser oscillators. This can be done also in multipass amplifiers by adding a negative lens between the successive passes into the amplifier medium but this solution does not allow pump power changes. Another solution that allows these changes while keeping the same divergence of the amplified beam is to cool the crystal to a temperature below –140°C, since at low temperature the thermal conductivity is increased by almost one order of magnitude as shown in Fig. 7 [42,43].

The focal length of the thermal lens increases in such a way that no more geometrical changes in the beam happen during the amplification. This technique can be applied to high-repetition-rate (kHz to multi-kHz) low-energy system [44] as well as lower repetition rate (10 Hz) systems that exhibit a lot more energy per pulse [40].

5.2 Pulse Duration Limitations

In the development of amplifier systems for high-power pulses with duration below 30 fs, there are two major effects that may limit the final pulse duration.

First, as discussed above, the finite bandwidth of the gain medium results in narrowing of the pulse spectrum during amplification. Assuming infinitely broadband input pulses injected into a Ti:sapphire amplifier with a gain of 10^7, the amplified output spectrum is ~47 nm FWHM. This bandwidth is capable of supporting pulses as short as 18 fs at millijoule pulse energy. For tens of millijoules energy, the gain-narrowing limit is ~25 fs. For all other materials, the gain-narrowing limit is more severe. In order to reduce the effect of gain

narrowing, some techniques have been used. One solution is based on generating gain-losses for the wavelength supporting the highest gain [45]. The spectral gain is modulated by the spectral transmittance of a Perot–Fabry inside a regenerative amplifier. This technique has lead to the production of 17 fs amplified pulses. Another solution is to shape the spectrum coming into the preamplifier with an acousto-optic device [46]. This modulator has improved the pulse duration from 30 fs to 17 fs for an amplified energy of 1 mJ. This technique has the advantage of being on-line and therefore is easy to implement. Another spectral modification in the case of a long-duration chirped pulse is that the leading edge of the pulse depletes the excited-state population so that the red leading edge of the pulse can experience a higher gain than the blue trailing edge of the pulse. That is the spectral shifting. It should be noted that gain narrowing, spectral shifting and gain saturation occur in all amplifier media, and are least severe for broadband materials such as Ti:sapphire.

The second limiting effect on pulse duration is the group velocity dispersion (GVD) that is due to the different components of the laser chain. The GVD introduces some spectral phase distortions that are harmful for the final pulse duration and shape. The pulse can be lengthened and can exhibit some wings. The temporal pulse profile is distorted because of its associated spectral phase. The spectral phase distortions arise from the material present in the laser chain and from the stretcher. These distortions are partially corrected by adjusting the length and the angle of incidence of the compressor and by cleverly choosing the number of grooves per millimetre of the compressor gratings. These compensations are valid for pulse duration greater than 30 fs. For shorter pulse duration, high-order phase distortions will limit the pulse duration and the temporal profile will exhibit some wings. Different techniques have been developed to compensate for the residual distortions [46,47,48,49,50,51,52]. They are based on active optical component; i.e. liquid-crystal spatial light modulator (SLM), acousto-optic modulator (AOM) or deformable mirrors (DM). The SLM and DM have to be placed in a spectral Fourier plane. An example of a DM system is illustrated in Fig. 8 [47]. The deformable mirror acts on the optical path length of the different spectral components to minimise the delay between each of these.

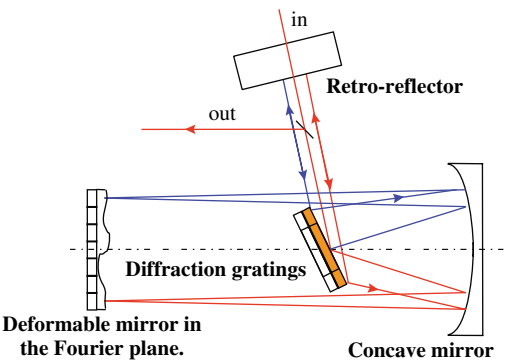

Fig. 8 Layout of an adaptive stretcher [47]

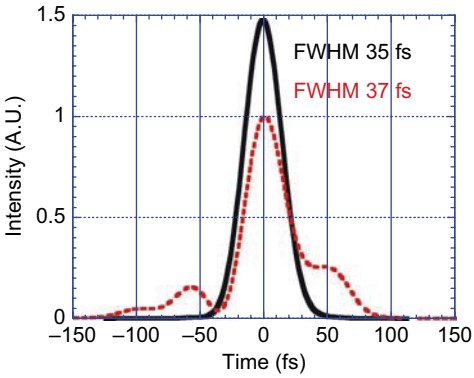

Fig. 9 Temporal pulse profile measured with the spider technique before (*dotted line*) and after (*solid line*) the correction by the adaptive optic [47]

The compensations available with such a set-up allow a good control of the temporal profile as shown in Fig. 9. In such experiment it should be noticed that an optimisation parameter has to be used in order to quantify the improvement in the temporal pulse profile. A phase measurement tool is necessary and two types are widely used. Chronologically these are the FROG [53] (frequency resolved optical gating) and the SPIDER [54] (spectral phase interferometry for direct electric-field reconstruction).

The other solution is the use of an acousto-optic programmable dispersive filter (Fig. 10) placed on-line in the laser system [46].

This solution presents the advantage of controlling the spectral phase distortions and also to shape the spectrum of the input pulse in order to compensate for the spectral gain narrowing. This component presents interesting capabilities in generating large chirp allowing using it as a stretcher in low-energy systems.

5.3 *Temporal Contrast of Intense Pulse*

The development of laser chains based on the chirped pulse amplification leads now to peak powers higher than 100 TW. The focused intensity can reach 10^{22} W/cm^2 [55]. To keep the laser–matter interaction in the femtosecond regime, the pulse has to exhibit a high temporal contrast. The most important problem

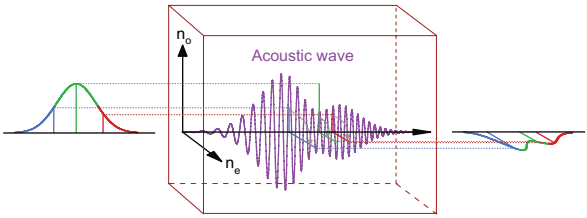

Fig. 10 Description of the acousto-optic programmable dispersive filter

consists in the presence of an amplified spontaneous emission (ASE) background coming from the amplification process. At the output of the laser the ratio between the femtosecond pulse intensity and the ASE level is about 10^6–10^7 leading to an ASE intensity as high as 10^{16} or 10^{15} W/cm^2, far above the ionisation threshold of most materials and susceptible to strongly modify the interaction process.

A classical CPA laser is seeded by a nJ energy level pulse originated from mode-locked oscillator. The temporal contrast of such a pulse when characterised on a high dynamic range is free of ASE pedestal and structures on at least 9 orders of magnitude.

So the ASE is usually rising up in the preamplifier where the total gain is 10^6. The measured contrast level (ratio between the maximum pulse intensity level and the ASE level) at the output of such an amplifier is of 7–8 orders of magnitude. This contrast is lowered in the power amplifiers leading to 6 or 7 orders of magnitude at the output of a 100 TW laser chain.

Different possible solutions for improving the contrast consist in seeding the preamplifier with more energetic pulses, amplifying these energetic pulses via a low ASE preamplifier and also temporally filtering the ASE versus the femtosecond pulse in a non-linear interferometer before the power amplifiers. This non-linear filter seems to be nowadays the most powerful technique to increase the contrast. The methods used are numerous: saturable absorber [56], non-linear Sagnac interferometer [57], non-linear-induced polarisation rotation in hollow fibre [58] or in air [59] and cross-polarised wave generation [60]. With this last technique also named XPW, a contrast improvement of almost 5 orders of magnitude at the millijoule level with 40 fs pulse duration has been demonstrated (Fig. 11). This technique is achromatic so that shorter pulse duration can be efficiently filtered.

The need for having clean temporal pulses at the output of the ultrafast system leads then to a change in the design of the laser. In order to implement the temporal filter, a double CPA scheme is relevant [61]. The pulse coming from the oscillator is amplified up to the millijoule level and temporally

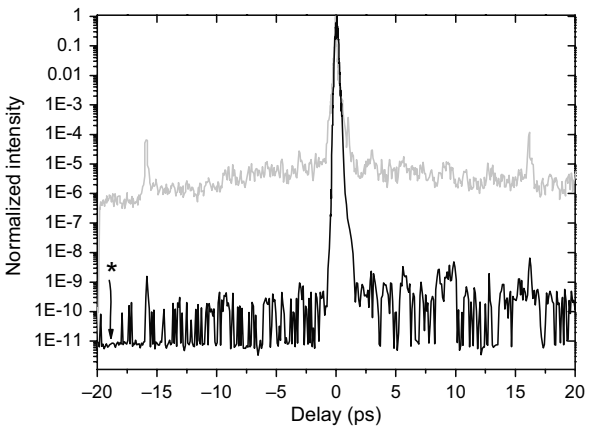

Fig. 11 Third-order correlation curves before (*grey curve*) and after (*black curve*) filtering by XPW non-linear filter [60]

recompressed. It is cleaned by passing through the non-linear filter. The second CPA system is then a power CPA system. The clean pulse is temporally stretched to few hundreds of picosecond (depending on the final energy level) and amplified allowing the possibility to have a pulse contrast in the range of 10 orders of magnitude after final recompression.

5.4 Focusability of Intense Femtosecond Lasers

The spatial quality of intense femtosecond pulses from chirped pulse amplification (CPA) systems is of great importance in order to reach very high peak intensity on target. In CPA laser systems, geometrical aberrations and surface quality from optical elements, clipping on mirrors, thermal effects and doping inhomogeneities in TiSa crystals affect the beam focusability. In other words, every effect than can degrade the spatial characteristics, i.e. energy distribution and wavefront, will lead to different propagation pattern and so to a poor focusability. Large part of the energy will be spread out into the wings of the focal spot. This will lead to an increase in focal spot dimensions and so to the decrease in intensity. A brief look at the theoretical definition of the intensity shows the importance of spatial quality:

$$I = \frac{E}{\pi r^2 \times \Delta\tau}$$

E is the energy of the pulse, r the radius of the focal spot at $1/e^2$ of the maximum intensity and $\Delta\tau$ the pulse duration. The focused intensity has a quadratic dependence with the radius of the beam compared to a linear dependence with the energy and the pulse duration. Then, it is more efficient to reduce the size of the focal spot than increase the energy by adding another amplifier stage to the laser chain or decreasing the pulse duration.

The efficient solution for wavefront correction is also like in the temporal domain in the use of adaptive optic. Either a deformable mirror (DM) [62] or a liquid-crystal spatial light modulator (SLM) can be used [63]. The DM has the advantage of being positioned at the end of the laser chain, thanks to its damage threshold, but the possibility to modulate the wavefront is low because the number of actuators is relatively small; i.e. ~40–100. The SLM presents the advantage of a high spatial resolution (few hundreds of actuators), but it can only be placed at the beginning of the laser because the damage threshold is very low.

The potentiality of the correction with a DM is illustrated in Fig. 11. This shows the wavefront correction on a 10 Hz–100 TW TiSa laser delivering 25 fs pulse duration with an energy of 2.5 J. The wavefront before correction exhibits mainly astigmatism with distortions of 0.7 μm peak to valley (PV) that gives a Strehl ratio of 35%. After the correction, the distortions are reduced

Fig. 12 Corrected wavefront of a 100 TW laser system [64]

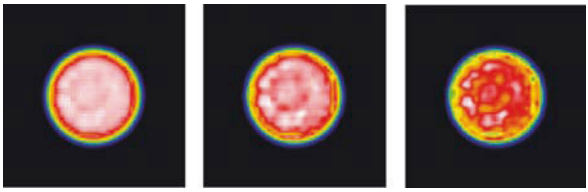

Fig. 13 Evolution of the energy distribution as a function of the propagation length [64]

to 0.22 μm PV (43 nm rms) and the Strehl ratio is higher than 90% [64] (Fig. 12). The Strehl ratio is the ratio between the experimental peak intensity and the calculated peak intensity of the experimental distribution associated to a flat wavefront.

The correction is very efficient in the far field, but nevertheless some drawbacks of that technique appear in the mid-field. The remaining phase distortions exhibit the frame of the actuators of the mirror even if the mirror is not segmented. This is due to each influence function of each actuator. These very low distortions have a relatively high spatial frequency that leads to a deterioration of the energy distribution during the beam propagation [64]. Figure 13 shows the evolution of the calculated energy distribution for different propagation lengths (Z).

Modulations appear in the beam profile with modulation in the range of 50% for a distance $Z = 10$ m. This is a very negative effect for all the components that are in laser chain after the deformable mirror.

6 Conclusion

Progress in high peak-power ultrafast lasers has been rapid in the 1990s, and new developments promise to continue to create exciting progress for the foreseeable future. Nowadays, the titanium-doped sapphire crystal technology allows for gain medium of 12 cm in diameter. Pulses of hundred joules with pulse duration less than 30 fs can be generated leading to a peak power of few

petawatts. After focusing with high-aperture off-axis parabola, intensity higher than 10^{23} W/cm^2 can be used for completely new physics of laser–matter interaction.

The capabilities of laboratory-scale laser systems will continue to improve in terms of available average and/or peak power and in terms of control and characterisation of the electromagnetic field of the pulse on a cycle-by-cycle basis. Developments in other areas of laser technology, such as diode-pumped lasers and adaptive optics for spatial and temporal wavefront control, can readily be incorporated into ultrafast systems.

Scientifically, these developments may make possible optical "coherent control" of chemical reactions and quantum systems and will extend ultrafast optical science into the X-ray region of the spectrum. Ultrafast X-ray techniques will allow us to observe reactions on a microscopic temporal and spatial scale and to develop a fundamental understanding of the most basic processes underlying the natural world. On a more applied level, the cost and complexity of ultrafast lasers will decrease, making feasible the widespread application of ultrafast technology for industrial and medical applications such as precision machining, thin film deposition, optical ranging, ophthalmological surgery and oncology.

References

1. D. Strickland and G. Mourou, Opt. Commun. **56**, 219 (1985).
2. P. Maine, D. Strickland, P. Bado, M. Pessot, and G. Mourou, IEEE J. Quantum Electron. **24**, 398 (1988).
3. M. Pessot, P. Maine, and G. Mourou, Opt. Commun. **62**, 419 (1987).
4. E. B. Treacy, IEEE J. Quantum Electron. **QE-5**, 454 (1969).
5. O. E. Martinez, J. P. Gordon, and R. L. Fork, J. Opt. Soc. Am. A **1**, 1003 (1984).
6. O. E. Martinez, J. Opt. Soc. Am. B **3**, 929 (1986).
7. O. E. Martinez, IEEE J. Quantum Electron. **QE-23**, 1385 (1987)
8. O. E. Martinez, IEEE J. Quantum Electron. **23**,59 (1987)
9. D. E. Spence, P. N. Kean, and W. Sibbett, Opt. Lett. **16**, 42 (1991).
10. T. Brabec, C. Spielman, P. F. Curley, and F. Krausz., Opt. Lett. **17**, 1292 (1992).
11. F. Krausz, M. E. Fermann, T. Brabec, P. F. Curley, M. Hofer, M. H. Ober, C. Spielman, E. Wintner, and A. J. Schmidt. IEEE J. Quantum Electron. **28**, 2097 (1992).
12. J. Herrmann, J. Opt. Soc. Am. B **11**, 498 (1994).
13. F. Krausz, C. Spielmann, T. Brabec, E. Wintner, and A. J. Schmidt, Opt. Lett. **17**, 204 (1992).
14. C.P. Huang, M. T. Asaki, S. Backus, M. M. Murnane, H. C. Kapteyn, and H. Nathel, Opt. Lett. **17**, 1289, (1992).
15. A. Stingl, M. Lenzner, C. spielmann, F. Krausz, and R. Sipocs, Opt. Lett. **19**, 204 (1994).
16. J. Zhou, G. Taft, C. Huang, M. M. Murnane, and H. C. Kapteyn, Opt. Lett. **19**, 1149 (1994).
17. U. Morgner, F. X. Krtner, S. H. Cho, Y. Chen, H. A. Haus, J. G. Fujimoto, E. P. Ippen, V. Scheuer, G. Angelow, and T. Tschudi, Opt. Lett. **24(**6), 411 (March 1999).
18. D. H. Sutter, G. Steinmeyer, L. Gallmann, N. Matuschek, F. Morier-Genoud, U. Keller, V. Scheuer, G. Angelow, and T. Tschudi. Opt. Lett. **24**, 631 (1999).

19. R. Ell, U. Morgner, F. X. Krtner, J. G. Fujimoto, E. P. Ippen, V. Scheuer, G. Angelow, T. Tschudi, M. J. Lederer, A. Boiko, and B. Luther-Davies, Opt. Lett. **26(**6), 373 (March 2001).
20. T. Fuji, A. Unterhuber, V. S. Yakovlev, G. Tempea, A. Stingl,F. Krausz, and W. Drexler, Appl. Phys. B. **77**(1), 125–8 (Aug. 2003).
21. L. Matos, D. Kleppner, O. Kuzucu, T. R. Schibli, J. Kim, E. P. Ippen, and F. X. Kaertner, Opt. Lett. **29**(14), 1683 (July 2004).
22. G. Cheriaux, P. Rousseau, F. Salin, J. Chambaret, B. Walker, and L. Dimauro, Opt. Lett. **21**, 414 (1996).
23. M. Hentschel,Z. Cheng,F. Krausz, and C. Spielmann, Appl. Phys. B. **70**, S161–4 (June 2000).
24. A. Baltuska, M. Uiberacker, E. Goulielmakis, R. Kienberger, V. Yakovlev, Th. Udem, T. Häntsch, and F. Krausz, IEEE J. Sel. Topics Quantum Electron. **9**, 972 (2003).
25. D. M. Gaudiosi, A. L. Lytle, P. Kohl, M. M. Murnane, H. C. Kapteyn, and S. Backus, Opt. Lett. **29(**22), 2665 (2004).
26. P. Moulton, Proc. IEEE **80**, 348 (1992).
27. L .M. Frantz and J. S. Nodvik, J. Appl. Opt. **34**, 2346 (1963).
28. C. Le Blanc, P. Curley, and F. Salin, Opt. Commun. **131**, 391 (1996).
29. J. V. Rudd, G. Korn, S. Kane, J. Squier, and G. Mourou, Opt. Lett. **18**, 2044 (1993).
30. C. LeBlanc, G. Grillon, J. P. Chambaret, A. Migus, and A. Antonetti, Opt. Lett. **18**, 140 (1993).
31. M. Lenzner, C. Spielmann, E. Wintner, F. Krausz, and A. J. Schmidt, Opt. Lett. **20**, 1397 (1995).
32. F. Salin, J. Squier, G. Mourou, and G. Vaillancourt, Opt. Lett. **16**, 1964 (1991).
33. J. Squier, S. Coe, K. Clay, G. Mourou, and D. Harter, Opt. Commun. **92**, 73 (1992).
34. G. Vaillancourt, T. Norris, J. Coe, P. Bado, and G. Mourou, Opt. Lett. **15**, 317 (1990).
35. K. Wynne, G. D. Reid, and R. M. Hochstrasser, Opt. Lett. **19**, 895 (1994).
36. C. Barty, G. Korn, F. Raksi, C. Rose-Petruck, J. Squier, A. Tian, K. Wilson, V. Yakovlev, and K. Yamakawa, Opt. Lett. **21**, 219 (1996).
37. C. Barty, T. Guo, C. Le Blanc, F. Raksi, C. Rose-Petruck, J. Squier, K. Wilson, V. Yakovlev, and K. Yamakawa, Opt. Lett. **21**, 668 (1996).
38. S. Backus, J. Peatross, C. P. Huang, M. M. Murnane, and H. C. Kapteyn, Opt. Lett. **20**, 2000 (1995).
39. V. Bagnoud and F. Salin, Appl. Phys. B **70**, 165 (2000).
40. M. Pittman, S. Ferré, J. P. Rousseau, L. Notebaert, J. P. Chambaret, and G. Chériaux, Appl. Phys. B **74(**6), 529–535 (June 2002).
41. M. Aoyama, K. Yamakawa, Y. Akahane, J. Ma, N. Inoue, H. Ueda, and H. Kiriyama, Opt. Lett. **28(**17), 1594 (Sep 2003).
42. W. Koechner, Solid-State Laser Engineering (Springer, Heidelberg, 1996).
43. A. DeFranzo and B. Pazol, Appl. Opt. **32**, 2224 (1993).
44. S. Backus, C. G. Durfee III, G. Mourou, H. C. Kapteyn, and M. M. Murnane, Opt. Lett. **22**(16), 1256 (August 1997).
45. C. P. J. Barty, C. L. Gordon III, and B. E. Lemoff, Opt. Lett. **19**, 1442 (1994).
46. F. Verluise, V. Laude, Z. Cheng, C. Spielmann, and P. Tournois, Opt. Lett. **25**, 575 (2000).
47. D. Yelin, D. Meshulach, and Y. Silberberg, Opt. Lett. **22**, 1793 (1997).
48. A. Efimov and D. H. reitze, Opt. Lett. **23**, 1612, (1998).
49. C. Dorrer, F. Salin, F. Verluise, and J. P. Huignard, Opt. Lett. **23**, 709 (1998).
50. E. Zeek, K. Maginnis, S. Backus, U. Russek, M. Murnane, G. Mourou, H. Kapteyn, and G. Vdovin, Opt. Lett. **24**, 493 (1999).
51. E. Zeek, R. Bartels, M. Murnane, H. C. Kapteyn, S. Backus, and G. Vdovin, Opt. Lett. **25**, 587 (2000).
52. G. Chériaux, O. Albert, V. Wänman, J. P. Chambaret, C. Félix, and G. Mourou, Opt. Lett. **26**, 169 (2000).

53. R. Trebino and D. J. Kane, J. Opt. Soc. Am. A **10**, 1101 (1993).
54. C. Iaconis and I. Walmsley, IEEE J. Quantum Electron. **QE-35**, 501 (1999).
55. S. -W. Bahk, P. Rousseau, T. A. Planchon, V. Chvykov, G. Kalintchenko, A. Maksimchuk, G. A. Mourou, and V. Yanovsky, Appl. Phys. B **80**, 823–832 (2005).
56. Y. Jiang, T. Lee, W. Li, G. Ketwaroo, and C. G. Rose-Petruck, Opt. Lett. **27**(11), 963 (June 2002).
57. A. Renault, F. Augé-Rochereau, T. Planchon, P. D'Oliveira, T. Auguste, G. Chériaux, and J.P. Chambaret, Opt. Commun. **248**(4–6), 535–541 (15 April 2005).
58. D. Homoelle, A. L. Gaeta, V. Yanovsky, and G. Mourou, Opt. Lett. **27(**18), 1646 (September 2002).
59. A. Jullien, F. Augé-Rochereau, G. Chériaux, and J. P. Chambaret, Opt. Lett. **29**(18), 2184–2186 (Sep 15, 2004).
60. A. Jullien, O. Albert, F. Burgy, G. Hamoniaux, J. P. Rousseau, J. P. Chambaret, F. Augé-Rochereau, G. Chériaux, J. Etchepare, N. Minkovski, and S. M. Saltiel, Opt. Lett. **30**(8), 920–922 (15 April 2005).
61. M. P. Kalashnikov, E. Risse, H. Schönnagel, and W. Sandner, Opt. Lett. **30**(8), 923 (April 2005).
62. F. Druon, G. Chériaux, J. Faure, J. Nees, M. Nantel, A. Maksimchuk, G. Mourou, J.C. Chanteloup, and G. Vdovin, Opt. Lett. **23**, 1043 (1998).
63. J. -C. Chanteloup, H. Baldis, A. Migus, G. Mourou, B. Loiseaux, and J. -P. Huignard, Opt. Lett. **23**, 475 (1998).
64. T. A. Planchon, J. P. Rousseau, F. Burgy, G. Chériaux, and J. P. Chambaret, Opt. Commun. **252**(4–6), 222–228 (15 Aug 2005).

Optical Parametric Amplification Techniques

Ian N. Ross

1 Introduction

From the very early days of lasers, the non-linear interaction between optical beams and transparent media was recognised as an important process, starting with the demonstration of second harmonic generation in 1961 [1], and the theory for this as well as for other three- and four-wave mixing processes was already well established in 1962 [2].

One of these processes was *optical parametric amplification* (OPA), or difference frequency mixing, and with the development of Q-switching techniques, intensities sufficient to generate significant gain in an OPA became available. It was soon realised that a key property of the OPA was that energy from a fixed wavelength source could be transferred onto a beam with a tunable wavelength. The prospect of tunable coherent pulses opened up a major development of the techniques of OPA and the growth of new non-linear crystals in the mid-1960s, and laid the foundations for many applications in spectroscopy. However, because the optical parametric amplification process contains initially one strong and two weak beams (in contrast to harmonic and sum frequency generation with one weak and two strong beams), high intensities are required for the strong pump beam and the development became limited by laser damage which prevented very high intensities being used at the then available pulse durations.

With the advent of mode-locking techniques and the resulting sub-ns pulses this difficulty was removed and it became possible to realise high gain and with it all forms of devices including optical parametric oscillators (OPO), optical parametric amplifiers (OPA) and even optical parametric generators (OPG) which could achieve significant pump depletion in a single pass with no input signal or idler beam.

A second difficulty in the early development arose because spectroscopic applications generally required very narrow bandwidth and this proved difficult

I.N. Ross
CLRC Rutherford Appleton Laboratory, Chilton, Didcot, Oxon OX11 0QX, UK
e-mail: I.N.Ross@rl.ac.uk

T. Brabec (ed.), *Strong Field Laser Physics*,
DOI: 10.1007/978-0-387-34755-4_3,

with optical parametric devices, since their gain bandwidths were generally much larger than the transform limit of the pulse duration. With the development of techniques for generating sub-ps pulses, however, this 'difficulty' became a major benefit, and there has been a resurgence of development in optical parametric devices from the 1990s to the present. This work was boosted both by new group velocity matching geometries [3, 4, 5, 6, 7, 8, 9, 10, 11] which greatly increased the gain bandwidth of the OPA and by the appearance of new crystals such as BBO and LBO, and has even led to the possibility of amplifying pulses of duration close to a single cycle.

It was also realised that, using the OPA as a *chirped pulse amplifier* [12] (CPA) in a technique we will refer to as optical parametric chirped pulse amplification (OPCPA) [13] and applying the technique to large aperture crystals such as KDP with high damage thresholds, it should be possible to achieve simultaneously high energy and large bandwidth (the latter leading to short pulse duration) and hence ultra-high power operation. Such systems would be expected to be focusable to intensities orders of magnitude higher than current laser systems, and would offer exciting new prospects for high field physics.

This article will concentrate on the recent short pulse, high-power applications of the OPA and will include the following:

(a) An analytical description of the OPA to provide tools for the design of OPA systems
(b) Considerations which are useful for achieving optimum designs
(c) A description of a number of designs exemplifying systems which are either in use or demonstrated, or which point to their future potential

2 The Principles and Analysis of Optical Parametric Amplifiers

Figure 1 shows the basic principle of an OPA. A strong pump beam incident on the medium creates a non-linear polarisation through the second-order polarisability and leads to the occurrence of gain in the medium at a 'signal' and an 'idler' wavelength. Conservation of energy requires that the sum of the signal and idler frequencies must equal that of the pump, and this of course allows continuous tunability over a wide spectral range. A second condition, that of conservation of momentum or 'phase matching', is usually required to achieve high gain and significant energy transfer, and it is this condition which controls the wavelengths of amplified signal and idler. The phase-matching condition, unlike the conservation of energy, has a tolerance, and this determines the respective spectral bandwidths of the signal and idler.

The reader is referred to the literature on non-linear optics for a more general description of the OPA and to several recent theoretical treatments of OPAs [14, 15, 16, 17]. A simple analysis, which extends that in the literature, is presented

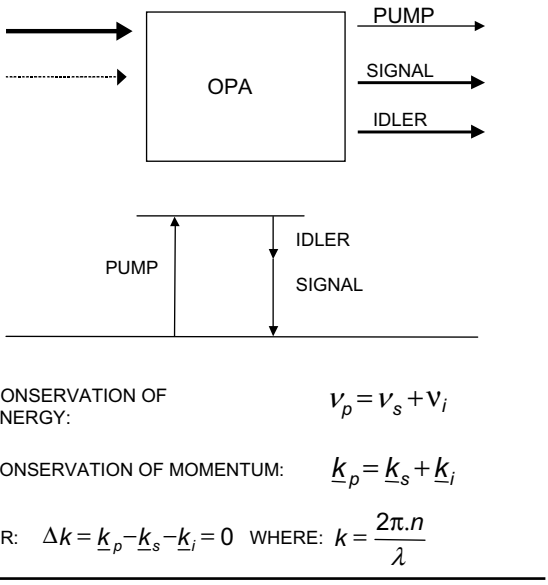

Fig. 1 Principles of operation of the optical parametric amplifier (OPA)

below, with the results in a form which is convenient for use in designing and optimising OPA systems.

The operation of a non-linear mixing process can be described by the coupled wave equations. We use the analysis of Armstrong et al. [2] which describes the optical parametric process for the case of plane monochromatic waves in the slowly varying envelope approximation for which the coupled wave equations become

$$\frac{\mathrm{d}A_\mathrm{s}^*}{\mathrm{d}z} = +\mathrm{i}K\frac{\omega_\mathrm{s}^2}{k_\mathrm{s}}A_\mathrm{p}^*A_\mathrm{i}\exp\mathrm{i}\Delta kz; \quad \frac{\mathrm{d}A_\mathrm{i}^*}{\mathrm{d}z} = +\mathrm{i}K\frac{\omega_\mathrm{i}^2}{k_\mathrm{i}}A_\mathrm{p}^*A_\mathrm{s}\exp\mathrm{i}\Delta kz;$$
$$\frac{\mathrm{d}A_\mathrm{p}}{\mathrm{d}z} = -\mathrm{i}K\frac{\omega_\mathrm{p}^2}{k_\mathrm{p}}A_\mathrm{s}A_\mathrm{i}\exp\mathrm{i}\Delta kz \tag{1}$$

where $K = \frac{2\pi}{c^2}\chi_\mathrm{eff}^{(2)}$, with $\chi_\mathrm{eff}^{(2)}$ the effective second-order non-linear susceptibility, A_p, k_p and ω_p are the amplitude, wave vector value and angular frequency of the pump wave respectively, with corresponding symbols for signal and idler waves and $\Delta k = \mathrm{I}\mathbf{k}_\mathrm{p} - \mathbf{k}_\mathrm{s} - \mathbf{k}_\mathrm{i}\mathrm{I} =$ phase mismatch.

2.1 Intensity Solution

Armstrong derives an analytical plane-wave solution for the development of the intensity of the three waves, including the effects of both significant depletion of

the pump and imperfect phase matching. In terms of physical quantities and assuming no idler input, this solution becomes

$$2gz = \pm \int_0^f \frac{\mathrm{d}f}{\sqrt{p(1-f)(f+\gamma_s^2)f - (\Delta k/2g)^2 f^2}} \tag{2}$$

where $g = 4\pi d_{\mathrm{eff}} \sqrt{\frac{I_p(0)}{2\varepsilon_0 n_p n_s n_i c \lambda_s \lambda_i}}$

$f = 1 - I_p/I_p(0)$ = fractional depletion of the pump beam

$\gamma_s^2 = \frac{\omega_p}{\omega_s}\frac{I_s(0)}{I_p(0)}$ = input signal to pump photon intensity ratio

$p = I_p(0)/I_p(0) + I_s(0)$ = pump to total input intensity ratio

$\theta(t) = \phi_p(t) - \phi_s(t) - \phi_i(t)$ = OPA phase (with $\theta(0)$ inserted for the input value)

The form of this solution is demonstrated in Fig. 2 which shows the evolution of pump and signal intensity as they propagate through a non-linear crystal. The example is for a type I BBO crystal operating near degeneracy with a pump wavelength of 532 nm. Curves are shown for the exactly phase-matched signal wavelength and for a wavelength (or angular) de-tuning giving a phase mismatch of 3π at $z = z_A$.

The cyclic nature of the process is at once apparent and indicates that 100% depletion of the pump is possible; however, this can only be achieved for beams of uniform intensity and at specific values of crystal length and beam intensity.

Real beams are not normally flat top in space and time, and this will result in reduced efficiency as illustrated in Fig. 3, which shows the input and output pump and phase-matched signal for a propagation distance giving maximum efficiency. The maximum pump depletion is now 48%. The input Gaussian temporal shape is seen to be both reduced in duration and severely modified in shape by saturated amplification in the OPA. This may be an important consideration in assessing performance for an OPCPA.

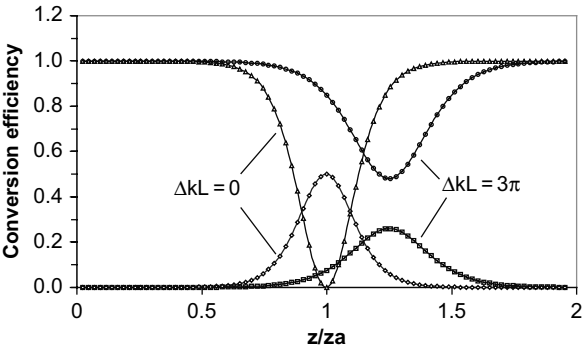

Fig. 2 Calculated evolution of pump and signal beam intensities propagating through an optical parametric amplifier under conditions both of exact phase matching and with a phase mismatch of 3π

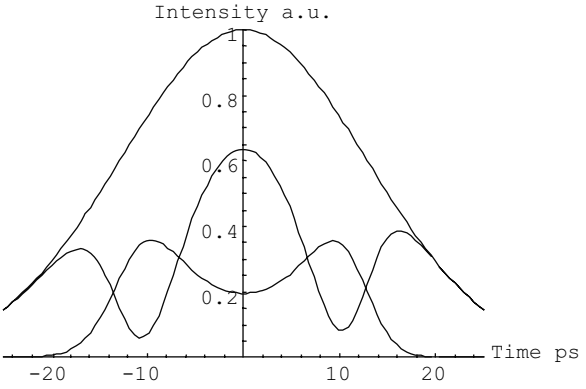

Fig. 3 Calculated temporal evolution of input and output pump and output signal intensities for a phase-matched OPA designed for maximum extraction efficiency. Input pulses have sech^2 temporal profiles

For small pump depletion, the solution reduces to the more familiar form: Signal beam gain,

$$G = 1 + (gz)^2 \left[\frac{\sinh \sqrt{(gz)^2 - (\Delta kz/2)^2}}{\sqrt{(gz)^2 - (\Delta kz/2)^2}} \right]^2 \tag{3}$$

or, for exact phase matching ($\Delta k = 0$):

$$G = \cosh^2(gz) \tag{4}$$

For example, a type I BBO OPA near degeneracy with a 532 nm 1 ps pump can operate without damage at pump intensities of 100 GW/cm^2 giving a gain of 10^6 for a 1.5 mm length of crystal. This illustrates the very high gains possible with very short path in the gain medium and represents a significant advantage of OPAs since, for ultra-short pulse amplification, material dispersion can be a major limitation.

2.2 Phase Solution

The contribution to phase during OPA has not received as much attention as intensity because in most instances it has not been important. However, as interest grows in the application of OPAs to ultra-short pulses, the amplified signal or idler phase becomes increasingly important. A solution similar to that for intensity is possible for the phases of each of the three waves and is similarly derived. The imaginary parts of the coupled wave equations can be written:

$$\frac{d\phi_s}{dz} = -K\frac{\omega_s^2}{k_s}\frac{\rho_p \rho_i}{\rho_s}\cos\theta; \quad \frac{d\phi_i}{dz} = -K\frac{\omega_i^2}{k_i}\frac{\rho_p \rho_s}{\rho_i}\cos\theta; \quad \frac{d\phi_p}{dz} = -K\frac{\omega_p^2}{k_p}\frac{\rho_s \rho_i}{\rho_p}\cos\theta \tag{5}$$

where the amplitude of each wave has been written in the form $\rho \exp(\mathrm{i}\phi)$.

Equation 5 is readily combined and integrated to give [2]

$$\cos\theta = -\left(\Gamma + \frac{\Delta k}{2\sqrt{\omega_\mathrm{p}}g}u_\mathrm{p}^2\right)\Big/ u_\mathrm{p}u_\mathrm{s}u_\mathrm{i} \tag{6}$$

where a new variable is defined such that $u_\mathrm{p}^2 = I_\mathrm{p}/\omega_\mathrm{p}I_0$ where

$$I_\mathrm{p} = \frac{c^2 k_\mathrm{p}}{8\pi\omega_\mathrm{p}}\rho_\mathrm{p}^2$$

and where analogous relations apply for the signal and idler, also $I_0 = I_\mathrm{p} + I_\mathrm{s} + I_\mathrm{i}$ and Γ is a constant of integration determined by the initial conditions.

Equation 6 can be used to eliminate θ from equation 5 and if there is assumed to be no input idler,

$$\frac{\mathrm{d}\phi_\mathrm{s}}{\mathrm{d}z} = -\frac{\Delta k}{2}\left(1 - \frac{\gamma^2}{\left(f+\gamma_\mathrm{s}^2\right)}\right); \qquad \frac{\mathrm{d}\phi_\mathrm{i}}{\mathrm{d}z} = -\frac{\Delta k}{2}; \qquad \frac{\mathrm{d}\phi_\mathrm{p}}{\mathrm{d}z} = -\frac{\Delta k}{2}\frac{f}{1-f} \tag{7}$$

where, as also required for the intensity analysis, use has been made of the Manley–Rowe relations.

The initial phases of pump and signal are determined by the input beams and the input phase of the idler adjusts itself to maximise the signal gain. By inspection of the coupled wave equation for the signal, it can be seen that this occurs at $\sin\theta = -1$ or $\Phi_\mathrm{i}(0) = \Phi_\mathrm{p}(0) - \Phi_\mathrm{s}(0) - \pi/2$.

Finally, by integrating equation 7, we can write down the equations for the phase of the three waves as

$$\begin{aligned} &\phi_\mathrm{s} = \phi_\mathrm{s}(0) - \frac{\Delta k z}{2} + \frac{\Delta k\gamma^2}{2}\int\frac{\mathrm{d}z}{f+\gamma_\mathrm{s}^2};\ \phi_\mathrm{i} = \phi_\mathrm{p}(0) - \phi_\mathrm{s}(0) - \frac{\pi}{2} - \frac{\Delta k z}{2}; \\ &\phi_\mathrm{p} = \phi_\mathrm{p}(0) - \frac{\Delta k}{2}\int\frac{f\,\mathrm{d}z}{1-f} \end{aligned} \tag{8}$$

Inspection of these equations allows one to make the following statements about the phase relationships in an OPA.

(a) The phase of the amplified signal is independent of the initial phase of the pump. This has the important consequence that it is possible to maintain the optical quality of the signal while using for example a pump with both spatial aberrations and temporal phase variations resulting from a chirp.
(b) Phase changes resulting from amplification of the signal and idler only occur at wavelengths for which there is a phase mismatch ($\Delta k \neq 0$).
(c) The phase of the idler is particularly simple (see equation 8), depending only on the initial pump and signal phases and the phase-mismatch term $\Delta kz/2$.

(d) A very good approximation to the phase of the signal can be obtained if the input signal intensity is small compared to the input pump intensity. In this case $\gamma^2 \ll f$ and there is only a small contribution to the integral part of the equation for Φ_s from the region of significant pump depletion. We can then use, after some manipulation, the low-depletion solution for the signal phase (see, for example, Ross et al. [13]):

$$\phi_s = \phi_s(0) - \frac{\Delta k z}{2} + \tan^{-1}\left[\frac{\Delta k}{2\sqrt{g^2 - (\Delta k/2)^2}} \tanh \sqrt{g^2 - (\Delta k/2)^2}.z\right] \quad (9)$$

(e) The OPA is a phase-sensitive amplifier, and the direction of energy flow is determined by the phase term θ. When there is no input idler field, the initial idler phase self-adjusts so that $\theta(0) = -\pi/2$ and energy is transferred from pump to signal and idler. By combining equations 2 and 6, it can be shown that at maximum depletion, $\cos\theta = 1$, or $\theta = 0$. With further propagation, θ becomes positive and the direction of energy flow is reversed.

An illustration of the OPA phase is given in Fig. 4 which plots both the intensity gain and the phase of the amplified signal beam as a function of the signal wavelength in our BBO example. The phase variation is close to quadratic (linear chirp) with a swing of about 1.5π over the bandwidth of significant gain. If, as is often the case, the optical system is designed to compensate for the quadratic and cubic spectral phase, the residual phase error falls to a very small value (0.024π). The peak gain in this example was 10^6.

2.3 OPA Spectral Bandwidth

The spectral bandwidth or 'gain bandwidth' is taken to be the FWHM of the gain against wavelength curve, and it is useful initially to consider the bandwidth in the absence of pump depletion. At wavelengths increasingly distant

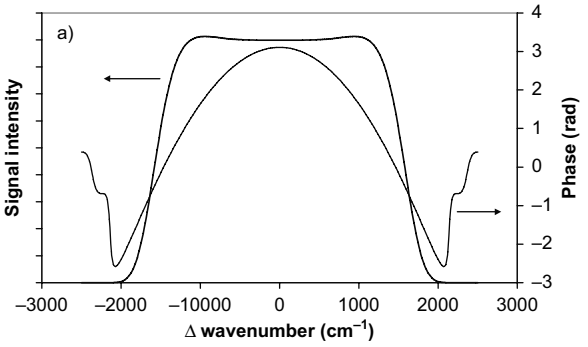

Fig. 4 The OPA spectral gain and phase for a BBO collinear OPA designed for maximum bandwidth at a peak gain of 10^6. The OPA is operated at degeneracy with a pump wavelength of 532 nm

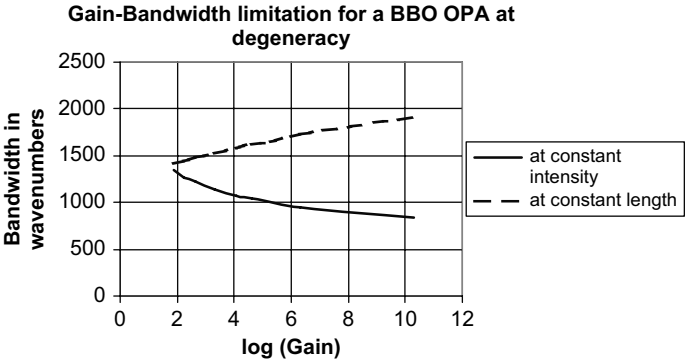

Fig. 5 The effect of gain on bandwidth for a BBO collinear OPA at degeneracy and at either constant pump intensity or constant crystal length

from the phase-matched wavelength, the phase mismatch (Δk) increases according to the material dispersion, and the gain reduces as given by equation 3. The 50% gain points correspond to a particular value of ΔkL and this leads to a FWHM bandwidth inversely related to the length of crystal. The gain, however, as indicated in equation 3, increases with increasing pump intensity ($g \approx \sqrt{I_p}$) as well as with increasing crystal length. Consequently, it is possible to satisfy a requirement for high gain and high bandwidth by using a maximum pump intensity and hence a minimum crystal length. This is in contrast to a conventional amplifier for which the gain bandwidth always decreases with increasing gain. Figure 5 illustrates this feature of OPAs by showing, for a BBO OPA at degeneracy, the variation of gain bandwidth with gain for either constant pump intensity or constant length.

2.4 Limiting Processes

This requirement to maximise the pump intensity to achieve maximum bandwidth leads us to look at the limits to this parameter. As with a conventional amplifier there is a 'power limit' for short pulses, usually determined by the B-integral parameter [18] characteristic of self-focusing, and an 'energy limit' for long pulses determined by the damage fluence. These limits for a BBO OPA are illustrated in Fig. 6, which also shows the line representing a gain of 10^6. This shows that if, as is normally accepted as the limit for chirped pulse amplification systems, we require the B-integral to be less than 1 then we can only achieve a gain of 10^6 for crystal lengths greater than 1.5 mm and this length sets a limit to the gain bandwidth. To achieve this bandwidth the energy limit also requires that the pulse duration must be below 2 ps in order to keep the fluence below 0.3 J/cm^2. It is only possible to increase the fluence and energy at

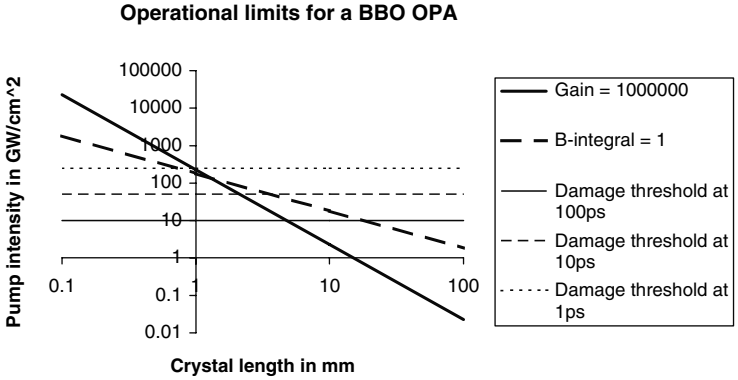

Fig. 6 The operational limits for a BBO OPA with a gain of 10^6 arising from the B-integral (intensity) limit and the energy (damage) limit

the same gain by increasing the pulse duration at a greater crystal length and this results in a reduction in bandwidth.

Note that in the example shown a high gain is achieved with a very short crystal length and the resulting 'power limit' is much greater than that for a conventional amplifier. Similarly short length ensures that material dispersion effects are small and this make the OPA attractive for ultra-short pulse applications.

2.5 Maximum Bandwidth Options

The example used above was BBO in collinear geometry at degeneracy (equal signal and idler wavelengths) and assumed a narrow bandwidth pump and for this case the gain bandwidth of the signal can be particularly high. For the optimised crystal length and intensity given by Fig. 6, the spectral gain curve is shown in Fig. 4 together with the OPA phase, both calculated using equations 3 and 9, respectively. The Fourier transform of the corresponding spectral amplitude and phase, assuming correction of the quadratic and cubic phase, is shown in Fig. 7 and indicates a potential pulse duration of 8.6 fs.

This does not however represent the maximum bandwidth and hence shortest pulse possible with a BBO OPA. A number of publications [3, 4, 5, 6, 7, 8, 9, 10, 11] present options for high bandwidth, and to briefly illustrate these, we consider the two separate cases: (i) a short broad-bandwidth pump pulse and (ii) a long narrow bandwidth pump pulse.

The main principle to be followed in all cases is to match the group velocities for pump, signal and idler since this ensures that, to first order, short pulses at the three wavelengths remain in step over the maximum length of crystal. To satisfy this requirement, it is usually necessary to operate the OPA with

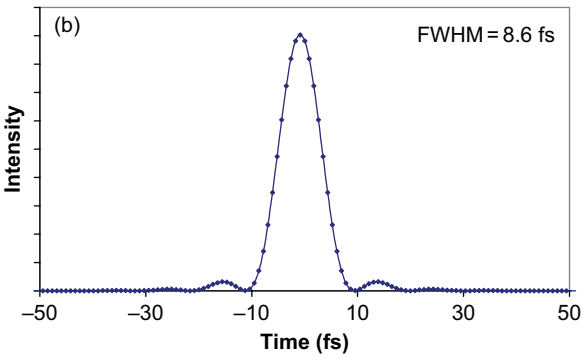

Fig. 7 The calculated shortest pulse profile as determined by the Fourier transform of the spectral amplitude and phase given by Fig. 4

non-collinear geometry and, as a consequence of this, to tilt the pulse front of one or more of the input pulses. This is best illustrated with a short pump and signal pulse example as shown in Fig. 8.

In this case by adjusting the pump to signal beam angle and the signal beam wavelength all the group velocities can be matched in one direction through the OPA. In addition, to maintain the synchronism over each pulse front it is necessary to apply a different pulse front tilt to the input pump and signal. Since a pulse front tilt corresponds to a dispersed pulse (generated, for example, using a prism or grating), care must be taken to ensure integrity of the pulses in the OPA and the dispersion must be compensated after the OPA. If the group velocity matching is not satisfied over the length of the crystal, the generated pulses are stretched in time and hence narrowed in spectrum. If the group velocities are well matched, the process only breaks down when the integrity of one or more of the pulses is affected by group velocity dispersion. The same principle applies if the pulses are chirped although the pulse duration is now

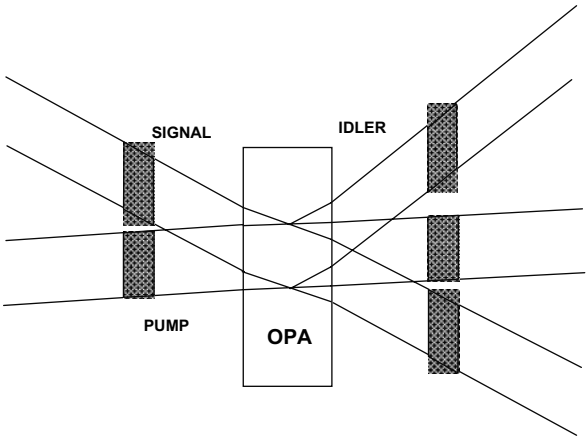

Fig. 8 Group velocity and pulse front matching for maximum bandwidth operation of an OPA

longer than the transform limit. Imperfect matching will also result in a spectral narrowing and consequently in this case in a shortening of the stretched pulses.

We separate out the special case of a narrow bandwidth pump because it is the preferred option for the highest powers where the OPA is used as a chirped pulse amplifier (CPA) in the technique known as OPCPA [13]. In this case, the group velocity mismatch between pump and signal is only significant if temporal slippage is a fraction of the *chirped* pulse duration (in contrast to the case above for which slippage relative to the shorter *bandwidth-limited pulse duration* is important). The group velocity matching condition now reduces to [19, 20]

$$\cos\beta = n_{\mathrm{gi}}/n_{\mathrm{gs}} \tag{10}$$

where β is the internal angle between signal and idler beams and $n_{\mathrm{gs}}, n_{\mathrm{gi}}$ is the group index of signal and idler, respectively.

The pulse front condition now allows a normal (undispersed) pulse front on the signal and generates an idler with a tilted pulse front (dispersed).

Figure 9 shows the variation of the optimum non-collinear angle with signal wavelength for a pump at 532 nm in BBO. The gain bandwidth at this optimised geometry can be estimated by evaluating the phase mismatch (Δk) as a function of signal wavelength using the material dispersion relation and finding the values (using equation 3) for which the gain is reduced by a factor 2.

Examples are shown in Fig. 10 for a number of pump wavelengths and materials.

One further option for generating ultra-high-gain bandwidth is through the use of a 'chirp compensation' technique [21]. This is best illustrated by Fig. 11 which gives for a fixed crystal angle the pairs of pump and signal wavelengths which maintain phase matching. If both pump and signal are chirped so that the correct wavelength pairs are maintained in synchronism during the pulses, then extreme values of gain bandwidth are possible. The technique requires the use of a chirped pump, often possible using a CPA pump laser, but the pump is not required to have as large a bandwidth as the signal. The ratio of chirps is also shown in Fig. 11 for the given example.

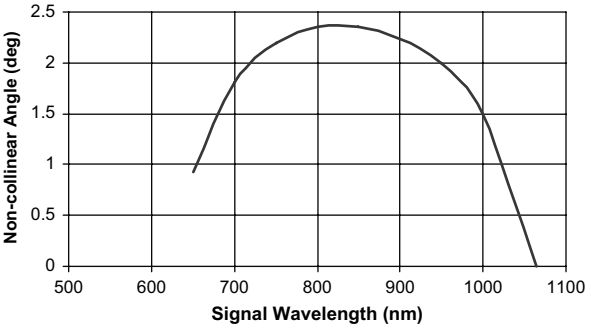

Fig. 9 The calculated internal non-collinear angle between pump and signal for maximum signal gain bandwidth in a BBO OPA using a long narrow bandwidth pump pulse

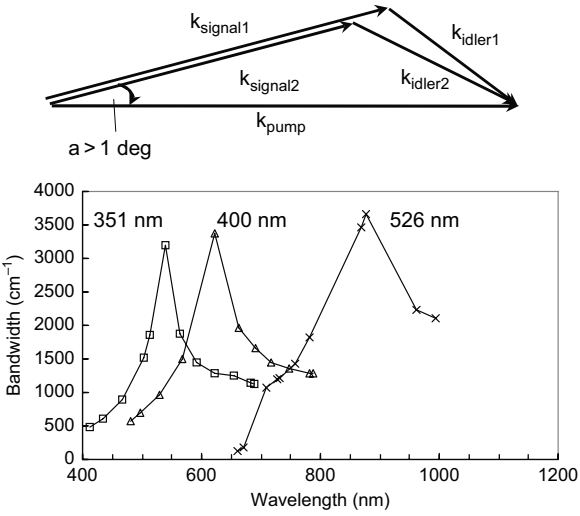

Fig. 10 Maximum signal gain bandwidths for an optimised non-collinear BBO OPA as a function of signal and pump wavelength

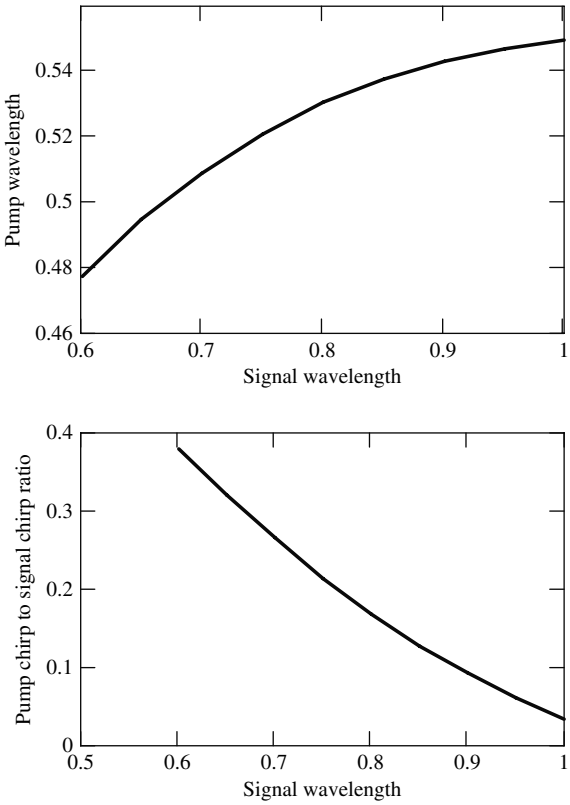

Fig. 11 Calculated variation of the required pump and signal wavelengths, together with the required pump to signal chirp ratio, to achieve exact phase matching over an arbitrary bandwidth

2.6 Energy Capacity

Non-linear crystals are widely used for frequency upconversion at high energies, when the energy limit is determined by the onset of damage at the fundamental wavelength for long pulses or by competition with other non-linear processes such as self-focusing at short pulse duration. Excellent quality large-aperture crystals are available and can equally be used as optical parametric amplifiers, although the limits are somewhat reduced since the strongest beam is now at the shortest wavelength. Typically we can use high-gain high-bandwidth crystals such as BBO and LBO up to energies of a few joules. For the highest energies, we must use KDP (or KD*P) which has lower gain and bandwidth but can be grown to sizes capable of operation at kilojoule energies.

2.7 Beam Quality

The attractive optical properties of optical parametric amplifiers can be reviewed as follows:

(a) There is no transfer of pump beam phase aberrations onto the amplified signal.
(b) The optical parametric amplification process involves no deposition of energy in the crystal, and in most applications there is very low linear absorption at the operating wavelengths. In consequence, there is little thermal distortion of the amplified signal beam.
(c) Passive optical distortions are generally small because high-quality crystals are available and it is possible to achieve the desired gain with a small thickness of material. Furthermore, amplifier schemes can be kept short to minimise air distortion, and this may even be eliminated by operating the OPAs in a vacuum.

2.8 Background Noise for an OPA ('ASE')

The issue of background noise (amplified spontaneous emission or ASE for conventional laser amplifiers) becomes increasingly important the higher the requirement for intensity on target. Current state of the art laser systems are capable of focused intensities of 10^{20} W/cm^2 or more, but these intensities are not useful for some experiments because it is not possible to keep the background intensity below the threshold for pre-damage to these targets. The source of this background for conventional lasers is spontaneous emission and the polarised ASE on target is then given by

$$I_{\mathrm{ase}} = \frac{F_{\mathrm{s}}}{32F^2\tau_{\mathrm{rad}}} . \frac{\Delta\lambda_{\mathrm{ase}}}{\Delta\lambda_{\mathrm{fl}}} . G_{\mathrm{ss}} \tag{11}$$

where G_{ss} is the small signal gain; F_s the saturation fluence; F the F.No. of focusing optic; τ_{rad} the upper state radiative lifetime; $\Delta\lambda_{fl}$ the fluorescence spectral bandwidth; and $\Delta\lambda_{ase}$ the output ASE spectral bandwidth.

For the OPA, spontaneous emission is not a useful concept. Instead the background noise can be considered to build up from the so-called vacuum fluctuations (one photon per mode) and the intensity on target is now given by [22]

$$I_{ase} = \frac{\pi n^2}{4F^2} \cdot \frac{h\nu c \Delta\lambda_{ase}}{\lambda^4} . G_{sat} \tag{6}$$

where G_{sat} is the saturated gain.

A comparison between these two in equivalent systems leads to the conclusion that OPAs offer a significant reduction in the background intensity. Examples will be given below.

3 OPCPA Schemes and their Optimisation

The coupling of chirped pulse amplification with optical parametric amplification is a powerful technique capable of generating extremely high powers with very short pulses. The following sections consider how best to achieve the highest performance with this scheme and illustrates the discussion by reference to several designs ranging from ultra-short μJ pulse generation to the future potential for multi-petawatt pulses.

3.1 The Amplification of Chirped Pulses

A chirped pulse is one with its spectrum dispersed in time with a monotonic increase (negative chirp) or decrease (positive chirp) of the wavelength with time. Generally, there is a close to linear chirp, but the small departure from linearity must be taken into account in assessing short pulse systems. Since, in an OPA, each wavelength corresponds to a value of phase mismatch as calculated from the dispersion relation, the amplification of a chirped pulse can be calculated by introducing into the analysis a time-dependent phase mismatch. Equations 2 and 8 can then be used to assess the intensity and phase performance, and these may also include a time and even a spatial dependence of the pump and signal intensities.

We may illustrate the OPA chirped pulse performance for a BBO OPA with a narrow bandwidth 526 nm pump and a chirped 140 nm broad bandwidth 1053 nm signal. Both pulses are assumed to have a flat-top spatial and a Gaussian temporal shape with equal duration. Figure 12 shows the calculated output signal intensity temporal profile for a crystal length giving maximum

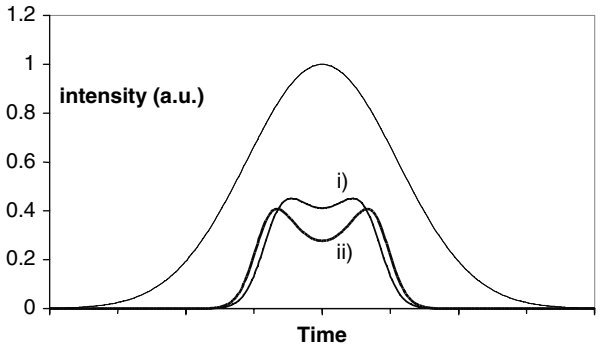

Fig. 12 Calculated evolution of output signal intensity for an OPA under conditions of (i) maximum extraction efficiency and (ii) maximum output spectral bandwidth. All input profiles are $sech^2$, and the input signal has a spectral FWHM of 140 nm stretched to a pulse duration equal to that of the pump pulse

pump to signal conversion efficiency. Since the signal pulse is assumed to be linearly chirped, these curves also represent the spectral profiles. This efficiency is 30% and the output signal bandwidth is 80% of the input signal bandwidth. Also shown is the intensity profile at a greater crystal length which now gives maximum spectral bandwidth and reflects that in general optimisation requires a compromise choice between the desirable parameters.

The curves in Fig. 12 also represent a typical amplified spectral shape under conditions of high efficiency. This is seen to be much squarer than the input pulse and consequently results in temporal wings on the re-compressed pulse which reduce the pulse contrast. Again a choice must be made. High contrast is possible using spectral profiling but generally comes with a reduction in both efficiency and output spectral bandwidth.

It is clear that, although often close to the actual shape in practise, the Gaussian profile does not represent the optimum temporal shape for pump and signal beams. Consideration of how best to optimise the profiles has been addressed [23, 24], with the conclusion that there are pairs of signal/pump pulse shapes which are matched for maximum pump depletion. The simplest pair is of course flat top for both signal and pump, but this may be difficult to realise in real systems. The characteristic of other complementary shapes is that the input signal should be an inverted version of the pump and intuitively this must be so since lower intensities of pump (reduced OPA gain) should be compensated by higher input signal intensities. Spectral filtering in a CPA pulse stretcher may be one route to appropriate shape control, but an approximation may also be effected in a multi-OPA-amplifier sequence by overdriving the earlier stage or stages to generate the inverted signal shape for the important final amplifier. An example is shown in Fig. 13 for an optimised three-stage PW OPCPA which has highly saturated initial stages to enable an output signal profile with both reasonable shape and higher values for efficiency and bandwidth.

It is a good working principle to strongly saturate all OPAs not only to optimise the beam profiles as indicated above but also because this results in a

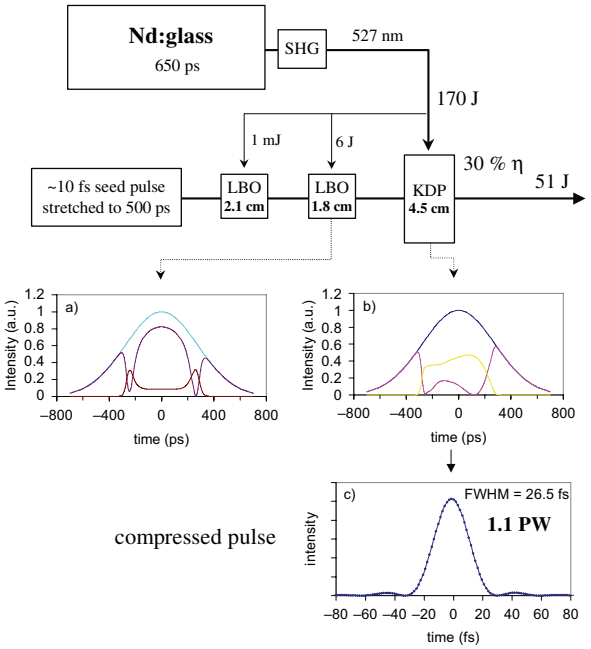

Fig. 13 A PW OPCPA scheme, showing the calculated input and output pump and output signal profiles for (**a**) the second and (**b**) the final OPA. The re-compressed pulse profile is estimated in (**c**) by taking the Fourier transform of the amplitude and phase of the output signal spectrum. Compressor throughput is assumed to be 60%

high level of stability for the output pulses, unlike the case of small signal gain, for which the amplified signal intensity is extremely sensitive to changes in the pump intensity. Under conditions of strong pump depletion, it is even possible to operate in a regime with a signal output variation less than the pump variation.

3.2 Tunable 10 fs High-Repetition-Rate OPCPA

A number of groups have developed kHz OPCPA systems [25, 26, 27]. The second harmonic of a high average power Ti:sapphire femtosecond system with a pulse duration of perhaps 150 fs is used to pump the OPA (usually BBO). The signal beam is generated by focusing a small fraction of the Ti:sapphire output into a material such as sapphire to generate a white light continuum. If the power of this fraction is adjusted to form a single self-focusing filament in the material, a stable continuum is generated having a linear chirp over typically a spectral range from 400 to 700 nm. One scheme for achieving short duration pulses which are spectrally tunable is to adjust the duration of this continuum to be longer than the OPA pump pulse so that only the bandwidth within the pump pulse duration is amplified and the centre wavelength can then be tuned by adjusting the delay between the pump and signal. The amplified signal is finally

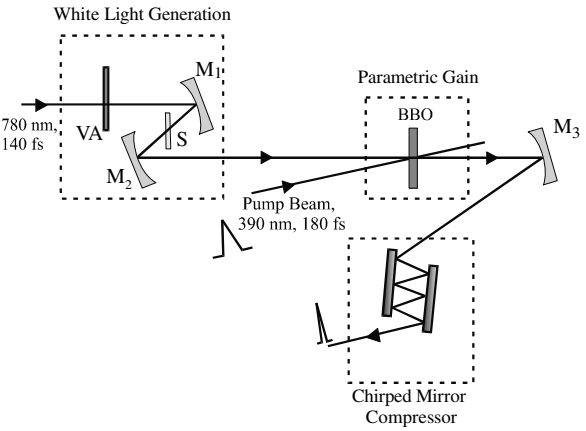

Fig. 14 Schematic of the arrangement used by Cerullo et al. [25, 26, 27] for generating amplified sub-10 fs tunable kHz pulses. The seed signal pulse uses white light generation in sapphire(S), amplification occurs in a BBO OPA and compression is achieved using chirped mirrors

re-compressed using typically prisms and/or chirped mirrors to achieve the shortest pulse corresponding to the amplified spectrum. A typical arrangement, taken from Cerullo et al. [25, 26, 27], is shown in Fig. 14.

Examples of their spectra obtained by amplifying different regions of the continuum are shown in Fig. 15, together with corresponding autocorrelation traces indicating pulse durations less than 10 fs over the spectral range 425–575 nm. Typically energies of 2 μJ are obtained at kHz repetition rate.

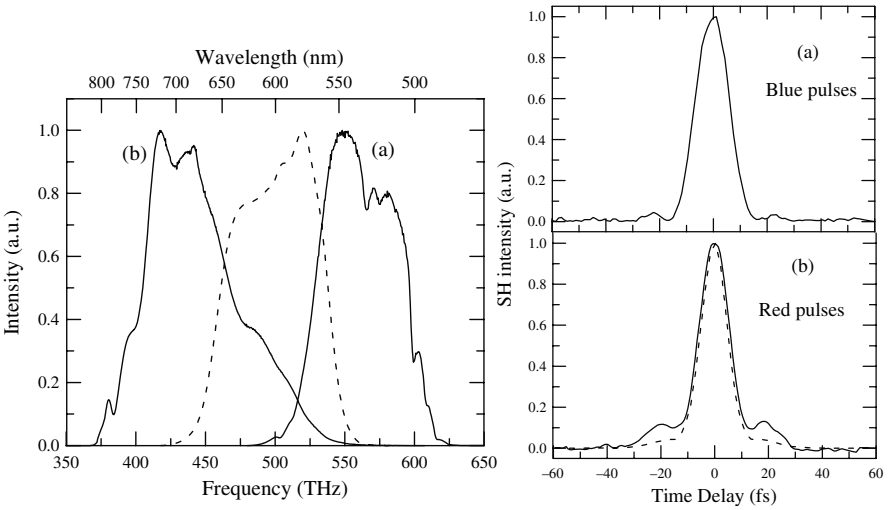

Fig. 15 The spectra and autocorrelation traces of the compressed pulses at different wavelengths for the kHz OPCPA system of Cerullo et al. [25, 26, 27]. Measured pulse durations assuming sech^2 profiles were 9.5 fs for the blue pulses and 8.5 fs for the red pulses

3.3 Broadband OPCPA Pre-amplifier

The OPCPA can offer significant advantages as a first-stage high-gain amplifier in many short pulse laser systems, from modest systems with no further amplification to large systems in which the output is fed into a further amplifier chain. Typically the OPCPA is pumped by a commercial frequency-doubled Q-switched Nd:YAG laser and can provide a gain up to 10,000 per stage over a bandwidth of greater than 1000 cm^{-1} and tunable from approximately 700 to 1064 nm (Fig. 16).

A three-stage OPCPA [28, 29, 30], as shown for Collier et al. in Fig. 17, forms an excellent pre-amplifier for a large Nd:glass laser, amplifying a sub-nJ pulse up to 20 mJ with sufficient pump depletion to provide a highly stable output pulse. A further advantage of the OPCPA used in this mode is its potential to reduce the level of background noise from a large system. When the output of a laser is focused onto target, the source of this background is dominated by that of the first-stage amplification and this is reduced by the substitution of an OPCPA, which has a lower level and duration of background noise than the ASE of a conventional amplifier.

For example using equations 10 and 11, a factor 20 reduction in background is estimated for an OPCPA amplifier in comparison to a typical saturated Ti:sapphire amplifier over the same ASE bandwidth and at the same wavelength.

3.4 A High Gain OPCPA for Amplification up to Joule Energies

The development of OPCPA systems up to ultra-high power and intensity [31, 32] is possible through the availability of large crystals of suitable nonlinear materials. LBO and BBO, available in sizes up to 2 cm, are capable of amplifying up to energies of a few joules, while KDP can be grown up to tens of centimetres and allow amplification up to the kJ level. Initial tests up to the

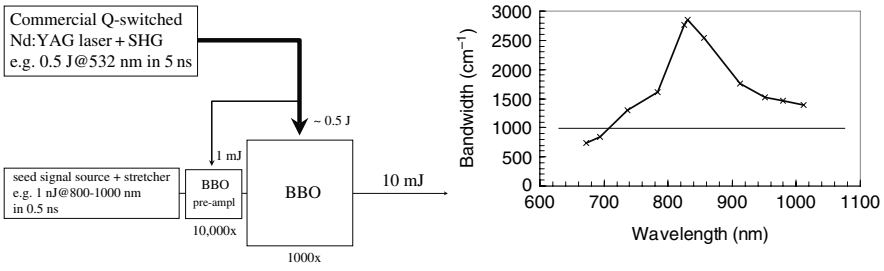

Fig. 16 Design schematic for a mJ 10 Hz OPCPA using a commercial Nd:YAG pump laser showing a gain bandwidth in excess of 1000 cm^{-1} over almost the entire tuning range of the OPA

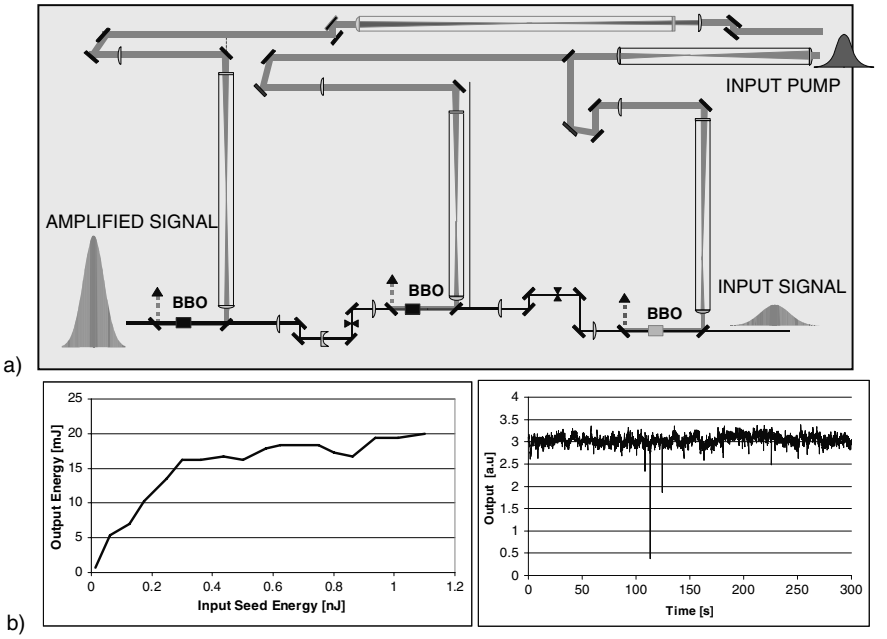

Fig. 17 (**a**) Experimental arrangement for a 3-amplifier Nd:YAG-pumped OPCPA for the amplification of nJ 1053 nm pulses at 10 Hz. (**b**) Saturated output performance of this amplifier showing an output energy of 20 mJ and a shot to shot rms stability of 10%

joule level have been conducted [31] and show that at this energy the performance is well matched to analytical simulations. Figure 18 shows the two-stage OPCPA pumped by a few joules at 527 nm and amplifying a chirped signal beam at 1050 nm. The measurements demonstrated a saturated gain of 10^{10} (Fig. 19a), a pump depletion of 40% and high-quality amplified beams with low spatial and spectral phase aberrations. Figure 19b demonstrates that the amplification resulted in only a modest increase of 15% in re-compressed pulse duration. These tests provided data for planning towards ultra-high power, the next stage being the demonstration of PW capability with an OPCPA system.

3.5 A PW OPCPA

The design schematic for a proposed PW OPCPA system pumped by a Nd:glass laser is given in Fig. 13. Oscillator pulses of 30 fs at 1050 nm are stretched to 300 ps and amplified in a three-stage OPCPA pumped by 175 J 750 ps pulses at the second harmonic of a 150 mm aperture Nd:glass laser system. LBO is the

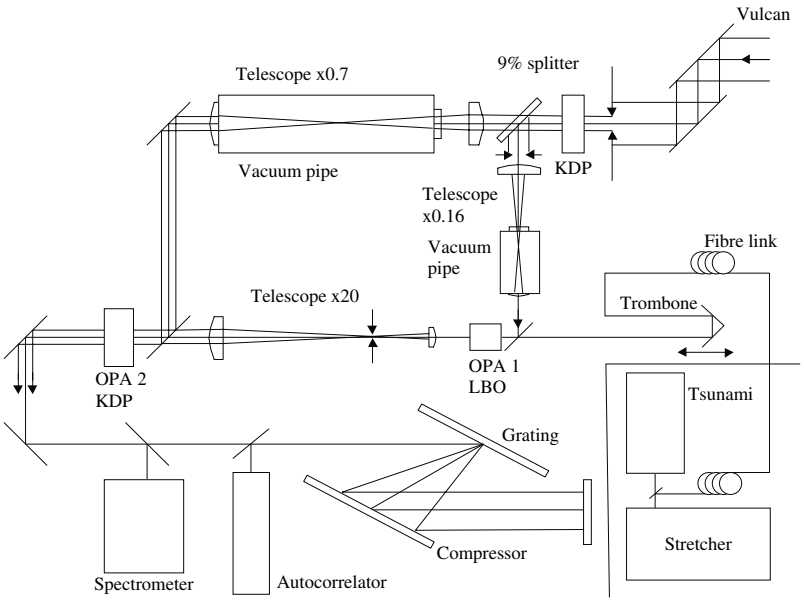

Fig. 18 Experimental arrangement for a joule level OPCPA pumped by the second harmonic of a Nd:glass laser

optimum material for the first two amplification stages, while only KDP can be grown to the aperture size required for the final stage. Pump and signal beams are spatially flat in the OPAs with Gaussian and sech^2 temporal distributions for input pump and signal, respectively. Strong saturation in the first two stages leads to an optimised input signal beam to the final amplifier and hence to a maximised re-compressed peak power. Taking into account losses in the compressor and phase effects in the OPAs a power of 1 PW is predicted at a pulse duration of 27 fs. Using equations 10 and 11 the background noise on a target at the focus of the re-compressed pulses is expected to be a factor of about 10 less than that for a PW Nd:glass laser.

3.6 Future Potential for a Multi-PW OPCPA

Perhaps the most important incentive of the OPCPA idea is that it is not limited to 1 PW and so it is of interest to estimate the maximum power that can be generated by an OPCPA system using current technology, and a scheme, similar to the above 'PW' design, and based now on a multi-beam Nd:glass pump laser, is proposed. The limiting factor in the OPCPA design is, in common with conventional CPA systems, the energy capacity of the compressor gratings. This design calls for square gratings with a groove density of 800 l/mm and an

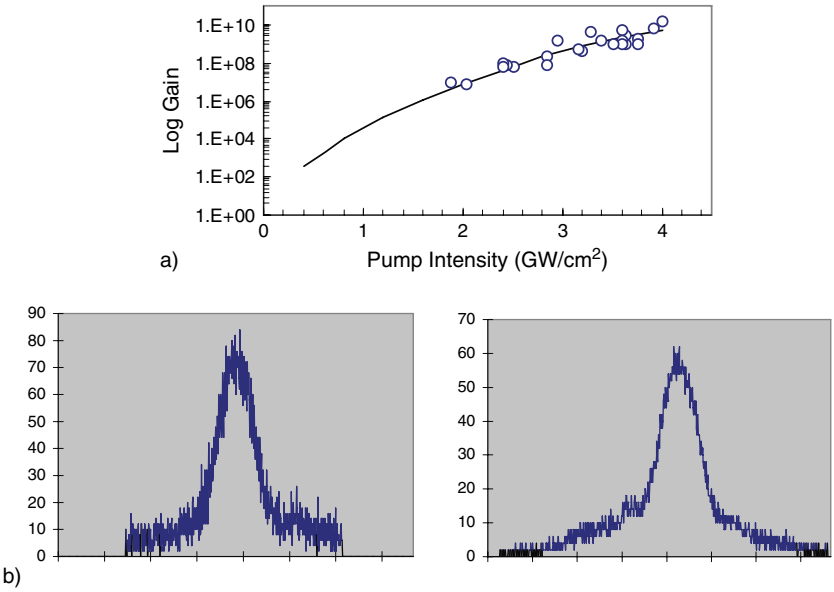

Fig. 19 (**a**) The 2-amplifier gain as a function of the pump intensity. Measured points (*circles*) are compared to the calculated curve (*continuous line*). (**b**) Re-compressed pulse autocorrelation traces for unamplified and amplified pulses. Estimated pulse durations are 250 and 300 fs, respectively

incident angle of 20° (diffraction angle = 30°) and current technology dictates a maximum size of 100 cm, and at a maximum fluence of 0.5 J/cm^2 the maximum energy capacity for a square incident beam is 4.7 kJ.

Figure 20 presents a schematic of this high-power design and includes the results of a simulation of its performance. Current glass laser technology [33] can provide an energy of approximately 3.4 kJ per beam in 1 ns at the pump wavelength of 526 nm and in a square 34 × 34 cm beam with flat profiles in both space and time. One beam drives a three-stage OPCPA to amplify a 1 nJ signal pulse which has been stretched from 20 fs to 400 ps. An output signal energy of 1.4 kJ is anticipated from the third stage. Two subsequent KDP booster amplifiers, each pumped by a second and third beam from the glass laser, enable further amplification of the signal up to 4.45 kJ, which is close to the capacity of the compressor. The peak power is calculated by taking the Fourier transform of the predicted output spectral amplitude and phase distribution and assumes that phase terms up to cubic can be compensated. A value of 22 fs was obtained giving finally an estimated power for this scheme of 163 PW.

The fluence in the OPAs is kept below 3 J/cm^2 for KDP and below 5 J/cm^2 for LBO, and with a total path in LBO and KDP of 29 and 57 mm, respectively, the effective overall B-integral on the signal beam is estimated to be less than 1.

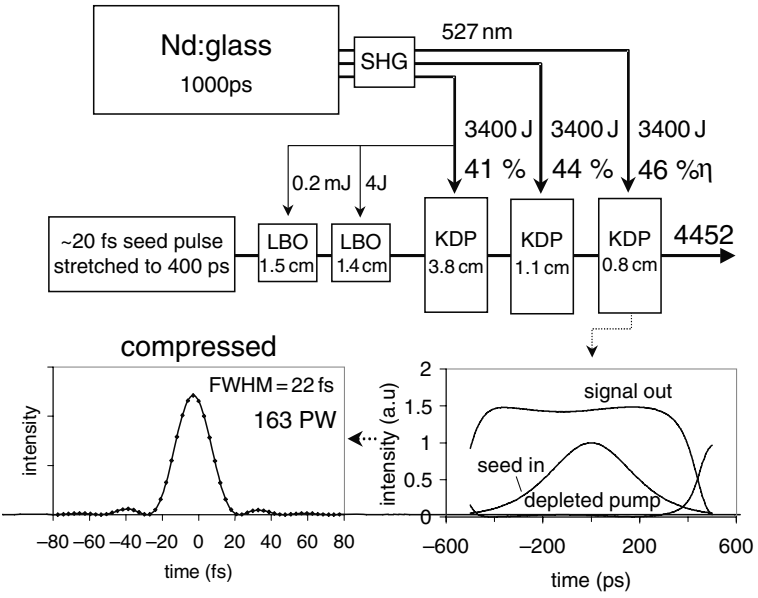

Fig. 20 'Maximum power' OPCPA design using a multi-beam Nd:glass laser as pump. *Curves* show the calculated input seed signal, output amplified signal and depleted pump pulses, respectively, together with the estimated re-compressed pulse assuming an ideal compressor with a throughput of 80%

The angular tolerance on the pump beams requires them to have a divergence no greater than 0.1 mrad which is more than 30× the diffraction limit. In addition, the OPCPA system could be placed in vacuum to minimise beam distortion on the amplified signal, and with the implementation if needed of an adaptive optic an output beam quality close to the diffraction limit can be expected. Focusing this beam to a focal spot size of say 3 μm would then provide intensities in excess of 10^{24} W/cm^2.

3.7 Phase-Preserving Chirped Pulse OPA

Carrier-envelope phase-stabilised pulses are of great importance for metrology and attoscience. For further information see the chapter of Krausz and Cundiff. Recently phase-preserving OPA was demonstrated [34, 35]. Phase-stabilised 12-fs, 1 nJ pulses from a commercial Ti:sapphire oscillator were directly amplified in an OPCPA [34] and re-compressed to yield near-transform-limited 17 fs pulses. The amplification process was demonstrated to be phase preserving. In another work [35], the angular dispersed idler output of an OPA, with a centre wavelength of 1 μm, was compressed to below 5 fs. The resulting

phase-stabilised quasi-monocyclic pulse was characterised by non-linear cross-correlation frequency-resolved optical gating.

4 Conclusion

The optical parametric amplifier is an important alternative and additional amplification technique in the generation of optical pulses. As well as being tunable it can also have high gain, high bandwidth, high energy and high beam quality, and is particularly suited to the generation of ultra-short and ultra-high peak power pulses.

Straightforward analytical equations governing the operation of the OPA enable a simulation of many practical designs. Optimisation of these designs is possible with due consideration to features of operation such as pump depletion, the maximisation of efficiency and bandwidth and operational limits due to self-focusing and damage.

Several schemes based on OPCPA show that OPAs will have a major role to play in current and future applications of ultra-short pulse ultra-high power systems.

5 Parameter Set

A_i = complex field
d_{eff} = effective second-order coefficient
Δk = phase mismatch
$\Delta\lambda$ = spectral bandwidth
Δ = gain bandwidth
f = fractional depletion of pump beam
F_s = saturation fluence
F = F.Number (optical)
g = amplifier gain parameter
G = signal gain
γ = photon intensity ratio
I = intensity
$\boldsymbol{k}$ = wave vector
L = length
λ = wavelength
n_i = refractive index
n_{gi} = group index
p = intensity ratio
ρ = wave amplitude
τ_{rad} = upper state radiative lifetime
θ = optical parametric amplifier phase parameter

u_i = normalised intensity
ω_i = angular frequency
φ_i = phase of the 'i' beam

References

1. P.A. Franken, A.E. Hill, C.W. Peters and G. Weinreich 'Generation of optical harmonics', Phys. Rev. Lett 7, 118 (1961)
2. J.A. Armstrong, N. Bloembergen, J. Ducuing and P.S. Pershan, 'Interactions between light waves in a nonlinear dielectric', Phys. Rev. 127, 1918–39 (1962)
3. P. DiTrapani, A. Andreoni, C. Solcia, P. Foggi, R. Danielius, A. Dubietis and A. Piskarskas, 'Matching of group velocities in three-wave parametric interaction with femtosecond pulses and application to travelling-wave generators', JOSA B 12, 2237–44 (1995)
4. J.M. Liu, G. Zhou and S.J. Pyo, 'Parametric gain of the generation and the amplification of ultrashort optical pulses', JOSA B 12, 2274–87 (1995)
5. R. Danielius, A. Piskarskas, A. Stabinis, G.P. Banfi, P. DiTrapani and R. Righini, 'Travelling-wave parametric generation of widely tunable, highly coherent femtosecond light pulses', JOSA B 10, 2222–32 (1993)
6. A. Piskarskas, A. Stabinis and A. Yankauskas, 'Phase phenomena in parametric amplifiers and generators of ultrashort light pulses', Sov. Phys. Usp. 29, 969–79 (1986)
7. R. Danelius, A. Piskarskas, V. Sirutkaitis, A. Stabinis and A. Yankauskas, 'Chirp reversal of picosecond light pulses in parametric amplification in quadratically nonlinear media', JETP Lett. 42, 122–24 (1985)
8. J. Wang, M.H. Dunn and C.F. Rae, 'Polychromatic optical parametric generation by simultaneous phase matching over a large spectral bandwidth', Opt. Lett. 22, 763–65 , (1997)
9. A. Shirakawa, I. Sikane, H. Takasaka and T. Kobayashi, 'Sub-5 fs visible pulse generation by pulse-front-matched non-collinear optical parametric amplification', App. Phys. Lett. 74, 2268–70 (1999)
10. G.M. Gale, M. Cavallari, T.J. Driscoll and F Hache, 'Sub-20 fs tunable pulses in the visible from an 82-MHz optical parametric oscillator', Opt Lett. 20 1562–64 (1995)
11. I.N. Ross, P. Matousek, M. Towrie, A.J. Langley, J.L. Collier, 'The prospects for ultrashort pulse duration and ultra-high intensity using optical parametric amplifiers', Optics Comm. 144, 125–33 (1997)
12. A. Dubeitis, G. Jonasauskas and A. Piskarskas, 'Powerful femtosecond pulse generation by chirped and stretched pulse parametric amplification in BBO crystal', Opt. Comm. 88, 437–40 (1992)
13. I.N. Ross, P. Matousek, M. Towrie, A.J. Langley and J.L. Collier, 'The prospects for ultra-short pulse duration and ultra-high intensity using optical parametric amplifiers', Optics Comm. 144, 125–33 (1997); N. Ishii et al., 'Multimillijoule chirped pulse amplification of few cycle pulses', Opt. Lett. 30, 567 (2005).
14. J.A. Armstrong, N. Bloembergen, J. Ducuing and P.S. Pershan, 'Interactions between light waves in a nonlinear dielectric', Phys. Rev. 127, 1918–39 (1962)
15. R.L. Sutherland, Handbook on Non-Linear Optics, Marcel Dekker, New York, 1996
16. R.A. Baumgartner and R.L. Byer, 'Optical parametric amplification', IEEE JQE-15, 432–44 (1979)
17. S. Reisner and J. Gutmann, 'Numerical treatment of UV-pumped, white-light-seeded single-pass non-collinear parametric amplifiers', JOSA B 16, 1801–13 (1999)
18. Laser Program Annual Report – Lawrence Livermore Laboratory UCRL-50021-75, 229–42 (1975)

19. T. Wilhelm, J. Piel and E. Riedle, 'Sub-20 fs pulses tunable across the visible from a blue pumped single-pass non-collinear parametric converter', Opt. Lett. 22, 1494–96 (1997)
20. I.N. Ross, P. Matousek, G.H.C. New and K. Osvay, 'Analysis and optimisation of optical parametric chirped pulse amplification', JOSA B, 19, 2945–54 (2002)
21. K. Osvay, I.N. Ross, JOSA B 13, 1431–38 (1996)
22. D.A. Kleinmann, 'Theory of optical parametric noise', Phys. Rev. 174, 1027 (1965)
23. I.A. Begishev, A.A. Gulanov, E.A. Erofeev, E.A. Ibragimov, Sh.R. Kamalov, T. Usmanov and A.D. Kadzhaev, 'Highly efficient parametric amplification of optical beams. 1. Optimisation of the profiles of interacting waves in parametric amplification', Sov. J. Quant. Electr. 20, 1100–03 (1990)
24. I.A. Begishev, A.A. Gulanov, E.A. Erofeev, Sh.R. Kamalov, V.I. Redkorachev and T. Usmanov, 'Total conversion of the pump energy into a subharmonic wave in parametric amplification of signals', Sov. J. Quant. Electr. 16, 1292–93 (1986)
25. G. Cerullo, M. Nisoli, S. Stagira, S. DeSilvestri, G. Tempea, F. Krausz and K. Ferencz, 'Mirror-dispersion-controlled OPA: a compact tool for sub-10 fs spectroscopy in the visible', App. Phys. B 70, S253–59 (2000)
26. A. Shirakawa, I. Sikane, H. Takasaka and T. Kobayashi, 'Sub-5 fs visible pulse generation by pulse-front-matched non-collinear optical parametric amplification', App. Phys. Lett. 74, 2268–70 (1999)
27. E. Riedle, M. Beutter, S. Lochbrunner, J. Piel, S. Schenkl, S. Sporlein, and W. Zinth, 'Generation of 10 to 50 fs pulses tunable through all of the visible and the NIR', App. Phys. B 71, 457–65 (2000)
28. J.L. Collier, C. Hernandez-Gomez, I.N. Ross, P. Matousek, C.N. Danson and J. Walczak, 'Evaluation of an ultra-broadband high-gain amplification technique for chirped pulse amplification facilities', App. Opt. 38, 7486–93 (1999)
29. I. Jovanovic, B.J. Comaskey, C.A. Ebbers, R.A. Bonner and D.M. Pennington, 'Replacing Ti:sapphire regenerative amplifiers with an optical parametric chirped pulse amplifier', CLEO/QELS 2001 conference post deadline paper
30. S.K. Zhang, M. Fujita, H. Yoshida, R. Kodama, M. Yamanaka, M. Izawa and C. Yamanaka, 'Gain and spectral characteristics of broadband optical parametric amplification', Jap. J. App. Phys 40, 3188–90 (2001)
31. I.N. Ross, J.L. Collier, P. Matousek, C.N. Danson, D. Neely, R.M. Allot, D.A. Pepler, C. Hernandez-Gomez and K. Osvay, 'Generation of terawatt pulses by use of optical parametric chirped pulse amplification', App. Opt. 39, 2422–27 (2000)
32. V.V. Lozhkarev et al., '100-TW femtosecond laser based on parametric amplification', JETP Lett. 82, 178 (2005)
33. C.C. Widmayer, O.S. Jones, D.R. Speck, W.H. Williams, P.A. Renard and J.K. Lawson, 'The NIF's power and energy ratings for flat–in-time pulses', Proc. 3rd Ann. Conf. on Solid State Lasers, SPIE 3492, 11–21 (1998)
34. C.P. Hauri, P. Schlup, G. Arisholm, J. Biegert and U. Keller, 'Phase preserving chirped-pulse optical parametric amplification to 17.3 fs directly from a Ti:sapphire oscillator', Opt. Lett. 29, 1369 (2005).
35. S. Adachi, P. Kumbhakar and T. Kobayashi, 'Quasi-monocyclic near-infrared pulses with a stabilized carrier-envelope phase characterized by noncollinear cross-correlation frequency resolved optical gating', Opt. Lett. 29, 1150 (2004).

Carrier-Envelope Phase of Ultrashort Pulses

Steven T. Cundiff, Ferenc Krausz, and Takao Fuji

1 Introduction

The phase of the electromagnetic field has typically not been a quantity of physical meaning in optics because all measurements are of intensity. Relative phases, for example, between two arms of an interferometer, can readily be measured and controlled, but not the phase of a single field. Recently, there has been significant progress in measuring and controlling the phase of the electromagnetic field of ultrashort pulses by using the envelope of the pulse as a phase reference [1, 2, 3, 4, 5, 6, 7, 8, 9, 10]. If we write the electric field of the laser pulse as

$$E(t) = A(t)\cos(\omega_1 t + \varphi), \tag{1}$$

then φ determines the carrier-envelope phase (CEP) (see Fig. 1).

At high intensities [11], where electrons are responding to the electric field itself, rather than the intensity, φ can become significant. Typically, this arises when there is a threshold such as occurs for tunneling. This is shown schematically in Fig. 1b.

Currently, it is possible to measure and control the pulse-to-pulse change in φ, which we designate at $\Delta\varphi$, for the pulse train emitted by a mode-locked oscillator. Measurement, based on above threshold ionization [8], of φ itself has been demonstrated for amplified pulses and the influence of φ on high harmonic generation demonstrated [9].[1]

[1] The term "absolute" phase is often used in referring to φ. This can be misleading as there is nothing absolute about the peak of the envelope used as a reference. This terminology has probably arisen to help distinguish between φ and $\Delta\varphi$ and to emphasize the fact that φ is not relative to a second reference beam.

S.T. Cundiff
JILA, National Institute of Standards and Technology and University of Colorado, Boulder, CO 80309-0440, USA
e-mail: cundiffs@jila.colorado.edu

T. Brabec (ed.), *Strong Field Laser Physics*,
DOI: 10.1007/978-0-387-34755-4_4,

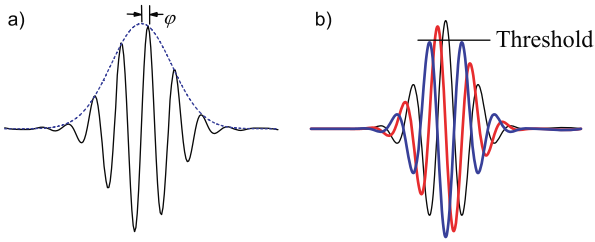

Fig. 1 Schematic showing the carrier-envelope phase. (**a**) Definition of φ of an ultrashort laser pulse. (**b**) Depending on φ, the field may not exceed a threshold, barely exceed it, or significantly exceed it

In this chapter, we first discuss how control of $\Delta\varphi$ in mode-locked oscillators has been achieved using frequency domain techniques. We then discuss the role of φ in high-intensity physics. Finally, we mention how control of $\Delta\varphi$ contributes to other areas.

1.1 Evolution of the Carrier-Envelope Phase

Because of dispersion, the group and phase velocities will differ and cause φ to evolve rapidly when propagating through any material except vacuum. For example, propagation through 10 μm of fused silica will cause φ to change by 1 rad for an 800 nm pulse. Correspondingly, 10 mm of air will have the same effect. In addition, phase shifts can occur due to diffraction or focusing of the pulse.

The evolution of φ during propagation inside the cavity of a mode-locked laser has the important consequence that the phase of each pulse in the emitted train will increase by an amount $\Delta\varphi$. If $\Delta\varphi$ happens to be a rational fraction of π, then φ is periodic; otherwise each pulse has a unique φ.

2 Measurement and Control of Carrier-Envelope Phase from Mode-Locked Lasers

Most high-intensity experiments use pulses that are originally produced by a mode-locked oscillator and subsequently amplified. Although the phase can be adjusted externally to the oscillator, it is desirable to start with a pulse train of constant φ, or at least evolving in a well-controlled manner. Thus, controlling $\Delta\varphi$ and ultimately φ is an important prerequisite for high-intensity experiments that are sensitive to φ.

Typically, an amplifier runs at a rate of 1-100 kHz, whereas the oscillator produces pulses at a repetition rate of 10-100 MHz. Thus, one pulse out of 10^2–10^5 is used from the pulse train emitted by the oscillator. This means that φ must be coherent for at least this many pulses, for systematic control to be achieved.

2.1 Cross-Correlation

Time domain measurement of $\Delta\varphi$ is performed by using a cross-correlator [1, 2]. A cross-correlator is similar to an interferometric autocorrelator, except that one arm of the scanning interferometer is longer than the other by a multiple, n, of the time between pulses (see Fig. 2). This means that pulse i in the pulse train is compared to pulse $i+n$, rather than with itself as would happen in an autocorrelator. In the resulting nonlinear interferogram, the shift of the interference fringes with respect to the peak of the envelope is due to $\Delta\varphi$. As noted above, propagation through air will shift φ. This is a significant effect in a cross-correlator because one arm is significantly longer, typically by $\sim$5 m. This means that either the path traversed by this arm must be evacuated [1] or the entire correlator must be evacuated [2]. Fortunately, only a rough vacuum is required.

The first cross-correlation measurements by Xu et al. [1] were performed on a laser that did not have active stabilization of $\Delta\varphi$, but coarse control was obtained by changing the insertion of a glass wedge in the laser cavity. This work also provided the important observation that $\Delta\varphi$ depends on intracavity power. Two typical correlations demonstrating a π shift in $\Delta\varphi$ from later work by Jones et al. [2], where the laser was actively stabilized as described below, are shown in Fig. 2.

2.2 Frequency Domain Description of Carrier-Envelope Phase Evolution in a Mode-Locked Pulse Train

Precision long-term stabilization of $\Delta\varphi$ can be achieved using the powerful tools developed for stabilization of single frequency lasers. To understand how $\Delta\varphi$ can be detected and stabilized using frequency domain techniques, we first

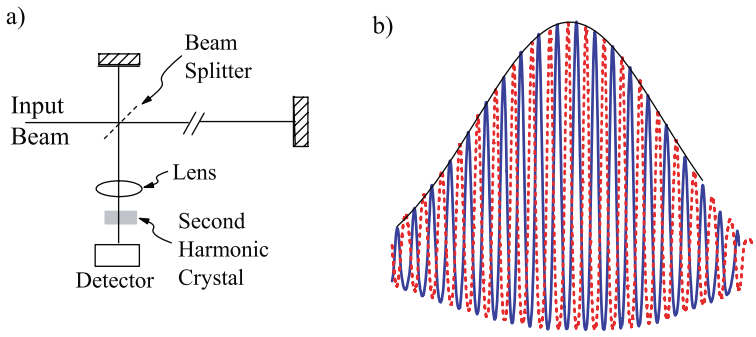

Fig. 2 (**a**) Schematic of a cross-correlator. The second harmonic crystal and detector can be replaced with a nonlinear photodiode. (**b**) Two typical cross-correlations showing a π phase shift in $\Delta\varphi$

need to describe the optical frequency spectrum of a train of ultrashort pulses, including $\Delta\varphi$.

If the spectrum of a mode-locked laser is measured using a typical spectrometer, a broad continuous spectrum will be observed. This spectrum is just that of the individual pulses. However, if a very high-resolution spectrometer were to be used, it would be observed that the spectrum actually consists of a comb of closely spaced lines, where the spacing corresponds to the repetition rate, f_{rep}, of the laser. Fourier analysis of a train of identical pulses easily shows that the frequency spectrum is indeed a comb, with the comb frequencies being integer multiples of f_{rep}. However, the phase evolution of the pulses means that the pulses are not identical. A more sophisticated analysis [12, 13, 14] yields the result that the optical frequencies of the comb lines are given by

$$\nu_n = nf_{\text{rep}} + f_0, \tag{2}$$

where the offset frequency, f_0, is connected to $\Delta\varphi$ by

$$\Delta\varphi = 2\pi f_0 / f_{\text{rep}}. \tag{3}$$

This correspondence between time and frequency is shown schematically in Fig. 3. The important result shown in (3) is that the pulse-to-pulse phase evolution causes a rigid shift of the frequency comb by f_0. Thus, if we can measure f_0, we can accurately determine $\Delta\varphi$ because frequency measurements can be very accurate.

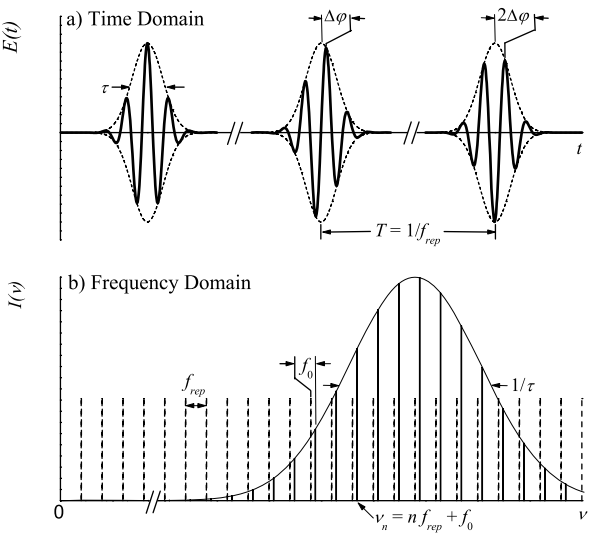

Fig. 3 Connection between time and frequency domains. (**a**) Train of ultrashort pulses in time showing pulse-to-pulse phase change $\Delta\varphi$. (**b**) Spectrum showing comb of lines separated by f_{rep} and offset by f_0

2.3 Frequency Domain Detection of $\Delta\varphi$

Given our understanding that $\Delta\varphi$ is manifest in the frequency domain as a rigid shift by f_0, we are faced with the question of how to measure f_0. It might be imagined that a very accurate absolute optical frequency reference could be used. However, this turns out to be impractical; instead, as we will discuss later, the techniques described here can be used to measure absolute optical frequencies. Measurement of f_0 is possible using a technique known as "self-referencing" [2, 15].

Self-referencing obtains f_0 by comparing the low- and high- frequency extremes of the spectrum. If the spectrum is sufficiently broad, the second harmonic of the low-frequency end of the spectrum will overlap with the high-frequency end. The heterodyne beat between these will yield a difference frequency given by

$$2\nu_n - \nu_{2n} = 2(nf_{\text{rep}} + f_0) - (2nf_{\text{rep}} + f_0) = f_0. \tag{4}$$

Thus, f_0 can be determined directly given a spectrum that spans an octave, i.e., a factor of 2 in optical frequency, which we designate as ν-to-2ν self-referencing. For narrow spectra, a higher-order version of this technique can be used. For example, if the second harmonic and third harmonic are compared (2ν-to-3ν), then a spectrum that spans only a half octave is required [15, 16]. The higher-order nonlinearities represent a disadvantage as higher intensities are needed, although the relaxed requirements on spectral width are an advantage.

2.4 Generation of an Octave-Spanning Spectrum

A transform-limited Gaussian or $sech()^2$ pulse with a full width at half maximum (FWHM) spectral width of an octave would have a temporal width of one cycle. Although sub-two-cycle pulses have been generated [17, 18], single-cycle pulses have not been achieved. However, the "octave" does not have to be at the FWHM, but rather can be significantly below that. In addition, it is not the temporal profile that counts, but rather the spectrum; thus strongly nonmonotonic spectra can be used. This allows the use of spectra that have been strongly broadened by self-phase modulation.

Using a low-repetition-rate laser (so that the pulse energy is correspondingly high) that generates 9 fs pulses, it is possible to achieve such an octave-spanning spectrum using self-phase modulation in standard optical fiber [3]. The discovery of strong spectral broadening of nanojoule pulses in microstructured fiber [19, 20] made it possible to achieve sufficient bandwidth from ordinary Ti:sapphire lasers. The spectral broadening in microstructured fiber occurs because it has a group-velocity-dispersion zero point within the spectral region of Ti:sapphire. In addition, microstructured fiber has a very strong

confinement, thereby increasing the effective nonlinearity. Similar effects have been observed in fiber tapers [21].

As discussed in Section 2.8, it is also now possible to generate an octave directly from a mode-locked oscillator.

2.5 Frequency Domain Stabilization

The heterodyne beat signal obtained with a ν-to-2ν interferometer can be used to stabilize the laser to produce a given value of f_0 and hence $\Delta\varphi$. Typically, a phase-locked loop is used to eliminate small frequency errors that could result in accumulated phase error. It is very important that the reference signal be coherently related to the repetition rate, either by deriving it from the repetition rate [2] or by using two synthesizers with a common timebase and locking the repetition rate to one and f_0 to the other [4].

To close the loop, there must be a laser parameter that controls f_0, which is determined by the difference between phase and group velocities inside the cavity. In a standard 10 fs Ti:sapphire laser [22], a prism sequence is used to compensate for group-velocity dispersion in the laser crystal. This results in the spectrum being spatially dispersed on the flat mirror at one end of the linear cavity. By making small rotations of this mirror, a linear phase shift with frequency, which is equivalent to a group delay [23], can be generated [13]. This has successfully been used to lock f_0 [2].

An alternative scheme is to use the pump power to control the intracavity power. This has been shown empirically to alter $\Delta\varphi$ [1, 4], although the exact mechanism remains unclear, with nonlinear phase shifts [1], nonlinear changes in the group velocity [24, 25], and spectral shifts [1, 26] all playing a role. Theoretical analysis has also shown that management of the intracavity dispersion, i.e., that consists of distinct regions with opposite signs of dispersion, affects the sensitivity of $\Delta\varphi$ to changes in intensity [27]. This technique has the advantage over the previous method of higher speed and also has been shown to reduce the amplitude noise [4].

2.6 Phase Noise and Coherence

As mentioned above, most high-intensity experiments use amplified pulses, and only a small fraction of the pulses emitted by the oscillator are actually amplified. Thus, coherence of φ must be maintained sufficiently long so that the phase of the pulses that are actually amplified is controlled. Clearly the longer phase coherence can be maintained, the better.

One obvious concern is that the highly nonlinear nature of the broadening in microstructure fiber will result in conversion of amplitude noise on the input to phase noise on the output. Measurement of this conversion using a pair of

ν-to-2ν interferometers yields a conversion coefficient of 3784 rad/nJ for 4.3 nJ of coupled pulse energy and a 4.5 cm long fiber [6]. For a well-designed laser, the amplitude noise is sufficiently small so that this process results in ~ 0.5 rad or less of phase noise.

The phase coherence of φ is directly reproduced in the phase of the heterodyne beat signal at f_0. By measuring the power spectrum of the phase noise, or the frequency noise, it is possible to determine the root-mean-square (RMS) phase fluctuation from the relationship

$$\Delta\varphi^{\mathrm{RMS}}|_{\tau_{\mathrm{obs}}} = \sqrt{2\int_{-\infty}^{-1/2\pi\tau_{\mathrm{obs}}} \frac{S_{f_0}(f)}{f^2}\,\mathrm{d}f} = \sqrt{2\int_{-\infty}^{-1/2\pi\tau_{\mathrm{obs}}} S_{\varphi}(f)\mathrm{d}f}, \qquad (5)$$

where $S_{f_0}(f)$ and $S_{\varphi}(f)$ are the power spectral density of the frequency noise and phase noise, respectively, and τ_{obs} is the observation time. Note that these expressions are only valid so long as $\Delta\varphi^{\mathrm{RMS}} < 2\pi$. This can be verified by measuring the power spectrum of the frequency noise using a frequency-to-voltage converter.

Measurement of $S_{f_0}(f)$ is shown in Fig. 4 [7]. Both in-loop (using the same signal as used to lock the laser) and out-of-loop (using a second length of microstructure fiber and a second ν-to-2ν interferometer) results are shown. The latter is important because of the aforementioned conversion of amplitude to phase noise in the fiber. In principle, the in-loop measurement does not properly account for this because the feedback can compensate for amplitude induced phase errors by adjusting the phase of the laser. Amplitude-to-phase conversion actually results in a degradation of the phase coherence of emitted pulses, but an improvement of the in-loop signal.

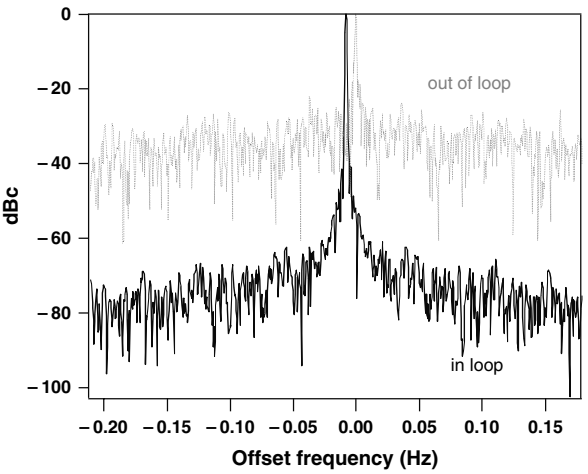

Fig. 4 Linewidth of f_0 (offset for clarity) as measured on a dynamic signal analyzer (FFT). The in-loop measurement (*solid*) was taken with a resolution bandwidth of 0.976 mHz, while the out-of-loop (*dashed*) measurement was taken at 0.488 mHz. Note that measurements of the linewidths are still resolution limited [7]

The measurement-limited linewidths in Fig. 4 are 0.976 mHz (0.488 mHz) out of loop (in loop). These results are confirmed by separate measurement of the phase noise spectrum, which is integrated as per (5) to yield an out-of-loop coherence time of at least 163 s, again measurement limited (coherence time is defined to be the time it takes to accumulate 1 rad of phase fluctuation). Earlier measurements suggest that nonlinear beam steering inside the cavity might contribute to the phase noise [5].

These long coherence times show that $\Delta\varphi$ of mode-locked oscillators is sufficiently stable so that the pulse train provided to an amplifier will indeed have reproducible phases. This enables high-intensity experiments sensitive to φ using phase-controlled pulses.

2.7 Detection of f_0 Using Quantum Interference

An alternative method of detecting φ is to use quantum interference rather than optical interference. Quantum interference occurs between m-photon and n-photon absorption pathways. When both photons come from the spectrum of a single femtosecond pulse, φ determines whether the interference is constructive or destructive. The simplest case is for $m = 1$ and $n = 2$, which is closely analogous to the ν-to-2ν interferometer. For a system in which parity is a good quantum number, it is forbidden for two states to be simultaneously coupled by both one- and two-photon transitions. Simultaneous one- and two-photon transitions are possible for continuum states that do not have parity as a good quantum number. Transitions between valence and conduction bands in a semiconductor are an example of a system in which such quantum interference can be observed.

Quantum interference control (QIC) of injected photocurrents in semiconductors was demonstrated using a two-color pulse consisting of a 100 fs pulse and its second harmonic, with the relative phases being controlled by dispersion or by a two-color interferometer [28, 29]. In this realization of QIC, an injected current is generated, despite the absence of a bias field because the interference depends on $\mathbf{k}$. Specifically, when the interference is constructive at $+\mathbf{k}$, it is destructive at $-\mathbf{k}$ and vice versa. An imbalance in carrier population with respect to k represents a current. A conceptual diagram of how QIC of injected photocurrents can be used to measure φ is given in Fig. 5.

The use of QIC to measure $\Delta\varphi$ was demonstrated by Fortier et al. [30]. In this demonstration, a mode-locked oscillator with f_0 locked to a known value was used to generate an oscillating photocurrent in a sample of low-temperature-grown GaAs. The photocurrent was collected with gold electrodes and detected by an electronic spectrum analyzer or lock-in amplifier. The signal to noise and bandwidth of the f_0 detection were limited because a simple load resistor was used for current-to-voltage conversion.

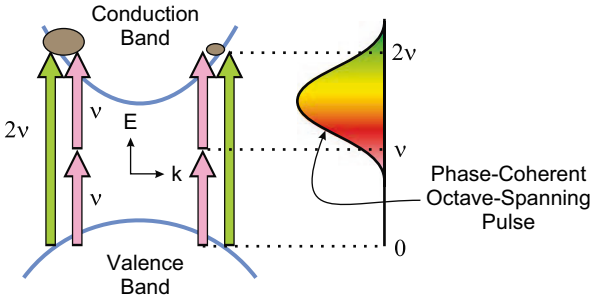

Fig. 5 Conceptual schematic showing quantum interference between one- and two-photon absorption in a direct-gap semiconductor. The interfering absorption pathways are driven by the spectral wings of a single octave-spanning pulse. The interference can cause an imbalance in the carrier-population distribution in momentum space (represented by *ovals*), resulting in a net flow of carriers. The direction and magnitude of the resulting photocurrent are sensitive to φ

By designing a custom transimpedance amplifier, it was possible to improve both the signal to noise and bandwidth of the f_0 signal produced by QIC of injected photocurrents. These improvements in turn enabled stabilization of the f_0 using QIC [31]. The obtained phase noise spectrum is shown in Fig. 6. The integrated RMS phase fluctuations are comparable to those obtained with a standard ν-to-2ν interferometer.

2.8 *Phase Stabilization with Octave-Spanning Ti:Sapphire Oscillator*

As mentioned in the previous section, a source of CEP noise is amplitude-phase conversion in microstructured fiber. Therefore, it is helpful to obtain an octave spectrum by self-phase modulation in a nonlinear crystal instead of microstructured fiber, or even directly from oscillator, to improve phase-locking quality.

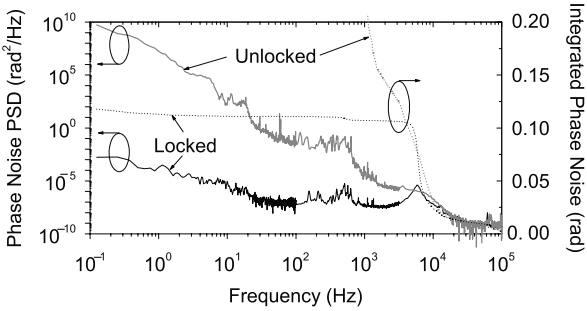

Fig. 6 Phase-noise power spectral density (*solid lines*) and integrated phase noise (*dotted lines*) measured when the laser is locked using QIC (*dark lines*) and unlocked (*lighter lines*) [31]

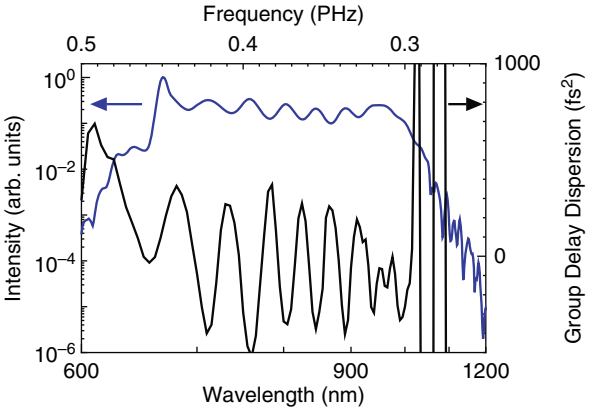

Fig. 7 Typical spectrum generated by the all-chirped mirror oscillator (blue curve) and net intracavity group-delay dispersion (GDD, *black curve*) [38]

An octave-spanning spectrum was demonstrated by moving the nonlinear medium inside the laser cavity [32, 33]. In this work, a glass plate was placed at a second waist inside the laser cavity. By managing the intracavity dispersion, it was possible to generate simultaneous time and space focii, and thus produce the high peak intensity needed for strong self-phase modulation.

Recently, broadband chirped mirror design and manufacturing techniques for multilayer mirrors have rapidly improved. Broadband chirped mirrors with high reflectivity from 600 to 1000 nm are now commercially available. Using these mirrors inside a Ti:sapphire cavity, the intracavity spectrum becomes broad, and the peak intensity of the pulse inside the cavity becomes so high that substantial white-light generation happens in the Ti:sapphire crystal. As a result, nearly one octave spectrum is generated directly from the oscillator (see Fig. 7) [17, 18, 24]. Locking f_0 without spectral broadening in microstructured fiber has been demonstrated [16, 35, 36]. Recently, the out-of-loop phase noise of such a system has been reported [37, 38]. The RMS phase fluctuation was $0.016\times2\pi$ rad, which is one order of magnitude better than the system with microstructured fiber. The phase-noise power spectral density and the integrated carrier-envelope phase error are shown in Fig. 8.

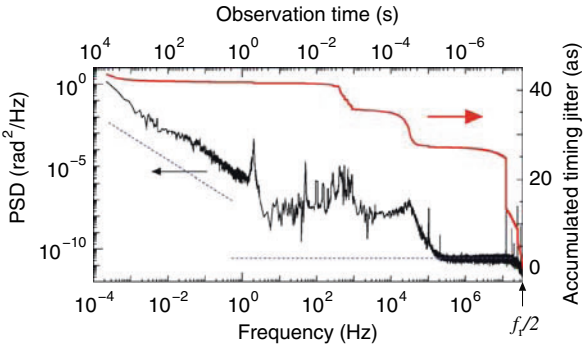

Fig. 8 Out-of-loop two-sided phase-noise power spectral density (PSD) and integrated carrier-envelope phase error. *Dotted line* shows noise floor of the detection system [38]

2.9 Phase Noise After Pulse Selection

When the carrier-envelope offset frequency is f_0, every $R^{\text{th}}(=f_{\text{rep}}/f_0)$ pulse has the same φ. When only such pulses are selected for amplification (pulse picking), an amplified pulse train with constant φ may result. As the phase-locked loop used for controlling and stabilizing φ of the seed oscillator will always have a finite bandwidth and the system used to detect φ will always be subject to noise, φ will fluctuate. Pulse picking can be understood as sampling of the seed oscillator φ and is therefore subject to aliasing.

It is very important to know how the CEP noise properties of the picked pulse sequence relate to those of the seed oscillator and how to estimate the power spectral density (PSD) of CEP fluctuations of the picked pulse train. Integrating this function within appropriate bounds yields the RMS phase error for a given integration time and bandwidth, which is the relevant metric for the quality of the CEP stabilization when considering experiments that are sensitive to φ [39].

From discrete Fourier transform theory, for the pulse train picked by a certain frequency, f'_{rep}, the original noise at higher frequency than f'_{rep} contributes to the noise of picked pulse train, S'_ϕ. The lowest frequency ν_{low} is defined by the inverse of observation time, τ_{obs}:

$$S'_\phi(n\nu_{\text{low}}) = \sum_m S_\phi(mf'_{\text{rep}} + n\nu_{\text{low}}). \tag{6}$$

This equation shows that the phase-noise PSD of the original pulse train is moved blockwise into the Nyquist range of the picked train and stacks up there. As a result, the RMS phase noise after picking the pulse train is identical to the original RMS phase noise. Therefore, the phase noise up to Nyquist frequency ($f_{\text{rep}/2}$) should be taken into account even if the pulse train picked much lower frequency than the original repetition rate for further applications.

3 Phase Stabilization of Intense Few-Cycle Pulses

As is discussed in the previous section, when the CEP frequency of an oscillator has been stabilized to f_0, every Rth pulse has the same phase. Normally in an amplifier system, the repetition rate of the pulse train is reduced to be comparable to the energy storage time of amplifier media. Then it is possible to have a phase-stabilized amplifier system just by seeding with an f_0-stabilized oscillator and adjusting the frequency of the Pockels cell to the fraction of f_0.

3.1 Phase-Stabilized Ti:Sapphire Amplifier System

The first phase-stabilized amplifier based on this concept was realized by Baltuška et al. [40] (Fig. 9). The phase-stabilized amplifier system delivers

~1 mJ, 20 fs, at a 1 kHz repetition rate. The output of the amplifier system was focused into a hollow wave guide and compressed by broadband chirped mirrors. The final output is ~0.5 mJ, 5 fs.

3.2 *Self-Stabilized φ from an Optical Parametric Amplifier*

In the previous sections, only active CEP stabilization schemes are introduced. As an alternative approach to stabilize CEP, difference-frequency generation can be used. When we define the comb frequencies as ν_n, the difference frequency between combs lines of the spectrum becomes

$$\nu_n - \nu_m = (nf_{\text{rep}} + f_0) - (mf_{\text{rep}} + f_0) = (n-m)f_{\text{rep}}, \tag{7}$$

which is independent of f_0. Therefore, φ of the difference frequency is always constant even if φ of the original pulse train is not stabilized. It is demonstrated with a similar system to a ν-to-2ν interferometer [41]. Additionally, phase noise

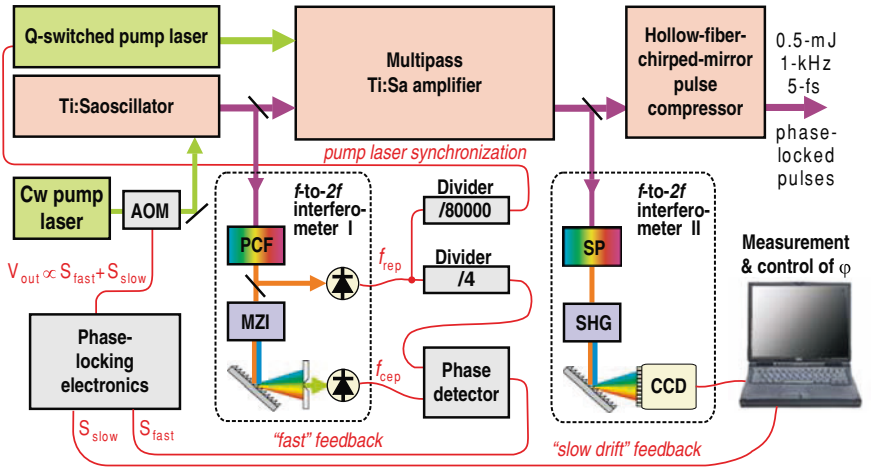

Fig. 9 Schematic of the phase-stabilized amplifier. AOM, acousto-optical modulator; PCF, photonic crystal fiber; MZ, Mach-Zehnder; SP, 2 mm sapphire plate; FDC, frequency-doubling crystal. The φ of the pulses delivered by the Ti:sapphire (Ti:Sa) oscillator is controlled by tracking the ν-to-2ν signal in interferometer I and controlling the pump power through a feedback based on the AOM. Frequency dividers /4 and /80,000 are used to derive, respectively, the reference frequency for the stabilization of $\Delta\varphi$ behind interferometer I and the repetition rate of pulses amplified in a multipass amplifier. The residual drift of φ behind the laser amplifier is monitored with interferometer II and pre-compensated by shifting φ of the oscillator [40]

is canceled by the difference-frequency process; hence the CEP stability may be better than active feedback CEP stabilization [42].

The same principle can be applied for the idler wave of an optical parametric amplifier(OPA) system [43]. The system is based on noncollinear OPA pumped by the second harmonic of the output of a Ti:sapphire regenerative amplifier. The seed pulse is white-light continuum generated by the second harmonic. The experimental phase stability is shown in Fig. 10. The phase stability is $\pi/10$, which is comparable to an active phase stabilization scheme. The idler wave can be compressed down to 4.3 fs with sub-micro-Joule energy [44].

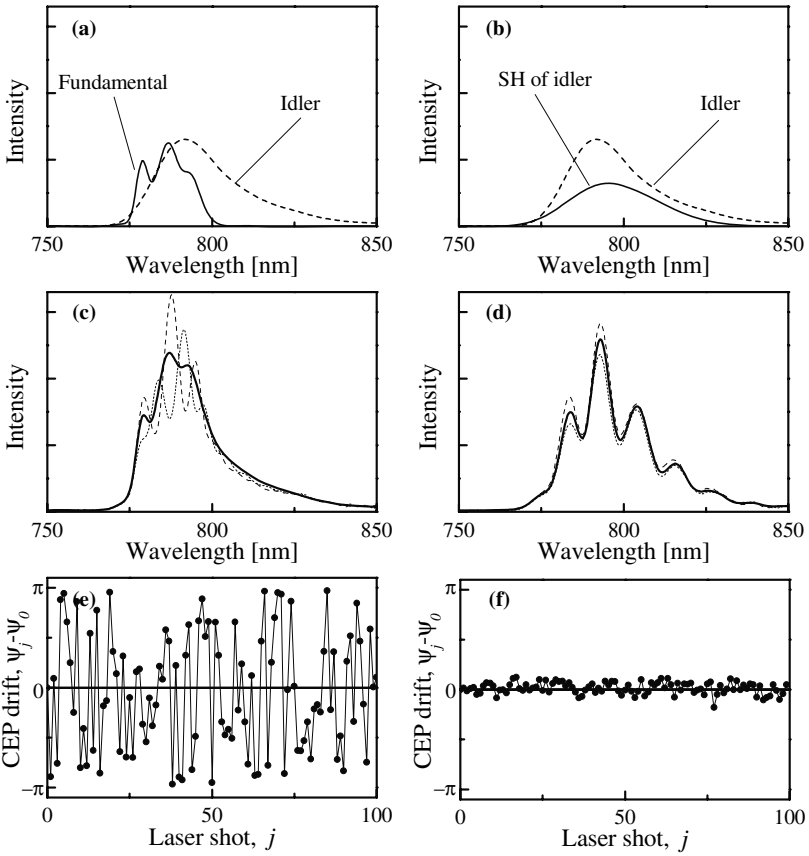

Fig. 10 Experimental results of self-stabilization measurements. (**a**),(**b**) Spectra of residual fundamental, idler, and its SH beams. (**c**),(**d**) *Solid curves* show interference pattern averaged for 1000 shots, while dotted curves represent single-shot interferograms. (**e**),(**f**) Relative CEP jumps wrapped on a $\pm\pi$ interval. Note that the stable phase pattern obtained from the interference of the idler and its second harmonic is a direct proof of CEP self-stabilization [43]

3.3 Cavity Buildup

The ability to stabilize and control the phase evolution of the pulse train produced by mode-locked lasers provides an alternate approach for achieving high-intensity femtosecond pulses. By controlling $\Delta\varphi$, successive pulses in the train can be coherently superimposed in an optical storage cavity [45, 46]. Recently, it has been demonstrated that sufficiently intense fields can be achieved in the buildup cavity to ionize atoms and produce harmonics [47, 48]. This technique has the advantage of not needing an amplification stage and pump laser(s) and operating at the repetition rate of the oscillator; thus the comb structure of the oscillator occurs in the generated harmonics [47]. However, the achieved intensities are much lower so far, which limits how high a harmonic can be generated. The limits on intensity are still under investigation.

4 The Role of φ in Strong-Field Interactions, Measurement of φ

Atoms exposed to high-intensity radiation tend to ionize. If the intensity is sufficiently high and the laser frequency sufficiently low, the laser electric field suppresses the Coulomb potential to an extent that allows the wave function of the most weakly bound electron to overcome the ionization barrier within a fraction of the laser oscillation cycle. This results in a microscopic current that near-adiabatically follows the variation of the optical field. Hence the motion of the detached electron wave packet, and thereby the induced macroscopic polarization, is directly controlled by the strong laser field. Microscopic processes occurring under these conditions tend to become increasingly sensitive to φ as the pulse duration approaches the field oscillation period [11].

Products of strong-field interactions include high-energy free electrons and photons. If the driving laser radiation is confined to a few cycles, the basic characteristics of these products, such as yields, energy, and momentum distribution, are affected by φ. Once fully characterized and with their carrier-envelope phase stabilized, few-cycle light pulses provide a unique means of controlling strong-field interactions. Single-shot measurements drawing on the self-referencing technique [49, 50] and optical parametric amplification [43] will constitute helpful diagnostic tools for phase-sensitive nonlinear optical experiments, with the latter even providing an output (idler) wave with a self-stabilized carrier-envelope phase.

4.1 Optical-Field Ionization of Atoms

Within the quasi-static approximation, the instantaneous optical-field ionization rate (i.e., electronic current) is a function of the instantaneous laser electric field strength. The instantaneous ionization rate is sensitive to φ as shown by

computations for $\varphi = 0$ and $\varphi = \pi/2$), corresponding to cosinusoidal and sinusoidal carrier fields, respectively. Somewhat surprisingly, the time-integrated ionization yield (i.e., the number of ionized atoms or free electrons the intense light pulse leaves behind) has been found to be independent of φ even for a pulse comprising less than two cycles within their full width at intensity half maximum [11], at least in the quasi-static approximation. Recently, an investigation based on the full numerical solution of the time-dependent Schrödinger equation indicated a slight dependence of the integrated ionization yield on φ [51].

The phase sensitivity of the integrated optical-field ionization yield can be substantially enhanced by ionizing atoms with a circularly polarized light wave and resolving the angular distribution of the photoelectrons [52]. If the ionizing few-cycle light is circularly polarized, the direction of the photoelectron momentum determining its drift motion after the laser pulse left the interaction volume depends on φ. Because electron rescattering off the parent ion is prevented in a circularly polarized field, the motion of the electrons subsequent to ionization can be accurately determined from Newton's equations. The final direction of the electron momentum rotates with the electric field vector. For long pulses, electrons are being detached over many optical cycles, and the electron distribution is isotropic because ionization is equally probable for any phase. In the case of a few-cycle pulse, significant ionization occurs only on a sub-cycle timescale because of the sensitive (exponential) dependence of instantaneous ionization rate on the electric field. As a consequence, φ determines the direction of the field at the moment of ionization and hence the direction of the freed electrons.

Figure 11 shows the angular distribution of the strong-field-ionized electrons produced in helium with a 800 nm pulse. The ionization rates were calculated by using a quasi-static model [53], while the electron trajectories were determined

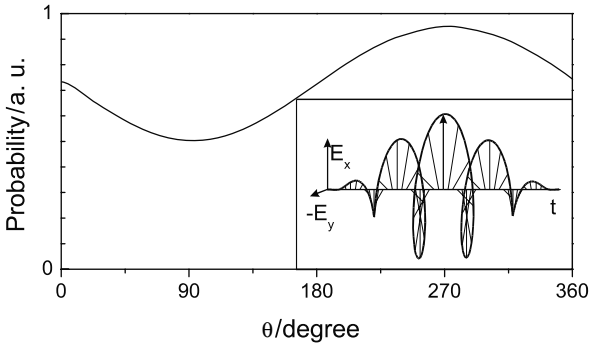

Fig. 11 Angular distribution of electrons freed by a strong circularly polarized 4.8 fs laser pulse ($E(t) = A(t)[\mathbf{e_x}\cos(\omega_L t + \varphi) + \mathbf{e_y}\sin(\omega_l t + \varphi)]$ with a peak field 6×10^{10} V/m^{-1}) in the plane perpendicular to the propagation direction of the pulse for $\varphi = 0$. Inset: Time-dependent electric field vector rotating around the direction of propagation. A change in φ changes the electric field direction at $t = 0$

analytically by integrating the classical equations of motion. For $\varphi = 0$, the angular distribution of the electrons peaks at $\theta = 270°$, a change $\Delta\varphi$ of φ rotates the electron trajectories by the same angle, i.e., shifts the angular distribution shown in Fig. 11 by $\Delta\varphi$ [52]. At moderate peak intensities, where ionization occurs only at the peak of the pulse, amplitude fluctuations do not change the direction of the electrons, which is hence unambiguously related to φ. These results suggest that ionization of atoms by a strong circularly polarized few-cycle light pulse may allow the determination of φ and thus the evolution of the electric and magnetic fields in the light wave packet. First experimental corroboration of these findings was obtained with 6 fs, 800 nm circularly polarized pulses [54].

4.2 Optical-Field-Induced Photoemission from a Metal Surface

Many applications call for linearly polarized light. However, changing of the polarization becomes increasingly difficult for bandwidths approaching the carrier frequency in the few-cycle regime. Hence, techniques for directly measuring φ of linearly polarized pulses are desirable. "Switching off" optical-field ionization for one of the two directions of the electric field vector, as it occurs on a metal surface (photoemission), is an option. In fact, the total number of photoelectrons emitted from a photocathode irradiated with p-polarized few-cycle laser pulses impinging at oblique incidence has been predicted to depend sensitively on φ [55].

This prediction, based on a simple model, has been recently corroborated by simulating photoemission for a metal (jellium) surface using time-dependent density functional theory [56]. The conduction-band electrons of a metal were modeled as a free electron gas confined in a rectangular potential well (jellium). Figure 12 depicts the predicted temporal evolution of the number of ejected

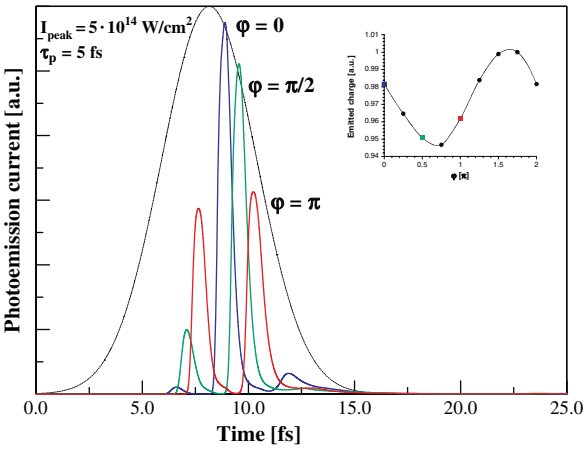

Fig. 12 Calculated instantaneous photocurrent emerging from a metal photocathode (jellium) upon exposure to an intense 5 fs pulse for different values of φ in the tunneling regime of ionization. The time delay between the pulse peak and emission current is caused by the finite time needed by emitted electrons to reach the "detector." Inset: Emitted charge per laser pulse as a function of φ

photoelectrons if a 5 fs, 800 nm p-polarized pulse with a peak intensity of $2 \times 10^{13}\mathrm{W/cm}^2$ impinges at an angle of 45° on the jellium surface. The inset in Fig. 12 reveals that the photocurrent integrated over the temporal extension of the laser pulse appears to remain sensitive to φ, in contrast to the ionization yield of a gaseous medium by the same radiation. The different behavior might be attributed to symmetry breaking due to the surface: only one half of each oscillation cycle contributes to the overall yield. As a result, the number of photoelectrons per laser pulse (readily measurable as a macroscopic current) provides access to φ and thus to the electromagnetic field evolution of linearly polarized few-cycle light pulses.

CEP detection with a metal was experimentally demonstrated by Apolonski et al. [57]. The schematic of the experiment is shown in Fig. 13. The photoemission signal is modulated by the stabilized f_0. As only φ was varying periodically at f_0 in the laser pulse train, the modulation $S(t) = S_0 \cos(2\pi f_0 t + \theta)$ of the photocurrent observed with sub-5 fs pulses clearly indicates the phase sensitivity of the nonlinear photoeffect. As a further check, a pair of thin fused silica wedges were introduced (see Fig. 13) in the laser beam and the variation of $S_0 \cos\theta$ measured

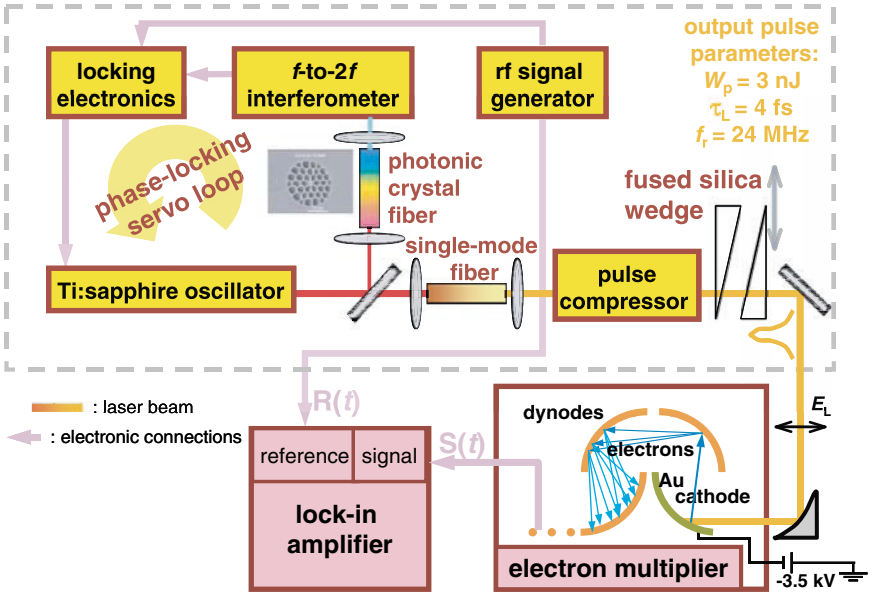

Fig. 13 Schematic of the experiment demonstrating φ sensitivity of photoemission from a metal surface. A 10 fs phase-controlled pulse train passes through a 1.5 mm long single-mode fiber and a dispersive delay line consisting of ultrabroadband chirped mirrors to produce sub-5 fs pulses at a 24 MHz repetition rate. The carrier-envelope phase difference of the pulses can be shifted by known amounts by translation of one of a pair of thin fused silica wedges. They are focused with an off-axis parabola onto a gold photocathode. The multiphoton-induced photocurrent is preamplified by an electron multiplier and selectively amplified by a lock-in amplifier triggered by the reference signal $R(t)$ at $f_{\mathrm{ref}} = 1$ MHz

with the lock-in amplifier as a function of the change ΔL in the path length through the plates. A representative series of measurements are depicted as triangles in Fig. 14. The sinusoidal variation of $S_0 \cos\theta$ can be accounted for by θ varying linearly with the path length, $\theta = \theta_0 + \pi(\Delta L/L)$. L_{fit} was evaluated as $L_{\text{fit,A}} = 20.3(+2.0/-1.5)$ μm and $L_{\text{fit,B}} = 19.3(+2.8/-1.9)$ μm from least-square fits (lines in Fig. 14) to the measured data obtained in two independent measurements depicted in panels (a) and (b) of Fig. 14, respectively. The experimental conditions and modeling of the experiments are described in the caption of Fig. 14.

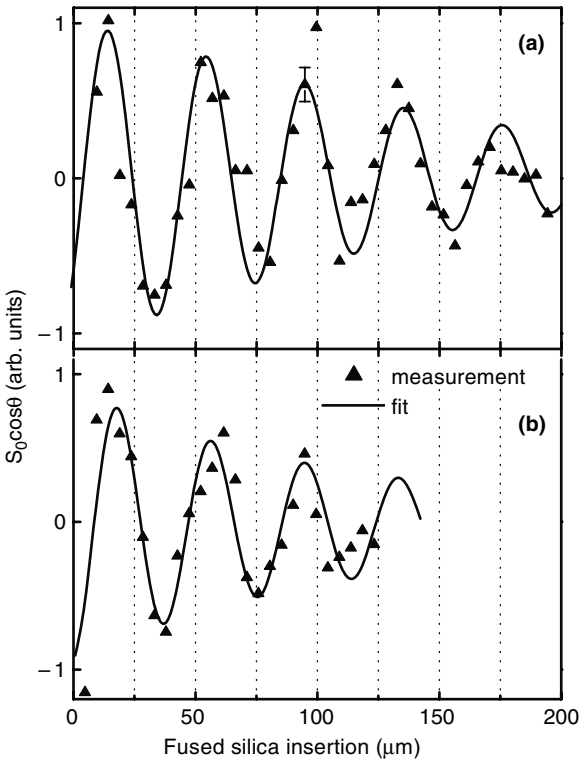

Fig. 14 In-phase component, $S_0 \cos\theta$, of the modulation of the photocurrent, $S(t)$, as a function of the change in path length through the fused silica glass wedges shown in Fig. 13. (**a**),(**b**) Photoemission signal recorded with pulses of a peak intensity of $I_p \approx 2 \times 10^{12}$ W/cm^2 and a duration (full width at half maximum) of $\tau_L = 4.5$ fs and 4.0 fs, respectively. The experimental data (*triangles*) are corrected for a constant (nonoscillating) phase offset of electronic origin. The lines are obtained by modeling the decrease of the photocurrent using the power law $S_0 \sim I_p^x$ with $x = 3.0$ and taking into account dispersive pulse broadening. Although the pulses broaden only by a few percentage upon traveling a distance of a few tens of micrometers in fused silica, the resulting decrease in their peak intensity is sufficient to notably decrease the photocurrent owing to the rapid I_p^x scaling. S_0 decays faster in (**b**) simply because the shorter pulse broadens more rapidly upon propagation

4.3 Generation of High-Order Harmonics and Attosecond Pulses

Atoms exposed to intense, linearly polarized femtosecond optical radiation emit coherent, high-order harmonics of the incident laser light [58, 59]. In a semiclassical approach, the microscopic origin of high-order harmonic radiation can be understood and described in terms of three elementary processes [52, 60]. An atom is ionized via tunneling ionization in the optical field and the freed electron gains energy from the laser pulse. As the direction of the linearly polarized electric field vector is reversed, the electron is driven back to the proximity of its parent ion and, with some probability, can radiatively recombine into its original ground state. This recombination gives rise to the emission of a high-energy photon in the extreme ultraviolet and soft X-ray (XUV) region. The dynamics outlined here take place within one oscillation cycle of the driving laser and is repeated each half laser cycle, forming a train of bursts for a multicycle driver laser pulse. The spectrum of this quasi-periodic emission is discrete, consisting of high-order odd harmonics of the pump laser radiation. Filtering the highest-frequency, shortest-wavelength part of the harmonic spectrum has been predicted to result in a train of bursts of attosecond duration [61]. This prediction has been recently confirmed experimentally [62].

Light pulses in the few-cycle regime benefit the process of ultrafast XUV pulse generation in several respects. They are capable of generating harmonics extending into the water window [63, 64] and enhance the harmonic photon yield as compared to longer-duration drivers. Most importantly, they are able to generate isolated XUV pulses of sub-femtosecond duration [65, 66]. Nevertheless, the time structure of the sub-femtosecond XUV emission is sensitive to the carrier-envelope phase.

If the driving laser pulses have a random φ, only a few percentage of them are able to generate a comparatively energetic XUV pulse with a clean sub-femtosecondtemporal structure. The overwhelming majority of laser pulses is unable to make a useful contribution to attosecond pump-probe measurements or even severely compromise temporal resolution. With φ stabilized, intense few-cycle laser pulses reproducibly and efficiently produce attosecond XUV pulses for time-resolved atomic spectroscopy.

High harmonic generation using a CEP-stabilized few-cycle pulse was demonstrated by Baltuška et al. [9] Coherent soft X-rays were generated by gently focusing the phase-stabilized 5 fs pulses (described in Section 3) into a 2 mm long sample of neon gas. Figure 15 shows a series of soft X-ray spectra produced under the conditions described in the caption for Fig. 15 for different values of φ of the 5 fs pump pulses. For $\varphi = \varphi_0$ (Fig. 15b), a broad structureless continuum appears in the cutoff region ($\hbar\omega > 120\,\mathrm{eV}$). Notably, with a change of the phase, the continuous spectral distribution of the cutoff radiation gradually transforms into discrete harmonic peaks, with the maximum modulation depth appearing for the settings of $\varphi = \varphi_0 \pm \pi/2$. This behavior is in agreement

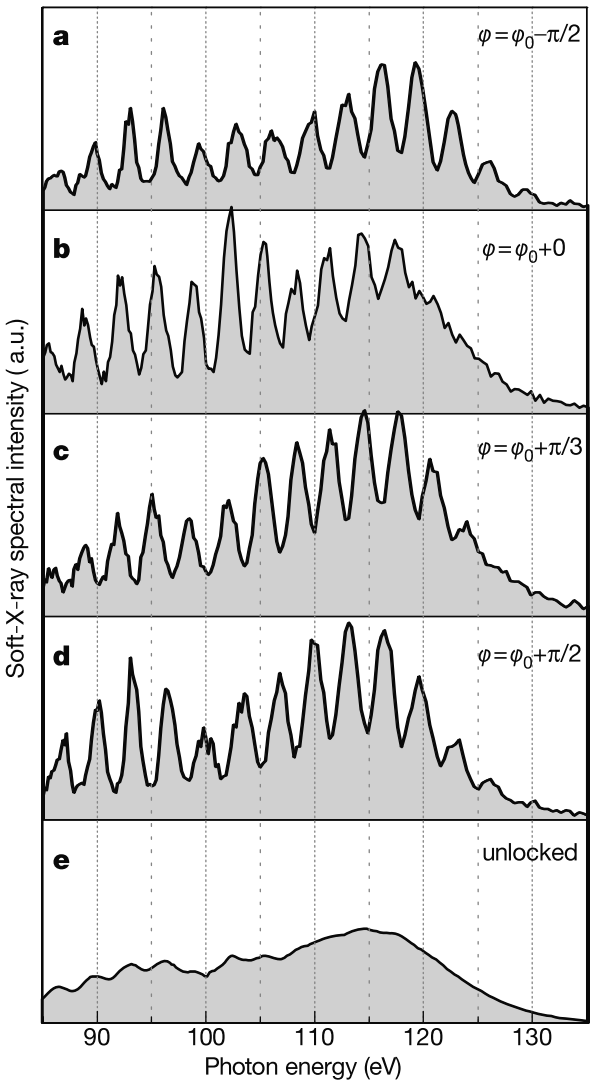

Fig. 15 Measured spectral intensity of few-cycle-driven soft X-ray emission from ionizing atoms. (**a**), (**b**), (**c**), (**d**), Data obtained with phase-stabilized pulses for different φ settings. (**e**) Spectrum measured without phase stabilization. The coherent radiation was generated by gently focusing 5 fs, 0.2 mJ laser pulses into a 2 mm long 160 mbar neon gas. The on-axis peak intensity of the pump pulse was estimated to be 7×10^{14} W/cm^2

with the intuitive picture presented above and allows us to identify φ_0 as zero with a residual ambiguity of $n\pi$, where n is an integer. This ambiguity in the determination of φ relates to the inversion symmetry of the interaction with the atomic gas medium. In fact, a π-shift in φ results in no change of the light waveform other than reversing the direction of the electromagnetic field vectors. This phase flip does not modify the intensity of the radiated X-ray photons, but it becomes observable in photoelectron experiments explained in Section 4.5.

4.4 Attosecond Pulse Generation and Application

When the generated soft X-ray in the cutoff region is isolated, an XUV attosecond pulse is obtained. Using the XUV attosecond pulse, the photoelectron spectrum change due to electric field was measured with attosecond time resolution [10, 67]. The momentum of electron change Δp by electric field $E_{\mathrm{L}}(t)$ is

$$\Delta p(t) = e\int_{t}^{\infty} E_{\mathrm{L}}(t')\mathrm{d}t' = eA_{\mathrm{L}}(t), \tag{8}$$

where e is the electron charge and $A_{\mathrm{L}}(t)$ is the vector potential in the Coulomb gauge. As a result, the photoelectron spectrum ejected from an atom by XUV light (here it is an isolated attosecond pulse) shifts because of the vector potential.

The experimental system is shown in Fig. 16. The generated XUV and the laser beams collinearly propagate, and the inner part (~3 mm) of the beam is

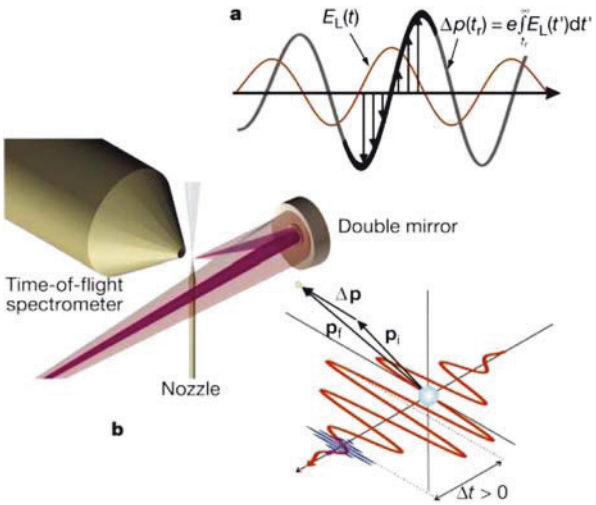

Fig. 16 Attosecond two-color sampling technique for probing electron emission from atoms. An extreme ultraviolet or X-ray pulse excites the atomic target and induces electron emission. A delayed probe light pulse transfers a momentum Δp to the ejected electron after its release. p_i and p_f represent the electron's initial and final momentum, respectively. (**a**) The transferred momentum sensitively depends on the phase and amplitude of the light field vector $E_{\mathrm{L}}(t)$ at the instant of release resulting in a time-to-energy mapping on an attosecond timescale. For processes lasting less than a light cycle, the oscillating light field constitutes a sub-femtosecond probe, whereas processes lasting longer than a cycle are sampled by the amplitude envelope of the laser pulse. In both cases, a sequence of light-affected electron energy spectra is recorded at different delays, Δt, from which the time evolution of electron emission is reconstructed. (**b**) The experiments use a 97 eV, sub-femtosecond soft X-ray pulse for excitation and a 750 nm (1.6 eV), sub-7 fs few-cycle light pulse for probing electron emission. The two pulses are collinearly focused into a krypton gas target by a two-component mirror similar to that used in Ref. [66]. The kinetic energy distribution of the ejected photon and Auger electrons was measured by the time-of-flight spectrometer

filtered with a zirconium filter (transmitting the XUV pulse and blocking the visible pulse). The inner (XUV) and the outer parts (visible) are delayed with a two-component Mo/Si broadband multilayer mirror (radius of curvature = −70 mm) placed 2.5 m downstream from the source and focused into a neon gas jet. The ejected photoelectron is detected by a time-of-flight spectrometer.

Figure 17 summarizes representative streaked neon photoelectron spectra recorded with the XUV and laser pulse impinging with a fixed relative timing set in the XUV generation process. For a cosine driver waveform ($\varphi = 0$), cutoff radiation (filtered by the Mo/Si multilayer) is predicted to be emitted in a single bunch at the zero transition of $E_L(t)$ following the pulse peak. The photoelectrons knocked off in the direction in the peak electric field at this instant should gain the maximum increase of their momentum and energy. Figure 17 corroborates this prediction. The clear upshift is consistent with the XUV burst coinciding with the zero transition of the laser electric field. Possible satellites would appear at the

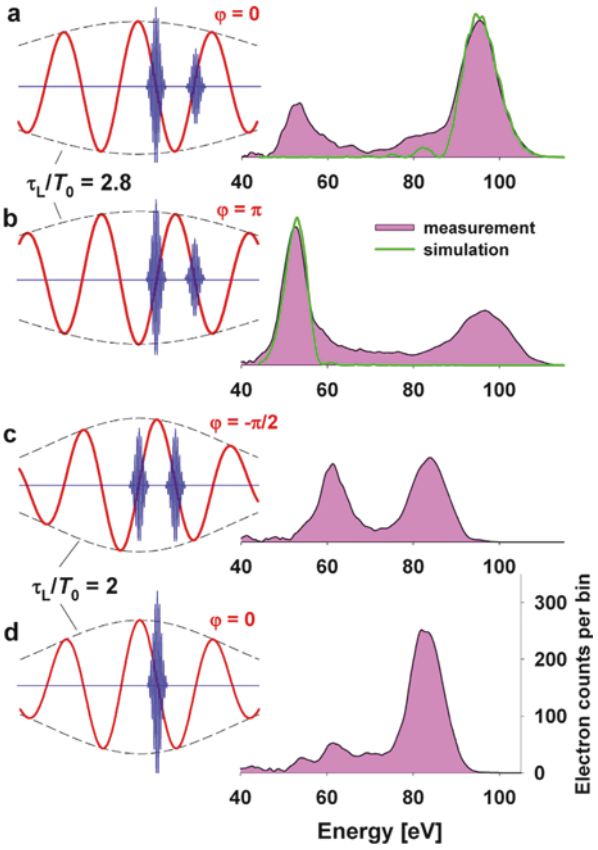

Fig. 17 Streaked photoelectron spectra recorded at a fixed delay of the probe laser light. Energy distribution of photoelectrons emitted from neon atoms excited by a sub-fs XUV pulse carried at a photon energy of $\hbar\omega_{XUV} < 93.5$ eV (selected by the Mo/Si mirror).

adjacent zero transitions of $E_L(t)$ and suffer an energy downshift. The absence of a downshifted spectral peak of substantial intensity indicates a clean single sub-femtosecond pulse generation. With the phase adjusted to yield a sine waveform ($\phi = \pi/2$), cutoff emission is predicted to come in twin pulses (Fig. 17c). The double-peaked streaked spectrum (Fig. 17c) clearly reflects this time structure. High-energy XUV photons are now distributed in two bursts, each of which is less than half as intense as the isolated burst produced by the cosine waveform (Fig. 17d). These measurements demonstrate how light waveform control allows shaping XUV emission on a sub-femtosecond timescale.

The series of photoelectron spectra obtained by scanning the delay between the visible pulse and the XUV pulse is shown in Fig. 18. Since the shift of the photoelectron spectrum is proportional to the vector potential of the electric field, the field oscillation is clearly observed. The delay uncertainty of the measurement is estimated as 250 as.

4.5 Carrier-Envelope Phase Measurement with Above Threshold Ionization

Above threshold ionization (ATI) means that an atom absorbs more photons than necessary for ionization [52], which results in the generation of photoelectrons with kinetic energy. It is an extremely nonlinear process (8–10th order) to ionize rare-gas atoms with visible pulses. Therefore, the phenomenon is extremely sensitive to the peak-field strength of the optical pulses. Since the peak-field strength of few-cycle pulses strongly depends on φ, the spectra of the photoelectrons from ATI can be ideal for determining φ. Measurement of φ with ATI has been demonstrated by Paulus et al. [8]. The experimental setup is shown in Fig. 19. By using a stereo detection system for the photoelectron, it is possible to measure the phase without $\pm\pi$ ambiguity. The measured ATI spectra corresponding to different φ are shown in Fig. 20. In particular, the high-energy parts of the photoelectron spectra show clear dependence on the CEP. By using this system, Lindner et al. directly observed the Gouy phase shift [68].

Fig. 17 (continued) The photoelectron spectrum peaks at $W_0 = \hbar\omega_{XUV} - W_b \sim 72\,eV$ in the absence of $E_L(t)$, where $W_b = 21.5\,V$ is the binding energy of the most weakly bound valence electrons in Ne. The spectrally filtered cutoff XUV bursts and the 5 fs, 750 nm driver laser pulses are depicted by blue and red lines, respectively. (**a**), (**b**) Streaked spectra obtained with "cosine" and "−cosine" laser pulses of a normalized duration of $\tau_L/T_0 = 2.8$ and of a peak electric field of $E_0 = 140$ MV/cm. The green lines on the right-hand side depict spectra computed with an XUV burst derived from the measured asymmetric XUV radiation filtered by the mirror under the assumption of zero spectral phase. The satellite pulse is not modeled in this way because the corresponding modulation of the spectrum is not considered in the calculation. The difference in broadening of the up- and down-shifted spectral features appears to be a consequence of the quadratic temporal frequency sweep resulting from the asymmetric spectral distribution of the XUV burst. (**c**, **d**) Streaked spectra obtained with "sine" and "cosine" laser pulses characterized by $\tau_L/T_0 = 2$ and $E_0 = 75$ MV/cm

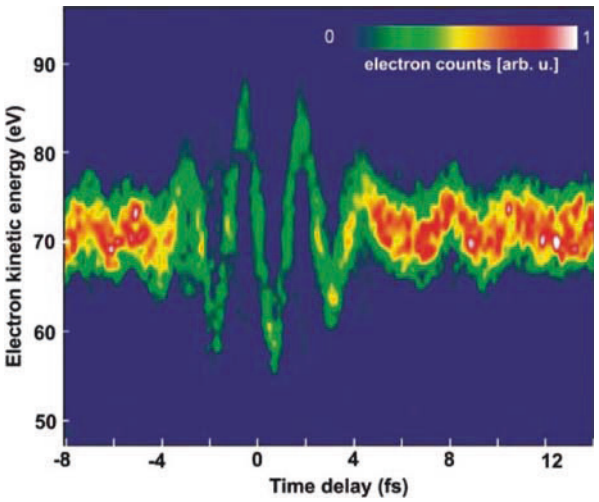

Fig. 18 A series of kinetic energy spectra of electrons detached by a 250 as, 93 eV XUV pulse from neon atoms in the presence of an intense 5 fs, 750 nm laser field, in false-color representation. The delay of the XUV probe is varied in steps of 200 as, and each spectrum is accumulated over 100 s. The detected electrons are ejected along the laser electric field vector with a mean initial kinetic energy of $p_i^2/2m \sim \hbar\omega_{\mathrm{XUV}} - W_{\mathrm{b}} = 93\,\mathrm{eV} - 21.5\,\mathrm{eV} = 71.5\,\mathrm{eV}$. The energy shift of the electrons versus the timing of the XUV trigger pulse that launches the probing electrons directly represents $A_{\mathrm{L}}(t)$

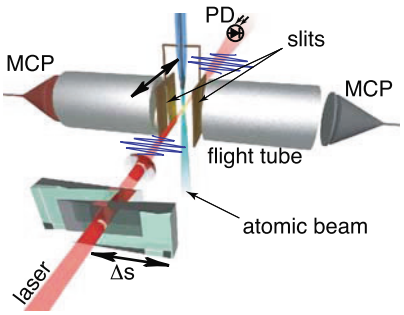

Fig. 19 "Stereo-ATI" spectrometer. Two opposing electrically and magnetically shielded time-of-flight spectrometers are mounted in an ultrahigh vacuum apparatus. Xenon atoms fed in through a nozzle from the top are ionized in the focus of a few-cycle laser beam. The focal length is 250 mm (the lens shown in the sketch is in reality a concave mirror), and the pulse energy is 20 μJ. The laser is linearly polarized parallel to the flight tubes. Note that the laser field changes sign while propagating through the focus. Slits with a width of 250 μm are used to discriminate electrons created outside the laser focus region. A photodiode (PD) and microchannel plates (MCP) detect the laser pulses and photoelectrons, respectively

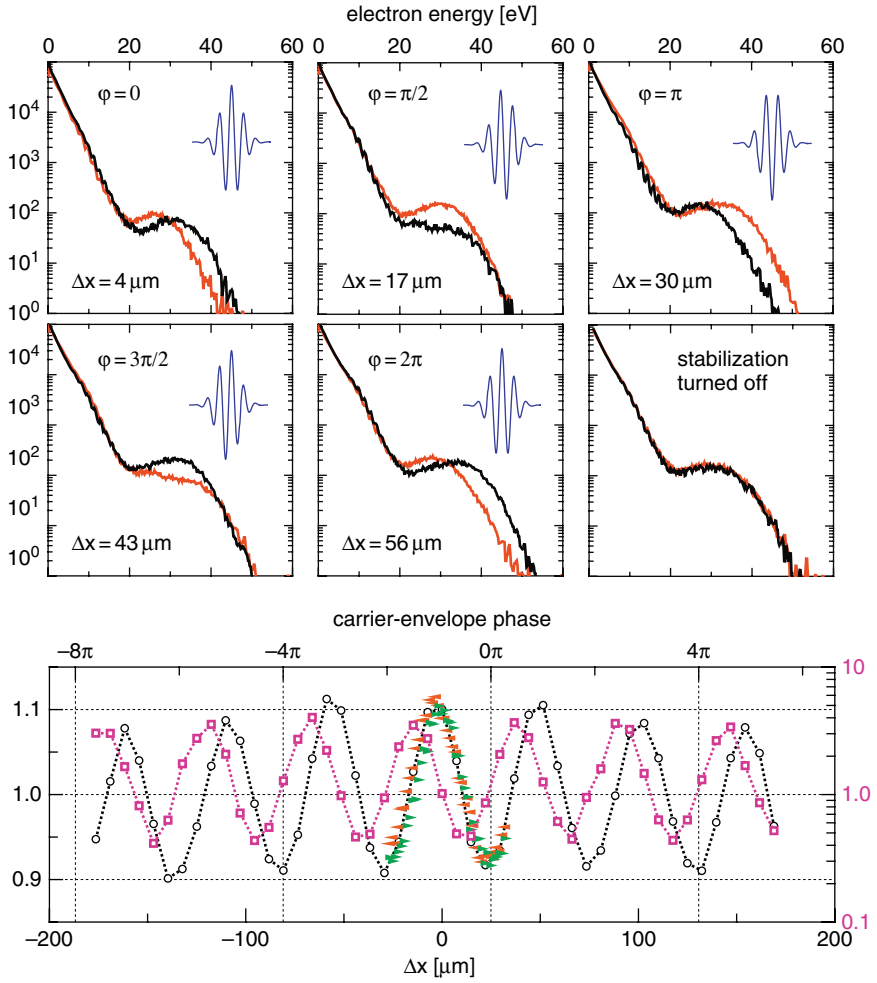

Fig. 20 (*Upper panels*) Photoelectron spectra for different φ controlled by fine movement of one of the wedges in Fig. 19. Δx indicates the added glass. Black curves correspond to emission to the right (positive direction); red curves to the opposite direction. The inset shows the deduced corresponding real-time variation of the electric field. Without phase stabilization, identical spectra were measured to the left and right as expected. (*Lower panel*) Left–right ratio of the total electron yield (*circles*) and high-energy electrons (*squares*) as a function of glass thickness Δx added or subtracted by moving one of the wedges. $\Delta x = 0$ corresponds to optimal dispersion compensation, i.e., the shortest pulses. Maximal left/right ratio for the total yield does not coincide with that for high-energy electrons. Note the different scales for low- and high-energy electrons. The upper x-scale indicates the φ of the pulse, as deduced from comparison with theory

5 Summary and Outlook

Clearly, φ is an important new parameter that can be explored in high-field experiments. Recent progress has shown that it can be "tamed" inside mode-locked oscillators and preserved through amplification. Many of the first experiments in these directions have been described in this chapter.

In addition to high-field experiments, control of the evolution of φ has already had a big impact on optical frequency metrology, the measurement of absolute optical frequencies referenced directly to cesium. Prior to the introduction of mode-locked lasers, absolute optical frequency measurement required the use of complex phase-coherent frequency chains [69, 70]. Although the potential of mode-locked lasers was recognized more than 20 years ago [71], only with recent improvements in the technology have significant measurements with mode-locked lasers been made. The enormous simplification made possible by self-referencing and related techniques [2, 72, 73] has led to an explosion of measurements and significant improvement in precision. For a review of optical frequency metrology with mode-locked lasers, see Ref. [74].

Closely related to optical frequency metrology has been the development of optical atomic clocks based on mode-locked lasers. An optical atomic clock uses an optical frequency transition as its "oscillator" instead of a microwave transition used in traditional atomic clocks. This significantly reduces the uncertainty in a given averaging time because of large frequency. The first demonstration using a trapped single Hg^+ ion yielded stability results comparable to the best cesium clocks [75]. An optical clock has also been demonstrated using I_2, which could lead to transportable clocks [76].

Remarkable advances have resulted from the synergy between precision optical techniques used in metrology and parallel progress in the generation of high-intensity pulses. Cross-fertilization between these seemingly disparate areas of research has resulted in truly remarkable strides over the past 5 years [77].

References

1. L. Xu, C. Spielmann, A. Poppe, T. Brabec, F. Krausz, T. W. Hänsch: Opt. Lett. **21**, 2008 (1996)
2. D. J. Jones, S. A. Diddams, J. K. Ranka, A. Stentz, R. S. Windeler, J. L. Hall, S. T. Cundiff: Science **288**, 635 (2000)
3. A. Apolonski, A. Poppe, G. Tempea, C. Spielmann, T. Udem, R. Holzwarth, T. W. Hänsch, F. Krausz: Phys. Rev. Lett. **85**, 740 (2000)
4. A. Poppe, R. Holzwarth, A. Apolonski, G. Tempea, C. Spielmann, T. W. Hänsch, F. Krausz: Appl. Phys. B **72**, 977 (2001)
5. F. W. Helbing, G. Steinmeyer, U. Keller, R. S. Windeler, J. Stenger, H. R. Telle: Opt. Lett. **27**, 194 (2002)
6. T. M. Fortier, J. Ye, S. T. Cundiff, R. S. Windeler: Opt. Lett. **27**, 445 (2002)
7. T. M. Fortier, D. J. Jones, J. Ye, S. T. Cundiff, R. S. Windeler: Opt. Lett. **27**, 1436 (2002)

8. G. G. Paulus, F. Lindner, H. Walther, A. Baltuška, E. Goulielmakis, M. Lezius, F. Krausz: Phys. Rev. Lett. **91**, 253004 (2003)
9. A. Baltuška, T. Udem, M. Uiberacker, M. Hentschel, E. Goulielmakis, C. Gohle, R. Holzwarth, V. S. Yakovlev, A. Scrinzi, T. W. Hänsch, F. Krausz: Nature **421**, 611 (2003)
10. R. Kienberger, E. Gooulielmakis, M. Uiberacker, A. Baltuška, V. S. Yakovlev, F. Bammer, A. Scrinzi, T. Westerwalbesloh, U. Kleineberg, U. Heinzmann, M. Drescher, F. Krausz: Nature **427**, 817 (2004)
11. T. Brabec, F. Krausz: Rev. Mod. Phys. **72** 545–591 (2000)
12. T. Udem, J. Reichert, R. Holzwarth, T. W. Hänsch Phys. Rev. Lett. **82**, 3568 (1999)
13. J. Reichert, R. Holzwarth, T. Udem, T. W. Hänsch: Opt. Commun. **172**, 59 (1999)
14. S. T Cundiff: J. Phys. D. **35** R43 (2002).
15. H. R. Telle, G. Steinmeyer, A. E. Dunlop, J. Stenger, D. H. Sutter, U. Keller: Appl. Phys. B **69**, 327 (1999)
16. T. M. Ramond, S. A. Diddams, L. Hollberg, A. Bartels: Opt. Lett. **27**, 1842 (2002)
17. U. Morgner, F. X. Kärtner, S. H. Cho, Y. Chen, H. A. Haus, J. G. Fujimoto, E. P. Ippen, V. Scheuer, G. Angelow, T. Tschudi: Opt. Lett. **24**, 411 (1999)
18. D. H. Sutter, G. Steinmeyer, L. Gallmann, N. Matuschek, F. Morier-Genoud, U. Keller, V. Scheuer, G. Angelow, T. Tschudi: Opt. Lett. **24**, 631 (1999)
19. J. K. Ranka, R. S. Windeler, A. J. Stentz: Opt. Lett. **25**, 25 (2000)
20. J. K. Ranka, R. S. Windeler, A. J. Stentz: Opt. Lett. **25**, 796 (2000)
21. T. A. Birks, W. J. Wadsworth, P. S. Russell: Opt. Lett. **25**, 1415 (2000)
22. M. T. Asaki, C. P. Huang, D. Garvey, J. P. Zhou, H. C. Kapteyn, M. M. Murnane: Opt. Lett. **18**, 977 (1993)
23. K. F. Kwong, D. Yankelevich, K. C. Chu, J. P. Heritage, A. Dienes: Opt. Lett. **18**, 558 (1993)
24. H. A. Haus, E. P. Ippen: Opt. Lett. **26**, 1654-1656 (2001)
25. P. M. Goorjian, S. T. Cundiff: Opt. Lett. **29**, 1363 (2004)
26. K. W. Holman, R. J. Jones, A. Marian, S. T. Cundiff, J. Ye: Opt. Lett. **28**, 851 (2003)
27. M. J. Ablowitz, B. Ilan, S. T. Cundiff: Opt. Lett. **29**, 1808 (2004)
28. R. Atanasov, A. Hache, J. L. P. Hughes, H. M. van Driel, J. E. Sipe: Phys. Rev. Lett. **76**, 1703 (1996)
29. A. Hache, Y. Kostoulas, R. Atanasov, J. L. P. Hughes, J. E. Sipe, H. M. van Driel: Phys. Rev. Lett. **78**, 306 (1997)
30. T. M. Fortier, P. A. Roos, D. J. Jones, S. T. Cundiff, R. D. R. Bhat, J. E. Sipe: Phys. Rev. Lett. **92**, 147403 (2004)
31. P. A. Roos, X. Li, R. P. Smith, J. A. Pipis, T. M. Fortier, S. T. Cundiff: Opt. Lett. **30**, 735 (2005)
32. R. Ell, U. Morgner, F. X. Kärtner, J. G. Fujimoto, E. P. Ippen, V. Scheuer, G. Angelow, T. Tschudi, M. J. Lederer, A. Boiko, B. Luther-Davies: Opt. Lett. **26**, 373 (2001)
33. U. Morgner, R. Ell, G. Metzler, T. R. Schibli, F. X. Kärtner, J. G. Fujimoto, H. A. Haus, and E. P. Ippen: Phys. Rev. Lett. **86**, 5462 (2001)
34. T. Fuji, A. Unterhuber, V. S. Yakovlev, G. Tempea, A. Stingl, F. Krausz, W. Drexler: Appl. Phys. B **77**, 125 (2003)
35. T. M. Fortier, D. J. Jones, S. T. Cundiff: Opt. Lett. **28**, 2198 (2003)
36. L. Matos, O. Kuzucu, T. R. Schibli, J. Kim, E. P. Ippen, D. Kleppner, F. X. Kärtner: Opt. Lett. **29**, 1683 (2004)
37. T. Fuji, J. Rauschenberger, A. Apolonski, V. S. Yakovlev, G. Tempea, F. Krausz, T. Udem, C. Gohle, T. W. Hänsch, W. Lehnert M. Scherer: Opt. Lett. **30**, 332 (2005)
38. T. Fuji, J. Rauschenberger, C. Gohle, A. Apolonski, T. Udem, V. S. Yakovlev, G. Tempea, T. W. Hänsch, F. Krausz: New J. Phys. **7**, 116 (2005)
39. C. Gohle, J. Rauschenberger, T. Fuji, T. Udem, A. Apolonski, F. Krausz, T. W. Hänsch, Opt. Lett. **30**, 2487 (2005)

40. A. Baltuška, M. Uiberacker, E. Gouliemakis, R. Kienberger, V. S. Yakovlev, T. Uddem, T. W. Hänsch, F. Krausz: IEEE J. Sel. Top. Quantum Electron. **9**, 972 (2003)
41. T. Fuji, A. Apolonski, F. Krausz: Opt. Lett. **29**, 632 (2004)
42. M. Zimmermann, C. Gohle, R. Holzwarth, T. Udem T. W. Hänsch: Opt. Lett. **29**, 310 (2004)
43. A. Baltuška, T. Fuji, T. Kobayashi: Phys. Rev. Lett. **88**, 133901 (2002)
44. S. Adachi, P. Kumbhakar, T. Kobayashi: Opt. Lett. **29**, 1150 (2004)
45. R. J. Jones, J. Ye: Opt. Lett. **27**, 1848 (2002)
46. R. J. Jones, J. Ye: Opt. Lett. **28**, 2812 (2004)
47. R. J. Jones, K. D. Moll, M. J. Thorpe, J. Ye: Phys. Rev. Lett. **94**, 193201 (2005)
48. C. Gohle, T. Udem, M. Herrmann, J. Rauschenberger, R. Holzwarth, H. A. Schuessler, F. Krausz, T. W. Hänsch: Nature **436**, 234 (2005)
49. M. Mehendale, S. A. Mitchell, J. L. Likforman, D. M. Vielleneuve, P. B. Corkum: Opt. Lett. **25**, 1672 (2000)
50. M. Kakehata, H. Takada, Y. Kobabyashi, K. Torizuka, Y. Fujihara, T. Homma, H. Takahashi: Opt. Lett. **26**, 1436 (2001)
51. I. P. Christov: Opt. Lett. **24**, 1425 (1999)
52. P. Dietrich, F. Krausz, P. B. Corkum: Opt. Lett. **25**, 16 (2000)
53. P. B. Corkum: Phys. Rev. Lett. **71**, 1994 (1993)
54. G. G. Paulus, F. Grasbon, H. Walther, P. Villoresi, M. Nisoli, S. Stagira, E. Priori, S. De Silvestri: Nature **414**, 182 (2001)
55. A. Poppe, A. Fürbach, Ch. Spielmann, F. Krausz: in *Trends in Optics and Photonics, OSA Proceedings Series Volume 28*, Optical Society of America, Washington D. C. pp. 31–35 (1999)
56. C. Lemell, X. -M. Tong, F. Krausz, J. Burgdörfer1: Phys. Rev. Lett. **90**, 076403 (2003)
57. A. Apolonski, P. Dombi, G. G. Paulus, M. Kakehata, R. Holzwarth, T. Udem, C. Lemell, K. Torizuka, J. Burgdörfer, T. W. Hänsch, F. Krausz: Phys. Rev. Lett. **92**, 073902 (2004)
58. A. L'Huillier, P. Balcou: Phys. Rev. Lett. **70**, 774 (1993)
59. J. J. Macklin, J. D. Kmetec, C. L. Gordon III: Phys. Rev. Lett. **70**, 766 (1993)
60. M. Lewenstein, P. Balcou, M. Yu. Ivanov, A. L'Huillier, P. B. Corkum: Phys. Rev. A **49**, 2117 (1994)
61. P. Antoine, A. L'Huillier, M. Lewenstein: Phys. Rev. Lett. **77**, 1234 (1996)
62. P. M. Paul, E. S. Toma, P. Berger, G. Mullot, F. Auge, Ph. Balcou, H. G. Muller, and P. Agostini: Science **292**, 1689 (2001); N. A. Papadogiannis, B. Witzel , C. Kalpouzos, D. Charalambidis: Phys. Rev. Lett. **83**, 4289 (1999)
63. Ch. Spielmann, N. H. Burnett, S. Sartania, R. Koppitsch, M. Schnürer, C. Kan, M. Lenzner, P. Wobrauschek, F. Krausz: Science **278**, 661 (1997)
64. Z. Chang, A. Rundquist, H. Wang, M. Murnane, H. C. Kapteyn: Phys. Rev. Lett. **79**, 2967 (1997)
65. M. Drescher, M. Hentschel, R. Kienberger, G. Tempea, Ch. Spielmann, G. A. Reider, P. B. Corkum, F. Krausz: Science **291**, 1923 (2001)
66. M. Hentschel, R. Kienberger, Ch. Spielmann, G. A. Reider, N. Milosevic, T. Brabec, P. Corkum, U. Heinzmann, M. Drescher, F. Krausz: Nature **414**, 509 (2001)
67. E. Gooulielmakis, M. Uiberacker, R. Kienberger, A. Baltuška, V. S. Yakovlev, A. Scrinzi, T. Westerwalbesloh, U. Kleineberg, U. Heinzmann, M. Drescher, F. Krausz: Sceince **305**, 1267 (2004)
68. F. Lindener, G. G. Paulus, H. Walther, A. Baltuška, E. Gouliemakis, M. Lezius, F. Krausz: Phys. Rev. Lett. **92**, 113001 (2004)
69. K. M. Evenson, J. S. Wells, F. R. Petersen, B. L. Danielson, G. W. Day: Appl. Phys. Lett. **22**, 192 (1973)
70. H. Schnatz, B. Lipphardt, J. Helmcke, F. Riehle, G. Zinner: Phys. Rev. Lett. **76**, 18 (1996)
71. J. N. Eckstein, A. I. Ferguson, T. W. Hänsch: Phys. Rev. Lett. **40**, 847 (1978)

72. S. A. Diddams, D. J. Jones, J. Ye, S. T. Cundiff, J. L. Hall, J. K. Ranka, R. S. Windeler, R. Holzwarth, T. Udem, T. W. Hänsch: Phys. Rev. Lett. **84**, 5102 (2000)
73. R. Holzwarth, T. Udem, T. W. Hänsch, J. C. Knight, W. J. Wadsworth, P. S. J. Russell: Phys. Rev. Lett. **85**, 2264 (2000)
74. S. T. Cundiff, J. Ye, J. L. Hall: Rev. Sci. Instrum. **72**, 3746 (2001)
75. S. A. Diddams, T. Udem, J. C. Bergquist, E. A. Curtis, R. E. Drullinger, L. Hollberg, W. M. Itano, W. D. Lee, C. W. Oates, K. R. Vogel, D. J. Wineland: Science **293**, 825 (2001)
76. J. Ye, L. S. Ma, J. L. Hall: Phys. Rev. Lett. **87**, art. 270801 (2001)
77. J. Ye, S. T. Cundiff, eds. : *Femtosecond Optical Frequency Comb Technology* (Springer, New York, 2004)

Free-Electron Lasers – High-Intensity X-Ray Sources

J. Feldhaus and B. Sonntag

1 Introduction

Extending the range of lasers into the X-ray regime will open up many new and exciting areas of basic and applied X-ray research [1,2,3,4,5,6]. Free-electron lasers (FEL) based on the self-amplified spontaneous emission (SASE) are expected to generate laser-like X-ray radiation within the next years [6,7,8,9,10]. The principle of operation of a SASE FEL is schematically depicted in Fig. 1. Electron bunches with extremely high charge density, small energy spread and low emittance pass at GeV energies through the periodic magnetic field of a long undulator. The spontaneous emission of the transversely accelerated electrons builds up an intense electromagnetic wave, which acts back on the electron bunches leading to a longitudinal density modulation. This micro-bunching causes the electrons to emit coherently giving rise to an exponential growth of the power of the radiation. Optical elements, hard to manufacture for the X-ray regime, are not required since saturation can be reached in a single pass.

2 The Motion of a Relativistic Electron Through an Undulator Under the Influence of an Electromagnetic Wave

An electron moving with relativistic velocity $\vec{v}_e$ along the axis (z) of an undulator is forced to oscillate in the transverse direction (x). Energy can be transferred from the electron to a superimposed radiation field if the time average of the scalar product $\vec{E} \cdot \vec{v}_e$ is positive along the undulator as depicted in Fig. 2. This occurs close to the undulator resonance where the electron falls

J. Feldhaus
Hamburger Synchrotronstrahlungslabor HASYLAB, Deutsches
Elektronen-Synchrotron DESY, Notkestrasse 85, 22603 Hamburg, Germany
e-mail: josef.feldhaus@desy.de

T. Brabec (ed.), *Strong Field Laser Physics*,
DOI: 10.1007/978-0-387-34755-4_5,

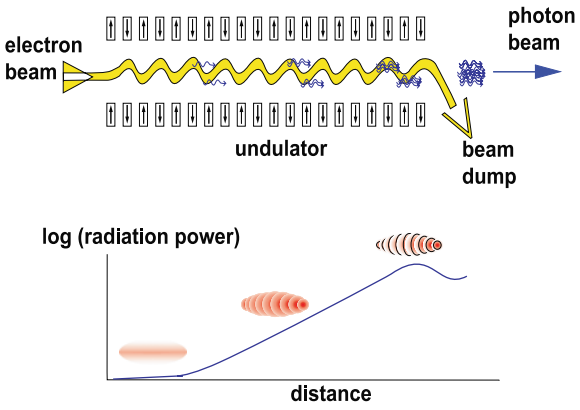

Fig. 1 Sketch of the self-amplification of spontaneous emission (SASE) in an undulator. In the *lower part* of the figure the longitudinal density modulation (microbunching) of the electron bunch is shown together with the resulting exponential growth of the radiation power along the undulator

back by one wavelength λ during one undulator period λ_u (see e.g. [10]). Let us assume an undulator field

$$\vec{B} = (0, B_0 \sin k_u z, 0), \tag{1}$$

with $k_u = 2\pi/\lambda_u$, and an electromagnetic wave

$$\vec{E} = (E_0 \cos(kz - \omega t), 0, 0), \tag{2}$$

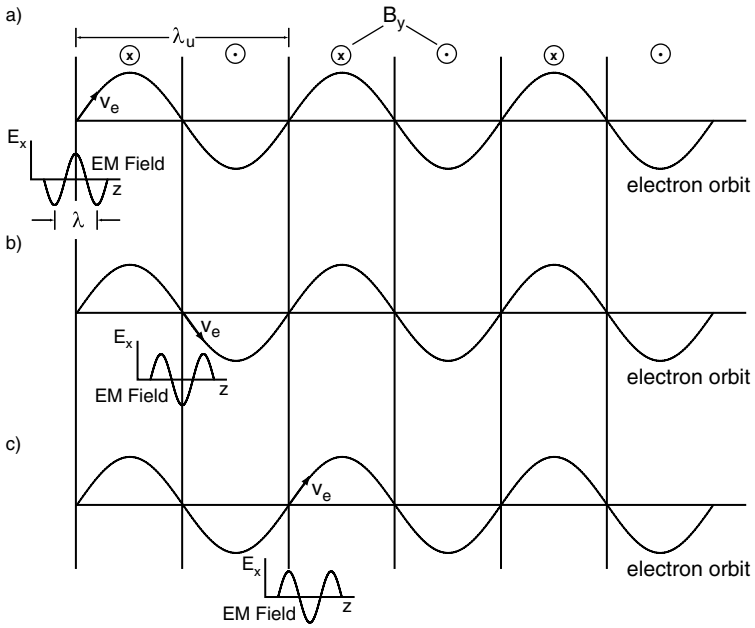

Fig. 2 The electron orbit in a periodic undulator field (undulator period λ_u). An electron and the field of an electromagnetic wave (wavelength λ) are shown at (*a*) $z = 0$, (*b*) $z = \lambda_u/2$, and (*c*) $z = \lambda_u$

with wavenumber $k = 2\pi/\lambda$. The motion of the relativistic electron obeys the following equations:

$$\frac{\mathrm{d}(\gamma\vec{\beta})}{\mathrm{d}t} = -\frac{e}{mc}(\vec{E} + c\vec{\beta} \times \vec{B}), \tag{3}$$

$$\frac{\mathrm{d}\gamma}{\mathrm{d}t} = -\frac{e}{mc}\vec{\beta}\vec{E}, \tag{4}$$

with $\gamma = \frac{E_e}{mc^2}$ and $\vec{\beta} = \frac{\vec{v_e}}{c}$. E_e is the electron energy. In a normal undulator and in the low gain regime of a FEL $\left|\vec{E}\right| << c\left|\vec{\beta} \times \vec{B}\right|$, we can approximate Eq. (3) by

$$\gamma\frac{\mathrm{d}\vec{\beta}}{\mathrm{d}t} = -\frac{e}{mc}\vec{\beta} \times \vec{B}, \tag{5}$$

yielding

$$\beta_x = \frac{e\lambda_u B_0}{2\pi\gamma mc}\cos k_u z. \tag{6}$$

Inserting Eq. (6) into Eq. (4) results in

$$\frac{\mathrm{d}\gamma}{\mathrm{d}t} = -\frac{eE_0K}{2\gamma mc}\{\cos[(k_u + k)z - \omega t] + \cos[(k_u - k)z + \omega t]\}, \tag{7}$$

with the undulator parameter

$$K = \frac{e\lambda_u B_0}{2\pi mc}. \tag{8}$$

Optimum energy transfer from the electron to the electromagnetic wave is obtained for

$$(k_u + k)z - \omega t = 0. \tag{9}$$

For a highly relativistic electron Eq. (9) is equivalent to the synchronisation condition

$$\lambda = \frac{\lambda_u}{2\gamma^2}\left(1 + \frac{K^2}{2}\right) \tag{10}$$

that also can be derived directly from Fig. 2. Note that in this case the second term in Eq. (7) oscillates rapidly along the undulator and averages out.

3 Microbunching

Comparing Eq. (7) and Eq. (4) we find that the interaction of the electron with the magnetic field of the undulator and the electromagnetic field is equivalent to an interaction with an effective axial electric field:

$$E_z^{\text{eff}} = \frac{eB_0E_0\lambda_u}{4\pi mc\gamma\beta_z}\cos[(k_u + k)z - \omega t]. \tag{11}$$

The corresponding "ponderomotive potential"

$$V_{\text{pond}} = \frac{e^2B_0E_0\lambda_u}{4\pi mc\gamma\beta_z(k_u + k)}\sin[(k_u + k)z - \omega t] \tag{12}$$

is propagating like a wave along the undulator axis. The synchronisation condition given in Eq. (10) states the requirement that for optimal energy exchange the axial velocity of the electron is equal to the phase velocity of the ponderomotive potential. The longitudinal motion of the electron in the ponderomotive potential can be described by a pendulum equation

$$\frac{d^2\Phi}{dz^2} = -\frac{2e^2B_0E_0}{(mc\gamma)^2}, \tag{13}$$

with Φ the phase of the electron relative to the ponderomotive potential and γ given by the synchronisation condition, Eq. (10). Figure 3 shows the result of a numerical solution of the pendulum equation for an extended electron bunch [11]. The electrons are initially spread uniformly over $-\pi < \Phi < \pi$ (left part of Fig. 3). This distribution is deformed along the undulator until most electrons are nearly vertically placed at saturation. A simulation of the real-space development of microbunching of the electron beam along the undulator is shown in Fig. 4 [3,4].

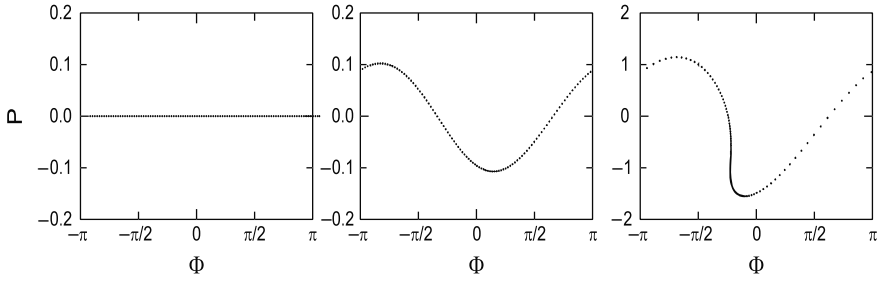

Fig. 3 Longitudinal phase space distribution of the electrons at (*left to right*) the entrance, in the middle, and close to the end (near saturation) of the undulator

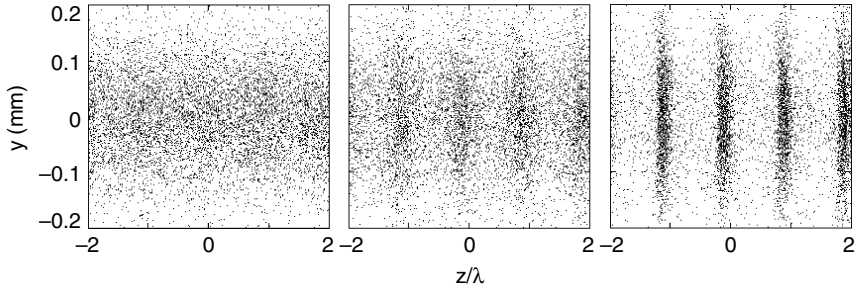

Fig. 4 Example of the development of microbunching of the electron beam along the undulator. The electron density is represented by the density of the *dots* (*left*: at the undulator entrance, *middle*: in the middle of the exponential growth regime, *right*: at the undulator exit, i.e. for saturation)

The electrons concentrated within a microbunch emit coherently. Since the power of the emitted radiation is proportional to the square of the number of electrons within a microbunch, the microbunching is driving the exponential growth of the radiation power shown in Fig. 1.

Beyond saturation the microbunching is destroyed and the radiation power drops. In the one-dimensional description assumed so far, the exponential growth of the radiation intensity is given by

$$I(z) = I(0)\mathrm{e}^{z/L_\mathrm{g}}, \tag{14}$$

with the gain length

$$L_\mathrm{g} = \frac{\lambda_\mathrm{u}}{4\pi\sqrt{3}\rho} \tag{15}$$

and the FEL parameter

$$\rho = \left\{ \frac{I}{I_\mathrm{A}} \frac{\gamma\lambda^2}{16\pi^2\sigma_\mathrm{t}^2} \frac{K^2}{\left(1+\frac{K^2}{2}\right)^2} \left[J_0\left(\frac{K^2}{4+2K^2}\right) - J_1\left(\frac{K^2}{4+2K^2}\right) \right]^2 \right\}^{1/3}. \tag{16}$$

I is the peak current of the electron bunch, $I_\mathrm{A} = 17.045$ A is the Alfvén current, $J_{0,1}$ are Bessel functions, and σ_t is the transverse root-mean-square size of the electron bunch. The one-dimensional linear description of the FEL process is based on the assumption that the amplitude of the electromagnetic wave changes slowly on the scale of the undulator period, i.e. $L_\mathrm{g} >> \lambda_\mathrm{u}$, which requires

$$\rho << 1. \tag{17}$$

Saturation is reached at the saturation length

$$L_{\mathrm{sat}} = 4\pi L_{\mathrm{g}}. \tag{18}$$

The fraction of the electron beam power P_{B} converted into radiation at saturation, P_{sat}, is approximately given by the FEL parameter ρ:

$$P_{\mathrm{sat}} = \rho P_{\mathrm{B}}. \tag{19}$$

For high gain the one-dimensional theory requires for the relative energy spread

$$\frac{\Delta\gamma}{\gamma} < \rho. \tag{20}$$

The finite energy spread, angular divergence, and transverse size of the electron beam, the diffraction of the electromagnetic wave, and space charge effects cause an increase of the gain length. This increase can be kept small if the emittance of the electron beam is smaller than that of the electromagnetic wave:

$$\varepsilon < \frac{\lambda}{4\pi}. \tag{21}$$

This ensures optimum overlap of electron and photon beam along the undulator, provided that the electron beam is perfectly aligned on the undulator axis.

4 Start-Up from the Spontaneous Emission

At present there are no X-ray sources capable of providing a monochromatic coherent photon beam of sufficient intensity and spatial and temporal parameters well matched to those of the electron beam to be used as an input seed radiation. Therefore X-ray FELs are based on the amplification of the noisy spontaneous emission generated at the entrance of the undulator. In this case a large number of transverse radiation modes are excited in the entrance section of the undulator. The modes experience very different amplifications along the undulator, and if saturation is reached at the end of the undulator only a limited number of modes are expected to survive, leading to a high degree of transverse (or spatial) coherence. In the linear gain regime, i.e. before saturation is reached, the statistical nature of the photon beam manifests itself in very spiky spectra in the frequency and the time domain [9]. For an electron bunch of sufficient duration T, with $\rho\omega T >> 1$, i.e. the electron bunch is much longer than the slippage of the radiation with respect to the electrons, the spectral width of the radiation, $\Delta\omega$, close to saturation is approximately

$$\Delta\omega \approx \rho\omega. \tag{22}$$

The characteristic width of the spikes, $\Delta\omega_{\text{spike}}$, is given by

$$\Delta\omega_{\text{spike}} \approx \frac{1}{T}. \tag{23}$$

From Eqs. (22), (23) the number of spikes can be estimated

$$n_{\text{spike}} \approx \rho\omega T. \tag{24}$$

The radiation consists of a superposition of wave trains, or modes, of coherence length

$$l_{\text{c}} \approx \tau_{\text{c}} c, \tag{25}$$

with the coherence time

$$\tau_{\text{c}} \approx \frac{1}{\rho\omega}, \tag{26}$$

Which are randomly distributed over the length of the electron bunch. Based on the assumption that the amplified spontaneous emission is completely random, the probability P of the radiation energy per pulse, W, can be approximated by the gamma distribution [9]

$$P(W) = \frac{M^M W^{M-1}}{\Gamma(M)\langle W\rangle^M} \exp\left(-M\frac{W}{\langle W\rangle}\right). \tag{27}$$

The parameter M can be interpreted as the number of modes contributing to the radiation. Figure 5 shows the probability distribution of the pulse energy measured at a wavelength of 109 nm during the first tests of the SASE FEL at the TESLA Test Facility at DESY, Hamburg [12]. The experimental result can

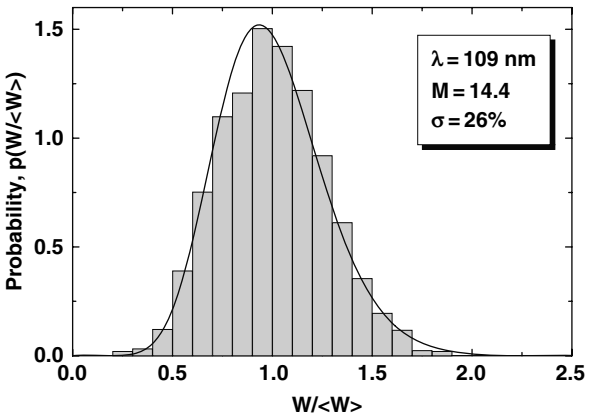

Fig. 5 Probability distribution of the radiation pulse energy E at 109 nm wavelength measured in the linear gain regime of the SASE FEL at DESY [12]

Table 1 Parameters of the VUV FEL FLASH at DESY

Parameter	Unit	Test facility (2000–2002)	User facility (expected)
Electron beam			
Beam energy	MeV	182–272	~300–1000
Energy spread (RMS)	MeV	0.3 ± 0.2	1
Bunch length (FWHM)	μm	~300	<120
Bunch diameter (FWHM)	μm	240 ± 70	160
Normalised emittance	mm mrad	$(6 \pm 3)\pi$	2π
Electron bunch charge	nC	1	1
Peak electron current	A	400 ± 200	2500
Number of bunches per train		1–1800	1–7200
Bunch separation	ns	444 or 1000	1000 (>111)
Repetition rate of pulse trains	Hz	1	up to 10
Undulator			
Undulator period λ_u	mm	27.3	27.3
Peak magnetic field B_0	T	0.46	0.46
Undulator gap	mm	12	12
Effective undulator length	m	13.5	27
Photon beam			
Wavelength λ	nm	180–80	6.4[b]
Spectral bandwidth	%	0.6[a]	0.36[b]
Beam size at undulator exit (FWHM)	μm	~250[a]	190[b]
Beam divergence (FWHM)	μrad	~300[a]	24[b]
Pulse duration (FWHM)	fs	~1000[a]	200[b]
Peak power	GW	~0.05[a]	2.8[b]
Pulse energy	mJ	~0.05[a]	0.56[b]
Number of photons per pulse		$\sim 2\times10^{13}$[a]	2×10^{13}[b]

[a] Experimental values for wavelengths close to 100 nm.
[b] Design values for 1 GeV electron beam energy.

be well approximated by a gamma distribution with $M = 14.4$. The parameters of the FEL are given in Table 1.

The stochastic nature of the SASE process is also reflected in the spectral distribution. The Fourier transform of the random intensity distribution along the radiation pulse results in narrow spikes in the spectral domain whose widths $\Delta\omega$ are given by the pulse duration $\Delta\omega \simeq 2\pi/\tau_{\mathrm{rad}}$. The upper panel of Fig. 6 shows the spectral distribution of a single radiation pulse measured at maximum electron bunch compression, corresponding to an average number of $M = 2.6$ modes. The pulse duration $\tau_{\mathrm{rad}} \simeq 50$ fs derived from the spectral line width is consistent with that estimated from the statistical intensity fluctuations and the measured gain length [13]. The lower panel of Fig. 6 shows the spectral distribution of a single radiation pulse for a somewhat weaker electron bunch compression. The pulse duration is now $\tau_{\mathrm{rad}} \simeq 100$ fs which is reflected in the narrower line widths and the larger number of modes, $M = 6$. The average spectral envelope $\Delta\omega_{\mathrm{avg}}$ is not much changed since it is determined by the

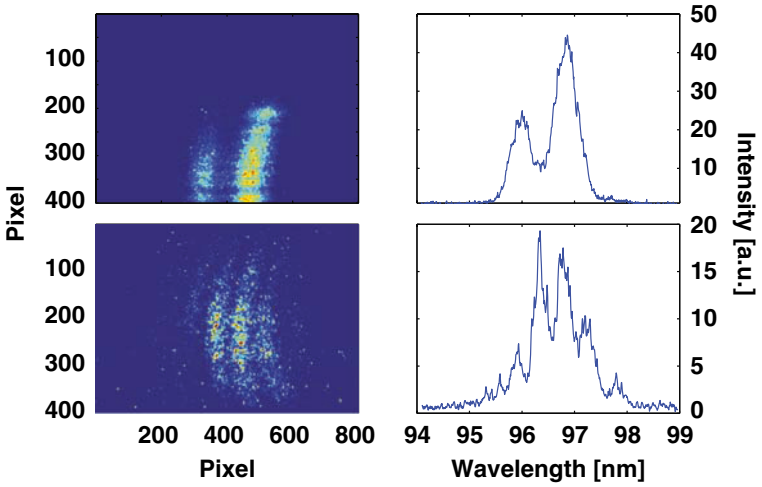

Fig. 6 Spectra of single FEL pulses. The CCD image of the horizontally dispersed FEL radiation is shown in a *false colour code* on the *left*. The spectral profiles scanned along the horizontal centre line of the CCD image are shown on the *right*. The *upper spectrum* is that of a short pulse (~50 fs) with an average of $M = 2.6$ modes, the *lower spectrum* belongs to a longer pulse (~100 fs) with $M = 6$ [13]

coherence length. However, the measured value of $\Delta\omega_{\mathrm{avg}}$ is approximately twice as large as that estimated from the gain length, and the profile is also distinctly asymmetric for the shortest pulses. More recent FEL simulations are in full agreement with these results [14]. They use a more realistic electron distribution based on the so-called start-to-end simulations of the electron bunch from the electron gun to the entrance of the undulator, revealing strong space charge effects which result in a large correlated energy spread.

A realistic, quantitative description of a SASE FEL is only possible by means of three-dimensional time-dependent numerical simulation codes. Several such codes have been developed over the last years (see e.g. [9,11]). They allow one to study the influence of all relevant electron beam parameters such as charge density, emittance, energy spread, the axial and transverse profiles of the electron bunch, and the finite pulse duration and may even include the interaction with the walls of the vacuum chamber and undulator field errors and misalignment. These codes have provided the basis for stringent tests of existing FELs and for optimising the parameters of future facilities.

5 Soft X-Ray SASE FEL Facilities

Proof-of-principle experiments on a short-wavelength SASE FEL were successfully performed at the TESLA Test Facility (TTF) at DESY [12,13,15]. Saturated SASE operation was achieved in the vacuum ultraviolet at wavelengths

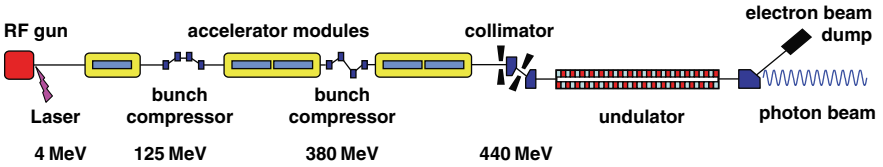

Fig. 7 Schematic layout of the FLASH facility at DESY. The electron beam energies indicated in the *bottom line* have been used during the commissioning of the facility at ~30 nm wavelength

between 80 and 120 nm. The GW radiation pulses were used for first exploratory experiments on clusters [16] and solids [17] demonstrating the unique properties of this new radiation source. Subsequently this FEL has been completely rebuilt and converted into the first FEL user facility for VUV and soft X-ray radiation, now called FLASH (Free electron LASer in Hamburg). The schematic layout of FLASH is shown in Fig. 7.

A low-emittance electron beam is generated in a laser-driven radiofrequency (RF) electron gun. Subsequently the electrons are accelerated in superconducting cavities operated at 1.3 GHz. In order to achieve high peak current the electron bunches are longitudinally compressed in bunch compressors. At FLASH this is done in two steps in order to preserve the high electron beam quality. The undulator, providing the periodic magnetic field for the generation of the FEL photon beam, is a planar permanent magnet structure with a fixed gap. Quadrupoles are mounted between the 4.5 m long undulator modules in order to keep the electron beam diameter small over the whole length of the undulator. Various devices for the diagnosis of the electron and photon beam are installed along the FEL and behind the undulator exit [18,19].

The superconducting cavities of the accelerator imply a special timing of the electron beam and thus of the FEL pulses; 1.3 GHz radiofrequency (RF) power from 5 and 10 MW clystrons fills the cavities with a strong electromagnetic field for up to ~1 ms at a typical repetition rate of 1, 5, or 10 Hz. Electron bunches can be accelerated only during these high-field periods. In principle the electron bunch structure can be rather flexible within a RF burst, up to a certain maximum total charge determined by the cryogenic power available for cooling the cavities to a temperature of 2 K. The FEL pulse structure of the VUV FEL FLASH at DESY at maximum current is displayed in Fig. 8.

The commissioning of the VUV-FEL has started in September 2004 at an electron beam energy of ~450 MeV. First lasing at 32 nm wavelength was observed in January 2005 with pulse energies around 10 μJ and pulse durations

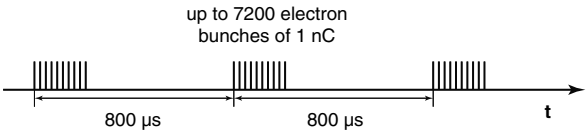

Fig. 8 The pulse structure of FLASH running at maximum current

of ~25 fs [20]. This is the shortest wavelength that has so far been reached by a SASE FEL. The FEL beam has been transported to the new experimental hall where it can be switched between five experimental stations. High-quality X-ray optics is used to guide the radiation beam to the experiment and focus it on the sample. The layout of the experimental area is shown in Fig. 9. Since August 2005 approximately 50% of the time has been scheduled for scientific experiments, the remaining time is mainly used for improving the performance of the facility towards routine operation in an extended wavelength range.

It will be possible to tune the photon energy of the FLASH FEL radiation from approximately 20 to 200 eV. Figure 10 compares the peak brilliance of the VUV FEL FLASH at DESY with that of the X-ray FELs proposed at DESY

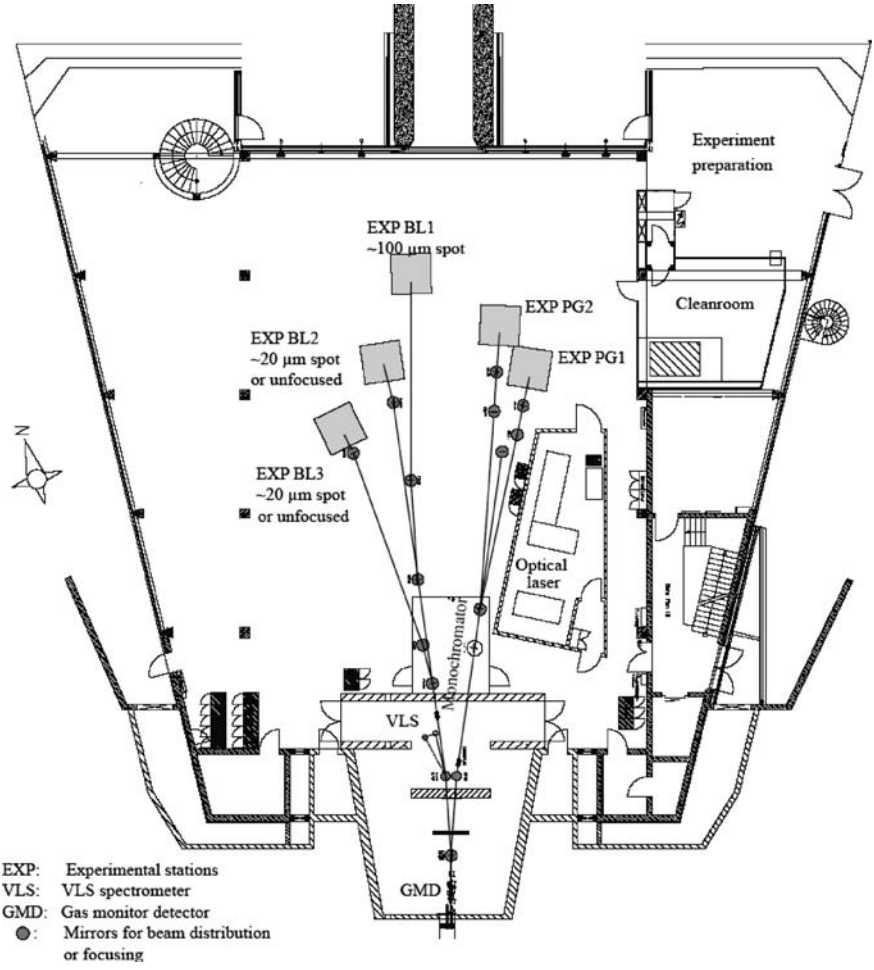

Fig. 9 The layout of the FLASH experimental hall at DESY

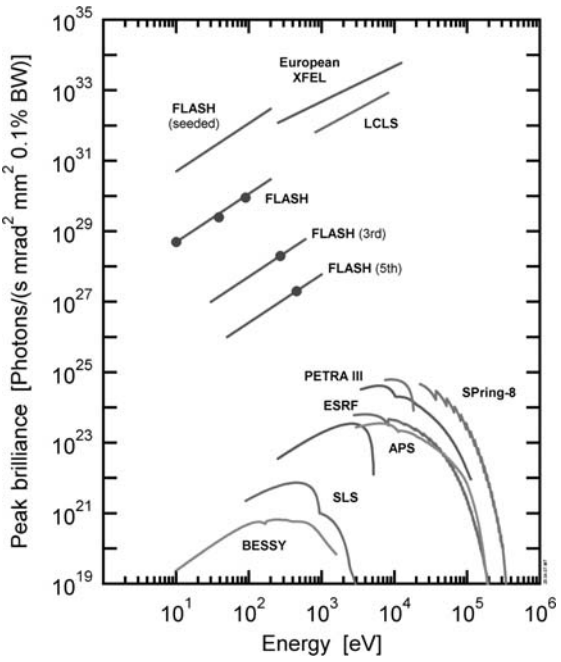

Fig. 10 Peak brilliance of proposed X-ray FELs and present undulator sources

[3,4] and Stanford (LCLS) [21], the spontaneous radiation emitted by these FEL undulators, and the undulator radiation of present third generation synchrotron radiation sources. The parameters of the electron beam, the undulator, and the photon beam are summarised in Table 1.

6 Hard X-Ray SASE Free-Electron Lasers

Free-electron lasers based on SASE are excellent candidates for extremely bright sources emitting femtosecond pulses of coherent hard X-ray radiation. The main components, such as the laser-driven RF electron gun, the superconducting linear accelerator, the bunch compressors, and the undulators will be very similar to those discussed for the soft X-ray FELs. To reach photon energies of 10 keV the electron energies have to be raised up to ~20 GeV and the length of the undulators increased to the order of 100 m.

There is growing excitement worldwide for the development of such unique X-ray sources. Several X-ray FELs have been proposed in Asia, Europe, and the United States. The best source for the current status of FEL projects is http://sbfel3.ucsb.edu/www/vl_fel.html. The first FEL for hard X-rays with wavelengths down to 1.5 Å will be the Linac Coherent Light Source (LCLS)

which is under construction at Stanford. It will use part of the existing LINAC at the Stanford Linear Accelerator Center [21]. The European XFEL in Hamburg will employ a superconducting linear accelerator, the construction of which is expected to start in 2008 [22]. This facility is designed as a multi-user facility with initially three different SASE FELs between which the electron beam can be switched. The photon energy of each FEL can be tuned by varying the undulator gap. The XFEL design parameters are collected in Table 2. The peak brilliance of LCLS and XFEL are included in Fig. 10. The commissioning of the two facilities is scheduled for 2009 and 2014, respectively.

A fundamental limit for the shortest obtainable wavelength is imposed by the growth of the uncorrelated energy spread of the electron beam due to the quantum fluctuation of the undulator radiation. The minimum wavelength is approximately

$$\lambda_{\min} \approx \frac{4\pi\varepsilon_{\mathrm{n}}[\mathrm{mm\ mrad}]}{\sqrt{I[\mathrm{kA}]L_{\mathrm{u}}[\mathrm{m}]}}, \tag{28}$$

where ε_{n} is the electron beam emittance normalised to the electron energy, I the peak current, and L_{u} the undulator length [9].

Table 2 Design parameters of the European X-FEL

Performance goals for the electron beam	
Beam energy range	10–20 GeV
Emittance (norm.)	1.4 mrad mm
Bunch charge	1 nC
Bunch length (1σ)	80 fs
Energy spread (uncorrelated)	<2.5 MeV rms
Main Linac	
Acc. gradient @ 20 GeV	23 MV/m
Linac length	Approx. 1.5 km
Beam current (max)	5 mA
Beam pulse length	0.65 ms
# Bunches p. pulse (max)	3250
Bunch spacing (min)	200 ns
Repetition rate	10 Hz
Avg. beam power (max)	650 kW
Performance goals for SASE FEL radiation	
Photon energy	15–0.2 keV
Wavelength	0.08–6.4 nm
Peak power	10–20 GW
Average power	40–80 W
Number photon per pulse	$0.5–4 \times 10^{12}$
Peak brilliance	$2.5–0.08 \times 10^{33}$*
Average brilliance	$1–0.03 \times 10^{25}$*

* In units of photons/(s mrad^2 mm^2 0.1% bw)

7 Seeding with Coherent Radiation

Since the process of amplification in a SASE FEL starts from noise the output radiation consists of a number of independent wave packets. Consequently the temporal structure and the spectral distribution of the radiation display a large number of uncorrelated sharp spikes (see Eqs. (22), (23), (24), (25), (26)) [23,9].

Figure 11 shows the spectrum calculated for 6.4 nm wavelength radiation from FLASH at DESY. For many scientific applications the removal of this random spiking is essential. It would be much more elegant if the FEL process could be controlled in such a way that Fourier-limited radiation pulses with adjustable duration could be produced. This is possible if the FEL is used not in the SASE mode (where it amplifies the shot noise in the electron beam), but rather as an amplifier seeded by coherent radiation. Since seed pulses of sufficiently intense, coherent radiation are presently not available at very short wavelengths, two different routes to achieve coherent seeding have been investigated.

One is to produce the coherent seed radiation in a SASE FEL tuned to the same wavelength [24]. This concept, also called self-seeding, has the advantage that it is independent of any external radiation source (which must be very stable, continuously tunable, operate at short wavelengths, and must be precisely matched to the electron beam in space and time, synchronised to <100 fs). The schematic layout of a self-seeded FEL for the soft X-ray region is shown in Fig. 12.

The first undulator, a short SASE FEL operating in the linear gain regime, produces radiation pulses with the characteristic features of SASE (Fig. 11) at a power level approximately three orders of magnitude below saturation in order not to spoil the electron beam quality. The electron beam is then sent through a magnetic chicane which is designed such that it destroys the density modulation introduced in the first undulator and delays the electron beam by the same

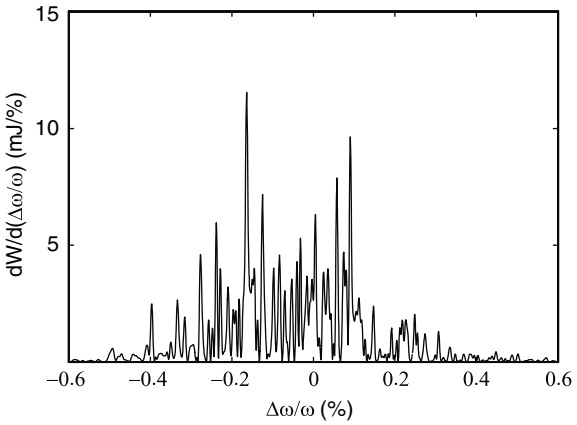

Fig. 11 Spectrum of a single radiation pulse close to saturation for a Gaussian axial profile of the electron beam

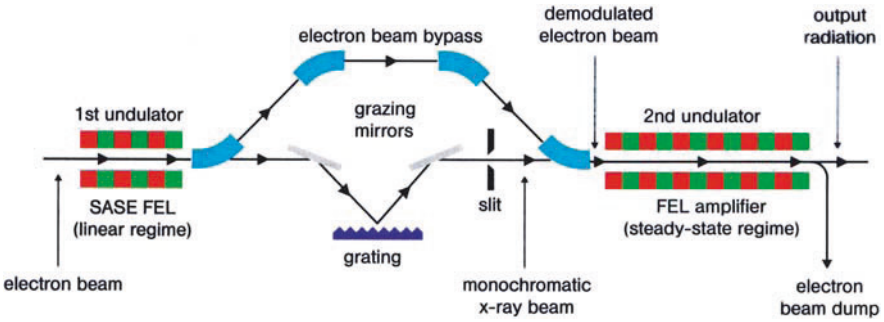

Fig. 12 Principle layout of a two-stage FEL providing full temporal and spatial coherence of the output radiation

amount as the radiation pulse. The radiation pulse is spectrally filtered by a narrow-band grating monochromator which stretches the pulse and provides a coherence length longer than the electron bunch length. This radiation is the seed for the second undulator which amplifies it to saturation.

The output radiation exhibits a narrow spectral line with only a small background of spontaneous radiation. The pulse energy is the same as that of a FEL operating in SASE mode, thus the spectral brightness has increased by almost two orders of magnitude. Due to the saturation in the FEL amplifier, the intensity of the single-line output radiation is rather insensitive to the fluctuating input seed intensity. The hardware components for a self-seeding mode of FLASH at DESY, covering a range of 6–60 nm wavelength, are currently under construction and will be installed and tested in the near future.

The other possible route to a temporally coherent X-ray FEL is to use an optical seed laser (or a higher harmonic generated in a nonlinear crystal or a gas) for the first stage of an FEL cascade making use of high-gain harmonic generation (HGHG). The schematic layout of a HGHG FEL is shown in Fig. 13. The first, short undulator, called the modulator, is tuned to the frequency of the coherent seed laser whose interaction with the electron beam introduces a small longitudinal energy modulation. The magnetic dispersion section converts this energy modulation into a density modulation. The second undulator, called the radiator, is tuned to the nth harmonic of the seed frequency. When the modulated electron beam passes the radiator, the radiation produced by the nth harmonic component is amplified to saturation. This concept was demonstrated in the mid-infrared by seeding with a CO_2 laser and generating the second harmonic in the radiator [25]. Later this scheme was employed to generate

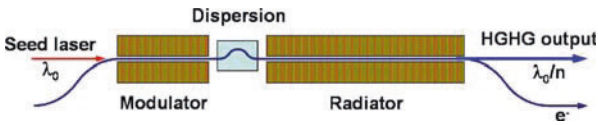

Fig. 13 Principle layout of the high-gain harmonic generation (HGHG) scheme

intense, coherent ultraviolet radiation at 266 nm wavelength as the third harmonic of 800 nm using a Ti:sapphire seed laser [26]. The radiation pulse energy at saturation was typically 100 μJ with a pulse duration of ~0.6 ps. The third harmonic of the output radiation at 88 nm wavelength, still at the 1 μJ level, was successfully used for first experiments probing the superexcited-state dynamics of methyl fluoride [27].

HGHG can be used to generate radiation pulses with <20 fs duration, and in principle the HGHG FEL can be cascaded to reach still shorter wavelengths. This concept is currently being discussed for the next generation of VUV and X-ray sources (see e.g. [28]). However, simulations and theoretical investigations have shown that the beam quality will eventually be degraded by noise which is also amplified [28,29]. At the present time it is not clear where the physical and technical limits are, therefore intensive research and development is ongoing.

8 Outlook

Recent advances in linear accelerators, new developments in laser-driven low-emittance electron guns, and the feasibility of ultra-precise long undulators open up the exciting possibility of building single-pass free-electron lasers based on self-amplified spontaneous emission. These FELs promise to provide extremely intense, polarised, ultra-short pulse radiation in the soft and hard X-ray regimes. Their high peak and average brilliance, the tunability of the photon energy, and the coherence of the radiation will make the FELs into unique sources for many areas of research. The discussions on the research with X-ray FELs have just started and we are sure there is exciting science waiting for us.

Acknowledgments The authors are indebted to many colleagues for stimulating discussions.

References

1. G. K. Shenoy and J. Stöhr editors, *LCLS – The First Experiments*, SLAC-R-611 (2000)s
2. P. G. ÓShea, H. P. Freund, Science **292**, 185 (2001)
3. G. Materlik and Th. Tschentscher editors, *TESLA Technical Design Report, Part V, The X-ray Free Electron Laser*, DESY 2001–011 (2001)
4. R. Brinkmann, B. Faatz, K. Flöttmann, J. Roßbach, J. R. Schneider, H. Schulte-Schrepping, D. Trines, Th. Tschentscher and H. Weise editors, *TESLA XFEL Technical Design Report Supplement*, DESY 2002–167 (2002)
5. M. Aeschlimann et al., *Visions of Science*, BESSY GmbH, Berlin-Adlershof (2001)
6. J. Feldhaus, J. Arthur and J. B. Hastings, J. Phys. B **38**, S799 (2005)
7. A. M. Kondratenko and E. L. Saldin, Part. Accel. **10**, 207 (1980)
8. R. Bonifacio, C. Pellegrini, L. M. Narducci, Opt. Commun. **50**, 373 (1984)
9. E. L. Saldin, E. A. Schneidmiller, M. V. Yurkov, *The Physics of Free Electron Lasers*, Springer, Berlin-Heidelberg (2000)
10. A. Yariv, *Quantum Electronics*, John Wiley & Sons, New York-Singapore

11. S. Reiche, *Numerical Studies for a Single Pass High Gain Free-Electron Lasers*, DESY-Thesis-2000-012
12. J. Andruszkow et al., Phys.Rev.Lett. **85**, 3825 (2000)
13. V. Ayvazyan et al., Eur. Phys. J. D **20**, 149 (2002)
14. M. Dohlus et al., Nucl. Instrum. Methods Phys. Res. A **530**, 217 (2004)
15. V. Ayvazyan et al., Phys.Rev.Lett. **88**, 10482 (2002)
16. H. Wabnitz et al., Nature **420**, 482 (2002)
17. J. Krzywinski et al., Proc. of the 2004 FEL Conference, p. 675 (available at http://www.JACoW.org/)
18. R. Treusch, Ch. Gerth, T. Lokajczyk and J. Feldhaus, Nucl. Instrum. Meth. Phys. Res. A **467–468**, 30 (2001)
19. J. Feldhaus and D. Nölle, Proc. of the EPAC 2004, Lucerne, Switzerland, p. 262 (available at http://www.JACoW.org/)
20. V. Ayvazyan et al., Eur. Phys. J. D **37**, 297 (2006)
21. Arthur J et al. *Linac Coherent Light Source (LCLS) Conceptual Design Report,* SLAC-R-593 SLAC, Stanford, USA (2002)
22. A. S. Schwarz, Proc. of the 2004 FEL Conference, p. 85 (available at http://www.JACoW.org/)
23. R. Bonifacio, L. De Salvo, P. Pierini, N. Piovella and C. Pellegrini, Phys. Rev. Lett. **73**, 70 (1994)
24. J. Feldhaus, E. L. Saldin, J. R. Schneider, E. A. Schneidmiller and M. V. Yurkov, Opt. Commun. **140**, 341 (1997)
25. L. H. Yu et al., Science **289**, 932 (2000)
26. L. H. Yu et al., Phys. Rev. Lett. **91**, 074801 (2003)
27. W. Li, R. R. Lucchese, A. Doyuran, Z. Wu, H. Loos, G. E. Hall and A. G. Suits, Phys. Rev. Lett. **92**, 083002 (2004)
28. D. Krämer, E. Jaeschke and W. Eberhardt, *The BESSY Soft X-Ray Free Electron Laser* BESSY GmbH, Berlin, Germany (2004)
29. E. L. Saldin, E. A. Schneidmiller and M. V. Yurkov, Optics Comm. **202**, 169 (2002)

Part II
Laser–Matter Interaction – Nonrelativistic

Numerical Methods in Strong Field Physics

Kenneth J. Schafer

1 Introduction

The numerical solution of the time-dependent Schrödinger equation (TDSE) for an atom or molecule in an intense, pulsed laser field is one of the most important theoretical tools available for the study of strong field phenomena. The reason for this is that in the regime where strong field effects occur the laser–electron interaction which tends to ionize the system is comparable in strength to the intra-atomic forces which bind the it. The presence of two equally strong, competing pieces in the Hamiltonian leads to an array of unexpected effects which are the subject of this book. It also necessitates a non-perturbative approach for its accurate description, and grid-based solutions of the TDSE allow us to treat the interactions on an equal footing, without making assumptions about the relative importance of the forces. They also have the flexibility to treat a wide range of physical systems and laser parameters, meaning that they can address a broad range of experimental data.

In this chapter we review some of the numerical methods available for solving the strong field TDSE on a space–time grid [1,2,3,4]. Our treatment is not comprehensive. We focus instead on introducing the main concepts that motivate the numerical methods that are most widely used; we give a brief introduction to these methods; and we illustrate some of the numerical tools that are available for extracting information from the time-dependent wave function for comparison with experiment. Throughout we wish to emphasize the relationship between the physics of strong field processes and the numerical methods used to describe them, how that physics determines which numerical methods will be most fruitful, and how the numerical methods can in turn be used to elucidate the physics of strong field processes in greater detail and even discover new phenomena.

The "three-step" model of strong field processes [5,6], though an oversimplification, nicely serves to illustrate the problem we wish to treat and the

K.J. Schafer
Department of Physics and Astronomy, Louisiana State University, Baton Rouge 70803-4001, LA, USA
e-mail: Schafer@rouge.phys.lsu.edu

T. Brabec (ed.), *Strong Field Laser Physics*,
DOI: 10.1007/978-0-387-34755-4_6,

numerical challenges we face. For now and in much of what follows, we assume that there is but a single electron in the system which strongly interacts with the laser. This electron is initially in a spatially localized bound state when it encounters a laser field of sufficient strength to cause some significant ionization. As the amplitude of the laser field rises and falls periodically, part of the bound state wave function evolves into a continuum wave packet, initially with very little energy. These wave packets can continue to interact with the ion core but they can also gain energy from the laser field. Part of each wave packet will move away from the ion core never to return. Another part will be driven back toward the ion core, returning after about one optical cycle. When it reaches the vicinity of the core several things can happen. The wave packet may scatter off the core, changing direction and possibly gaining additional energy from the laser field in the process. The wave packet can also coherently overlap with the remaining bound state amplitude, which leads to a time-dependent dipole moment and stimulated photon emission. The returning electron can also interact with another bound electron, leading to multiple ionization.

Even in this highly simplified picture, one that ignores, for example, resonant excitation pathways or complicated driving fields, one can appreciate the numerical challenges involved in solving the strong field TDSE. The methods used must be able to accurately represent a solution which is, at any given time, a superposition of bound motion, oscillating wave packets near the ion core, and purely outgoing ionizing wave packets. In addition to this, we are most often interested in calculating the dependence of various observables on the laser intensity, and the level of effort required to integrate the TDSE rises rapidly with increasing intensity or wavelength. For these reasons, the numerical methods employed in strong field physics, and the ones we will concentrate on, tend to be very simple and robust. The wave functions and the operators that make up the Hamiltonian are described by their finite difference representations, and the propagators that evolve the wave function in time are unitary approximations to the full propagator that are second-order accurate in the time step δt. It cannot be overemphasized that all of the elements of the calculation, from the choice of potential and electromagnetic gauge, to the representation of the operators and the propagator, must work together to produce the most efficient algorithm.

The numerical methods commonly used in strong field physics have been developed primarily to treat interactions of rare gas atoms with near-infrared radiation at a wavelength of about 800 nm, corresponding to the Ti:sapphire lasers currently found in most laboratories. Through relentless development these lasers have been pushed to their performance limits: they can produce amplified pulses with peak intensities above 10^{15} W/cm^2 and pulse durations barely longer than an optical cycle, which is about 2.5 fs [7]. The last few years, however, have seen a proliferation of new sources with the potential for driving strong field processes. These include mid-infrared lasers with wavelengths between 2 and 4 μm, which will also operate in the high-intensity, few cycle regime [8], and attosecond sources, available as both single attosecond pulses [9] or a train of sub-femtosecond pulses [10], in the XUV regime. XUV or soft X-ray

free-electron lasers are also developing toward shorter pulse durations and higher peak intensities [11]. Looking further ahead, facilities such as the Linear Coherent Light Source at Stanford, scheduled to open at the end of the decade, promise to eventually deliver intense coherent X-ray pulses with a duration of a few femtoseconds. All of these sources will require that the numerical methods that are so well adapted for IR lasers be greatly extended and improved.

2 Single Active Electron Approximation

We begin with the TDSE for a one-electron atom in strong laser field. We use atomic units, $e = \hbar = m_e = 1$. For wavelengths much larger than the atomic length scale and non-perturbative intensities we can use the classical electron–field interaction in the dipole approximation. In the length gauge this is

$$\mathrm{i}\frac{\partial}{\partial t}\psi(\boldsymbol{r},t) = \left[-\frac{1}{2}\nabla^2 + V(\boldsymbol{r}) + (\hat{\mu}\cdot\boldsymbol{r})\mathcal{E}(t)\right]\psi(\boldsymbol{r},t), \tag{1}$$

where $V(\boldsymbol{r})$ is the binding potential, $\mathcal{E}(t)$ is the time-dependent laser field, and $\hat{\mu}$ is the polarization which is constant for linear polarization and varies with time for elliptic or circular polarization. Eq. (1) is essentially exact for one-electron atoms. Its solution for that case is an important benchmark for both the performance of numerical algorithms and comparisons among different strong field methods. Experiments on hydrogenic atoms are very difficult to carry out, however, and so there have been few comparisons of such exact calculations to experimental data [12,13].

Equation (1) can be used to treat a wide variety of multielectron systems with a suitable choice of the one-electron potential $V(\boldsymbol{r})$. This model, known as the single active electron approximation or SAE [14], assumes that only one electron at a time interacts strongly with the laser field. For systems such as the alkali metal atoms or a negative ion, this approximation makes intuitive sense since the valence electron sits outside a closed shell. The SAE is more widely applicable than this, however, because it can be applied whenever the probability of simultaneous, multiple excitations of the system is small. For the rare gases, where the valence electrons are part of a filled shell, extensive calculations have found it to be a good approximation when the photon energy is much smaller than the energy necessary to remove one electron from the system [1,15,16]. In this case the ionization is dominated by sequential processes in which one electron is completely removed before another is excited. The contribution of different electrons to observables such as the time-dependent dipole moment or the photoelectron spectrum can therefore be calculated separately and added together (either coherently or incoherently as is appropriate). It is also often the case that the electron orbitals that are aligned along the field (such as the $m = 0$ orbitals for a laser linearly polarized along the z direction)

experience a much higher ionization rate than the other electrons, and sufficient accuracy can be obtained by considering only these orbitals.

The most obvious shortcoming of the SAE is that it ignores the simultaneous interaction of more than one electron with the laser field. For the laser wavelengths most often employed in experiments (~ 800 nm) this turns out to be an excellent approximation except in situations where a doubly excited state is resonantly coupled by the laser to the ground state. The largest practical shortcoming of the SAE in strong field physics is that it ignores the possibility that the active electron may interact with other electrons in the system, a non-resonant process that can lead to non-sequential multiple ionization, a topic which we will discuss in the section on multiple electron effects.

The great virtue of the SAE is not only the reduction in complexity that it provides as a one-electron approximation but also the fact that it is a linear equation which automatically allows for the kind of superposition (bound + continuum) solutions which are the hallmark of strong field processes. SAE calculations can also be done *exactly* to within numerical error. This means that they can be used as a benchmark in determining the extent of one-electron versus multielectron effects in an experiment. Since it is often not possible to calculate non-sequential processes with high accuracy, proof that a non-sequential process has in fact been observed may come from the departure of the experimental results from the calculated sequential results [17]. Conversely, in reference [18] a highly accurate match between SAE theory and experimental data was used to rule out what were initially assumed to be multiple electron effects in high-energy photoelectron spectra [19].

2.1 SAE Potentials

The potentials used to model intra-atomic forces in SAE calculations may be divided into two classes, model potentials and pseudopotentials. Model potentials are used for their simplicity, which allows for fast computation in one dimension or for a tractable treatment of electron–electron interactions in multiple dimensions. They can also be used to examine the effect of certain features of the atomic system, for example, by eliminating excited states from the calculation. Pseudopotentials are constructed to facilitate detailed comparison to experiment and so strive for as accurate as possible a representation of the active electron wave function.

2.1.1 Model Potentials

By far the most commonly used model potential in strong field physics is the one-dimensional "soft Coulomb" potential

$$V(x) = \frac{-q}{\sqrt{x^2 + a^2}}. \tag{2}$$

It contains no singularity, which would be difficult to treat numerically in one dimension, and supports a Rydberg series of states close to threshold [2]. The form of the potential can be motivated by considering the hydrogenic potential in cylindrical coordinates $V(\rho, z) = -q/\sqrt{\rho^2 + z^2}$ and replacing ρ^2 with a constant, a^2. By choosing q and a^2 appropriately the ionization potential of different systems can be reproduced, which allows for a qualitative match to three-dimensional ionization rates when the ionization is non-resonant. As an example, if we use $q = 1$ and take a^2 equal to $\langle \rho^2 \rangle$ in the hydrogen ground state ($a^2 = 2$) we obtain the hydrogen ionization potential of $E_I = 1/2$ au. For this value of the softening parameter there is also an analytic wave function available [20] which can be used as an additional check on the accuracy of the one-dimensional discretization. Of course, matching the ground state energy does not guarantee that the excited states energies will be correct, and indeed they are overbound. The first excited state is typically bound by approximately $E_I/2$.

2.1.2 Pseudopotentials

For three-dimensional SAE calculations we use a one-electron pseudopotential that has as its ground state the valence state that we are interested in. The potentials take the form

$$V(\boldsymbol{r}) = \sum_{\ell} V_\ell(r)|\ell\rangle\langle\ell| - 1/r, \tag{3}$$

where the short-range potentials V_ℓ can depend on the angular momentum of the electron. This form of the potential, which is non-local in space, allows for great flexibility in treating different atomic systems when spherical coordinates are used.

We have done extensive SAE calculations on both the rare gases and the alkali metals. For the rare gases the potentials are constructed from the valence orbitals of the atoms obtained from a Hartree–Slater calculation for the ground and singly excited states of the atom. The exchange correlation parameter is adjusted so that the orbital energy agrees with the experimentally determined value. We also modify the Hartree–Slater equations to incorporate the correct, long-range Coulomb attraction. The valence orbital, of angular momentum ℓ, is then used to construct the ℓ-dependent potential for that value of the angular momentum [14]. For example, for the xenon $5p$ orbitals we obtain the $\ell = 1$ potential from a ground state calculation and the $\ell = 0$ and $\ell = 2$ potentials from $5p^5 6s$ and $5p^5 5d$ calculations, respectively. For $\ell > 2$ we use the $\ell = 2$ potential. The effective potential used in the TDSE calculations is constructed by removing the nodes from the valence orbital of interest and then inverting the single-particle Schrödinger equation for this pseudo-orbital to obtain $V_\ell(r)$. Further fine adjustments of the individual potential in each ℓ channel allows us to achieve excellent agreement with experimental excitation energies.

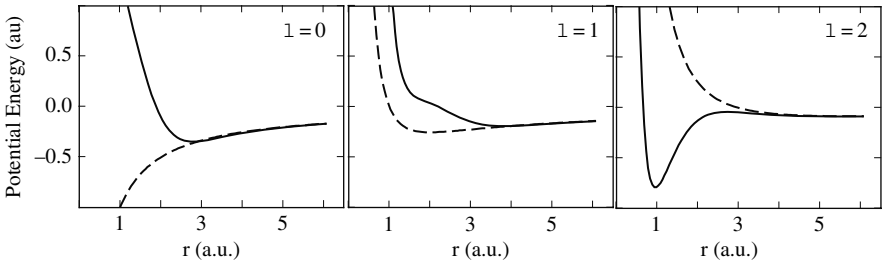

Fig. 1 *Solid line*: potassium SAE potential for $\ell = 0 - 2$ after reference [21]. We plot the sum of the pseudopotential and the centrifugal term. The corresponding potential for hydrogen is shown as a *dashed line*

For alkali metal atoms, use semi-empirical pseudopotentials given by Stevens in [21] to describe the valence electron–ion core interaction. The short-range potentials include a core potential term which accounts for the shielding of the nuclear charge by the core electrons, as well as the orthogonality constraints imposed by the exclusion principle, and a polarization term which accounts for the polarization of the ion charge cloud through dipole and quadrupole potentials proportional to r^{-4} and r^{-6}, respectively. To obtain the correct energies and transition matrix elements, the short-range terms V_c and V_{pol} are in general dependent on the angular momentum channel. Since the pseudopotential is ℓ-dependent it is non-local; however, the range over which it is non-local is restricted to distances close to the ion core. The potential is effectively local for distances greater than about 5–10 au. As an example, Fig. 1 shows the pseudopotential for potassium in the lowest three angular momentum channels. We plot the sum of the pseudopotential and the centrifugal term $\ell(\ell+1)/2r^2$. The corresponding hydrogen potentials are shown for each channel. For distances greater than about 5 au the two potentials agree, which means that the short-range potentials have become negligible.

2.1.3 Modifying the Pseudopotentials

The pseudopotentials and model potentials discussed above can often be modified to either illuminate the physics of some strong field process or reproduce a known spectroscopic feature which is not already well described by the potential. The latter example is the well-known Cooper minimum which occurs in all the alkali metal atoms at an energy below 1 eV. If one calculates the one-photon matrix element using the Stevens potentials as published, they all exhibit a Cooper minimum in the $s \rightarrow p$ channel as they should. The energy of the minimum in the cross-section, however, ranges between 1 and 10 eV for the various atoms. The precise position of the minimum depends sensitively on the details of the short-range part of the potential. By making small changes to the polarization term in the Stevens potential, the Copper minima can be well reproduced without changing the excitation energies by more than a fraction of a percent.

2.2 Choice of Gauge

The choice of electromagnetic gauge has a large influence on the numerical effort involved in strong field calculations, through both the number of spherical harmonics $\ell_{\max}$ and the time step δt required for convergence [22]. In the length gauge the TDSE in the dipole approximation for an electron in a time-varying field polarized along the z axis is

$$\mathrm{i}\frac{\partial \psi_l}{\partial t} = (H_0 + \mathcal{E}(t)z)\psi_l, \tag{4}$$

where H_0 is the field–free ion–valence electron Hamiltonian and $\mathcal{E}(t)$ is the laser electric field.

This gauge is preferred near the ion core where the interaction is reasonably small, even for intense fields. When the electron is ionized, however, it travels far from the ion core where the interaction grows rapidly. This has two undesirable consequences. First, the large interaction requires that a small time step be used in the time integration. Second, the oscillations in the electron's motion induced by the field, which are on the order of the free-electron oscillation amplitude $\sim \mathcal{E}/\omega^2$, require the use of a very large number of angular momentum functions.

If we define the vector potential $A(t)$ and an auxiliary function $\Phi(t)$ by the relations

$$-\frac{\partial A(t)}{\partial t} = \mathcal{E}(t); \quad \frac{\partial \Phi}{\partial t} = \frac{1}{2}A^2(t), \tag{5}$$

then for local potentials we can use the gauge transformation

$$\psi_l(\boldsymbol{r}, t) = \mathrm{e}^{-\mathrm{i}(A(t)z + \Phi(t))}\psi_v(\boldsymbol{r}, t) \tag{6}$$

to write the TDSE in the velocity gauge as

$$\mathrm{i}\frac{\partial \psi_v}{\partial t} = \left(H_0 - \mathrm{i}A(t)\frac{\partial}{\partial z}\right)\psi_v. \tag{7}$$

In this gauge the phase factor that describes the free-electron-like oscillations in the ionized electron's wave function is mostly removed, which results in a large reduction in the number of angular momentum channels needed for convergence. The interaction is also bounded when the electron travels far from the ion core. This has the practical effect that the size of the angular momentum basis no longer scales with the box size. Close to the ion core, however, the interaction $A(t)p_z$ can be very large which again makes the equation hard to integrate. The two interactions are comparable in strength at a distance from the ion core on the order of the free-electron oscillation

amplitude. Calculations that employ a small computational box, such as those used to describe ionization rates or high harmonic generation, can generally be done in the length gauge. Calculations of photoelectron spectra, which require large box sizes so that the ionizing wave function can be analyzed at the end of the laser pulse, may be more efficient in the velocity gauge.

2.3 SAE Calculations

Once we have an SAE potential and have chosen an electromagnetic gauge for the interaction term, we solve the one-electron TDSE by integrating Eq. (1) for a particular laser wavelength, peak intensity, and pulse duration [1]. The laser pulse usually takes the form

$$\mathcal{E}(t) = F(t)\mathcal{E}_0 \sin(\omega t + \varphi(t)), \tag{8}$$

where $\mathcal{E}_0$ is the peak amplitude of the electric field, ω is the central frequency of the laser, and $F(t)$ is an envelope function. The phase $\varphi(t)$ is a constant for transform-limited pulses and varies in time for chirped pulses. For few cycle pulses, even a constant value of φ, known as the carrier envelope offset (CEO) phase, has important consequences for the ionization dynamics [23]. When carrying out calculations in the velocity gauge we begin by specifying $\mathcal{E}(t)$, which can be directly measured in an experiment [24], and calculating $A(t)$ from it. The important requirement is that both $\mathcal{E}$ and A must be zero at the end of the calculation. Furthermore, care should be taken in specifying the envelope function $F(t)$ so that $A(t)$ oscillates around an average value of zero during the pulse. Though this requirement is not strictly speaking necessary, it is very difficult to integrate the TDSE accurately otherwise.

We start from a well-defined initial state which may be a combination of eigenstates. It is important that the initial state consist of a superposition of eigenstates of the *discrete* field-free Hamiltonian. Use of analytic approximations introduces spurious couplings between the grid eigenstates. For the time integration we use a short time approximation to the full (time-ordered) evolution operator to propagate the wave function from time t_n to time $t_{n+1} = t_n + \delta t$:

$$|\,\psi(t_{n+1})\rangle = \mathrm{e}^{-\mathrm{i}\hat{H}_{\bar{n}}\delta t}\,|\,\psi(t_n)\rangle. \tag{9}$$

For a time-dependent Hamiltonian such as we typically encounter in laser–matter interactions $\hat{H}_{\bar{n}}$ is the Hamiltonian at the intermediate time $t_n + \delta t/2$. Since we have ignored the time-ordering operator that appears in the full propagator, the short time propagator is itself second-order accurate in time. This means that there is little advantage in evaluating the short time propagator to higher order than this, unless it is required for some other reason, such as maintaining unitarity.

Knowing the time-dependent wave function we can calculate time-dependent observables such as the dipole moment $\langle \hat{\epsilon} \cdot \boldsymbol{r} \rangle$ responsible for photoemission [25,26,27,28,29] and asymptotic quantities such as the probability to find the electron in an excited state or with a particular outgoing energy (photoelectron spectrum) [30,31,32,33,28,34], the angular distribution of the emitted electrons [35], etc. We can also calculate time-dependent quantities which, while not directly observable, can give us insight into the dynamics. An example is projecting onto a particular dressed state while the laser is on as a means of identifying resonant pathways into the continuum [36].

2.4 Discrete Form of the TDSE

In this section we discuss the discrete form of the TDSE in both the length and velocity gauges. In one dimension computational efficiency is rarely a crucial issue, and a variety of methods can be employed to obtain numerical wave functions. As a concrete example, we consider a finite difference representation of the wave function on a uniform grid $x_j = (j - N/2)\delta x$ $\{j = 1 \ldots N\}$. The time-dependent coefficients $\psi_j(t)$ describe the amplitude of the wave function $\psi(x, t)$ at the grid points x_j. A three-point finite difference treatment of the TDSE results in an equation of motion for these coefficients:

$$\mathrm{i}\frac{\partial \psi_j}{\partial t} = \left[\hat{H}_0\,\psi\right]^j + \left[\hat{H}_1\,\psi\right]^j, \tag{10}$$

where the field-free (electron–ion) term is

$$\left[\hat{H}_0\,\psi\right]^j = -\frac{1}{2(\Delta x)^2}\left[\psi_{j+1} - 2\psi_j + \psi_{j-1}\right] + V_j\psi_j \tag{11}$$

with $V_j \equiv V(x_j)$ and the electron–laser interaction term in either the length (L) or velocity (v) gauge is

$$\left[\hat{H}_1^L\,\psi\right]^j = \mathcal{E}(t)x_j\psi_j \text{ or } \left[\hat{H}_1^v\,\psi\right]^j = \frac{-\mathrm{i}A(t)}{2\Delta x}\left[\psi_{j+1} - \psi_{j-1}\right]. \tag{12}$$

The boundary conditions for the solution are that $\psi_j = 0$ at the left and right boundaries of the grid. Higher accuracy at a given grid spacing may be obtained by using either a higher-order finite difference discretization or a spectral method for evaluating the derivative terms [37].

In three dimensions the interaction in the length gauge for a laser linearly polarized along the z direction is proportional to $r\cos(\theta) \propto rY_1^0$ which strongly suggests that we begin by expanding the time-dependent state vector in a mixed basis of discrete radial functions times spherical harmonics,

$$|\psi(\boldsymbol{r},\, t)\rangle \rightarrow \sum_{\ell=|m|}^{\ell_{\max}} \psi_\ell(r_j, t)|\ell, m\rangle, \tag{13}$$

where $\langle\theta, \phi|\ell, m\rangle = Y_\ell^m(\theta, \phi)$. For now we restrict ourselves to linear polarization which means that the m_ℓ quantum number is conserved. For this reason, the m_ℓ label is suppressed in the following equations. We discuss elliptically polarized driving fields, for which m_ℓ is not conserved, below. It is usually convenient to make a transformation to the scaled coefficients $\phi_\ell^j = r_j \psi_\ell^j$ which satisfy the normalization condition

$$\Delta r \sum_{\ell=|m|}^{\ell_{\max}} \sum_{j=1}^{N_r} |\phi_\ell^j|^2 = 1. \tag{14}$$

We could substitute this form of the wave function into the TDSE directly and use a point finite difference representations of the operators on a uniform radial grid $r_j = j\Delta r\ \{j = 1 \ldots N_r\}$ to obtain equations of motion for the coefficients $\phi_\ell{}^j$. A characteristic feature of spherical and other non-cartesian coordinate systems is that the initial state in the calculation has significant amplitude near one of the boundaries ($r = 0$ in this case). Finite differencing schemes can incur large errors near the $r = 0$ boundary (where the order of the method may not be preserved due to an inconsistency in the application of the boundary conditions), and this requires a small grid spacing to counteract. The errors associated with using low-order finite difference operators in spherical coordinates can be greatly reduced by avoiding discretizing the TDSE directly. Instead we begin by inserting the discrete wave function (13) into the Lagrange-type functional [3,38,39]:

$$\mathcal{L} = \left\langle \psi | i\frac{\partial}{\partial t} - T - V - H_{\mathrm{I}} | \psi \right\rangle, \tag{15}$$

where H_{I} is the electron–laser interaction in either gauge, and requiring that ψ^* obey the Euler–Lagrange condition

$$\frac{\mathrm{d}}{\mathrm{d}t}\left(\frac{\partial \mathcal{L}}{\partial \dot{\psi}^*}\right) - \frac{\partial \mathcal{L}}{\partial \psi^*} = 0. \tag{16}$$

This is equivalent to requiring that the action associated with this functional be stationary with respect to small variations of the time-dependent coefficients. In the limit $\Delta r \rightarrow 0$ this procedure leads directly to the usual TDSE for $\psi(\boldsymbol{r},\, t)$. For a discrete wave function, the procedure leads to a discrete version of the TDSE that consistently accounts for the boundary conditions imposed on ψ at small r because the functional includes the $r = 0$ boundary condition explicitly.

We use a uniform radial grid that is offset by $\Delta r/2$ from the standard grid: $r_j = (j - 1/2)\Delta r\ \{j = 1 \ldots N_r\}$. We note that the variational procedure can

also be used to derive discrete versions of the TDSE on a non-uniform grid [40]. Carrying out the angular integrals in Eq. (15), discretizing the kinetic energy with a three-term finite difference formula, and making the transformation $\phi_\ell^j = r_j \psi_\ell^j$, we derive equations for the time evolution of the coefficients. We omit the details of the derivation, which are fairly involved and are given in full in reference [3], and quote the result first in the length (L) gauge:

$$\mathrm{i}\frac{\partial \phi_\ell^j}{\partial t} = \left[\hat{H}_0\,\phi\right]_\ell^j + \left[\hat{H}_\mathrm{I}\,\phi\right]_\ell^j, \tag{17}$$

where the atomic term is

$$\left[\hat{H}_0\,\phi\right]_\ell^j = -\frac{1}{2(\Delta r)^2}\left[\alpha_j \phi_\ell^{j+1} - 2\beta_j \phi_\ell^j + \alpha_{j-1}\phi_\ell^{j-1}\right] + V_\ell^j \phi_\ell^j \tag{18}$$

and the interaction term is

$$\left[\hat{H}_\mathrm{I}^L\,\phi\right]_\ell^j = \mathcal{E}(t)\, r_j \left[c_\ell \phi_{\ell+1}{}^j + c_{\ell-1}\phi_{\ell-1}{}^j\right]. \tag{19}$$

The dimensionless radial coefficients α_j and β_j are

$$\alpha_j = \frac{r_{j+1/2}^2}{r_j r_{j+1}} = \frac{j^2}{j^2 - 1/4}; \quad \beta_j = \frac{r_{j+1/2}^2 + r_{j-1/2}^2}{2r_j^2} = \frac{j^2 - j + 1/2}{j^2 - j + 1/4}. \tag{20}$$

The angular coefficients c_ℓ are just the usual $3j$ coefficients

$$c_\ell = \sqrt{\frac{(\ell + m + 1)(\ell - m + 1)}{(2\ell + 1)(2\ell + 3)}}. \tag{21}$$

The field-free Hamiltonian matrix, $\hat{H}_0$, is diagonal in the ℓ quantum number and tridiagonal in the radial index j. Likewise, $\hat{H}_\mathrm{I}^L$ is diagonal in j and tridiagonal in ℓ. Far from the $r = 0$ boundary both α_j and β_j approach 1, and we recover the standard second-order finite difference equations. Setting all the αs and βs $= 1$ and using a grid that is not offset we recover the "naive" second-order accurate discretization of the TDSE alluded to above. The variational formulation reduces the error in the ground state energy by about a factor of 5 over the naive discretization for the same grid spacing (typically, we use $\Delta r = 0.25$ au with a variety of pseudopotentials). An exception to this rule is the $\ell = 0$ Coulomb problem. In this anomalous case, the naive discretization gives a better energy than the variational derivative. The problem comes at the $r = 0$ boundary and can be fixed by the replacement $\beta_1 \to \beta_1 + \delta\beta_1$ where

$$\delta\beta_1 = \frac{Z\Delta r}{8}(1 + Z\Delta r). \tag{22}$$

This simple re-scaling of the first diagonal coefficient in the kinetic energy matrix yields an excellent quality wave function with an error of about 10^{-5} in the total energy.

In the velocity gauge the interaction is proportional to

$$\frac{\partial}{\partial z} = \cos(\theta)\frac{\partial}{\partial r} - \frac{\sin(\theta)}{r}\frac{\partial}{\partial \theta}. \tag{23}$$

This more involved form might suggest using cylindrical coordinates, but the resulting simplicity will be overwhelmed by the need for a much greater number of grid points. Continuing with the spherical basis, the variational procedure yields, after some additional effort, the interaction Hamiltonian as the sum of two terms

$$\begin{aligned}
\left[\hat{H}_{\mathrm{I}}^{v}\phi\right]_{\ell}^{j} &= \left[\hat{H}_{1}^{v}\phi\right]_{\ell}^{j} + \left[\hat{H}_{2}^{v}\phi\right]_{\ell}^{j}, \\
\left[\hat{H}_{1}^{v}\phi\right]_{\ell}^{j} &= \frac{\mathrm{i}A(t)}{r_j}\left[(\ell+1)c_{\ell}\phi_{\ell+1}^{j} - \ell c_{\ell-1}\phi_{\ell-1}^{j}\right], \\
\left[\hat{H}_{2}^{v}\phi\right]_{\ell}^{j} &= \frac{\mathrm{i}A(t)}{2\Delta r}\left[c_{\ell}\left(\alpha_j\phi_{\ell+1}^{j+1} - \alpha_{j-1}\phi_{\ell+1}^{j-1}\right) + c_{\ell-1}\left(\alpha_j\phi_{\ell-1}^{j+1} - \alpha_{j-1}\phi_{\ell-1}^{j-1}\right)\right].
\end{aligned} \tag{24}$$

The first term, weighted by $1/r_j$, is tridiagonal in the ℓ coordinate. The second term couples the radial and angular coordinates and is tridiagonal in both. This increased complexity makes time propagation in the velocity gauge more difficult than in the length gauge. As discussed above, however, for large box calculations the gain in efficiency from using fewer angular functions and larger time steps more than compensates the additional complication.

2.5 Time Propagation

The Hamiltonian in both the length and velocity gauges consists of two pieces: $\hat{H}_0$, the atomic Hamiltonian which is diagonal in the ℓ quantum number, and the interaction piece $\hat{H}_{\mathrm{I}}$. In both gauges we use a split-operator expansion of the full short time propagator which is unitary and correct to $\mathcal{O}(\delta t)^3$:

$$\psi(t+\delta t) = \mathrm{e}^{-\mathrm{i}(\hat{H}_0+\hat{H}_1)\delta t}\,\psi(t) \approx \mathrm{e}^{-\mathrm{i}\hat{H}_1\delta t/2}\,\mathrm{e}^{-\mathrm{i}\hat{H}_0\delta t}\,\mathrm{e}^{-\mathrm{i}\hat{H}_1\delta t/2}\psi(t). \tag{25}$$

The interaction term is evaluated at the midpoint of the time step. The action of the exponentials on the time-dependent wave function cannot be calculated directly due to the non-diagonal nature of the matrices representing $\hat{H}_0$ and $\hat{H}_{\mathrm{I}}$. We therefore resort to approximations to the full exponentials which are themselves unitary and correct to the same order in δt as the split-operator method. The propagator for $\hat{H}_0$ is approximated by the Crank–Nicolson form [40]

$$e^{-i\hat{H}_0\delta t} \approx \left[1+i\hat{H}_0\delta t/2\right]^{-1}\left[1-i\hat{H}_0\delta t/2\right] + \mathcal{O}(\delta t)^3. \tag{26}$$

The application of this operator requires the solution of a sparse set of linear equations at every time step:

$$z^n \equiv \left[1 - i\hat{H}_0\delta t/2\right]\phi^n, \tag{27}$$

$$\left[1 + i\hat{H}_0\delta t/2\right]\phi^{n+1} = z^n. \tag{28}$$

Gaussian elimination and back substitution work well due to the diagonal dominance of the matrices. Each value of the ℓ index can be handled separately and the solution of the linear equations can be greatly speeded up by making this the *inner* loop in the computation.

The interaction propagator could also be handled via the Crank–Nicolson method as was done in references [1,4], but the purely off-diagonal nature of the angular coupling also makes it possible to use an explicit method, a 2×2 splitting technique previously used by Richardson and others [41,42] for cartesian grids. We demonstrate this method in the length gauge and leave the slightly more involved treatment necessary for the velocity gauge for an appendix. In the length gauge, $\hat{H}_{\mathrm{I}}^L$ is diagonal in j and so we may solve

$$e^{-i\hat{H}_{\mathrm{I}}\delta t/2}\phi^j = e^{-i\hat{L}^j}\phi^j \tag{29}$$

at each radial point separately. We use ϕ^j as a shorthand for the column vector composed of the coefficients ϕ_ℓ^j $\{\ell = 0 \ldots \ell_{\max}\}$. The matrix that must be exponentiated, $\hat{L}^j$, is tridiagonal in the ℓ index. It can be split into even and odd pieces $\hat{L}^j = \hat{L}^{\mathrm{e}} + \hat{L}^{\mathrm{o}}$ as shown below:

$$\begin{bmatrix} 0 & a_0 & & & & \\ a_0 & 0 & a_1 & & & \\ & a_1 & 0 & a_2 & & \\ & & a_2 & 0 & a_3 & \\ & & & a_3 & 0 & \\ & & & & & \ddots \end{bmatrix} = \begin{bmatrix} \boxed{\begin{matrix} 0 & a_0 \\ a_0 & 0 \end{matrix}} & & & \\ & \boxed{\begin{matrix} 0 & a_2 \\ a_2 & 0 \end{matrix}} & & \\ & & \ddots & \\ & & & \ddots \end{bmatrix} + \begin{bmatrix} 0 & & & & \\ & \boxed{\begin{matrix} 0 & a_1 \\ a_1 & 0 \end{matrix}} & & & \\ & & \boxed{\begin{matrix} 0 & a_3 \\ a_3 & 0 \end{matrix}} & & \\ & & & \ddots & \end{bmatrix}, \tag{30}$$

where the matrix elements are $a_\ell = \mathcal{E}(t) c_\ell r_j \delta t/2$. The even and odd matrices consist of 2×2 block-diagonal pieces which can be exactly exponentiated using

$$\exp\left\{-\mathrm{i}\begin{bmatrix} 0 & a \\ a & 0 \end{bmatrix}\right\} = \begin{bmatrix} \cos a & -\mathrm{i}\sin a \\ -\mathrm{i}\sin a & \cos a \end{bmatrix}$$

A single propagation step in the length gauge is accomplished via

$$\mathrm{e}^{-\mathrm{i}\hat{H}^l \delta t} = \mathrm{e}^{-\mathrm{i}\hat{L}^e \delta t/2} \mathrm{e}^{-\mathrm{i}\hat{L}^o \delta t/2} \frac{\left[1 - \mathrm{i}\hat{H}_0 \delta t/2\right]}{\left[1 + \mathrm{i}\hat{H}_0 \delta t/2\right]} \mathrm{e}^{-\mathrm{i}\hat{L}^o \delta t/2} \mathrm{e}^{-\mathrm{i}\hat{L}^e \delta t/2}. \tag{32}$$

Although the matrices $\hat{L}^e$ and $\hat{L}^o$ do not commute, the symmetric placement of the operators makes this approximate propagator unitary and correct to $\mathcal{O}(\delta t)^3$. The computation scales linearly with the total number of grid points.

2.6 Advanced Topics

2.6.1 Elliptic Polarization

The algorithms we have been considering are specifically adapted to doing calculations on linearly polarized light. This means the wave function has two non-trivial dimensions. Three-dimensional calculations are needed to treat elliptical or circular polarized light. For these cases, the m dimension becomes a non-trivial index to our wave function since the laser field couples the various m states. In principle we need up to $2\ell_{\max}$ m states, but if the polarization vector rotates in a plane, then only half of the values need to be explicitly calculated. Muller [4] has proposed an efficient scheme for treating elliptic polarizations with the same two-dimensional code used for linear polarization calculations. At each time step the coordinate system is counter-rotated to the laser field, meaning that the laser polarization is always parallel to the z axis at every propagation step. The rotation operation can be carried out more efficiently than the laser coupling can be calculated, which makes this method attractive. As an alternative, Madsen and co-workers [43] use a weighted representation of the spherical harmonics to cover the whole range of the angular coordinates with an optimal (for a given value of ℓ) number of points.

2.6.2 Mixed Gauge Propagation

To take maximum advantage of both the length and velocity gauges, we have developed a mixed gauge time propagation technique for solving the TDSE which uses the length gauge near the ion core and the velocity gauge at large distances. We switch gauges in a transition zone that is located away from the ion core. This insures that the potential is strictly local in the transition zone (the

short-range ℓ-dependent terms having decayed) and the local gauge transformation Eq. (6) can be used. The mixed gauge approach allows us to use non-local pseudopotentials near the ion core, which give a superior description of the atomic potentials as compared to local pseudopotentials, while minimizing the numerical effort.

To implement the mixed gauge time propagation we use two partially overlapping radial grids. The length gauge grid extends from $r = 0$ to r_L and the velocity gauge grid extends from r_v to R, which is the maximum grid radius. The grids overlap, $r_v < r_L$, and the midpoint of the transition zone is r_0. At each time step t_n we propagate both wave functions forward in time to $t_{n+1} = t_n + \delta t$ on their separate grids. Due to the presence of the artificial boundaries, some error accumulates in ψ_L near r_L and in ψ_v near r_v. Before taking the next propagation step we replace the "bad" part of the wave function on each grid with "good" wave function that we obtain by using the gauge transformation on the wave function from the other grid. For instance, after every time step, the portion of ψ_L between r_0 and r_L is replaced by the gauge-transformed ψ_v at the same radial grid points. Typically, $r_L = 30$ au and $r_v = 20$ au. The key to this method is that the errors at each propagation step are localized near the artificial boundaries. This is due to the fact that we use a finite difference discretization of the TDSE.

2.7 Computational Scaling

For grid-based finite difference calculations the total computational effort scales as $C = N_r N_\ell N_t$ where $N_r = R/\Delta r$ is the number of radial grid points, $N_\ell = \ell_{\max} + 1$ is the number of angular momentum functions, and $N_t = T_{\text{pulse}}/\delta t$ is the number of time steps. This linearity in the computational parameters, even when using non-local SAE potentials, is an essential element of grid-based SAE calculations. It is not the whole story, however, since the computational effort is non-linear in several of the laser parameters. For example, raising the intensity leads to faster outgoing electrons which requires both a bigger computational box and a smaller time step to treat with the same accuracy. Similarly, using a longer pulse requires more time steps and a bigger box. The choice of gauge is crucial to these considerations, since in general it takes fewer spherical harmonics to represent the motion far from the ion core in the velocity gauge, and the time step may also be somewhat larger than for the length gauge.

2.8 Photoelectron Spectra

The most direct way to connect the numerical solution of the TDSE to experimental results is to calculate energy-resolved quantities using the wave function at the end of the integration when the interaction Hamiltonian has been

switched off. Measurements of photoelectron spectra, and especially energy-resolved angular distributions, are sensitive probes of ionization dynamics and are "single-atom" quantities in the sense that macroscopic effects are usually avoided in experiments by keeping the gas pressure low (there are, however, still intensity-averaging effects from the distribution of intensities experienced by atoms at different positions within the focal volume of the laser). The efficient extraction of energy-resolved information is not, however, straightforward given a numerical wave function spread over a large grid. Though it can in principle be accomplished by projecting $|\psi(\boldsymbol{r}, t_f)\rangle$ onto states of definite energy, this requires either the calculation of these states (as eigenstates of the asymptotic Hamiltonian) or their approximation by an analytic form. In the general case neither of these alternatives is attractive since the computation and storage of eigenstates is prohibitive in multiple dimensions and analytic approximations fail if the energy region of interest is close to a threshold or if the wave function has not yet reached a region where asymptotic states can be used.

As an alternative, we have developed and extensively used a window function technique that allows for the efficient calculation of energy-resolved quantities [30,44]. We define the window function of order n with a resolution of 2γ around an energy E as

$$W(E, \gamma, n) = \frac{\gamma^{2^n}}{(H_0 - E_k)^{2^n} + \gamma^{2^n}}, \tag{33}$$

where H_0 is the field-free Hamiltonian. The window around each energy is almost rectangular (the more so the higher n is) and has a half-width of 2γ independent of n. We apply W to the wave function and obtain the energy-resolved ket $|\Omega(\boldsymbol{r}, E)\rangle$ (we suppress the n and γ labels on the kets):

$$|\Omega(\boldsymbol{r}, E)\rangle = W(E, n, \gamma)|\psi(\boldsymbol{r}, t_f)\rangle = \sum_{\ell} \Omega_\ell(E, r)|\ell, m\rangle. \tag{34}$$

Since the field-free Hamiltonian is diagonal in ℓ we can find the coefficients Ω_ℓ by solving an implicit equation for the factorized form of the windowoperator. For instance for $n = 1$ (which we have found to be adequate) we solve

$$\left(H_0^\ell - E + \mathrm{i}\gamma\right)\left(H_0^\ell - E - \mathrm{i}\gamma\right)\Omega_\ell = \gamma^2 \phi_\ell. \tag{35}$$

This equation has the same form as the Crank–Nicolson propagator we discussed earlier and can be solved quickly using sparse matrix techniques.

Using the energy window method, the probability to find an electron with an energy in the range $E \pm \gamma$ is given by $\langle \Omega(\boldsymbol{r}, E)|\Omega(\boldsymbol{r}, E)\rangle$. As an example, energy-resolved angular distributions are found by integrating over the radial and azimuthal coordinates:

$$\begin{aligned}\mathcal{F}(E,\theta) &= \Delta r \sum_j \int \mathrm{d}\phi \, \langle \Omega(E, r_j, \theta, \phi) | \Omega(E, r_j, \theta, \phi) \rangle \\ &= \sum_{\ell=0}^{2\ell_{\max}} \beta_\ell(E) P_\ell(\theta),\end{aligned} \tag{36}$$

where we have used standard angular momentum algebra to re-express the result as a sum over $2\ell_{\max}$ Legendre polynomials. The angle-integrated photoelectron probability $P(E)$ is $2\beta_0(E)$, but if this is all that is desired it is simpler to calculate $P(E)$ directly from

$$P(E) = \Delta r \sum_{j=1}^{N_r} \sum_{\ell=|m|}^{\ell_{\max}} |\Omega_\ell(E, r_j)|^2. \tag{37}$$

Although we most often calculate energy spectra using a uniform grid of energies separated by 2γ, it is also possible to calculate momentum distributions, $\mathcal{H}(p,\theta)$, for comparison to momentum-resolved imaging experiments [45]. This can be done by making a transformation from energy to momentum via $E = p^2/2$ and accounting for the difference in phase space between the two distributions using the norm-conserving transformation $\mathcal{H}(p,\theta) = \mathcal{F}(p^2/2,\theta)/p$. Calculating $\mathcal{H}(p,\theta)$ using values from a uniform energy grid, however, results in a sparsity of points at low momentum. To obtain a uniform spacing in momentum we use a non-uniform spacing in energy and take account of the integration weight $2\gamma_k$ associated with the energy E_k. An example of a theoretically calculated "velocity image map" using this method is shown in Fig. 6.

2.8.1 Sample Results

In Fig. 2a we show total (angle-integrated) ATI spectra for potassium and sodium, at a wavelength of 3.2 μm, corresponding to a photon energy of 0.39 eV. Ionization of K requires a minimum of 11 photons at this wavelength. The laser pulse has a trapezoidal shape, consisting of one cycle ramp and five cycles of constant intensity. The peak intensity is 10^{12} W/cm^2, which corresponds to a ponderomotive energy of 1 eV. The difference in the ionization yields is due to the higher ionization potential of sodium as compared with potassium. These results are representative of calculations over a range of laser intensities, and they were performed with the mixed gauge propagation code with $\ell_{\max} = 16$ and $\delta t = 0.1$ au. Calculations using the length gauge for the entire radial grid required $\ell_{\max} = 200$ and $\delta t = 0.02$ au for a similar level of convergence. The difference in numerical effort is a factor of ~ 100.

Figure 2a illustrates a striking phenomena in the alkali metals. The production of high-order photoelectrons is very sensitive to the atomic species. K exhibits a plateau extending up to about $10U_p$, whereas the Na distribution

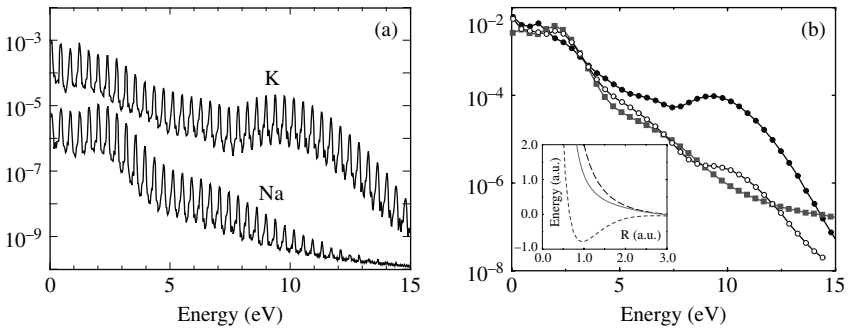

Fig. 2 (**a**) ATI spectra for potassium (*upper curve*) and sodium (*lower curve*) at 10^{12} W/cm^2 and 3.2 μm. The ponderomotive energy is 1 eV and the rescattering cutoff at $10U_p$ is clearly visible for K. (**b**) Partial rates for K (*black circles*), Na (*squares*), and a "modified" K atom (*white circles*), where the *d* potential has been substituted with the H *d* potential. In the *inset* we show the *d* potential for K (*short-dashed line*), Na (*solid line*), and H (*long-dashed line*)

shows essentially no change of slope beyond $3U_p$. One way to gain insight into the physics behind this strong field effect is to investigate its dependence on specific features of the atomic potential. To investigate the role of the *d* potential in producing high-energy electrons, we exchange the K *d* potential by the H *d* potential, leaving the *s* and *p* potentials unchanged. This modified pseudopotential reproduces the total ionization rate and the low-energy portion of the ATI spectrum of the full K atom. In Fig. 2b we show partial ATI rates for K, Na, and the modified K. The Na spectrum has been scaled so that the total yield agrees with the modified K yield. The effect of manipulating the K *d* potential is remarkable. The high-energy part of the spectrum is reduced by almost two orders of magnitude when using the H *d* potential and is now similar to the Na spectrum. By manipulating one specific feature of the electron–ion potential we can significantly alter the rescattering process. We note that this change in the *d* potential results in only small changes of the *d* state energies. We have also tested several pseudopotentials which give correct *d* state energies and find that the high-energy part of the photoelectron spectrum is unchanged.

2.9 Photoemission Spectra

The photoemission from an isolated atom in a strong field can be calculated from a knowledge of its time-dependent dipole moment

$$d(t) = \langle \psi(t)|z|\psi(t)\rangle. \tag{38}$$

We assume in what follows that the laser is polarized along the *z* direction. In a gas of atoms the polarization is proportional to the density times the single-atom dipole moment. The non-linear component of the polarization is the input

to the time-dependent Maxwell equation that describes the propagation of the emitted radiation through the gas. The single-atom spectrum is proportional to the square of the Fourier transform of the dipole expectation value over the laser pulse:

$$|\mathcal{D}(\omega)|^2 = \left|\frac{1}{T}\int_0^T \mathrm{d}t \mathrm{e}^{-\mathrm{i}\omega t} d(t)\right|^2. \tag{39}$$

Due to the inversion symmetry of the isolated atom, this spectrum is dominated by odd harmonics of the driving field when no other symmetry-breaking mechanism is present. These strong field high harmonics, as is well known, form a broad plateau that can reach into the soft X-ray regime. They also form the basis for attosecond pulse generation.

In an experiment, a gas of atoms is driven to emit harmonic radiation which is strongly modified as it propagates through the non-linear medium. A full description of harmonic generation must also account for these macroscopic phase-matching effects, which are beyond the scope of this article. We will concern ourselves with the details of the single-atom calculations and techniques that can be used to extract information from them about the dynamics of an atom in a strong field.

In practice, it is very hard to calculate the dipole moment directly from the time-dependent wave function because of the form of the matrix element, which heavily weights the behavior of the electron far from the ion core. This means that small errors in the wave function propagation show up as large errors in the time-dependent dipole. It is better to start by calculating the acceleration of the electron which is

$$a(t) = \frac{\mathrm{d}^2}{\mathrm{d}t^2}\langle z\rangle = -\langle [H,[H,z]]\rangle, \tag{40}$$

where H is the full Hamiltonian including the laser interaction. The dipole strength is related to the Fourier transform of the acceleration, $\mathcal{A}(\omega)$, by

$$\mathcal{D}(\omega) = \mathcal{A}(\omega)/\omega^2. \tag{41}$$

Intuitively we expect the acceleration to be dominated by contributions from regions near the ion core where the electron experiences a large force. Indeed, for a spherically symmetric potential the acceleration is proportional to the expectation value $\langle \partial V(r)/\partial z\rangle$ which is z/r^3 for hydrogen. This weighting of the region close to the ion core helps make the calculation more tractable. That said, individual calculations of the high harmonic spectrum for a specific set of laser parameters are almost impossible to converge. There are two reasons for this. The first one is physical and stems from the fact that the individual harmonics in the spectrum are calculated as a coherent sum over several

quantum pathways that lead to the same final emission energy. These individual contributions are rapidly varying with laser intensity and wavelength, which means that very small changes in the laser parameters or the details of the calculation can lead to large changes in individual harmonics. Fortunately, such convergence is hardly warranted. What is of physical relevance is the highly non-linear intensity scaling of the harmonic's amplitude and phase, and these *trends* can be converged with moderate effort. Realistically, two different single-atom calculations that showed the same dependence on laser intensity but differed in fine details and overall magnitude by a factor of two would not be cause for great concern.

The second reason high harmonic calculations are difficult to converge is numerical and stems from reflections of the ionized wave packets from the grid boundary. The proper damping of these reflections is crucial for calculating, for example, the characteristic high-energy cutoff of the spectrum. Wave packets that reflect from the grid boundary gain a great deal of additional energy from the laser field and completely mask the physical cutoff in the spectrum. Because of the broad spectrum of energies that make up the wave packets it is not possible to design "optimal" absorbing boundaries for the grid. Instead we use a very soft ($\cos^{1/8}$) mask function spread over several hundred grid points [46]. By using a large enough angular momentum basis we can avoid reflections in the "ℓ coordinate". It is a good idea to remove any flux that reaches the maximum ℓ value and to keep track of the amount of flux lost via this route. It should be kept at the level of a few percent of the flux absorbed by the radial mask function.

When using ℓ-dependent pseudopotentials we must calculate the acceleration by evaluating the double commutator in Eq. (40) numerically. This is expensive and requires roughly the same effort as the time propagation. Fortunately, there are high-quality approximations to the above-threshold portion of the spectrum available, and we turn to a discussion of these next.

2.10 Approximate Dipole Calculation

A useful way to gain insight into the physics of harmonic generation is to calculate approximations to the full time-dependent dipole that restrict the number or character of the states that can participate in the process. For instance, the role of the bound states can be systematically investigated by defining a subspace projection operator $\hat{P}_n$:

$$\hat{P}_n = |1\rangle\langle 1| + |2\rangle\langle 2| + \cdots + |n\rangle\langle n|. \tag{42}$$

The projected wave function at a time t is $|\Phi_n(t)\rangle = \hat{P}_n|\psi(t)\rangle$, where $|\psi(t)\rangle$ is the full time-dependent wave function. The approximate dipole moment is calculated by requiring that the transition either begin or end in the projected subspace:

$$\langle d \rangle(t) = \langle \psi(t)|z|\psi(t)\rangle \approx \langle \psi(t)|\hat{P}_n z + z\hat{P}_n|\psi(t)\rangle - \langle \psi(t)|\hat{P}_n z \hat{P}_n|\psi(t)\rangle. \quad (43)$$

As $n \to \infty$ and $\hat{P}_n \to 1$, the approximate dipole goes over to the full dipole. The last term makes up for double-counting of transitions between states in the projected subspace. An equivalent way to write the approximate dipole that makes this clear is

$$\langle d \rangle(t) \approx \langle d_n \rangle(t) = \langle \psi|z|\Phi_n\rangle + \langle \Phi_n|z|\psi\rangle - \langle \Phi_n|z|\Phi_n\rangle. \quad (44)$$

This applies equally well when we calculate the acceleration form of the dipole.

In the rare gas atoms it was found that using just $\hat{P}_1$, where the state $|1\rangle$ is the field-free ground state, is an excellent approximation to the full high harmonic spectrum, both amplitude and phase, for all harmonics above the ionization threshold [46]. This provides a validation for the rare gases of the physical model underlying the strong field approximation, which assumes that excited bound states play no role in the HHG process [47]. It also provides a very fast algorithm for calculating the HHG spectrum, because the projection operator eliminates all of the angular momentum channels except those adjacent to the channel containing the ground state.

In the alkali metal atoms, on the other hand, there exists a very strong dipole coupling between the *ns* ground state and the first excited *np* state. This strong coupling, which is absent in the rare gases, can be expected to play a role in strong field processes at MIR wavelengths [48]. Figure 3 shows a single-atom harmonic spectrum calculated for a potassium atom in a 3.2 μm, 80 cycle laser pulse with a peak intensity of 1 TW/cm^2. The spectrum exhibits many similarities with the better-known near-IR excitation of rare gas atoms, especially the general form of the spectrum and the cutoff. As an example of the role played by the strong ground–first excited state coupling, we compare the full result to two approximate dipoles calculated using

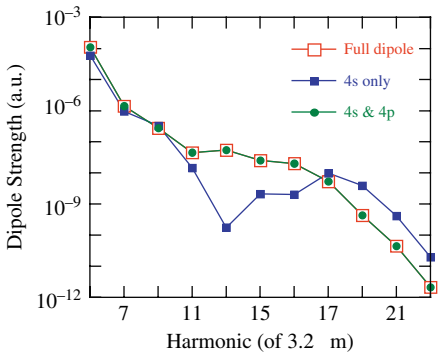

Fig. 3 Single-atom harmonic spectrum for K. The full calculation is compared to approximate dipoles calculated using the continuum wave packet plus the 4*s* and the $4s + 4p$ states

$$\hat{P}_1 = |4s\rangle\langle 4s| \tag{45}$$

and

$$\hat{P}_2 = |4s\rangle\langle 4s| + |4p\rangle\langle 4p|. \tag{46}$$

The black squares in Fig. 3 are the result of including the dipole interaction between the time-dependent wave function and the ground (4 s) state. This approximation, which as we said works very well in the rare gases, fails here, showing differences in both the conversion efficiency and the harmonic cutoff energy. However, when we include the first excited state in the projected subspace, as shown with black circles (inside the white squares), we get agreement with the full result, demonstrating explicitly the role played by the excited state in the harmonic generation process.

2.11 Relation to the Strong Field Approximation

As discussed in a separate chapter, the strong field approximation (SFA) is an chapter of L'Huillier and Lewenstein alternate route to investigating strong field processes [47]. The SFA is itself a single active electron approximation, but one that ignores the role of excited states and the effect of the ion–electron interaction on the continuum dynamics of the electron. Even with these approximations, the full SFA is difficult to solve in the general case of a pulsed laser interacting with an atom. Its real efficacy derives from its evaluation via a saddle point method that emphasizes stationary contributions to the rapidly oscillating integrals that occur in the theory. In this saddle point SFA picture, the amplitude for any strong field process can be expressed as a *coherent* sum over only a few quantum orbits. These space–time trajectories follow a sequence of release into the continuum (ionization), acceleration in the IR field, and return to the ion core, where the electron can either rescatter or recombine. They provide a powerful framework for interpreting strong field processes [47].

The key features in an SFA explanation of any strong field process are the precise quantum orbits involved, their weights, and the scaling of these with increasing laser intensity. The quantum orbits and their intensity scalings are simple to calculate since the continuum dynamics in the SFA are essentially that of a classical electron in a strong laser field. This tends to be a good approximation, since the density of states in the continuum is high and the ionizing, oscillating wave packet spends most of its time outside the steepest part of the ionic potential. The calculation of the amplitude for a given process, however, depends sensitively on the details of the electron dynamics, and given the drastic assumptions in the SFA they can be suspect. TDSE calculations, which include a much better description of the electron dynamics, lack the powerful interpretive framework of quantum orbits for understanding their results. The two

approaches can be made much more useful if the quantum orbits and their weights can be extracted from the TDSE calculations. Sometimes, as in the case of resonant ionization, this cannot be done since the SFA does not apply. But often it can, and we briefly review two such cases, one pertaining to HHG and the second to high-order ATI spectra.

The SFA description of HHG gives a picture of the photoemission on a sub laser-cycle timescale in terms of the times at which the electrons that follow the various quantum orbits return to the ion core. The electric field with component $e^{i\omega_k t}$ will peak at times corresponding to the return of electrons with an energy E_k at the time of return which satisfies $\hbar\omega_k = I_p + E_k$ where I_p is the ionization potential. It follows that by applying a window function to the full dipole acceleration spectrum (amplitude and phase) calculated with the TDSE around a frequency ω_k and Fourier transforming to the time domain, we can examine the time dependence of the emission:

$$\mathcal{E}_k(t) = e^{-i\omega_k t} \int d\omega\, e^{-i(\omega-\omega_k)t}[\mathcal{A}(\omega)F(\omega-\omega_k)], \tag{47}$$

where F is the window function. To examine sub-cycle time dependences, we use a filter that is much wider than one harmonic interval. By sliding the window in energy we can build up a picture of the time dependence. An example, calculated by Tate et al. for argon driven by a 2 μm laser, is shown in Fig. 4. The return times and energies for the classical trajectories predicted by the SFA are shown as dark lines. The strength of the windowed emission along a given trajectory can be used to extract the weight of the process. At these wavelengths the correspondence to the SFA trajectories is very good. In similar calculations at 800 nm in the rare gases we have found that though the SFA quantum orbits are themselves very well reproduced in the TDSE calculations, their weights are often completely different, which can have large consequences for attosecond pulse generation [49].

Similar to HHG, the semi-classical orbits that give rise to high-energy electrons in above-threshold ionization spectra can be identified via the SFA. Bauer [50] has shown that these orbits, and their weights, can be extracted from a TDSE calculation using the window function technique discussed above.

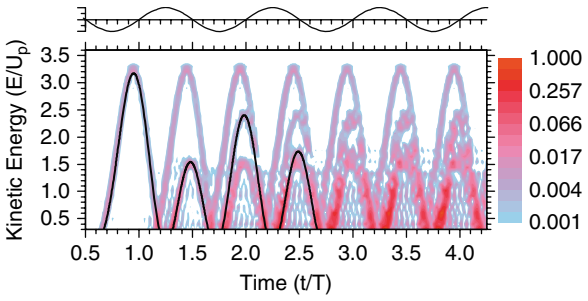

Fig. 4 Quantum orbits calculated via the TDSE for an argon atom interacting with intense, 2 μm light. The semi-classical predictions are shown as *solid black lines* in the *left half* of the figure

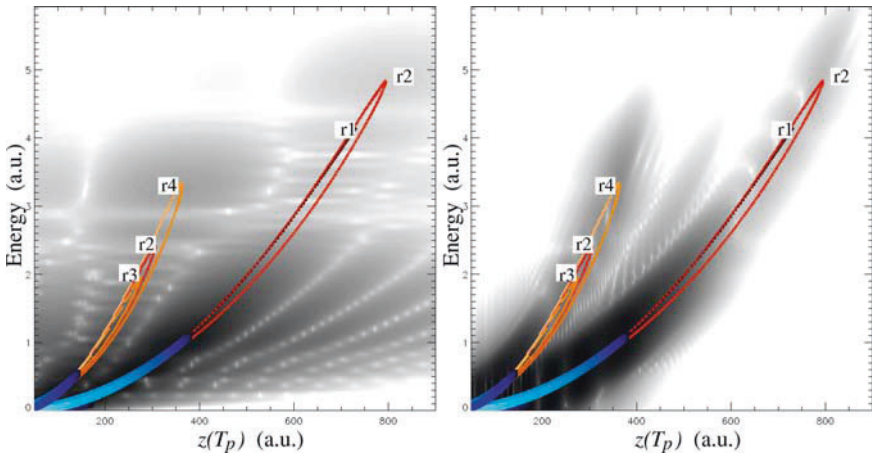

Fig. 5 The emergence of quantum wave packets aligned along the quasi-classical orbits. In this TDSE calculation the resolution of the energy analysis is either very narrow (*left*) or very wide (*right*). The wide resolution plot is compared to the semi-classical prediction (*heavy lines*). The coordinates transverse to the laser polarization have been integrated over

When the energy window used in the analysis is very narrow, as in Fig. 5 (left), only interferences due to energy-resolved, spatially delocalized states can be seen. But when the energy window is made much wider than the photon energy, the classical orbits (again shown as heavy lines) clearly emerge.

2.12 Restricted Ionization Model

In this section we give an example of how a standard SAE calculation can be modified to gain greater insight into a physical process. We treat the case of an atom subject to a combined attosecond pulse train and infrared field:

$$\mathcal{E}_{\mathrm{X}}(t) + \mathcal{E}_{\mathrm{IR}}(t). \tag{48}$$

The intensity of the XUV field is chosen such that the ionization is significantly enhanced over that due to the IR field alone, which means that the XUV field dominates the ionization step. We still expect that the continuum dynamics will be dominated by the IR laser, however, since the ponderomotive energy scales as λ^2. We can of course test these assumptions by comparison to exact calculations.

Our goal is to directly calculate the excited portion of the time-dependent wave function under the assumptions outlined in the previous paragraph. We begin with the TDSE

$$\mathrm{i}\frac{\partial}{\partial t}|\psi\rangle = (H_\mathrm{A} + H_1 + H_\mathrm{X})|\psi\rangle. \tag{49}$$

Here H_A is the atomic Hamiltonian, H_1 is the interaction with the fundamental IR field, and H_X is the interaction with the high-frequency XUV field. The ground state wave function $|\phi_0\rangle$ satisfies

$$H_\mathrm{A}|\phi_0\rangle = E_0|\phi_0\rangle \tag{50}$$

and the XUV field has an average frequency given by $\bar{\omega}_X$ such that

$$H_\mathrm{X} = \widetilde{H}_\mathrm{X}\mathrm{e}^{-\mathrm{i}\bar{\omega}_\mathrm{X}t} + \mathrm{c.c.} \tag{51}$$

This means that $\widetilde{H}_\mathrm{X}$ includes the (possibly complex) slowly varying envelope of the XUV field. We define a detuning $\Delta = E_0 + \bar{\omega}_\mathrm{X}$. Next we write the wave function as

$$|\psi(t)\rangle = \mathrm{e}^{-\mathrm{i}H_\mathrm{A}t}|\phi_0\rangle + \mathrm{e}^{-\mathrm{i}\Delta t}|\widetilde{\psi}(t)\rangle. \tag{52}$$

So far this is still exact, because we have not specified what $|\widetilde{\psi}(t)\rangle$ is. But the idea is clear: the full wave function is split into two pieces, a ground state portion that oscillates at a frequency set by E_0 and a "continuum" portion $|\widetilde{\psi}(t)\rangle$ that has been formed via one-photon absorption and oscillates at approximately Δ. Substituting this form of the wave function into Eq. (1) and canceling terms gives an equation for the time evolution of $|\widetilde{\psi}(t)\rangle$:

$$\mathrm{i}\frac{\partial}{\partial t}|\widetilde{\psi}(t)\rangle = \mathrm{e}^{+\mathrm{i}\bar{\omega}_\mathrm{X}t}(H_1 + H_\mathrm{X})|\phi_0\rangle + (H_\mathrm{A} + H_1 + H_\mathrm{X} - \Delta)|\widetilde{\psi}(t)\rangle. \tag{53}$$

In the first bracket we drop rapidly varying terms which oscillate at $\bar{\omega}_X \pm \omega_1$ compared to the slowly varying term $\widetilde{H}_\mathrm{X}$. In the second bracket we drop the $H_\mathrm{X}(t)$ term because we expect the time evolution to be dominated by the IR field once the electron is excited out of the ground state. Making these approximations gives

$$\mathrm{i}\frac{\partial}{\partial t}|\widetilde{\psi}(t)\rangle = \widetilde{H}_\mathrm{X}|\phi_0\rangle + (H_\mathrm{A} + H_1 - \Delta)|\widetilde{\psi}(t)\rangle. \tag{54}$$

This is our main result. The time evolution of $|\widetilde{\psi}(t)\rangle$ has two components: an inhomogeneous source term corresponding to the absorption of a single XUV photon from the ground state and a homogeneous term corresponding to time evolution in the continuum at the "average" energy Δ.

In practice $H_\mathrm{X}(t) = \mathcal{E}_\mathrm{X}(t)\,\hat{\mu}\cdot\boldsymbol{r}$, where $\hat{\mu}$ is the polarization direction of the XUV field. If we define a source wave function $|\phi_\mathrm{s}\rangle = \hat{\mu}\cdot\boldsymbol{r}\,|\phi_0\rangle$ then to take a short time step we use

$$|\widetilde{\psi}(t+\delta t)\rangle = \mathrm{e}^{-\mathrm{i}(H_\mathrm{A}+H_\mathrm{I}-\Delta)\delta t}|\widetilde{\psi}(t)\rangle + \delta t\, \widetilde{E}_\mathrm{X}|\phi_\mathrm{s}\rangle, \tag{55}$$

where $\widetilde{E}_X$ is the slowly varying envelope (possibly complex) of the XUV field. As an example of how the XUV envelope is calculated, consider a full XUV field given by

$$\mathcal{E}_\mathrm{X}(t) = F(t)\sum_q \mathcal{E}_q \sin(q\omega_\mathrm{l}(t-t_\mathrm{d}) - \varphi_q). \tag{56}$$

$F(t)$ is the envelope of the whole XUV pulse, t_d is the overall time shift of the attosecond pulse train, and phase locking is determined by the variation of φ_q with q. The slowly varying envelope of the positive frequency part is then

$$\widetilde{E}_\mathrm{X}(t) = \frac{1}{2}F(t)\sum_q \mathcal{E}_q\, \mathrm{e}^{-\mathrm{i}(q\omega_\mathrm{l}-\bar{\omega}_X)(t-t_\mathrm{d})}\, \mathrm{e}^{\mathrm{i}(\bar{\omega}_X t_\mathrm{d}+\varphi_q)}. \tag{57}$$

There are several uses for such a restricted ionization model. One of the most fruitful is to study the effect of the atomic potential on the ionizing wave function, by turning on or off the atomic potential in the term $H_\mathrm{A} = T + V_\mathrm{A}$ which drives the continuum dynamics. Figure 6 demonstrates this effect for a helium atom ionized by an attosecond pulse train while subjected to a moderately strong IR field. With this restricted ionization model the interaction between the continuum wave packet and the ion core can be studied as a function of the IR field intensity and the delay between the XUV and IR fields.

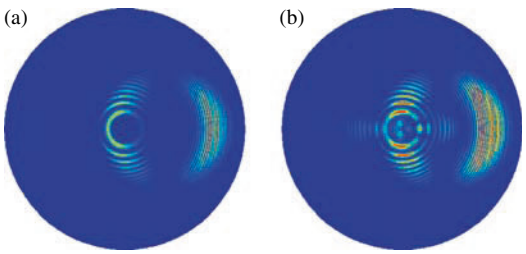

Fig. 6 Comparison of velocity distributions calculated for a helium atom subject to an IR laser pulse (800 nm, 5×10^{13} W/cm^2) and attosecond pulse train with one pulse per IR cycle and an average energy close to the ionization threshold. The radial coordinate is proportional to momentum, and the polarization of the electric fields is along the horizontal. In (**a**) we neglect the atomic potential in the continuum dynamics, in (**b**) we include it

3 Multiple Active Electrons

To calculate strong field phenomena that involve explicit multielectron effects requires going beyond the SAE. Interest in multiple active electron (MAE) effects has been driven first and foremost by the discovery of a significant probability for non-sequential double ionization (NSDI) in helium at IRfrequencies and intensities above 10^{14} W/cm^2 [17]. NSDI has subsequently been studied in all the rare gases and several molecular systems. More recent motivations include experimental data on the ionization of heavy molecular systems which requires physics beyond the SAE for its explanation and the use of attosecond pulses, in combination with few cycle IR pulses, to study correlated processes such as Auger decay in the time domain [51].

The conceptually simplest approach to multiple electron systems is to simply solve the full n-electron TDSE. This requires the solution of a partial differential equation of dimension $3n$ (without spin and with perhaps some small reduction in dimensionality due to symmetries). It remains a computational *tour de force* even for two-electron systems, especially at the IR wavelengths used in NSDI experiments [52,53]. The details of such calculations are beyond the scope of this chapter. The interest in MAE effects, coupled with the prohibitive cost of solving the TDSE directly, has spawned a number of methods for studying MAEs in a simplified manner. In this section we discuss a number of these more tractable approximations.

3.1 The Aligned Electron Model

The simplest approach to studying MAEs in a computationally tractable manner is to reduce the spatial extent of the electron wave functions. The "aligned electron model" (AEM) restricts each electron to move on a line, which is taken to be the direction of the laser polarization [54,55,56]. The soft core form of the Coulomb potential discussed above is now used to describe the electron–electron interaction as well as the electron–ion interaction. For two electrons the Hamiltonian in the length gauge is (a slightly different form of this model is used in reference [54])

$$H = H_1(x_1) + H_2(x_2) + V_{12} + (x_1 + x_2)\mathcal{E}(t), \tag{58}$$

$$\begin{aligned} H_i &= -\frac{1}{2}\frac{\partial}{\partial x_i} - \frac{2}{\sqrt{x_i^2 + a^2}}, \\ V_{12} &= \frac{C}{\sqrt{(x_1 - x_2)^2 + \epsilon}}. \end{aligned} \tag{59}$$

The single-particle softening parameter a^2 and the electron–electron softening parameter ϵ can be adjusted to mimic chosen parameters of a real system, e.g., the ionization potential of helium [56]. The correlation strength, C, can also be varied to study in a systematic way the effect of varying the amount of correlation between the electrons [57]. The numerical solution is usually carried out on a uniform cartesian grid on n dimensions, meaning that two- or three-electron systems can be studied.

The split-operator method is again an efficient choice for time propagation:

$$e^{-iH\delta t}\psi(t+\delta t) \approx e^{-iV_{12}\delta t/2}e^{-iH_1\delta t}e^{-iH_2\delta t}e^{-iV_{12}\delta t/2}\psi(t). \tag{60}$$

The electron–laser interaction $\mathcal{E}(t)x_i$ can be separated out into its own exponential or grouped with the H_i term. The kinetic energy terms can be evaluated very accurately using fast Fourier transforms. We have found that it is preferable to use the fourth-order finite difference method of Muller [4] coupled to the Crank–Nicolson form of the propagator to evaluate the $\exp(-iH_i\delta t)$ terms. The method is faster on the moderately sized grids (1024×1024) that we have tested and is as accurate as the FFT for all practical purposes. Given its linear scaling with increasing number of grid points (as opposed to the non-linear scaling of the FFT), this advantage will only increase for the larger grids needed to calculate photoelectron spectra. Though the two-electron AEM is a two-dimensional system, being cartesian it requires many more grid points for its solution than the two-dimensional SAE problem discussed earlier. For example, a box size of 256 au discretized using 1024 points along each dimension requires 10^6 grid points, as compared to the $\sim$ 32,000 points needed for an $r - \ell$ decomposition with the same box size.

Like its single-particle counterpart, the two-electron AEM exhibits many of the strong field phenomena of full dimensional systems. For example, the well-known "knee" structure in the double ionization probability as a function of laser intensity is reproduced. Though it gives qualitatively correct behavior, the relative amount of, e.g., double versus single ionization differs markedly from the experimental data on real atoms. The great strength of the model is that it can be solved exactly and so can be used to evaluate the role of physical effects such as correlation and to benchmark alternative theoretical treatments such as mean field theories [54]. Bauer has used the AEM to compare exact, SAE, mean field, and classical treatments of NSDI [56]. Ruiz et al. have treated a three-dimensional version of helium by using the two-electron AEM but allowing the electrons to move off axis in a constrained way [58].

3.2 Orbital-Dependent Potentials

An approach that goes beyond the AEM for treating many-electron systems while retaining some of the desirable features of the SAE is to use the *ansatz* that

the wave function can be approximated by a combination of time-dependent single-particle orbitals. These orbitals $\phi_i(\boldsymbol{r}_i, t)$ evolve according to a single-particle equation that looks much like the single-particle TDSE:

$$\mathrm{i}\frac{\partial}{\partial t}\phi_i(\boldsymbol{r}_i, t) = \widetilde{H}_i(t)\phi_i(\boldsymbol{r}_i, t). \tag{61}$$

This allows us to use all of the SAE machinery discussed above to evaluate the time evolution of the orbitals. One immediate consequence is that the Hamiltonians $\widetilde{H}_i$ must depend on the orbitals themselves, which means they must be calculated at every time step in a self-consistent manner, but this also means that we can build some correlation effects into the calculation while still solving n three-dimensional equations instead of one $3n$-dimensional equation.

The early pioneering work of Kulander [59,60] used time-dependent Hartree–Fock (TDHF) theory to study the strong field ionization of helium and xenon. In TDHF theory the wave function of the system is approximated by a single Slater determinant

$$\psi(\boldsymbol{r}_1, \ldots, \boldsymbol{r}_n, t) = \mathcal{A}\prod_{i=1}^{n}\phi_i(\boldsymbol{r}_i, t), \tag{62}$$

where $\mathcal{A}$ is the antisymmetrization operator. The Hamiltonian $\widetilde{H}_i$ includes single-particle terms such as the kinetic energy, the interaction with the nucleus, and the interaction with the field. It also includes a Hartree term, due to the Coulomb interaction of the ith electron with the charge density of the other electrons, and an exchange term [1]. The Hartree term depends only on the density of the individual orbitals, while the exchange term depends explicitly on the orbitals themselves. This dependence makes the correlation term non-local and hence expensive to calculate. In practice it is usually replaced by a density-dependent term, the *exchange–correlation* term. The calculation of the density-dependent terms can easily be as time consuming as the propagation itself.

The attractive features of TDHF are that some degree of correlation between the orbitals is included through the enforced orthogonality of the orbitals, and that it allows for the possibility that multiple excitations could play a role in the ionization dynamics. Already in the first studies of strong field phenomena via TDHF theory, however, it was realized that the TDHF method contains basic flaws. The wave function, being a single Slater determinant, enforces unphysical correlations between, for example, single and double ionization probabilities. It is also unable to smoothly evolve to the final superposition state (bound + continuum) which is the hallmark of strong field ionization. Furthermore, the non-linearity of the equations destroys any hope of calculating accurate ionization rates when there is a significant probability of ionization. This is because as the wave function ionizes, the electron density near the core decreases, which causes the electron repulsion term to diminish. This increases the binding of the

remaining density to the core, which shuts off ionization. The hallmark of this effect is a non-exponential decay in situations where it would be expected; see references [59,1] for additional details and examples. There has been work on "extended" TDHF, in which some of the constraints on the orbitals are relaxed so that physically desirable superposition states can occur [61]. While there is an improvement in the sense that single ionization is more sensibly described and features such as some version of the NSDI "knee" occur, the agreement with exact benchmark calculations is still insufficient.

Another method which may provide a tractable route to calculating MAE effects is time-dependent density functional theory (TDDFT) (see [62,63] and references therein). The basic quantity in DFT is the electron density

$$\rho(\boldsymbol{r}, t) = \sum_{i=1}^{n} |\phi_i(\boldsymbol{r}_i, t)|^2. \tag{63}$$

The theory is implemented via the time-dependent Kohn–Sham equations [64] which are of the form in Eq. (62). The Hamiltonian includes the Kohn–Sham potential which is constructed in principle from the electron density alone using functionals for the correlation and exchange energies. As in TDHF the potential depends on the orbitals through the density and the equations are nonlinear, though this presents no real problem in the time propagation. In practice TDDFT also has seemingly severe flaws. First, since TDDFT provides the electron density (albeit in terms of orbitals) it can be problematic to define observables such as the photoelectron spectrum or the probability of double ionization (see reference [56] for example). Second, the construction of high-quality time-dependent exchange–correlation potentials $v_{\mathrm{xc}}(t)$ is difficult since the exchange–correlation functional itself is not known for most systems. Though there has been some success in using TDDFT to qualitatively study HHG in molecular systems [63], no TDDFT calculation has been able to reproduce the NSDI "knee" even qualitatively using the best existing exchange–correlation functionals.

Recently, Lein and Kümmel [65] have carried out an ingenious calculation of the *exact* $v_{\mathrm{xc}}(t)$ for a correlated system (the two-electron AEM) undergoing strong field ionization. Their conclusion is that the failure of TDDFT to reproduce the NSDI knee can be understood as a manifestation of a basic flaw in TDDFT which use approximate exchange–correlation functionals. They find that the exact correlation potential develops a quasi-discontinuous step as one electron is ionized and moves away from the nucleus. This behavior, which they argue is related to the known discontinuity in the exact ground state DFT exchange–correlation energy when the electron number passes through an integer, is smoothed out when approximate functionals are used, which leads to the suppression of the NSDI knee. To cement their case, the authors add a discontinuous piece to $v_{\mathrm{xc}}(t)$ "by hand" and find that their TDDFT is then able to reproduce the correct NSDI behavior. This work points to a promising

future for TDDFT in strong field physics *if* functionals incorporating discontinuous behavior can be formulated and *if* they yield reasonable agreement with experiment.

Finally, we make mention of an extension to TDHF theory that can in principle provide an exact description of strong field correlated dynamics. Scrinzi, Brabec, and co-workers have formulated and tested a multi-configuration TDHF theory for studying strong field ionization from systems with many electrons [66,65]. In this version of TDHF the single Slater determinant restriction is relaxed and the *ansatz* for the wave function now consists of the linear combination of all the Slater determinants that can be formed from N linearly independent orbitals $\phi_i(\boldsymbol{r}_i, t)$. If the set of N orbitals ϕ_i form a complete set in the single-particle Hilbert space then the MCTDFH equations reduce to the full n-electron TDSE. But the theory may converge to the correct answer with a much smaller basis set. The reason is that the uncorrelated single-particle orbitals, which are chosen to optimally cover the initial correlated state of the system, evolve in time so as to maintain their coverage of the wave function. Provided that no new, strongly correlated structures appear in the wave function, the initial (small) basis set can suffice for the whole time evolution.

The most useful properties of MCTDHF are its ability to converge to a stable answer as the basis size is increased, as demonstrated for the interaction of up to six active aligned electrons in reference [65], and the way in which correlation is built in as the basis set size increases. By using more and more uncorrelated basis functions, the correlation of the full wave function is systematically increased. This allows for the systematic study of the role of correlation in strong field processes, something that has been lacking up to now. As an example, Caillat et al. [65] have shown that correlation is crucial in the understanding of the size dependence of the ionization probability of large "molecules" which are modeled as a one-dimensional system. The method, which will require large-scale computational resources if it is to describe three-dimensional systems, remains under active development.

In closing we wish to emphasize what we see as two key aspects of numerical methods in strong field physics. First, they are a fully integrated part of strong field theory, widely used along with more approximate theories such as the SFA, classical simulations, and simple models to explain the wealth of experimental data; and second, the proliferation of new experimental sources over the next decade, and the resultant flood of new data on strong field processes, will be the main driver of new theoretical developments.

4 Appendix: Velocity Gauge Time Propagation

Propagation in the velocity gauge is handled in a manner very similar to that used for the length gauge. Referring to Eq. (24) we use the symmetric splitting

$$e^{-i\hat{H}'\delta t} \approx e^{-i\hat{H}_2\delta t/2} e^{-i\hat{H}_1\delta t/2} \frac{[1-i\hat{H}_0\delta t/2]}{[1+i\hat{H}_0\delta t/2]} e^{-i\hat{H}_1\delta t/2} e^{-i\hat{H}_2\delta t/2}. \tag{64}$$

The terms involving $\hat{H}_1$ (Eq. (25)) are of the same form as the interaction term in the length gauge and are treated in the same way:

$$e^{-i\hat{H}_1\delta t/2}\phi = e^{\hat{M}^j}\phi^j, \tag{65}$$

where the non-zero elements of the antisymmetric matrix of $\hat{M}^j$ are $a_\ell = A(t)r_j^{-1}(\ell+1)c_\ell\delta t/2$. Again the full matrix is split into even and odd 2×2 block-diagonal matrices and the exponentiation is accomplished using the relation

$$\exp\left\{\begin{bmatrix} 0 & a \\ -a & 0 \end{bmatrix}\right\} = \begin{bmatrix} \cos a & \sin a \\ -\sin a & \cos a \end{bmatrix}. \tag{66}$$

Exponentiating the terms involving $\hat{H}_2$ (Eq. (25)) is more complicated since they couple ϕ_ℓ^j to the four adjacent coefficients $\phi_{\ell\pm1}^{j\pm1}$. To do it, we use the 2×2 splitting method twice in succession, first in the ℓ dimension and then in the j dimension. The exponent $-i\hat{H}_2\delta t/2$ can be written as a super-matrix, $\widetilde{N}$, which is tridiagonal in ℓ:

$$\widetilde{N} = -i\hat{H}_2\delta t/2 = \begin{bmatrix} 0 & \hat{a}_0 & 0 & \\ \hat{a}_0 & 0 & \hat{a}_1 & \\ 0 & \hat{a}_1 & 0 & \\ & & & \ddots \end{bmatrix}. \tag{67}$$

Each of the elements $\hat{a}_\ell$ are themselves matrices that are tridiagonal in j:

$$\hat{a}_\ell = c_\ell \frac{A(t)}{2\Delta r}\frac{\delta t}{2} \begin{bmatrix} 0 & \alpha_1 & 0 & \\ -\alpha_1 & 0 & \alpha_2 & \\ 0 & -\alpha_2 & 0 & \\ & & & \ddots \end{bmatrix} \tag{68}$$

with α_j given by Eq. (20). We now split the super-matrix $\widetilde{N}$ into even and odd pieces which consist of 2×2 blocks just as in Eq. (30)

$$e^{\widetilde{N}} = e^{\widetilde{N^e}} e^{\widetilde{N^o}}. \tag{69}$$

Before applying each of these exponentials, we diagonalize them using a similarity transformation:

$$\frac{1}{\sqrt{2}}\begin{bmatrix}1 & 1\\ 1 & -1\end{bmatrix}\exp\left\{\begin{bmatrix}0 & \hat{a}_\ell\\ \hat{a}_\ell & 0\end{bmatrix}\right\}\begin{bmatrix}1 & 1\\ 1 & -1\end{bmatrix}\frac{1}{\sqrt{2}}=\begin{bmatrix}\mathrm{e}^{\hat{a}_\ell} & 0\\ 0 & \mathrm{e}^{-\hat{a}_\ell}\end{bmatrix}.$$

The application of the operators $e^{\pm\hat{a}_\ell}$ is then made by further splitting the matrices $\hat{a}_\ell$ into even and odd pieces in the j index as in Eq. (30), and then using Eq. (66). The various even and odd matrices are placed symmetrically in Eq. (64) so that it remains unitary.

References

1. K. C. Kulander, K. J. Schafer, and J. L. Krause, in M. Gavrila, ed., *Atoms in Intense Laser Fields* (Academic Press, San Diego, 1992), pp. 247–300.
2. J. H. Eberly, R. Grobe, C. K. Law, and Q. Su, in M. Gavrila, ed., *Atoms in Intense Radiation Fields* (Academic Press, New York, 1992), pp. 301–334.
3. K. Schafer, M. Gaarde, K. Kulander, B. Sheehy, and L. F. DiMauro, in L. F. DiMauro, R. R. Freeman, and K. C. Kulander, eds., *ICOMP VIII Proceedings* (American Institute of Physics, New York, 2000), pp. 45–58.
4. H. G. Muller, Laser Phys. **9**(1), 138 (1999).
5. K. J. Schafer, B. Yang, L. F. DiMauro, and K. C. Kulander, Phys. Rev. Lett. **70**, 1599 (1993).
6. P. B. Corkum, Phys. Rev. Lett. **71**, 1994 (1993).
7. T. Brabec and F. Krausz, Rev. Mod. Phys. **72**(2), 545 (2000), http://link.aps.org/abstract/RMP/v72/p545.
8. B. Sheehy, J. Martin, T. Clatterbuck, D. Kim, L. DiMauro, P. Agostini, K. Schafer, M. Gaarde, and K. Kulander, in L. F. DiMauro, R. R. Freeman, and K. C. Kulander, eds., *ICOMP VIII Proceedings* (American Institute of Physics, New York, 2000), pp. 59–69.
9. M. Hentschel, R. Kienberger, C. Spielmann, G. A. Reider, N. Milosevic, T. Brabec, P. Corkum, U. Heinzmann, M. Drescher, and F. Krausz, Nature **414**(6863) 509 (2001), http://www.nature.com/doifinder/10.1038/35107000.
10. P. M. Paul, E. S. Toma, P. Breger, G. Mullot, F. Augé, P. Balcou, H. G. Muller, and P. Agostini, Science **292**, 1689 (2001).
11. L. H. Yu, L. DiMauro, A. Doyuran, W. S. Graves, E. D. Johnson, R. Heese, S. Krinsky, H. Loos, J. B. Murphy, G. Rakowsky, et al., Phys. Rev. Lett. **91**(7), 074801, 074801 (4 pages) (2003), http://link.aps.org/abstract/PRL/v91/e074801.
12. M. Dorr, R. M. Potvliege, and R. Shakeshaft, Phys. Rev. A (Atomic, Molecular, and Optical Physics) **41**(1), 558 (1990), http://link.aps.org/abstract/PRA/v41/p558.
13. E. Cormier and P. Lambropoulos, J. Phys. B **30**, 77 (1997).
14. K. C. Kulander and T. N. Rescigno, Comp. Phys. Comm. **63**, 523 (1991).
15. A. L'Huillier, P. Balcou, S. Candel, K. J. Schafer, and K. C. Kulander, Phys. Rev. A **46**, 2778 (1992).
16. M. Bellini, C. Lyngå, A. Tozzi, M. B. Gaarde, T. W. Hänsch, A. L'Huillier, and C. G. Wahlström, Phys. Rev. Lett. **81**, 297 (1998).
17. B. Walker, B. Sheehy, L. Dimauro, P. Agostini, and E. Al., Phys. Rev. Lett. **73**, 1227 (1994).
18. M. J. Nandor, M. A. Walker, L. D. V. Woerkom, and H. G. Muller, Phys. Rev. A **60**, R1771 (1999).
19. M. P. Hertlein, P. H. Bucksbaum, and H. G. Muller, J. Phys. B **30**, L197 (1997).
20. W.-C. Liu and C. W. Clark, Journal of Physics B: Atomic, Mol. Opt. Phys. **25**(21), L517 (1992), http://stacks.iop.org/0953-4075/25/L517.

21. W. J. Stevens, P. G. Jasien, M. Krauss, and H. Basch, Can. J. Chem. **70**, 612 (1992).
22. E. Cormier and P. Lambropoulos, J. Phys. B **29**, 1667 (1996).
23. G. G. Paulus, F. Lindner, H. Walther, A. Baltuska, E. Goulielmakis, M. Lezius, and F. Krausz, Phys. Rev. Lett. **91**(25), 253004, 253004 (4 pages) (2003), http://link.aps.org/abstract/PRL/v91/e253004.
24. C. Iaconis and I. A. Walmsley, Opt. Lett. **23**, 792 (1998).
25. B. W. Shore, *The Theory of Coherent Atomic Excitation* John Wiley & Sons, Inc., New York, 1990).
26. J. L. Krause, K. J. Schafer, and K. C. Kulander, Phys. Rev. Lett. **68**, 3535 (1992).
27. J. J. Macklin, J. D. Kmetic, and C. L. Gordon, Phys. Rev. Lett. **70**, 766 (1993).
28. X. Chen, A. Sanpera, and K. Burnett, Phys. Rev. A **51**, 4824 (1995).
29. K. J. Schafer and K. C. Kulander, Phys. Rev. Lett. **78**, 638 (1997).
30. K. J. Schafer and K. C. Kulander, Phys. Rev. A (Atomic, Molecular, and Optical Physics **42**(9), 5794 (1990), http://link.aps.org/abstract/PRA/v42/p5794.
31. V. Reed and K. Burnett, Phys. Rev. A **43**, 6217 (1991).
32. K. J. Schafer and K. C. Kulander, Phys. Rev. A **45**, 8026 (1992).
33. R. Blank and M. Shapiro, Phys. Rev. A **51**, 4762 (1995).
34. E. Cormier and P. Lambropoulos, J. Phys. B **28**, 5043 (1995).
35. B. R. Yang, K. J. Schafer, B. Walker, K. C. Kulander, and L. F. DiMauro., Phys. Rev. Lett. **71**, 3770 (1993).
36. H. G. Muller, Phys. Rev. Lett. **83**, 3158 (1999).
37. C. Cerjan and R. Kasloff, Phys. Rev. A **47**, 1852 (1993).
38. S. E. Koonin, *Computational Physics* Benjamin Cummings, 1986).
39. J. W. Negle, Rev. Mod. Phys. **54**, 913 (1982).
40. J. L. Krause and K. J. Schafer, J. Phys. Chem. A. **103**, 10118 (1999).
41. J. L. Richardson, Comp. Phys. Comm. **63**, 84 (1991).
42. H. DeRaedt, Comp. Phys. Report **7**, 1 (1987).
43. J. Hansen, T. Srevik, and L. B. Madsen, Phys. Rev. A **68**, 031401(R) (2003).
44. K. J. Schafer, Comput. Phys. Comm. **63**, 427 (1991).
45. A. Wetzels, A. Gurtler, F. Rosca-Pruna, S. Zamith, M. J. J. Vrakking, F. Robicheaux, and W. J. van der Zande, Phys. Rev. A (Atomic, Molecular, and Optical Physics) **68**(4), 041401, 041401 (4 pages) (2003), http://link.aps.org/abstract/PRA/v68/e041401.
46. J. L. Krause, K. J. Schafer, and K. C. Kulander, Phys. Rev. A (Atomic, Molecular, and Optical Physics) **45**(7), 4998 (1992), http://link.aps.org/abstract/PRA/v45/p4998.
47. M. Lewenstein, P. Balcou, M. Y. Ivanov, A. L'Huillier, and P. B. Corkum, Phys. Rev. A **49**, 2117 (1994).
48. B. Sheehy, J. D. D. Martin, L. F. DiMauro, P. Agostini, K. J. Schafer, M. B. Gaarde, and K. C. Kulander, Phys. Rev. Lett. **83**, 5270 (1999).
49. M. B. Gaarde and K. J. Schafer, Phys. Rev. A **65**, R031406 (2002).
50. D. Bauer, Phys. Rev. Lett. **94**(11), 113001, 113001 (4 pages) (2005), http://link.aps.org/abstract/PRL/v94/e113001.
51. M. Drescher, M. Hentschel, R. Kienberger, M. Uiberacker, V. Yakovlev, A. Scrinzi, T. Westerwalbesloh, U. Kleineberg, U. Heinzmann, and F. Krausz, Nature **419**, 803 (2002).
52. J. S. Parker, L. R. Moore, K. J. Meharg, D. Dundas, and K. T. Taylor, Journal of Physics B: Atomic, Mol. Opt. Phys. **34**(3), L69 (2001), http://stacks.iop.org/0953-4075/34/L69.
53. H. W. van der Hart, B. J. S. Doherty, J. S. Parker, and K. T. Taylor, Journal of Physics B: Atomic, Mol. Opt. Phys. **38**(13), L207 (2005), http://stacks.iop.org/0953-4075/38/L207.
54. M. S. Pindzola, D. C. Griffin, and C. Bottcher, Phys. Rev. Lett. **66**(18), 2305 (1991), http://link.aps.org/abstract/PRL/v66/p2305.
55. R. Grobe and J. H. Eberly, Phys. Rev. Lett. **68**(19), 2905 (1992), http://link.aps.org/abstract/PRL/v68/p2905.

56. D. Bauer, Phys. Rev. A (Atomic, Molecular, and Optical Physics) **56**(4), 3028 (1997), http://link.aps.org/abstract/PRA/v56/p3028.
57. W.-C. Liu, J. H. Eberly, S. L. Haan, and R. Grobe, Phys. Rev. Lett. **83**(3), 520 (1999), http://link.aps.org/abstract/PRL/v83/p520.
58. C. Ruiz, L. Plaja, L. Roso, and A. Becker, Phys. Rev. Lett. **96**(5), 053001, 053001 (4 pages) (2006), http://link.aps.org/abstract/PRL/v96/e053001.
59. K. C. Kulander, Phys. Rev. A (General Physics) **36**(6), 2726 (1987), http://link.aps.org/abstract/PRA/v36/p2726.
60. K. C. Kulander, Phys. Rev. A **38**, 778 (1988).
61. N. E. Dahlen and R. van Leeuwen, Phys. Rev. A (Atomic, Molecular, and Optical Physics) **64**(2), 023405, 023405 (7 pages) (2001), http://link.aps.org/abstract/PRA/v64/e023405.
62. X.-M. Tong and S.-I. Chu, Phys. Rev. A (Atomic, Molecular, and Optical Physics) **57**(1), 452 (1998), http://link.aps.org/abstract/PRA/v57/p452.
63. X. Chu and S.-I. Chu, Phys. Rev. A (Atomic, Molecular, and Optical Physics) **64**(6), 063404, 063404 (9 pages) (2001), http://link.aps.org/abstract/PRA/v64/e063404.
64. W. Kohn and L. J. Sham, Phys. Rev. **140**, 1133 (1965).
65. M. Lein and S. Kummel, Phys. Rev. Lett. **94**(14), 143003, 143003 (4 pages) (2005), http://link.aps.org/abstract/PRL/v94/e143003.
66. M. Kitzler, J. Zanghellini, C. Jungreuthmayer, M. Smits, A. Scrinzi, and T. Brabec, Phys. Rev. A (Atomic, Molecular, and Optical Physics) **70**(4), 041401, 041401 (4 pages) (2004), http://link.aps.org/abstract/PRA/v70/e041401.

Principles of Single Atom Physics: High-Order Harmonic Generation, Above-Threshold Ionization and Non-Sequential Ionization

Maciej Lewenstein and Anne L'Huillier

1 Introduction

The physics of atoms in strong laser fields has been a subject of intensive studies in the last 20 years. Atoms subjected to short-pulse high-intensity fields, of magnitude comparable to the Coulomb nucleus attraction field, respond non-perturbatively. Electrons initially in the ground state can absorb a large number of photons, much more than the minimum number required for ionization, thus being ionized with a high kinetic energy. This process has been called above-threshold ionization (ATI). Atoms subject to strong laser fields can emit one or several electrons. In some conditions, these electrons are emitted "simultaneously", a process called direct or non-sequential ionization. Finally, efficient XUV photon emission in the form of high-order harmonics of the fundamental laser field (HHG) has been observed.

Our intention in this chapter is not to review in detail these phenomena. There have been at least three recent books which provide excellent reviews of the subject of atoms in strong laser fields in general, Refs. [1, 2, 3]. The development of this field of research is also well described in the Proceedings of the International Conferences on Multiphoton Processes [4, 5, 6, 7, 8, 9], the Proceedings of the "Super-Intense-Laser-Atom-Physics" meetings [10, 11, 12], and in numerous review articles (see, for example, [13, 14], as well as [15] for ATI, [16] for both ATI and non-sequential ionization, [17, 18, 19] for HHG, and [20] for two-electron atoms in strong laser fields). Our aim is to emphasize the common features of HHG, ATI, and non-sequential ionization: the experimental conditions and methods (Section 2), the history (Section 3), and the theoretical description (Sections 4 and 5).

Our chapter is organized as follows: We begin by a brief discussion of the experimental conditions for observing HHG, ATI, and non-sequential ionization (Section 2). In Section 3, we present some typical experimental results and

M. Lewenstein
Institute of Photonic Sciences, Parc Mediterrani de la Tecnologia, Av. del Canal Olimpic s/n, 08860 Castelldefels, Barcelona, Spain
e-mail: maciej.lewenstein@icfo.es

T. Brabec (ed.), *Strong Field Laser Physics*,
DOI: 10.1007/978-0-387-34755-4_7,

give a historical perspective for each of the phenomena. In Section 4, we review the theoretical approaches to describe the phenomena in question. In Section 5, we present a simple formulation of one of these approaches, called the strong field approximation (SFA) and apply it to HHG, ATI, and non-sequential ionization. We emphasize in particular its quasi-classical interpretation. Finally, we conclude in Section 6.

2 Experimental Conditions and Methods

A typical (general) experimental setup for studying atoms in strong laser fields is shown in Fig. 1. We discuss in turn the different elements of this setup.

2.1 Lasers

Lasers used to study atoms in strong electromagnetic fields have changed considerably during the past decade. The intensity available has increased from 10^{14} W cm^{-2} to 10^{19} W cm^{-2}. The pulse duration has decreased from $\sim$10 ps to $\sim$10 fs. The shortest laser pulses used today to study atoms in strong laser fields are about 5 fs (two cycles) long. The advantage of using short pulses is that atoms get exposed to a higher laser intensity before they ionize. This leads to electrons with higher kinetic energy, a larger amount of non-sequential ionization relative to sequential ionization and higher-order harmonics.

The repetition rate of the lasers has increased from a few shots per minute for the Neodyme-glass lasers to 10–100 kHz for the recent titanium–sapphire (Ti:S) lasers, allowing experimentalists to improve considerably the statistics of the data, as well as to have access to a larger dynamical range. For example, precision measurements of ATI spectra extending over five or more decades have become possible (see, for instance, [21] and references therein) using lasers with very high repetition rates.

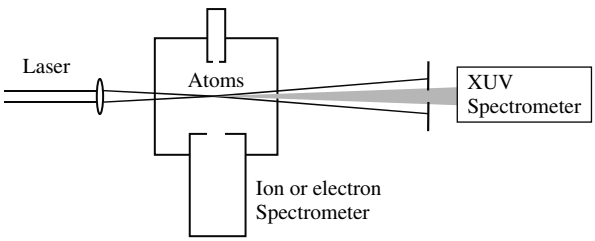

Fig. 1 Typical schematic experimental setup in the study of atoms in strong laser fields. An intense short-pulse laser is focused into an interaction chamber which contains a gas of atoms. Ions or electrons can be detected, e.g., with time-of-flight techniques. Alternatively, the radiation which is emitted on axis can be analyzed with an extreme-ultraviolet spectrometer

Many types of lasers have been used, ranging from excimer lasers (XeF [22] or KrF [23], with wavelengths 193 nm and 248 nm, respectively), Nd:YAG, Nd:Glass (1 μm), Ti:S (800 nm), dye lasers, etc. In addition, the second harmonics of these lasers [24, 25, 26], as well as different sum- or difference-frequency mixing processes, involving, for example, an optical parametric amplifier [27, 28] or a Nd:YFL mode-locked laser to get into the mid-infrared range [29], have also been employed. The processes of interest scale roughly as λ^{-2}, which make long wavelength lasers more interesting. In the last ten years, the "favorite" tool has become the Ti:S laser, providing very short-pulse durations, high laser intensities at high repetition rates.

The different parameters of the laser pulses, such as the polarization, the focusing characteristics, the spatial, and temporal profiles, are often varied in the experiments. For example, the studies of harmonic generation with pulses of varying degree of ellipticity have been historically important to confirm the quasi-classical description of the process (see below). Recent experiments do not simply vary a given parameter, but attempt to shape a laser pulse (by varying, for example, its phase, or its degree of ellipticity) in order to get a specific result. Bartels and coworkers [30] have thus managed to enhance the generation of one harmonic relative to the others by an order of magnitude by varying the phase of the laser with a deformable mirror. The pulse was shaped using an evolutionary algorithm.

2.2 Ionization Experiments

In the ionization experiments, the atomic gas is usually introduced with a leak valve, in order to get a uniform gas density in the interaction region. Pressures varying from 10^{-8} to 10^{-5} mbar are optimized in order to get the maximum number of events, but at the same time to avoid space charge effects in the interaction region as well as collisions in the detector tube. In the recent cold-target recoil-ion momentum spectroscopy experiments [31, 32], supersonic gas jets are also used, providing cold atoms in the interaction region (30 K). Many different atomic species have been investigated, especially in the early days: alkalis, alkaline-earths, hydrogen (see, for example, [33]), and rare gases (we do not discuss here the ionization of molecules or clusters in strong laser fields). The first two species have relatively low ionization energies and, in the near-infrared and visible regions, ionize mostly in the so-called multiphoton regime, where the atom is not much perturbed by the laser field. The atoms that have been most studied experimentally have been the different rare gases, from He to Xe. The detection of ions with different charge states requires a time-of-flight spectrometer, with an acceleration stage where ions are accelerated, a field-free tube where ions travel at different speeds, and a detector, e.g., multichannel plates or an electron multiplier. The experimental measurement consists in varying the laser energy and in detecting the number of ions produced as a function of the laser intensity. Recently, measurements of recoil-ion momenta have been performed using imaging detectors [31, 32].

Electron energy spectra have been recorded with many different detectors. The simplest one is the time-of-flight (TOF) tube, providing good resolution, but limited efficiency. TOF detectors also allow one to record angular distributions by varying the laser polarization with respect to the axis of the flight tube. The detection efficiency can be increased by using a magnetic bottle [34] or a parabolic electrostatic mirror [35]. Of course, the information on the angle of emission is lost but the detection efficiency increases from a few percent to 50%. Imaging techniques [36, 37, 38] are now becoming more and more popular since they allow one to get "the whole picture" (energy and angle) at once. Recently, coincidence techniques have been used to detect only those electrons accompanying a double ionization process [37, 38] (see the chapter of Ullrich and Voitkiv).

2.3 Photon Detection

In the high-order harmonic generation experiments, the gas medium is provided by a gas jet, hollow fiber [39, 40], or a (small) gas cell [41]. The atomic density is usually much higher than that in the ionization experiments, up to a few hundred mbar, since the number of photons increase rapidly with the atomic density. This aspect is described in more detail in the chapter of Salières and Christov. Rare gases are also the "favorite" species, for obvious technical reasons. In addition, some work has been done with alkali ions [42], as well as alkali atoms using mid-infrared lasers [29]. Photons are separated in energy and detected by an XUV spectrometer, including a grating, sometimes a refocusing mirror, and a detector (electron multiplier). Lately, experimental investigations of high-order harmonics have concentrated on the characterization of the radiation in different conditions, in both space [43, 44, 45, 46, 47, 48] and time [49, 50, 51, 52, 53, 54]. The characterization of the spatial properties requires imaging techniques. The temporal properties of the short-pulse radiation are usually measured by a cross-correlation or autocorrelation technique based on photoelectron spectroscopy.

3 Typical Experimental Results and Historical Perspective

We now present a few typical experimental results and give a small historical background for the three phenomena. Again, our emphasis is not to make a thorough review but to illustrate the common features of the three phenomena.

3.1 High-Order Harmonic Generation

Harmonic generation in gases in the multiphoton regime have been studied since the end of the 60's. In this regime, the harmonic intensity diminishes rapidly with the harmonic order and only a few orders can be observed. In contrast, at high intensities, a typical harmonic spectrum exhibits a fast decrease for the first few harmonics, followed by a long plateau, which ends

up by a rapid cutoff. An experimental spectrum is shown for example in Fig. 2 [55]. It is the first HHG result obtained in a gas of neon with a short-pulse (125 fs) 800 nm Ti:S laser. It shows odd harmonic peaks up to the 111th order (even harmonics are forbidden owing to the inversion symmetry). The increase of the harmonic efficiency at low orders is simply due to the grating response not taken into account in the data. The spectrum shows a beautiful plateau up to the $\sim$ 87th harmonic. The efficiency then drops rapidly.

Recent experiments using very short laser pulses (in the 10 fs regime) show even higher orders, corresponding to energies $\sim$ 500 eV [56, 57]. An example is shown in Fig. 3 [19]. The spectral range of the harmonic emission as well as the conversion efficiency is presented for three different rare gases: Ar, Ne, and He. The efficiency is highest in Ar, but the highest photon energies are obtained in He.

As discussed in more detail in the chapter of Salières and Christov, efficient HHG requires not only efficient radiation of single atoms but also macroscopic constructive interference of contributions of participating radiation sources, i.e., efficient phase matching [58, 59]. The properties of the harmonic emission (ultrashort-pulse duration, high brightness, good coherence) make it a unique source of XUV radiation, used in a growing number of applications ranging from atomic [60, 61] and molecular

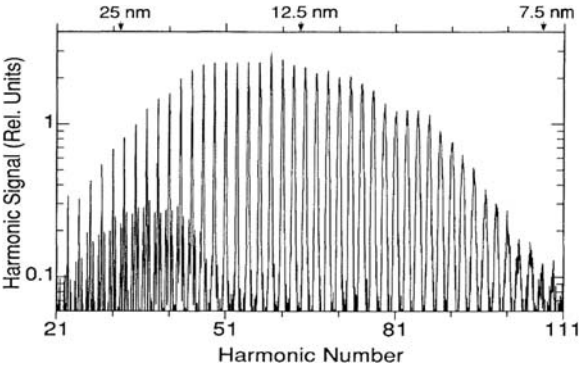

Fig. 2 Harmonic spectrum taken in neon with a 125 fs 800 nm titanium–sapphire laser. The intensity is 1.3×10^{15} W cm^{-2}. The first increase is simply due to the grating response. The decrease at high energies is the harmonic cutoff. The spectrum extends up to the 111th harmonic (from [55])

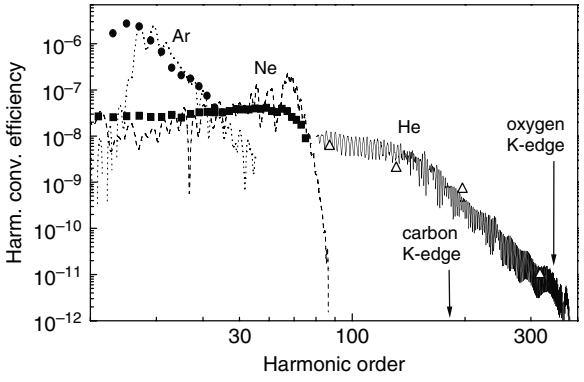

Fig. 3 Harmonic conversion efficiency in Ar (*filled circles*), Ne (*filled squares*), and He (*open triangles*) with a 7 fs 800 nm laser pulse. The intensities are, respectively, 5×10^{14} W cm^{-2}, 2×10^{15} W cm^{-2}, and 3×10^{15} W cm^{-2}. Results of calculations including propagation effects are presented as *dotted*, *dashed*, and *solid curves*, respectively (from [19])

[62, 63, 64] spectroscopy to solid-state [65, 66, 67] and plasma [68, 69, 70] physics. The harmonic radiation is intense enough to induce non-linear optical processes in the XUV range, as recently demonstrated by [71, 72, 73]. It can also be used to generate extremely short (attosecond) light pulses [74, 75, 76, 77] (see the chapter of Scrinzi and Muller). Recently, it was shown that the process of HHG itself can be used for attosecond spectroscopy of molecular orbitals. The harmonic radiation is proportional to the dipole matrix element between the recombining electron and the molecular orbital of the valence electron. By using a tomographic method, the molecular orbital could be reconstructed from the measured harmonic spectrum and information could be gained on the structure of the molecule [78, 79, 80].

One can select the following milestones in the short history of this subject:

- *First observations:* The first experimental observations of the plateau in the HHG spectrum were done in Chicago [22] and in Saclay [81] at the end of the 1980 s.
- *Early work:* Most of the early work has concentrated on the extension of the plateau, i.e., the generation of harmonics of higher frequency and shorter wavelength going progressively from $\sim$20 nm at the end of the 1980 s to $\sim$7 nm in the mid-1990 s [23, 55, 82, 83, 84]. Today, harmonic spectra produced with short and intense laser pulses extend to the water window (below the carbon K-edge at 4.4 nm) [56, 57].
- *Simple man's theory:* A breakthrough in the theoretical understanding of HHG process in low-frequency laser fields was initiated by Krause and coworkers [85] who showed that the cutoff position in the harmonic spectrum follows the universal law $I_p + 3U_p$, where I_p is the ionization potential, whereas $U_p = e^2E^2/4m\omega^2$ is the ponderomotive potential, i.e., the mean kinetic energy acquired by an electron oscillating in the laser field. Here e is the electron charge, m is its mass, and E and ω are the laser electric field and its frequency, respectively. An explanation of this universal fact in the framework of a "simple man's theory" was found shortly afterwards [86, 87, 88, 89][1]. According to this model (also called three-step model) (see also note 1) harmonic generation occurs in the following manner: first the electron tunnels out from the nucleus through the Coulomb energy barrier modified by the presence of the (relatively slowly varying) electric field of the laser. It then undergoes oscillations in the field, during which the influence of the Coulomb force from the nucleus is practically negligible. If the electron comes back to the vicinity of the nucleus, it may recombine back to the ground state, thus producing a photon of energy I_p plus the kinetic energy acquired during the oscillatory motion. According to classical mechanics, the maximal kinetic energy that the electron can gain is indeed $\simeq 3.2U_p$. A fully quantum mechanical theory, which is based on a strong field approximation (SFA) and recovers the simple man's theory, was formulated soon after [90, 91].

[1] It is worth reminding that the first formulation of the "Simple man's model" was proposed in 1987.

- *Ellipticity studies:* The simple man's theory leads to the immediate consequence that harmonic generation in elliptically polarized fields should be strongly suppressed, since the electron released from the nucleus in such fields practically never comes back, and thus cannot recombine [89, 92]. Several groups have demonstrated this effect [93, 94, 95], and have since then performed systematic experimental [96, 97, 98, 99, 100] and theoretical [101, 102, 103] studies of the polarization properties of harmonics generated by elliptically polarized fields.
- *Optimization and control:* Progress in experimental techniques and theoretical understanding stimulated numerous studies of optimization and control of HG. These studies involved among others (for more complete references see [17, 18, 19])
  - Optimization of the laser parameters [30]
  - Generation by multicolored fields [24, 25, 26, 27, 28]
  - Optimization of the generating medium [19, 39, 40, 41]
  - Characterization and optimization of the spatial and temporal properties [43, 44, 45, 46, 47, 48, 49, 50, 51, 52, 53, 54]
- *HHG and quantum orbits:* The microscopic physics (the quantum orbits) behind high-order harmonic generation was shown in a series of experiments investigating the temporal coherence of the harmonics [104, 105, 21]. These quantum paths are easily predicted by the SFA approach, as described in more detail in Section 5. Analysis techniques to extract these quantum paths from (more exact) theoretical approaches, in particular the numerical integration of the time-dependent Schrödinger equation [106, 107, 108], were also developed.
- *Attosecond physics:* Future applications of high harmonics will undoubtedly involve attosecond physics, i.e., the physics of generation, control, detection, and application of subfemtosecond laser pulses. Three types of proposals for reaching the subfemtosecond limit have been put forward over the last few years: those that employ ellipticity effects [109, 110, 111], those that rely on phase locking between consecutive harmonics [92, 112, 113, 114, 115, 116], and those that concern single harmonics [117, 118, 119]. The latter two proposals have been realized in spectacular experiments: trains of 250 as pulses, corresponding to the coherent superposition of harmonics 11–19 generated in argon, were measured by Agostini et al. [74] (see also [120] for earlier indications), whereas a single isolated 650 as pulse was observed by Krausz and his collaborators [75, 121]. These limits have recently been extended to 170 as for pulses in a train [77, 122] using compression of the intrinsically chirped attosecond pulses [123] in aluminum filters as well as 250 as for single attosecond pulses [76].

3.2 Above-Threshold Ionization

The phenomenon of ATI was the first characteristic phenomenon of the intense laser-atom interactions detected experimentally ([124, 125], see also [15]). From

the fundamental point of view, it is equally important as HHG, but its significance for practical applications is more limited. It is "cleaner" in a way than HHG, since macroscopic effects amount to performing a volume integration and in accounting for the effect of the laser pulse on the ionized electrons, which is a much simpler task than accounting for phase matching effects in harmonic generation. The "gap" between single atom (microscopic) calculations and the actual experimental results is smaller in ATI than in HHG, and comparisons between theory and experiment are more precise and reliable.

We present in Fig. 4 a typical low-energy ATI spectrum [126], obtained in xenon, with a 100 ps 1064 nm Nd:YAG laser. It shows a number of electron peaks separated by the laser photon energy. The energy of these peaks is given by

$$E = (n + s)\hbar\omega - I_{\mathrm{p}}, \tag{1}$$

where n is the minimum number of photons needed to exceed the atomic binding energy and s is usually called the number of "excess" or "above-threshold" photons carried by the electron.

As in HHG, in the multiphoton regime, the intensity of ATI peaks diminishes rapidly with the peak order. As the intensity approaches the non-perturbative regime, the AC-Stark shift of the atomic states begins to play a significant role in the structure of this spectrum. The first effect is the shift of the ionization potential given roughly by the ponderomotive energy, U_{p}. If the electron exits the laser focus while the laser is still on, it is accelerated by the gradient of the field. The quiver motion is converted into radial motion away from the focal volume, increasing the kinetic energy by U_{p} and exactly canceling the shift of

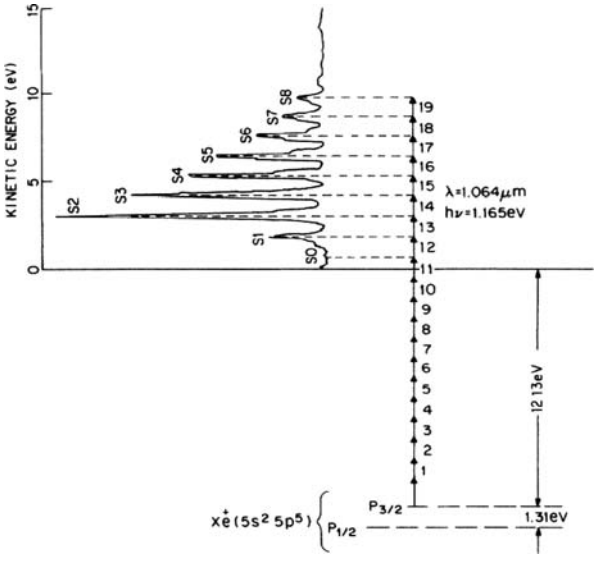

Fig. 4 Schematic ATI spectrum obtained in xenon with 100 ps 1064 nm pulses at intensities exceeding 10^{13} W cm^{-2}. The photoelectron peaks are labeled by SN where N is the minimum number of photons necessary for ionization of the Xe ground state leaving the ion in the $^2P_{3/2}$ state, which is expected to be the dominant contribution (from [126])

the continuum. The electron energies are still given by Eq. 1. However, when the ponderomotive energy exceeds the photon energy, the lower ATI peaks disappear from the spectrum. This has been called *peak shifting* [125], since the strongest ATI peak moves to higher order as the intensity increases. An example of this effect is shown in Fig. 4: the peak labeled $S0$ has completely disappeared, while the peak $S1$ is partly suppressed compared to higher-order contributions.

If the laser pulse is short enough (<1 ps), the field turns off before the electron can escape from the focal volume. Then the quiver energy is returned to the field and the ATI spectrum becomes much more complicated. The observed electron energies correspond directly to the energy above the shifted ionization potential:

$$E(\text{short pulse}) = (n+s)\hbar\omega - (I_\text{p} + U_\text{p}). \tag{2}$$

In this case, electrons from different regions of the focal volume are emitted with different ponderomotive shifts. Any enhancement of the ionization probability due to resonance effects on AC-Stark shifted states will lead to a substructure in the ATI spectrum [16, 127, 128, 129].

The above discussion is appropriate to the case of linear polarization where the excited states of the atom can play a significant role in the excitation. In a circularly polarized field, the orbital angular momentum must increase one unit with each photon absorbed so that multiphoton ionization is allowed only to states which see a large centrifugal barrier. The lower energy scattering states cannot penetrate to the vicinity of the initial state so that the ATI spectrum in circular polarization peaks at high energy and is very small near threshold [130].

The experimental precision in detecting electron spectra increased significantly from the mid-1990 s owing essentially to higher laser repetition rates. Thus, ATI spectra with many decades in number of counts could be recorded. Amazingly, the spectra exhibit features somewhat similar to the HHG plateau. After a steep decrease for the first orders, up to $2U_\text{p}$, the intensity of the ATI peaks varies much less rapidly with a large plateau extending to $\sim 10U_\text{p}$. An example of such an effect is shown in Fig. 5 [131], obtained in xenon with 800 nm, 120 fs pulses at 1.5×10^{14} W cm^{-2}. As described in more detail below, this effect originates from the rescattering of the electronic wave packet on the nucleus after some evolution in the laser field. While with linear polarization, electrons are typically generated along the polarization's direction, angular distributions exhibit a much more complex (off-axis) structure at the edge of the plateau(s), called "scattering rings" [132]. Similarly as for HHG we point out the following milestones in the short history of this subject:

- *First observations:* The first experimental observations of above-threshold ionization were done by Agostini and coworkers in Saclay in 1979 [124]. The effect of the ponderomotive potential leading to "peak switching" was shown by Kruit and coworkers in 1983 [125].

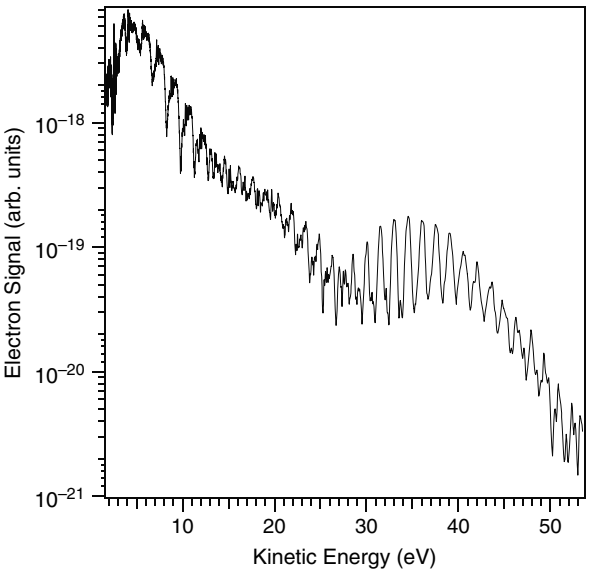

Fig. 5 ATI spectrum in xenon with 120 fs 800 nm pulses at 1.5×10^{14} W cm^{-2}. There are clearly two parts in the spectrum, a rapid decrease, due to direct tunneling, and a plateau due to rescattering (from [131])

- *Early work:* Most of the early work has concentrated on the low-energy part of the spectrum, with the following important results (for more complete references, see [13, 14, 15, 16]):
  - Effect of the ponderomotive potential for long pulses [125]
  - Influence of the laser polarization [130]
  - ATI with short laser pulses, AC-Stark shifted resonances [127, 128, 129], population trapping [133]
  - Transition from the multiphoton to the tunneling regime, showing progressive disappearance of the substructures in the spectrum with increasing intensity, going from Xe to He [134]
- *ATI plateaus and scattering rings:* Second-generation ATI experiments started in the mid-1990 s triggered by the development of high-repetition-rate lasers. High kinetic energy electron spectra with an extended plateau [135, 136, 137] as well as rings in the electron angular emission (in particular at the edges of the plateau) [132, 138, 139] were observed.
- *Simple man's theory:* The better understanding reached in HHG processes, thanks to the simple man's model [86, 87, 88, 89],[2] made its impact on ATI as well. ATI could now be understood as a combination of dominant direct tunneling process (without returning to the vicinity of the nucleus) and indirect processes in which the electron is rescattered one or several times onto the nucleus. The ATI plateau and scattering rings were thus interpreted in terms of rescattering processes, in the framework of the simple man's theory

[2] See Note 1.

[140, 141]. More sophisticated quantum approaches [142, 143] showed that the contributions of the relevant quasi-classical electron trajectories (orbits) were interfering, so that the orbits were eventually called "quantum orbits".

- *Ellipticity studies:* Perhaps the most complex and rich structure in ATI spectra has been obtained in experiments in which the ATI electrons were generated by elliptically polarized laser pulses. In contrast to ATI with linear polarization, where the high-order ATI spectrum contains a single plateau with a cutoff around $10U_p$, a staircase spectrum with several steps was observed for elliptical polarization [144, 145, 146].
- *Enhancement of ATI peaks:* The latest experiments [131, 147, 148, 149] report an enhancement of groups of ATI peaks at specific values of the laser intensity. These effects have been attributed to resonances with particular Rydberg states [150, 151], to "channel closing" effects [148, 152], and to interfering quantum orbits [151, 153].

3.3 Non-sequential Ionization

Although ATI and HHG experiments are usually performed on multielectron systems, the rare gases, they involve essentially the response of a single electron to a laser field. However, at sufficiently high laser intensities, atoms undergo multiple ionization. Such processes, observed for the first time in 1975 in alkaline-earth atoms [154], necessarily involve many electrons. The simplest way to understand multiple ionization when an atom is exposed to a strong laser field is via the so-called sequential stripping mechanism, i.e., a sequence of single electron ionization acts: ionization of the atom, then of the singly charged ion, then of the doubly charged ion, and so on [155, 156].

The experimental study of the number of multiply charged ions produced as a function of the laser intensity reveals that sequential ionization is not the only mechanism responsible for double and multiple ionization. The existence of a "knee" in the double ionization result observed for the first time in 1983 in xenon [157, 158] indicates the existence of another process "direct" or "non-sequential" responsible for the double ionization. We show in Fig. 6 results obtained in helium with a 100 fs titanium–Sapphire laser by DiMauro and coworkers [135]. The number of singly and doubly charged ions is reported as a function of the laser intensity in a double-logarithmic plot. The saturation effect observed for the singly charged ions is due to saturation of ionization, which happens when most of the atoms in the interaction volume get ionized. The first part of the doubly charged ion curve follows that of the singly charged ions and saturates at the same intensity. It means that both ion charges come from the same species, i.e., the neutral atom in its ground state, so that the double ionization occurs via a non-sequential process. At higher intensities, the number of He^{2+} ions increases again, owing to sequential ionization.

Ion data such as those shown in Fig. 7 remained the only experimental signature of multiple ionization processes in strong laser fields during a quarter

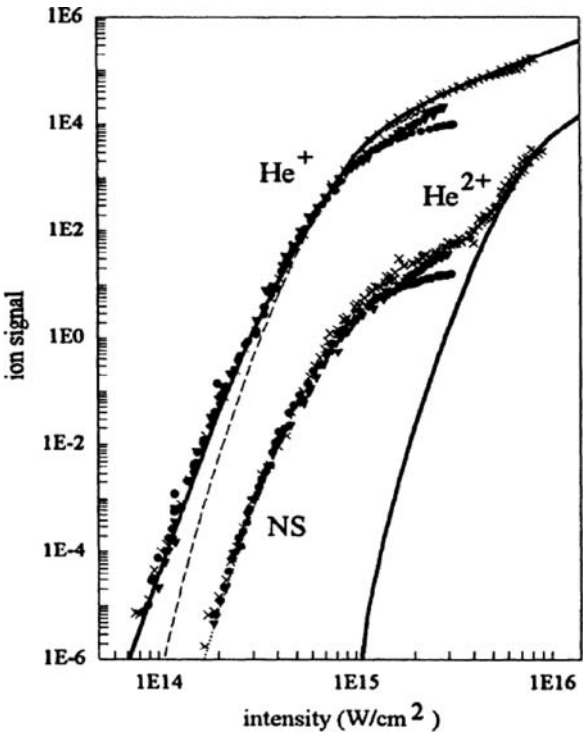

Fig. 6 Ion yields in helium with a 100 fs 780 nm laser pulse. The *solid curves* are TDSE calculations for ionization of He and He^+. The *dashed curve* is a calculation using a tunneling ADK rate [165] (from [135])

of a century. Very recently, however, recoil-ion momentum spectroscopy measurements, directly reflecting the energy distribution of the electrons emitted in a non-sequential ionization process, as well as electron–ion coincidence techniques, gave a much better experimental insight into the origin of the non-sequential process [31, 32, 37, 38, 159]. We show in Fig. 8 a recoil-ion momentum measurement, performed in neon [31, 32]. Analysis of the momenta distribution shows that the most probable explanation for the non-sequential process is tunneling followed by rescattering leading to emission of a second electron.

Similarly as for HHG and ATI, we point out below our selection of the milestones in the short history of non-sequential ionization:

- *First observations:* The "knee" in the ionization yield of xenon was observed in 1983 [157, 158].
- *Early work:* The main effort during the 1980s was to test the limits of the sequential stripping mechanism with the available laser powers [156, 160] and to understand the process responsible for the ionization of the different charge states (multiphoton or tunneling) [155, 156, 160, 161]. The theory of direct tunneling ionization had been formulated already in the 1960 s by Keldysh [162], and developed by Faisal [163] and Reiss [164] (KFR theory).

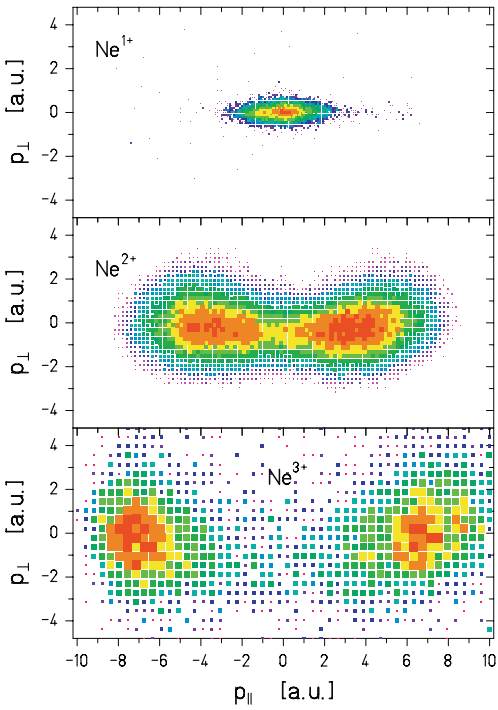

Fig. 7 Momentum distributions of Ne ions irradiated by 30 fs 800 nm laser pulses at intensities of 1.3×10^{15} W cm^{-2} for Ne^+ and Ne^{2+} and 1.5×10^{15} W cm^{-2} for Ne^{3+} ions. The broad distributions observed for the multiply charged ions, compared to the singly charged ions, confirm the interpretation in terms of rescattering (from [31, 32])

Ammosov et al. [165] used this theory to derive tunneling ionization rates (ADK rates) that have been extensively used in comparison with experimental results.

- *Experiments with short pulses and high repetition rates:* Non-sequential ionization was "revived" at the beginning of the 1990 s with the development of short-pulse high-repetition-rate lasers. Beautiful "knees" were observed in the double ionization of helium using short-pulse Ti:S lasers [135, 166]. It was rapidly extended to higher charge states and other atoms [167].
- *Simple man's theory and theoretical progress:* This model also made its impact on the understanding of non-sequential ionization. As a consequence of electron rescattering on a parent ion, a second electron could be ejected [89]. Another mechanism called *shakeoff* by analogy with single-photon double ionization was proposed. In this model, ionization of the second electron is due to adjustment of the wave functions after the ionization of the first electron [166, 168]. Finally, collective tunneling was also discussed [169]. Several important theoretical approaches were developed in the late 1990 s. The so-called CRAPOLA model [170], which treats the first electron in the framework of the single active electron (SAE) approximation [171], but accounts for the effects of the first electron onto a second electron, was the first to give evidence for dominance of the rescattering mechanism in non-sequential ionization. The simple man's model stimulated further

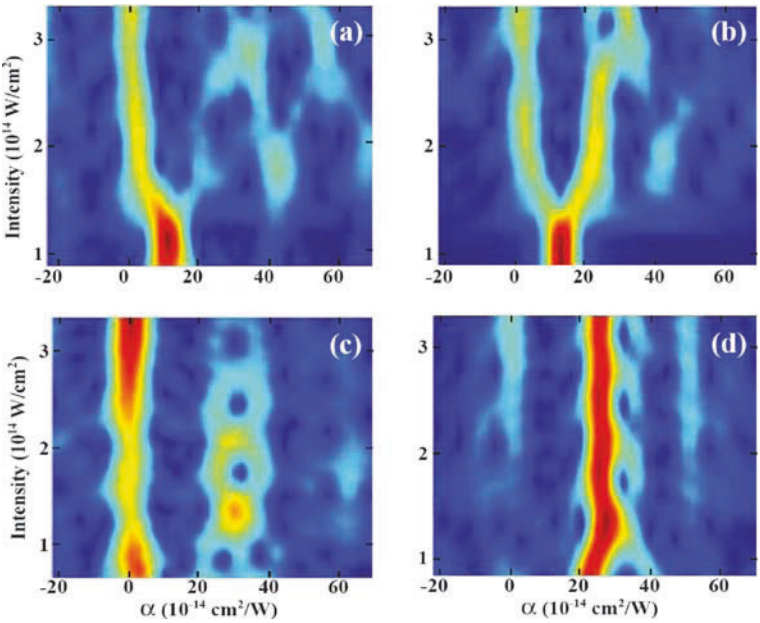

Fig. 8 Quantum path distributions for the 27th and 15th harmonics in argon. The figures on the left are obtained from TDSE calculations, whereas the ones on the right are due to the SFA (from [107])

developments of the strong field approximation (SFA) [172, 173], with, for example, inclusion of the Coulomb rescattering [174, 175]. Finally, enormous progress has been achieved in numerical simulations of multielectron ionization processes [176, 177, 178, 179, 180, 181, 182].

- *Ellipticity studies:* If rescattering is the dominant process leading to non-sequential ionization, it should be very sensitive to the laser degree of polarization. This was indeed the findings of a series of experiments performed in the late 1990 s [94, 183, 184].
- *Electron and ion momentum distributions:* Using cold-target recoil-ion momentum spectroscopy (COLTRIMS) [31, 32] and electron–ion coincidence [37, 38, 185], it is now possible to get new insights into the physics of non-sequential ionization and to confirm in particular the correctness of the rescattering mechanism.

In conclusion, there are obviously many common points in the physics (as well as in the history) behind the three phenomena reviewed in this chapter. A unified view of HHG, ATI, and non-sequential ionization, originating from simple man's model, formulated within the strong field approximation and expressed in terms of quantum orbits, is slowly emerging [153, 186]. It will be presented in

more details in Section 5. In the next section, we review the theoretical methods that have been used to treat the problem of an atom in a strong laser field.

4 Theoretical Methods

The theoretical problem consists in finding the time-dependent wave function of an atom with several active electrons. Strictly speaking, we need to solve the time-dependent Schrödinger equation that describes the interaction of a many-electron atom with a laser field. During many years, theorists have concentrated their effort on solving the problem of a hydrogen atom, or more generally, a single active electron (SAE) [171] atom in a strong laser field. In this SAE approximation, the role of electronic structure in an atom is to determine an effective (for instance, Hartree–Fock) static potential felt by the (active) electron interacting with the laser field (for a discussion of some two-electron effects, see, for instance, [187, 188, 189]). In this section, we review the main methods that have been used to calculate the response of a single atom to a laser field within the SAE approximation.

We can identify four types of methods that have been used to solve the "one-electron" problem: the numerical methods, the classical phase space averaging method, the pseudo-potential model, and the strong field approximation, which we will present in some detail in Section 5.

- *Numerical methods:* The aim of these methods is to solve numerically the time-dependent Schödinger equation (TDSE) describing an atom in the laser field. Since the laser field oscillates periodically (at least in the adiabatic case, i.e., for long pulses), one of the possible approaches is to use a Floquet analysis ([190]; for a recent review, see [14, 191]). However, the direct integration of the TDSE is far more often used (for a review, see [13, 192]). In one dimension, such integration can be performed using either the finite element (Crank-Nicholson), or split operator techniques; in the context of ATI and HHG, it has been first used by the Rochester group [15, 193], but then employed by many others as a test method. In three dimensions, the numerical methods have been pioneered by Kulander [171, 194], who used a 2D finite element ("grid") method. Pretty soon it was realized that basis expansion methods that employ the symmetry of the problem (i.e., the spherical symmetry of a bare atom, or the cylindrical symmetry of an atom in a linearly polarized field) work much better [195, 196]. Modern codes use typically expansions in angular momentum basis and solve the coupled set of equations for the radial wave function using finite grid methods (cf. [85]), Sturmian expansions [197, 198], or B-spline expansions [199, 200]. Most of those codes are quite powerful and allow one to calculate the atomic response directly in three dimensions [23, 197, 198, 201, 202] without adiabatic approximation [117]. Many seminal results concerning especially harmonic generation have been obtained using direct numerical

methods: For example, the first observation of the $I_p + 3U_p$ law [85], the importance of pulse shape and blue shifting effects [203, 204, 205], and the proposal of subfemtosecond pulse generation [19, 117, 206, 207, 208].

- *Classical phase space averaging method:* A lot of useful information about atom-intense laser interaction processes can be gained from a purely classical analysis of the electron driven by the laser field. In order to mimic quantum dynamics, classical Newton equations are solved for an ensemble of trajectories generated from an initial electron distribution in the phase space. This distribution is supposed to reproduce the true quantum initial state of the system, so that averages over this distribution are analogs of quantum averages. Such approach has been developed in the context of HHG by Maquet and his collaborators [209, 210].
- *Pseudo-potential model:* Many important results in the theory of harmonic generation have been obtained by Becker and his collaborators who have solved exactly (and to a great extent analytically) the zero range pseudo-potential model [211]. In this model, the electron is bound to the nucleus via the potential

$$V(\mathbf{r}) = \frac{2\pi}{\kappa m}\delta(\mathbf{r})\frac{\partial}{\partial r}r, \tag{3}$$

where m is the electron mass. This potential supports a single bound state with the energy $-I_p = -\kappa^2/2m$. This model, originally formulated in the case of a linearly polarized field, was extended to one-color [101] and two-color [212] fields with arbitrary polarization and used to study the polarization properties of harmonics generated by elliptically polarized fields [213]. It also accounts for the ground state depletion [214]. Structures in the harmonic spectra are associated in this model to above-threshold ionization channel closings [215], rather than with quantum interferences between the contributions of different electronic trajectories [216]. Nevertheless, Becker's model leads to the same final formulas for the induced atomic dipole moment as the SFA theory described below, and essentially to the same results (for a detailed comparison, see [103]).

5 Strong Field Approximation

In this section, we present the strong field approximation (SFA) to the time-dependent Schrödinger equation. It is a generalization of the Keldysh–Faisal–Reiss approximation [162, 163, 164]. A first formulation of the SFA for harmonics can be found in [217]. We begin by a general derivation and a discussion of the conditions of validity, before applying the theory to the three phenomena reviewed in this paper. More details of our version of the SFA can be found in the series of Refs. [90, 91, 102, 143, 216, 218], and in the review [17, 18].

5.1 Derivation of SFA

We consider an atom (or an ion) in a single electron approximation under the influence of the linearly polarized laser field $\mathbf{E}(t) = (E(t)\cos(\omega t), 0, 0)$. In the length gauge, the Schrödinger equation takes the form

$$\mathrm{i}\hbar|\Psi(\mathbf{x},t)\rangle = \left[-\frac{\hbar^2\nabla^2}{2m} + V(\mathbf{x}) - E(t)\cos(\omega t)ex\right]|\Psi(\mathbf{x},t)\rangle. \tag{4}$$

Initially (i.e., before the turn-on of the laser pulse), the system is in the ground state, denoted as $|0\rangle$, which in general has a spherical symmetry.

We assume that $I_\mathrm{p} \gg 1$ in units of the laser photon energy (typically $I_\mathrm{p} \simeq 5-20$ laser photons) and that U_p is comparable or larger than I_p. We start our discussion by considering the case when ionization is weak, so U_p should be large, but still below the saturation level, U_sat, when all atoms ionize during the interaction time. In this regime of parameters, the tunneling theory [162, 163, 164, 165] becomes valid [156]. The intensities are large enough ($10^{14}-10^{15}$ W cm^{-2}) so that intermediate resonances, including dynamically induced ones (see, for instance, [127]), play no role. The electron undergoes transitions to continuum states which we label by the kinetic momentum of the outgoing electron $|\mathbf{q}\rangle$. These are eigenstates of the free Hamiltonian corresponding to outgoing electrons with kinetic momentum $\mathbf{q}$:

$$\left[-\frac{\hbar^2\nabla^2}{2m} + V(\mathbf{x})\right]|\mathbf{q}\rangle = \frac{q^2}{2m}|\mathbf{q}\rangle. \tag{5}$$

Since we use an expansion into eigenstates of the free Hamiltonian, we account in principle for the Coulombic correction to the asymptotic phase shift of the states $|\mathbf{q}\rangle$ when $V(\mathbf{x})$ is a long-range potential. The electron leaves the atom typically when the field reaches its peak value. The effect of the force due to the potential, $-\nabla V(\mathbf{x})$, is then negligible. As the electron is accelerated in the field, it immediately acquires a high velocity, so that the role of $V(\mathbf{x})$ is even less pronounced. That is particularly true if the electron returns to the nucleus with a large kinetic energy of the order of U_p. At the turning points, the electron velocity might be quite small but these points are located typically very far from the nucleus.

The above considerations suggest that the following assumptions should be valid in the regime of parameters that we consider:

(a) The contribution to the evolution of the system of all bound states except the ground state $|0\rangle$ can be neglected.
(b) In the continuum, the electron can be treated as a free particle moving in the electric field with no or little effect of $V(\mathbf{x})$.

For intensities much smaller than saturation intensity, we can additionally neglect the depletion of the ground state. Otherwise, the depletion of the ground

state has to be taken into account, as discussed in Section 5.2. Assumption (b) is non-questionable for short-range potentials, but is also valid for hydrogen-like atoms, provided U_p is large enough. Generally speaking, assumptions (a) and (b) hold when there are no intermediate resonances and when the Keldysh parameter $\gamma = \sqrt{I_p/2U_p}$ is smaller than one, i.e., in the tunneling or over-the-barrier ionization regimes. The latter condition requires $I_p \leq 2U_p$ and implies that (i) when the electron is born in the continuum it is under the influence of a very strong laser field and (ii) when it comes back to the nucleus it has a large kinetic energy, so that the atomic potential force can be neglected. Obviously, the latter implication concerns only highly energetic electrons, e.g., in the case of HHG those responsible for the production of harmonics of order $(2M+1)\hbar\omega \geq I_p$.

There are, as we mentioned, several theoretical approaches that incorporate assumption (b) in solving Eq. (4) [162, 163, 164, 165]. We here follow Ref. [219, 220], since this approach is more closely related to standard methods of quantum optics, in the sense that it neglects, or treats as a perturbation, part of the interaction Hamiltonian. Quite generally (both for short-range and long-range potentials), the continuum–continuum (C–C) matrix element can be expanded into the most singular part and "the rest" (less singular or regular), as

$$\langle \mathbf{q}|e\mathbf{x}|\mathbf{q}'\rangle = ie\hbar\nabla_{\mathbf{q}}\delta(\mathbf{q}-\mathbf{q}') + \mathbf{g}(\mathbf{q},\mathbf{q}'). \tag{6}$$

The first term on the right side in Eq. (6) describes the motion of the free electron in the laser field. The second term is responsible for electron rescattering processes. On the energy shell ($q^2/2m = (q')^2/2m$), this term is related to the scattering amplitude for the potential $V(\mathbf{x})$. If during rescattering the electron absorbs at least one photon, $|q^2/2m - (q')^2/2m| \geq 1$. Far from the energy shell $g(\mathbf{q},\mathbf{q}')$ depends on the momentum transfer $\mathbf{q}-\mathbf{q}'$.

Assumption (a) implies that the time-dependent wave function can be expanded as

$$|\Psi(x,t)\rangle = \mathrm{e}^{\mathrm{i}I_p t/\hbar}(a(t)|0\rangle + \int \mathrm{d}^3\mathbf{q}\, b(\mathbf{q},t)|\mathbf{q}\rangle), \tag{7}$$

where $a(t)$ is the ground state amplitude and $b(\mathbf{q},t)$ are the amplitudes of the corresponding continuum states. We have factored out here free oscillations of the ground state amplitude with the bare frequency I_p. The Hamiltonian governing the evolution of $\Psi(x,t)$ can then be projected onto the space spanned by $|0\rangle$ and the continuum states $|\mathbf{q}\rangle$. The projected Hamiltonian can be divided into two parts:

$$H = H_0 + H_1, \tag{8}$$

where

$$
\begin{aligned}
H_0 = &- I_\mathrm{p}|0\rangle\langle 0| + \int \mathrm{d}^3\mathbf{q}\ \frac{\mathbf{q}^2}{2m}|\mathbf{q}\rangle\langle\mathbf{q}| \\
&- E(t)\cos\omega t \int \mathrm{d}^3\mathbf{q}[d_x(\mathbf{q})|0\rangle\langle\mathbf{q}| + \mathrm{h.c.}] \\
&- \mathrm{i}\hbar e E(t)\cos\omega t \int \mathrm{d}^3\mathbf{q} \int \mathrm{d}^3\mathbf{q}'|\mathbf{q}\rangle\nabla_{q_x}\delta(\mathbf{q}-\mathbf{q}')\langle\mathbf{q}'|,
\end{aligned}
\tag{9}
$$

while

$$
H_1 = -E(t)\cos\omega t \int \mathrm{d}^3\mathbf{q} \int \mathrm{d}^3\mathbf{q}'|\mathbf{q}\rangle g_x(\mathbf{q},\mathbf{q}')\langle\mathbf{q}'|. \tag{10}
$$

Here $\mathbf{d}(\mathbf{q}) = \langle\mathbf{q}|e\mathbf{x}|0\rangle$ denotes the atomic dipole matrix element for the bound-free transition and $d_x(\mathbf{q})$ is the component parallel to the polarization axis. H_0 includes dominant effects of the motion of the electron in the laser field, whereas H_1 takes care for rescattering.

The Schrödinger equation for the amplitude $b(\mathbf{q}, t)$ reads

$$
\begin{aligned}
\hbar\dot{b}(\mathbf{q},t) = &- \mathrm{i}\left(\frac{\mathbf{q}^2}{2m} + I_\mathrm{p}\right) b(\mathbf{q},t) + \mathrm{i}E(t)\cos(\omega t)\ d_x^*(\mathbf{q}) \\
&- \hbar e E(t)\cos(\omega t)\ \frac{\partial b(\mathbf{q},t)}{\partial q_x} \\
&+ \mathrm{i}E(t)\cos(\omega t) \int \mathrm{d}^3\mathbf{q}' g_x(\mathbf{q},\mathbf{q}') b(\mathbf{q}',t).
\end{aligned}
\tag{11}
$$

In writing Eq. (11), we have neglected the depletion of the ground state, setting $a(t) = 1$ on the right hand side. The whole information about the atom is thus reduced to the form of $\mathbf{d}(\mathbf{q})$ and $\mathbf{g}(\mathbf{q},\mathbf{q}')$.

A generalized strong field approximation may now be formulated as a systematic perturbation theory with respect to H_1. Zeroth-order SFA corresponds to the exact solution of the Schrödinger equation generated by H_0 only. The Schrödinger equation reduces to the first two lines in Eq. (11), and its solution takes the form

$$
\begin{aligned}
b_0(\mathbf{q},t) = &\ \mathrm{i}\int_0^t \mathrm{d}t' E(t')\cos(\omega t') d_x(\mathbf{q} + e(\mathbf{A}(t) - \mathbf{A}(t'))/c) \\
&\times \mathrm{e}^{-\mathrm{i}\int_{t'}^t \mathrm{d}t''[(\mathbf{q}+e(\mathbf{A}(t)-\mathbf{A}(t''))/c)^2/2m + I_\mathrm{p}]/\hbar},
\end{aligned}
\tag{12}
$$

where $\mathbf{A}(t)$ is the vector potential. Introducing the canonical momentum $\boldsymbol{p} = \boldsymbol{q} + e\boldsymbol{A}(t)/c$, we get

$$b_0(\mathbf{q}, t) = \mathrm{i}\int_0^t \mathrm{d}t' E(t')\cos(\omega t') d_x(\mathbf{p} - e\mathbf{A}(t')/c) \times \mathrm{e}^{-\mathrm{i}\int_{t'}^t \mathrm{d}t''[(\mathbf{p}-e\mathbf{A}(t''))/c)^2/2m + I_\mathrm{p}]/\hbar}. \tag{13}$$

The interpretation of this result is straightforward. $b_0(\boldsymbol{q}, t)$ is a sum of probability amplitudes that the electron is born in the continuum at time t' with the canonical momentum $\boldsymbol{p}$. These amplitudes are given by the first two factors in the integrand of Eq. (13). They are then propagated until time t, and acquire a phase factor $\exp(-\mathrm{i}S(\mathbf{p}, t, t'))$, where $S(\mathbf{p}, t, t')$ is the quasi-classical action:

$$S(\mathbf{p}, t, t') = \int_{t'}^t \mathrm{d}t'' \left(\frac{(\mathbf{p} - e\mathbf{A}(t''))/c)^2}{2m} + I_\mathrm{p} \right). \tag{14}$$

The effect of the atomic potential is assumed to be small between t' and t, so that $S(\mathbf{p}, t, t')$ actually describes the motion of an electron freely moving in the laser field with a constant canonical momentum $\mathbf{p}$. Note, however, that $S(\mathbf{p}, t, t')$ does incorporate leading effects of the binding potential through its dependence on I_p. This zeroth-order solution will be used to describe high-order harmonic generation (Section 5.2), as well as the "direct" tunneling process in ATI (see Section 5.3).

Inserting the zeroth-order solution on the right hand side of Eq. (11), we obtain the first-order correction to SFA with respect to the rescattering term

$$b_1(\mathbf{q}, t) = -\int_0^t \mathrm{d}t' \int_0^{t'} \mathrm{d}t'' \int \mathrm{d}^3\mathbf{p}'\, E(t')\cos(\omega t') \times g_x(\mathbf{p} - e\mathbf{A}(t')/c, \mathbf{p}' - e\mathbf{A}(t')/c)\mathrm{e}^{-\mathrm{i}S(\mathbf{p},t,t')} \times E(t'')\cos(\omega t'') d_x(\mathbf{p}' - e\mathbf{A}(t'')/c)\mathrm{e}^{-\mathrm{i}S(\mathbf{p}',t',t'')}. \tag{15}$$

The above expression has also a simple physical meaning. The electron makes transitions to the continuum at t' with the amplitude

$$E(t'')\cos(\omega t'') d_x(\mathbf{p}' - e\mathbf{A}(t'')/c).$$

The kinetic momentum of the electron is then $\mathbf{q}' = \mathbf{p}' - \mathrm{e}\mathbf{A}(\mathbf{t}'')/\mathrm{c}$. The amplitude is then propagated until t', when the electron undergoes rescattering, followed by subsequent propagation until t. The propagation in both cases consists of accumulation of phase factors, expressed as exponentials of i times the corresponding quasi-classical actions. This first-order correction to the solution of

the Schrödinger equation will be used in the description of ATI processes (Section 5.3).

5.2 Strong Field Approximation for HHG

The harmonic components are given by the Fourier transform of the time-dependent dipole moment $ex(t) = \langle \Psi(x,t)|ex|\Psi(x,t)\rangle$. $ex(t)$ can be expanded (in the zeroth-order approximation) as

$$ex(t) = \int \mathrm{d}^3\mathbf{q}\; d_x^*(\mathbf{q}) b_0(\mathbf{q},t) + \mathrm{c.c.}, \tag{16}$$

where $b_0(\mathbf{q},t)$ is given by Eq. (12). The time-dependent dipole moment can be expressed as

$$\begin{aligned} ex(t) = & \mathrm{i}\int_0^t \mathrm{d}t' \int \mathrm{d}^3\mathbf{p}\; E(t')\cos(\omega t') d_x^*(\mathbf{p} - \mathrm{e}\mathbf{A}(\mathbf{t})/\mathrm{c}) \\ & \times d_x(\mathbf{p} - e\mathbf{A}(t')/c)\mathrm{e}^{-\mathrm{i}S(\mathbf{p},\mathbf{t},\mathbf{t}')} + \mathrm{c.c.} \end{aligned} \tag{17}$$

The integral over p can be approximated using the saddle point method as

$$\begin{aligned} ex(t) = & \mathrm{i}\int_0^t \mathrm{d}\tau \left(\frac{\pi}{\nu + i\tau/2m\hbar}\right)^{3/2} \\ & \times d_x^*(\mathbf{p}_s - e\mathbf{A}(t)/c)\;\exp\left(-\mathrm{i}S(\mathbf{p}_s,t,\tau)\right) \\ & \times E(t-\tau)\cos(\omega(t-\tau)) d_x(\mathbf{p}_s - e\mathbf{A}(t-\tau)/c) + \mathrm{c.c.}, \end{aligned} \tag{18}$$

where ν is a positive regularization constant. We have introduced a new variable, the return time $\tau = t - t'$, which is the time the electron spends in the continuum between the moments of tunneling from the ground state and recombination back to the ground state. The saddle point value of the momentum (stationary point of the quasi-classical action) is given by

$$\mathbf{p}_s = \mathbf{p}_s(t,\tau) = \int_{t-\tau}^{t} \mathrm{d}t'\; e\mathrm{A}(t')/c\tau. \tag{19}$$

Note the characteristic prefactor $(\nu + \mathrm{i}\tau/2m\hbar)^{-3/2}$ in (20) coming from the effect of quantum diffusion. It cuts off very efficiently the contributions from large τs and allows often one to extend the integration range from *0* to infinity.

This expression (Eq. (18)) can be generalized to an elliptically polarized field $\boldsymbol{E}(t)$, and ground state depletion can be taken into account (for details, see [91, 102]):

$$\begin{aligned} e\boldsymbol{x}(t) = \mathrm{i}\int_0^t \mathrm{d}\tau \left(\frac{\pi}{\nu + \mathrm{i}\tau/2m\hbar}\right)^{3/2} \mathbf{d}^*(\mathbf{p}_s - e\mathbf{A}(t)/c)\ \exp\left(-\mathrm{i}S(\mathbf{p}_s, t, \tau)\right) \\ \times \mathbf{E}(t-\tau)\cdot\mathbf{d}(\mathbf{p}_s - e\mathbf{A}(t-\tau)/c)a^*(t)a(t-\tau) + \text{c.c.} \end{aligned} \tag{20}$$

The field-free dipole transition element from the ground state to the continuum state characterized by the momentum $\boldsymbol{p}$ can be approximated by [91, 221]

$$\mathbf{d}(\mathbf{p}) = \mathrm{i}\frac{2^{7/2}\alpha^{5/4}}{\pi}\frac{\mathbf{p}}{(\mathbf{p}^2 + \alpha)^3}, \tag{21}$$

with $\alpha = 2mI_\mathrm{p}$, for the case of hydrogen-like atoms and transitions from s states.

Finally, the amplitude of the ground state fulfills in general the integrodifferential equation:

$$\dot{a}(t) = \int_0^t \mathrm{d}\tau\Gamma(t,\tau)a(t-\tau),$$

where

$$\begin{aligned} \Gamma(t,\tau) = \left(\frac{\pi}{\nu + \mathrm{i}\tau/2m\hbar}\right)^{3/2} \mathbf{E}^*(t)\cdot\mathbf{d}^*(\mathbf{p}_s - e\mathbf{A}(t)/c)\ \exp(-\mathrm{i}S(\mathbf{p}_s, t, \tau)) \\ \times \mathbf{E}(t-\tau)\cdot\mathbf{d}(\mathbf{p}_s - e\mathbf{A}(t-\tau)/c). \end{aligned} \tag{22}$$

When the pulses are not too short and not too strong, and the change of $a(t)$ on the time scale of one period of the fundamental frequency is small, we can make a series of approximations: $\dot{a}(t) \simeq -\int_0^t \mathrm{d}\tau\Gamma(t,\tau)a(t)$, so that

$$a(t) = \exp\left(-\int_0^t \gamma(t')\mathrm{d}t'\right),$$

where $\gamma(t) = \int_0^t \mathrm{d}\tau\Gamma(t,\tau)$. Furthermore, $\gamma(t)$ can be approximated by its average over one laser period $\bar{\Gamma}(t) = \frac{1}{T}\int_t^{t+T}\gamma(t')\mathrm{d}t'$ where $T = 2\pi/\omega$. The intensity-dependent ionization rate is twice the real part of the (complex) decay rate $\bar{\Gamma}(t)$.

Expressions (20) and (22) result from a single active electron approximation. In the case of rare gas atoms, all electrons on the outer shell can be "active". In the case of He, with two (equivalent) s electrons in the ground state, the total dipole moment and the total ionization rate are simply given by twice the above expressions (Eqs. (20) and (22), respectively). In the case of the other noble gases (six p electrons on the outermost shell in the ground state, two in each of the $m = -1, 0, 1$ states), the procedure is more complex. The two expressions (Eqs. (20) and (22)) should be replaced by twice the sum of contributions from each magnetic quantum number $m = -1, 0, 1$; each of those contributions should be calculated by replacing Eq. (21) by an appropriate field-free dipole matrix element describing the transition from the $\ell = 1, m = -1, 0, 1$ states to the continuum. Fortunately, the dependence of the dipole moment and ionization rate on the details of the ground state wave function is rather weak, and typically reduces to an overall prefactor [91, 102] that determines the strength of the dipole but not the form of its intensity dependence. For these reasons, in most of the calculations for noble gases other than helium, we still use the s-wave function to describe the ground state (Eq. (21)), but multiply the results by an effective number of active electrons, $n_{\mathrm{el}} \simeq 4$. Total ionization rates of helium and neon calculated with $n_{\mathrm{el}} = 2, \simeq 4$, respectively, agree very well with the ADK ionization rates [165].

The two expressions (20) and (22) have the characteristic semi-classical form that can be analyzed in the spirit of Feynman path integrals: they contain (from right to left) transition elements from the ground state to the continuum at $t - \tau$, a propagator in the continuum proportional to the exponential of i times the quasi-classical action, and finally transition elements from the continuum to the ground state. Applying the saddle point technique to calculate the integral over τ (and t if one calculates the corresponding Fourier components or time averages), one can transform both expressions into sums of contributions corresponding to quasi-classical electron trajectories (labeled by n), characterized by the moment when the electron is born in the continuum $t_n - \tau_n$, its canonical momentum $\boldsymbol{p}_n(t_n, \tau_n)$ (see Eq. (19)), and the moment when it recombines t_n [91, 216]. Since we deal here with tunneling processes (i.e., where electrons pass through a classically forbidden region), these trajectories are in general complex. Typically, only the trajectories with short return times $\mathrm{Re}(\tau)$ contribute significantly to the dipole moment (Eq. (20)); The number of relevant trajectories with, for example, return times shorter than one period is ~ 2.

The Kth Fourier component of the dipole moment (Eq. (20)) can then be written in the form

$$e\boldsymbol{x}_K = \sum_n a_n \exp\{-\mathrm{i}S[\mathbf{p}_n, t_n, \tau_n]/\hbar\}, \tag{23}$$

where the sum runs over the relevant trajectories (quantum orbits), a_n is a corresponding amplitude, and S denotes the action. This corresponds indeed to a Feynman's path integral: The sum is, in fact, an infinite-dimensional

functional integral, which reduces, in the framework of the SFA, to a sum over a few quantum orbits.

To understand in more detail how this reduction works, we apply the saddle point technique, not only to calculate the integral over **p** but also to evaluate the remaining integrals over τ and t. This method is asymptotically exact provided U_p, I_p, and K are large enough. The saddle point equations that arise from the derivatives of the classical action (Eq. (14)) take the form

$$\nabla_{\mathbf{p}} S(\mathbf{p}, t, \tau) = \mathbf{x}(t) - \mathbf{x}(t-\tau) = \mathbf{p}\tau/m - \int_{t-\tau}^{t} \mathrm{d}t'' \, e\mathbf{A}(t'')/mc = 0, \quad (24)$$

$$\frac{\partial S(\mathbf{p}, t, \tau)}{\partial \tau} = \frac{(\mathbf{p} - e\mathbf{A}(t-\tau)/c)^2}{2m} + I_p = 0, \quad (25)$$

$$\frac{\partial S(\mathbf{p}, t, \tau)}{\partial t} = \frac{(\mathbf{p} - e\mathbf{A}(t)/c)^2}{2m} - \frac{(\mathbf{p} - e\mathbf{A}(t-\tau)/c)^2}{2m} = K\hbar\omega. \quad (26)$$

The first of these equations indicates, as already mentioned, that the only relevant electron trajectories are those such that the electron leaves the nucleus at time $t - \tau$ and returns at t. Eq. (25) has a somewhat more complicated interpretation. If I_p were zero, it would simply state that the electron leaving the nucleus at $t - \tau$ should have a velocity equal to zero. In reality, $I_p \neq 0$ and in order to tunnel through the Coulomb barrier the electron must have a negative kinetic energy at $t - \tau$. This condition cannot be fulfilled for real τs, but can easily be fulfilled for complex τs. The imaginary part of τ can then be interpreted as a tunneling time, just as it has been done in the seminal paper of Ammosov et al. [165]. Finally, we can rewrite the last expression (26) as

$$\frac{(\mathbf{p} - e\mathbf{A}(t)/c)^2}{2m} + I_p = E_{kin}(t) + I_p = K\hbar\omega. \quad (27)$$

This is simply the energy conservation law, which gives the final kinetic energy of the recombining electron that generates the Kth harmonic.

These equations can be used to derive for instance the cutoff law. Indeed, Eq. (27) clearly says that the maximum emitted harmonic frequency is given by the maximum possible kinetic energy the electron has at the moment t of collision with the nucleus. Qualitatively, this conclusion is fully consistent with the classical model of Refs. [88, 89]. Quantitatively, there are differences, since Eqs. (24) and (25), which have to be considered together with Eq. (27), naturally account for the tunneling process and its influence on the electron kinetic energy at the moment it encounters the nucleus again. Perhaps the most important quantum mechanical effect, however, is implied by expression (23): the amplitude of the Kth harmonic is a sum of *interfering* contributions corresponding to different electronic trajectories. The interfering contributions have

a phase (given by the real part of the classical action) which is intensity dependent. We can write Eq. (23) as

$$e\boldsymbol{x}_K = \sum_n a_n \exp\{-\mathrm{i}\alpha_n I\}, \tag{28}$$

where the coefficient α_n is the factor in front of the laser intensity for each quantum path labeled by n. To illustrate the meaning of this expression, we present in Fig. 8 quantum path distributions obtained in argon, using TDSE (left) and SFA (right) for the 27th (top) and 15th (bottom) harmonics [107]. Each vertical line represents a quantum path, and the color code indicates their respective weight. There are mainly two of them with the TDSE, whereas the SFA seems to emphasize only one. The induced intensity-dependent phase, approximately given by $S = U_p\tau$, where τ is the electron return time [216, 218], plays an important role in propagation, phase matching, and attosecond pulse generation (for more details, see the chapter of Salières and Christov). The fact that several quantum orbits contribute to harmonic generation has been experimentally shown [104, 105, 21]. As an example, we present in Fig. 9 an experimental result [104] showing a spatial distribution resulting from the interference of two (equivalent) 15th harmonic beams, separated by a time delay of 0 fs on the left and 15 fs on the right. There are clearly two spatial regions (a central one and an outer ring) with two different coherence times, since the interferences have disappeared after 15 fs on the outer ring, but are still present on the central part. This effect is due to the influence of two different quantum orbits (see Fig. 8), leading to different spatial and temporal characteristics.

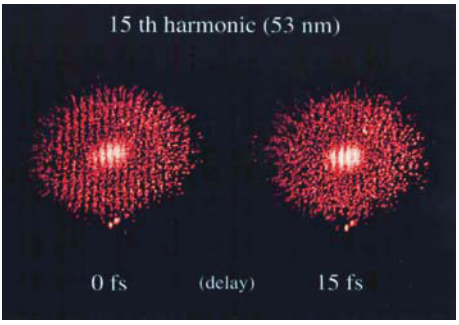

Fig. 9 Spatial distribution resulting from the interference of two (equivalent) 15th harmonic beams generated in Ar, separated by a time delay of 0 fs on the left and 15 fs on the right. There are two spatial regions, with two different coherence times. This effect has been interpreted in terms of two contributing quantum paths, with different phase behavior, leading to different spatial and temporal properties (from [104])

5.3 Generalized Strong Field Approximation for ATI

ATI is described by the combination of Eqs. (13) ("direct" tunneling) and (15) (rescattering), taken at the end of the laser pulse $t = t_F$. Note that, in the limit $t \to \infty$, we can assume $\mathbf{A}(t \to \infty) = 0$ (see [143] for details), so that canonical and kinetic momenta are the same ($\boldsymbol{p} = \boldsymbol{q}$). To analyze these expressions in a quasi-classical sense, we perform the integrals entering those expressions using a saddle point method. This method [90, 91] is expected to be accurate when both U_p and I_p, as well as the involved momenta $\mathbf{p}$ and $\mathbf{p}'$, are large. Since the quasi-classical actions are proportional to I_p, U_p, q^2, etc., the factors $\exp(-iS/\hbar)$ are rapidly oscillating, and the integrals can be approximated by the value of the integrands at the stationary points of the quasi-classical actions. Such a procedure is legitimate provided d_x and g_x are slowly varying and in particular are non-singular at the saddle points of the actions (see discussion in [91]). As shown below, the advantage of our approach is that it captures the essential underlying physics.

The zeroth order term describing direct tunneling becomes then

$$b_0(\mathbf{q}, t_F) \propto i \sum_n \mathcal{A}_n E(t'_n) \cos(\omega t'_n) d_x(\mathbf{p} - e\mathbf{A}(t'_n)/c) e^{-iS(\boldsymbol{p}, t_F, t'_n)}, \tag{29}$$

where the sum is extended over the saddle points enumerated by n, t'_n denotes the time at which the electron tunnels out, t_F is the final time, and $\mathcal{A}_n$ is the amplitude of the nth saddle point contribution.

The saddle points are derived from the condition

$$\frac{(\mathbf{p} - e\mathbf{A}(t'_n)/c)^2}{2m} + I_p = 0. \tag{30}$$

In general, the trajectories are complex, and there are four families of solutions of Eq. (30): $t + 2\pi k, -t + 2\pi k, t^* + 2\pi k, -t^* + 2\pi k$, where k is an integer. The summation over this sequence of saddle points leads eventually to appearance of peaks in the spectrum at $p^2/2m = N\hbar\omega - I_p - U_p$, where N is an integer. Only two of these families contribute to Eq. (29), since the action $S(\boldsymbol{p}, t_F, t'_n)$ must have a negative imaginary part to describe appropriately an exponential decay of the ionization amplitudes.

It is interesting to note that even for $I_p = 0$, and $\theta = 0$ (angle between p and the direction of the field), there does not exist real solutions (real quantum orbits) for $p > \sqrt{4U_p m}$. This indicates that there is a cutoff for electrons of kinetic energies higher than $2U_p$. Note also that since there are contributions of two families of trajectories to each of the ATI peaks, the probability amplitude of direct tunneling displays in general interference effects. We stress that this is a generic feature that occurs also when we consider rescattering events.

A similar analysis can be done for the first-order solution (15). In this case, the result is

$$b_1(\mathbf{q}, \mathbf{t}_\mathrm{F}) = -\sum_{\mathrm{sp}} \mathcal{A}_n E(t'_n) \cos(\omega t'_n) g_x(\mathbf{p} - e\mathbf{A}(t'_n)/c, \mathbf{p}'_n - e\mathbf{A}(t'_n)/c) \times \mathrm{e}^{-\mathrm{i}S(\mathbf{p}, t_\mathrm{F}, t'_n)} E(t''_n) \cos(\omega t''_n) d_x(\mathbf{p}'_n - e\mathbf{A}(t''_n)/c) \mathrm{e}^{-\mathrm{i}S(\mathbf{p}'_n, t'_n, t''_n)}, \tag{31}$$

where the saddle points are stationary points of the sum of actions $S(\mathbf{p}, t_\mathrm{F}, t') + S(\mathbf{p}', t', t'')$, with respect to t', t'', and $\mathbf{p}'$.

The saddle points are solutions of the following set of equations:

$$\frac{(\mathbf{p}'_n - e\mathbf{A}(t'_n - \tau)/c)^2}{2m} + I_\mathrm{p} = 0, \tag{32}$$

$$\mathbf{p}'_n \tau/m - \frac{e}{mc} \int_{t'_n - \tau}^{t'_n} \mathbf{A}(\tilde{t}) \mathrm{d}\tilde{t} = 0, \tag{33}$$

$$\frac{(\mathbf{p} - e\mathbf{A}(t'_n)/c)^2}{2m} - \frac{(\mathbf{p}'_n - e\mathbf{A}(t'_n)/c)^2}{2m} = 0, \tag{34}$$

where we have introduced the return time $\tau = t'_n - t''_n$.

The first of the above equations in the limit $I_\mathrm{p} \to 0$ expresses the fact that the main contribution comes from the electrons that leave the nucleus at time $t''_n = t'_n - \tau$ with zero kinetic momentum, but with canonical momentum $\mathbf{p}'$. The second equation determines the value of $\mathbf{p}'$ which allows the electron to return to the nucleus at t'_n. Finally, the third equation describes rescattering at t'_n and simply states that the kinetic energy is conserved in this process. Neither the canonical momenta ($\boldsymbol{p}$) nor even the kinetic momenta ($\mathbf{p} - e\mathbf{A}/c$) have to be conserved at t'_n. The kinetic momenta may undergo a change of sign (backward scattering).

Generally, there are many families of solutions of Eqs. (32, 33, 34). In the limit $I_\mathrm{p} \to 0$, each of these families contains different values of τ corresponding to trajectories with one or several returns of the electron to the nucleus at t'_n. Due to quantum diffusion, trajectories with a single return are the most relevant ones. Even when we restrict ourselves to the families of trajectories with single returns, there are still four families corresponding to different values of t'_n. Each of the families contains an infinite number of solutions $t'_n + 2\pi k$, where k is an integer. Only some of these families contribute, however, to Eq. (31) since they must also fulfill the condition that the imaginary parts of $S(\mathbf{p}, t_\mathrm{F}, t')$ and $S(\mathbf{p}', t', t'')$ are negative.

For $\theta = 0$, $I_\mathrm{p} = 0$, the saddle point equations become particularly simple. For instance, Eq. (34) implies that we deal either with forward scattering

$$\boldsymbol{p} = \boldsymbol{p}'_n \tag{35}$$

or backward scattering

$$\boldsymbol{p} = -\boldsymbol{p}'_n + 2e\boldsymbol{A}(t'_n)/c. \tag{36}$$

On the other hand,

$$t'_n - \tau = \arccos(p'_n/\sqrt{4U_p m}), \tag{37}$$

i.e., $t'_n - \tau$ is real, provided p'_n is real and $p'_n/\sqrt{4U_p m} \leq 1$. One may ask how large p can be to have real solutions of the saddle point equations and thus lack of decay of probability amplitudes (i.e., plateau structures). For the forward scattering obviously the condition is $p'_n/\sqrt{4U_p m} \leq 1$, i.e., $p^2/2m \leq 2U_p$. Forward scattering is expected in this limit to affect most significantly low-energy part of the ATI spectrum. It is a little trickier to consider the case of backward scattering. Setting $2e\mathbf{A}(t'_n)/c$ to its extremal value $-2\sqrt{4U_p m}$, we obtain for the case of backward scattering that $p \geq -3\sqrt{4U_p m}$, i.e., $p^2/2m \leq 18U_p$. This estimate is obviously exaggerated, but it clearly indicates that backward scattering might in principle affect the parts of the ATI spectra that correspond to much higher energies, which indeed is the case (see Ref. [143] for detailed calculations of ATI spectra using the SFA).

Again, as an illustration of this formalism, we present in Fig. 10 an experimental ATI spectrum, obtained for elliptical polarization [21]. To each plateau

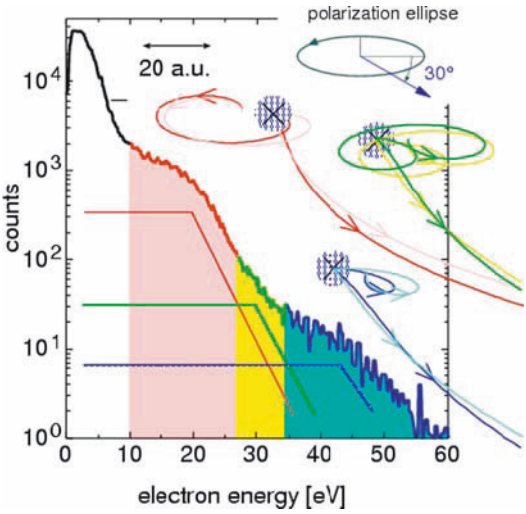

Fig. 10 ATI spectrum in xenon for an elliptically polarized laser field with ellipticity $\xi = 0.36$ and intensity 7.7×10^{13} W cm^{-2} for emission at an angle with respect to the polarization axis as indicated. The different steps of the spectrum are shaded differently. For each step (from *left* to *right*), the responsible quantum orbits, calculated from the stationary action principle (see text) are displayed above (from *top* to *bottom*). The *crosses* mark the position of the atom, and the length scale of the orbits is given in the upper left of the figure (from [21])

shown in this figure, it is possible to associate a quantum orbit (or quantum path), derived from Eqs. (32, 33, 34).

5.4 Generalized Strong Field Approximation for Non-sequential Ionization

To our knowledge, a time-dependent formulation of the SFA for multielectron problems such as non-sequential ionization has not been presented in the literature so far [222][3]. A related generalized $\hat{S}$-matrix theory [172, 173, 186] has been very successful in explaining experimental momentum distributions. It was also stressed [174, 175] that to get full quantitative agreement with the experiment, Coulomb refocusing of the electron trajectories has to be accounted for. In the following, we will not attempt to derive the time-dependent version of the SFA for two electrons, but we will rather follow the "minimal correlation" approach of Becker and his coworkers, which leads to a description of non-sequential ionization in the form of a Feynman sum over few relevant electronic trajectories.

Here the process in question involves two electrons, which have the final momenta $\mathbf{p}_1$ and $\mathbf{p}_2$, respectively. Let $I_{2\mathrm{p}}$ be ionization potential for two-electron ionization (i.e. $-I_{2\mathrm{p}}$ is the ground state energy), and let $I_{1\mathrm{p}}$ be the ionization potential for a singly charged ion (i.e., $-I_{1\mathrm{p}}$ is the energy threshold for continuum states with one electron freed from the nucleus). Let $t_n - \tau$ denote the time at which the first electron tunnels out, t_n the time at which it rescatters on the nucleus, and τ the return time, i.e., the time the first electron needs to come back to the nucleus. Let $\mathbf{p}_n$ denote the canonical momentum of the first electron born in the continuum at $t_n - \tau$. With this notation the stationary action equations become

$$\frac{(\mathbf{p}_n - e\mathbf{A}(t_n - \tau)/c)^2}{2m} + I_{2\mathrm{p}} - I_{1\mathrm{p}} = 0, \tag{38}$$

$$\mathbf{p}_n \tau - \frac{e}{c}\int_{t_n-\tau}^{t_n} \mathbf{A}(\tilde{t})\mathrm{d}\tilde{t} = 0, \tag{39}$$

$$\frac{(\mathbf{p}_1 - e\mathbf{A}(t_n)/c)^2}{2m} + \frac{(\mathbf{p}_2 - e\mathbf{A}(t_n)/c)^2}{2m} - \frac{(\mathbf{p}_n - e\mathbf{A}(t_n)/c)^2}{2m} + I_{1\mathrm{p}} = 0. \tag{40}$$

Again, there are typically several physically relevant families of solution of these equations. Summation over such families in the expression of the form Eq. (23) leads eventually to appearance of peaks in the energy spectrum at

$$\frac{\mathbf{p}_1^2}{2m} + \frac{\mathbf{p}_2^2}{2m} = N\hbar\omega - 2U_{\mathrm{p}} - I_{2\mathrm{p}},$$

[3] Some steps toward such formulation have been achieved.

where N is an integer. The analysis of the above equations. allows both for qualitative understanding of the non-sequential ionization process and for quite accurate quantitative description of momentum distributions [172, 173, 186].

6 Conclusion

We have presented a review of the physics of atoms in strong laser fields, concentrating on the single atom response. We hope that the readers of this chapter will share our opinion that even the "simple" single atom physics is only apparently simple, and is in fact very rich and leads to a whole variety of fascinating phenomena and applications.

We have focused in this chapter on an accurate description and explanation of HHG, ATI, and non-sequential ionization provided by SFA, which in turn, when analyzed using the stationary phase principle, leads to a unified description of all of the considered processes in terms of Feynman integrals, or better to say Feynman sums over few relevant electronic trajectories.

The readers should not get the impression that SFA explains and describes everything and that there are no more open challenging problems in the physics of single atoms in strong fields. Our aim was to convince the readers that a lot has been already achieved in this area, and a lot can be understood using the elegant language of Feynman's path integrals. Nevertheless, the area is still full of open problems and challenges.

In HHG for instance, the problem of optimization of generation process is far from being solved and may lead to many surprises in the future. Applications of HHG has just begun to arise, and one expects a lot of activities in this area. Optimal generation of attosecond pulses, or pulse trains, is another issue. Attophysics is being now born and there are numerous open questions concerning applications of attosecond XUV pulses, in particular for time-resolved attosecond spectroscopy (TRAS). The first steps toward this direction has been recently achieved by Krausz and his collaborators, who have used attosecond pulses for monitoring an Aug decay [223] as well as for visualizing an optical light wave [224].

ATI seems to be the area in which many of the fundamental questions have been already answered. Even this point of view is misleading: for instance, ATI and more generally electron scattering in the presence of strong laser light is becoming a test ground for attophysics [76, 122].

Finally, the systematic study of multielectron ionization and electron correlation processes in strong laser fields has just begun. Both in experiments and in the theory there are fundamental questions, involving for instance control of rescattering effects, role of laser pulse duration. We may expect a lot of activities in this area in the next future.

Acknowledgements We thank A. Sanpera, P. Salières, Ph. Balcou, K. J. Schafer, F. Krausz, and T. Brabec for discussion and encouragement. This work has been supported by the Deutsche Forschungsgemeinschaft (SFB 407, GK 282) and by the Swedish Science Council. This paper was originally written in 2001 and reviews mostly the research performed in the field until that time. More complete descriptions of the evolution of the field during the last seven years can be found elsewhere.

References

1. F. H. M. Faisal. *Theory of Multiphoton Processes* (Plenum, New York, 1987).
2. M. Gavrila, editor, *Atoms in Intense Laser Fields* (Academic Press, San Diego, 1992).
3. M. H. Mittleman, *Theory of Laser-Atom Interactions*, 2nd ed. (Plenum, New York, 1993).
4. P. Lambropulos and S. J. Smith (Eds.), *Multiphoton Processes*, Proc. of ICOMP III, in Springer Series on Atoms and Plasmas, vol. 2, (Springer-Verlag, Berlin, 1984).
5. S. J. Smith and P. L. Knight (Eds.), *Multiphoton Processes*, Proc. of ICOMP IV, in Cambridge Studies of Modern Optics, vol. 8 (Cambridge University Press, Cambridge, 1988).
6. G. Mainfray and P. Agostini (Eds.), *Multiphoton Processes*, Proc. of ICOMP V, (Commissariat à l'Energie Atomique, Centre d'Etudes de Saclay, Saclay, 1991).
7. S. L. Chin and D. K. Evans (Eds.), *Multiphoton Processes*, Proc. of ICOMP VI, (World Scientific Publishing, Singapore, 1994).
8. P. Lambropoulos and H. Walther (Eds.), *Multiphoton Processes: 1996*, Proc. of ICOMP VII, (The Institute of Physics, Bristol, 1997).
9. L. F. DiMauro, R. R. Freeman, and K. Kulander (Eds.), *Multiphoton Processes*, Proc. of ICOMP VIII, (Springer, Berlin, 2000).
10. A. L'Huillier, B. Piraux, and K. Rzażewski (Eds.), *Super-intense Laser-atom Physics III*, (Kluwer, Dordrecht, 1994).
11. H.-G. Muller, (Eds.), *Super-intense Laser-atom Physics VI*, (Kluwer, Dordrecht, 1996).
12. B. Piraux and K. Rzażewski (Eds.), *Super-intense Laser-atom Physics VII*, (Kluwer, Dordrecht, 2001).
13. M. Protopapas M, C. H. Keitel, and P. L. Knight, Rep. Prog. Phys. **60**, 389 (1997).
14. C. J. Joachain, M. Dörr, and N. Kylstra, Adv. Atom. Mol. Opt. Phys. **42**, 225 (2000).
15. J.H. Eberly, J. Javanainen, and K. Rzaażwski, Phys. Rep. **204** (5), 331 (1991)
16. L. F. DiMauro and P. Agostini, Adv. At. Mol. Opt. Phys. **35**, 79 (1995).
17. P. Salières, A. L'Huillier, Ph. Antoine, and M. Lewenstein, Adv. Atom. Mol. Opt. Phys. **41**, 83 (1999).
18. P. Salières and M. Lewenstein, Measur. Sci. Tech. **12** (11), 1818 (2001).
19. T. Brabec and F. Krausz, Rev. Mod. Phys. **72**, 545 (2000).
20. P. Lambropoulos, P. Maragakis, and J. Zhang, Phys. Rep. **305**, 203 (1998).
21. P. Salières, B. Carré, L. Le Déroff, F. Grasbon, G. G. Paulus, H. Walther, R. Kopold, W. Becker, D. B. Milošević, A. Sanpera, and M. Lewenstein, Science **292**, 902 (2001).
22. A. McPherson, G. Gibson, H. Jara, U. Johann, T. S. Luk, I. McIntyre, K. Boyer, and C. K. Rhodes, J. Opt. Soc. Am. B **4**, 595 (1987).
23. S. G. Preston, A. Sanpera, M. Zepf, J. W. Blyth, C. G. Smith, J. S. Wark, M. H. Key, K. Burnett, M. Nakai, D. Neely, and A. A. Offenberger, Phys. Rev. A **53**, R31 (1996).
24. M. D. Perry and J. K. Crane, Phys. Rev. A **48**, R4051 (1993).
25. H. Eichmann, A. Egbert, S. Nolte, C. Momma, B. Wellegehausen, W. Becker, S. Long and J. K. McIver, Phys. Rev. A **51**, R3414 (1995).
26. S. Watanabe, K. Kondo, Y. Nabekawa, A. Sagisaka and Y. Kobayashi, Phys. Rev. Lett. **73**, 2692 (1994).

27. H. Eichmann, S. Meyer, K. Riepl, C. Momma and B. Wellegehausen, Phys. Rev. A **50** R2834 (1994).
28. M. B. Gaarde, P. Antoine, A. Persson, B. Carrè, A. L'Huillier and C.-G. Wahlström, J. Phys. B **29**, L163 (1996).
29. B. Sheehy, J. D. D. Martin, L. F. DiMauro, P. Agostini, K. J. Schafer, M. B. Gaarde, and K. C. Kulander, Phys. Rev. Lett. **83**, 5270 (1999).
30. R. Bartels, S. Backus, E. Zeek, L. Misoguti, G. Vdovin, I. P. Christov, M. M. Murnane, H. C. Kapteyn, Nature **406**, 164 (2000).
31. Th. Weber, M. Weckenbrock, A. Staudte, L. Spielberger, O. Jagutzki, V. Mergel, F. Afaneh, G. Urbasch, M. Vollmer, H. Giessen, and R. Dörner et al. Phys. Rev. Lett. **84**, 443 (2000).
32. R. Moshammer, B. Feuerstein, W. Schmitt, A. Dorn, C. D. Schröter, J. Ullrich, H. Rottke, C. Trump, M. Wittman, G. Korn, K. Hoffmann and W. Sandner, Phys. Rev. Lett. **84**, 447 (2000).
33. G. G. Paulus, W. Nicklich, F. Zacher, P. Lambropoulos, and H. Walther, J. Phys. B **29**, L249 (1996).
34. P. Kruit and F. H. Read, J. Phys. E: Sci. Instrum. **16**, 313 (1983).
35. D. J. Trevor, L. D. Van Woerkom, and R. R. Freeman, Rev. Sci. Instrum. **60**, 6 (1989).
36. H. Helm, N. Bjerre, M. J. Dyer, D. L. Huestis, and M. Saeed, Phys. Rev. Lett. **70**, 3221 (1993).
37. Th. Weber, H. Giessen, M. Weckenbrock, G. Urbasch, A. Staudte, L. Spielberger, O. Jagutzki, V. Mergel, M. Vollmer, and R. Dörner, Nature **405**, 658 (2000).
38. B. Witzel, N. A. Papadogiannis, and D. Charalambidis, Phys. Rev. Lett. **85**, 2268 (2000).
39. A. Rundquist, C. Durfee III, Z. Chang, C. Herne, S. Backus, M. Murnane, and H. C. Kapteyn, Science **280**, 1412 (1998).
40. E. Constant, D. Garzella, P. Breger, E. Mvel, Ch. Dorrer, C. Le Blanc, F. Salin, and P. Agostini, Phys. Rev. Lett. **82**, 1668 (1999).
41. Y. Tamaki, J. Itatini, Y. Nagata, M. Obara, and K. Midorikawa, Phys. Rev. Lett. **82**, 1422 (1999).
42. C.-G. Wahlström, S. Borgström, J. Larsson, and S.-G. Pettersson, Phys. Rev. A **51**, 585 (1995).
43. J. W. G. Tisch, A. R. Smith, J. E. Muffet, M. Ciarocca, J. P. Marangos, and M. H. R. Hutchinson , Phys. Rev. A **49**, R28 (1994).
44. J. Peatross and D. D. Meyerhofer, Phys. Rev. A **51**, R906 (1995).
45. P. Salières, T. Ditmire, M. D. Perry, A. L'Huillier, and M. Lewenstein, J. Phys. B **29**, 4771 (1996).
46. M. Nisoli, E. Priori, G. Sansone, S. Stagira, G. Cerullo, S. De Silvestri, C. Altucci, R. Bruzzese, C. de Lisio, P. Villoresi, L. Poletto, M. Pascolini, and G. Tondello, Phys. Rev. Lett. **88**, 033902 (2002).
47. T. Ditmire, E. T. Grumbell, R. A. Smith, J. W. G. Tisch, D. D. Meyerhofer and M. H. R. Hutchinson, Phys. Rev. Lett. **77**, 4756 (1996).
48. L. Le Déroff, P. Salières, B. Carré, D. Joyeux, and D. Phalippou, Phys. Rev. A **61**, 043802 (2000).
49. T. E. Glover , R. W. Schoenlein, A. H. Chin, and C. V. Shank, Phys. Rev. Lett. **76**, 2468 (1996).
50. J. M. Schins, P. Breger, P. Agostini, R. C. Constantinescu, H. G. Muller, A. Bouhal, G. Grillon, A. Antonetti, and A. Mysyrowicz, J. Opt. Soc. Am. B **13**, 197 (1996).
51. E. S. Toma, H. G. Muller, P. M. Paul, P. Breger, M. Cheret, P. Agostini, C. Le Blanc, G. Mullot, and G. Cheriaux , Phys. Rev. A **62** 061801 (2000).
52. M. Drescher, M. Hentschel, R. Kienberger, G. Tempea, C. Spielmann, G. A. Reider, P. B. Corkum, and F. Krausz, Science **291**, 1923 (2001).
53. J. Norin, J. Mauritsson, A. Johansson, M. K. Raarup, S. Buil, A. Persson, O. Dühr, M. B. Gaarde, K. J. Schafer, U. Keller, C.-G. Wahlström, and A. L'Huillier, Phys. Rev. Lett. **88**, 193901 (2002)

54. T. Sekikawa, T. Katsura, S. Miura, and S. Watanabe, Phys. Rev. Lett. **88**, 193902 (2002)
55. J. J. Macklin, J. D. Kmetec, and C. L. Gordon III, Phys. Rev. Lett. **70**, 766 (1993).
56. Z. Chang, A. Rundquist, and H. Wang, M. M. Murnane, and H. C. Kapteyn, Phys. Rev. Lett. **79**, 2967 (1997).
57. C. Spielmann, N. Burnett, S. Sartania, R. Koppitsch, M. Schnurer, C. Kan, M. Lenzner, P. Wobrauschek, and F. Krausz, Science **278**, 661 (1997).
58. A. L'Huillier, L.-A. Lompré, G. Mainfray, and C. Manus, in *Atoms in Intense Laser Fields*, ed. by M. Gavrila (Academic Press, New York 1992).
59. A. L'Huillier, Ph. Balcou, S. Candel, K. J. Schafer, and K. C. Kulander Phys. Rev. A **46**, 2778 (1992).
60. J. Larsson, E. Mevel, R. Zerne, A. L'Huillier, C.-G. Wahlström, and S. Svanberg, J. Phys. B **28**, L53 (1995).
61. M. Gisselbrecht, D. Descamps, C. Lyngå, A. L'Huillier, C.-G. Wahlström, and M. Leyer, Phys. Rev. Lett. **82**, 4607 (1999).
62. S. L. Sorensen, O. Bjorneholm, I. Hjelte, T. Kihlgren, G. Ohrwall, S. Sundin, S. Svensson, S. Buil, D. Descamps, and A. L'Huillier, J. Chem. Phys. **112**, 8038 (2000).
63. M. Bauer, C. Lei, K. Read, R. Tobey, J. Gland, M. M. Murnane, and H. C. Kapteyn, Phys. Rev. Lett. **87**, 025501 (2001).
64. L. Nugent-Glandorf, M. Scheer, D. A. Samuels, A. M. Mulhisen, E. R. Grant, X. Yang, V. M. Bierbaum, and S. R. Leone, Phys. Rev. Lett. **87**, 193002 (2001).
65. R. Haight and D.R. Peale, Phys. Rev. Lett. **70**, 3979 (1993).
66. F. Quéré, S. Guizard, G. Petite, Ph. Martin, H. Merdji, B. Carré, and J.-F. Hergott, Phys. Rev. B **61**, 9883 (2000).
67. T. Sekikawa, T. Ohno, Y. Nabekawa, and S. Watanabe, J. Lumin. **87**, 827 (2000).
68. W. Theobald, R. Hässner, C. Wülker, and R. Sauerbrey, Phys. Rev. Lett. **77**, 298 (1996).
69. P. Salières, L. Le Déroff, T. Auguste, P. Monot, P. d'Oliveira, D. Campo, J.-F. Hergott, H. Merdji, and B. Carré, Phys. Rev. Lett. **83**, 5483 (1999).
70. D. Descamps, C. Lyngå, J. Norin, A. L'Huillier, C.-G. Wahlström, J.-F. Hergott, H. Merdji, P. Salières, M. Bellini, and T. W. Hänsch, Opt. Lett. **25**, 135 (2000).
71. Y. Kobayashi, T. Sekikawa, Y. Nabekawa, and S. Watanabe, Opt. Lett. **23**, 64 (1998).
72. T. Sekikawa, T. Ohna, T. Yamazaki, Y. Nabekawa, and S. Watanabe, Phys. Rev. Lett. **83**, 2564 (1999).
73. D. Descamps, L. Roos, C. Delfin, A. L'Huillier, and C.-G. Wahlström, Phys. Rev. A **64**, 031401 (R) (2001).
74. P. M. Paul, E. S. Toma, P. Breger, G. Mullot, F. Augé, P. h. Balcou, H. G. Muller, and P. Agostini, Science **292**, 1689 (2001).
75. M. Hentschel, R. Klenberger, Ch. Spielmann, G. A. Reider, N. Milošević, T. Brabec, P. Corkum, U. Heinzmann, M. Drescher, and F. Krausz, Nature **414**, 511 (2001).
76. R. Kienberger et al., Nature **427**, 817 (2004).
77. R. López-Martens et al., Phys. Rev. Lett. **94**, 033001 (2005).
78. M. Lein, N. Hay, R. Velotta, J. P. Marangos, and P. L. Knight, Phys. Rev. A **66**, 023805 (2002).
79. J. Itatani, J. Levesque, D. Zeidler, H. Niikura, H. Pépin, J. C. Kieffer, P. B. Corkum, D. M, Villeneuve, Nature **432**, 867 (2004).
80. T. Kanai, S. Minemoto, and H. Sakai, Nature **435**, 470 (2005).
81. M. Ferray, A. L'Huillier, X. F. Li, L. A. Lompré, G. Mainfray, and C. Manus, J. Phys. B **21**, L31 (1988).
82. A. L'Huillier and Ph. Balcou, Phys. Rev. Lett. **70**, 774 (1993).
83. M. D. Perry and G. Mourou, Science **264**, 917 (1994).
84. Z. Chang, A. Rundquist, H. Wang, H. Kapteyn, M. Murname, X. Liu, and B. Shan, proceedings of the *Applications of High Field and Short Wavelength Sources VII* topical meeting, Santa Fe, March 19–22 (1997).
85. J. L. Krause, K. J. Schafer, and K. C. Kulander, Phys. Rev. Lett. **68**, 3535 (1992).

86. H.B. van Linden van den Heuvell in Ref. [5], p. 25.
87. P. B. Corkum, N. H. Burnett and F. Brunel, Phys. Rev. Lett. **62**, 1259 (1989).
88. K. C. Kulander, K. J. Schafer, and J. L. Krause, in *Super-Intense Laser-Atom Physics*, Eds. B. Piraux, Anne L'Huillier, and K. RzaŻewski, NATO ASI Series B, vol. 316, p. 95 (Plenum Press, New York, 1993).
89. P. B. Corkum, Phys. Rev. Lett. **71**, 1994 (1993).
90. A. L'Huillier, M. Lewenstein, P. Salières, Ph. Balcou, M. Yu. Ivanov, J. Larsson, and C. G. Wahlström, Phys. Rev. A **48**, R3433 (1993).
91. M. Lewenstein, Ph. Balcou, M.Yu. Ivanov, Anne L'Huillier, and P. Corkum, Phys. Rev. A **49**, 2117 (1994).
92. P. B. Corkum, N. H. Burnett, and M. Y. Ivanov, Opt. Lett. **19**, 1870 (1994).
93. K. S. Budil, P. Salières, A. L'Huillier, T. Ditmire, and M. D. Perry, Phys. Rev. A **48**, R3437 (1993).
94. P. Dietrich, N. H. Burnett, M. Y. Ivanov, and P. B. Corkum, Phys. Rev. A **50**, R3585 (1994).
95. Y. Liang, M. V. Ammosov, and S. L. Chin, J. Phys. B **27**, 1296 (1994).
96. N. H. Burnett, C. Kan, and P. B. Corkum, Phys. Rev. A **51**, R3418 (1995).
97. F. A. Weihe, S. K. Dutta, G. Korn, D. Du, P. H. Bucksbaum, and P. L. Shkolnikov, Phys. Rev. A **51**, R3433 (1995).
98. Ph. Antoine, B. Carré, A. L'Huillier, and M. Lewenstein, Phys. Rev. A **55**, 1314 (1997).
99. F. A. Weihe and P. H. Bucksbaum, J. Opt. Soc. Am. B **13**, 157 (1996).
100. D. Schulze, M. Dörr, G. Sommerer, P. V. Nickles, T. Schlegel, W. Sandner, M. Drescher, U. Kleineberg, and U. Heinzmann, Phys. Rev. A **57**, 3003 (1998).
101. W. Becker, A. Lohr, and M. Kleber, J. Phys. B **27**, L325 (1994); **28**, 1931 (1995) (corrigendum).
102. Ph. Antoine, A. L'Huillier, M. Lewenstein, P. Salières, and B. Carré, Phys. Rev. A **53**, 1725 (1996).
103. W. Becker, A. Lohr, M. Kleber, and M. Lewenstein, Phys. Rev. A **56**, 645 (1997).
104. M. Bellini, C. Lyngå, A. Tozzi, M. B. Gaarde, C. Delfin, T. W. Hänsch, A. L'Huillier, and C.-G. Wahlström, Phys. Rev. Lett. **81**, 297 (1998).
105. C. Lyngå, M. B. Gaarde, C. Delfin, M. Bellini, T. W. Hnsch, A. L'Huillier, and C.-G. Wahlstr"m, Phys. Rev. A **60**, 4823 (1999).
106. Ph. Balcou, A. S. Dederichs, M. B. Gaarde, and A. L'Huillier, J. Phys. B **32**, 2973 (1999).
107. M. B. Gaarde and K. J. Schafer, Phys. Rev. A **65**, 031406(R) (2002).
108. M. Gaarde, F. Salin, E. Constant, Ph. Balcou, K. J. Schafer, K. C. Kulander, and A. L'Huillier, Phys. Rev. A **59**, 1367 (1999).
109. P. B. Corkum, N. H. Burnett, and M. Y. Ivanov, Opt. Lett. **19**, 1870 (1994).
110. C. Altucci, C. Delfin, L. Roos, M. B. Gaarde, A. L'Huillier, I. Mercer, T. Starczewsky, and C.-G. Wahlström: Phys. Rev. A **58**, 3934 (1998).
111. E. Constant, V. D. Taranukhin, A. Stolow and P. B. Corkum, Phys. Rev. A **56**, 3870 (1997).
112. G. Farkas and C. Toth, Phys. Lett. A **168**, 447 (1992).
113. S. E. Harris, J. J. Macklin, and T. W. Hänsch, Opt. Comm. **100**, 487 (1993).
114. Ph. Antoine, A. L'Huillier, and M. Lewenstein, Phys. Rev. Lett **77**, 1234 (1996).
115. M. Y. Ivanov, P. B. Corkum, T. Zuo, and A. Bandrauk, Phys. Rev. Lett. **74**, 2933 (1995).
116. C.-G. Wahlström, C. Altucci, Ph. Antoine, M. Bellini, M. B. Gaarde, T. W. Hänsch, A. L'Huillier, C. Lyngå, I. Mercer, E. Mevel, and R. Zerne, in *Multiphoton Processes 1996*, Eds. P. Lambropoulos and H. Walther, (IOP Publishing, Bristol, 1997).
117. K. J. Schafer, K. C. Kulander, Phys. Rev. Lett. **78**, 638 (1997).
118. P. Salières, Ph. Antoine, A. de Bohan, and M. Lewenstein, Phys. Rev. Lett. **81**, 5544 (1998).
119. I. P. Christov, M. M. Murnane, and H. C. Kapteyn, Phys. Rev. Lett. **78**, 1251 (1997).

120. N. A. Papadogiannis, B. Witzel, C. Kalpouzos, and D. Charalambidis, Phys. Rev. Lett. **83**, 4289 (1999).
121. R. Kienberger et al., Science **297**, 1144 (2002).
122. P. Johnsson et al., Phys. Rev. Lett. **95**, 013001 (2005).
123. Y. Mairesse et al., Science **302**, 1540 (2003).
124. P. Agostini, F. Fabre, G. Petite, and N. K. Rahman, Phys. Rev. Lett. **42**, 1127 (1979).
125. P. Kruit, J. Kimman, H. G. Muller, and M. J. Van der Wiel, Phys. Rev. A **28**, 248 (1983).
126. R. R. Freeman, T. J. McIlrath, P. H. Bucksbaum, and M. Bashkansky, Phys. Rev. Lett. **57**, 3156 (1986).
127. R. R. Freeman, P. H. Bucksbaum, H. Milchberg, S. Darack, D. Schumacher, and M. E. Geusic, Phys. Rev. Lett. **59**, 10 (1987).
128. H. G. Muller, P. Agostini and G. Petite, Chapter 1 in Ref. [2] pp. 1–42.
129. R. R. Freeman, P. H. Bucksbaum, W. E. Cooke, G. Gibson, T. J. McIlrath, and L. D. van Woerkom, Chapter 2 in Ref. [2] pp. 43–65.
130. P. H. Bucksbaum, M. Bashkansky, R. R. Freeman, T. J. McIlrath, and L. F. DiMauro, Phys. Rev. **56**, 2590 (1986).
131. P. Hansch, M. A. Walker, and L. D. Van Woerkom, Phys. Rev. A **55**, R2535 (1997).
132. B. Yang, K. J. Schafer, B. Walker, K. C. Kulander, P. Agostini, and L. F. DiMauro, Phys. Rev. Lett. **71**, 3770 (1993).
133. M. P. deBoer and H. G. Muller, Phys. Rev. Lett., **68**, 2727 (1992).
134. E. Mevel, P. Breger, R. Trainham, G. Petite, P. Agostini, A. Migus, J. P. Chambaret, and A. Antonetti, Phys. Rev. Lett. **70**, 406 (1993).
135. B. Walker, B. Sheehy, L. F. DiMauro, P. Agostini, K. J. Schafer, and K. C. Kulander, Phys. Rev. Lett. **73**, 1227 (1994).
136. G. G. Paulus, W. Nicklich, H. Xu, P. Lambropoulos, and H. Walther, Phys. Rev. Lett. **72**, 2851 (1994).
137. B. Walker, B. Sheehy, K.C. Kulander, and L.F. DiMauro, Phys. Rev. Lett. **77**, 5031 (1996).
138. D. Feldman, in ref. [7].
139. G. G. Paulus, W. Nicklich, and H. Walther, Europhys. Lett. **27**, 267 (1994).
140. K. C. Kulander and K. J. Schafer, in ref. [5].
141. K. J. Schafer and K. C. Kulander, in ref. [5].
142. W. Becker, A. Lohr, and M. Kleber, J. Phys. B **27**, L325 (1994).
143. M. Lewenstein, K. C. Kulander, K. J. Schafer, and P. Bucksbaum, Phys. Rev. A **51**, 1495 (1995).
144. G. G. Paulus, F. Zacher, H. Walther, A. Lohr, W. Becker, and M. Kleber, Phys. Rev. Lett. **80**, 484 (1998).
145. G. G. Paulus, F. Grasbon, A. Dreischuh, H. Walther, R. Kopold, and W. Becker, Phys. Rev. Lett. **84**, 3791 (2000).
146. R. Kopold, D. B. Miloševiŭ, and W. Becker, Phys. Rev. Lett. **84**, 3831 (2000).
147. M. P. Hertlein, P. H. Bucksbaum, and H. G. Muller, J. Phys. B **30**, L197 (1997).
148. G. G. Paulus, F. Grasbon, H. Walther, R. Kobold, and W. Becker, Phys. Rev. A **64**, 021401(R) (2001);
149. E. Cormier, D. Garzella, P. Breger, P. Agostini, G. Chériaux and C. Leblanc, J. Phys. B **34**, L9 (2001).
150. M. J. Nandor, M. A. Walker, L. D. Van Woerkom, and H. G. Muller, Phys. Rev. A **60**, R1771 (1999).
151. H. G. Muller and F. C. Kooiman, Phys. Rev. Lett. **81**, 1207 (1998).
152. R. Kobold, W. Becker, M. Kleber, and G. G. Paulus, J. Phys. B **35**, 217 (2002).
153. R. Kopold, W. Becker, and D. B. Milošević, in print in special issue of J. Mod. Opt. on "Quantum Challenges 2001", ed. M. Lewenstein and M. Wilkens.
154. V. V. Suran and I. P. Zapesnochnyi, Sov. Tech. Phys. Lett. **1**, 420 (1975).

155. S. Augst, D. Strickland, D. D. Meyerhofer, S. L. Chin, and J. H. Eberly, Phys. Rev. Lett. **63**, 2212 (1989).
156. Th. Auguste, P. Monot, L. A. Lompré, G. Mainfray, and C. Manus, J. Phys. B **25**, 4181 (1992).
157. A. L'Huillier, L.A. Lompre, G. Mainfray, and C. Manus, Phys. Rev. A **27**, 2503 (1983).
158. A. L'Huillier, L.A. Lompre, G. Mainfray, and C. Manus, J. Phys. B **16**, 1363 (1983).
159. A. Rudenko, K. Zrost, B. Feuerstein, V. L. B. Jesus, C. D. Schröter, R. Moshammer, and J. Ullrich, Phys. Rev. Lett. **93**, 253001 (2004).
160. T. S. Luk, U. Johann, H. Egger, H. Pummer, and C. K. Rhodes, Phys. Rev. A **32**, 214 (1985).
161. M. D. Perry, A. Szöke, O. L. Landen, and E. M. Campbell, Phys. Rev. Lett. **60**, 1270 (1988).
162. L. V. Keldysh, Sov. Phys. –JETP, **20**, 1307 (1965).
163. F. Faisal, J. Phys. B **6**, L312 (1973).
164. H. R. Reiss, Phys. Rev. A **22**, 1786 (1980).
165. M. V. Ammosov, N. B. Delone and V. P. Kraïnov Sov. Phys. – JETP, **64**, 1191 (1986).
166. D. N. Fittinghoff, P. R. Bolton, B. Chang, and K. C. Kulander, Phys. Rev. Lett. **69**, 2642 (1992).
167. S. Larochelle, A. Talebpour, and S. L. Chin, J. Phys. B **31**, 1201 (1998).
168. R. Wehlitz, F. Heiser, O. Hammers, B. Langer, A. Mentzel, and U. Becker, Phys. Rev. Lett. **67**, 3764 (1991).
169. J. Bauer and K. Rzżewski, J. Phys. B **29**, 3351 (1996).
170. J. B. Watson, A. Sanpera, D. G. Lappas, P. L. Knight, and K. Burnett, Phys. Rev. Lett. **78**, 1884 (1997).
171. K. C. Kulander, Phys. Rev. A **36**, 2726 (1987).
172. A. Becker and F. Faisal, Phys. Rev. A **59**, R1742 (1999).
173. A. Becker and F. Faisal, Phys. Rev. Lett. **84**, 3546 (2000).
174. M. Yu. Ivanov, Th. Brabec, and N. Burnett, Phys. Rev. A **54**, 742 (1996).
175. G. L. Yudin and M. Yu. Ivanov, Phys. Rev. A **63**, 033404 (2001).
176. J. S. Parker, E. S. Smyth, and K. T. Taylor, J. Phys. B **31**, L571 (1998).
177. L. R. Moore, J. S. Parker, D. Dundas, K. J. Merhag, and K. T. Taylor, in Ref. [10](c), p. 107.
178. M. A. Kornberg and P. Lambropoulos, J. Phys. B **32**, L603 (1999).
179. P. Lambropoulos, L. A. A. Nikolopoulos, L.B. Masden, and M. G. Makris, in Ref. [10](c), p. 153.
180. R. Panfili, C. Szymanowski, W.-C. Liu, and J. H. Eberly, in Ref. [9], p. 265.
181. B. Piraux and G. Lamago Kamta, in Ref. [10](c), p. 127.
182. G. Lamago Kamta and A. Starace, in Ref. [10](c), p.143.
183. D. N. Fittinghoff, P. R. Bolton, B. Chang, and K. C. Kulander, Phys. Rev. A **49**, 2174 (1994).
184. K. Kondo, A. Sagisaka, T. Tamida, Y. Nabekawa, and S. Watanabe, Phys. Rev. **48**, 2531 (1993).
185. R. Lafon, J. L. Chaloupka, B. Sheehy, P. M. Paul, P. Agostini, and L. F. DiMauro, Phys. Rev. Lett. **86**, 2762 (2001)
186. R. Kopold, W. Becker, H. Rottke, and W. Sandner, Phys. Rev. Lett. **85**, 3781 (2000).
187. D. G. Lappas, A. Sanpera, J. B. Watson, K. Burnett, P. L. Knight, R. Grobe, and J. H. Eberly, J. Phys. B **29**, L619 (1996).
188. S. Erhard and E. K. U. Gross, in *Multiphoton Processes 1996*, Eds. P. Lambropoulos and H. Walther, (IOP Publishing, Bristol, 1997).
189. K. T. Taylor, J. S. Parker, D. Dundas, E. Smyth, and S. Vivirito, in *Multiphoton Processes 1996*, Eds. P. Lambropoulos and H. Walther, (IOP Publishing, Bristol, 1997).
190. R. Potvliege and R. Shakeshaft, Phys. Rev. A **46**, 424 (1989).

191. C. J. Joachain, in [7].
192. K. C. Kulander, K. J. Schafer, and J. L. Krause, in *Atoms in Intense Laser Fields*, Ed. M. Gavrila, (Academic Press, New York, 1992).
193. J. H. Eberly, Q. Su, and J. Javanainen, Phys. Rev. Lett. **62**, 881 (1989).
194. K. C. Kulander, Phys. Rev. A **35**, R445 (1987).
195. P. L. DeVries, J. Opt. Soc. Am. B **7**, 517 (1990).
196. K. J. LaGutta, J. Opt. Soc. Am. B **7**, 639 (1990).
197. Ph. Antoine, B. Piraux, and A. Maquet, Phys. Rev. A **51**, R1750 (1995).
198. Ph. Antoine, D. B. Milošević, B. Piraux, and M. Gajda, in print Laser Phys. **7**, 3 (1997).
199. E. Cormier and P. Lambropoulos, J. Phys. B **29**, 1667 (1996).
200. E. Cormier and P. Lambropoulos, J. Phys. B **30**, 77 (1997).
201. M. Protopapas, D. G. Lappas, and P. L. Knight, Phys. Rev. Lett. **79**, 4550 (1997).
202. A. Sanpera, P. Jonsson, J. B. Watson, and K. Burnett, Phys. Rev. A **51**, 3148 (1995).
203. J. B. Watson, A. Sanpera, and K. Burnett, Phys. Rev. A **51**, 1458 (1995).
204. S. C. Rae, K. Burnett, and J. Cooper, Phys. Rev. A **50**, 3438 (1994).
205. J. B. Watson, A. Sanpera, K. Burnett, and P. L. Knight, Phys. Rev. A **55**, 1224 (1997).
206. I. P. Christov, M. M. Murnane, and H. C. Kapteyn, Phys. Rev. Lett. **78**, 1251 (1997).
207. N. Miloševic, A. Scrinzi, and T. Brabec, Phys. Rev. Lett. **88**, 093905 (2002).
208. M. Kitzler, N. Miloševic, A. Scrinzi, F. Krausz, and T. Brabec, Phys. Rev. Lett. **88**, 173904 (2002).
209. G. Bandarage, A. Maquet, T. Ménis, R. Taïeb, and J. Cooper, Phys. Rev. A **46**, 380 (1992).
210. V. Véniard, A. Maquet, and T. Ménis, in Ref. [10](a), p. 225.
211. W. Becker, S. Long, and J. K. McIver, Phys. Rev. A **41**, 4112 (1990).
212. S. Long, W. Becker, and J. K. McIver, Phys. Rev. A **52**, 2262 (1995).
213. A. Lohr, S. Long, W. Becker, and J. K. McIver, in Ref. [10](b).
214. W. Becker, S. Long, and J. K. McIver, Phys. Rev. A **50**, 1540 (1994).
215. W. Becker, S. Long, and J. K. McIver, Phys. Rev. A **46**, R5334 (1992).
216. M. Lewenstein, P. Salières, and A. L'Huillier, Phys. Rev. A **52**, 4747 (1995).
217. F. Ehlotzky, Nuovo Cim. **14D**, 517 (1992).
218. P. Salières, A. L'Huillier, and M. Lewenstein, Phys. Rev. Lett. **75**, 3376 (1995).
219. M. Lewenstein, J. Mostowski, and M. Trippenbach, J. Phys. B **18**, L461 (1985).
220. J. Grochmalicki, J. R. Kukliński, and M. Lewenstein, J. Phys. B **19**, 3649 (1986).
221. H. A. Bethe and E. E. Salpeter, *Quantum Mechanics of One and Two Electron Atoms*, (Academic, New York, 1957).
222. A. Heinrich, Diploma Thesis, University of Hannover (2001).
223. M. Drescher et al., Nature **419**, 803 (2002).
224. E. Goulielmakis, et al., Science **305**, 1267 (2004).

Ionization of Small Molecules by Strong Laser Fields

Hiromichi Niikura, V.R. Bhardwaj, F. Légaré, I.V. Litvinyuk, P.W. Dooley, D.M. Rayner, M. Yu Ivanov, P.B. Corkum, and D.M. Villeneuve

1 Introduction

Ionization is fundamental to many technologies. Mass spectrometry relies on ionization, as does femtosecond laser machining. Ionization is the fundamental nonlinearity behind attosecond science – the worldwide effort to generate optical pulses that last only a single atomic unit of time. Molecular ionization and the fate of the molecular fragments (ions and electrons) will be the focus of this review.

Ionization of atoms and molecules in intense, infrared or near-infrared laser fields is fundamentally different from that in low-intensity fields. The latter requires either a photon with sufficient energy to directly ionize or an electronic resonance that aids in the ionization. An example of the latter is resonance-enhanced multiphoton ionization (REMPI). When the laser intensity becomes great enough, the need for electronic resonances is removed. Indeed, the electronic levels are strongly modified by the presence of the intense field, and the idea of resonances is less applicable.

Intense field ionization can be divided into two regimes that we will discuss soon – multiphoton vs tunnel ionization. We will concentrate on the latter regime, since it fits most current high-intensity experiments with titanium:sapphire lasers.

The process of removing electrons from atoms and molecules can be divided into several distinct steps. It starts with the detachment of the electron from the core, a process which is rich in interesting complications. The freed electron can then move under the influence of the laser electric field and can possibly recollide with the core. Recollision leads to well-known phenomena like high harmonic generation that can be used as a source of short-wavelength sub-femtosecond pulses. The motion of the molecular ion in the laser field is another source of study, leading to methods of controlling chemical bonds.

H. Niikura
Steacie Institute for Molecular Sciences, National Research Council of Canada,
100 Sussex Drive, Ottawa K1A 0R6, ON, Canada
e-mail: Hiromichi.Niikura@nrc-cnrc.gc.ca

T. Brabec (ed.), *Strong Field Laser Physics*,
DOI: 10.1007/978-0-387-34755-4_8,

Clearly, many of the things that we are learning about molecules have the potential for application elsewhere, particularly in chemistry. The spectrum of high harmonics from molecules contains information about the electronic orbitals that are ionized and their symmetries. The recolliding electrons, after diffracting from the molecular core, also contain information about the molecular geometry. Both of these effects can be used as probes of molecular structure in pump-probe experiments, with the possibility of femtosecond and even sub-femtosecond time resolution.

2 Experimental Setup

Although strong field molecular ionization is being studied in many laboratories worldwide [1, 2, 3, 4, 5, 6], we will focus on experiments performed at the National Research Council of Canada. That allows us to present a unified experimental section.

A kilohertz Ti:sapphire laser system was used in all the experiments, with a 39 fs pulse duration at 800 nm wavelength and an energy of 800 μJ. The 800 nm pulse could optionally pump an optical parametric amplifier (OPA) that produced tunable near-infrared pulses with a duration of 60 fs. The laser was focused into the vacuum chambers with $f/2$ 50 mm focal length on-axis parabolic mirrors.

Several vacuum chambers were used for experiments. One was a simple time-of-flight mass spectrometer containing molecules at a pressure of 10^{-6} Torr. A uniform electric field was applied and ions were observed through a 1 mm diameter hole in one electrode. The signal was detected with a micro-channel plate detector and recorded with a multichannel scaler. Another chamber had a constant electric field acceleration region and a time- and position-sensitive delay line anode detector. This detector system was able to collect multiple ions per laser shot and to determine their initial three-dimensional velocities.

For experiments in which the ellipticity of the laser polarization was varied, a sequence of optical elements were used to change the ellipticity while maintaining the direction and magnitude of the major axis of the ellipse. The laser beam passed through a rotating half-wave plate, a rotating polarizer and finally an achromatic quarter-wave plate with a fixed vertical optical axis. The fixed quarter-wave plate ensured that the major axis of the ellipse remained vertical. The polarizer before it controlled the magnitude of the minor axis. The half-wave plate was then used to keep the magnitude of the major axis constant. The ellipticity, defined as the ratio of the two electric field components, was less than 0.02 for linear polarization.

For all wavelengths, the intensity was calibrated by measuring the saturation intensity of Xe^+ and comparing it with that calculated by the ADK model. This provides an intensity reference that allows different laboratories, with different lasers and focusing geometries, to compare their actual intensities.

3 The Initial Ionization Process

We first consider ionization of atoms by intense laser fields. We then generalize to molecules with single electrons and then to multielectron systems.

With typical ionization potentials of 12–20 eV, atoms can only be ionized directly by lasers with wavelengths shorter than about 150 nm. For the more typical visible or infrared lasers, ionization by strong laser fields can be divided into two regimes: multiphoton and tunneling. Multiphoton ionization occurs when an electron gains energy by absorbing a number of photons simultaneously. Tunnel ionization occurs when the optical frequency of the field is low enough that the electron has time to tunnel through the potential barrier, as seen in Fig. 1.

One can use a classical analysis to estimate the laser intensity that is required to tunnel ionize an atom, called the "over-the-barrier" threshold, $I_{\mathrm{th}} = KI_{\mathrm{p}}^4/(16Z^2)$, where I_{p} is the ionization potential of the atom and Z is the charge state of the ion that is produced by ionization. In atomic units, $K = 1$, but if I_{p} is in eV and I_{th} is in W/cm^2 then $K = 6.4 \times 10^{10}$. Below this dividing line the electron is bound. Strong field physics still occurs, for example, the Stark shift can be very large [7] – and through this very large Stark shift we can control either internal [8, 9] or external [10, 11, 12, 13, 14] degrees of freedom of a molecule. However, in this review we will restrict our considerations to ionization phenomena – intensities above (or near) I_{th}.

While classical physics can provide an approximate dividing line, ionization is quantum mechanical in nature. Most femtosecond laser experiments are performed in an intensity region where tunnel ionization is important. The parameter that determines if the tunneling approximation is valid is the Keldysh parameter [15], $\gamma = (I_{\mathrm{p}}/2U_{\mathrm{p}})^{1/2}$, where $U_{\mathrm{p}} = e^2E^2/(4m\omega^2)$ is the ponderomotive potential, e and m are the electronic charge and mass, E is the electric field strength at which the atom ionizes and ω is the angular frequency of the laser

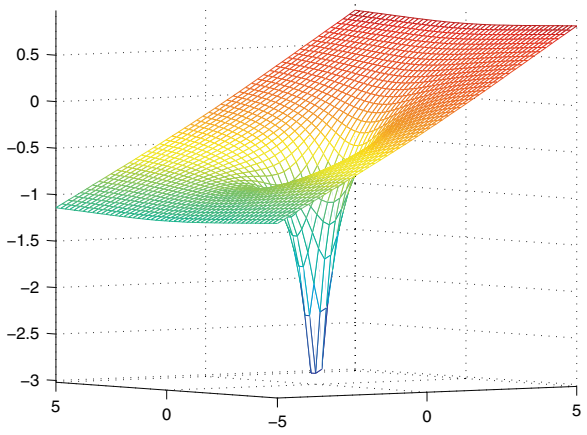

Fig.1 The combined laser field and Coulomb potential of the ion plotted as a function of the distance from the ion, illustrating the barrier suppression responsible for tunnel ionization. The potential is $V(r) = -1/r + Ex$, where E is the instantaneous laser electric field

radiation. If $\gamma < 1$, the tunneling conditions are satisfied [15]. For $\gamma \gg 1$ a multiphoton picture is more appropriate.

A theoretical model was developed by Ammosov, Delone and Krainov, called the ADK model [16], that has been successful in describing tunnel ionization of atoms. It has been further improved in the PPT model [17, 18, 19] and the Yudin–Ivanov model [20]. All these models predict a steeply increasing ion yield as the laser intensity approaches I_{th}.

Since molecules are usually larger than atoms and the atomic tunnel ionization calculations assume a short-range potential, it has been thought up to now that molecules will be easier to ionize than atoms with the same ionization potential. In reality, neutral molecules at their equilibrium internuclear separation tend to be more difficult to ionize than equivalent atoms [21, 22, 23, 24], sometimes much more difficult [22].

The starting point for understanding ionization in molecules is to compare their ionization with atoms. Early models simply substituted molecular ionization potentials in atomic tunneling models such as ADK [16]. It was assumed that the molecule's relatively low ionization potentials and lower-lying excited states would raise their ionization rates beyond tunneling rates. Even an early adaptation of the atomic tunneling model to molecules, where the extended range of the molecular potential was taken into account, predicted easier ionization [25, 26].

The first indication that this was not the case came from diatomic molecules, where results on HCl [21] and especially O_2 [23] began to cast these predictions in doubt. The O_2 results are important because O_2 has the same I_p as Xe and allows direct experimental comparison.

The question is: Are these isolated special cases or is the behavior general and does it extend to larger molecules with low ionization potentials? Direct comparison with rare gas of the same ionization potential is not possible in general, so a consistent approach for comparing the ionization of molecules and atoms with diverse ionization potentials is required.

We have developed an experimental approach that allows I_{sat} to be defined in a manner that can be directly connected to theory and that can be applied consistently between different laboratories. We refer the reader to [22, 27] for details. Figure 2 shows I_{sat} plotted as a function of ionization potential. The solid line is the ionization potential dependence of I_{sat} calculated using ADK tunneling theory [16]. The inset shows the results on an expanded scale where the rare gas atoms He and Ne can be included. There is good agreement with the ADK results for He, Ne and Xe, validating our experimental approach. For molecules the key observation is that tunneling theory does not provide an upper bound for the saturation intensity. All the organic molecules studied show I_{sat} is greater than that predicted by ADK theory, some by as much as a factor of 4.

As yet there is no clear understanding of the general resistance of molecules to strong field ionization. It seems that there might be a combination of causes. Based largely on the results on O_2 and the observation that N_2 does not show

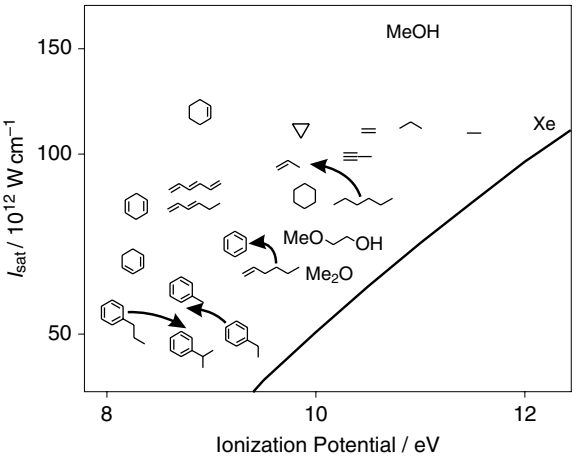

Fig. 2 One might think that, because molecules are more spatially extended than atoms, their electrons can pick up more energy from a laser field, and hence that molecules will be easier to ionize than an equivalent atom. This is not true. Most molecules are more difficult to ionize than an atom that has the same ionization potential. In some cases, the orbital symmetry of the highest orbital makes it very difficult to ionize. This graph shows the appearance intensity for ionization of a number of organic molecules, plotted against their ionization potential. The curve shows the appearance intensity predicted by the ADK model for that ionization potential

suppression, it has been proposed [28] that interference in the exit channel suppresses ionization in species with anti-symmetrical electronic ground states. We have observed such quantum interference by studying the elliptical dependence of recollision processes in benzene [29]. However, this mechanism for ionization suppression is by no means established. The theory predicts suppression in other molecules with anti-symmetric ground states such as F_2. Although N_2 and F_2 have similar ionization potentials, due to differences in molecular symmetry, theory predicts ionization of F_2 to be suppressed by two orders of magnitude relative to N_2. Contrary to this, very small variation of the measured ratio of N_2^+/F_2^+ with the laser intensity (Fig. 3) indicates no suppression of ionization of F_2 relative to N_2. A similar study comes to the same conclusion for S_2 [30]. Also questioning the role of interference is the fact that we have been unable to observe the expected ellipticity dependence in the recollision-driven dissociation of O_2.

It is intuitively obvious that ionization probability should depend on the orientation of the molecule with respect to the laser polarization axis. However, until recently all the experiments were performed on samples with isotropic angular distributions, and therefore reported spherically averaged single ionization rates. Using short laser pulses to dynamically align molecules in the gas phase, we for the first time measured the angular dependence of the strong field single ionization probability for N_2. We found that a nitrogen molecule aligned

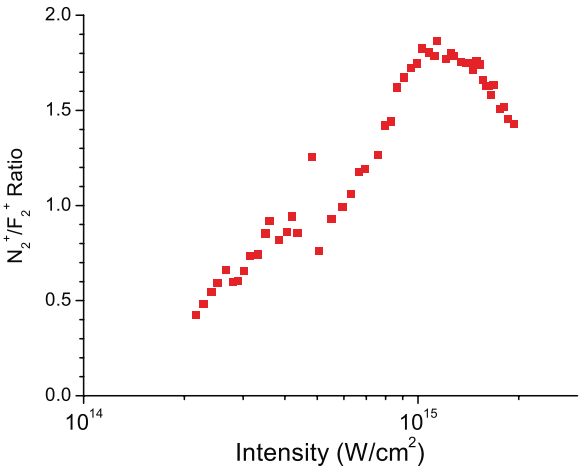

Fig. 3 Measurement of N_2^+/F_2^+ ratio as a function of laser intensity for 800 nm light. N_2 and F_2 have nearly identical ionization potentials, 15.58 and 15.69 eV, respectively, and have singlet electronic ground states. F_2 has an anti-symmetric configuration compared to the symmetric configuration of N_2. The interference model predicts the ionization of F_2 to be suppressed by two orders of magnitude relative to N_2. However, the ratio shown above is very small, varying from 0.4 to 1.8 with intensity, suggesting no suppression of ionization in F_2

parallel to an electric field is about 4 times more likely to be ionized by a 40 fs, 3×10^{14}W/cm^2 pulse than the one aligned perpendicular to the field [31]. This result is in good agreement with predictions of the theory extending ADK to small molecules [32]. This theory also predicts that for O_2, due to the symmetry of its outermost orbital, the angular dependence of ionization probability exhibits a maximum at 45° orientation. That prediction is yet to be tested experimentally.

The treatments applied to diatomic molecules largely ignore one of the most important differences between atoms and molecules, especially for larger molecules. This is the multielectron nature of the problem. Single-active-electron models can treat rare gas atoms successfully because their excited states are well above their ionization potentials. This is not generally the case in molecules.

In the quasi-static tunneling regime, where the laser frequency is well below any molecular resonance, multielectron effects can be most simply addressed through the polarizability of the molecule. In a strong ionizing field, screening of the ion core by the induced dipole effectively raises the ionization barrier, resulting in suppression of tunnel ionization [8]. A simple modeling, using several electrons in a box [33], supports this qualitative picture.

Another significant difference between atoms and molecules is the presence of nuclear coordinates in the latter. Those degrees of freedom can couple dynamically to the electric field, resulting in alignment and deformations on timescales comparable to the pulse duration and affecting the observed

ionization rates. For example, it is clear that light molecules like F_2, N_2 and O_2 can undergo significant alignment before being ionized by pulses of 40 fs or longer (and H_2/D_2 molecules even by much shorter pulses). For complete understanding of molecular ionization, one will have to account for those dynamic effects as well.

In summary, for small molecules in the adiabatic limit [34], our best understanding is that the basic ideas of tunnel ionization are valid, but they must be adapted to a realistic electronic wave function and the knowledge that tunneling occurs through a potential barrier that includes the influence of all of the molecule's electrons. Thus, H_2 will be quite atomic-like while C_{60} is quite different from an atom.

4 The Characteristics of the Newly Formed Electron

The act of ionization forms not only an ion, but also an electron. Since the electron can only be launched during the fraction of each cycle when the field is strong, electron wave packets are formed [35]. For small molecules and low charge states, the laser field dominates the motion of the electron after detachment. It is the most important force determining the motion of the wave packet. After birth, the electron is accelerated away from the parent ion but, as the field reverses, the electron can be driven back [36]. Depending on the electron's phase of birth in the laser field the electron can recollide with its parent, exciting the second electron or knocking it free. This process is known as non-sequential double ionization [36, 37].

Although the classical-like motion of the electron in the strong field is most important, tunneling determines some of the characteristics of the electron wave packet and studying these characteristics gives insight into tunnel ionization. In particular, once the electron passes through the tunneling barrier, its motion perpendicular to the laser field is not influenced by the field [38]. The electron velocity perpendicular to the laser field is determined by the uncertainty in the position and velocity at the time of tunneling through the barrier. This lateral motion is readily observed.

This section concentrates on experiments to measure the lateral momentum. We use double ionization and fragmentation as a diagnostic. For atoms, it is known theoretically [39] and experimentally [38] that the lateral velocity distribution is Gaussian. We show that it can be qualitatively different in molecules. For C_6H_6, the distribution of lateral velocities has a local minimum at zero lateral velocity and a global maximum at ~ 3 Å/fs [29]. At still higher lateral velocities, the distribution function falls rapidly to zero just as in an atom. We also show that the lateral velocity spread is slightly different for H_2 molecule aligned parallel and perpendicular [35].

We now know, in a general way, the probability of the electron emerging from an atom or molecule as a function of the laser field strength. We next

concentrate on the characteristics of the newly emerging electron. As it departs the ion, the electron, which is confined laterally by the structure of the tunnel region (Fig. 1), acquires a velocity $v_\perp$ in the direction perpendicular to the laser field, in addition to a parallel velocity $v_|$. The transverse velocity is a characteristic signature of the intrinsic quantum mechanical nature of strong field ionization. It determines the subsequent expansion of the electron wave packet in the lateral direction [36, 38] as long as the electron is distant from the ion. For atoms, the initial transverse velocity has a Gaussian distribution with 1/e width given by $v_\perp = (E/\sqrt{2I_p})^{1/2}$ (in atomic units), where I_p is the ionization potential of the atom and E is the peak electric field amplitude [39].

After the electron is detached, it moves in the laser field as a free electron [40]. Its oscillatory motion can bring the electron back to the ion, where it recollides with its parent [36]. During this free evolution, the field controls the electron motion. In elliptically polarized light, the electron is displaced from the ion in the direction of the minor component of the electric field (Fig. 4). This gives us the experimental means to measure the transverse velocity distribution [36, 38].

As the laser ellipticity, defined as the ratio of the electric field components ($\varepsilon = E_y/E_x$) increases, the transverse displacement increases. Ultimately the transverse displacement of the electron wave packet exceeds the wave packet radius and the electron never returns to the ion. Above this ellipticity, any phenomena caused by the electron–ion recollision are no longer observed. We use non-sequential ionization to measure the diameter of the electron wave packet at the time of recollision, and hence $v_\perp$.

In atoms, the probability of non-sequential excitation and double ionization vs polarization ellipticity has a Gaussian distribution and is always a maximum for linear polarization ($\epsilon = 0$) and falls off rapidly with increasing ellipticity of the laser polarization. The width of the Gaussian distribution is governed by the ionization potential and the laser intensity. For a laser intensity of 10^{15} W/cm^2 at 800 nm, double ionization of Ne has a 1/e width of $\varepsilon \sim 0.13$, which

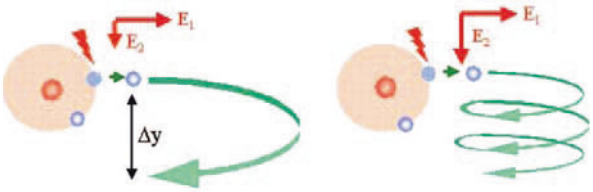

Fig. 4 Illustration of the trajectory of the electron in elliptically polarized light. The *left panel* shows how a small amount of elliptical polarization causes the just-detached electron to move laterally, so that it is less likely to recollide with the parent ion. The *right panel* illustrates circularly polarized light, whereby the electron trajectory never returns to the parent ion. By means of controlling the ellipticity of the laser light, one can control the electron trajectory or even turn off the recollision process. This technique is important in clarifying the shape of the electron wave packet and its influence upon recollision

corresponds to a transverse displacement of 12 Å [38]. Since the effective collision cross-section is small (~ 1 Å^2), the transverse displacement allows us to measure the spatial distribution of the wave packet when it returns to the ion in 1.77 fs. From this distribution we determine the transverse velocity at the time of ionization to be 7 fs/Å, in close agreement with the calculated value of 7.5 fs/Å.

Recollision must certainly occur in molecules. However, in addition to electronic excitation and double ionization, in molecules the nuclear degrees of freedom can be excited, resulting in fragmentation of the molecule. The dependence of double ionization (or recollision-induced fragmentation) on the ellipticity of the laser polarization identifies non-sequential double ionization in molecules. We review measurements of the lateral spread of the electron wave packet in H_2 [35] and C_6H_6 [29]. We show that transverse velocity spread depends slightly on the molecular alignment with respect to the laser polarization in H_2 [35]. In C_6H_6 [29], we show that both fragmentation and double ionization have identical ellipticity dependence. At intensities of 10^{14} W/cm^2, for 1.4 μm light illuminating C_6H_6 we show that all fragmentation is due to recollision. We begin with H_2. As a two-electron molecule it is similar to helium, but has a nuclear degree of freedom. We study the sensitivity of tunnel ionization to the direction of the internuclear axis by observing the expansion of the electron wave packet.

We infer the alignment direction of the molecule via inelastic scattering. Ionization results in a vibrational wave packet moving on the field-modified Σ_g potential energy surface until electron recollision occurs. During the recollision, the electron can either ionize the H_2^+ ion or inelastically scatter, producing excited H_2^+ leading to dissociation. In either case, high kinetic energy protons are produced. Their direction labels the molecular alignment. By selecting only those fragments that travel in a particular direction relative to the laser polarization axis, we can effectively have an ensemble of aligned molecules.

Figure 5 shows the ellipticity dependence of the recollision yield. At each ellipticity, the signal count is integrated in the kinetic energy range 4–9 eV. All high kinetic energy fragments have the same ellipticity dependence. The three curves in the figure are for argon and for H_2 molecules aligned parallel and perpendicular to the laser polarization. Argon, with almost the same ionization potential as hydrogen, is used as a reference for which the transverse velocity can be accurately calculated. For argon (open squares in Fig. 5) the measured transverse velocity spread is ~ 5.6 Å/fs, in excellent agreement with 5.4 Å/fs predicted by the atomic tunneling theory.

The ellipticity dependence is slightly different for parallel and perpendicular orientations of the H_2 molecule. The measured transverse velocity spread is 4.2 Å/fs and 5.0 Å/fs for molecules aligned perpendicular and parallel to the laser field, respectively. It is interesting to note that although Ar has almost the same ionization potential as H_2, the transverse velocity spread of Ar is larger than that for either orientations of H_2. There are no theoretical predictions of the electron wave packet spread in molecules; however, qualitatively we expect

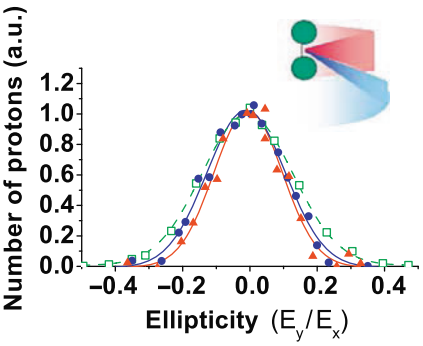

Fig. 5 The lateral spreading of the electron wave packet after ionization of H_2 can be determined by varying the ellipticity of the laser light. Here we show the number of H^+ ions whose kinetic energy is greater than 4 eV. This signal is due to excitation to the H_2^+ Σ_u surface after an inelastic scattering event from the recolliding electron. As the ellipticity increases, the electron wave packet is pushed sideways more and more, mapping out the lateral shape of the wave packet. The ellipticity dependence is shown for H_2 parallel (*circles*) and perpendicular (*triangles*) to the laser polarization direction, and also for argon (*squares*), an atom with almost the same ionization potential as hydrogen. The narrowest distribution is from the perpendicular H_2

a smaller wave packet spread from the broader tunnel that characterizes a perpendicular molecule.

We now concentrate on C_6H_6. With 12 atoms, benzene might be expected to be quite different from an atom. In fact there are differences and similarities. The overall width of the transverse velocity distribution is similar to that for atoms. However, interference between different electron trajectories during the tunneling process results in a structure in the polarization dependence of ion yields that is not observed for rare gas atoms. Also, fragmentation in C_6H_6 can be switched on or off with small changes in the ellipticity of the laser polarization.

Figure 6 shows the ellipticity dependence of the $C_6H_6^{2+}$ signal and the sum of the most important fragments. Individually every fragment shows the same ellipticity dependence as the double ionization. We observe $C_4H_n^+$ ($n = 2, 3, 4$) and $C_5H_n^+$ ($n = 2, 3$) fragmentation channels with $C_4H_4^+$ as the most dominant channel. Also shown for comparison purposes is the ellipticity dependence of Xe^{2+} obtained at 10^{14} W/cm^2. All the measurements were made at laser wavelength of 1.4 μm instead of 800 nm. At 800 nm, for molecules with relatively low values of I_p (< 10 eV), the ionization process is complex and the recollision energy is low.

The solid curve in Fig. 6 shows the best-fit Gaussian distribution to the experimental data of Xe. The half-width of the Xe distribution is consistent with the calculated values from the tunneling model (a width of ~ 0.16 translates to a measured transverse velocity distribution of 6.4 Å/fs while the calculated distribution is 7 Å/fs). For C_6H_6, a Gaussian fit to the measured data (dotted

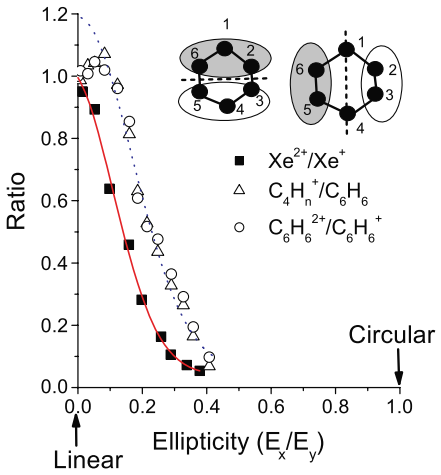

Fig. 6 Ellipticity dependence of benzene (C_6H_6) and xenon. The xenon signal is the ratio of doubly to singly charged xenon ions, a measure of the probability of recollision. The benzene signal is the ratio of a fragment of benzene, or doubly charged benzene, to the parent ion. Again, both signals are indicative of recollision. Benzene has a wider ellipticity dependence compared with a similar atom, xenon. This suggests that the lateral spreading of the electron wave packet is greater for benzene. Furthermore, there is a dip for $\varepsilon = 0$, indicative of the lack of electrons with $v_\perp = 0$

curve) deviates significantly for $\varepsilon < 0.1$. However, its width of $\varepsilon \sim 0.25$ corresponds to a measured transverse velocity of 5.15 Å/fs. An atom with the same ionization potential will have a transverse spread of 5 Å/fs. Both double ionization and fragmentation have the same ellipticity dependence. So, if double ionization is due to recollision, then fragmentation must also be due to recollision. At the intensity of this measurement ($\sim 10^{14}$W/cm^2) and at all intensities less than this, there is no fragmentation without recollision.

The transverse distribution is estimated by assuming a small cross-section and ignoring Coulomb focusing [41]. In C_6H_6, both non-sequential double ionization and fragmentation are maximum not at an ellipticity of $\varepsilon = 0$ (like in atoms) but at $\varepsilon \sim 0.1$. We show that this effect is due to the destructive interference between the two components of the wave function in the highest occupied molecular orbital.

The highest occupied molecular orbitals in C_6H_6 are doubly degenerate π-orbitals. They both have two nodal planes, one is the plane of the molecule and the other is perpendicular to this plane. A representation of the two degenerate highest occupied molecular orbitals is shown in Fig. 7. Dashed lines indicate nodal planes perpendicular to the molecular plane.

For simplicity, consider C_6H_6 with its plane perpendicular to the laser polarization. When viewed in three dimensions, a saddle-like structure of the potential surface is created by the ionic and laser fields. The saddle point is at a

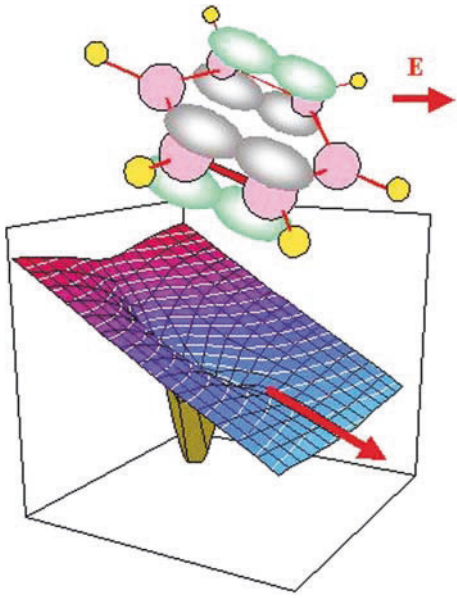

Fig. 7 Illustration of the highest occupied molecular orbital of benzene. Positive and negative lobes are shown in *different colors* to illustrate the symmetry of the wave function. Because of the wave function symmetry, no electrons are detached with zero perpendicular velocity. This leads to a hole in the ellipticity dependence, as seen in the previous figure

distance of a few Angstroms from the ionic core. For tunnel ionization the electron must pass through this restricted region of the saddle. The symmetry of the wave function should be preserved in the saddle region. Electrons from either side of the node travel equal distances to the center of the saddle region, however, with opposite phases. Therefore they interfere destructively.

The momentum distribution of the electrons $\Phi(p)$ in the transverse dimensions is given by the Fourier transform of the spatial wave function $\Psi(r)$ in the saddle region, $\Phi(p) = \int \Psi(r) e^{-ipr} dr$. For an asymmetric wave function, $\Phi(0) = 0$. Since there are no electrons with zero transverse momentum, none return to the ion in linearly polarized light. This can be understood in terms of destructive interference of the components of the electron wave function after departing the saddle region. Due to destructive interference, there are never any electrons on-axis, so there must be a minimum in the non-sequential double ionization/fragmentation, as is observed.

In elliptically polarized light, the transverse field component compensates for the initial momentum, forcing some of the off-axis electrons to return to the ionic core, increasing the double ionization/fragmentation probability. However, in near-circularly polarized light, the transverse field imparts so much momentum that the electrons far overshoot the ionic core and the probability of double ionization/fragmentation drops to zero.

We have described what we would expect for a C_6H_6 molecule aligned perpendicular to the laser polarization. However, our experiments are performed with randomly oriented molecules. Let us now consider two other

orientations. (1) If the laser field is in the molecular plane of C_6H_6 but with polarization parallel to the nodal plane (dashed line in Fig. 7), the argument presented above applies. Therefore we expect a minimum in double ionization/fragmentation probability for linearly polarized light. (2) Since the molecular plane is itself a nodal plane, we again expect a minimum for linearly polarized light, when the laser polarization is perpendicular to the nodal plane (dashed line in Fig. 7).

Any other orientations result in incomplete interference. So, when one considers an ensemble of randomly oriented C_6H_6 molecules, interference results in a local minimum of non-sequential double ionization/fragmentation signal for linear polarization as observed in Fig. 6.

As the molecule becomes still larger, other atomic properties disappear. Although we do not show it here, in C_{60} the electron preserves a significant fraction of its Fermi velocity when it departs from the molecule [8], giving us a "look inside" a large molecule in a strong laser field.

5 The Fate of the Ion: Bond Softening

So far, we have discussed ionization and the characteristics of the departing electron. Now we have two fragments to follow, the electron and the ion. First we concentrate on the molecular ion. Compared to atoms, molecular vibrations and rotations add richness (and another level of complexity) to the interaction of molecules with strong fields. A strong external field couples the electronic (ionization and excitation) and nuclear (rotation, vibration and dissociation) motions. A complex hierarchy of timescales, including response times for electronic and nuclear motion, field oscillation period and pulse envelope rise time, determines the dynamics of such a system.

Many features of molecules interacting with strong laser fields can be illustrated using the example of the one-electron molecule, the hydrogen ion. Despite its apparent simplicity, H_2^+ exhibits most of the interesting strong field molecular physics seen in more complex systems. At the same time, it possesses a single vibrational coordinate (internuclear separation R) and it is free of electron–electron interaction. It is also helpful that just a pair of electronic states is sufficient to account for its behavior in strong fields.

The Born–Oppenheimer approximation allows the electronic and nuclear degrees of freedom to be separated. A molecule can be described by a set of potential energy surfaces, with electronic energy levels and wave functions parametrically depending on the internuclear separation (see Fig. 8(a)). Since the free-molecule Hamiltonian for H_2^+ possesses inversion symmetry, all the electronic eigenstates are either symmetric (g-states) or anti-symmetric (u-states) with respect to inversion. The two relevant electronic states (attractive $1s\sigma_g$ and repulsive $2p\sigma_u$) closely correspond to symmetric and anti-symmetric linear combinations of the 1 s and 2p orbitals of atomic hydrogen.

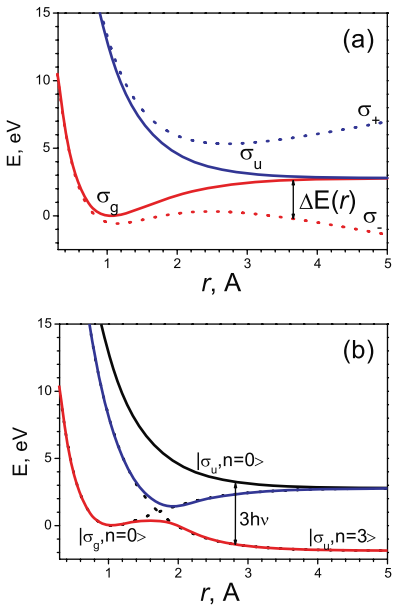

Fig. 8 This figure shows a few of the potential energy curves of H_2, both field-free and under the influence of an intense laser field. There are two states shown, the ground state σ_g and the first excited state σ_u. In the presence of an electric field, these two states are coupled, as shown by the *dotted lines*. In (**a**), the low-frequency, quasi-static model is used, so that bond softening occurs with the σ_g state, while bond hardening occurs with the σ_u state. In (**b**) the Floquet picture is shown. Here the σ_u surface is dressed down by three photons, and an avoided crossing is formed. In both cases, the laser-dressed state is a superposition of the σ_g and σ_u states, and the electrons will be polarized by the applied field. The induced polarization lowers the energy of the system, and so the molecule will try to align with the applied laser polarization

An external electric field breaks the inversion symmetry and modifies electronic energies (by introducing Stark shifts) as well as electronic eigenstates (by mixing *g*- and *u*- states). For molecules aligned along the field, the resulting adiabatic electronic states acquire significant dipole moment (see Fig. 8(b)). The field polarizes the molecule, shifting the electron density towards one of the nuclei. Such polarization disrupts electron sharing and weakens the chemical bond. For a constant field, the induced dipole moment increases with internuclear separation, as does the Stark shift. The lowest potential energy surface becomes repulsive for large *R*. For sufficiently strong fields, the local potential minimum cannot hold any bound vibrational states, and the molecule dissociates. Classically this means that the polarizability of the molecule in a strong field increases with internuclear distance, and that dissociation minimizes the total energy of the system. Now known as bond softening, it was observed in static fields for H_2^+ many decades ago and in laser fields about a decade ago [21, 42].

In the case of a time-periodic electric field, the Floquet picture presents a framework for understanding molecule–field interactions. In the Floquet picture, upon an adiabatic turn-on of an oscillating electric field, each eigenstate of a free molecule evolves into a corresponding eigenstate of the time-periodic Hamiltonian (field-dressed state). A field-dressed state describes a common state of molecule and electric field. Upon quantization of the field, the field-dressed state can be represented by a coherent superposition of Floquet states. Floquet states are separated by a quasi-energy equal to the photon energy, with each state corresponding to a different number of photons in the field. A manifold of Floquet states (Floquet ladder) is formed around each state of a field-free molecule. The Floquet states possess the same symmetry (g or u) as a corresponding field-free state. In the Floquet representation the time evolution of the system is seen as transitions between the Floquet states while absorbing and emitting photons. Coupling between the electric field and nuclear motion causes avoided crossings of potential energy surfaces of g and u Floquet states separated by an odd number of photons (parity conservation forbids two-photon transitions between g and u states). The coupling depends on the orientation of the molecule and intensity of the field. At sufficiently high intensity for molecules aligned along the field, the potential barrier becomes suppressed and the molecule dissociates into $H_2^+ \rightarrow H + H^+$ channel (see Fig. 8(b)). This process is usually referred to as bond softening (BS).

Bond softening was predicted theoretically for Ar_2^+ ions by Bandrauk and Sink in 1981 [43] and first observed experimentally in H_2^+ by Bucksbaum and co-workers in 1990 [42]. The kinetic energy of the BS fragments is low. The fragments are emitted preferentially along the direction parallel to electric field.

Bond softening can be controlled by modulated laser pulses [44]. A laser pulse composed of two wavelengths generated by an optical parametric amplifier is modulated at the difference frequency. If the molecule is ionized at one of the amplitude peaks, the vibrational wave packet may reach the outer turning point when the laser intensity is either high (another peak) or low (a node). If the intensity is low, the wave packet is not able to dissociate. On the other hand, if the intensity is high, the potential energy surface is been pulled down by the laser field, and dissociation can occur. By changing the modulation period, it was shown [44] that bond-softening dissociation could be either turned off or on.

6 The Fate of the Ion: Enhanced Ionization

The difficulty of ionizing neutral molecules relative to atoms is in sharp contrast with stretched ions [3, 45, 46, 47, 48]. As the molecule dissociates, the ionization rate of an ion increases until it reaches a maximum at a critical distance. This distance is approximately the distance where molecular bonds break. At larger distances, the rate decreases again. This general process is known as enhanced

ionization. A multielectron molecule exposed to a sufficiently long pulse will explosively ionize at or near the critical distance [47].

It may seem strange to a reader that, although we are dealing with ultra-short pulses, we have not discussed dynamics. There are many important dynamics issues and most are beyond the scope of this review. An early example of the new opportunities that molecules bring to strong field ionization is seen in experimental studies of enhanced ionization [46]. In this experiment, a vibrational wave packet was launched in I_2^+ with a pump pulse. A delayed probe pulse can catch the dissociating molecule at different internuclear separations. Varying the pump-probe delay allows the ionization rate to be probed as a function of the internuclear separation.

The coupling of bound states causes bond softening. This coupling also influences ionization. If ionization occurs in H_2^+, it produces a pair of protons repelling each other by a strong Coulomb force. The kinetic energy of the protons would equal the potential energy of the Coulomb repulsion, $U = 1/(4\pi\epsilon_0 R)$ (plus the small kinetic energy gained in bond softening), reflecting the internuclear distance at the moment of ionization.

Experimental kinetic energy distributions of protons measured for high laser intensities ($>4 \times 10^{14}$ W/cm^2) [49, 50], are dominated by fragments with energies around 3 eV, as shown in Fig. 9. The experimental kinetic energy distributions indicate that H_2^+ is ionized at large internuclear distances ($R>5$ atomic units), exceeding the equilibrium bond length ($R = 2$ au) by more than a factor of 2. The angular distribution of the fragments is strongly directional along the

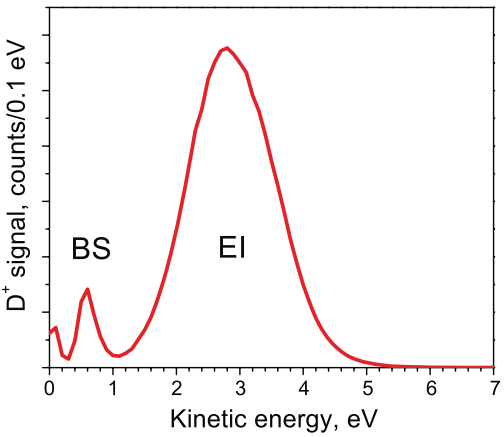

Fig. 9 An experimental spectrum is shown of the kinetic energy release (per D^+ fragment) from deuterium in an intense 800 nm laser field. The peak intensity was 5×10^{14} W/cm^2, with a pulse duration of 50 fs. The laser was circularly polarized so as to turn off electron recollision. The large peak labeled *EI* at 3 eV is due to enhanced ionization (also called charge resonant enhanced ionization, CREI). The smaller peak near 0.5 eV, labeled *BS*, is due to bond-softening dissociation. Additional peaks due to fast sequential double ionization would appear above 5 eV

laser polarization vector. Similar observations were also made for other diatomic and triatomic molecules [51, 52, 53, 54].

Numerical solution of the time-dependent Schrödinger equation for H_2^+ in strong field [45, 48] confirms that the ionization rate for molecules aligned parallel to the field increases by orders of magnitude when the internuclear distance is increased from the equilibrium value to the critical length $R_c = 6$ au. This phenomenon is known as enhanced ionization.

As with bond softening, enhanced ionization in H_2^+ arises from the coupling of the 1 sσ_g and 2pσ_u states. A strong field mixes the two states, resulting in two field-modified states σ_+ and σ_-. These electronic states correspond to the electron being localized near the left or right proton. As the laser field oscillates, these states appear as potential wells that move up and down. The electron usually moves from side to side in phase with the laser field so as to stay in the lower well. As the internuclear separation increases, the oscillating field can effectively trap significant electron population in the upper potential well. In an alternative view, this can be seen as a non-adiabatic transition between the 1 sσ_g and 2pσ_u states. The electron trapped in the σ_+ state can reach the continuum by tunneling through the internal potential barrier. At a critical internuclear distance, that potential barrier is lowered by the adjacent nucleus and the ionization rate increases, as seen in Fig. 10. The ionization rate reaches its maximum for relatively large bond lengths, 2–3 times the equilibrium distance.

Figure 9 shows the kinetic energy spectrum for deuterons resulting from ionization of D_2 by a circularly polarized 800 nm, 50 fs laser pulse with peak

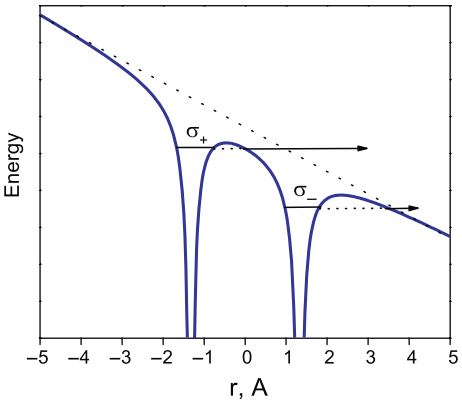

Fig. 10 This sketch shows how enhanced ionization works. The potential energy surface seen by an electron is influenced by the two ions plus the applied electric field. The electron is in a superposition of the two electronic states, $\sigma_+ = \sigma_g + \sigma_u$ and $\sigma_- = \sigma_g - \sigma_u$. As the laser field changes direction, the electron will try to follow by staying in the lower potential well. Sometimes it will not respond quickly enough and will find itself trapped in the upper well. When that happens, it has a higher probability of tunneling through the barrier that separates the two wells and will then escape to the continuum. This enhanced ionization occurs preferentially at a particular internuclear separation

intensity of 5×10^{14} W/cm^2. The peaks corresponding to bond softening (0.6 eV) and enhanced ionization (2.8 eV) can be easily identified. To experience enhanced ionization, a molecule must first reach the critical distance by undergoing bond softening. Only those dissociating molecules, which fail to ionize at the critical distance will appear as low-energy bond-softened fragments. Strong field ionization and dissociation are dynamically coupled, so that the exact evolution of the system and relative amplitudes of its various channels depend strongly on intensity and temporal characteristics of the laser pulse.

Current experimental data and numerical simulations suggest the following sequence of events taking place in a hydrogen (deuterium) molecule interacting with a 5×10^{14} W/cm^2, 800 nm, 50 fs laser pulse. First, the molecule is field ionized, and the resulting molecular ion starts to undergo bond-softening dissociation. When its bond length reaches the critical value, enhanced ionization takes place, followed by Coulomb explosion. As one lowers the laser intensity, enhanced ionization becomes less and less probable until at intensities below 10^{14} W/cm^2 only the bond-softening peak remains.

In molecules with many electrons, the dynamics is more complex, with many more electronic states being involved. However, just like in H_2^+, initial ionization by the field triggers dissociation of the ion. When a dissociating ion approaches the critical geometry, enhanced ionization turns on, and highly charged ions are produced through sequential multielectron ionization.

7 The Fate of the Electron: Measuring the Dynamics of Double Ionization

In this section, we discuss the formation and evolution of an electron wave packet. We can indirectly infer the *few-cycle dynamics* of the electron wave packet [55] using few cycle pulses interacting with atoms. However, we can directly measure its *sub-cycle dynamics* using non-sequential *molecular* ionization [35].

Ionization of a molecule simultaneously forms two wave packets. One is the electron wave packet described above. The other is a nuclear vibrational wave packet. We introduced the concept of a molecular clock and showed how nuclear motion in H_2^+ can be used to time-resolve [35] the electron wave packet formed by ionization of H_2. Alternatively, the electron can be used to measure nuclear motion [56].

Now we proceed to characterize the electron wave packet as it returns to its parent ion more fully – its time structure and magnitude. In so doing we measure the dynamics of non-sequential double ionization. We begin by calculating the electron's recollision probability as a function of time.

We treat the motion of electron wave packet semi-classically [35, 55, 57]. We follow many electron trajectories and count the number of trajectories which can go through the small collision area, ~ 1 Å^2 using a hard sphere model. Each

trajectory is weighted by the ADK ionization probability as a function of optical phase, and given a distribution of initial velocities. Since we will concentrate on H_2, we use the lateral velocity of the electron wave packet measured above as the initial condition for the calculation.

The magnitude of the electron recollision probability is shown in Fig. 11. Although a single electron, we plot it as a current density – the current density that gives an equivalent probability of inelastic scattering. The ion sees an electron current rising to $\sim 10^{11}$amp/cm^2 in a fraction of a fs. The electron probability passes the ion in a spike lasting ~ 1 femtosecond. However, as the field reverses, the electron can wash back giving a second (and subsequent) surge as seen in Fig. 11. The first current peak has a duration of about 1 fs and contains $\sim 50\%$ of the density.

We chose to use the parameters for H_2 because it gives us a method to confirm the current density in Fig. 11. The basic idea behind the experiment is to use H_2^+ motion as a clock to measure the time structure of the returning electron wave packet. Tunnel ionization of H_2 forms two correlated wave packets simultaneously at a peak of the laser cycle: one is the electron and the other is the vibrational wave packet on its ionic surface. Until the electron returns to the parent ion, the vibrational wavepacket moves on the potential energy surface of H_2^+ (X Σ_g). The half vibrational period of H_2^+ is $\sim$10 fs, which is somewhat longer than the timescale of electron's return. We use this well-known vibrational motion to provide a "molecular clock" against which we can time-resolve the current pulse with femtosecond resolution.

To read the molecular clock we use the inelastic scattering during the electron–ion recollision. At a time of recollision the vibrational wave packet

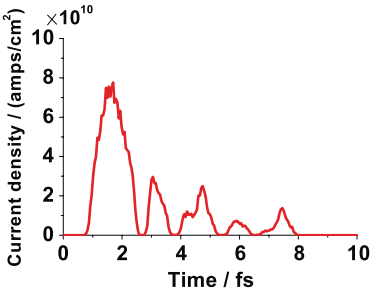

Fig. 11 The electron that is detached from a parent molecule is accelerated in the laser field and can return to the parent ion with considerable kinetic energy. The electron can (**a**) elastically scatter (**b**) inelastically scatter or (**c**) recombine and give off an xuv photon. Although this is only a single electron, it is instructive to estimate the equivalent current density. This figure shows the number of electrons whose trajectories pass inside the cross-sectional area for inelastic scattering from the $H_2^+\Sigma_g$ to $H_2^+\Sigma_u$ potential surface. This is then divided by the time of the encounter to determine the current density. This enormous current is significantly greater than what can be achieved with conventional electron guns, because the "photocathode" is the molecule itself

on H_2^+ (X Σ_g) is promoted to the Σ_u state, leading to the dissociative fragments of H^+. The kinetic energy of H^+ indicates the internuclear separation of H_2^+ when the electron collides with the parent ion. We measure the kinetic energy distribution of H^+ dissociating from H_2^+ followed by ionization only due to electron recollision. To select this recollision channel alone, we use linear and elliptically polarized laser light and take the differences between them in the kinetic energy distribution of H^+.

We select the laser field perpendicular to the molecular axis in order to avoid bond-softening or enhanced ionization processes. This configuration ensures us that there is no laser-induced coupling between Σ_g and Σ_u, allowing us to assess the motion of vibrational wave packet as a reliable time clock.

Figure 12 is a plot of the observed kinetic energy distribution of H^+. The dotted line is the calculated kinetic energy distribution associated with the contribution of the first electron's return in Fig. 11. To obtain the curves we calculate the motion of the vibrational wave packet quantum mechanically on the field-free potential energy surface of H_2^+(X Σ_g) and promote it to Σ_u surface according to the electron recollision probability shown in Fig. 5. The solid line is the incoherent sum of the kinetic energy distribution of H^+ produced by all five electron micro-bunches. The agreement between the observed and calculated confirms the time-dependent electron current density in Fig. 11.

Although we have concentrated on clarifying ionization, the electron is a valuable tool for probing molecules. It is controlled by the laser field, so it can be experimentally "steered". The recollision electron, slaved to the field, is the convenient, short-wavelength probe that has been lacking in laser physics until now.

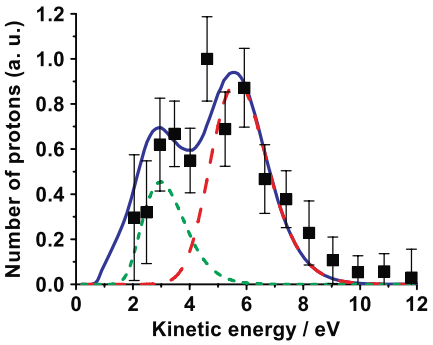

Fig. 12 Observed (*square*) and calculated (*solid curve*) kinetic energy distribution of H^+ fragments caused by electron recollision. H_2 was aligned perpendicular to the laser polarization. When H_2 is ionized, it goes to the H_2^+ Σ_g state. When the electron recollides a fraction of an optical cycle later, it can collisionally excite to the H_2^+ Σ_u surface, which then dissociates into H and H^+. The motion on the H_2^+ Σ_g surface after ionization and before recollision occurs at a well-known speed and forms the "molecular clock". The agreement confirms the time structure of electron current density. The *dashed lines* show the calculated contribution from the first electron bunch (*long dash*) and third electron micro-bunch (*short dash*)

8 Conclusion

We have seen that high-intensity (but often very low energy) femtosecond pulses readily ionize molecules. Ionization is behind many technologies – laser machining and mass spectrometry are two examples. A better understanding of molecular ionization will be helpful as lasers play an increasing role in these applications.

When ionization is driven to extremes, many electrons can be extracted from a molecule in just a few femtoseconds. If done fast enough, even the lightest ions are confined by their inertia [58]. Then they Coulomb explode, yielding an image of the original atomic positions [59, 60]. It now seems practical [58] to image many small molecules by optically driven Coulomb explosion imaging.

We have also seen that strong laser fields modify the potential energy surface enough to overcome the strong bonds of many molecular ions. While bond breaking in neutral molecules by the non-resonant Stark shift will be uncommon, Stark shifts are still quite large. Via Stark shifts, intense pulses can be used to manipulate and control both the internal and external degrees of freedom of the molecule.

Finally, we have seen that the newly ionized electrons can be directed and controlled, making them tools for probing their parent ion [56]. Most importantly, it appears that the recollision electron might allow molecular imaging via "recollision electron diffraction" [35, 61].

References

1. T. D. G. Walsh, L. Strach, and S. L. Chin, "Above-threshold dissociation in the long-wavelength limit," J. Phys. B **31,** 4853 (1998).
2. G. N. Gibson, M. Li, C. Guo, and J. Neira, "Strong-field dissociation and ionization of H_2^+ using ultrashort laser pulses," Phys. Rev. Lett. **79,** 2022 (1997).
3. J. H. Posthumous, A. J. Giles, M. R. Thompson, W. Shaikh, A. J. Langley, L. J. Frasinski, and K. Codling, "The dissociation dynamics of diatomic molecules in intense laser fields," J. Phys. B **29,** L525 (1996).
4. M. Schmidt, P. D'Oliveira, P. Meynadier, D. Normand, and C. Cornaggia, "Strong laser field interaction with diatomic molecules: From the ultra-short to long-pulse regime," J. Nonlinear Opt. Phys. Mat. **4,** 817 (1995).
5. A. Hishikawa, H. Hasegawa, and K. Yamanouchi, "Sequential three-body Coulomb explosion of CS_2 in intense laser fields appearing in momentum correlation map," Chem. Phys. Lett. **361,** 245 (2002).
6. H. Rottke, C. Trump, and W. Sandner, "Multiphoton ionization and dissociation of H_2O," J. Phys. B **31,** 1083 (1998).
7. H. Sakai, A. Tarasevitch, J. Danilov, H. Stapelfeldt, R. W. Yip, E. Ellert, E. Constant, and P. B. Corkum, "Optical deflection of molecules," Phys. Rev. A **57,** 2794 (1998).
8. V. R. Bhardwaj, P. B. Corkum, and D. M. Rayner, "Internal laser-induced dipole force at work in C_{60} molecule," Phys. Rev. Lett. **91,** 203004 (2003).
9. T. Brixner, N. H. Damrauer, P. Niklaus, and G. Gerber, "Photoselective adaptive femtosecond quantum control in the liquid phase," Nature **414,** 57 (2001).

10. H. Stapelfeldt, H. Sakai, E. Constant, and P. B. Corkum, "Deflection of neutral molecules using the nonresonant dipole force," Phys. Rev. Lett. **79,** 2787 (1997).
11. D. M. Villeneuve, S. A. Aseyev, P. Dietrich, M. Spanner, M. Y. Ivanov, and P. B. Corkum, "Forced molecular rotation in an optical centrifuge," Phys. Rev. Lett. **85,** 542 (2000).
12. P. W. Dooley, I. V. Litvinyuk, K. F. Lee, D. M. Rayner, M. Spanner, D. M. Villeneuve, and P. B. Corkum, "Direct imaging of rotational wave-packet dynamics of diatomic molecules," Phys. Rev. A **68,** 23406 (2003).
13. H. Sakai, C. P. Safvan, J. J. Larsen, K. M. Hilligs, K. Hald, and H. Stapelfeldt, "Controlling the alignment of neutral molecules by a strong laser field," J. Chem. Phys. **110,** 10235 (1999).
14. F. Rosca-Pruna, E. Springate, H. L. Oerhaus, M. Krishnamurthy, N. Farid, C. Nicole, and M. J. J. Vrakking, "Spatial alignment of diatomic molecules in intense laser fields: I. experimental results," J. Phys . B **34,** 4919 (2001).
15. L. V. Keldysh, "Ionization in the field of a strong electromagnetic wave," Sov. Phys. JETP **20,** 1307 (1965), (JETP 47, 1945 (1964)).
16. M. V. Ammosov, N. B. Delone, and V. P. Krainov, "Tunnel ionization of complex atoms and of atomic ions in an alternating electromagnetic field," Sov. Phys. JETP **64,** 1191 (1986).
17. A. M. Perelemov, V. S. Popov, and M. V. Terent'ev, "Ionization of atoms in an alternating electric field," Sov. Phys. JETP **23,** 924 (1966).
18. A. M. Perelomov, V. S. Popov, and M. V. Terent'ev, "Ionization of atoms in an alternating electric field: II," Sov. Phys. JETP **24,** 207 (1967).
19. A. M. Perelemov and V. S. Popov, "Ionization of atoms in an alternating electric field. III," Sov. Phys. JETP **25,** 336 (1967).
20. G. Yudin and M. Y. Ivanov, "Nonadiabatic tunnel ionization: Looking inside a laser cycle," Phys. Rev. A **64,** 13409 (2001).
21. P. Dietrich and P. B. Corkum, "ionization and dissociation of diatomic molecules in intense infrared laser fields," J. Chem. Phys. **97,** 3187 (1992).
22. S. M. Hankin, D. M. Villeneuve, P. B. Corkum, and D. M. Rayner, "Nonlinear ionization of organic molecules in high intensity laser fields," Phys. Rev. Lett. **84,** 5082 (2000).
23. A. Talebpour, C.-Y. Chien, and S. L. Chin, "The effects of dissociative recombination in multiphoton ionization of O_2," J. Phys . B **29,** L677 (1996).
24. C. Guo, M. Li, J. P. Nibarger, and G. N. Gibson, "Single and double ionization of diatomic molecules in strong laser fields," Phys. Rev. A **58,** R4271 (1998).
25. M. J. Dewitt and R. J. Levis, "Observing the transition from a multiphoton-dominated to a field-mediated ionization process for polyatomic molecules in intense laser fields," Phys. Rev. Lett. **81,** 5101 (1998).
26. M. J. DeWitt and R. J. Levis, "Concerning the ionization of large polyatomic molecules with intense ultrafast lasers," J. Chem. Phys. **110,** 11368 (1999).
27. S. M. Hankin, D. M. Villeneuve, P. B. Corkum, and D. M. Rayner, "Intense-field laser ionization rates in atoms and molecules," Phys. Rev. A **64,** 013405 (2001).
28. J. Muth-Bohm, A. Becker, and F. H. M. Faisal, "Suppressed molecular ionization for a class of diatomics in intense femtosecond laser fields," Phys. Rev. Lett. **85,** 2280 (2000).
29. V. R. Bhardwaj, D. M. Rayner, D. M. Villeneuve, and P. B. Corkum, "Quantum interference effects in double ionization and fragmentation of C_6H_6," Phys. Rev. Lett. **87,** 417 (2001).
30. M. J. DeWitt, E. Wells, and R. R. Jones, "Ratiometric comparison of intense field ionization of atoms and diatomic molecules," Phys. Rev. Lett. **87,** 153001 (2001).
31. I. V. Litvinyuk, K. F. Lee, P. W. Dooley, D. M. Rayner, D. M. Villeneuve, and P. B. Corkum, "Alignment-dependent strong field ionization of molecules," Phys. Rev. Lett. **90,** 233003 (2003).
32. X. M. Tong, Z. X. Zhao, and C. D. Lin, "Theory of molecular tunneling ionization," Phys. Rev. A **66,** 033402 (2002).

33. M. Lezius, V. Blanchet, M. Y. Ivanov, and A. Stolow, "Polyatomic molecules in strong laser fields: Nonadiabatic multielectron dynamics," J. Chem. Phys. **117,** 1575 (2002).
34. M. Lezius, V. Blanchet, D. M. Rayner, D. M. Villeneuve, A. Stolow, and M. Y. Ivanov, "Nonadiabatic multielectron dynamics in strong field molecular ionization," Phys. Rev. Lett. **86,** 51 (2001).
35. H. Niikura, F. Légaré, R. Hasbani, A. D. Bandrauk, M. Y. Ivanov, D. M. Villeneuve, and P. B. Corkum, "Sub-laser-cycle electron pulses for probing molecular dynamics," Nature **417,** 917 (2002).
36. P. B. Corkum, "A Plasma perspective on strong field multiphoton ionization," Phys. Rev. Lett. **71,** 1994 (1993).
37. D. N. Fittinghoff, P. R. Bolton, B. Chang, and K. C. Kulander, "Observation of nonsequential double ionization of helium with optical tunneling," Phys. Rev. Lett. **69,** 2642 (1992).
38. P. Dietrich, N. H. Burnett, M. Ivanov, and P. B. Corkum, "High harmonic generation and correlated two electron multiphoton ionization with elliptically polarized light," Phys. Rev. A **50,** 3585 (1994).
39. N. B. Delone and V. P. Krainov, "Energy and angular electron spectra for the tunnel ionization of atoms by strong low-frequency radiation," J. Opt. Soc. Am. B **8,** 1207 (1991).
40. P. B. Corkum, N. H. Burnett, and F. Brunel, "Above threshold ionization in the long wavelength limit," Phys. Rev. Lett. **62,** 1289 (1989).
41. T. Brabec, M. Y. Ivanov, and P. B. Corkum, "Coulomb focussing in intense field Atomic Processes," Phys. Rev. A **54,** 2551 (1996).
42. P. H. Bucksbaum, A. Zavriyev, H. G. Muller, and D. W. Schumacher, "Softening of the H_2^+ molecular bond in intense laser fields," Phys. Rev. Lett. **64,** 1883 (1990).
43. A. D. Bandrauk and M. L. Sink, "Photodissociation in intense laser fields: Predissociation analogy," J. Chem. Phys. **74,** 1110 (1981).
44. H. Niikura, P. B. Corkum, and D. M. Villeneuve, "Controlling vibrational wave packet motion with intense modulated laser fields," Phys. Rev. Lett. **90,** 203601 (2003).
45. T. Seideman, M. Y. Ivanov, and P. B. Corkum, "The role of electron localization in intense field molecular ionization," Phys. Rev. Lett. **75,** 2819 (1995).
46. E. Constant, H. Stapelfeldt, and P. B. Corkum, "Observation of enhanced ionization of molecular ions in intense laser fields," Phys. Rev. Lett. **76,** 4140 (1996).
47. M. Y. Ivanov, T. Seideman, and P. B. Corkum, "Explosive ionization of molecules in intense laser fields," Phys. Rev. A **54,** 1541 (1996).
48. T. Zuo and A. D. Bandrauk, "Charge-resonance-enhanced ionization of diatomic molecular ions by intense lasers," Phys. Rev. A **52,** R2511 (1995).
49. A. Zavriyev, P. H. Bucksbaum, J. Squier, and F. Saline, "Light-induced vibrational structure in H_2^+ and D_2^+ in intense laser fields," Phys. Rev. Lett. **70,** 1077 (1993).
50. T. D. G. Walsh, F. A. Ilkov, and S. L. Chin, "The dynamical behaviour of H_2 and D_2 in a strong, femtosecond, titanium:sapphire laser field," J. Phys . B **30,** 2167 (1997).
51. L. J. Frasinski, K. Codling, P. Hatherly, J. Barr, I. N. Ross, and W. T. Toner, "Femtosecond dynamics of multielectron dissociative ionization by use of a picosecond laser," Phys. Rev. Lett. **58,** 2424 (1987).
52. K. Boyer, T. S. Luk, J. C. Solem, and C. K. Rhodes, "Kinetic energy distributions of ionic fragments produced by subpicosecond multiphoton ionization of N_2," Phys. Rev. A **39,** 1186 (1989).
53. D. T. Strickland, Y. Beaudoin, P. Dietrich, and P. B. Corkum, "Optical studies of inertially confined molecular iodine ions," Phys. Rev. Lett. **68,** 2755 (1992).
54. D. Normand, L. A. Lompre, and C. Cornaggia, "Laser-induced molecular alignment probed by a double-pulse experiment," J. Phys . B **25,** L497 (1992).
55. V. R. Bhardwaj, S. A. Aseyev, M. Mehendale, G. L. Yudin, D. M. Villeneuve, D. M. Rayner, M. Y. Ivanov, and P. B. Corkum, "Few cycle dynamics of multiphoton double-ionisation," Phys. Rev. Lett. **86,** 3522 (2001).

56. H. Niikura, F. Légaré, R. Hasbani, M. Y. Ivanov, D. M. Villeneuve, and P. B. Corkum, "Probing molecular dynamics with attosecond resolution using correlated wave packet pairs," Nature **421,** 826 (2003).
57. G. L. Yudin and M. Y. Ivanov, "Physics of correlated double ionization of atoms in intense laser fields: Quasistatic tunneling limit," Phys. Rev. A **63,** 033404 (2001).
58. F. Légaré, I. Litvinyuk, P. Dooley, F. Quéré, A. D. Bandrauk, D. M. Villeneuve, and P. B. Corkum, "Time-resolved double-ionization with few cycle laser pulses," Phys. Rev. Lett. **91,** 093002 (2003).
59. E. P. Kanter, P. J. Cooney, D. S. Gemmell, K.-O. Groeneveld, W. J. Pietsch, A. J. Ratkowski, Z. Vager, and B. J. Zabransky, "Role of excited electronic states in the interactions of fast (MeV) molecular ions with solids and gases," Phys. Rev. A **20,** 834 (1979).
60. Z. Vager, R. Naaman, and E. P. Kanter, "Coulomb explosion imaging of small molecules," Science **244,** 426 (1989).
61. M. Lein, N. Hay, R. Velotta, J. P. Marangos, and P. L. Knight, "Role of the intramolecular phase in high-harmonic generation," Phys. Rev. Lett. **88,** 183903 (2002).

Probing Molecular Structure and Dynamics by Laser-Driven Electron Recollisions

J.P. Marangos, S. Baker, J.S. Robinson, R. Torres, J.W.G. Tisch, C.C. Chirila, M. Lein, R. Velotta, and C. Altucci

1 Introduction

We review recent advances in measurement of electronic structure and nuclear dynamics in molecules using the sub-cycle electron dynamics inherent to high-order harmonic generation. The mechanism of high harmonic generation (HHG) is closely tied to the driven electron dynamics in a strong laser field. A consequence of this is the ultra-fast (few hundred attosecond) duration of emitted XUV harmonics. This property is the subject of an active programme of research to find application in attosecond domain measurements. Whilst the high photon energy and short duration of radiation is a consequence of the influence of the laser field, the amplitude of emission depends upon properties of the atomic or molecular system. Thus the HHG signal carries information about the atomic and molecular structure that, over the last few years, we have started to understand how to interpret. The aim of this contribution will be to describe techniques for ultra-fast measurement of molecular structure and dynamics that are based upon our understanding of the electron dynamics driven by a laser pulse within an optical cycle and the role of molecular structure.

In the strong-field limit (intensity $> 10^{14}$ W cm^{-2}) HHG can be well understood using the semi-classical model proposed by Corkum [1,2], which separates the process into three distinct steps. First, an intense linearly polarised laser pulse ionises an atom or molecule through field ionisation (predominately quantum tunnelling through the field-suppressed potential barrier) when the electric field amplitude is near a peak, launching an electron wavepacket into the continuum. In the next step, the electron wavepacket moves in response to the laser field: first being accelerated away from the parent ion and then returning at some later time (typically 0.5–1.5 fs for a laser field at 800 nm) as the laser field reverses direction. During this step the electron wavepacket gains energy from the laser field, which is then emitted as a

J.P. Marangos
Blackett Laboratory, Imperial College, Prince Consort Road, London SW7 2BZ, UK
e-mail: j.marangos@imperial.ac.uk

T. Brabec (ed.), *Strong Field Laser Physics*,
DOI: 10.1007/978-0-387-34755-4_9,

high-energy photon if recombination occurs on the return of the wavepacket to the parent ion: this is the third step in Corkum's model. The spectrum extends up to a cut-off energy set by the maximum possible electron return energy which from classical considerations is $3.17U_p + I_p$ (where U_p is the ponderomotive (quiver) energy of a free electron in the field and I_p the ionisation potential of the state). In this strong-field limit the excursion of the laser-driven electron from the atom will amount to many atomic radii and so there are distinct moments within the optical cycle when an electron on a given trajectory (energy) is ionised and returns.

A unique feature of this process is that under appropriate (to an extent experimenter-controlled) circumstances the soft X-ray radiation is emitted for a duration much less than the optical period (the optical period is 2.67 fs for a 800 nm laser) and exactly synchronised with the phase of the laser driving the process. A typical ultra-fast high-power laser pulse might have an energy of $\sim$1 mJ and a duration of 30 fs. This will be focussed into a sample of the target gas to an intensity in the range 10^{14}–10^{15} W cm^{-2}. For a central wavelength of 800 nm the pulse will comprise $\sim$10 optical cycles, therefore there are a number of cycles near the peak of the pulse that are essentially identical to each other. A harmonic is emitted within every half-cycle resulting in a train of ultra-fast XUV pulses, separated by half the optical period, i.e. 1.35 fs, which is referred to as an attosecond pulse train or APT. Each XUV pulse has a duration given by the inverse of the available spectral bandwidth. APTs have been extensively investigated by a number of groups most notably in Lund [3,4] and Saclay [5]. The generation of an isolated attosecond pulse (rather than a pulse train) has also been achieved by the group of Krausz [6,7]. This is important since it allows pump–probe measurements of isolated ultra-fast events to be carried out. To do this requires laser pulses in the few-cycle limit, i.e. durations $\sim$5 fs [8], such that there is only a single recollision at the highest energy the emission from which can be spectrally selected to generate the attosecond pulse.

It is also possible to use the laser-driven electron recollision in a more direct way to make attosecond domain measurements. Because the electrons return in a brief and well-synchronised moment with an appreciable momentum (returning with kinetic energy in the 10–100 eV range for typical fields) the recollision can be used as a probe in several ways. For instance Corkum and colleagues pointed out that the ionisation event forms correlated electron/nuclear wavepackets in a molecule; these can be used to measure vibrational or dissociation dynamics from the kinetic energy released when the molecules are ionised by the returning electron [9,10].

The emission of harmonics from a molecular target of aligned molecules has been shown to carry structural information about the molecule with a very high temporal resolution [11,12,13,14,15,16]. This is possible because the HHG amplitude is dependent upon the dipole amplitude for the transition between the continuum state and the ground state. As the return electron energy is in the range of 10–100 eV the de Broglie wavelengths in the wavepacket span the spatial scales of interest in the ground state wavefunction and so the dipole is

sensitive to the electronic structure of the molecular ground state [16]. In the strong-field limit it is argued that the continuum state can be treated approximately as a superposition (wavepacket) of plane waves unaffected by the binding potential [15] and in this case the dipole matrix amplitude takes the form of a Fourier transform (x-p) of the ground state wavefunction.

2 Laser-Driven Electron Dynamics Within an Optical Cycle

We will now examine in a bit more detail the electron dynamics connected to the HHG process in the strong-field limit. Tunnel ionisation occurs only near the peak of the electric field amplitude (Fig. 1) due to the exponential dependence of the tunnelling rate on the factor $-\frac{2(2I_p)^{3/2}}{3E(t)}$ [17,18,19] (where I_p is the ionisation potential of the bound state and $E(t)$ the electric field amplitude, both in atomic units) and this ensures that (a) the highest energy electronic state is field ionised first and (b) the ionisation is confined in time to $\sim\pm 200$ as (or $<1/10$th of an optical cycle) around the cycle peak. The liberated electron wavepacket moves in response to the laser field: first being accelerated away from the parent ion and then returning at a later time (typically 0.5–1.5 fs for a laser field at 800 nm) as the laser field reverses direction. The motion of the electron in the laser field is essentially classical motion of a charge in an oscillating electric field taking into account the constraints on the phase of the field at which the electron first

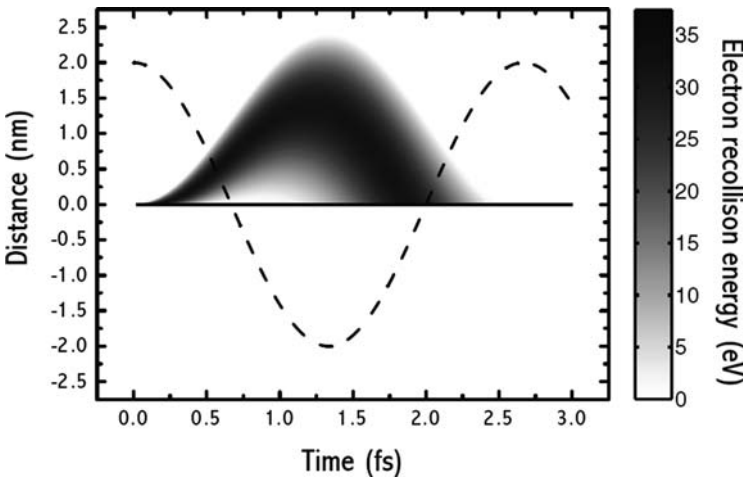

Fig. 1 This shows the electron trajectory displacement (*vertical scale*) and return energy (*darker* = higher return energy) within the trajectories launched by ionisation in the optical half-cycle peaking at $t = 0.0$ fs. The laser electric field as a function of time is shown as a *dashed line*

appeared in the continuum and assuming that it appeared close to the parent ion with an initial momentum close to zero [2,20].

Only electrons tunnel-ionised after the peak of the cycle may return; those arriving in the continuum before the peak never receive sufficient acceleration from the field to come back and so they directly ionise. During this step the electron wavepacket gains energy by virtue of the laser field up to a maximum value of $3.17U_p$ for electrons born at ~1/20th of a cycle (300 mrad after the peak or 133 as for a 800 nm field). This energy is emitted as a high-energy photon if recombination occurs on the return of the wavepacket to the parent ion giving the cut-off energy of $3.17U_p + I_p$.

Electrons born into the continuum between the peak of the electric field and 1/20th of a cycle follow the so-called "long trajectories", travelling far from the core before the electric field reverses direction. Electrons launched into the continuum between 1/20th of a cycle and the zero-crossing of the electric field follow "short trajectories", that is, their path in the continuum is short since the electric field reverses direction relatively quickly following their birth. For electrons born at 1/20th of a cycle after the peak the short and long trajectories converge and of course this corresponds to the highest energy return and so gives rise to the highest energy photon emission (the harmonic cut-off). Within each "class" of trajectories, the energy of the colliding wavepacket varies depending on its time of birth [5,20]: e.g. for electrons following shorter trajectories, those which follow the very shortest paths return with relatively low energy since they have experienced little acceleration by the field. Long trajectories have the opposite dependence, with the electrons spending longer in the field returning with smaller energy. Some long trajectories give rise to multiple electron returns but their role in HHG is usually insignificant. Thus, there exists a direct relationship between the wavepacket return time and the energy of the harmonic photon emitted: for short trajectories, successively higher orders of harmonics are generated at longer time delays. This property of HHG is fundamental to the new technique demonstrated in this work, since it allows a range of pump–probe delays to be accessed by analysis of a single harmonic spectrum (this will be discussed in Section 4).

It is useful to be more concrete about the properties of the returning electron. These are determined by the peak intensity (field) of the pulse and the carrier wave frequency as this sets the scale of the ponderomotive energy: $U_P = e^2E_0^2/4m_e\omega^2$ (where E_0 is the electric field amplitude and ω the angular frequency of the field). The return electron kinetic energy will range from a few eV for the very lowest energy electrons up to $3.17U_p$ for the highest returns (to this should be added the ground state binding energy I_p to get the energy of the photon emitted). For a 800 nm field focussed to an intensity of 5×10^{14} W cm^{-2}, $U_p = 32$ eV and so the highest return energy is slightly above 100 eV. Assuming that the electrons returning in this field have a kinetic energy in the range of 10–100 eV the de Broglie wavelength of the return electron wavepacket spans the range from 3.9×10^{-10} m (for 10 eV electrons) to 1.22×10^{-10} m (for 100 eV electrons); the latter wavelength is close to the size of a typical diatomic

molecule. At this same intensity a field of 1.6 μm will have return energies up to 400 eV, so the shortest de Broglie wavelength in the wavepacket will be 0.61×10^{-10} m, i.e. close to the size of a hydrogen atom.

3 Signatures of Molecular Structure in the HHG Signal

The investigation of high-order harmonic generation in aligned ensembles of molecules [11,12,21] has recently emerged as an important area in strong-field ultra-fast physics. This is because it may be possible to use the molecular alignment to control harmonic emission [21] and potentially enhance attosecond pulse generation [22]. It has been shown that the dependence of HHG on the molecular structure [13,14] can give new insights into measuring molecular structure on a sub-femtosecond timescale. The tomographic reconstruction of the electronic state of the N_2 molecule was recently demonstrated [12]. The newly developed capabilities for fixing the molecular frame axis in the laboratory frame underpin these recent developments [24].

That the molecular structure can be extracted from measurements of the HHG signal from aligned molecules arises through the nature of the process in the strong-field limit, i.e. when the Keldysh parameter $\gamma \leq 1$ (for 800 nm laser light this means $>10^{14}$ W cm^{-2}). To see this we consider the strong-field approximation. The same effects will show up in other treatments; indeed several of the effects described here were first found using numerical solutions of the TDSE for model H_2 and H_2^+ systems [13,14]. Nevertheless the SFA is the most transparent formulation in which to understand the connection between the HHG signal and the molecular electronic structure. The Lewenstein integral for the electron coordinate along the laser polarisation axis in the stationary phase approximation performed on the momentum space reads

$$z(t) = 2\mathrm{Re}\left\{ \mathrm{i} \int_0^\infty \mathrm{d}\tau |a_\mathrm{G}(t)|^2 \left(\frac{\pi}{\varepsilon + \mathrm{i}\tau/2}\right)^{3/2} \times \right. \\ \left. E_0 \cos(t-\tau) d_z(p_\mathrm{st}(t,\tau) - A_z(t-\tau)) \cdot d_z^*(p_\mathrm{st}(t,\tau) - A_z(t)) \cdot \exp[-\mathrm{i}S_\mathrm{st}(t,\tau)] \right\} \quad (1)$$

where t is the recollision time, τ is the time spent by the electron in the continuum, $t-\tau$ is the ionisation instant, $E(t)$ is the electric field of the driving pulse linearly polarised along the z-direction, $A(t)$ is the vector potential, S_st is the stationary dipole phase, i.e. the phase accumulated by the electronic wavepacket due to its motion in the electric field. The term p_st is the stationary momentum and is given by $p_\mathrm{st}(t,\tau) = -\int_{t-\tau}^{t} A(t')\mathrm{d}t'/\tau$ while the term $\left(\frac{\pi}{\varepsilon+\mathrm{i}\tau/2}\right)^{3/2}$ derives from the stationary phase approximation over the momentum space

and takes into account the spreading of the electronic wavepacket. Finally, the term $a(t-\tau)$ is the ground state amplitude and is calculated taking into account the ionisation-dependent depletion, i.e.

$$a_{\mathrm{G}}(t) = \exp\left\{ -\int_{-\infty}^{t-\tau} \frac{w(t')}{2}\,\mathrm{d}t' \right\} \tag{2}$$

where the rate $w(t)$ can be estimated by means of ADK theory [17].

In the Lewenstein integral the whole information about the molecule is contained in the term $d_z(p_{\mathrm{st}}(t,\tau)+A(t-\tau))\cdot d_z^*(p_{\mathrm{st}}(t,\tau)+A(t))$ where d_z and d_z^* are the matrix dipole elements between the ground state $|0\rangle$ and a state of the continuum $|k\rangle$ (which is usually taken to be a plane wave with momentum along the laser polarisation):

$$\mathbf{d}(k) = \langle k|\mathbf{r}|0\rangle \tag{3}$$

The dipole terms are calculated at the ionisation instant $t-\tau$ (d_z) and recombination instant t (d_z^*), respectively.

Since in the strong-field limit, the continuum states are close to plane waves $\exp(\mathbf{ik}.\mathbf{r})$, for a molecule with well-defined alignment it is in principle possible to extract the molecular state wavefunction ψ_0 from measurements of the harmonic spectrum [12]. In a simplified picture, this can be seen in the following way. For z-polarised light a recollision wavepacket can be written as the sum (integral) over the possible momenta of plane waves:

$$\psi_{\mathrm{c}}(z,t) = \int a(k)\mathrm{e}^{\mathrm{i}kz-\mathrm{i}E_k t}\mathrm{d}k \tag{4}$$

where the factor $a(k)$ describes the amplitudes for different $\mathbf{k}$ in the superposition and can be seen to arise from the other terms in Equation (1) describing ionisation and propagation in the field. The harmonic spectrum from one such recollision in a single molecule is given by $S(w)\sim\omega^4|\mathbf{D}(\omega)|^2$ where $\mathbf{D}(\omega)$ is the Fourier transform of the time-dependent dipole moment $\mathbf{D}(t) = <\psi_{\mathrm{c}}|-e\mathbf{r}|\psi_0>\exp[\mathrm{i}I_{\mathrm{p}}t]+\mathrm{c.c.}$ so that we have

$$S(\omega) \sim e^2\omega^4|a(k(\omega))< \exp(\mathrm{i}k(\omega)z)|\mathbf{r}|\psi_0>|^2 \tag{5}$$

The term within the bracket has the form of a Fourier transform of the function $\mathbf{r}\,\psi_0(\mathbf{r})$ and can be seen to be the same as the matrix element in Equation (3). [Under certain conditions, the form of Equation (5) remains valid even if more than one recollision contribute to a harmonic frequency ω, but the factor $a(k)$ may lose the simple meaning given in Equation (4).] This

motivates the concept of retrieval from the measurement of the dipole moment over all **k** which can be achieved by multiple measurements of the HHG spectrum (each over all k) for the different orientations of the molecule [12]. Whilst this is a very powerful idea it is not the only way to extract significant structural information from Equation (5) and instead we will examine here a simpler to implement idea. This is the measurement of recombination interference signatures for certain values of k that give almost directly the internuclear separation. In principle these data can be obtained from a single alignment angle and in a few laser shots and so can lend itself readily to measurement of bond length changes in a pump–probe experiment.

Numerical simulations of the HHG from H_2^+ and H_2 as a function of the angle θ between laser polarisation and the internuclear axis showed for a specific harmonic order a characteristic minimum of the calculated dipole amplitude and modulation of the phase at an angle of 30°–45° [13,14] as can be seen in Fig. 2a. This was shown to be due to interference between the dipole amplitudes from the two atomic centres in the molecule when they were separated by half a de Broglie wavelength λ_B, i.e. the modulation arose in the recombination step in the HHG process. It was shown that a simple calculation of the electron de Broglie wavelength of a particular harmonic order compared to the internuclear separation in the direction of the recolliding electron was sufficient to approximately reproduce the position of interference minimum computed in a full numerical simulation (see Fig. 2b).

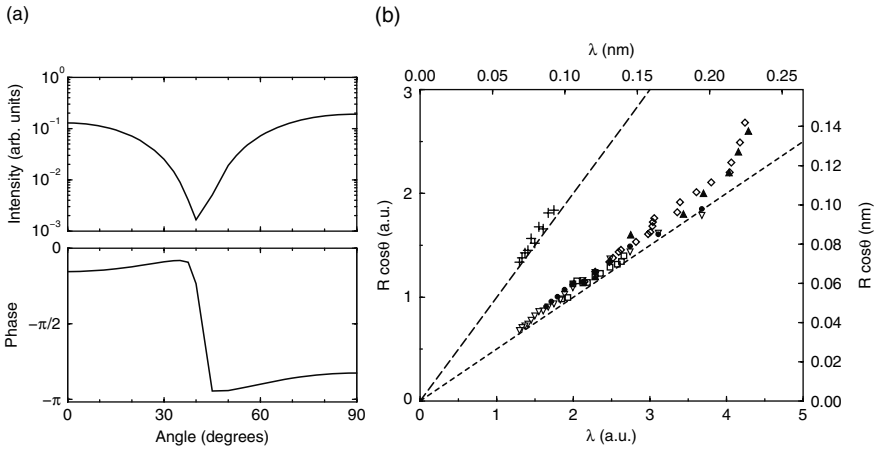

Fig. 2 (**a**) Calculated dipole amplitude (*upper*) and phase (*lower*) for H_2^+ in a field of intensity 5×10^{14} W cm^{-2} (800 nm) shown as a function of the angle between the laser polarisation vector and the internuclear axis, (**b**) projected internuclear separation vs electron wavelength. *Lower set* of points: interference minima for the 2D model molecules. (∇) H_2^+ at $R = 2$ a.u., $I = 10^{15}$ W cm^{-2}, various θ; (•) H_2^+ at $R = 2$ a.u., $I = 5 \times 10^{14}$ W cm^{-2}, various θ; (□) H_2 at $R = 1.4$ a.u., $I = 5 \times 10^{14}$ W cm^{-2}, various θ; ($\diamond$) H_2^+ at $\theta = 40°$, $I = 5 \times 10^{14}$ W cm^{-2}, various R; (▲) H_2 at $\theta = 0°$, $I = 5 \times 10^{14}$ W cm^{-2}, various R. *Upper set* of points (+): interference maxima for H_2^+ at $R = 2$ a.u., $I = 10^{15}$ W cm^{-2}, various θ

Consider a molecular wavefunction for the HOMO (highest occupied molecular orbital) of a diatomic molecule of the form of a linear combination of atomic orbitals (LCAO) of two identical wavefunctions φ_0 centred at each atomic core. If this molecule has an internuclear separation R this can be written as

$$\psi_0(\mathbf{r}) = \frac{1}{\sqrt{2}}(\varphi_0(\mathbf{r} + \mathbf{R}/2) + \varphi_0(\mathbf{r} - \mathbf{R}/2)) \tag{6}$$

Now we assume that this molecule is aligned at an angle θ to the field polarisation direction. By substitution of Equation (6) into the velocity matrix element (not the dipole), which is essentially a Fourier transform of the molecular orbital within the assumption of plane waves for the continuum states as before, we obtain

$$d(k) \sim d_{\text{atom}}(k) \cos\left(k\frac{R}{2}\cos\theta\right) \tag{7}$$

This expression provides for the interference between the contributions to the emission from the atomic centres. For any molecule where the form of the HOMO is well described by the form (6) we can anticipate two-centre interference – indeed for multiple-centred wavefunctions we can anticipate a more complex interference signature.

In summary the conditions for interference were found to correspond to the simple conditions for constructive and destructive interferences, respectively:

$$\begin{aligned} R\cos\theta &= n\lambda_{\text{B}} \\ R\cos\theta &= \left(n + \frac{1}{2}\right)\lambda_{\text{B}} \end{aligned} \tag{8}$$

where R is the internuclear separation and n an integer. In the case of the first destructive interference $n = 0$. For anti-symmetric electronic states (+ in Equation (6) replaced by –) these conditions become reversed so the first corresponds to destructive interference and the second to constructive interference. In these expressions it is implicit that a plane wave approximation has been made. The detailed dispersion relation that is adopted to connect λ_{B} to the electron energy (and thus to the harmonic frequency) is discussed below.

Earlier experiments employing adiabatic alignment showed the modulation of the HHG yield as a result of partial alignment in the molecular ensemble [11]. A limit in these experiments was that the adiabatic alignment technique as used was only able to induce relatively weak degrees of alignment in the sample [25]. Recent work using the impulsive alignment technique [26] has shown much larger alignment-dependent modulations of HHG indicative of higher degrees of alignment with the added benefit that the alignment is field free at the

rotational revivals and sub-revivals [12,14,15,21]. In this technique the molecular alignment is controlled by an initial ultra-fast laser pulse that excites a rotational wavepacket (coherent superposition of rotational states) in the molecules [27]. The rotational wavepacket exhibits strong molecular axis alignment at a regular period corresponding to rotational revivals, half-revivals and quarter revivals. For a rotational period T these occur at delays of T, $T/2$ and $T/4$ (and integer multiples thereof). A second higher-intensity ultra-fast laser pulse then produces high harmonic emission from the molecules when they are close to the maximum degree of alignment. By varying the precise delay of this pulse the HHG emission intensity for different angular distributions can be measured. Alternatively the delay can be fixed to correspond to maximum alignment and the relative polarisation of alignment field and HHG drive laser can be varied to probe the HHG response for different alignment directions.

The simultaneous observation of the ionisation along with the intensity of the soft X-ray emission by Kanai et al. [15] allowed the efficiency of the first (ionisation) step of the process to be separated from the efficiency of the final step when the electron wave recombines to the initial molecular state. In their measurements CO_2 was found to have a minimum in the harmonic emission when the ionisation was maximum. Increased ionisation was accompanied by maximum harmonic emission in the cases of O_2 and N_2, but in the case of CO_2 this was more than offset by the reduced efficiency of the recombination step of the process. The parts of the molecular electronic state of CO_2 located near the two oxygen atoms make equal but opposite contributions to the X-ray emission due to the anti-symmetric nature of the π_g HOMO. The suppression of the harmonic emission occurred when the two oxygen atoms in the molecule, which are a distance of 0.232 nm apart, are separated by exactly one complete wavelength of the electron wave in the direction of the laser polarisation. The soft X-ray emission amplitude from each of the two oxygen atoms is then exactly out of phase which leads to destructive interference in the total emission.

We show in Fig. 3 a robust signature of this interference seen in CO_2 measured by our own group and collaborators [16] that illustrates the effect of two-centre interference upon the HHG spectrum. A strong minimum in harmonic orders 27–39 is seen; these correspond to the position expected for the recombination interference and provide information for the dispersion

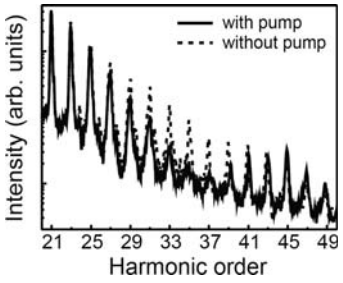

Fig. 3 Measured harmonic spectra from CO_2 generated by 30 fs pulses with (*solid curve*) and without (*dashed curve*) pump beam (pump and probe pulses with parallel polarisation). Pump–probe delay $t = 21.1$ ps

relation of the returning electrons [28]. Other effects, e.g. angle dependence of ionisation rate, can also play a role, as illustrated in recent calculations [29]. However, the experimental results of Kanai [15], where the strong anti-correlation between the ionisation rate and the harmonic signal is shown, the robustness of the dip seen in [16], and other recent experiments support the important role played by the recombination interference mechanism. These most recent experiments have observed a phase-jump between harmonics either side of the dip [30] (as predicted by Lein [13,14]) using the RABITT technique [31] that further confirms its nature.

The observation of interference dips in harmonic spectra from CO_2 molecules is a first step towards developing techniques of wider applicability [15, 16]. Likewise the recent tomographic reconstruction of the HOMO of N_2 from the scans of HHG spectra for different alignment angles [12] is a closely related advance. The full analysis of the reconstruction of structure by this pair of techniques for these two simple molecules is still being tackled. For instance the concept of tomographic reconstruction of a *single-electron* wavefunction (the HOMO of N_2) as determined in [12] rather than the physically more appropriate *multi-electron wavefunction* of the real molecule has been questioned. Recently a more sophisticated calculation (including exchange effects) has shown the reconstructed wavefunction to be still closer to the appropriate multi-electron than the single-electron wavefunction of N_2. At the time of writing the reconstruction measurements have only been published for N_2 but progress towards performing these for other molecules is being made. It is not yet clear for two-centre interference measurements how general the two or multi-centre interference signatures will be and whether their observation will be confined only to molecules where the wavefunction can be accurately described as a simple linear combination of atomic orbitals centred at the atomic locations.

An important issue for both techniques, and for variants built upon these basic ideas, is the extent to which the SFA is an applicable theory for structural reconstruction. The great simplicity of SFA in reducing the HHG emission to a simple mapping of the angle dependence of the transition dipole moment is very attractive and powerful. SFA, however, neglects the Coulombic binding potential in the continuum states and the laser field is ignored in the bound states, and therefore accuracy of the dipole moment calculations and gauge invariance are compromised. Alternative, more accurate, approaches lose the simple relationship between HHG emission and dipole matrix element and so do not lend themselves immediately to the retrieval of molecular structure. There is clearly a lot of work to be carried out in this area both by the theorist, for instance to examine what can be done to preserve the simple ideas offered by SFA in a more accurate theoretical framework [32,33], and by the experimenter to learn how to do these experiments in a way that reduces the reconstruction difficulties, for instance by ensuring that a large recollision momentum is achieved to improve the accuracy of the SFA.

We would argue that despite these difficulties there are considerable prospects to use these techniques as time-resolved probes. Even if there are uncertainties in the retrieval there are certain situations where large structural changes are happening quickly, accompanied perhaps by symmetry changes in the electronic wavefunction, and so a time-resolved method even if it is not exact will provide enormous new insight into chemical physics. The incorporation of the HHG probe techniques into a pump–probe scenario is envisaged. In fact two pumps – one to induce alignment and a second to investigate some photochemical change – are required. The performing of the HHG measurement at known molecular axis alignment and with variable delay with respect to the second probe should suffice to provide a new class of ultra-fast measurements that can follow structural changes. Short laser pulses (of 10 fs or less) in the second pump and probe will be required to achieve high temporal resolution, but these are now becoming available over a wide range of wavelengths. The position in the spectrum of the interference dip minimum can be followed in time through such a measurement and through this the temporal evolution of the internuclear separation will be determined. The limits in the SFA affect primarily the accurate calculation of the amplitude of the dipole moment and will have a more minor effect upon the position of the interference minimum making this technique fairly robust against the theoretical uncertainty.

4 Chirp-Encoded Measurements of Proton Dynamics in Molecules

In the case of molecular structure determination considered above it can be reasonably assumed that the atomic nuclei are too massive to move appreciably during the electron return time. That said, recent data have shown that if a pump– probe configuration is employed (in which the first pulse creates vibrational modes in a spherical molecule such as SF_6) then the harmonic signal generated by the probe will modulate as a function of delay time. It has been noted that the Fourier transform of this modulation includes signatures of all the active Raman modes indicating that the HHG signal is sensitive to small changes in internuclear separation ($\sim$0.01 Å) caused by the vibrational motion [34].

If the molecule contains very light nuclei, such as protons or deuterons, then appreciable motion can occur on the electron return timescale. This is especially interesting as it is very difficult to see this very fast motion by any conventional means. We will describe a technique that has allowed us to study the ultra-fast rearrangement of protons in a molecule following tunnel ionisation in a strong field.

At recollision of the electron wavepacket with the parent ion the probability that recombination occurs, and therefore the strength of the harmonic signal emitted, is related to the quantum mechanical overlap between the wavefunctions of the electron wavepacket and the molecular ground state at the moment

of recollision. Lein predicted [35] that the harmonic signal will be weaker from a molecule whose nuclei move quickly compared to that from a molecule with slower nuclear motion, since the overlap of the wavefunctions decreases as the internuclear separation increases. In addition, since successive orders of harmonics are generated at later times (if short electron trajectories are isolated as was the case in our experiments) [36], the ratio of the harmonic signal for instance between D_2 and H_2 should increase as the harmonic order increases. The "rate" of increase of this ratio with harmonic order then yields information concerning the differing nuclear motion in the two species, and thus represents a measurement of the nuclear motion on an attosecond timescale. We have studied HHG in gaseous H_2 and D_2 to confirm this effect, detecting a clear signature of the nuclear motion that occurs during the time interval between the ionisation and recombination steps.

In these experiments the ionisation step can be thought of as the "pump" process in this technique, since, in the case of a molecule, a vibrational wavepacket is simultaneously launched at the moment of ionisation since the nuclear state makes an instantaneous transition to the ground state potential of the molecular ion. The "probe" is the recollision of the electron wavepacket with the parent ion. This is in common with the earlier technique using correlated electron and nuclear wavepackets of Niikura et al. [9,10]. In contrast the earlier technique used recollision-induced ionisation, rather than recombination followed by emission of radiation, for the probe signal, and requires a variation of laser wavelength over a significant range in order to obtain the required pump–probe delays. In the new technique the inherent chirp in HHG emission permits a range of delays to be simultaneously measured simply by observing the harmonic spectrum.

In these experiments we choose to study the interaction with a very short laser pulse so as to isolate other processes that could be excited in a longer pulse (for instance molecular alignment, vibrational modes and other channels to ionisation). The intense laser field acting as the pump for HHG was provided by 8 fs pulses centred at approximately 775 nm. The 8 fs pulses were generated by the compression of ~0.75 mJ, 30 fs pulses (Femtolasers CompactPRO), which had been spectrally broadened through self-phase modulation in a differentially filled, 0.25 mm inner diameter, 1 m long hollow fibre. The laser beam was focused by a 400 mm focal length off-axis paraboloid beneath a solenoid gas jet operating at a repetition rate of 2 Hz. The beam waist was located 9 mm before the gas jet to ensure that short electron trajectories dominated the harmonic signal. The intensity at the interaction region was estimated to be 2×10^{14} W cm^{-2}. The harmonic signal was spectrally dispersed in a grazing incidence flat field spectrometer and made incident upon an imaging multichannel plate (MCP) detector. The harmonic spectrum was extracted by spatial integration of the MCP image. Since the first ionisation potential in the two species was very similar (15.43 eV for H_2, 15.46 eV for D_2), it was expected that the difference in phase-matching conditions for harmonic generation in the two cases is insignificant. This was confirmed by observation that the harmonics

generated in H_2 and D_2 had identical far-field spatial distributions. To make the comparison it was essential that H_2 and D_2 were delivered to the interaction region at an equal density which was verified by an independent interferometric measurement of the electron density through full ionisation of the sample in a high-power laser pulse.

The calculations for D_2 and H_2 are based on a model derived from the strong-field approximation (SFA) for vibrating molecules [35]. The model involves the propagation of the nuclear wavepacket $\chi(R,\tau)$ in the Born–Oppenheimer (BO) potential of the molecular ion, calculated by numerical solution of the vibrational time-dependent Schrödinger equation. Here, R is the internuclear distance and τ is the electron travel time between ionisation and recombination (equivalent to the delay time Δt when viewed as a pump–probe scheme). The initial wavepacket $\chi(R,0)$ launched in the BO potential of the ion is assumed to be real and identical to $\chi_0(R)$ (the vibrational ground state) of the neutral molecule. The initial state is calculated by imaginary-time propagation in the BO potential of H_2. Following Itatani et al. [12], the intensity of a harmonic with frequency ω is proportional to $\omega^2|a[k(\omega)]v[k(\omega)]|^2$, where $|a[k(\omega)]|$ is the amplitude for finding the active electron recolliding with the core with momentum $\hbar k$, and $v[k(\omega)]$ is the recombination amplitude in velocity form (not to be confused with the velocity gauge for the laser–electron interaction). The wave vector $k(\omega)$ is obtained using the relation $\hbar^2k^2/(2m) = \hbar\omega$ (i.e. the photon energy is equated to the electron kinetic energy). Including nuclear and electronic coordinates, the recombination amplitude reads

$$v[k] = \int \chi_0(R)\left\langle \Psi_0(R)|k|\mathrm{e}^{\mathrm{i}kx}\Psi_0^+(R)\right\rangle \chi(R,\tau(k))\mathrm{d}R \tag{6}$$

where $\Psi_0(R)$ and $\Psi_0^+(R)$ are the electronic ground states of the neutral molecule and the molecular ion, respectively. The relation determining the travel time $\tau(k)$ is taken from the simple man's model [1], assuming that only short trajectories near the peak of the laser pulse contribute to harmonic generation. Denoting as $r[k]$ all independent factors that can be written as prefactors of the integral over R, we have $v[k] = r[k]c[\tau(k),k]$, where the nuclear correlation function $c[\tau(k),k]$ collects the effects of the nuclear motion.

Assuming isotopic invariance for $a[k(\omega)]$, i.e. for the ionisation step and for the dynamics of the free electron before recombination, the ratio of harmonic intensities in two isotopes is given by the ratio of the moduli squared of the nuclear correlation functions in the two species.

We compare our experimental results with this calculation based on the strong-field approximation which collects the effect of the nuclear motion in the compact nuclear correlation function. The harmonics are approximately proportional to the modulus squared of the nuclear correlation function, $c(\tau) = \int \chi_0(R,0)\chi(R,\tau)f(k,R)\mathrm{d}R$, where $\chi_0(R,0)$ and $\chi(R,\tau)$ are the initial and propagated vibrational wavepackets in the molecular ion, R is the internuclear distance and τ is the travel time, which is equivalent to our delay time,

Δt and $f(k,R)$ describes the effect of two-centre interference. The calculated curve is scaled to account for the slight difference in photoionisation cross-sections for H_2 and D_2. We have confirmed in test calculations that the influence of the Stark shifts in the Born–Oppenheimer potential is negligible for the present set of parameters. Two-centre interference in H_2^+ (or D_2^+) gives rise to a small but clearly discernable shift which is included through the $f(k,R)$ factor. As shown in Fig. 4a, we find good quantitative agreement between our measurements and the calculation.

The time evolution of the internuclear separation in each molecule was reconstructed from the recorded intensity spectra and their ratio by use of a genetic algorithm. As shown in Fig. 4b the agreement with the exact calculation is good. Therefore, the measurement of the harmonic spectrum ratio can be used to determine proton (deuteron) motion in H_2 and D_2 molecules $\sim$1 fs after ionisation, with a temporal resolution of $\sim$100 as (the difference in recollision times between successive harmonic orders). Here we use the data from H_2/D_2 primarily to test and confirm the method, since the potential surface and so the calculated dynamics of the proton are known in the case of H_2. Therefore the agreement between the measurement and the calculated ratio of the nuclear autocorrelation function is confirmation that the chirp of the electron is satisfactorily given by the semi-classical treatment validating the frequency to time mapping and other assumptions in the theoretical treatment such as the vertical ionisation.

The above demonstration of the measurement of the proton dynamics in a H_2^+ ion is a proof of principle for the chirp-encoded recollision technique. A similar experiment was conducted on CH_4^+ and revealed the ultra-fast onset of rearrangement of the protons in the few femtoseconds following ionisation

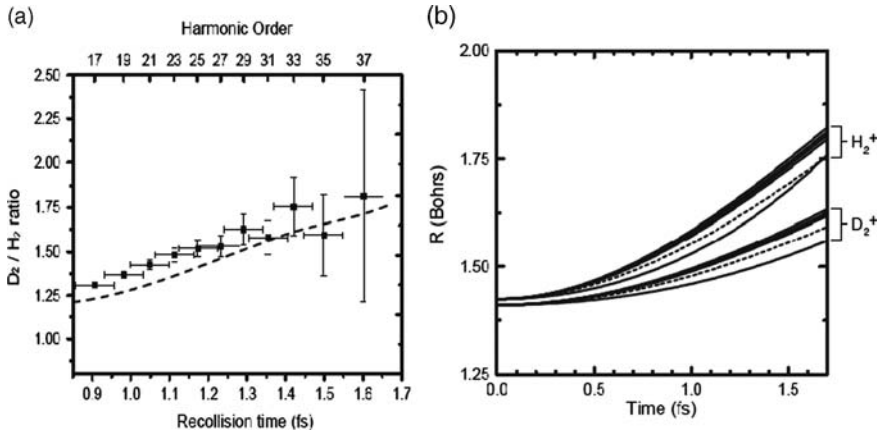

Fig. 4 (**a**) Ratio of harmonic intensities for D_2/H_2 plotted as a return time (*black squares* with errors); *the dashed curve* is the calculated ratio of the square of the nuclear correlation function. (**b**) Retrieved mean internuclear separation $<R>$ as a function of time. Retrieved data from experiment using genetic algorithm (*solid lines*) exact calculation using potentials (*dashed lines*)

that takes the molecule from the equilibrium tetrahedral structure of neutral CH_4 to the C_{2v} structure of the cation [37].

Further refinements of the technique are now needed. These include a fuller accounting of effects that may alter the photon energy to return time mapping, e.g. Coulomb effects, two-centre interference; in principle the mapping can be checked in situ using the two-colour techniques recently reported by Dudovich and co-workers [38]. Extension to longer measurement times can be achieved by employing longer wavelength lasers.

It should be noted that the comparison of deuterated to protonated molecules of the same type was an experimental convenience that circumvented the need to more fully characterise the order dependence of the returning electron amplitude and the momentum-dependent factor in the transition dipole; nevertheless this could in principle be dispensed with. For instance measuring the harmonic spectrum over a range of intensities can in principle give us the extra information needed to unravel these factors from those depending solely on the return time. The technique should be extendable to many organic molecules containing protons, the ultra-fast rearrangements of which cannot be resolved by existing techniques. In principle the use of the temporal encoding of the return energy of the electrons might allow us to measure changes occurring within the states of the electrons remaining within the ion core during the "probe" electrons sojourn in the continuum. So for instance states excited by the strong field or by the removal of the electron (shake-off processes) might be time resolved with a temporal resolution of better than 100 as.

5 Conclusion

The techniques set out above are in their infancy. There remains much to do to explore their limitations and overcome these if a more general applicability is to be found. Nevertheless the proofs of principle already achieved and the rapid pace of development are very encouraging. Closely related techniques; for instance that look at the diffraction of the recolliding electrons after they are elastically scattered [39,40], are also promising new methods for ultra-fast structural analysis. Moreover exploration of these techniques is contributing new knowledge to our understanding of the interaction of molecules with strong laser fields. What is already clear is that laser-driven electron recollision is a probe with unique characteristics that can in principle provide sub-femtosecond temporal resolution and high spatial resolution structural information.

References

1. Corkum, P. B., *Phys. Rev. Lett.* **71,** 1994–1997 (1993).
2. Lewnstein, M., et al., *Phys. Rev. A* **49,** 2117 (1994).
3. Antoine, P., L'Huillier, A., and Lewenstein, M., *Phys. Rev. Lett.* **77,** 1234–1237 (1996).

4. Mauritsson, J., *Phys. Rev. Lett.* **97,** 013001 (2006).
5. Mairesse, Y., et al., *Science* **302,** 1540–1543 (2003).
6. Dreschler, M., et al., *Science* **291,** 1923 (2001).
7. Kienberger, R., et al., *Nature* **427,** 817–821 (2004).
8. Nisoli, M., et al., *Appl. Phys. B* **65,** 189.196 (1997).
9. Niikura, H., et al., *Nature* **417,** 917–922 (2002)
10. Niikura, H., et al., *Nature* **421,** 826–829 (2003).
11. Velotta, R., et al., *Phys. Rev. Lett.* **87,** 183901 (2001).
12. Itatani, J., et al., *Nature* **432,** 867 (2004).
13. Lein, M., Hay, N., Velotta, R., Marangos, J. P., and Knight, P. L., *Phys. Rev. Lett.* **88,** 183903 (2002)
14. Lein, M., Hay, N., Velotta, R., Marangos, J. P., and Knight, P. L, *Phys. Rev. A* **66,** 023805 (2002).
15. Kanai, T., Minemoto, S., and Sakai, H., *Nature* **435,** 470 (2005).
16. Vozzi, C., et al., *Phys. Rev. Lett.* **95,** 153902 (2005).
17. Ammosov, M. V., et al., *Sov. Phys. JETP* **64,** 1191 (1986).
18. Tong, X. M., et al., *Phys. Rev. A* **66,** 033402 (2002).
19. Ivanov, M. Y., et al., *J. Mod. Opt.* **52,** 165 (2005).
20. Paulus, G. G., et al., *J. Phys .B* **27,** L703 (1994).
21. Kaku, M., Masuda, K., and Miyazaki, K., *Jpn. J. Appl. Phys.* **43,** L591 (2004).
22. Itatani, J., Zeidler, D., Levesque, J., Spanner, M., Villeneuve, D. M., and Cokum, P. B., *Phys. Rev. Lett.* **94,** 123902 (2005).
23. Pfeifer, T., Walter, D., Gerber, G., Emelin M. Yu, Ryabikin M. Yu, Chernobrovtseva, M. D., and Sergeev, A. M., *Phys. Rev. A* **70,** 013805 (2004).
24. Stapelfeldt, H. and Seidemann, T., *Rev. Mod. Phys.* **75,** 543 (2003).
25. Lein, M., de Nalda, R., Heesel, E., Hay, N., Springate, E., Velotta, R., Castillejo, M., Knight, P. L., and Marangos, J. P., *J. Mod. Opt.* **52,** 465 (2005).
26. Rosca-Pruna, J. and Vrakking, M. J. J., *J. Chem. Phys.* **116,** 6567 (2002).
27. Torres, R., de Nalda, R., and Marangos, J. P., *Phys. Rev. A* **72,** 023420 (2005).
28. Vozzi, C., et al., *J. Phys. B* **39,** S457 (2006).
29. Le, A. T., Tong, X. M., and Lin, C. D., *Phys. Rev. A* **73,** 041402 (2006).
30. P.Salieres – private comm.
31. Paul, P. M., et al., *Science* **292,** 1689 (2001).
32. Gordon, A. and Kärtner, F. X., *Phys. Rev. Lett.* **95,** 223901 (2005).
33. Chirilă, C. C. and Lein, M., *J. Mod. Opt.* **54,** 1039 (2007).
34. Wagner, N. L., et al., *PNAS* **103,** 13279 (2006).
35. Lein, M., *Phys. Rev. Lett.* **94,** 053004 (2005).
36. Baker, S, et al., *Science* **312,** 424 (2006).
37. Frey, R. E. and Davidson, E. R., *J. Chem. Phys.* **88,** 1775 (1988).
38. Dudovich, N., et al., *Nat. Phys.* **2,** 781 (2006).
39. Lein, M., Marangos, J. P., and Knight, P. L., *Phys. Rev. A* **66,** 051404 (2002).
40. Spanner, M., et al., *J. Phys. B* **37,** L243 (2004).

Intense Laser Interaction with Noble Gas Clusters

Lora Ramunno, Thomas Brabec, and Vladimir Krainov

1 Introduction

The interaction of intense short-laser pulses with atomic clusters has become an important area of research, particularly for understanding the physics of laser-generated plasmas [1]. Clusters are small particles of condensed matter, with sizes ranging from 10^2 to 10^6 atoms. As such, they are intermediate to macroscopic condensed matter and microscopic systems, such as atoms and molecules. Intense laser–cluster interaction creates small-scale plasmas (nanoplasmas). While these nanoplasmas are transient, because the clusters eventually explode, they nevertheless allow the investigation of fundamental laser–matter interaction processes such as ionization and laser energy absorption mechanisms. Since cluster sizes can span the transition region between microscopic and macroscopic systems, these processes can be investigated as a function of system size.

Interest in laser-induced cluster explosion was sparked by the experimental observation [2, 3, 4, 5, 6, 7] that highly charged, highly energetic ions are created during the interaction of intense lasers with noble gas clusters. The charge state and energy of these ions considerably exceeds those resulting from single-atom experiments with comparable laser intensities. While the average particle density in cluster experiments ($10^{19}\,\mathrm{cm}^{-3}$) is not much higher than in conventional atomic gas density experiments, the local density inside the clusters, $10^{22} - 10^{23}\,\mathrm{cm}^{-3}$, is close to solid state. Thus cluster beams are near-transparent to laser light, yet they absorb laser energy very efficiently [8], combining the advantages of both atomic gas and solid density targets.

This efficient energy absorption has now been confirmed by a wealth of experiments for a broad set of laser parameters, including wavelengths ranging from 100 nm to 1 μm, intensities ranging from 10^{15} to $10^{19}\,\mathrm{W/cm}^2$, and pulse durations ranging from 30 fs to 0.5 ps. To date, most experiments were performed in the near-infrared, corresponding to the Ti:sapphire laser wavelength

L. Ramunno
Physics Department, University of Ottawa, Ottawa K1N 6N5, ON, Canada
e-mail: lora.ramunno@uottawa.ca

T. Brabec (ed.), *Strong Field Laser Physics*,
DOI: 10.1007/978-0-387-34755-4_10,

of 800 nm [8, 9, 10, 11, 21]; a few were performed at the KrF wavelength (248 nm) [22, 23]. Free-electron lasers (FEL) will allow the investigation of nanoplasmas in the vacuum-ultra-violet (VUV) to X-ray wavelength regime. A first set of FEL–noble gas interaction experiments was performed at 100 nm [24, 25], and experiments at shorter wavelengths (30 nm) are under way [26].

In contrast to noble gas clusters, there are fewer experimental studies of metal clusters in intense laser fields [27, 28, 29, 30, 31]. Unlike in noble gas clusters – where the atoms are bonded via weak van der Waals forces and the electrons are thus initially localized and bound to the nuclei – the ground state of metal clusters consists of delocalized valence electrons. As a result, quantum many-body effects play a role only at low laser intensities ($< 10^{14}$ W/cm^2), making the theoretical analysis much more difficult. For a review of metal clusters see Ref. [32].

In this chapter, we review the current understanding of noble gas cluster interaction with intense lasers. We begin by presenting some of the most interesting experimental results and possible applications. Next, we outline the major physical processes underlying the dynamics of intense laser–cluster interaction, which is followed by a discussion of the mechanisms of laser energy absorption by electrons. Finally, we show that laser–cluster interaction is an interesting tool for the investigation of plasmas in the strongly coupled regime and for investigating the interplay between collective and collisional processes that take place on a few femtosecond to attosecond time scales.

2 Experiments and Applications

The interaction of lasers with noble gas clusters has many possible applications. Primarily, these are a consequence of the energetic electrons and ions that are created though this interaction. For example, at moderate laser intensities ($\sim 10^{15} - 10^{16}$ W/cm^2) electrons with energies of a few keV [33] and ions of charge states 10+ and higher, with energies of tens to hundreds of keV, are created [34, 35].

The potential of using highly energetic ions from laser–cluster interaction to trigger nuclear reactions has been demonstrated recently through the observation of nuclear fusion in large deuterium clusters [36, 37, 38]. This has generated considerable interest, especially for the possibility of a tabletop neutron source. The use of clusters for fusion, however, is limited by several constraints. While laser-induced cluster explosion does lead to the creation of energetic ions, it also reduces the density by orders of magnitude, ultimately creating a plasma with the density of an atomic gas. Thus the requirements of high ion energy and high ion density are difficult to fulfil simultaneously.

The highly charged ions of laser–cluster interaction can also lead to the emission of X-ray radiation [39]. Clusters present an alternative to intense X-ray generation from laser-driven solid-state targets [40], and efforts have been made to optimize the life time and energy absorption of clusters and thus the X-ray yield [41]. Intense Kα and Kβ emission from krypton at

12.66 and 14.1 keV was observed in the interaction of 10^{18} W/cm^2 laser pulses with krypton clusters [42]. The highest laser energy to (Kα) X-ray conversion efficiency observed is 10^{-6}, corresponding to 45 nJ X-ray pulse energy. This is close to the conversion efficiency of $\approx 10^{-5}$ obtained from intense laser–solid target interactions [43].

Finally, noble gas clusters can also be used to create plasma waveguides [44, 45] that are suitable to guide high-intensity laser pulses in under-dense plasmas. Guiding of intense laser pulses in plasmas is important for laser wakefield accelerators, X-ray lasers and high harmonic generation. The waveguide is created in the following way. The laser-heated clusters expand on a sub-ps time scale and eventually merge to form a locally uniform plasma in 10–100 ps. This hot plasma leads to the formation of a shock wave and a subsequent waveguide structure over a nanosecond time scale. The advantage of using clusters over atomic gases is a longer and better-quality waveguide.

3 Fundamental Concepts of Intense Laser–Cluster Interaction

Over the past decade considerable effort has been put into understanding the physical mechanisms driving the dynamics of laser–cluster interaction [46, 47, 48, 49, 50, 51, 52, 53, 54, 55, 56, 57, 58, 59, 60, 61, 62]. The dynamics generally follows three basic steps: (i) ionization creates free electrons within the cluster (inner ionization); (ii) electrons absorb energy from the laser field, and many escape the cluster (outer ionization) creating an overall positive space charge throughout the cluster; and (iii) due to electrostatic and hydrodynamics forces, the cluster eventually explodes.

While the mechanisms discussed below apply to the long-wavelength (visible and near-infrared) regime, this overall cycle of ionization, electron heating, positive cluster charge up, and eventual explosion applies over a broad range of wavelengths from the infrared to the XUV regime. Of course, the specific optical field ionization mechanisms change with wavelength. For example, tunnel ionization dominates in the infrared regime, whereas single-photon or multi-photon ionization dominates in the short wavelength of 100 nm and below [24].

3.1 Inner Ionization

At the leading edge of the laser pulse, the weakest bound electrons of the noble gas atoms are ionized. This happens through optical field (tunnelling) ionization, beginning when an intensity of around 10^{14} W/cm^2 is reached. Due to the presence of these (quasi) free electrons, the noble gas cluster becomes metallic. After the inner ionization of the first valence electron, other ionization mechanisms, in addition to optical field ionization, become relevant. These include:

Impact ionization. When the kinetic energy of a free electron is larger than the ionization potential of a bound electron, the free electron can share its energy with the bound electron during an atom–electron or ion–electron collision, resulting in the creation of two free electrons. Simulations show that impact ionization is very important for the creation of the most highly charged ions observed in clusters [60].

Charge-enhanced ionization [48, 55]. This effect was first discovered in intense laser interaction with diatomic molecules. After the first electron is removed, the field of the ion lowers the Coulomb barrier of the neighbouring atom. This lowers the ionization potential for the second electron, as illustrated in Fig. 1a, thereby facilitating optical field ionization. In clusters, a similar process can occur. However, the total electric field within the cluster is much

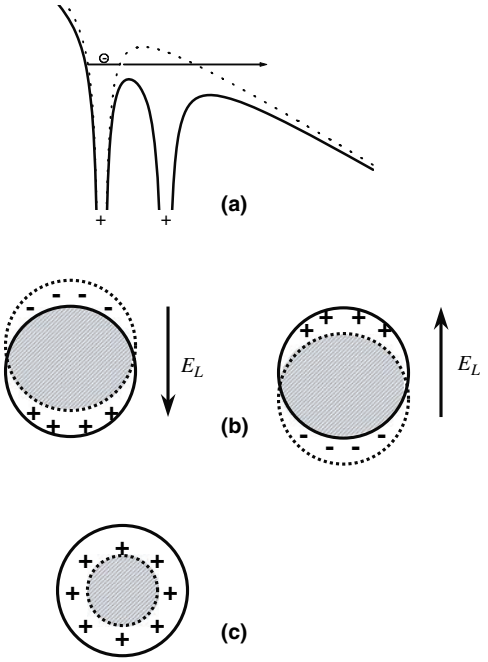

Fig. 1 (**a**) Schematic of charge-enhanced ionization in a diatomic molecule. *The dotted line* is the Coulomb potential felt by the most weakly bound electron of an atom in the presence of an intense laser field, when the adjacent atom has not been ionized. *The solid line* is the modified potential felt by this electron when the adjacent atom has been ionized. As shown, the ionization barrier of the electron has been effectively lowered by the adjacent ion, leading to enhanced ionization. (**b**) Illustration of the motion of an electron cloud (*dotted circle*) relative to an ion cloud (*solid circle*) in response to an oscillating laser field. Every half cycle, there is a region of the ion cloud that becomes unshielded by the electron cloud; shielded regions are *shaded*. This leads to a macroscopic field at the cluster poles which augments the laser field and leads to enhanced ionization. (**c**) Illustration of a cluster during laser–cluster interaction after significant outer ionization has occurred. There are not enough electrons to shield the entire cluster, but they still do shield the core, indicated by the *shaded region*. This leaves an outer ring of positive charge which can lead to enhanced ionization in the unshielded region

more complex due to the presence of many electrons. It thus exhibits strong fluctuations, which add a stochastic component to charge-enhanced ionization [58].

Polarization-enhanced ionization [16, 58]. To a first approximation the metal-like cluster behaves like two uniformly charged spheres: a positively charged ionic sphere and a negatively charged electronic sphere. Unlike the much heavier ionic sphere whose motion is practically unaffected by the laser pulse, the lighter electron sphere can be driven quite strongly by the laser field in the direction of the laser polarization, as illustrated in Fig. 1b. As a result, two sections of the cluster can become unshielded by the electron cloud every half cycle. These cluster "poles" then experience a very large space charge which adds to the laser electric field and enhances ionization. The highest charge states are created at the cluster poles leading to asymmetric Coulomb explosion of the cluster, which has been experimentally observed [16].

Cluster charge-enhanced ionization. Since outer ionization (described below) reduces the number of electrons within the cluster, a net positive cluster charge results and the electrons can no longer completely shield the ions. Numerical simulations have shown that for large clusters ($\sim 10^5$ atoms), the electrons will shield the core of the cluster, while leaving a ring around the cluster core unshielded [58], see Fig. 1c. The radius of the electron cloud is thus much less than the radius of the cluster.[1] The resulting electric field adds to the laser electric field and enhances optical field ionization.

Enhanced ionization due to ion shielding. In a charge-neutral plasma, electrons can shield the field of an ion. As a result, the long-range Coulomb potential of the ion is modified to a short-range, exponentially damped potential. This serves to reduce the ionization potential, enhancing ionization [53]. Calculations based on Debye shielding show that the ionization potential can be reduced by up to a factor of two when the electron–ion interaction strength in the plasma becomes large (i.e. the plasma is strongly coupled). However, current analysis so far does not take into account the field of neighbouring ions, the strong plasma electric field fluctuations in the strong coupling limit, and the overall positive charge of the clusters. As discussed qualitatively in Ref. [53], these effects would induce a Stark shift that increases the ionization potential and may counteract the effect of Debye shielding. A quantitative calculation of the ionization potential is one of the open challenging questions in plasma and nanoplasma physics.

[1] In general, the radius of the electronic cloud is determined by both the net postive cluster charge and the electronic temperature.

3.2 Outer Ionization

Outer ionization refers to the removal of electrons from the cluster. Near the leading edge of the laser pulse, when the cluster is quasi-neutral, electrons can escape easily. Eventually this results in a positive charging of the cluster and a corresponding build-up of a Coulomb potential outside the cluster. This potential will act against further outer ionization.

Further electrons will escape, however, if they absorb sufficient energy from the laser field to overcome the Coulomb barrier. A truly free electron will not absorb energy from a laser monochromatic field. However, the free electrons within the cluster experience the combined electric fields of the driving laser and of the cluster itself, which does result in the absorption of photons. This is because a third body of some sort is required to fulfil energy and momentum conservation during photon absorption. Discussion of cluster electron heating mechanisms is presented in detail in the next section.

3.3 Cluster Explosion

At the trailing edge of the laser pulse the cluster begins to expand. The explosion is driven by two forces: hydrodynamic and electrostatic. The former results from the pressure associated with the ideal gas of the heated free electrons inside the cluster and leads to cluster expansion. This mechanism dominates in the parts of large clusters that remain neutral due to shielding, as discussed above. The electrostatic force occurs as a result of the incomplete shielding, which causes the positive ions to repel each other and Coulomb explosion to take place. The time for an intermediate-sized deuterium cluster to double in size is around 30 fs and fora Xe cluster is around 300 fs. After 10–100 ps, depending on the initial cluster sizes in a given cluster beam, the exploding clusters will merge, creating a macroscopic low-density plasma.

4 Electronic Heating Mechanisms

In addition to the processes discussed above, the energetic explosion of laser-irradiated clusters is driven by energy absorption by electrons in the combined electric field of the laser and the cluster. While crucial to understanding laser–cluster interaction dynamics, the roles of the various proposed energy absorption mechanisms are still not well understood. We hope our discussion will contribute to a better understanding. Again, we focus here on long-wavelength laser irradiation.

One way to understand the different heating mechanisms is by modelling the collective electronic motion by means of a driven oscillator model. An equation of motion can be derived from hydrodynamic (Vlasov) plasma equations [63]

by modelling the electron and ion distributions as interpenetrating negative and positive spheres, as introduced in the last section. It is understood that the parameters introduced below describing the cluster state will change as a function of time due to both ionization and cluster explosion, but we assume these changes are relatively small over a single laser cycle. The equation of motion along the direction of laser polarization for centre of mass $x(t)$ of a rigid electron cloud is

$$\ddot{x} + 2\nu\dot{x} + \omega_{\mathrm{m}}^2 x + F_{\mathrm{nl}}(x) = -|Q_{\mathrm{e}}|E_{\mathrm{L}}(t)/M_{\mathrm{e}}, \tag{1}$$

where ν is a damping coefficient arising from microscopic collisions (including both interparticle collisions, and random electron collisions with the cluster surface); $Q_{\mathrm{e}} < 0$ and M_{e} are the charge and mass of the electron cloud, respectively; E_{L} is electric field of the laser; and F_{nl} contains nonlinear force terms. The dot and double dot refer to the first and second time derivatives, respectively. Due to the cluster's spherical geometry, the fundamental plasmon resonance is at the Mie frequency,

$$\omega_{\mathrm{m}} = \omega_{\mathrm{p}}/\sqrt{3} = \sqrt{e^2 Z n_{\mathrm{i}}/(3\epsilon_0 m_{\mathrm{e}})}, \tag{2}$$

where SI units have been used. The bulk plasma frequency is ω_{p}, Z is the average ion charge, n_{i} is the ion density within the cluster, e is the unit charge, m_{e} is the electron mass, and ϵ_0 is the vacuum dielectric constant.

The non-neutrality of the cluster leads to a net macroscopic cluster field which affects the motion of the electron cloud. If the particle distributions are both uniform, this macroscopic field is harmonic within the cluster radius, and Coulombic outside. Whenever part of the electron cloud is driven over this Coulombic region (i.e. the cluster surface) by the laser field, anharmonic oscillatory motion will result. This is the case illustrated in Fig. 1b and is a much different phenomenon than the random electron–surface collisions that contribute to a transferring of energy from collective electron motion to random thermal motion. Damping via random surface collisions has also been referred to as Landau damping [62], though it is different from the usual meaning of pure collisionless Landau damping in bulk plasmas. In the limit of uniform density distribution and when the electron cloud excursion over the cluster surface has a length much less than the cluster radius, an expression for F_{nl} in Eq. (1) can be found explicitly [64].

Nonlinear motion can also result when the particle distributions are non-uniform, even if no part of the electron sphere is driven over the cluster boundary. This can occur, for example, when significant outer ionization has taken place, and the electronic radius is less than the ionic radius; this is illustrated in Fig. 1c.

We can transform Eq. (1) into an equation for the total (kinetic plus potential) energy $E(t)$ of the electron sphere, i.e. the total energy contained in the collective motion. Multiplying Eq. (1) by $\dot{x}$ and integrating over time yields

$$\begin{aligned} E(t) &\equiv \frac{M_e}{2}\dot{x}^2 + \frac{M_e\omega_m^2}{2}x^2 + V_{nl}(x) \\ &= -2M_e\nu\int_{-\infty}^{t}\dot{x}^2 dt' - |Q_e|\int_{-\infty}^{t}\dot{x}(t')E_L(t')dt'. \end{aligned} \tag{3}$$

The first term of the last line of Eq. 3 determines the amount of energy lost from the collective motion to random, thermal motion via collisions (i.e. dissipation). The second term of the last line is the total amount of energy absorbed from the laser field, E_{tot}. The quantity $V_{nl}(x) = \int \dot{x}F_{nl}(x)dt'$ contains the part of the potential arising from the nonlinear force terms in the cluster. When damping is present, eventually all the absorbed energy gets transferred from the collective motion to thermal energy so that $E(\infty) = 0$.

Armed with this simple driven oscillator model, we now discuss the heating mechanisms governing laser–cluster interaction. They can be grouped into two major categories: (1) collisional heating, governed by the damping parameter ν, and (2) nonlinear cluster heating, governed by the nonlinear potential.

4.1 Collisional Heating

Collisional heating arises from processes that contribute to the damping term in the equation of motion, Eq. (1). Since collisional heating is present in the limit of even a linear potential, in the following we neglect the nonlinear terms in Eqs. (1, 3) for simplicity.

In the absence of damping, $\nu = 0$, and the total energy absorption over a laser pulse in a driven harmonic oscillator model is proportional to the spectral component of the driving field only at the Mie frequency, $|\tilde{E}_L(\omega_m)|^2$ [65]. Here, the tilde refers to the Fourier transform.

The presence of damping mechanisms broadens the range of frequencies that can contribute to heating. This can be understood by examining the general solution of the linear version of Eq. (1) in the Fourier domain. The solution for the velocity $v = \dot{x}$ of the electron cloud is

$$\tilde{v}(\omega) = \frac{-|Q_e|}{M_e}\tilde{E}_L(\omega)\tilde{S}_m(\omega), \tag{4}$$

where we refer to $\tilde{S}_m(\omega) \equiv i\omega/(\omega_m^2 - \omega^2 + 2i\nu\omega)$ as the Mie spectrum. Absorption of laser energy only takes place when there exists a significant overlap between the laser spectrum $\tilde{E}_L(\omega)$ and the Mie resonance [7, 55]. For this reason, collisional heating is also referred to as "resonance heating".

Assuming that ω_m and ν do not change over time, the expression from Eq. (3) for the total energy absorbed from the laser pulse can be rewritten as

$$-|Q_e| \int_{-\infty}^{\infty} \dot{x}(t')E_L(t')dt' = \frac{Q_e^2}{2\pi M_e} \int_{-\infty}^{\infty} \Re[\tilde{S}_m(\omega)]|\tilde{E}_L(\omega)|^2 d\omega, \quad (5)$$

where $\Re$ refers to the real part of an imaginary quantity. From Eq. (5), we see that if the laser and Mie spectra do not significantly overlap, then there will be very little laser energy absorbed. This case is illustrated in Fig. 2a, where we plot $|\tilde{E}_L(\omega)|^2$ and $\Re[\tilde{S}_m(\omega)]$ for typical laser–cluster interaction parameters. In the time domain, this means that the electron cloud motion x and the laser field oscillation are nearly in-phase, giving $\int vE_L = 0$ over a laser cycle. However, if there is significant overlap in the two spectra, as illustrated in Fig. 2b, then collisional heating can become large. In this case, the motion of the electron sphere will be dephased from the laser field oscillation, and $\int vE_L$ does not vanish over a laser cycle.

Throughout intense laser–cluster interaction, ionization and cluster expansion cause the Mie resonance to change as a function of time. If at some point during the interaction the overlap described above becomes large, and if this is sustained over a long enough time, significant collisional heating may occur. In the long-wavelength limit (visible and near-infrared), collisional heating does not play a role in the early stages of the laser pulse. This is because clusters have solid-state density, which by Eq. (2) gives ω_m much larger than the laser frequency. However, if Zn_i (and thus ω_m) is decreased sufficiently during the laser pulse (due to cluster explosion), and if the cluster explosion is at the same time not too rapid so that the resonance with the laser frequency is not passed through too quickly, collisional heating may occur to a significant degree.

Finally, we make a connection between the damped harmonic oscillator model discussed here and the familiar Drude-based model for cluster heating developed in Ref. [7]. Solving Eq. (1) in the linear regime, we find that the cycle-averaged rate of total laser energy absorption for $E_L = E_o \cos \omega t$ gives the well-known expression

$$\frac{dE_{tot}}{dt} = -|Q_e| < \dot{x}E_L > = 3\epsilon_o V_e \frac{\omega_m^2 \omega^2}{(\omega^2 - \omega_m^2)^2 + 4\nu^2\omega^2} \nu E_o^2, \quad (6)$$

where V_e is the volume of the electron sphere. The damped harmonic oscillator model for clusters can thus be understood as the same mechanism behind the Drude-based model.

Damping mechanisms. Damping of the collective Mie oscillation comes predominantly from two sources that contribute to ν: (1) scattering of individual electrons by the cluster surface [62] and (2) particle–particle scattering.

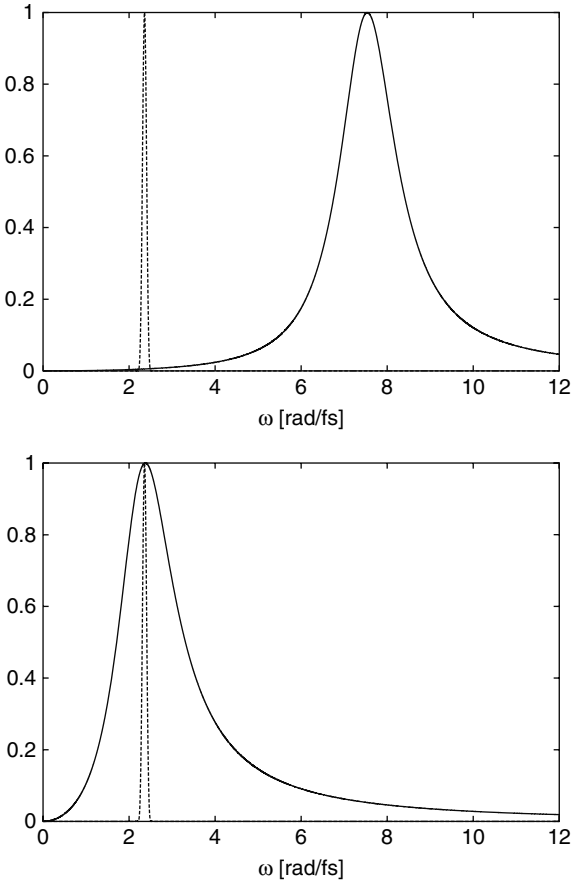

Fig. 2 Laser spectrum $|\tilde{E}_{\mathrm{L}}(\omega)|^2$ (*dashed line*) and the real part of the Mie spectrum $\Re[\tilde{S}_{\mathrm{m}}(\omega)]$ (*solid line*) versus angular frequency ω. The amplitudes of the spectra were normalized to one. The laser spectrum was calculated from a time-domain field envelope profile with $\sin^2$ shape, with a full width at half-max of 30 fs and a wavelength of 800 nm (corresponding to an angular frequency of 2.4 rad/fs). The parameters for the Mie spectrum in (**a**) are $Zn_{\mathrm{i}} = 5.4 \times 10^{22}\mathrm{cm}^{-3}$ (giving $\omega_{\mathrm{m}} = 7.5\,\mathrm{rad/fs}$) and $\nu = 0.8\,\mathrm{fs}^{-1}$, corresponding to typical laser–cluster interaction parameters. In this case, there is very little overlap between the spectra, so little collisional heating is expected. In (**b**), we set Zn_{i} to be an order of magnitude lower, which gives an ω_m near the laser frequency. In this case, there is a large overlap, and collisional heating could be a dominant heating mechanism, if the cluster explosion is not too rapid

When the ionic charge states are high, electron–ion collisions dominate over electron–electron collisions [66]. The scattering of individual electrons by ions in the presence of a laser field can lead to inverse Bremsstrahlung heating (IBH) [49]. In a recent work it was found that damping appears to be dominated by electron–ion collisions for shorter (20 fs), moderately intense ($10^{14} - 10^{15}$ W/cm^2) near-infrared laser pulses [67].

Recently, a new mechanism was proposed that may serve to enhance IBH [61]. Usual IBH rates are based on the assumption of a Coulombic ion potential, which is an approximation to the true potential, especially very close to the ion. A Hartree–Fock analysis of IBH from a noble gas ion shows that the true potential would enhance large angle scattering events, which yield the strongest contribution to heating. The analysis is based on a field-free Hartree–Fock calculation, i.e. it neglects the effect of the strongly fluctuating plasma electric field on the ionic bound state. In order to determine the IBH enhancement more accurately, a more detailed analysis taking into account the effect of the plasma electric field on the ionic bound state will be necessary.

4.2 Nonlinear Cluster Heating

The linear versions of Eqs. (1, 3) are only valid when the ion sphere is uniformly distributed and infinitely extended with no cluster surface. As discussed, presence of a boundary and/or non-uniformity gives rise to the nonlinear (anharmonic) terms in Eqs. (1, 3). The nonlinearity is thus a result of the macroscopic interaction between the electron sphere and the ion field, quite distinct from the microscopic interaction of individual electrons with the cluster surface. As discussed above, the latter phenomenon contributes to damping and randomizes the motion of the electrons. Instead, the nonlinear surface interaction gives rise to an energy absorption mechanism independent of microscopic collisions.

The nonlinear terms in Eqs. (1, 3) lead to (i) dephasing between electron cloud and laser, even in the case where there would be very little dephasing in the linear limit, and (ii) nonlinear motion of the electron cloud. Both effects result in energy absorption. This effect was first identified in Ref. [58], where it was termed "laser dephasing heating". Unfortunately, this name is not ideal, as it neither emphasizes the nonlinearity behind the process nor captures its distinctiveness from collisional/resonant heating. The nonlinearity-based mechanism due to the surface was confirmed in a subsequent work, where it was called "nonlinear resonant heating" [68]. This name is also somewhat misleading, since the nonlinear energy absorption process does not rely on a vicinity to a resonance. Therefore, we refer to this process here as "nonlinear cluster heating".

The importance of nonlinear cluster heating is seen in Fig. 3, where the velocity of the electron cloud (current) of an Ar_{10000} cluster during laser irradiation is plotted versus time [58]. The driving laser wavelength is 800 nm, the peak intensity is 8×10^{15} W/cm^2, and the pulse duration is 100 fs. The time interval included in Fig. 3 begins approximately 30 fs before the laser pulse peak. The solid line is the macroscopic current retrieved from numerical analysis. The dotted line is the current of a free electron in the laser field, which would be proportional to the vector potential of the laser field, $A(t) \propto \int E_L(t)$.

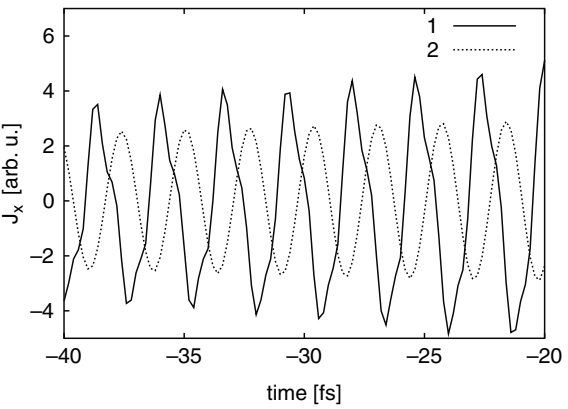

Fig. 3 (*1*) The macroscopic electron current in the direction of the laser field versus time, for a Ar_{10000} nanoplasma near the peak of a 800 nm, $8\times10^{15}W/cm^2$ laser pulse with a full width at half-maximum of 100 fs. (*2*) The current of a single free electron in the same laser field. Both plots were scaled to a similar size to facilitate comparison [58]

The motion of a free electron is in phase with the laser field and does not lead to energy absorption. Comparison of the two curves clearly shows a strong nonlinear component (higher harmonics) and dephasing. Since in this example the laser frequency is far from the Mie resonance throughout the laser pulse, the origin of the dephasing is the nonlinear interaction.[2]

Both collisional and nonlinear effects contribute to electron heating. Collisional heating plays a role for laser frequencies close to the Mie resonance, where it may be the dominant absorption mechanism. Whether resonance occurs or not depends on the specific experimental parameters. Coulomb explosion limits collisional heating to only a fraction of the laser–cluster interaction. Since nonlinear surface heating does not depend on resonance, it heats electrons over the whole cycle of the laser–cluster interaction. Sorting out which mechanisms prevail in which regions of parameter space remains an open issue.

5 Collective Versus Collisional Phenomena

Collective phenomena occur when microscopic particles respond to external perturbations coherently. In laser–cluster interaction, this occurs most strongly when the laser frequency is near resonance, possibly resulting in the excitation of a plasmon. Collisions destroy collective motion by transferring energy into random, thermal motion. If the collision time is small enough, collisional processes will dominate and destroy any collective motion before it has time to build.

---

[2] A recent estimate of nonlinear cluster heating indicated results that were too small to explain the total energy absorption [61]. The authors used the shielded laser field inside the cluster, E_s [7] for the calculation of the energy absorption, $\int_{-\infty}^{t}\dot{x}(t')E_s(t')$, rather than the full laser field, as required by Eq. (3).

Collision times are strongly affected by the interaction strength between particles. In plasmas, the interaction strength between electrons and between electrons and ions are characterized by electron–electron and electron–ion coupling parameters, defined, respectively, by [69]

$$\Gamma_{ee} = V_{ee}/k_B T_e,$$
$$\Gamma_{ei} = Z\,\Gamma_{ee}^{3/2},$$

where $k_B T_e$ is the average electron thermal energy and $V_{ee} = 1/a$ is the average electrostatic energy between neighbouring electrons. The average distance between electrons is $a = [3/(4\pi n_e)]^{1/3}$, where n_e is the electron density within the cluster. The parameter Γ_{ei} represents the ratio of ion to electron charge within the Debye sphere. The Debye length $\lambda_d = [T_e/(4\pi n_e)]^{1/2}$ determines the length over which charge fluctuations are screened by the electron plasma.

For $\Gamma_{ei} \leq 0.1$, corresponding to the limit of low particle density and high temperature, the plasma is "weakly coupled" and behaves as a macroscopic, fluid-like ensemble. In the high-density, low-temperature limit ($\Gamma_{ei} \geq 1$ and $\Gamma_{ee} \geq 0.1$) the plasma is "strongly coupled". In this regime, collisional processes dominate since they occur on timescales comparable to or faster than the oscillation time of collective effects.

We have shown in a recent work [67] that the coupling strength of the nanoplasmas created through laser interaction with noble gas clusters can be tailored through varying the laser intensity. This makes feasible both controlled experimental access to the transition region between strongly and weakly coupled plamas and a direct numerical analysis through molecular dynamics-type computational methods. We simulated Xe_{5000} and Xe_{500} cluster interaction with 20 fs, 800 nm laser pulses of varying intensity, and plot in Fig. 4 the coupling parameters Γ_{ei} (circles) and Γ_{ee} (squares) as determined at the end of the laser pulse [67]. Since higher-intensity pulses create hotter electrons, both

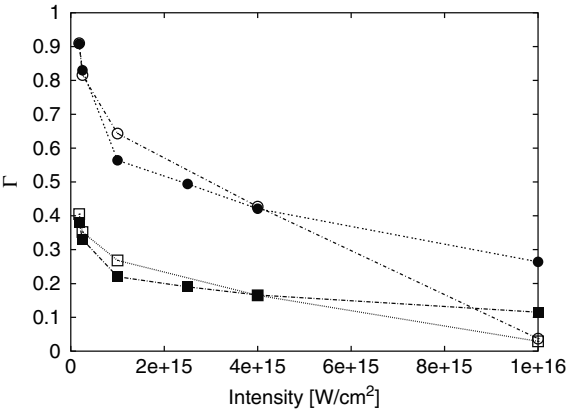

Fig. 4 Coupling parameters Γ_{ee} (*squares*) and Γ_{ei} (*circles*) for nanoplasmas created through the interaction of Xe_{5000} (*filled symbols*) and Xe_{500} (*open symbols*) with 20 fs, 800 nm laser pulses for intensities from 1.8×10^{14} to 10^{16} W/cm^2 [67]

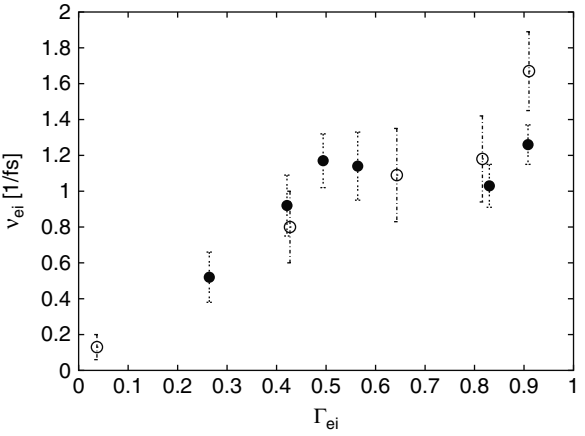

Fig. 5 Electron–ion collision frequency ν_{ei} for Xe_{5000} (*filled circles*) and Xe_{500} (*open circles*) nanoplasmas versus Γ_{ei} [67]

Γ_{ee} and Γ_{ei} become larger as the intensity is decreased. Both parameters span the range from weakly to strongly coupled and are largely cluster size-independent.

Clusters thus present an opportunity for a systematic, combined experimental and theoretical study of ultrafast electron kinetics in plasmas as a function of coupling strength. We conducted such a study through a numerical experiment that measures plasmon decay times for the nanoplasmas of Fig. 2 as a function of coupling strength in a pump-probe scenario. A plasmon is excited through a short second laser pulse near resonant to the Mie frequency. The plasmon decay time τ is extracted by fitting the electron current within the cluster (parallel to the laser electric field) to the damped oscillator model.

In Fig. 5 we plot $1/\tau$ versus Γ_{ei} for the Xe_{5000} (filled circles) and Xe_{500} (open circles) nanoplasmas. As coupling strength increases, so does the damping rate, from 0.1 fs^{-1} for $\Gamma_{ei} = 0.04$ to $\sim$1.5 fs^{-1} for $\Gamma_{ei} = 0.9$. The latter corresponds to 700 as. For $\Gamma_{ei} \sim 1$, we find $1/\tau \sim \omega_m/2\pi$, i.e. collective motion decays over one oscillation.

As discussed earlier, there are two possible damping mechanisms: particle–particle collisions and single electron collisions with the surface. Electron–ion collisions dominate over electron–electron collisions if the average ion charge state is high [66]. In our case, it ranges from 3.5 to 7.5. Damping via random, single electron–surface collisions is ruled out here by comparing the results for the two cluster sizes in Fig. 5. Thus $1/\tau$ is the electron–ion collision frequency ν_{ei}. Random surface collisions likely do not play a strong role in this regime for two reasons. First the average path an electron travels between surface collisions is enhanced for stronger coupling, due to many particle collisions. Second, since the cluster is positively charged, the electron distribution within the clusters thus has a smaller effective radius than the ion distribution. This leads to fewer random collisions with the cluster surface.

Experimentally, one could probe plasmon decay via loss absorption spectroscopy to measure the spectral width of the plasmon resonance. Since the decay time is comparable to the oscillation period for $\Gamma_{ei} \sim 1$, however, a broad source

spanning the whole spectral range is required. This makes time-domain experiments an interesting alternative. The technology required to extend four wave mixing pump-probe techniques – the workhorse of nonlinear femtosecond laser spectroscopy [70] – into the necessary wavelength (vacuum-ultra-violet), time (attosecond), and intensity regime is starting to be within reach [71].

6 Conclusion

The interaction of noble gas clusters with intense lasers is inherently rich and complex. While we have presented an overview of the major features of this interaction as it is currently understood, there are many open issues that remain due to this complexity. These range from the quantitative determination of the true ionization potentials in complex cluster fields, to the role of non-Coulombic potentials beyond the field-free approximation, to the determination of which heating mechanism dominates in which interaction regime. Though our discussion here was aimed primarily at long-wavelength radiation, first experiments and theoretical analyses in the VUV regime indicate there is much that needs to be resolved there as well. Understanding the details of laser–cluster interaction, while interesting in its own right, will also be an important stepping-stone to understanding the details of strong laser interaction with much larger systems, such as solid surfaces and bulk media, for which there are a host of potentially useful applications.

References

1. V.P. Krainov, and M.B. Smirnov, Phys. Rep. **370**, 237 (2002).
2. K. Boyer, and C.K. Rhodes, J. Phys. B: At. Mol. Opt. Phys. **27**, L633 (1994).
3. A. McPherson, B.D. Thompson, A.B. Borisov, K. Boyer, and C.K. Rhodes, Nature **370**, 631 (1994).
4. A.B. Borisov, A. McPherson, B.D. Thompson, K. Boyer, and C.K. Rhodes, J. Phys. B: At. Mol. Opt. Phys. **28**, 2143 (1995).
5. K. Kondo et al., J. Phys. B: At. Mol. Opt. Phys. **30**, 2707 (1997).
6. W.A. Schroeder et al., J. Phys. B: At. Mol. Opt. Phys. **31**, 5031 (1998).
7. T. Ditmire, T. Donnelly, A.M. Rubenchik, R.W. Falcone, and M.D. Perry, Phys. Rev. A **53**, 3379 (1996).
8. T. Ditmire, R.A. Smith, J.W.G. Tisch, and M.H.R. Hutchinson, Phys. Rev. Lett. **78**, 3121 (1997).
9. S. Dobosz et al., Phys. Rev. A **56**, R2526 (1997).
10. M. Lezius, S. Dobosz, D. Normand, and M. Schmidt, J. Phys. B: At. Mol. Opt. Phys. **30**, L251 (1997).
11. J. Zweiback, T. Ditmire, and M.D. Perry, Phys. Rev. A **59**, R3166 (1999).
12. S. Ter-Avetisyan et al., Phys. Rev. E **64**, 036404 (2001).
13. M. Schnürer et al., Eur. Phys. J. D **14**, 331 (2001).
14. E. Parra, I. Alexeev, J. Fan, K.Y. Kim, S.J. McNaught, and H.M. Milchberg, Phys. Rev. E **62**, R5931 (2000).
15. V. Kumarappan, M. Krishnamurthy, D. Mathur, and L.C. Tribedi, Phys. Rev. A **63**, 023203 (2001).

16. V. Kumarappan, M. Krishnamurthy, and D. Mathur, Phys. Rev. Lett. **87**, 085005 (2001).
17. E. Springate et al., Phys. Rev. A **61**, 063201 (2000).
18. M. Lezius, S. Dobosz, D. Normand, and M. Schmidt, Phys. Rev. Lett. **80**, 261 (1998).
19. G.C. Junkel-Vives et al., Phys. Rev. A **64**, 021201(R) (2001).
20. J. Abdallah Jr. et al., Phys. Rev. A **63**, 032706 (2001).
21. K.Y. Kim et al., Phys. Rev. A **71**, 011201(R) (2005).
22. H. Honda, E. Miura, K. Katsura, B. Takahashi, and K. Kondo, Phys. Rev. A **61**, 023201 (2000).
23. M. Mori et al., J. Appl. Phys. **90**, 3595 (2001).
24. H. Wabnitz et al., Nature **420**, 482 (2002).
25. T. Laarmann et al., Phys. Rev. Lett. **92**, 143401 (2004).
26. Private communication, Thomas Moeller.
27. L. Köller, et al., Phys. Rev. Lett. **82**, 3783 (1999).
28. E.E.B. Campbell, et al., Phys. Rev. Lett. **84**, 2128 (2000).
29. V.R. Bhardwaj, P.B. Corkum, and D.M. Rayner, Phys. Rev. Lett. **91**, 203004 (2003).
30. M. Smits, C.A. de Lange, A. Stolow, and D. M. Rayner, Phys. Rev. Lett. **93**, 203402 (2004).
31. T. Döppner, Th. Fennel, Th. Diederich, J. Tiggesbäumker, and K. H. Meiwes-Broer, Phys. Rev. Lett. **94**, 013401 (2005).
32. F. Calvayrac, P.-G. Reinhard, E. Suraud, and C.A. Ullrich, Phys. Rep. **337**, 493 (2000).
33. E. Springate, S.A. Aseyev, S. Zamith, and M.J.J. Vrakking, Phys. Rev. A **68**, 053201 (2003).
34. S. Sakabe et al., Phys. Rev. A **69**, 023203 (2004).
35. M. Krishnamurthy et al., J. Phys. B: At. Mol. Opt. Phys. **39**, 625 (2006).
36. T. Ditmire et al., Nature **398**, 489 (1999).
37. J. Zweiback et al., Phys. Rev. Lett. **84**, 2634 (2000).
38. K.W. Madison et al., Phys. Rev. A **70**, 053201 (2004).
39. S.B. Hansen et al., Phys. Rev. E **71**, 016408 (2005).
40. K.B. Fournier et al., Phys. Rev. Lett. **67**, 016402 (2003).
41. Y. Fukuda et al., Phys. Rev. A **67**, 061201 (2003).
42. R.C. Issac et al., Phys. Plasmas **11**, 3491 (2004).
43. J.A. King et al., Rev. Sci. Inst. **76**, 076102 (2005).
44. T. Ditmire, R.A. Smith, and M.H.R. Hutchinson, Opt. Lett. **23**, 322 (1998).
45. V. Kumarappan, K.Y. Kim, and H.M. Milchberg, Phys. Rev. Lett. **94**, 205004 (2005).
46. I. Last, and J. Jortner, Phys. Rev. A **62**, 013201 (2000).
47. H.M. Milchberg, S.J. McNaught, and E. Parra, Phys. Rev. E **64**, 056402 (2001).
48. C. Rose-Petruck, K.J. Schafer, K.R. Wilson, and C.P.J. Barry, Phys. Rev. A **55**, 1182 (1997).
49. V.P. Krainov, Sov. Phys. – JETP **92**, 960 (2001).
50. M.B. Smirnov, and V.P. Krainov, Phys. Plasmas **10**, 443 (2003).
51. M.B. Smirnov, and V.P. Krainov, Phys. Rev. A **69**, 043201 (2004).
52. T. Bornath, P. Hilse, and M. Schlanges, Laser Phys. **17**, 591 (2007).
53. A.V. Gets, and V.P. Krainov, J. Phys. B **39**, 1787 (2006).
54. C. Siedschlag, and J.M. Rost, Phys. Rev. Lett. **89**, 173401 (2002).
55. U. Saalmann, and J.M. Rost, Phys. Rev. Lett. **91**, 223401 (2003).
56. C. Siedschlag, and J.M. Rost, Phys. Rev. Lett. **93**, 043402 (2004).
57. R. Santra, and C.H. Greene, Phys. Rev. Lett. **91**, 233401 (2003).
58. C. Jungreuthmayer, M. Geissler, J. Zanghellini, and T. Brabec, Phys. Rev. Lett. **92**, 133401 (2004).
59. C. Jungreuthmayer, L. Rammuno, J. Zanghellini, and T. Brabec, J. Phys. B **38**, 3029 (2005).
60. M. Krishanmurthy et al., J. Phys. B **39**, 625 (2006).
61. C. Deiss et al., Phys. Rev. Lett. **96**, 013203 (2006).

62. Ph.A. Korneev, S.V. Popruzehnko, S.F. Zaretsky, and W. Becker, Las. Phys. Lett. **2**, 452 (2005).
63. W.L. Kruer, *The physics of laser plasma interactions*, Westview Press, Colorado (2003).
64. P. Mulser, and M. Kanapathipallai, Phys. Rev. A **71**, 063201 (2005).
65. L. D. Landau, and E.M. Lifshitz, *Mechanics*, Pergamon Press, Oxford (1960).
66. E.M. Lifshitz, and L.P. Pitaevskii, *Kinetic Theory*, Pergamon Press, Oxford (1981).
67. L. Ramunno, C. Jungreuthmayer, H. Reinholz, and T. Brabec, J. Phys. B: At. Mol. Opt. Phys. **39**, 4923 (2006).
68. M. Kundu and D. Bauer, Phys. Rev. Lett. **96**, 123401 (2006).
69. S. Ichimaru, *Statistical Plasma Physics Volume II: Condensed Plasmas*, Westview Press, Colorado (2004).
70. Y.L. Shen, *The principles of nonlinear optics*, Wiley, New York (1984).
71. M.Y. Shverdin, D.R. Walker, D.D. Yavuz, G.Y. Yin, and S.E. Harris, Phys. Rev. Lett. **94**, 033904 (2005).

Laser-Induced Optical Breakdown in Solids

Matthias Lenzner and Wolfgang Rudolph

1 Introduction

One of the unique features of femtosecond light pulses is the high peak power at moderate pulse energies, which enables many interesting applications in fundamental and applied science. When interacting with condensed matter, irreversible material changes occur if the pulse fluence exceeds a certain critical value. On one hand, such processes severely limit the performance of optical components such as coatings and windows (laser damage) and are undesired. On the other hand, permanent laser-induced material modifications have found interesting applications for laser micro- and nanostructuring as well as for the production of three-dimensional waveguides.

Laser-induced breakdown has been studied since the invention of the laser using ever shorter pulses. The underlying physical processes are very complex as they involve matter far from thermal equilibrium under excitation conditions where perturbative approaches known from nonlinear optics fail.

The primary energy deposition in dielectric materials with UV, VIS, and NIR pulses is through the electronic system, followed by energy transfer to the lattice and resulting in material ablation if a certain excitation fluence is exceeded. Although the actual damage mechanisms depend on the material under study and are still an area of active research (and controversy), much can be learned from the initial excitation of the electrons. As an illustration, Fig. 1 shows the fluence region of a 100 fs pulse for which damage in wide-gap materials occurs together with some important benchmarks of light–matter interaction. At low fluences, region A, the interaction leads to anharmonic oscillations of bound electrons, which can trigger processes like self-phase modulation. With increasing fluence, the binding potential is changed under the influence of the external electric field up to a point where the probability

M. Lenzner
Department of Physics, City College of CUNY, Convent Ave & 138th Street,
New York, NY 10031, USA
e-mail: mlenzner@sci.ccny.cuny.edu

T. Brabec (ed.), *Strong Field Laser Physics*,
DOI: 10.1007/978-0-387-34755-4_11,

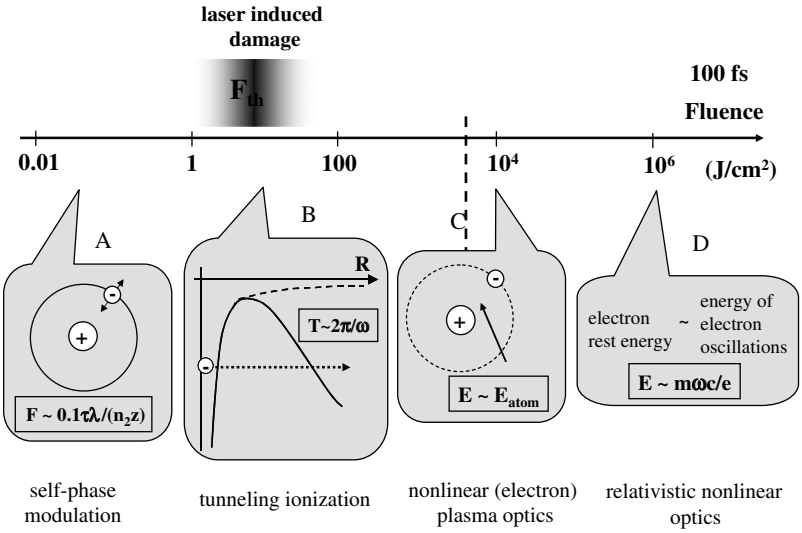

Fig. 1 Examples of laser pulse–electron interaction for different fluences, see, for example, [1, 2]. The range of typical threshold fluences for laser-induced damage is indicated. A: The fluence at which the pulse spectrum approximately doubles in a z = 1 mm dielectric plate of nonlinear index n_2 is shown

that the electron can tunnel (ionization) during one optical period $2\pi/\omega$ approaches unity, region B. At larger fluences, region C, the laser field approaches the Coulomb field between an electron and nucleus as a result of which the electron dynamics is driven by the external field with the nucleus as a perturbation. At even higher fluences, region D, the energy of the electron accelerated in the laser field reaches the rest mass energy, resulting in relativistic effects. The damage fluences of most dielectric materials are within a relatively narrow fluence region close to region B, but well below regions C and D. If we identify a permanent laser-induced material modification with damage, the fluence region can be divided into two parts with a well-defined boundary. Below this boundary, some material properties, e.g., the refractive index, are changed without material ablation; at the boundary (threshold fluence F_{th}) and at higher fluences the material breaks down and is ablated.

In this chapter, we review the energy deposition mechanisms that can lead to femtosecond laser-induced breakdown and ablation in solids. We will concentrate on wide-gap dielectric materials and only briefly mention important features in the interaction with (narrow-gap) semiconductors and metals. We will conclude with an introduction of fs laser-based material structuring as an emerging application.

2 Damage Induced by Nano- and Picosecond Pulses

Since the invention of the laser, numerous research groups have studied optical damage with laser pulses at various wavelengths and pulse durations [3, 4, 5, 6]. A large class of commonly used (bulk) optical materials [7], optical coatings [8, 9], and more recently liquids [10, 11] (important, e.g., for ophthalmic surgery) have been investigated. In parallel to the experimental work, significant efforts have been made to develop theoretical models of optical breakdown in dielectric materials.

Being intrinsically transparent to VIS–NIR pulses, dielectric materials are excited via heating of electrons in the conduction band (CB) involving quasi-free electron absorption followed by impact ionization. At a certain electron density, the plasma becomes highly absorptive for the remainder of the pulse leading to melting and evaporation of material (ablation). If (linear) absorption centers (as a source for CB electrons) are absent, the optical pulse acts on background carriers [12, 13, 14, 15] in the CB. Because of their stochastic distribution, the threshold fluence for ps and ns pulses exhibits relatively large fluctuations [16].

With ns and ps pulses, a dependence of the damage fluence F_{th} on the pulse duration τ_{p}, $F_{\mathrm{th}} \propto \tau_{\mathrm{p}}^{\kappa}$ where $\kappa \approx 1/2$, was found for bulk materials [17, 18, 19, 20] and coatings [8, 21]. This $\sqrt{\tau_{\mathrm{p}}}$ dependence is characteristic of situations where one-dimensional transport of the excitation occurs during the pulse. For example, the pulse is absorbed in a thin surface layer (spot area A), the produced heat propagates normal to the surface (z direction), and lateral diffusion can be neglected (spot size $>>$ absorption depth). The pulse deposits an energy $\alpha_{\mathrm{a}} W$, which is distributed over a volume $A\sqrt{D\tau_{\mathrm{p}}}$ during the pulse, with α_a being the absorption coefficient and D being the heat diffusion constant. The corresponding temperature change $\Delta T = \kappa\alpha_{\mathrm{a}} W/(A\sqrt{D\tau_{\mathrm{p}}})$ will lead to damage (melting) if a certain threshold value (melting temperature) is reached. The corresponding incident laser fluence $F_{\mathrm{th}} = W_{\mathrm{th}}/A \approx Q\sqrt{\tau_{\mathrm{p}}}$ where Q contains the material parameters exhibits the $\sqrt{\tau_{\mathrm{p}}}$ dependence. A more rigorous approach involves solving the diffusion equation for the half space. The solution shows the surface temperature to also increase as $\Delta T \propto F/\sqrt{\tau_{\mathrm{p}}}$ [5]. A similar $\sqrt{\tau_{\mathrm{p}}}$ law controlled by heat diffusion was found when small (linear) absorption centers (impurities or defects) are present [8, 22, 23] and the absorbed laser power scales as πa^2 (a – radius of the inclusion).

3 Damage Induced by Femtosecond Laser Pulses

A deviation from the $\sqrt{\tau_{\mathrm{p}}}$-scaling of the breakdown threshold was first reported for pulses in the range of 4–10 ps [24]. Later, this deviation was confirmed for the case of femtosecond pulses, see Fig. 2 for example. The damage threshold with fs pulses is more deterministic as compared with longer pulses; stochastic background electrons in the CB lose their importance as photoionization of valence band (VB) electrons takes over owing to the high field strength of fs

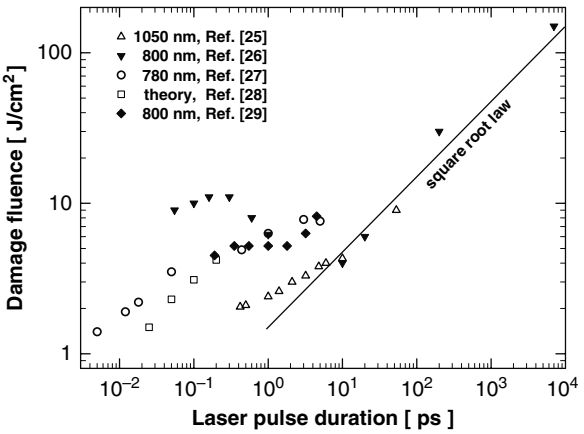

Fig. 2 Damage fluence thresholds of fused silica. All experiments are performed with multiple pulses in air. Data are from references [25, 26, 27, 28, 29]

pulses. As a consequence, damage is more likely be controlled by the intrinsic material properties of bulk and thin-film samples.

Numerous experimental studies dealt with the dependence of the critical pulse fluence F_{th} on the pulse duration τ_p [9, 27, 30, 31, 32, 33], the laser wavelength λ [30, 34, 35, 36], and the material [9, 27, 30, 32, 34, 35, 36]. These experiments were conducted on fluorides, oxides, and glasses using near infrared and visible laser pulses with durations as short as a few femtoseconds.

The actual processes leading to femtosecond laser pulse-induced dielectric breakdown and ablation are complex and still under investigation. Proposed mechanisms for material breakdown and removal include Coulomb explosion [37], plasma formation [38], thermal melting (heterogeneous and homogeneous nucleation) [37, 38], and material cracking due to thermoelastic stresses [39]. Most of the damage processes occur after the optical pulse for $\tau_p < 100$ fs.

Common to all these scenarios is that a critical amount of energy density has to be deposited in the material before breakdown occurs. In the sub-ps pulse regime, the absorption of near IR photons in dielectrics leads to the excitation of electrons to the CB. Models that identify the onset of damage with the production of a certain critical CB electron density N_{cr} were suggested early on [18] and proved successful in explaining the observed $F_{th}(\tau_p)$ behavior until today [27, 30, 31, 33]. The exact value of this critical density is not known. One limit was defined by using an excited electron density at which the energy in the excited electron system equals the binding energy of the lattice [40]. For alkali-halides, for example, this requires an electron density of about 10^{19} cm^{-3} [7]. Another critical density was introduced by setting the plasma frequency equal to the excitation frequency [41]. At this point, the material starts to absorb strongly. For laser pulses at 800 nm this happens at $N_{cr} \approx 10^{21}$ cm^{-3}. After the critical electron density is reached, melting, vaporization, and ablation start. There are indications that the critical electron density may also depend on the pulse duration [42].

4 Light–Matter Interaction

Figure 3 illustrates the main processes associated with the excitation of dielectric materials with femtosecond pulses.

Photoionization and impact ionization produce CB electrons until a critical density is reached. One can formally write a rate equation for the CB electron density n:

$$\frac{\mathrm{d}n}{\mathrm{d}t} = \alpha + \beta - \vartheta, \tag{1}$$

where α and β are the rates for impact and photoionization, respectively. ϑ is a relaxation term taking into account electron trapping [9, 43]. The latter term can explain the pulsewidth dependence of the threshold in dual-pulse ablation experiments [43].

4.1 Photoionization

In metals and most semiconductors of practical interest, the radiation of available femtosecond sources is absorbed via linear (one-photon) or free carrier absorption. In either case, Beer's law applies and assuming a certain quantum efficiency, ionization rates and resulting electron densities can be calculated easily. Saturation effects and plasma shielding have to be taken into account at high electron densities. The so-excited electron

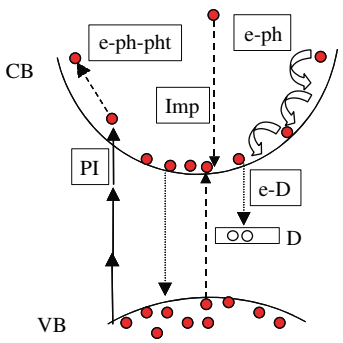

Fig. 3 Schematic diagram of energy deposition and dissipation in wide-gap dielectric materials through excitation of electrons from the valence band (VB) to the conduction band (CB) in the presence of defect states (D). Contributing processes are photoionization (PI), impact ionization (Imp), electron–phonon–photon scattering (e–ph–pht, free carrier absorption), electron–phonon scattering (e–ph, cooling of the electron gas), electron–electron scattering (e–e), and electron-defect interaction (e-D) including the creation of self-trapped excitons

system interacts with the lattice, which can be described by the two-temperature model [44].

The physics of dielectric materials having a bandgap energy that is larger than the photon energy of the incident laser pulse, $\mathcal{E}_g > \hbar\omega$, is more sophisticated. In the absence of states within the energy gap (due, for example, to defects or traps), the deposition of energy has to take place via a nonlinear optical process.

Initially, electron–hole pairs are excited by high-field excitation. This phenomenon was described more than 40 years ago by Keldysh [45]. According to this model, electrons are promoted to the conduction band by a combination of what is usually called multiphoton ionization (MPI) and tunneling ionization. Keldysh's theory emphasized that MPI and tunneling are not competing mechanisms but merely two limiting cases of the same ionization process.

For ionization to occur, the electron has to overcome the atomic potential modified by the incident electric field. The Keldysh parameter

$$\gamma = \omega\tau = \frac{\omega}{|eE|}\sqrt{m_r \mathcal{E}_g} \tag{2}$$

roughly represents the ratio of the time τ needed to tunnel through the resulting potential barrier and the period of the oscillating electric field, $T = 2\pi/\omega$. The quantity $\mathcal{E}_g$ is the ionization potential, m_r and e are the effective mass and charge of the electron, respectively. A Keldysh parameter $\gamma \ll 1$ means that the electron has enough time for tunneling before the field changes magnitude and sign (see Fig. 4 C). In this limit tunneling ionization is the dominant excitation mechanism. In the other limit, $\gamma \gg 1$, multiphoton absorption plays the major role in the ionization (see Fig. 4 A). According to [45], the ionization rate can be written as

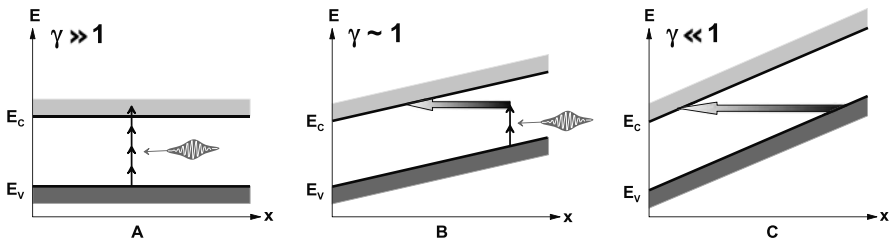

Fig. 4 Band model of high-field laser excitation of a wide-gap solid. The laser pulse intensity is increasing from A to C. The gradient of the potential (tilt of the band structure) is caused by the electric field of the laser pulse. E_C is the lower boundary of the conduction band, E_v is the upper boundary of the valence band, γ is the Keldysh parameter explained in the text

$$\beta = \frac{2\omega}{9\pi}\left(\frac{\omega m_r}{\gamma_1 \hbar}\right)^{3/2} Q(\gamma, x) \times \exp\left\{-\pi\langle x+1\rangle \frac{K(\gamma_1) - L(\gamma_1)}{L(\gamma_2)}\right\}, \tag{3}$$

where $\gamma_1 = \gamma/\sqrt{1+\gamma^2}$, $\gamma_2 = \gamma_1/\gamma$, K, L are complete elliptical integrals of first and second order, respectively, $\langle z\rangle$ denotes the integer part of z, and

$$Q(\gamma, x) = \left(\frac{\pi}{2K\sqrt{2}}\right)^{1/2} \sum_{k=0}^{\infty}\left[-k\pi \frac{K(\gamma_1) - L(\gamma_1)}{L(\gamma_2)} \times \Phi\left(\pi\sqrt{\frac{2\langle x+1\rangle - 2x + k}{2K(\gamma_2)L(\gamma_2)}}\right)\right], \tag{4}$$

$$x = \frac{2\varepsilon_g}{\pi\hbar\omega\gamma_1} L(\gamma_2), \tag{5}$$

with $\Phi(z) = \int_0^z \exp(y^2 - z^2)\mathrm{d}y$.

As explained above, the derived formula for the excitation rate reduces to multiphoton absorption in the high-frequency limit and to the equation for tunneling at low frequencies and strong fields. Figure 5 shows the ionization rate according to the Keldysh model as a function of laser intensity. At low fluences ($\gamma \gg 1$), a simple multiphoton absorption model fits the data well. The sudden changes in the ionization rates occur at excitation intensities where the – now increased–effective bandgap reaches a value that requires an additional photon for excitation. Even though the Keldysh model needs to be modified for a more accurate description (see, for example, [46, 47]), it explains the main features of the excitation well.

Recently, there has been theoretical work about the enhancement of photoionization due to the presence of already ionized electron–hole pairs [48]. The electrical field of these pairs superposes the electrical field of the light wave and thereby leads to an exponential enhancement of the photoionization rate as well

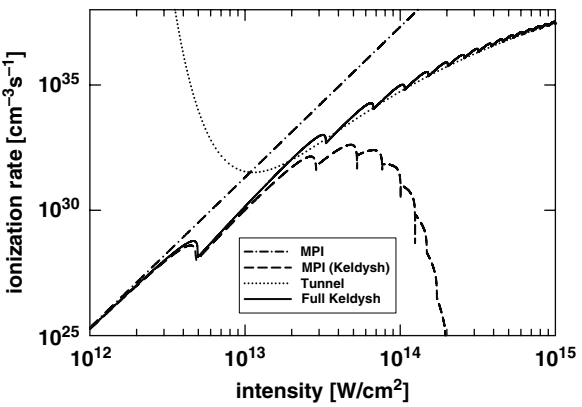

Fig. 5 Calculated photoionization rates as a function of laser intensity for $\lambda_0 = 800\,\mathrm{nm}$ in quartz ($\mathcal{E}_g = 9\,\mathrm{eV}$). MPI is 6-photon-ionization with a rate $\sigma_6 I^6$ and $\sigma_6 = 2.1 \times 10^{-47}\mathrm{cm}^9\mathrm{s}^{-1}\mathrm{W}^{-5}$

as the impact ionization rate (see below). This additional ionization is supposed to supersede the traditional avalanche ionization for pulses shorter than ≈10 fs which is about the time for an electron to be accelerated to an energy sufficient for impact ionization [49].

4.2 Impact Ionization

Electrons that are excited into the conduction band are continuously accelerated by the laser field. Energy deposition into the electron system is possible because momentum conservation is assured by the interaction with lattice phonons; this process is known as free carrier absorption. After reaching a critical value, the excess energy of these electrons can be transferred to valence electrons by impact, promoting these to the conduction band (impact ionization) see Fig. 6.

As a consequence, the conduction band electron density grows exponentially. The impact ionization rate from Equation (1) can formally be written as

$$\alpha = \alpha_f(E)n, \tag{6}$$

where $\alpha_f(E)$ is the impact ionization coefficient. This equation stems from the DC avalanche breakdown in gases and crystals but has been shown to apply to laser pulse-induced breakdown as well [12, 50].

The dependence of α_f on the electric field E is difficult to derive because α_f contains information about two physical processes: free carrier absorption and impact ionization. In an effort to find an analytical approach that describes a broad class of dielectric materials, several models have been developed. A common ansatz is Keldysh's impact ionization formula:

$$\alpha_f = \eta[(\mathcal{E} - \mathcal{E}_c)/\mathcal{E}_c]^2, \tag{7}$$

where η is a constant and $\mathcal{E}$ is the kinetic energy of the electron [28]. Up to this point, almost all publications modeling dielectric breakdown with rate

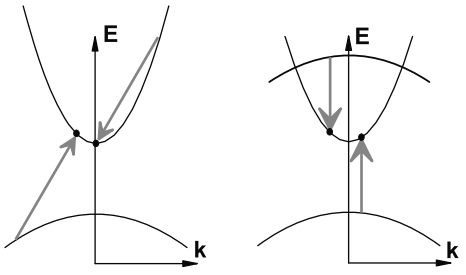

Fig. 6 Two possible paths of impact ionization. An electron, highly excited into the conduction band by free carrier absorption, ionizes a second electron from the valence band, observing energy and momentum conservation

equations agree. However, the size of the assumed constants η differs as well as the postulated critical energy $\mathcal{E}_c$.

In order to fulfill energy and momentum conservation, the free electron needs to be promoted to a critical energy $\mathcal{E}_c$ [28, 45, 51]:

$$\mathcal{E}_c \approx 1.5\left(\varepsilon_g + \frac{e^2E^2}{4m_r\omega^2}\right). \tag{8}$$

Equation (8) contains the sum of the bandgap energy and the ponderomotive potential, i.e., the energy of the electron oscillating in the laser field; the factor 1.5 results from the common assumption that the effective electron and hole mass are equal at the extrema of CB and VB. The "flux-doubling" model [15, 30, 52, 53] assumes that (i) as soon as an electron acquires the critical energy it ionizes a second electron and the excess energy is equally distributed between the collision partners and (ii) the shape of the electron distribution remains basically unchanged during the laser pulse. This model yields an impact parameter that is proportional to the field squared, i.e., $\alpha_f(E) = \alpha_i I$, where $\mathrm{I} \propto \mathrm{E}^2$ is the pulse intensity. This approach is strictly applicable only for photon energies sufficiently small compared to the bandgap energy [14].

There is another estimate where the impact ionization coefficient $\alpha_f(E)$ is proportional to E in the high-field limit [54]. This model, developed for DC high-field electronic transport, considers a nonuniform distribution of electrons in the conduction band. It was used to explain the increasing threshold fluences for very short pulses (see Fig. 2) [31].

A quantum-mechanical method to calculate "the rate at which conduction band electrons absorb energy" (i.e., free carrier absorption) is employed in [55]. Here, the calculated absorption rate (which is significantly different from the classical one) is used as starting point to calculate the avalanche coefficient using the flux-doubling model.

Because the agreement between these models and experimental results is sometimes unsatisfactory, more sophisticated numerical models are established to describe the temporal evolution of the electron gas in the conduction band. In Ref. [28], for example, Equation (7) was replaced by a completely quantum-mechanical description. Here, the impact ionization contribution to the development of the distribution function in the Boltzmann equation was calculated from a collision integral. This approach, usually referred to as "full kinetic model" involves an extensive numerical apparatus but it allows to treat free carrier absorption and impact ionization separately, quantum-mechanically. It also considers the energy dependence of these processes [49, 56]. More recently, a set of rate equations were developed that use discrete electronic levels in the conduction band to account for the dependence of the impact ionization rate on the electron energy [57].

In summary, impact ionization in dielectric materials with femtosecond pulses will remain an interesting research area for years to come because of

the vast complexity of processes involved. For example, the role of the actual band structure of the material under investigation is largely unexplored.

4.3 Scaling Laws

Many experimental observations concerning the threshold fluence behavior and also its order of magnitude could be explained by the rate Equation (1) when the impact ionization term was approximated by $\alpha = \alpha_i n I$ and the PI term by the multiphoton absorption term $\beta = \beta_m I^m$. It is instructive to look at the predictions of this model concerning the dependence of the damage fluence on the bandgap with the assumption that the $\mathcal{E}_g$ dependence stems from $\beta(\mathcal{E}_g)$. Under certain conditions [58], one can derive from Keldysh's theory [45]:

$$\beta_m \approx \frac{\omega}{9\pi}\left(\frac{m_r \omega}{\hbar}\right)^{3/2}\left(\frac{e^2}{8\omega^2 m_r c\varepsilon_0}\right)^m \frac{\exp(2m)}{(n_0\mathcal{E}_g)^m}, \tag{9}$$

where ω is the carrier angular frequency of the laser pulse, $m = \mathrm{mod}(\mathcal{E}_g/\hbar\omega)$ is the order of the multiphoton absorption process, m_r is the reduced mass, e is the electron charge, c is the velocity of light in vacuum, and n_0 is the refractive index. In a broad parameter range for the impact ionization coefficients and sub-ps pulse durations, this $\beta(\mathcal{E}_g)$ results in an approximately linear increase of F_{th} with $\mathcal{E}_g$ [9]. There is experimental evidence supporting these results, see Fig. 7.

4.4 Multiple Pulse Effects

The damage threshold of dielectric materials typically decreases with the number of pulses that illuminate one and the same sample site. This phenomenon,

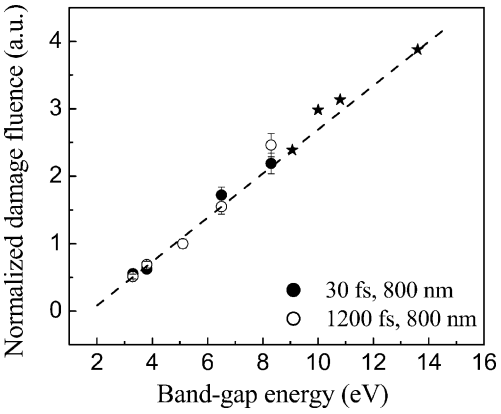

Fig. 7 Measured F_{th} as a function of bandgap energy. To illustrate the similar slopes of the data sets, the data points were normalized to the damage fluence at 5.1 eV. *Circles*–oxide films [9], *asterisks*–1053 nm, 400 fs, fluoride bulk materials [30]

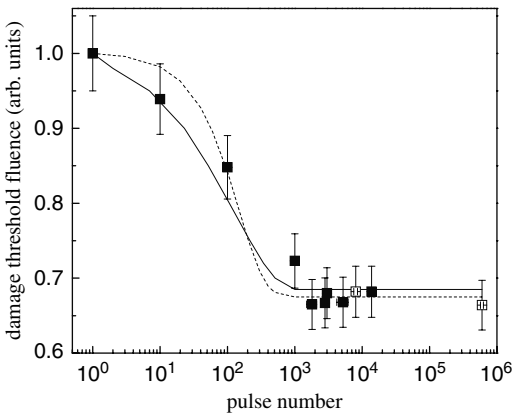

Fig. 8 Damage fluence vs number of pulses ($\tau \approx 30$ fs, 1 kHz repetition rate) on the same sample spot (*squares*). The lines represent modeling results (*dashed line*–Equation (11), *solid line*–numerical model) from [60]. The sample was a Ta_2O_5 film deposited on fused silica

sometimes called incubation, has been observed for different pulse repetition rates and pulse durations [4, 31, 32, 33, 53, 59, 60]. An example is shown in Fig. 8.

The international organization for standardization recommends a phenomenological fit function that relates the single pulse damage fluence $F_{\mathrm{th},1}$ to the M-pulse threshold

$$F_{\mathrm{th}}(M) = F_{\mathrm{th},\infty} + \frac{F_{\mathrm{th},1} - F_{\mathrm{th},\infty}}{1 + \Delta^{-1}\log_{10}(M)}, \tag{10}$$

where Δ is a fit parameter [61].

In wide-gap materials, optical excitation can result in the formation of self-trapped excitons (STEs) and color centers [53, 62, 63, 64, 65], cf. Fig. 3. These excitations can be long lived with lifetimes up to months at room temperature depending on the material. The formation of STEs following optical excitation usually proceeds on a ps or sub-ps time scale [43, 66, 67]. While most likely not critically important for single pulse exposures, the accumulation of such defect states that can act as additional absorption centers affects the multiple pulse damage behavior. Since these defect states are within the bandgap, an absorption of lower nonlinear order than what is necessary for an interband transition suffices, increasing the absorption with pulse number. Indeed, a model taking into account such processes can explain the principal $F_{\mathrm{th}}(M)$ behavior, cf. Fig. 8. For a material that can be excited by a three photon absorption, for example,

$$F^3_{\mathrm{th}}(M) = F^3_{\mathrm{th},\infty} + \left[F^3_{\mathrm{th},1} - F^3_{\mathrm{th},\infty}\right]\left(1 - \frac{T_{VB}}{T_S}B\right)^{M-1}, \tag{11}$$

where T_S, T_{VB}, and B is the formation time of defects (STEs), the interband recombination time, and the ratio of N_{cr} and the maximum possible defect density, respectively [60].

5 Applications

The advantage of material processing with femtosecond pulses is most obvious for wide-gap dielectrics, which are transparent to near infrared and visible laser light. Unlike for (linearly) absorbing materials such as metals and semiconductors, cw-high-power laser machining can be utilized for dielectric materials only to a limited extent. Not only can the high peak power of femtosecond pulses turn these materials into absorbing targets, but also the involved nonlinear absorption processes cause a high degree of spatial confinement (in three dimensions) of the deposited energy. This together with the associated deterministic breakdown thresholds makes femtosecond machining attractive [25, 27, 29, 34, 68] in particular for microstructuring. This application field also matches the commercially available fs laser systems with limited average power, typically not exceeding 10 W.

Several noteworthy features of femtosecond laser ablation (as opposed to machining with nanosecond pulses) have been observed:

- It is possible to process transparent materials.

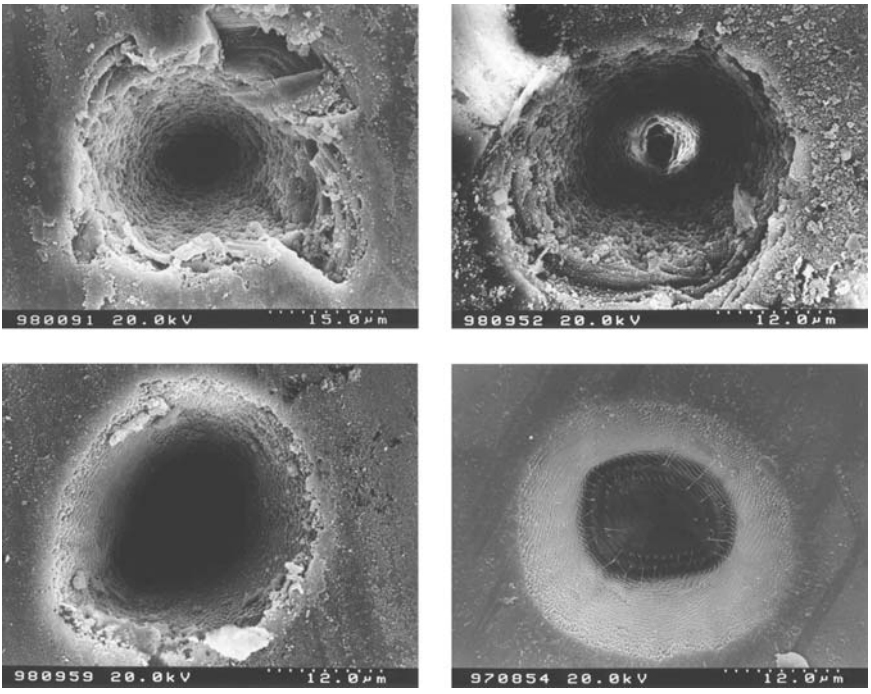

Fig. 9 Scanning electron micrographs of fused silica ablated by ultrashort laser pulses with a peak fluence of F_0. $\lambda = 780\,\text{nm}$, 80 shots. Pulse duration and fluence are (*upper left*) $\tau_p = 3\,ps, F_0 = 19.9\ \text{J/cm}^2$, (*upper right*) $\tau_p = 220\,\text{fs}, F_0 = 10.7\ \text{J/cm}^2$, (*lower left*) $\tau_p = 20\,\text{fs}, F_0 = 11.1\ \text{J/cm}^2$, (*lower right*) $\tau_p = 5\,\text{fs}, F_0 = 6.9\ \text{J/cm}^2$

- More regular damage patterns as well as a higher reproducibility of structures from shot to shot are found [69].
- High intensities in the focal region at low average power result in low thermal load to the surrounding material and the material in the beam path.
- The penetration depth of the pulses can be controlled by changing the pulse duration; it can be as low as 100 nm [27].
- Only a small fraction of pulse energy is converted to heat and momentum (small heat-affected zone or shock-affected zone) [70].

To qualitatively demonstrate this phenomenon, typical ablation pictures for fused silica taken from a scanning electron microscope are shown in Fig. 9. Holes for different pulse durations between 5 fs and 3 ps were machined with 80 pulses from a Ti:sapphire laser system at a repetition rate of 1 kHz. It is obvious that the 5 fs ablation morphology (Fig. 9, lower right) is much more deterministic than in the case of longer pulses (Fig. 9, upper row). Differences are visible even when compared with the 20 fs pulses (Fig. 9, lower left). Although the applied fluence is higher for the picosecond pulses, it amounts to the same multiple of the damage threshold fluence for all pulse durations. The more stochastic behavior of long-pulse ablation as explained in Section 2 accounts for the difference in edge quality.

Femtosecond lasers are not necessarily advantageous for the processing of linearly (in the NIR–VIS) absorbing materials such as metals or semiconductors since the energy deposition itself does not depend much on pulse duration. In most materials, the electrons transfer the energy to the lattice on a time scale of a few ps, after which melting and evaporation occur. By carefully choosing the parameter range (wavelength, pulse duration, fluence) of the processing laser, one can structure these materials with the same high precision using more cost-efficient, longer-pulse, laser systems.

Another interesting application of high-intensity laser pulses is processing of transparent materials *within* the bulk. Not only can decorative accessories be produced this way, but also three-dimensional optical waveguides can be written within the materials [71]. The physical mechanism of this permanent modification of the refractive index is not completely resolved. Structural changes of the atomic network rather than optical breakdown are likely to occur [72]. At higher intensities, material can also be ablated if the debris is removed by, e.g., a wetting fluid. Microfluidic devices can be manufactured using this technique [73].

Acknowledgment We would like to thank M. Mero for helpful discussions.

References

1. S. A. Akhmanov, V. A. Vysloukh, and A. S. Chirkin, *Optics of Femtosecond Laser Pulses*, AIP, New York, 1992.
2. J.-C. Diels and W. Rudolph, *Ultrashort Laser Pulse Phenomena*, Academic Press, New York, 1996, second edition 2006.

3. A. M. Guenther, editor, *Laser-Induced Damage in Optical Materials: 25-year index 1969–1993*, SPIE, Washington, 1994.
4. G. J. Exarhos et al., editors, *Proceedings of the Laser-Induced Damage in Optical Materials, Collected papers, Boulder, 1999–2003*, SPIE, Bellingham, WA, 2004.
5. R. M. Wood, *Laser Damage in Optical Materials*, Hilger, Boston, 1986.
6. Y. Sidorin, editor, Special section of applications of laser ablation and micromachining, Opt. Eng. **44**, 051101–051109 (2005).
7. W. L. Smith, Opt. Eng. **17**, 489 (1978).
8. T. W. Walker, A. H. Guenther, and P. E. Nielsen, IEEE J. Quant. Electr. **17**, 2041 (1981).
9. M. Mero, J. Liu, W. Rudolph, D. Ristau, and K. Starke, Phys. Rev. B **71**, 115109 (2005).
10. D. X. Hammer et al., IEEE J. Quant. Electr. **32**, 670 (1996).
11. A. Vogel et al., Appl. Phys. B **68**, 271 (1999).
12. N. Bloembergen, IEEE J. Quant. Electr. **10**, 375 (1974).
13. A. I. Rubinstein and V. M. Fain, Sov. Phys. - Solid State **15**, 332 (1973).
14. A. S. Epifanov, A. A. Manenkov, and A. M. Prokhorov, Sov. Phys. - JETP **43**, 377 (1976).
15. M. Sparks et al., Phys. Rev. B **24**, 3519 (1981).
16. M. Bass and H. H. Barrett, IEEE J. Quant. Electr. **8**, 338 (1972).
17. E. Yablonovich, Appl. Phys. Lett. **19**, 495 (1971).
18. E. Yablonovich and N. Bloembergen, Phys. Rev. Lett. **29**, 907 (1972).
19. D. W. Fradin, N. Bloembergen, and J. P. Letellier, Appl. Phys. Lett. **22**, 635 (1973).
20. W. L. Smith, J. H. Bechtel, and N. Bloembergen, Phys. Rev. B **15**, 4039 (1977).
21. W. H. Lowdermilk and D. Milam, IEEE J. Quant. Electr. **17**, 1888 (1981).
22. M. R. Lange, J. K. McIver, and A. H. Guenther, Thin Solid Films **125**, 143 (1985).
23. M. D. Feit and A. M. Rubenchik, Implications of nanoabsorber initiators for damage probability curves, pulselenghts scaling and laser conditioning, in *Laser-induced Damage in Optical Materials*, edited by G. J. Exarhos et al., volume 5273, pages 74–81, 2004.
24. M. J. Soileau, W. E. Williams, E. W. V. Stryland, T. F. Boggess, and A. L. Smirl, Natl. Bur. Stand. (U.S.) Spec. Publ. **669**, 387 (1984).
25. B. C. Stuart, M. D. Feit, A. M. Rubenchik, W. B. Shore, and M. D. Perry, Phys. Rev. Lett. **74**, 2248 (1995).
26. D. Du, X. Liu, G. Korn, J. Squire, and G. Mourou, Appl. Phys. Lett. **64**, 3071 (1994).
27. M. Lenzner et al., Phys. Rev. Lett. **80**, 4076 (1998).
28. A. Kaiser, B. Rethfeld, M. Vicanek, and G. Simon, Phys. Rev. B **61**, 11437 (2000).
29. H. Varel et al., Appl. Phys. A **62**, 293 (1996).
30. B. C. Stuart et al., Phys. Rev. B **53**, 1749 (1996).
31. A.-C. Tien, S. Backus, H. Kapteyn, M. Murnane, and G. Mourou, Phys. Rev. Lett. **82**, 3883 (1999).
32. A. Rosenfeld, M. Lorenz, R. Stoian, and D. Ashkenasi, Appl. Phys. A **69**, S373 (1999).
33. J. Jasapara, A. V. V. Nampoothiri, W. Rudolph, D. Ristau, and K. Starke, Phys. Rev. B **63**, 045117 (2001).
34. C. B. Schaffer, A. Brodeur, and E. Mazur, Meas. Sci. Technol. **12**, 1784 (2001).
35. A. P. Joglekar et al., Appl. Phys. B **77**, 25 (2003).
36. D. M. Simanovskii, H. A. Schwettman, H. Lee, and A. J. Welch, Phys. Rev. Lett. **91**, 107601 (2003).
37. R. Stoian, D. Ashkenasi, A. Rosenfeld, and E. E. B. Campbell, Phys. Rev. B **62**, 13167 (2000).
38. B. Rethfeld, K. Sokolowski-Tinten, D. von der Linde, and A. S. Anisimov, Appl. Phys. A: Mater. Sci. Process. **79**, 767 (2004).
39. M. F. Koldunov, A. A. Manenkov, and I. L. Pokotilo, Quantum. Electron. **32**, 335 (2002).
40. B. C. Stuart et al., J. Opt. Soc. Am. B **13**, 459 (1996).
41. A. Vaidyanathan, T. W. Walker, and A. H. Guenther, J. Quant. Electr. **16**, 89 (1980).

42. F. Quéré, S. Guizard, and P. Martin, Europhys. Lett. **56**, 138 (2001).
43. M. Li, S. Menon, J. P. Nibarger, and G. N. Gibson, Phys. Rev. Lett. **82**, 2394 (1999).
44. C. Momma, S. Nolte, B. N. Chichkov, F. von Alvensleben, and A. Tünnermann, Appl. Surf. Science **109/110**, 15 (1997).
45. L. V. Keldysh, Sov. Phys. JETP **20**, 1307 (1965).
46. F. H. M. Faisal, J. Phys. B **6**, L89 (1973).
47. H. R. Reiss, Phys. Rev. A **22**, 1786 (1980).
48. G. L. Yudin et al., Laser Phys. **14**, 51 (2004).
49. L. Sudrie et al., Phys. Rev. Lett. **89**, 186601 (2002).
50. E. Yablonovich, Appl. Phys. Lett. **23**, 121 (1973).
51. B. K. Ridley, *Quantum Processes in Semiconductors*, Clarendon, Oxford, 1993, pp. 276–278.
52. B. G. Gorshkov, A. S. Epifanov, and A. A. Manenkov, Sov. Phys. - JETP **49**, 309 (1979).
53. S. C. Jones, P. Bräunlich, R. T. Casper, X. A. Shen, and P. Kelly, Opt. Eng. **28**, 1039 (1989).
54. K. K. Thornber, J. Appl. Phys. **52**, 279 (1981).
55. T. Q. Jia, R. X. Li, Z. Liu, and Z. Z. Xu, Appl. Phys A **74**, 503 (2002).
56. D. Arnold and E. Cartier, Phys. Rev. B **46**, 15102 (1992).
57. B. Rethfeld, Phys. Rev. Lett. **92**, 187401 (2004).
58. J. Zeller et al., Femtosecond dynamics of highly excited dielectric thin films, in *Proceedings of the Laser-Induced Damage in Optical Matls. 2003, SPIE Vol. 5273*, edited by G. J. Exarhos et al., pages 515–525, The International Society for Optical Engineering, 2004.
59. J. Bonse, J. M. Wrobel, J. Krüger, and W. Kautek, Appl. Phys. A: Mater. Sci. Process. **72**, 89 (2001).
60. M. Mero et al., Opt. Eng. **44**, 051107 (2005).
61. I. O. for Standardization, *EN ISO 11146*, 1997.
62. S. Guizard, P. Martin, G. Petite, P. D'Oliveira, and P. Meynadier, J. Phys.: Condens. Matter **8**, 1281 (1996).
63. C. Görling, U. Leinhos, and K. Mann, Opt. Commun. **216**, 369 (2003).
64. J. B. Lonzaga, S. M. Avanesyan, S.C. Langford, and J. T. Dickinson, J. Appl. Phys. **94**, 4332 (2003).
65. A. Hertwig, S. Martin, J. Krüger, and W. Kautek, Appl. Phys. A **79**, 1075 (2004).
66. P. Martin et al., Phys. Rev. B **55**, 5799 (1997).
67. M. Mero, A. Sabbah, J. Zeller, and W. Rudolph, Appl. Phys. A, 317 (2005).
68. P. S. Tsai, B. Friedman, J. Squier, and D. Kleinfeld, Opt. Photonics News **15**, 24 (2004).
69. M. Lenzner, J. Krüger, W. Kautek, and F. Krausz, Appl. Phys. A **68**, 369 (1999).
70. W. Kautek and J. Krüger, SPIE Proceedings **2207**, 600 (1994).
71. C. B. Schaffer and E. Mazur, Opt. Photonics News **12**, 20 (2001).
72. W. Liu et al., Appl. Phys. B **76**, 215 (2003).
73. C. B. Schaffer, A. O. Jamison, and E. Mazur, Appl. Phys. Lett. **84**, 1441 (2004).

Part III
Laser-Driven X-ray Sources

Macroscopic Effects in High-Order Harmonic Generation

Pascal Salières and Ivan Christov

1 Introduction

The use of powerful ultrashort laser pulses offers new perspectives in light–matter interaction because the external field may reach very high values before the atom is fully ionized. Recent experiments have shown that by using 800 nm laser pulses of duration around 10 fs, harmonics of order higher than 300 can be generated in noble gases, extending the spectral range of the emission to the water window [1, 2] and to the keV regime [3] (see the chapter of Lewenstein and L'Huillier). Moreover, the properties of the macroscopic harmonic emission (ultrashort pulse duration, high brightness, good coherence) make it a very unique source of XUV radiation, used in a growing number of applications ranging from atomic [4, 5] and molecular [6, 7, 8] spectroscopies to solid-state [9, 10, 11] and plasma [12, 13, 14] physics. The last two properties stem from the fact that harmonic generation is a coherent process so that the phase of the harmonic emission at a given time and position is determined by the generating laser field. This allows (under certain conditions) the coherent growth of the harmonic field in the nonlinear medium and the "transfer" of the laser coherence properties to the harmonic beam. However, both the physics of the emission and the generating conditions are very different from the ones relative to low-order harmonic generation (classical nonlinear optics) and very specific problems and processes arise in this new situation.

The generation of high harmonics takes place in a gas medium since there exist no solid-state materials that are transparent to the XUV radiation and that can stand the high laser intensities necessary to produce these harmonics. Although the dispersion of the gases is much lower than that of the solid materials, phase matching is required to achieve significant increase in the harmonic signal. This means that the driving polarization and the high-frequency light must have the same phase velocity as they travel through the generating medium. However, since the gases are isotropic the well-established

P. Salières
CEA-Saclay, IRAMIS/SPAM, 91191 Gif-sur-Yvette, France
e-mail: pascal.salieres@cea.fr

T. Brabec (ed.), *Strong Field Laser Physics*,
DOI: 10.1007/978-0-387-34755-4_12,

phase-matching techniques are not applicable and new ones have to be developed. Different generating conditions have been tried to optimize the conversion efficiency: laser tightly focused in a gas jet or cell, laser guided in a hollow core fiber filled with gas. Moreover, the high laser intensity may induce a strong ionization of the nonlinear medium. The resulting space- and time-dependent free-electron dispersion has important consequences for the propagation of both laser and harmonic fields.

In this chapter, we study how the macroscopic harmonic field builds up in the medium and review the main limiting factors to the harmonic yield. We first recall the propagation equations in order to introduce the main propagation effects: they define optimal generating conditions and determine the macroscopic properties of the harmonic emission. We then discuss the non-adiabatic phenomena occurring with ultrashort few-cycle laser pulses and the possibility of generating macroscopic attosecond x-ray pulses. Finally, we present some new proposals for phase matching.

2 Propagation Equations

In order to calculate the macroscopic response of the system, one has to solve the Maxwell equations for the fundamental and harmonic fields. A now standard approach has been developed by Anne L'Huillier and co-workers in the case of not too short laser pulses using the slowly varying envelope and paraxial approximations [15, 16]. Several groups have used similar approaches to study the effects of phase matching and to perform direct comparison of the theory with experiments [17, 18, 19]. Recently, the emphasis on ultrashort laser pulses has led to more general resolutions of the propagation equations [20, 21, 22, 23, 24]. For a review, see [25, 26].

First, we present simplified propagation equations in order to introduce the relevant parameters and discuss the main phenomena occurring during the propagation. Starting from the general wave equation describing the propagation of a linearly polarized electromagnetic field in an isotropic, globally neutral, non-magnetic, dielectric medium, one obtains, in the slowly varying envelope and paraxial approximations, the following coupled equations:

$$\Delta_{\perp}\mathcal{E}_1(\boldsymbol{r},t) + 2\mathrm{i}k_1(\boldsymbol{r},t)\frac{\partial\mathcal{E}_1(\boldsymbol{r},t)}{\partial z} = 0, \tag{1a}$$

$$\Delta_{\perp}\mathcal{E}_q(\boldsymbol{r},t) + 2\mathrm{i}k_q(\boldsymbol{r},t)\frac{\partial\mathcal{E}_q(\boldsymbol{r},t)}{\partial z} = -\frac{q^2\omega_1^2}{\epsilon_0 c^2}\mathcal{P}_q^{\mathrm{NL}}(\boldsymbol{r},t)\mathrm{e}^{\mathrm{i}(qk_1-kq)z}, \tag{1b}$$

where $\mathcal{E}_1(\boldsymbol{r},t)$ and $\mathcal{E}_q(\boldsymbol{r},t)$ denote the slowly varying envelopes of the fundamental and qth harmonic fields, respectively, propagating in the medium with

wavevectors $\boldsymbol{k}_1$ and $\boldsymbol{k}_q$. The depletion of the fundamental field is neglected, considering the low conversion efficiency obtained in gases. The source term for the harmonic field (right-hand side of Eq. (1b)) is provided by the envelope of the qth Fourier component of the nonlinear polarization: $\mathcal{P}_q^{\mathrm{NL}}(\boldsymbol{r},t) = n_{\mathrm{a}}(z,t)d_q(\boldsymbol{r},t)$, where $n_a(z,t)$ is the atomic density and $d_q(\boldsymbol{r},t)$ denotes the qth harmonic component of the total atomic dipole moment that includes the contributions of all active electrons (see the chapter of Lewenstein and L'Huillier). These equations are written in the moving reference frame, assuming a constant group velocity for the laser and harmonic pulses, given the low atomic densities used in experiments. The "slow" time dependence in the above equations accounts for the temporal profile of the fundamental field that enters Eq. (1a) through the boundary condition for $\mathcal{E}_1$.

An important simplification to the problem is obtained by assuming that the polarization is a *local* function of the incident electric field, both in space and time. The field creating a polarization in $(\boldsymbol{r},t)$ is $\mathcal{E}_1(\boldsymbol{r},t)$. In space, this approximation is valid for the dilute media used in experiments. In time, it implies that the polarization follows "instantaneously" or adiabatically the changes in the envelope of the electric field. This is questionable for high intensities and ultrashort pulses, and a number of non-adiabatic phenomena have been reported both in simulations and in experiments (see Section 6).

For not too short pulses, it is then possible to propagate independently temporal slices of the laser envelope, except for the ionization that of course builds up during the pulse. The amplitude and phase of the fundamental field are obtained by solving the propagation equation (1a), allowing the calculation of the nonlinear polarization and the solution of the propagation equation (1b) of the harmonic field.

3 Main Propagation Effects

The main processes governing the propagation of the harmonic field in the nonlinear medium – absorption, phase matching and amplification – are described in the following.

3.1 Absorption

Except for low orders, the harmonic photon energy is larger than the ionization potential of the generating rare gas, so that a significant portion of the emitted radiation may be reabsorbed. For low degree of medium ionization the reabsorbtion by the neutrals sets an upper limit on the achievable harmonic yield, as will be shown below. It enters Eq. (1b) through the imaginary part of the refractive index and thus of the harmonic wavevector: $\mathrm{Im}(k_q) = r_0\lambda_1 f_2 n_{\mathrm{a}}/q = n_{\mathrm{a}}\sigma_q/2$, where r_0 is the classical electron

radius, f_2 the imaginary part of the atomic scattering factor, n_a the atomic density and σ_q the photoionization cross-section. One can define an absorption length $L_{abs} = 1/n_a\sigma_q$ as the length over which a freely propagating field is attenuated by a factor exp(0.5).

3.2 Phase Matching

As is clear when considering Eq. (1b), an efficient energy transfer between the polarization and harmonic fields requires that they propagate with the same phase velocity. If this is not the case, destructive interferences between partial waves emitted at different z-positions in the medium come into play, stopping the coherent growth of the macroscopic harmonic field. From Eq. (1b), one can derive a phase-matching condition generalized to the strong field regime [27]: $\boldsymbol{k}_q = q\boldsymbol{k}_1 + \nabla\Phi_q$, where Φ_q is the intrinsic phase of the harmonic dipole moment d_q. In the following, we analyze this term and the main dispersion phenomena that play a role in phase matching.

3.2.1 Dipole Phase

In the strong field regime, the dipole phase strongly depends on the laser intensity (see the chapter of Lewenstein and L'Huillier), so that the laser focusing in the nonlinear medium may result in large longitudinal and transverse gradients of this phase, influencing phase matching. The origin of this intrinsic phase is the action acquired by the electron wavefunction on the trajectory leading to the emission of the considered harmonic. It can be approximated by $\Phi_q \simeq -U_p\tau \simeq -\theta I_1$, where U_p is the ponderomotive potential and τ the duration of the trajectory. In a first approximation, it varies linearly with the laser intensity I_1; the slope θ depends on the return time and exhibits a weak dependence on both the laser intensity and the harmonic order. In fact, it has quite a generic behavior for the high harmonics. When the harmonic is in the cutoff region, there is a single trajectory giving rise to the emission, characterized by $\theta_{cutoff} \simeq 13.7 \times 10^{-14}$ rad cm^2/W. In the plateau region, there are mainly two such trajectories corresponding, respectively, to $\theta_{short} \simeq 1.4 \times 10^{-14}$ rad cm^2/W and $\theta_{long} \simeq 25.7 \times 10^{-14}$ rad cm^2/W. Due to these different slopes, the best phase matching conditions will be different for the different trajectories, as will be shown below.

3.2.2 Geometric Dispersion

The focusing of the laser beam in the nonlinear medium introduces a phase advance on axis known as the Gouy phase. In the focal region of a Gaussian beam, the correction to the fundamental wavevector can be written as $\delta\boldsymbol{k}_{1,geo} = -2/z_1\,\hat{\mathbf{z}}$, where z_1 is the confocal parameter. The correction to the

harmonic wavevector due to the diffraction of the freely propagating harmonic beam is of the same order of magnitude, so that for sufficiently high orders, one obtains $\Delta \boldsymbol{k}_{\mathrm{geo}} = q\delta \boldsymbol{k}_{1,\mathrm{geo}} - \delta \boldsymbol{k}_{q,\mathrm{geo}} \simeq -2q/z_1\, \hat{\mathbf{z}}$.

In the case of the guiding of the laser beam in a hollow-core fiber, the correction to the propagation constant writes $\delta \boldsymbol{k}_{1,\mathrm{geo}} = -\lambda_1 u_{11}^2/4\pi a^2\, \hat{\mathbf{z}}$, where a is the bore radius and $u_{11} = 2.405$ [28], resulting in $\Delta \boldsymbol{k}_{\mathrm{geo}} \simeq -q\lambda_1 u_{11}^2/4\pi a^2\, \hat{\mathbf{z}}$. Note that this mismatch is close to the Gaussian one in the case where $a \simeq 1.2 w_0$, where w_0 is the Gaussian beam waist.

3.2.3 Atomic Dispersion

The linear atomic polarizability may also play a role in phase matching, even though its role is small for low atomic density. The correction to the fundamental wavevector can be approximated to $\delta \boldsymbol{k}_{1,\mathrm{atom}} = \pi\alpha_1 n_{\mathrm{a}}/\lambda_1\, \hat{\mathbf{z}}$, where α_1 is the static polarizability. The harmonic wavevector is modified by $\delta \boldsymbol{k}_{q,\mathrm{atom}} = -r_0\lambda_1 f_1 n_{\mathrm{a}}/q\, \hat{\mathbf{z}}$, where f_1 is the real part of the atomic scattering factor. The resulting mismatch is

$$\Delta \boldsymbol{k}_{\mathrm{atom}} = q\delta \boldsymbol{k}_{1,\mathrm{atom}} - \delta \boldsymbol{k}_{q,\mathrm{atom}} \simeq n_{\mathrm{a}} \left[\pi\alpha_1 \frac{q}{\lambda_1} + r_0 f_1 \frac{\lambda_1}{q} \right] \hat{\mathbf{z}}. \tag{2}$$

3.2.4 Electronic Dispersion

High-harmonic generation is intrinsically linked to ionization. While the dispersion induced by the resulting ions is negligible due to their lower polarizability, the one induced by free electrons is a very important parameter as soon as there is a significant portion of ionization. Indeed, it affects the fundamental much more than the harmonic wave: $\Delta \boldsymbol{k}_{\mathrm{elec}} = q\delta \boldsymbol{k}_{1,\mathrm{elec}} - \delta \boldsymbol{k}_{q,\mathrm{elec}} = r_0\lambda_1 n_{\mathrm{e}}(-q + 1/q)\, \hat{\mathbf{z}} \simeq -r_0 q\lambda_1 n_{\mathrm{e}}\, \hat{\mathbf{z}}$, where n_e is the free-electron density.

3.2.5 Generalized Phase-Matching Condition

We can now write a detailed phase-matching condition: $\boldsymbol{k}_q^0 = q\boldsymbol{k}_1^0 + \Delta \boldsymbol{k}_{\mathrm{geo}} + \Delta \boldsymbol{k}_{\mathrm{atom}} + \Delta \boldsymbol{k}_{\mathrm{elec}} - \theta \nabla I_1$, where $|\boldsymbol{k}_q^0| = q|\boldsymbol{k}_1^0| = 2\pi q/\lambda_1$. The way the different vectors compensate – or not – each other determines how the harmonic field builds up in the nonlinear medium. The geometric and electronic contributions are opposite to the atomic contribution. The dipole phase factor has a direction determined by the $\boldsymbol{r}$ position in the focal volume. It is thus possible to find different phase-matching regimes depending on the generating parameters: the gas density influences the atomic and electronic dispersions, the laser intensity modifies both the electronic dispersion and the dipole phase factor, the laser focusing or guiding changes the latter as well as the geometric dispersion, the position of the jet relative to the focus determines the gradients of the dipole

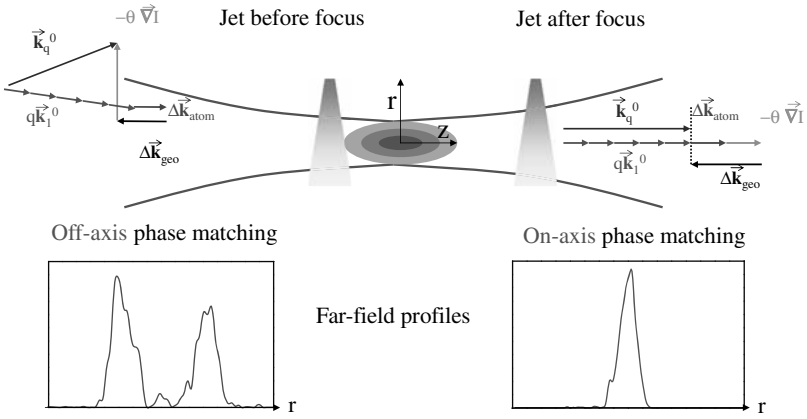

Fig. 1 Illustration of the phase-matching conditions for two positions of the gas jet relative to the laser focus. The corresponding spatial profiles measured for the 39th harmonic generated in neon are shown below (from [29])

phase. In order to illustrate these different regimes, we give below two examples: first in the case of a focused laser beam and second, for a guided beam.

When the laser beam is focused in the nonlinear medium, the position of the focus can serve as a phase-matching parameter, as illustrated in Fig. 1. When the jet is placed after the focus, the dipole phase gradient adds to the atomic dispersion to compensate for the geometric dispersion (and also possibly for the electronic dispersion, not shown here) resulting in a good phase matching on axis. If the jet is placed before the focus, the dipole phase gradient is now directed in the opposite direction preventing phase matching on axis. However, it is possible by going off axis to achieve a good phase matching thanks to the transverse gradient of the dipole phase [29, 27]. A signature of the way phase matching is achieved in the medium is provided by the spatial profile of the resulting harmonic beam. And indeed, a distortion from a narrow-centered profile to a large annular distribution has been observed when changing the jet/focus position [29], as illustrated in Fig. 1: the 39th harmonic was generated in a 1 mm long neon jet by a laser beam focused at $3 \times 10^{14} \mathrm{W/cm^2}$ with a confocal parameter of 5 mm. Note finally that, when the jet is after the focus, only a small gradient of the dipole phase is necessary to achieve phase matching, which favors the contribution of the short trajectory that presents the smaller slope θ_{short}. The situation is reversed when the jet is before the focus and more favorable to the long trajectory.

When the laser beam is guided in a hollow-core fiber, there is no longitudinal gradient of the intensity and thus of the dipole phase. Therefore, the only way to balance the net negative dispersion that comes from both the geometric dispersion and the free-electron dispersion is to vary the atomic dispersion by playing on the gas density [30, 31, 32]. Thus, there exists a maximum of the harmonic yield as a function of the gas pressure inside the capillary, as shown in Fig. 2.

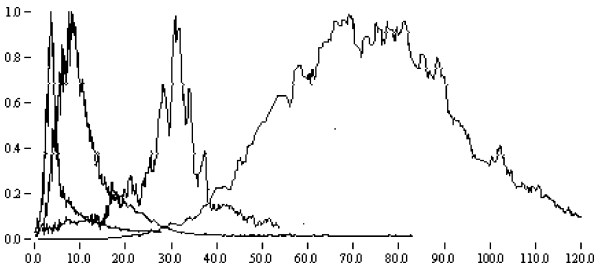

Fig. 2 Pressure dependence of the harmonic yield in a hollow capillary for several gases. In order of increasing optimum pressure, the *curves* correspond to xenon, krypton, argon, and hydrogen. From [31]

The more dispersive the gas, the lower the optimum pressure for phase matching. With this technique, a spatially homogeneous phase matching can be achieved over long distances (see Section 3.3). Note that this type of optimization is only possible for a low degree of ionization (typically below 10%, see also Section 8) where the electronic dispersion is small.

More generally, if there is no exact compensation of the different dephasing terms, we are left with a phase mismatch term: $\Delta \boldsymbol{k}_{\text{tot}} = q\boldsymbol{k}_1 + \nabla\Phi_q - \boldsymbol{k}_q$ that determines a coherence length $L_{\text{coh}} = \pi/|\Delta \boldsymbol{k}_{\text{tot}}|$, the distance over which the nonlinear polarization and the harmonic field get dephased by π. This is the elementary length over which the harmonic field builds up constructively.

3.3 Amplification

Amplification here is understood in the general meaning of an energy transfer between the laser and harmonic beams. In a focused geometry, the interaction range between the laser field and the harmonic field is limited to the size of the confocal parameter. This is because the harmonic generation is a very high order nonlinear process and as such it is very sensitive to the peak intensity of the laser pulse. Therefore, the typical length L_{amp} over which the amplitude of the polarization is high enough to contribute to the macroscopic emission is limited to a few mm. Moreover, the propagation of the laser field may be affected by a strong ionization: since the ionization is higher on axis than in the wings of the laser beam, there is a strong radial gradient of the free-electron density, equivalent to a diverging lens. This induces a defocusing of the laser beam as it propagates through the nonlinear medium. The reduced intensity sets a limitation on the amplification length [33]. This is particularly important when using long generating media, where L_{amp} becomes smaller than L_{med}, the medium length.

The limitations of the focused geometry can be circumvented by using guided geometry which ensures quasi-planar propagation of the waves over distances far exceeding the confocal parameter. Currently there are two basic schemes which experimentally implement guided-wave high-harmonic generation. One uses self-guided pulses where the self-guided propagation results from a dynamic quasi-equilibrium between beam convergence due to self-focusing

and beam divergence resulting from the ionization [34, 35, 36]. However, the self-focusing occurs for a narrow set of parameters of the laser pulse and of the gas, which limits the interaction length to about 1 cm. Nevertheless, a conversion efficiency $\sim 10^{-6}$ for the 49th harmonic generated in neon has been observed, which surpasses by more than one order of magnitude that one in the focused geometry. More flexible control over the parameters for phase-matched propagation is achieved by using a hollow capillary. In this way, very long interaction lengths can be obtained. This is particularly helpful for harmonic orders corresponding to very long absorption lengths (low-absorption cross-section), like the 29th generated in argon. In addition, the spatial filtering that results from the guided geometry improves the spatial quality of both the laser and the XUV beams. An increase in the harmonic signal between two and three orders of magnitude has been obtained over a distance of 3 cm [31].

4 Optimal Generating Conditions

How will the macroscopic harmonic yield be affected by the various above-mentioned limitations? A useful insight into this problem is given by a simple one-dimensional model that allows an analytical solution of the propagation equation for the harmonic field [32]. The number of harmonic photons emitted on axis per unit of time and area is given by

$$N_{\mathrm{ph}} \simeq n_{\mathrm{a}}^2 d_q^2 \frac{4L_{\mathrm{abs}}^2}{1+4\pi^2(L_{\mathrm{abs}}^2/L_{\mathrm{coh}}^2)} \left[1+\exp\left(-\frac{L_{\mathrm{med}}}{L_{\mathrm{abs}}}\right)-2\cos\left(\frac{\pi L_{\mathrm{med}}}{L_{\mathrm{coh}}}\right)\exp\left(-\frac{L_{\mathrm{med}}}{2L_{\mathrm{abs}}}\right)\right]. \tag{3}$$

The value of the photon flux as a function of the ratio of the different characteristic lengths is illustrated in Fig. 3. When L_{abs} becomes much smaller than

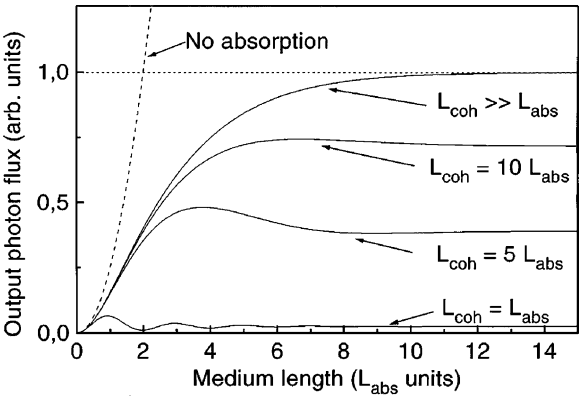

Fig. 3 Number of photons emitted on axis as a function of the medium length (in units of absorption length). The *dotted line* corresponds to a zero absorption case. From [32]

both L_{med} and L_{coh}, the output saturates at a value proportional to $4d_q^2/\sigma_q^2$, independent of the medium density. Note that since an upper limit on d_q is set by ionization when increasing the laser intensity, it follows that there is a maximum value for the harmonic conversion efficiency. A rule of thumb to ensure that the macroscopic response is more than half the maximum response is obtained from Fig. 3 in the form of two conditions: $L_{\mathrm{med}} > 3L_{\mathrm{abs}}$ and $L_{\mathrm{coh}} > 5L_{\mathrm{abs}}$ [32].

Figure 4 illustrates the variation with pressure of these characteristic lengths in a typical case. For a pressure of 60 Torr, the dispersion terms cancel out leading to an infinite coherence length. If L_{med} is too short (0.5 mm case shown in dotted line), it prevents the optimal conditions to be fulfilled simultaneously. In contrast, this can be realized in a large pressure range (from 55 to 115 Torr) if L_{med} is large enough (2.5 mm case shown in dashed line). And indeed, a saturation of the harmonic yield due to absorption has been observed at these pressures in experiments [37]. The influence of the medium length has also been studied in [38].

An absorption-limited emission has been demonstrated by several groups in different generating conditions (gas jet or cell, hollow-core fiber), rare gases (xenon, argon, neon) and harmonic orders [30, 31, 32, 35, 37]. Using ultrashort laser pulses (less than 10 fs), it is possible to achieve such an emission at wavelengths down to 10 nm [39]. For shorter wavelengths, the coherence length remains the main limiting factor due to the strong free-electron dispersion resulting from the high degree of ionization necessary to generate these high harmonics. Since ionization builds up during the laser pulse, phase matching may be achieved only transiently and at different times depending on the position (intensity) in the medium. In order to get the maximum harmonic intensity, a phase-matched absorption-limited emission must be obtained at the highest possible laser intensity (that provides the highest d_q) [40, 41]. Typical conversion efficiencies reach a few 10^{-5} at 55 nm in xenon, a few 10^{-6} at 30 nm in argon, a few 10^{-8} down to 10 nm in neon.

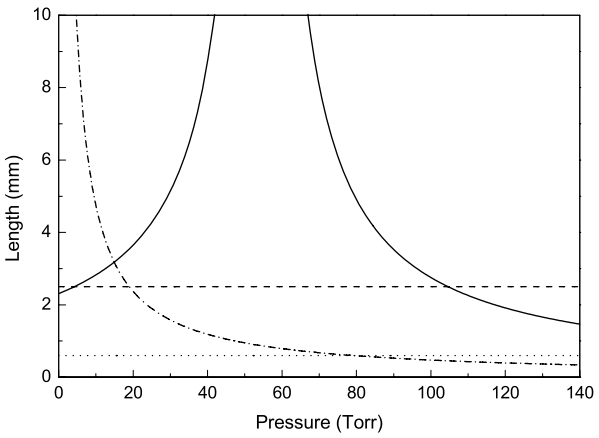

Fig. 4 Calculated absorption length (*dot-dashed line*) and coherence length (*solid line*) for H47 generated in neon at $4\times10^{14}\mathrm{W/cm^2}$ (laser beam ($z_1 = 9$ cm) focused 2.5 cm after the jet, ionization rate 0.3%, dipole phase $-\theta I_1$ with $\theta = 20\times 10^{-14}\mathrm{rad\ cm^2/W}$). Medium lengths of 0.5 mm (2.5 mm) are indicated in *dotted* (*dashed*) *lines*. From [37]

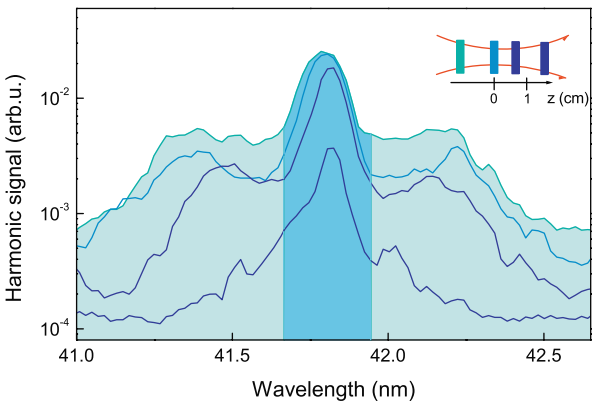

Fig. 5 Spectral profiles of the 19th harmonic generated in a 1 mm long neon jet by a 130 fs, 800 nm laser pulse focused ($f/80$) at $4 \times 10^{14}\mathrm{W/cm^2}$. From *bottom* to *top*, the jet is moved from after to before the focus, as indicated in the *inset*. The *color shades*, *dark blue* vs. *light blue*, refer to the contributions of the short (long) trajectory, resp. From [45]

5 Influence on the Macroscopic Properties

The way phase matching is achieved in the medium determines the harmonic emission profile, as shown in the preceding section. More generally, it can affect the coherence properties of the macroscopic emission: the spatial [42, 43] as well as the temporal [44, 45] coherence. In order to illustrate the latter effect, Fig. 5 presents the spectral profile of the 19th harmonic generated in neon for different jet/focus positions. When the jet is moved from after to before the focus, the harmonic spectrum broadens considerably and symmetrically, indicating a chirp of the emission. Indeed, since the dipole phase varies rapidly with the laser intensity, the harmonic emission by the short laser pulse presents a temporally varying phase. This phase modulation is all the more important as the electron trajectory leading to the emission is long (large slope θ_{long}). The long trajectory being favored when the jet is before the focus, this position leads to a larger chirp and consequently a larger spectral width. This result corroborates the measurements of the coherence times inside the harmonic beam reported in [46, 47].

Like the intensity-dependent dipole phase, the ionization-induced free-electron dispersion may result in a degradation of the harmonic beam coherence, especially in a focused geometry [48, 49, 50]. Both are time- and space-dependent factors that degrade the correlation between the harmonic fields, particularly in the focal region where the intensity is high.

6 Few-Cycle Laser Pulse (Non-adiabatic) Phenomena

When the atom is exposed to a strong fast-increasing field, its response may be strongly distorted for three main reasons. First, the laser field amplitude varying significantly over the optical period may modify the electron trajectories leading to harmonic emission: an electron entering the continuum when the laser intensity is increasing experiences an additional acceleration before

returning, resulting in a blue shift of the emitted harmonic [51, 52, 53]. Second, the value of the carrier-envelope phase will determine the number of laser half-cycles contributing to the emission in the cutoff region of the spectrum, and consequently its shape (see Section 7) [54, 55]. Third, the transient ionization becomes a dominating mechanism which affects both the single-atom interactions and the propagation of laser pulses through the gas medium, where macroscopic effects like plasma dispersion take place (a phase-matching mechanism relying on this effect will be presented in the last section) [23, 56]. To illustrate the distorted ionization dynamics, let us now consider the response of an atom which is illuminated by a strong laser pulse which consists of only few periods of the carrier under the envelope. Figure 6(a) compares the time-dependent ionization calculated by ab initio solution of the three-dimensional Schrödinger equation (solid line) with the results from the quasi-static theory (for the quasi-static approximation see, e.g., [57] and the references therein).

The major difference between the quasi-static approximation of light–atom interaction and the (ab initio) solution of the Schrödinger equation is that the former relies on the concept of "ionization rate". It is important to stress that the rate must be a positively defined quantity while the time derivative of the ionization probability as calculated by the Schrödinger equation is not (see Fig. 6(b)). This effect can be neglected for pulses much longer than the period of the carrier frequency because of the time averaging over many periods which takes place in that case. However, the return of the wavepacket to the core when the field reverses its sign strongly modulates the ionization yield in the case of a few-cycle laser pulse (see the deeps in the solid curve in Fig. 6(a)), which in return reshapes the laser pulse through the medium polarization. In fact, the negative values of the time derivative of the ionization probability lead to a negative loss experienced by the laser pulse, which means that the atomic polarization periodically restores energy back to the pulse at each half-cycle of the carrier [58]. This is an essentially *non-adiabatic* effect which is ignored in

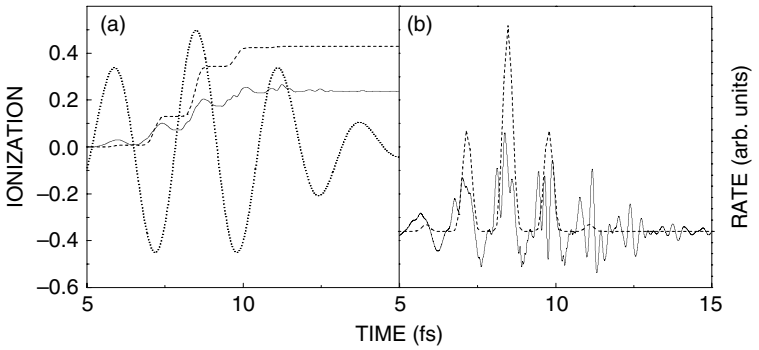

Fig. 6 Time dependence of the ionization (**a**) and the ionization "rate" (**b**) for a hydrogen atom. *Solid line* numerical results; *dashed line* quasi-static approximation. The *dotted line* in (**a**) shows the laser field. From [58]

the quasi-static theory where the ionization rate is always a positively defined quantity. Moreover, during the propagation the phase of the laser field changes due to the dispersion, which also reflects on the ionization via the dependence of the ionization on the absolute phase of the laser field [58, 59]. These non-adiabatic effects should be taken into consideration when propagation and phase-matching issues are of importance. It should be noted that there exists another interpretation of the non-adiabatic response based on the assumption that the ionization of the atom can be calculated by using a static field ionization rate, for each instantaneous value of the electric field [60]. However, by still using the "rate" concept one ignores the essentially non-adiabatic effect that is due to the return of the electron wavepacket to the core, as discussed above.

7 Generation of Attosecond X-Ray Pulses

One of the most attractive challenges faced by extreme nonlinear optics is the generation of short-wavelength pulses with ultrashort duration. Since the harmonic comb spans hundreds of harmonic orders, its time counterpart should consist of series of x-ray pulses with unprecedentedly low duration, provided the different harmonic orders are in phase [61, 62]. In fact, the time dependence of the harmonic emission can be understood intuitively as ultrashort bursts emitted by the atom at each re-collision of the electron with the core, which happens twice per laser period (linear polarization is assumed) [63]. However, a more detailed analysis based on quasi-classical considerations reveals that the emission within each half laser cycle is more complex and it consists of the contributions of the two electron trajectories with the shortest return times [64]. Further, depending on the geometry of harmonic generation, the propagation may enhance the contribution of only one of these trajectories thanks to a better phase matching (see Section 3). As a result, the harmonic radiation at the output of the medium consists of a train of sharp short-wavelength pulses with sub-femtosecond duration, with only one pulse per half-cycle. Experimentally, a first indication of this attosecond localization of the harmonic emission was reported in [65] and more recently, a train of 250 as pulses has been measured, corresponding to the coherent superposition of harmonics 11–19 generated in argon [66]. For a detailed discussion see the chapter of Scrinzi and Muller.

Of course, a train of attosecond pulses with a terahertz repetition rate could find practical applications under some specific conditions. It is evident, however, that the unique time resolution offered in the attosecond timescale can be more easily exploited if isolated attosecond pulses are generated. The earlier proposals for generation of single attosecond pulses are based on the sensitivity of the harmonic efficiency to the degree of ellipticity of the laser light [67]. By irradiating the atom with two perpendicularly polarized laser fields of slightly different carrier frequency, the harmonic emission can be localized to the time interval where the net polarization is linear. A first experimental attempt in this

direction has been made using two chirped laser pulses delayed in time, resulting in a temporal gate of duration ≈ 4 fs [68]. More recently, a new scheme for polarization gating was proposed, based on two time-delayed circularly polarized laser pulses [69, 70]. This technique would allow generating intense isolated attosecond pulses in the plateau region of the spectrum, as demonstrated in a recent experiment [71].

A different approach for generation of isolated attosecond pulses makes use of the fact that when the atom is illuminated by $\sim$20 fs laser pulse, the harmonics close to the end of the plateau acquire a quadratic phase modulation (linear chirp, see Section 4), which allows further compression of these harmonics to sub-femtosecond pulse duration [52, 21]. However, the time envelope of the compressed harmonic pulse shows some structure on femtosecond timescale.

A direct method for generation of a clean single attosecond pulse is offered by the high-harmonic generation with a few-cycle laser pulse [72]. When $\sim$5 fs laser pulse is used (800 nm) such that the maximum of the carrier wave coincides with the maximum of the envelope (cosine wave under the envelope), the harmonic emission close to the end of the plateau is localized to only one half-period near the pulse peak (if the atom is still not fully ionized) or to any one half-period *before* if the atom is fully ionized. Therefore, in this case the end of the harmonic plateau merges in a broad continuous band which is generated during the re-collision of the most energetic electron with the core. In this way the detrimental interference that comes from the contributions from the neighboring half-periods of the laser pulse is eliminated (they still contribute but to much lower photon energies). In other words, the harmonic generation close to the end of the plateau does not depend on the history of light–atom interaction in this case. Thus, the generated x-ray continuum at the end of the plateau can further be extracted by a filter or a x-ray mirror to produce a single attosecond pulse per laser pulse [72]. This regime of HHG is also favored by the decreased ionization of the atom when illuminated with a few-cycle laser pulse, which leads to generation of shorter wavelengths with higher efficiency. Of course, the quasi-single-cycle regime of HHG requires appropriate intensity and phase of the laser field (e.g., a cosine wave under the envelope). In case of non-optimal relation between intensity and phase, the end of the plateau can be modulated by the contributions from different half-cycles of the laser field (e.g., in case of a sine wave under the envelope [73]). It should be mentioned, however, that if the laser field is strong enough, a single attosecond pulse can be generated for arbitrary value of the carrier phase. In fact, there are two sources of dependence of the harmonic emission on the carrier phase of the laser pulse. One stems from the fluctuations of the phase in the femtosecond laser system, while the other comes from the dispersive phase as the laser pulse propagates through the ionizing gas, which leads to a slip of the carrier frequency with respect to the envelope. Experimentally, the generation of isolated 250 as XUV pulses has been demonstrated using the above technique of few-cycle laser pulses plus spectral filtering of the cutoff region [74, 75]. For more details, see the chapter of Scrinzi and Muller.

8 New Proposals for Phase Matching

In principle, the generation of attosecond x-ray pulses presumes high degree of ionization of the gas. This, however, limits the conversion efficiency because the plasma-induced negative dispersion adds to that due to the geometry and destroys the phase matching between the driving polorization and the harmonics. There exist new proposals to enhance the generation of high harmonics and attosecond pulses in the high ionization regime.

For laser intensities in the range 10^{14}–10^{16} W/cm^2 where the ionization of the gas may be very strong, quasi-phase-matching techniques can be used. In the following, we detail two schemes for quasi-phase-matched regime of HHG and attosecond pulse generation in modulated hollow waveguides. One scheme uses thin glass plates with holes positioned periodically along a hollow-core fiber, which are intended to periodically modulate the phase of the fundamental pulse to match that of the harmonics [76]. Another scheme uses a weak corrugation of the walls of a tapered hollow fiber to periodically modulate the peak intensity of the laser pulse. In this way the harmonics near the cutoff are generated in selected regions along the fiber [77]. When the period of modulation of the fiber diameter is close to twice the coherent length of the cutoff harmonics, the signal builds up along the propagation and an enhancement of about three orders of magnitude is predicted. However, the bandwidth that can be phase-matched by using a periodic (sine) corrugation is limited because the frequencies at the extremes may have significantly different coherent lengths, especially for HHG with ~5 fs laser pulses for which the continuum near the end of the plateau may span more than 20 harmonic orders. To overcome this limitation a corrugated hollow waveguide with aperiodic groove spacing (linearly chirped fiber) can be used [78]. In this way, different portions of the fiber enhance different groups of frequencies and therefore a quasi-phase-matched regime of HHG can be achieved for the entire bandwidth of the x-rays generated by the single atom.

The propagation is modeled by a numerical solution of the three-dimensional scalar wave equations written for the laser field $E_1(r,t)$ and for the harmonic field $E_q(r,t)$ in a local frame of reference, moving with the speed of light along the fiber axis (z) [58]:

$$-\frac{2}{c}\frac{\partial^2 E_1}{\partial z \partial t} + \Delta_\perp E_1 = \frac{1}{\varepsilon_0 c^2} n_0 \left[\frac{e^2}{m} P(E_1) E_1 + I_\mathrm{p} \frac{\partial}{\partial t}\left(\frac{1}{E_1}\frac{\partial P(E_1)}{\partial t}\right)\right] - \frac{1}{c^2}\left[1 - \eta^2(n_\mathrm{a})\right]\frac{\partial^2 E_1}{\partial t^2}, \tag{4a}$$

$$-\frac{2}{c}\frac{\partial^2 E_q}{\partial z \partial t} + \Delta_\perp E_q = \frac{1}{\varepsilon_0 c^2} n_0 \left[\frac{e^2}{m} P(E_1) E_q + \left\langle \ddot{d}_q \right\rangle\right], \tag{4b}$$

where the first term in the right-hand side of Eqs. (4a, 4b) describes the dispersion that is due to the transient plasma, the second term in Eq. (4a) accounts for

the ohmic power dissipation that is due to ionization and the third term describes the dispersion by the neutrals. $\eta(n_a)$ is the index of refraction as a function of the atomic density, $n_a = n_o[1 - P(E_1)]$ where n_o is the initial (neutral) gas density and $P(E_1)$ the ionization probability of the gas with ionization potential I_p. Depending on the duration of the laser pulse, the average dipole acceleration $\langle \ddot{d}_q \rangle$ in Eq. (4b) and the ionization probability $P(E_1)$ can be calculated either by a direct solution of the Schrödinger equation or by using semi-classical theory. The dependence $\eta(n_a)$ above is easily calculated for some gases by using the approach of Ref.[79]. On the other hand, the absorption of the neutral gas can be taken into account by transforming the field to the spectral domain and then applying an appropriate filter.

The most important results on the propagation of an attosecond pulse in a chirped tapered waveguide are presented in Figs. 7, 8. Curve 2 in Fig. 7 shows the output harmonic spectrum. It is seen that the harmonic band between orders 89 and 105 preserves its continuous distribution during propagation and remains close to the shape of the spectrum generated by a single atom (curve 1 in Fig. 7).

In time domain, the frequency band at the end of the plateau corresponds to a single x-ray pulse as short as 200 as (solid line in Fig. 8b), which emerges at the output of the waveguide. It can be seen from Fig. 8 that at the beginning of the waveguide the attosecond pulse is generated close to the peak of the laser pulse, while at the output the attosecond pulse is shifted to the leading front of the laser pulse. Although the laser pulse is stretched and shifted in time due to the plasma dispersion, Fig. 8b proves that for an appropriate set of parameters the regime of single attosecond pulse generation can be preserved during the propagation in a hollow waveguide (see also [80]). At the same time the peak enhancement of the attosecond pulse energy is about three orders of magnitude.

Experimentally, high-harmonic generation in a quasi-phase-matched (QPM) regime has recently been demonstrated in a hollow-core fiber with periodically

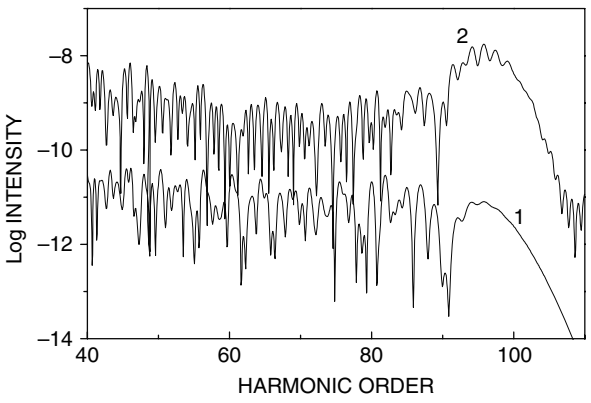

Fig. 7 Harmonic spectra for quasi-phase-matched generation of an attosecond pulse in a chirped waveguide. Curve *1* – at the input; curve *2* – at the output. From [78]

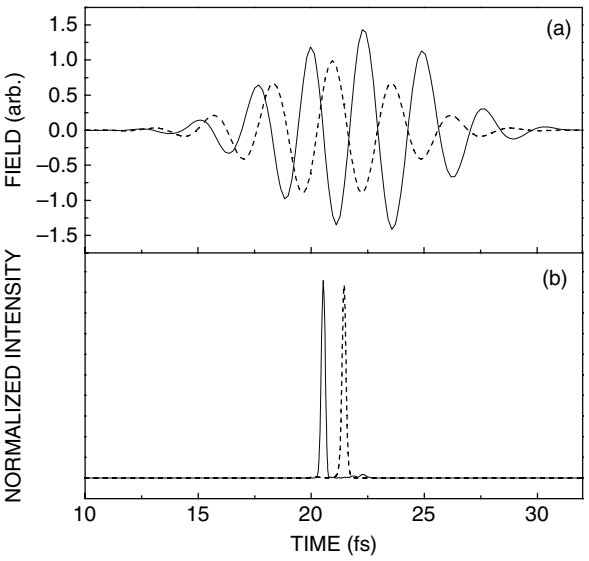

Fig. 8 (**a**) time profile of the laser pulse at the input of the waveguide (*dashed line*) and at the output (*solid line*). (**b**) Attosecond x-ray pulse at the input (*dashed line*) and at the output (*solid line*). From [78]

modulated inner diameter [81, 82]. These first experiments have proven that the efficiency of HHG near the end of the plateau can be enhanced significantly when the period of modulation of the fiber approaches its optimal value (see Fig. 9). It is important to point out that better operation in QPM regime is expected for the harmonics that are generated close to the peak of the laser pump pulse (the cutoff harmonics) because those are propagated under conditions of almost constant degree of ionization, and hence their coherent length is better defined.

In the case of the generation in a gas jet (focused geometry), different techniques have been proposed to realize QPM, based on a spatial modulation

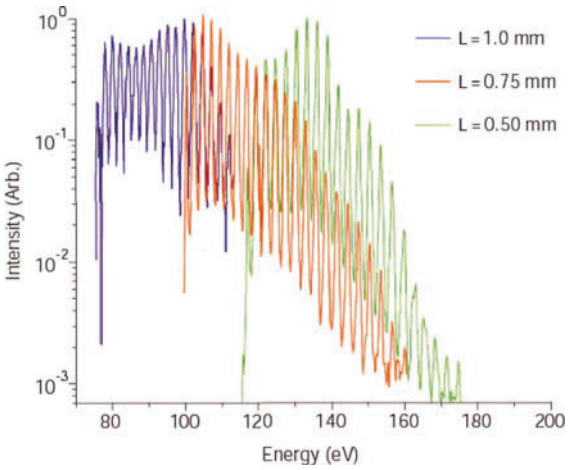

Fig. 9 Experimentally measured spectra (log scale) from QPM in He for different periodicities of the modulated fibers (2.5 cm in length). *Blue* 1 mm periodicity; *red* 0.75 mm periodicity; *green* 0.5 mm periodicity

of either the gas density [83] or the generating laser beam [84]: a relatively weak counter-propagating pulse disrupts the generation at the zones with destructive contribution to the harmonic signal, so that a quasi-phase-matched regime is achieved. Another manipulation of the fundamental field has been proposed to control and improve phase matching: when the laser beam is focused to two separated foci along the propagation axis, a better control of both the geometric dispersion and the atomic phase is possible [85]. Alternatively, truncated Bessel beams have been shown to modify phase matching (and consequently the harmonic spatial properties) as compared to Gaussian beams [86]. Finally, there is a growing activity on the enhancement of phase matching by adaptive control of the laser wavefront with a genetic algorithm, for harmonic generation in a jet, a cell or a fiber [87, 88, 89].

For very high laser intensities (typically above 10^{16} W/cm^2) another mechanism for phase matching may become dominant. This is the so-called "non-adiabatic self-phase matching" (NSPM) [23, 26] where the influence of the phase advance of the fundamental wave due to dispersion can be compensated thanks to dynamic changes in the electron density within an optical cycle. In the presence of ionization, the laser field experiences a linearly growing phase shift with the propagation. For multi-cycle laser pulses the change of free-electron density during one laser cycle is negligible and as a consequence the quasi-classical action along the trajectory leading to the harmonic emission remains constant. However, for a very short laser pulse the trajectories of the freed electrons are governed by slightly different electric field evolutions at different positions along the propagation. Therefore, the quasiclassical phase changes with the distance and that change is opposite in sign with respect to the dispersive phase. For a few-cycle laser pulse these phase contributions may cancel resulting in a growth of the harmonic signal. These theoretical predictions show that NSPM may enhance HHG significantly for very short wavelengths ($\sim$1 keV), thus making HHG in the soft x-ray regime possible.

Another proposal for efficiently generating water-window harmonics at high intensity is to use the dispersion characteristics of exploding atomic clusters that can transiently compensate the free-electron dispersion, dramatically improving phase matching [90]. Finally, let us note that phase matching of high-order frequency mixing processes is also a field of current research [91, 92].

In conclusion, we have detailed the main macroscopic effects playing a role in high-order harmonic generation, and in particular phase matching. This is a rich process, determined by the interplay between the microscopic atomic response and the propagation of the fields in the medium. It allows controlling and optimizing not only the conversion efficiency but also the macroscopic properties of the harmonic emission, and in particular its attosecond structure. The current trend is toward an improved control of the nonlinear interaction, through a precise control of both the laser beam and the gas medium.

References

1. Z. Chang, A. Rundquist, H. Wang, M. M. Murnane, H. C. Kapteyn: Phys. Rev. Lett. **79**, 2967 (1997)
2. C. Spielmann, N. Burnett, S. Sartania, R. Koppitsch, M. Schnurer, C. Kan, M. Lenzner, P. Wobrauschek, F.Krausz: Science **278**, 661 (1997)
3. J. Seres, E. Seres, A. J. Verhoef, G. Tempea, C. Streli, P. Wobrauschek, V. Yakovlev, A. Scrinzi, C. Spielmann, F. Krausz: Nature **433**, 596 (2005)
4. J. Larsson, E. Mevel, R. Zerne, A. L'Huillier, C.-G. Wahlström, S. Svanberg: J. Phys. B **28**, L53 (1995)
5. M. Gisselbrecht, D. Descamps, C. Lynga, A. L'Huillier, C.-G. Wahlström, M. Leyer Phys. Rev. Lett. **82**, 4607 (1999)
6. S. L. Sorensen, O. Bjorneholm, I. Hjelte, T. Kihlgren, G. Ohrwall, S. Sundin, S. Svensson, S. Buil, D. Descamps, A. L'Huillier: J. Chem. Phys. **112**, 8038 (2000)
7. M. Bauer, C. Lei, K. Read, R. Tobey, J. Gland, M.M. Murnane, H.C. Kapteyn: Phys. Rev. Lett. **87**, 025501 (2001)
8. L. Nugent-Glandorf, M. Scheer, D.A. Samuels, A.M. Mulhisen, E.R. Grant, X. Yang, V.M. Bierbaum, S.R. Leone: Phys. Rev. Lett. **87**, 193002 (2001)
9. R. Haight, D.R. Peale: Phys. Rev. Lett. **70**, 3979 (1993)
10. F. Quéré, S. Guizard, G. Petite, Ph. Martin, H. Merdji, B. Carré, J.-F. Hergott: Phys. Rev. B **61**, 9883 (2000)
11. T. Sekikawa, T. Ohno, Y. Nabekawa, S. Watanabe: J. Lumin. **87**, 827 (2000)
12. W. Theobald, R. Hässner, C. Wülker, R. Sauerbrey: Phys. Rev. Lett. **77**, 298 (1996)
13. P. Salières, L. Le Déroff, T. Auguste, P. Monot, P. d'Oliveira, D. Campo, J.-F. Hergott, H. Merdji, B. Carré: Phys. Rev. Lett. **83**, 5483 (1999)
14. D. Descamps, C. Lynga, J. Norin, A. L'Huillier, C.-G. Wahlström, J.-F. Hergott, H. Merdji, P. Salières, M. Bellini, T.W. Hänsch: Opt. Lett. **25**, 135 (2000)
15. A. L'Huillier, L.-A. Lompré, G. Mainfray, C. Manus. In *Atoms in Intense Laser Fields*, ed. by M. Gavrila (Academic Press, New York 1992).
16. A. L'Huillier, Ph. Balcou, S. Candel, K. J. Schafer, K. C. Kulander: Phys. Rev. A **46**, 2778 (1992)
17. J. E. Muffet, C.-G. Wahlström, M. H. R. Hutchinson: J. Phys. B **27**, 5693 (1994)
18. J. Peatross, M. V. Fedorov, K. C. Kulander: J. Opt. Soc. Am. B **12**, 863 (1995)
19. S. C. Rae, K. Burnett, J. Cooper: Phys. Rev. A **50**, 3438 (1994)
20. I. P. Christov, M. M. Murnane, H. C. Kapteyn: Phys. Rev. A **57**, R2285 (1998)
21. P. Salières, Ph. Antoine, A. de Bohan, M. Lewenstein: Phys. Rev. Lett. **81**, 5544 (1998)
22. I. P. Christov: Phys. Rev. A **60**, 3244 (1999)
23. G. Tempea, M. Geissler, M. Schnürer, T. Brabec: Phys. Rev. Lett. **84**, 4329 (2000)
24. E. Priori, G. Cerullo, M. Nisoli, S. Stagira, S. De Silvestri, P. Villoresi, L. Poletto, P. Ceccherini, C. Altucci, R. Bruzzese, C. de Lisio: Phys. Rev. A **61**, 063801 (2000)
25. P. Salières, A. L'Huillier, Ph. Antoine, M. Lewenstein: Adv. Atom. Mol. Opt. Phys. **41**, 83 (1999)
26. T. Brabec , F. Krausz: Rev. Mod. Phys. **72**, 545 (2000)
27. Ph. Balcou, P. Saliéres, A. L'Huillier, M. Lewenstein: Phys. Rev. A **55**, 3204 (1997)
28. E. A. J. Marcatili, R. A. Schmeltzer: Bell Syst. Tech. **43**, 1783 (1964)
29. P. Salières, A. L'Huillier, M. Lewenstein: Phys. Rev. Lett. **74**, 3776 (1995)
30. A. Rundquist, C. Durfee, Z. Chang, C. Herne, S. Backus, M. Murnane, H. Kapteyn: Science **280**, 1412 (1998)
31. C. Durfee III, A. Rundquist, S. Backus, C. Herne, M.M. Murnane, H.C. Kapteyn: Phys. Rev. Lett. **83**, 2187 (1999)
32. E. Constant, D. Garzella, P. Breger, E. Mével, Ch. Dorrer, C. Le Blanc, F. Salin, P. Agostini: Phys. Rev. Lett. **82**, 1668 (1999)
33. K. Miyazaki: J. Nonlinear Opt. Phys. Mat. **4**, 567 (1995)

34. H. R. Lange, A. Chiron, J-F. Ripoche, A. Mysyrowicz, P. Breger, P. Agostini: Phys. Rev. Lett. **81**, 1611 (1998)
35. Y. Tamaki, J. Itatani, Y. Nagata, M. Obara, K. Midorikawa: Phys. Rev. Lett. **82**, 1422 (1999)
36. V. Tosa, H. T. Kim, I. J. Kim, C. H. Nam: Phys. Rev. A **71**, 63807 (2005)
37. J.-F. Hergott, M. Kovacev, H. Merdji, C. Hubert, Y. Mairesse, E. Jean, P. Breger, P. Agostini, B. Carré, P. Salières: Phys. Rev. A **66**, 021801(R), (2002)
38. C. Delfin, C. Altucci, F. De Filippo, C. de Lisio, M.B. Gaarde, A. L'Huillier, L. Roos, C.-G. Wahlström: J. Phys. B **32**, 5397 (1999)
39. M. Schnürer, Z. Cheng, M. Hentschel, G. Tempea, P. Kálmán, T. Brabec, F. Krausz: Phys. Rev. Lett. **83**, 722 (1999)
40. S. Kazamias, D. Douillet, F. Weihe, C. Valentin, A. Rousse, S. Sebban, G. Grillon, F. Augé, D. Hulin, Ph. Balcou: Phys. Rev. Lett. **90**, 193901 (2003)
41. E. Takahashi, Y. Nabekawa, K. Midorikawa: Opt. Lett. **27**, 1920 (2002)
42. L. Le Déroff, P. Salières, B. Carré: Opt. Lett. **23**, 1544 (1998)
43. M. B. Gaarde, F. Salin, E. Constant, Ph. Balcou, K. J. Schafer, K. C. Kulander, A. L'Huillier: Phys. Rev. A **59**, 1367 (1999)
44. M. B. Gaarde, Ph. Antoine, A. L'Huillier, K. J. Schafer, K. C. Kulander: Phys. Rev. A **57**, 4553 (1998)
45. P. Salières, B. Carré, L. Le Déroff, F. Grasbon, G. G. Paulus, H. Walther, R. Kopold, W. Becker, D. B. Milosević, A. Sanpera, M. Lewenstein: Science **292**, 902 (2001)
46. M. Bellini, C. Lynga, A. Tozzi, M. B. Gaarde, C. Delfin, T. W. Hänsch, A. L'Huillier, C.-G. Wahlström: Phys. Rev. Lett. **81**, 297 (1998)
47. C. Lynga, M. B. Gaarde, C. Delfin, M. Bellini, T. W. Hänsch, A. L'Huillier, C.-G. Wahlström: Phys. Rev. A **60**, 4823 (1999)
48. T. Ditmire, J. K. Crane, H. Nguyen, M. D. Perry: J. Nonlinear Opt. Phys. Mat. **4**, 737 (1995)
49. T. Ditmire, E. T. Grumbell, R. A. Smith, J. W. G. Tisch, D. D. Meyerhofer, M. H. R. Hutchinson: Phys. Rev. Lett. **77**, 4756 (1996)
50. Le Déroff, P. Salières, B. Carré, D. joyeux, D. Phalippou: Phys. Rev. A **61**, 043802 (2000)
51. J. B. Watson, A. Sanpera, K. Burnett: Phys. Rev. A **51**, 1458 (1995)
52. K. J. Schafer, K. C. Kulander: Phys. Rev. Lett. **78**, 638 (1997)
53. H. J. Shin, D. G. Lee, Y. H. Cha, K. H. Hong, C. H. Nam: Phys. Rev. Lett. **83**, 2544 (1999)
54. A. Baltuska, Th. Udem, M. Uiberacker, M. Hentschel, E. Goulielmakis, Ch. Gohle, R. Holzwarth, V. S. Yakovlev, A. Scrinzi, T. W. Hänsch, F. Krausz: Nature **421**, 611 (2003)
55. M. Nisoli, G. Sansone, S. Stagira, S. De Silvestri, C. Vozzi, M. Pascolini, L. Poletto, P. Villoresi, G. Tondello: Phys. Rev. Lett. **91**, 213905 (2003)
56. C. Kan, N. H. Burnett, C. E. Capjack, R. Rankin: Phys. Rev. Lett. **79**, 2971 (1997)
57. V. P. Krainov: J. Opt. Soc. Amer. B **14**, 425 (1997)
58. I. P. Christov: Opt. Express **6**, 34 (2000)
59. I. P. Christov: Opt. Lett. **24**, 1425 (1999); Appl. Phys. B **70**, 459 (2000)
60. A. Scrinzi, M. Geissler and T. Brabec: Phys. Rev. Lett. **83**, 706 (1999)
61. G. Farkas, C. Toth: Phys. Lett. A **168**, 447 (1992)
62. S. E. Harris, J. J. Macklin, T. W. Hänsch: Opt. Comm. **100**, 487 (1993)
63. M. Protopapas, D. G. Lappas, C. H. Keitel, P. L. Knight: Phys. Rev. A **53**, R2933 (1996)
64. Ph. Antoine, A. L'Huillier, M. Lewenstein: Phys. Rev. Lett. **77**, 1234 (1996)
65. N. A. Papadogiannis, B. Witzel, C. Kalpouzos, D. Charalambidis: Phys. Rev. Lett. **83**, 4289 (1999)
66. P. M. Paul, E. S. Toma, P. Breger, G. Mullot, F. Augé, P.h. Balcou, H. G. Muller, P. Agostini: Science **292**, 1689 (2001)
67. P. B. Corkum, N. H. Burnett, M. Y. Ivanov: Opt. Lett. **19**, 1870 (1994)

68. C. Altucci, C. Delfin, L. Roos, M. B. Gaarde, A. L'Huillier, I. Mercer, T. Starczewsky, C.-G. Wahlström: Phys. Rev. A **58**, 3934 (1998)
69. R. López-Martens, J. Mauritsson, P. Johnsson, A. L'Huillier, O. Tcherbakoff, A. Zaïr, E. Mével, E. Constant: Phys. Rev. A **69**, 53811 (2004)
70. Z. Chang: Phys. Rev. A **70**, 43802 (2004)
71. I. J. Sola, E. Mével, L. Elouga, E. Constant, V. Strelkov, L. Poletto, P. Villoresi, E. Benedetti, J. -P. Caumes, S. Stagira, C. Vozzi, G. Sansone: Nat. Phys. **2**, 319 (2006)
72. I. P. Christov, M. M. Murnane, H. C. Kapteyn: Phys. Rev. Lett. **78**, 1251 (1997)
73. A. de Bohan, P. Antoine, D. Milosevic, B. Piraux: Phys. Rev. Lett. **81**, 1837 (1998)
74. M. Hentschel, R. Klenberger, Ch. Spielmann, G. A. Reider, N. Milosevic, T. Brabec, P. Corkum, U. Heinzmann, M. Drescher, F. Krausz: Nature **414**, 511 (2001)
75. R. Kienberger, E. Goulielmakis, M. Uiberacker, A. Baltuska, V. Yakovlev, F. Bammer, A. Scrinzi, Th. Westerwalbesloh, U. Kleineberg, U. Heinzmann, M. Drescher, F. Krausz: Nature **427**, 817 (2004)
76. I. P. Christov, H. C. Kapteyn, M. M. Murnane: Opt. Express, **3** 360 (1998); I. P. Christov: Phys.Rev. A **60**, 3244 (1999)
77. I. P. Christov, H. C. Kapteyn, M. M. Murnane: Opt. Express **7**, 362 (2000)
78. I. P. Christov: J. Opt. Soc. Am. B **18**, 1877 (2001)
79. A. Delgarno, A. E. Kingston: Proc. R. Soc. A **259**, 424 (1966)
80. N. H. Shon, A. Suda, Y. Tamaki, K. Midorikawa: Phys. Rev. A **63**, 3806 (2001)
81. A. Paul, R. A. Bartels, R. Tobey, H. Green, S. Weiman, I. P. Christov, M. M. Murnane, H. C. Kapteyn, S. Backus: Nature **421**, 51 (2003)
82. E. A. Gibson, A. Paul, N. Wagner, R. Tobey, D. Gaudiosi, S. Backus, I. P. Christov, A. Aquila, E. M. Gullikson, D. T. Attwood, M. M. Murnane, H. C. Kapteyn: Science **302**, 95 (2003)
83. P. L. Shkolnikov, A. Lago, A. E. Kaplan: Phys. Rev. A **50**, R4461 (1994)
84. S. L. Voronov, I. Kohl, J. B. Madsen, J. Simmons, N. Terry, J. Titensor, Q. Wang, J. Peatross: Phys. Rev. Lett. **87**, 3902 (2001)
85. L. Roos, E. Constant, E. Mevel, Ph. Balcou, D. Descamps, M. B. Gaarde, A. Valette, R. Haroutunian, A. L'Huillier: Phys. Rev. A **60**, 5010 (1999)
86. M. Nisoli, E. Priori, G. Sansone, S. Stagira, G. Cerullo, S. De Silvestri, C. Altucci, R. Bruzzese, C. de Lisio, P. Villoresi, L. Poletto, M. Pascolini, G. Tondello: Phys. Rev. Lett. **88**, 33902 (2002)
87. P. Villoresi, S. Bonora, M. Pascolini, L. Poletto, G. Tondello C. Vozzi, M. Nisoli, G. Sansone, S. Stagira, S. De Silvestri: Opt. Lett. **29**, 207 (2004)
88. D. Yoshitomi, J. Nees, N. Miyamoto, T. Sekikawa, T. Kanai, G. Mourou, S. Watanabe: App. Phys. B **78**, 275 (2004)
89. T. Pfeifer, R. Kemmer, R. Spitzenpfeil, D. Walter, C. Winterfeldt, G. Gerber, C. Spielmann: Opt. Lett. **30**, 1497 (2005)
90. J. W. G Tisch: Phys. Rev. A **62**, 041802 (2000)
91. S. Meyer, H. Eichmann, T. Menzel, S. Nolte, B. Wellegehausen, B. N. Chichkov, C. Momma: Phys. Rev. Lett. **76**, 3336 (1996)
92. Ph. Balcou, A. S. Dederich, M. B. Gaarde, A. L'Huillier: J. Phys. B **32**, 2973 (1999)

Attosecond Pulses: Generation, Detection, and Applications

Armin Scrinzi and Harm Geert Muller

1 Introduction

The shortest laser pulses that can currently be produced in the visible are barely longer than a single cycle and are thus approaching the extreme limit for pulses with such a spectral content. The much higher frequencies available in the UV, and especially VUV, allow much shorter pulses, and it is a fortuitous coincidence that the short visible pulses can be directly used to generate ultrashort XUV pulses with durations of a few hundred attoseconds (1as $= 10^{-18}$ s). Such pulses may for the first time allow the time-resolved observation of valence and inner-shell electronic processes in atoms and small molecules, such as the dynamics of field ionization or complex relaxation processes in hollow atoms. In this chapter, the status of theory and experiment on generation and detection of attosecond pulses is given, and first applications are discussed.

Mechanisms for attosecond pulse generation have been investigated theoretically for almost two decades, concentrating on highly non-linear laser–matter interactions for the generation of the required bandwidth on the one hand and on the complex questions of pulse propagation and phase matching on the other hand [11,2]. This has led to increasing theoretical confidence about the presence of attosecond pulses in harmonic generation, but their direct measurement posed a big experimental challenge. In recent years, attosecond pulses have been detected [32,16] and pulse duration, time of emission [28], and even chirp [19] have been measured. Currently attention is focusing on applications, such as time-resolved spectroscopy of inner-shell dynamics [10], direct imaging of the electric field of light [14], or the observation of electronic relaxation during strong field ionization [23]. Other important developments will be the generation of harmonic pulses with higher energies and higher frequencies as well as the tools to control and manipulate the pulses.

A. Scrinzi
Institute for Photonics, Vienna University of Technology, Gusshausstr. 27, A-1040 Vienna, Austria
e-mail: ascrinzi@pop.tuwien.ac.at

T. Brabec (ed.), *Strong Field Laser Physics*,
DOI: 10.1007/978-0-387-34755-4_13,

The fundamental mechanism for attosecond pulse generation is the sharpening of the sinusoidal time dependence of a laser field by a highly non-linear response of a medium. Section 2 discusses these microscopic aspects of attosecond pulse generation.

Propagation of pulses in a medium and the important question of phase matching are discussed in the contribution of Salières and Christov in this book. Section 3 lists the aspects of propagation that are most important for attosecond pulses and presents a numerical experiment, where all essential physical processes have been included and which shows that surprisingly smooth and intense harmonic attosecond pulses are generated.

Experiments on pulse detection and alternative methods for pulse characterization are the subject of Section 4, and Section 5 reviews pump–probe applications of attosecond pulses and proposals for the observation of sub-femtosecond dynamics of electrons.

2 Ultrashort Time Structures in the Non-linear Response

The mechanism for attosecond pulse generation discussed here is based on a strongly non-linear response of a medium to the laser field. Even a simple, instantaneously reacting non-linearity produces the additional spectral bandwidth needed for short pulse generation. For the time structure of the pulses the frequency dependence of the spectral phases is crucial. Here it is useful to look at the problem in the time domain instead, where one can easily see that, irrespective of the nature of the non-linear response, one may always expect the transformation of smooth to sharp time structures, if coherence can be maintained in a strongly non-linear process. Figure 1 illustrates this remark: high powers of a sine function appear as a comb of Gaussian spikes. This simple structure has a broad spectrum with phase locking among the spectral

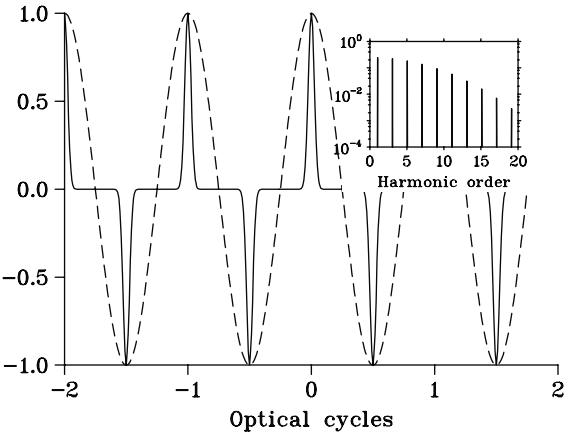

Fig. 1 Generation of sharp time structures in strongly non-linear processes: the functions $f(t) = \sin(2\pi t)$ and $f^{41}(t)$. The *inset* shows the corresponding harmonic power spectrum

components. At present, the two most promising non-linear mechanisms, where coherence is maintained, are excitation of D_2 near a Raman resonance [18,15] and generation of high harmonics by strong pulses [12]. Here we concentrate on the latter mechanism.

2.1 High Harmonic Generation

The production of a plateau of high harmonic radiation with constant intensity was first observed in experiments [12] and later reproduced in numerical simulations [22] and was explained in the time domain by the recollision picture [24,8]. In brief, harmonics are generated by an electron which is ionized at a given phase of the laser field, then is accelerated by the electric field, and finally recollides with the nucleus. Classical considerations show that a maximum electron energy of $3.17U_\mathrm{p}$ is achieved for release at a phase of $\phi = 18°$ after a peak of the electric field strength, which leads to recollision 234° later near a node of the field [24,8,25]. ($U_\mathrm{p} = E_0^2/4\omega^2$ is the ponderomotive potential for field amplitude E_0 and laser frequency ω.) This means that ionization precedes recollision and high harmonic generation by more than half an optical cycle. The mechanism for generating non-linear distortion is far from instantaneous, but rather involves the integrated effect of the field over the entire time interval between ionization and recollision. As a consequence, the time structure of the generated harmonics is likely to be different from, and more complicated than, the train of Gaussian pulses appearing at the field maxima of the driver laser depicted in Fig. 1.

The recollision picture has been elaborated into a semiquantitative quantum mechanical theory within the frame of the strong field approximation [25] (see the chapter of Lewenstein and L'Huillier in this book). Already the classical picture shows that the highest frequencies are only produced during very brief moments and that the highest harmonics must appear with a very sharp time structure. This is confirmed by a time–frequency analysis of the atomic response to the laser field. The harmonic spectrum is obtained as the modulus of the Fourier transform of the acceleration of the dipole expectation value:

$$\ddot{\boldsymbol{d}}(t) = \frac{\mathrm{d}^2}{\mathrm{d}t^2}\langle\Psi(t)|\boldsymbol{r}|\Psi(t)\rangle, \tag{1}$$

where Ψ is the time-dependent electronic wave function. For the time–frequency analysis the dipole acceleration is multiplied by a narrow window function $g(t)$ and Fourier transformed:

$$h_g(t,\omega) = \left|\mathcal{F}\left[g(t'-t)\ddot{\boldsymbol{d}}(t')\right](\omega)\right|^2. \tag{2}$$

$\mathcal{F}$ denotes the Fourier transform with respect to the t' coordinate. The window function was chosen as the Gaussian $g(t) = \exp(-t^2/a^2)$ with a width of $a = 260$ as, corresponding to 1/10 of the laser optical cycle. The electronic wave function was calculated by numerical integration of the time-dependent Schrödinger equation [37]. The result for a hydrogen atom in a linearly polarized 5 fs laser pulse with a peak intensity of 5×10^{14} W/cm^2 and wavelength 800 nm is shown in Fig. 2. Harmonic frequencies increase as the laser field strength rises. The maximum frequency is generated at a delay after the peak field, which can be related to the trajectory for maximal electron acceleration: release and recollision times of this trajectory are marked in the plot. The total harmonic spectrum exhibits the characteristic plateau and a sharp cutoff around the maximum harmonic energy $\omega_{\text{cut}} \approx I_p + 3.2U_p$. Note that because the time-window is far shorter than the laser period, the laser harmonic structure seen in the total spectrum is absent in the time–frequency plot.

The highest frequencies are produced only during a very brief period of a few hundred attoseconds. By separating these highest harmonics from the others by means of a band-pass filter, one may therefore expect a pulse duration on that scale, provided filtering can be performed without temporal and phase distortions of the transmitted harmonics. If instead of the 5 fs pulse a longer pulse is chosen, a train of short pulses separated by 1/2 the optical period is generated. With the very short pulse, the carrier-envelope offset of the laser plays an important role for a more detailed discussion see the chapter of Cundiff, Krausz, and Fuji. In our example, the carrier-envelope offset is chosen such that the peak field coincides with the maximum of the envelope (cosine pulse). When the phase is shifted by 1/4 optical period the field has two equal maxima and maximal harmonic frequencies are generated twice and instead of a single short pulse a double pulse is generated. In any case, the delay between field maxima and attosecond pulse generation remains independent of the laser phase. The time-locking of the XUV pulse to the laser field was a prerequisite

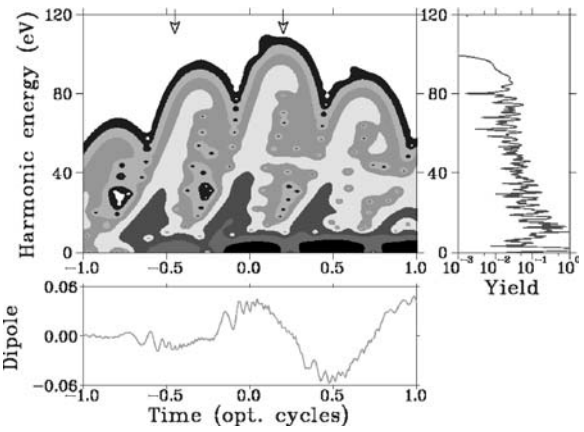

Fig. 2 Atomic dipole, harmonic yield and time–frequency analysis for hydrogen exposed to a 5 fs laser pulse at wavelength 800 nm and intensity 5×10^{14} W/cm^2. Peak laser field strength is reached at time 0. The *arrows* mark start and end time of the classical electron trajectory with maximum energy. Atomic dipole and harmonic yield are in arbitrary units

for the first experimental observation of single attosecond pulses [16], which was performed without control over the laser phase. More generally, it allows exact timing of the attosecond pulse relative to the laser pulse on a timescale well below the optical period. This is needed for all attosecond experiments.

The plot also shows that harmonics below the cutoff energy are generated over an extended period of time with a well-defined time structure. For a given harmonic frequency, there are two intensity maxima, which can be associated with a long and a short classical electron trajectory, respectively [25]. The different lengths of the trajectories create different phases of the harmonics. In propagation, the different phases lead to different phase-matching conditions, which may lead to amplification of the contributions from one trajectory and suppression of the other contribution, resulting in a sharp time structure also for harmonics in the plateau [33,2]. A closer analysis shows that the harmonics near the short trajectory are emitted with a nearly linear chirp. This prediction was confirmed experimentally [28]. By compensating the chirp, trains of pulses as short as 170 as could be generated [27].

3 Propagation Effects

While the microscopic mechanisms of ultrashort pulse generation in non-linear interactions are well understood and seem to be robust with respect to variations of the laser parameters, accumulation of the microscopic contributions and propagation in a medium is a highly complex process, the details of which are only beginning to be understood. All questions affecting the efficiency of high harmonic generation arise again and in sharpened form for attosecond pulse generation. The most important problems are temporal phase matching between the fundamental and the harmonic pulse, intensity dependence of the harmonic phase, destruction of the fundamental pulse during propagation in the highly non-linear medium, absorption of the XUV radiation, transverse spatial coherence of the harmonic pulse, and the resulting spatiotemporal structure of the harmonic pulse. These and related questions are discussed in detail in the chapter of Salières and Christov in this book. The contribution of the separate effects strongly depends on the laser parameters, most importantly on laser intensity. Non-linear propagation of the fundamental pulse, rapid ionization, and the transverse coherence of the harmonic pulse require special attention, since very short and very intense laser pulses are most efficient for attosecond pulse generation. The XUV pulse must be propagated over significant distances without losing its temporal structure and it should be focusable to high intensities for non-linear optics experiments.

The highly non-linear nature of many of the effects makes it difficult to estimate their interplay in an experiment. This has motivated large-scale numerical calculations to predict and interpret experiments for a given set

of parameters [30,6,38]. In such a simulation it is important to simultaneously include all relevant effects listed above as well as the response on the atomic level. Important simplifications of Maxwell's equations can be made, since high harmonic generation experiments are performed in dilute gases with plasma wavelength much larger than the laser wavelength. This means that modifications of the laser electric field over a single optical period remain small and back-propagating waves can be neglected. Based on this assumption, one derives equations that are first order in time. The slowly varying envelope approximation was adapted to the special demands of ultrashort pulses [26,4]. Propagation equations are split into one equation for the laser pulse and a separate equation for the harmonic pulse, since the two parts are affected quite differently by the effects listed above. For the long-wavelength laser pulse, ionization and free-electron dispersion are most important, while propagation of the short wavelength remains essentially linear with a source term that depends only on the low-frequency laser field. After transformation into a frame of reference that moves at the velocity of light ($\tau = t - z/c$, $\xi = z$), the propagation equation for the laser field $E_\mathrm{l}(\xi,\tau)$ reads [30]

$$\begin{aligned}\partial_\xi E_\mathrm{l}(\xi,\tau) - \hat{D}E_\mathrm{l}(\xi,\tau') = &-\frac{1}{2c}\int_{-\infty}^{\tau}\omega_\mathrm{p}^2(\xi,\tau')E_\mathrm{l}(\xi,\tau')\mathrm{d}\tau' \\ &-\frac{I_\mathrm{p}}{2\varepsilon_0 c}\frac{\partial_\tau n_\mathrm{e}(\xi,\tau)}{E_\mathrm{l}(\xi,\tau)} - \frac{\zeta^{(1)}}{c}\partial_\tau(1-n_\mathrm{e}(\xi,\tau))E_\mathrm{l}(\xi,\tau).\end{aligned} \tag{3}$$

Here $\omega_\mathrm{p} = (e^2 n_\mathrm{e}/m\varepsilon_0)^{1/2}$ is the plasma frequency and $c, e, m, \varepsilon_0, I_\mathrm{p}$, and $\zeta^{(1)}$ refer to the vacuum velocity of light, electron charge, electron mass, permittivity of free space, atomic ionization potential, and linear susceptibility of neutral atoms, respectively. The free-electron density is denoted by $n_\mathrm{e}(t)$. Diffraction is generated by $\hat{D} = (c/2)\nabla_\perp^2 \int_{-\infty}^{t} dt'$. The first term on the right-hand side is the known free-electron dispersion, which leads to a strong non-linearity through the variation of the free-electron density $n_\mathrm{e}(t)$ with time. The second term represents energy loss by ionization, which is proportional to the increase of free-electron concentration [13]. Contributions from this term become sizable when a significant portion of the atoms is ionized during a single laser cycle. The last term accounts for the linear response of neutral atoms to the field, which leads to a different refractive index for laser and XUV pulses, where the latter is set equal to 1. When neutral atoms are rapidly depleted by ionization, this term effectively introduces significant non-linearity also.

The linear propagation equation for the harmonic pulse, in turn, includes XUV absorption α_h and the source term for harmonics P_h:

$$\left(\partial_\xi + \alpha_\mathrm{h}\right)E_\mathrm{h}(\xi,\tau) - \hat{D}E_\mathrm{h}(\xi,\tau') = \frac{-1}{2\varepsilon_0 c}\partial_\tau P_\mathrm{h}(\xi,\tau) + \mathrm{c.c} \tag{4}$$

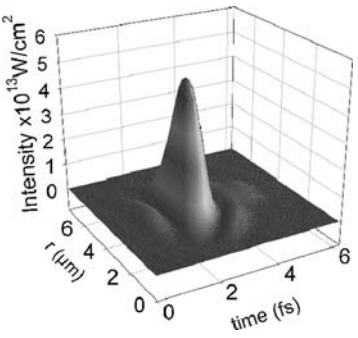

Fig. 3 Spatiotemporal shape of an attosecond pulse (r is the transverse coordinate)

Absorption data for a given atomic species can be obtained from experiments. The source term P_{h} is the complete microscopic response

$$P_{\mathrm{h}}(\xi, t) = \langle \Psi_{\xi}(t) | \boldsymbol{r} | \Psi_{\xi}(t) \rangle, \tag{5}$$

where $\Psi_{\xi}(t)$ is the electronic wave function of an atom subject to the field of the laser $E(\xi, t')$ that has passed the given location until time t. Here the evolution history is fully included, i.e., P_{h} depends not only on the field $E(\xi, t)$, but also on all field values before t. As pointed out above, such *non-adiabatic* microscopic response is dominant for high harmonic generation, i.e., the frequency, intensity, and phase of harmonic generation at one moment depend, in a non-trivial manner, on electron release processes preceding it by more than half a laser cycle.

Numerical solution of the coupled equations above shows that an intense, spatially well-defined, and smooth single attosecond pulse is generated by a few-cycle laser pulse in a dilute gas. The pulse depicted in Fig. 3 is for harmonic frequencies near the cutoff of the harmonic plateau. These highest harmonics are produced at the peak laser intensity during a very short time (cf. Fig. 2) and therefore one can explain the smooth structure. More surprising is the observation of a single pulse below the maximal harmonic frequencies, where many different times contribute. Similar parameters were used in the first measurement of an isolated attosecond pulse [16]. Numerical and experimental findings support the theoretical prediction that phase matching favors one single contribution and suppresses all others [2], which leads to "self-cleaning" of the harmonic pulse.

4 Attosecond Pulse Measurements

Short wavelength, low intensity, and short duration make the measurement of attosecond pulses a difficult task, since commonly used autocorrelation and cross-correlation techniques cannot be extended into the attosecond time and

XUV wavelength regime [21,3]. For autocorrelation, there are few non-linear mechanisms [21] that are efficient enough at short wavelengths. To date, the only successful autocorrelation measurement of attosecond time structure exploited a specific range of relatively long harmonic wavelength for the two-photon ionization of He [41]. The method in principle is limited to photon energies below the ionization potential of the chosen atomic species. The time resolution of the more efficient cross-correlation techniques, such as two-color above-threshold ionization of gases [3], is limited to a few femtoseconds by the shortest feasible laser pulse duration. Even shortening the effective duration of the field with which one cross correlates, by using it in higher order, would not allow sub-cycle resolution [40]. A variety of new measurement techniques for attosecond pulses have been proposed that mostly rely on cross-correlation between the laser electric field and the attosecond pulse. In these techniques the dependence of XUV photoionization and photoelectron spectra on the phase of the laser field at the instant of XUV ionization is exploited. For XUV pulses shorter than the laser optical cycle, modulations of the electron spectra are observed, when the time delay between laser and XUV pulses is changed on a sub-laser-cycle timescale.

Here we discuss in detail the two methods that have provided experimental evidence for attosecond pulses to date. The first method is based on interference of two-photon transitions and it is best understood in terms of non-linear optics. It is applicable with low-intensity laser fields and also allows the characterization of long XUV pulses. The second method uses a streak camera principle to map the temporal shape of the XUV pulse into the electron spectrum. This process can be basically described using classical mechanics. It is naturally applied to single, sub-femtosecond pulses and requires a strong laser field for streaking. Since the first experiments it has been realized that both methods can be interpreted within the same quantum mechanical theory and that algorithms developed for frequency-resolved optical gating are applicable for the analysis of both methods [29].

4.1 Interference of Two-Photon Transitions

When the power spectrum of harmonics is known, the temporal structure of the XUV pulse can be reconstructed by measuring the relative phases of the harmonics. In the present method, the phase measurement is performed by observing the phase dependence of side-band peaks in the photoelectron spectrum of XUV harmonic radiation, which are generated by an additional laser field. Such a dependence, as first noticed by Veniard *et al.* [42], is brought about by the quantum interference between alternative paths to the side-band peak between the $(2N+1)\omega_{\mathrm{IR}} - I_{\mathrm{p}}$ and $(2N-1)\omega_{\mathrm{IR}} - I_{\mathrm{p}}$ ATI photoelectron peaks. (I_{p} denotes the ionization potential and ω_{IR} is the IR laser frequency.) Note that harmonic radiation generated in rotationally symmetric media does not contain

even harmonics and therefore the peak at the $2N\omega_{IR}$ position can only be created by a two-color, harmonic plus laser transition. For large $N$the corresponding matrix element is [32,42]

$$T_{2N} = I_{IR} I_{XUV} \Big[|M_{2N-1}|^2 + |M_{2N+1}|^2 + 2|M_{2N-1} M_{2N+1}| \cos(2\omega_{IR}\tau + \varphi_{2N-1} - \varphi_{2N+1}) \Big], \tag{6}$$

where laser intensity is denoted by I_{IR} and it is assumed that both harmonics have equal intensity of I_{XUV}. The phases of the harmonics are φ_{2N-1} and φ_{2N+1}, respectively, and τ denotes the delay between laser and harmonic pulses. A small atomic contribution to the phases is omitted for clarity [39]. $M_{2N\pm1}$ are the lowest-order perturbative amplitudes for the two alternative transitions XUV$\pm$IR to the same side-band peak. For high harmonics, both amplitudes are of comparable strength and one obtains a pronounced modulation of the side-band peak with the relative delay between laser and harmonic pulses. The delay time τ_0, where the peak is maximal, gives the phase difference between neighboring harmonics $2\omega_{IR}\tau_0 = \varphi_{2N+1} - \varphi_{2N-1}$.

Measurement of the harmonic phases by this technique (known as reconstruction of attosecond beating by interference of two-photon transitions, RABBITT) is in fact a form of spectral interferometry [17]. The side bands to the harmonics are the sum (XUV + IR) and difference (XUV−IR) frequencies of the involved fields and could be considered as two frequency-converted versions of the XUV field. If the IR has sufficiently narrow bandwidth it simply shifts the XUV spectrum to another frequency without any distortion of the relative phases and amplitudes of its spectral components. The frequency difference (shear) between the converted spectra is $2\omega_{IR}$, and the spectrally resolved interference at electron energy E reveals the relative phase of spectral components at $\omega = E + I_p + \omega_{IR}$ and $\omega' = E + I_p - \omega_{IR}$.

By determining the relative phase of all pairs of frequencies spaced by $2\omega_{IR}$, RABBITT thus leads to unambiguous determination of the XUV phases on a spectral sampling grid with this spacing (i.e., on the central frequencies of all harmonics). Such a sampling allows complete reconstruction of a pulse that can be contained within an IR half-cycle. To completely characterize a longer XUV pulse, correspondingly denser spectral sampling is needed. Under conditions where the harmonics are spectrally narrow, the single RABBITT measurement described above does effectively provide complete knowledge of the spectrum on a much denser spectral grid, since no explicit phase determination is needed at frequencies where the amplitude is known to vanish. The reconstruction with the extra zero samples then leads to a train of identical attosecond beatings.

If, on the other hand, one has independent information that one is dealing with a single sub-cycle pulse comprising a range of harmonic frequencies in its spectrum, its chirp can be extracted from the phase differences on the coarse grid provided by the laser harmonics. In the case of a single, sub-laser-cycle

XUV pulse with a correspondingly broad spectrum, the practical problem occurs that the two-photon signals start to overlap the one-photon signals in energy. In that case, intensity dependence or angular distribution of the photoelectrons can be used to separate one- and two-photon signals. The interference between the XUV and XUV + IR signals, peculiar to this situation, contracts the spectral sampling grid to ω_{IR}, which provides some compensation for the extra effort.

When one wants to fully characterize with this method a pulse exceeding the laser period, one needs a denser sampling also at frequencies between the harmonics. That, in principle, could be obtained by performing a second RABBITT measurement with a different IR frequency that makes the spectral shear such that the central frequency of one harmonic interferes with a frequency component out of the center of the neighboring harmonic [31].

4.2 Attosecond Streak Camera Techniques

A second class of techniques that allows to detect *single* attosecond pulses goes by the name of "attosecond streak camera" [7,20]. There the complete information about the attosecond pulse duration can be extracted from the shift and distortion of the XUV photoelectron peak in a simultaneously present laser field. The essence of this idea can be described in a simple classical model. Single-photon XUV electrons are set free at a time t with an initial momentum $\boldsymbol{p}(t)$ and are then accelerated by the laser field to a final momentum

$$\boldsymbol{p}_\infty = \boldsymbol{p}(t) - \int_t^\infty \mathrm{d}t' e\boldsymbol{E}(t') = \boldsymbol{p}(t) + \frac{e}{c}\boldsymbol{A}(t), \tag{7}$$

where $\boldsymbol{E}$ and $\boldsymbol{A}$ are field and vector potentials of the laser pulse and c is the velocity of light. The spectrum of electrons released during the whole XUV pulse is obtained as

$$b(\boldsymbol{p}_\infty) = \int_{-\infty}^{\infty} \mathrm{d}t f_{\mathrm{X}}(t) a_i\left(\boldsymbol{p}_\infty - \frac{e}{c}\boldsymbol{A}(t)\right), \tag{8}$$

where a_i is the initial momentum distribution of XUV photoelectrons and $f_{\mathrm{X}}(t)$ is the XUV pulse intensity envelope. Because of energy conservation, the initial distribution is concentrated around the sphere $\boldsymbol{p}^2 = 2m_{\mathrm{e}}(\omega_{\mathrm{X}} - I_{\mathrm{p}})$, where ω_{X} is the center frequency of the XUV pulse and I_{p} is the ionization potential of the medium. The angular distribution depends on the chosen medium. Shift and broadening of the initial electron momentum spectrum leading to the detected spectrum $b(\boldsymbol{p}_\infty)$ are determined by strength and variation of the vector potential $\boldsymbol{A}(t)$ during the ionization process, respectively, see Fig. 4.

The classical picture presented above needs modifications, when XUV ionization cannot be considered instantaneous compared to variations of the laser

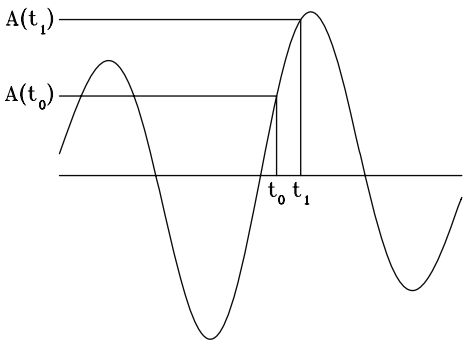

Fig. 4 Boost of electron momenta as a function of release time. *The solid line* indicates the vector potential A of a laser pulse. The momentum shift is proportional to A at the time of release. XUV pulse duration between t_0 and t_1 causes broadening of the momentum distribution by $A(t_1) - A(t_0)$

field. This is the case when the laser field varies significantly during the XUV optical period, i.e., the condition $\omega_X >> \omega_0$ is violated. Quantum mechanical calculations show that for currently considered experimental parameters these corrections are negligible [20].

The proposals for experimental realization of that scheme differ in laser parameters and experimental geometry. In the original proposal [7] circular polarization and observation of the angular distribution of XUV photoelectrons was favored. In recent experiments streaking was obtained using the same linearly polarized laser pulse that generated the attosecond pulse. The advantage of that setup is that the XUV pulse is generated at a well-defined phase of the laser pulse, which allows its exact timing on a sub-laser-cycle timescale, even when the laser phase cannot be controlled. In the first set of experiments [9,16] electron momenta were measured perpendicular to the polarization of laser and XUV pulses. More recently, a different experimental geometry was proposed, which significantly improves the electron yield and allows direct experimental discrimination between single and multiple attosecond pulses [20]. The essence of that proposal is to observe the electron spectrum in polarization direction. Depending on the sign of the laser vector potential at the instance of release, electrons are either accelerated or decelerated. When there is only a single XUV pulse, a single photoelectron peak is produced, which is shifted to either larger or smaller energies. When, on the other hand, there is a train of XUV pulses separated by half an optical period, one of two subsequent electron peaks is shifted to higher energies, while the energy of the other is lowered, which leads to the observation of two separate electron peaks. The separation between the peaks only depends on laser intensity and phase of the laser at the instant of photoelectron emission. This experiment has been realized and has provided the final experimental confirmation of single attosecond pulses ([19], see below).

The same geometry also allows to determine the chirp of the XUV pulse. A positive chirp means that early electrons are emitted at slightly lower energies than later ones, which causes broadening of the spectrum. To measure the chirp one uses the different slopes of the vector potential A at two subsequent nodes. Assume that around the first node A *increases* during the XUV pulse, which

causes early electrons to be decelerated, whereas later ones are accelerated. This further adds to the spectral broadening caused by the chirp. When the XUV pulse arrives half an optical period later, the vector potential *decreases* during the pulse, which compensates for the chirp. This is how measuring streaked spectra at different time delays allows recovery of the XUV time structure. In fact, general time–momentum distributions of electron emission can be recovered by a tomographic procedure [19]. A systematic theory of XUV pulse recovery and its practical implementation was given in Ref. [29].

4.3 Gating by the Laser Field

In a third type of cross-correlation technique [36], single XUV photon ionization is gated by strong laser field. The ionizing medium is chosen such that a single XUV photon is insufficient for ionization. A strong laser field is used to lower the ionization threshold and open the single photoionization channel during peaks of the laser field. Calculations show a strong dependence of the ionization yield on the laser phase. As in the methods discussed above, time resolutions on the scale of half the laser period can be achieved and, at least in principle, single pulses can be distinguished from multiple pulses.

4.4 Experiments

The first experiments to unambiguously establish the existence of attosecond pulses used attosecond cross-correlation techniques [32,16]. More recently, Tzallas *et al.* have also measured the autocorrelation of an attosecond pulse train using two-photon ionization of He as the non-linear process [41].

4.4.1 A RABITT Measurement

The first experimental proof of attosecond time structures was found in harmonics generated from a 40 fs, 800 nm pulse on argon [32]. Earlier experiments, using ponderomotive streaking [40], had shown that the XUV pulses emerging from this process have a time duration of about 11 fs. The XUV spectrum was determined from the photoelectron spectrum generated by the XUV pulse in a noble gas. The electron energies translate into XUV frequencies by simply adding the ionization potential of the ionized atom (in this case also argon). From the observed width of the electron peaks it follows that the individual harmonics have rather narrow bandwidth, not far from the limit expected for an 11 fs pulse. Apparently the conditions of this experiment were such that the individual harmonics were produced without too much chirp, and as a consequence their beating should produce a nearly periodic, 11 fs long beat pattern, with 1.35 fs (half an optical cycle) periodicity. The exact phases between the

harmonics were determined by the RABBITT scheme discussed above. The photoelectrons were produced in the presence of a fairly weak (10^{10} W/cm^2) part of the fundamental beam, the phase of which could be varied by turning a glass delay plate through which the IR beam passed. The XUV + IR two-photon ionization yield was measured as a function of this IR phase and showed a strong dependence on it (fringe contrast about a factor 2). The periodicity of the modulation was 400 nm, as expected from interference between quantum paths differing by two IR photons (emitting vs. absorbing one) and revealed the relative phase of the two involved harmonics. The relative phases of the 11th to the 19th harmonic were determined, showing that (except for the last one) they were almost perfectly phased for producing a single bandwidth-limited, 250 as wide attosecond beat pulse in the 1.35 fs periodicity interval. Due to the phase shift of the 19th harmonic a weak second pulse appeared slightly after it.

4.4.2 Attosecond Streak Camera Measurements

The first measurement of attosecond pulses based on the streak camera principle reported pulse durations of 650 ± 150 as and produced indirect evidence for a *single* pulse with less than 10% of the pulse energy outside the central peak [16]. In that experiment, a light pulse with peak intensity $\sim 5 \times 10^{13}$ W/cm^2 at a central wavelength of $\lambda \approx 750$ nm and a 90 eV X-ray pulse ($\lambda \approx 14$ nm) were colinearly focused into a low-pressure krypton gas jet (see Fig. 5). The XUV pulse was produced from the laser pulse by high harmonic generation in a Ne gas jet with subsequent filtering. Both pulses were linearly polarized with identical polarization directions. The delay between the pulses was varied in time steps of 150 as by a mirror mounted on a piezo-element. Photoelectrons from the Kr 4p shell were collected from a rather large angle of $\theta = \pm 40^\circ$ around the axis perpendicular to polarization. The angular distribution of Kr 4p electrons is nearly isotropic at a photon energy of 90 eV. Both width and position of the photoelectron peak at about 75 eV vary with the delay. The width of the electron peak has two distinct origins: First, electron momenta are spread by the laser vector potential during the time that the XUV pulse lasts, as discussed above. The second contribution to broadening is connected to the specific observation geometry chosen, where electrons were collected with a large aperture perpendicular to the laser polarization. The large opening angle enhances the total electron yield and amplifies the variations of width, providing a robust experimental observable (see Ref. [16]).

A periodic variation of the width of the photoelectron spectra was observed as a function of delay time. The period of the variation was approximately half the optical period of the laser, but at the center of the laser pulse a pronounced blue shift by almost 30% was seen, which was as cribed to self-phase modulation of the laser pulse during passage through the Ne gas jet. The fact that modulations were observed at all provides a save estimate for the XUV pulse duration of 650 ± 150 as. Longer pulses would have washed out any modulation of the width.

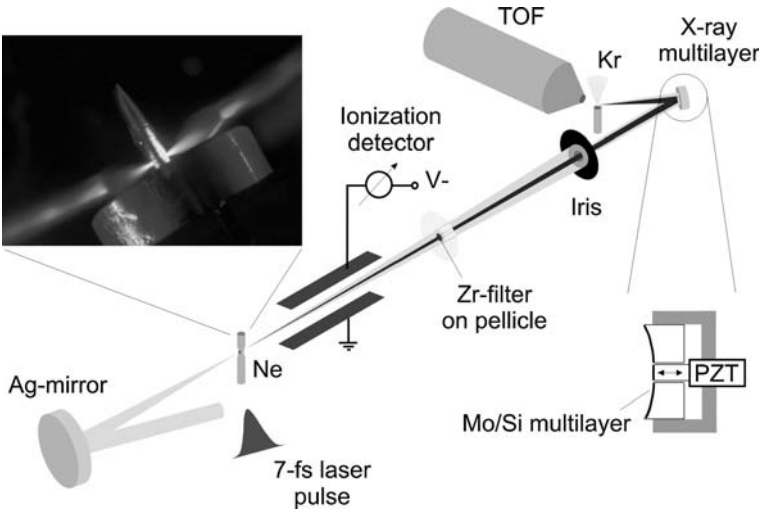

Fig. 5 Setup of the streak camera measurement of attosecond pulses. A 7 fs laser pulse is focused into a neon gas jet for harmonic generation. (The *photo* shows the interaction region). An ionization detector serves to determine the harmonic flux. The beam is split into a central part containing a range harmonics and the annular laser beam surrounding it by a Zr filter. The delay of the harmonic part relative to the laser is varied by moving the central part of a Mo/Si mirror mounted on a piezo-element. Both beams are focused into a krypton gas jet. Electron spectra are determined by time of flight (from Ref. [9])

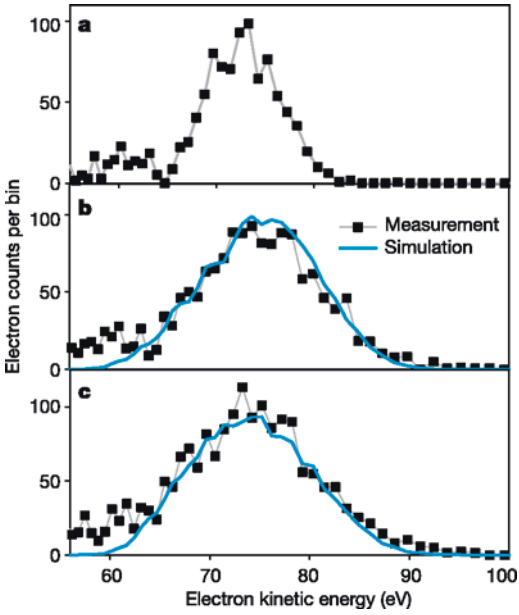

Fig. 6 Measurement of a single 250 as pulse. Spectra taken near two subsequent nodes of the vector potential (peaks of the field) differ little, showing that the pulse is weakly chirped (from Ref. [19])

For this first streak camera measurement phase-stabilized laser pulses were not available yet and intensity was not sufficiently well controlled to decide whether the measured harmonics were from the cutoff or from the plateau region. The experiment therefore provided only indirect evidence for production of a *single* pulse, which had to rely on comparison with the numerical simulation [30]. In experiment [19] the use of phase-stabilized pulses with known intensity and a measurement geometry where electrons were recorded in polarization direction rather than perpendicular to it provided the experimental proof for single pulse production. For each time delay between XUV and laser pulse only a single photoelectron peak was observed, whose position was modulated in a sine-like shape, which is the signature of a single attosecond pulse (see discussion above). In the same experiment the chirp of the pulse was determined by comparing streaked electron spectra obtained with different time delays. It was found that the pulses from the cutoff spectral region were nearly transform limited with a pulse duration of $250(-5+30)$ as (Fig. 6).

5 Applications

Processes on the attosecond timescale occur in the bound state electronic motion of atoms and small molecules, in laser–atom interactions, and in certain electronic relaxation processes in solids. According to the time–energy uncertainty, the characteristic energies corresponding to attosecond pulses are on the scale of $\sim$10 eV, which shows that even quite energetic excitation dynamics is accessible to time-resolved observation.

First proposals for the observation of electronic dynamics by means of attosecond pulses all concern atomic physics problems. Attosecond time-resolved atomic physics experiments will be most advantageous in complex dynamical situations, where many states are involved and an understanding of the physics in terms of a wave packet becomes simpler than the interpretation by many interfering quantum mechanical states. However, most likely first attosecond spectroscopy experiments will concentrate on alternative observations of known spectroscopic processes, such as, for example, atomic relaxation or the resonant Auger mechanism [5]. Another case where fieldfree electronic structure is destroyed and a quasi-continuous spectrum is created is in strong electric fields. Attosecond pulses can be used to probe the electronic structure of an atom or a small molecule while it is being ionized by a strong field.

Apart from applications to electronic dynamics, attosecond pulses were also used to fully map out the field of a laser pulse [14], providing the first direct image of the electric field in a light pulse and giving direct proof of the high stability of the few-cycle pulses.

Below we first discuss the general problems of an attosecond measurement on the textbook example of observing quantum beats of an atomic

superposition state, we give a brief review of a recent attosecond pump–femtosecond probe experiment and outline a possible ionization dynamics experiment.

5.1 Quantum Beats of Low-Lying States

The most elementary electronic motion in atomic bound states is the quantum beats of electron density that are generated by the superposition of two bound states with different energies. For the hydrogen atom, the energy difference between ground and first excited states is about 10 eV, the corresponding beat period is about 400 as. Attosecond pulses provide the time resolution to observe such oscillations. As an observable one can probe the electron density near the nucleus, since XUV ionization is strongly favored for small distances from the nucleus. This can be understood in a classical picture, as the XUV field does not carry any significant momentum, and momentum exchange by collision with the nucleus is required to accelerate the electron to the rather large XUV photoelectron energy. In a superposition state, the electron density near the nucleus oscillates at the beat period and causes an observable modulation of the ionization yield.

Figure 7 shows the variation of the photoelectron yield from hydrogen atoms in a 1s–2s superposition state interacting with an attosecond-pulse for different XUV pulse delays [35]. We have chosen pulse parameters that seem in reach for state-of-the-art HHG systems [30,34]: XUV intensity $I_X = 10^{12}$ W/cm^2, $\lambda_X = 13$ nm, and full width at half maximum duration $\tau_X = 150$as. The ratio of populations is assumed to be $P(1s)$:$P(2s) = 1$:1. The coherent macroscopic ensemble of superposition states is created by the same laser pulse that generates the attosecond pulse. Since both the quantum phase of the superposition state and the generation time of the attosecond pulse are locked to the laser phase, timing on a sub-laser-cycle timescale can be realized. In an experiment, a noble gas rather than hydrogen atoms would be used and energy-selective detection of photoelectrons would enhance the signal-to-noise ratio [35].

This elementary example shows the basic requirements for attosecond experiments: a sufficiently short and intense attosecond pulse, preparation of a coherent macroscopic ensemble of the target, and timing control of the pulse on an attosecond scale. Short pulses and the timing control have been achieved

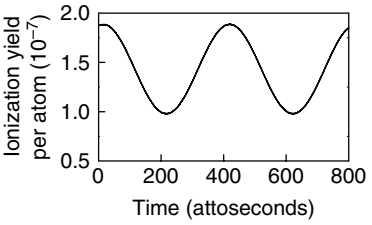

Fig. 7 Modulation of the total photoelectron yield by the quantum beats of a superposition state for pulse parameters described in the text

in the first attosecond measurements. Techniques for target preparation remain to be developed.

5.2 Time-Domain Observation of an Auger Decay

The new possibilities of ultra-fast time-resolved spectroscopy were demonstrated in an experiment, where an Auger decay was observed in the time domain [10] by techniques similar as in the attosecond pulse detection described above [16]. In this experiment, a vacancy was created in krypton by ejecting a 3d-electron using a sub-femtosecond XUV pump pulse. The vacancy is filled from the $n = 4$ shell by an Auger decay at a rate of about 8 fs. The probe pulse was a 6.5 fs laser pulse, which created a side band in the Auger electron spectrum. The intensity of the side band decreases with the delay time of the laser after the XUV pulse at a rate that corresponds to the Auger decay. By deconvolution of the laser pulse and the Auger decay, a decay time of $7.9(+1.0 - 0.9)$ fs was found, corresponding to a decay width of $\Gamma = 84 \pm 10$ meV, in good agreement with the known spectral width of the transition 88 ± 4 meV.

5.3 Ionization Dynamics Experiments

Ionization in strong fields occurs during fractions of a laser cycle on an attosecond timescale. It is an important process, which is only poorly understood in multielectron systems. Attosecond pulses allow a direct observation of the ionization dynamics and the subsequent relaxation processes in the ion. It seems to be a case for time-resolved spectroscopy, since in a strong laser interaction many states of the system become involved and the wave-packet picture becomes applicable.

The generic setup of an ionization dynamics experiment is the same as for the experiments discussed above: cross correlate a laser pulse with an attosecond XUV pulse on an atomic or molecular target. The strong laser ionizes the system and the ion is probed by the XUV pulse at various instances during the ionization process. There are two different, but related observables reflected in the XUV photoelectron spectrum: first, the change of ionization potential during relaxation of the ion changes the final XUV energies and, second, the electron density near the nucleus determines the total XUV photoelectron yield, as discussed above.

The rather high laser intensities involved in such an experiment cause severe distortions and backgrounds. Streaking of XUV photoelectron energies by the laser, which was used for the measurement of pulse durations, here causes unwanted blurring of the XUV spectrum. The effect can be reduced by using very short XUV pulses and observing perpendicular to the laser polarization axis, but in any case a deconvolution of ionic relaxation and laser streaking will

be necessary. Since laser ionization is investigated, a large background of laser photoelectrons is generated. Fortunately the bulk of laser electrons has energies below $2U_p$ [8]. Using large XUV intensities and higher frequencies may serve to separate the XUV photons from the background.

5.4 Trains of Attosecond Pulses

Even trains of attosecond pulses can be useful tools for probing systems, especially since they are synchronized with sub-cycle precision to the carrier of the driving pulse that generated them. They can be used to enhance ionization at specific phases of the laser field. This kind of control makes it possible to investigate the role of various types of trajectories in, e.g., harmonic generation or non-sequential double ionization [1].

6 Perspectives

All experimental setups described above combine a conventional laser with an XUV pulse. The simple reason is that correlation experiments need a non-linear process at their heart, which is facilitated by the strong laser. Even in cases where this is not obvious, such as pump–probe experiments with single-photon processes, the pump should be intense enough to significantly change the system, so that the probe can detect the difference, and the signal is proportional to the intensity of both pump and probe.

The near future will therefore bring more laser–XUV cross-correlations experiments, which, in principle, are limited in their time resolution to a fraction of the laser optical period. In the case of the near-infrared Ti:sapphire lasers mostly used now, the laser optical period is 2.6 fs and it has been demonstrated, both theoretically and experimentally, that resolutions of about 0.1 fs can be achieved [19].

To go beyond that limit, one needs attosecond XUV pulses to drive the system to be observed to a non-linear response, even if this non-linearity is only the saturation of a resonant process. While for specific systems and longer wavelength that can be achieved even at presently available attosecond XUV intensities, in general, there remains strong demand for higher-intensity attosecond pulses.

References

1. Antoine, P., Gaarde, M., Salieres, P., Carre, B., L'Huillier, A., Lewenstein, M.: On the phase of harmonic polarization in harmonic generation processes. In: P. Lambropoulos, H. Walther (eds.) Multiphoton Processes 1996: Inst. Phys. Conf. Ser. No 154, p. 142. IOP, Bristol (1996)

2. Antoine, P., L'Huillier, A., Lewenstein, M.: Attosecond pulse trains using high-order harmonics. Phys. Rev. Lett. **77**, 1234 (1996)
3. Bouhal, A., Evans, R., Grillon, G., Mysyrowicz, A., Breger, P., Agostini, P., Constantinescu, R.C., Muller, H.G., von der Linde, D.: Cross-correlation measurement of femtosecond noncollinear high-order harmonics. J. Opt. Soc. Am. B **14**, 950–956 (1997)
4. Brabec, T., Krausz, F.: Intense few–cycle laser fields: frontiers of nonlinear optics. Rev. Mod. Phys. **72**, 545 (2000)
5. Carlson, T.A., Mullins, D.R., Beall, C.E., Yates, B.W., Taylor, J.W., Lindle, D.W., Grimm, F.A.: Angular distribution of ejected electrons in resonant auger processes of protect ar, kr, and protect xe. Phys. Rev. A **39**, 1170–1185 (1989)
6. Christov, I.P., Murnane, M.M., Kapteyn, H.C.: Generation and propagation of attosecond x-ray pulses in gaseous media. Phys. Rev. A **57**, R2285 (1998)
7. Constant, E., Taranukhin, V.D., Stolow, A., Corkum, P.B.: Methods for the measurement of the duration of high-harmonic pulses. Phys. Rev. A **56**, 3870–3878 (1997)
8. Corkum, P.B.: Plasma perspective on strong-field multiphoton ionization. Phys. Rev. Lett. **71**, 1994 (1993)
9. Drescher, M., Hentschel, M., Kienberger, R., Tempea, G., Spielmann, C., Reider, G., Corkum, P., Krausz, F.: X-ray pulses approaching the attosecond frontier. Science **291**, 1923 (2001)
10. Drescher, M., Hentschel, M., Kienberger, R., Uiberacker, M., Yakovlev, V., Scrinzi, A., Westerwalbesloh, T., Kleineberg, U., Heinzmann, U., Krausz, F.: Time-resolved atomic inner-shell spectroscopy. Nature **419**, 803 (2002)
11. Farkas, G., Tóth, G.: Proposal for attosecond light pulse generation using laser induced multiple-harmonic conversion processes in rare gases. Phys. Lett. A **168**, 447–450 (1992)
12. Ferray, M., L'Huillier, A., Li, X., Lompré, L., Mainfray, G., Manus, C.: Multiple-harmonic conversion of 1064 nm radiation in rare gases. J. Phys. B **21**, L31 (1988)
13. Geissler, M., Tempea, G., Scrinzi, A., Schnürer, M., Krausz, F.: Light propagation in field-ionizing media: Extreme nonlinear optics. Phys. Rev. Lett. **83**, 2930 (1999)
14. Goulielmakis, E., Uiberacker, M., Kienberger, R., Baltuska, A., Yakovlev, V., Scrinzi, A., Westerwalbesloh, T., Kleineberg, U., Heinzmann, U., Drescher, M., Krausz, F.: Direct measurement of light waves. Science **305**, 1267–1269 (2004)
15. Harris, S.E., Sokolov, A.V.: Subfemtosecond pulse generation by molecular modulation. Phys. Rev. Lett. **81**, 2894 (1998)
16. Hentschel, M., Kienberger, R., Spielmann, C., Reider, G.A., Milosevic, N., Brabec, T., Corkum, P., Heinzmann, U., Drescher, M., Krausz, F.: Attosecond metrology. Nature **414**, 509 (2001)
17. Iaconis, C., Walmsley, I.: Spectral phase interferometry for direct electric-field reconstruction of ultrashort optical pulses. Opt. Lett. **23**, 792 (1998)
18. Kaplan, A.E.: Subfemtosecond pulses in mode-locked 2 pi solitons of the cascade stimulated raman scattering. Phys. Rev. Lett. **73**, 1243–1246 (1994)
19. Kienberger, R., Goulielmakis, E., Uiberacker, M., Baltuška, A., Yakovlev, V., Bammer, F., Scrinzi, A., Westerwalbesloh, T., Kleineberg, U., Heinzmann, U., Drescher, M., Krausz, F.: Atomic transient recorder. Nature **427**, 817 (2004)
20. Kitzler, M., Milosevic, N., Scrinzi, A., Krausz, F., Brabec, T.: Quantum theory of attosecond xuv pulse measurement by laser dressed photoionization. Phys. Rev. Lett. **88**, 173,904 (2002)
21. Kobayashi, Y., Yoshihara, O., Nabekawa, Y., Kondo, K., Watanabe, S.: Measurement of high-order harmonic pulse width and electron recombination time by field ionization. Opt. Lett. **21**, 417–419 (1996)
22. Krause, J.L., Schafer, K.J., , Kulander, K.C.: High-order harmonic generation from atoms and ions in the high intensity regime. Phys. Rev. Lett. **62**, 3535–3538 (1992)
23. Krausz, F.: Attosecond physics. Presented at "High Field Attosecond Physics", January 9–15, Obergurgl, Austria (2005)

24. Kulander, K.C., Schafer, K.J., Krause, J.L.: Title missing. In: B. Piraux (ed.) Proceedings of the Workshop, *Super Intense Laser Atom Physics* (SILAP) III, Plenum, New York (1993)
25. Lewenstein, M., Balcou, P., Ivanov, M.Y., L'Huillier, A., Corkum, P.B.: Theory of high-harmonic generation by low-frequency laser fields. Phys. Rev. A **49**, 2117 (1994)
26. L'Huillier, A., Balcou, P., Candel, S., Schafer, K.J., Kulander, K.C.: Calculations of high-order harmonic-generation processes in xenon at 1064 nm. Phys. Rev. A **46**, 2778–2790 (1992)
27. López-Martens, R., Varjú, K., Johnsson, P., Mauritsson, J., Mairesse, Y., Salières, P., Gaarde, M.B., Schafer, K.J., Persson, A., Svanberg, S., Wahlström, C.G., L'Huillier, A.: Amplitude and phase control of attosecond light pulses. Phys. Rev. Lett. **94**, 033,001 (2005)
28. Mairesse, Y., de Bohan, A., Frasinski, L.J., Merdji, H., Dinu, L.C., Monchicourt, P., Breger, P., Kovaev, M., Taïeb, R., Carré, B., Muller, H.G., Agostini, P., Salières, P.: Attosecond synchronization of high-harmonic soft x-rays. Science **302**, 1540 (2003)
29. Mairesse, Y., Quere, F.: Frequency-resolved optical gating for complete reconstruction of attosecond bursts. Phys. Rev. A **71**, 011,401(R) (2005)
30. Milosevic, N., Scrinzi, A., Brabec, T.: Numerical characterization of high harmonic attosecond pulses. Phys. Rev. Lett. **88**, 093,905 (2002)
31. Muller, H.G.: Reconstruction of attosecond harmonic beating by interference of two-photon transitions. Appl. Phys. B **74**, S17 (2002)
32. Paul, P.M., Toma, E.S., Breger, P., Mullot, G., Auge, F., Balcou, P., Muller, H.G., Agostini, P.: Observation of a train of attosecond pulses from high harmonic generation. Science **292**, 1689–1692 (2001)
33. Peatross, J., Fedorov, M.V., Kulander, K.C.: Intensity-dependent phase-matching effects in harmonic generation. J. Opt. Soc. Am. B **12**, 863 (1995)
34. Schnürer, M., Cheng, Z., Hentschel, M., Tempea, G., Kálmán, P., Brabec, T., Krausz, F.: Absorption-limited generation of coherent ultrashort soft-x-ray pulses. Phys. Rev. Lett. **83**, 722–725 (1999)
35. Scrinzi, A.: Ionization of multielectron atoms by strong static electric fields. Phys. Rev. A **61**(4), 041,402(R) (2000)
36. Scrinzi, A., Brabec, T., Walser, M.: 3d numerical calculations of laser–atom interactions. In: B. Piraux, K. Rzaszewski (eds.) Proceedings of the Workshop *Super–Intense Laser–Atom Physics*, p. 313. Kluwer Academic Publishers (2001)
37. Scrinzi, A., Piraux, B.: Two-electron atoms in short intense laser pulses. Phys. Rev. A **58**, 1310 (1998)
38. Shon, N.H., Suda, A., Midorikawa, K.: Generation and propagation of attosecond pulses in he gas with sub-10 fs driver pulses. Phys. Rev. A **60**, 2587 (1999)
39. Toma, E.S., Muller, H.G.: The two-electron mechanism of the formation of doubly charged ions by the multiphoton ionization of ba atoms with two-laser radiation. J. Phys. B **35**, 3435 (2002)
40. Toma, E.S., Muller, H.G., Paul, P.M., Breger, P., Cheret, M., , Agostini, P., Blanc, C.L., Mullot, G., Cheriaux, G.: Ponderomotive streaking of the ionization potential as a method for measuring pulse durations in the xuv domain with fs resolution. Phys. Rev. A **62**, 61,801 (2000)
41. Tzallas, P., Charalambidis, D., Papadogiannis, N.A., Witte, K., Tsakiris, G.D.: Direct observation of attosecond light bunching. Nature **426**, 267–271 (2003)
42. Véniard, V., Taïeb, R., Maquet, A.: Phase dependence of $(n+1)$-color $(n>1)$ ir-uv photoionization of atoms with higher harmonics. Phys. Rev. A **54**, 721–728 (1996)

High-Order Harmonics from Plasma Surfaces

Alexander Tarasevitch, Clemens Wünsche, and Dietrich von der Linde

1 Introduction

The generation of harmonics of the highest possible order has always been a major challenge in nonlinear optics. Generally, nonlinear optical processes become more efficient at higher laser intensities. However, qualitative changes in the nature of the nonlinearity of the laser–matter interaction take place in certain characteristic intensity regimes. One is related to the inner-atomic electric field strength (for the hydrogen atom – 10^9 V/cm, corresponding to a laser intensity of about 10^{16} W/cm^2). At this intensity level, perturbative nonlinear optics breaks down [1, 2]. One of the remarkable effects in this intensity regime is harmonic generation up to the 300th order in noble gases [3, 4].

For intensities exceeding 10^{16} W/cm^2 matter is highly ionized. New nonlinear plasma physics rather than neutral atom nonlinear optics comes into play. The crucial parameter in this intensity regime is the dimensionless amplitude of the laser field $a_0 = eE/(m\omega_0 c)$ which is equal to the normalized electron quiver momentum p_{osc}/mc. Here E is an electric field strength of the laser pulse, m and e are the electron mass and charge, ω_0 is a laser frequency, and c is the speed of light. Significant qualitative changes in the nonlinear interaction take place in the relativistic regime, $a_0 > 1$. The corresponding light intensity is usually quoted as $I\lambda^2 \sim 1.37 \times 10^{18}$ W/cm^{2}μm^2, where I and λ are the laser intensity and wavelength, respectively.

On a femtosecond time scale, the motion of the ions can be neglected and nonlinearities of the electron current $\boldsymbol{j} = -en_e\boldsymbol{v}$ are responsible for nonlinear optical effects. The electron density n_e and the velocity $\boldsymbol{v}$ are nonlinear functions of the electromagnetic fields, and both sources of nonlinearity contribute to high-order harmonic generation (HOHG). In underdense plasmas, the two contributions tend to cancel each other and the resulting harmonic efficiency

A. Tarasevitch
University of Duisbrug-Essen, Institute of Experimental Physics, Lotharstr. 1, 47048 Duisburg, Germany
e-mail: alexander.tarasevitch@uni-due.de

T. Brabec (ed.), *Strong Field Laser Physics*,
DOI: 10.1007/978-0-387-34755-4_14,

in bulk plasmas is low [5, 6, 7, 8]. The situation is quite different in overdense plasmas where harmonic generation occurs in reflection geometry.

High-order harmonic generation from solids was observed for the first time many years ago by Carman et al. [9, 10] who used nanosecond laser pulses. A key point of the theoretical explanation was the assumption of a step-like plasma density gradient. Electrons driven across this steep gradient by the laser field perform a strongly anharmonic motion which leads to the generation of odd and even harmonics.

Recent theoretical work has suggested that HOHG from solid surfaces can be orders of magnitude more efficient [11, 12, 13, 14, 15] than HOHG in gaseous media. The crucial point is to carry laser–solid interaction into the relativistic regime using femtosecond laser pulses of very high intensity. The essential features of HOHG in this regime have been interpreted by Lichters et al. [16, 17] and von der Linde et al. [18, 19]) in terms of a *phase modulation* effect. They have used the "oscillating mirror model" of HOHG, originally developed by Bulanov et al. [20]. This model also offers a descriptive view of HOHG in the time domain. According to this picture, the harmonic frequencies result from the anharmonic distortion of the laser carrier wave upon reflection from a rapidly oscillating surface.

Detailed numerical simulations of the complex collective electron dynamics, in particular particle-in-cell (PIC) simulations [16, 17, 20, 21], have greatly contributed to the understanding of harmonic generation at a plasma–vacuum boundary. In [16], it was shown that the results of PIC simulations and the predictions of the simple oscillating mirror model are in good agreement. However, most of the calculations have been carried out at much lower than solid density and mostly for step-like density profiles. These restrictions make direct comparisons with experiments difficult because the density and the density profile of the plasma are key parameters in HOHG from solid surfaces.

Although the generation of femtosecond laser pulses with relativistic intensities is state of the art [22], the conditions for relativistic interaction with a solid density plasma are rather difficult to actually achieve. Typically, prepulses and/or a slowly rising leading front of the laser pulse lead to a premature ionization of the target, and significant expansion of the plasma sheet may occur before the arrival of the pulse maximum. The plasma expansion lowers the thresholds of various types of plasma instabilities which can distort the plasma sheet or even destroy the conditions for harmonic generation [23, 24, 25, 26]. This difficulty has prevented relativistic interaction in most previous experiments [27, 28, 29, 30, 31]. Only recently has successful HOHG using femtosecond pulses in the relativistic regime been reported [32, 33, 34, 35].

2 Modeling of High-Order Harmonic Generation

2.1 Oscillating Mirror Model

Harmonic generation by an intense light wave incident on a plasma–vacuum boundary involves very complex, collective interaction of the electrons with the

electromagnetic fields. The oscillating mirror approximation [11, 16, 17, 18, 19] consists of two distinct steps. The first step is to neglect the details of the electron spatial distribution and to represent the collective electronic motion by the motion of some characteristic electronic boundary, e.g., the critical density surface. This surface represents the oscillating mirror from which the incident light is reflected. The ions are regarded as fixed, positive background charges. In the second step, the emission from the moving boundary is calculated, in particular the harmonic spectrum generated upon reflection of the incident light.

2.2 Oscillations of the Plasma Surface

Let an intense light wave impinge on an overdense plasma with a sharp boundary ($L \ll \lambda$). The overdense plasma is highly reflective. The electrons near the plasma boundary are driven by the total electric and magnetic fields resulting from the incident and reflected waves. Inside the plasma, the electromagnetic fields decay exponentially over a distance given by the skin depth.

The equation of motion of an electron near the boundary is

$$\frac{\mathrm{d}(m\gamma \boldsymbol{v})}{\mathrm{d}t} = -e\boldsymbol{E}_\mathrm{l} - e\boldsymbol{E} - \frac{e}{c}\boldsymbol{v} \times \boldsymbol{H} = \boldsymbol{F}_\mathrm{p} + \boldsymbol{F}_\mathrm{em}, \tag{1}$$

where γ is the Lorentz factor of the electrons. $\boldsymbol{E}_\mathrm{l}$ is the longitudinal electric field resulting from the electron–ion charge separation which gives rise to the restoring force $\boldsymbol{F}_\mathrm{p} = -e\boldsymbol{E}_\mathrm{l}$. The light wave with the electric and magnetic field strengths of $\boldsymbol{E}$ and $\boldsymbol{H}$ is acting on the electron with the force $\boldsymbol{F}_\mathrm{em}$.

We are interested in the motion of the plasma surface layer. A qualitative picture of this motion can be obtained by considering the orbit of a *single free electron* under the action of the electromagnetic wave of frequency ω_0, neglecting for a moment the restoring force $\boldsymbol{F}_\mathrm{p}$. The electron performs the well-known "figure-of-eight" motion in a plane spanned by the wave vector and the electric field [36]. Figure 1a and b illustrate the situation for a slab of plasma for p- and

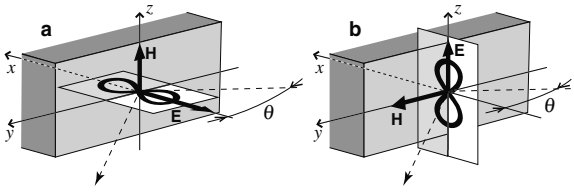

Fig. 1 Directions of the electric and magnetic fields and "figure-of-eight" orbit of an electron: (**a**) for p-polarized light, (**b**) for s-polarized light. The *dashed line* indicates the incident and the reflected light

s-polarized incident light, respectively. For p-polarization, the electron orbit is in the plane of incidence, and the normal component of the electron motion oscillates at ω_0 (Fig. 1a). On the other hand, for s-polarization, the plane of the orbit is perpendicular to the plane of incidence. In this case, the electron moves back and forth across the boundary *twice* during one cycle of the field, i.e., we have a normal motion of the electron surface at $2\omega_0$ (Fig. 1b).

It is quite useful to perform a Lorentz transformation from the laboratory frame K to a new frame K' which moves along the y-axis with a velocity of $V = c \sin\theta$ [37] (see also [16, 20, 21, 38]). Here θ is the angle of incidence in the laboratory frame, as shown in Fig. 1. This transformation allows the general case of oblique incidence in the laboratory frame to be reduced to normal incidence in the moving frame. It will considerably simplify the second step, i.e., the calculations of the emission caused by the oscillating electrons, which will be discussed later.

In the moving frame, the incident wave propagates normally to the plasma surface, while plasma itself moves with the velocity $-V$ along the y-axis. The frequency ω_0 changes to $\omega_0' = \omega_0 \cos\theta$. The amplitudes of the electric and magnetic fields of an incident p-polarized wave are in the K frame given by

$$\boldsymbol{E}_{\mathrm{i}0} = (-E_0 \sin\theta, E_0 \cos\theta, 0), \quad \boldsymbol{H}_{\mathrm{i}0} = (0, 0, E_0). \tag{2}$$

In the K' frame they take the form [36]

$$\boldsymbol{E}'_{\mathrm{i}0} = (0, E_0 \cos\theta, 0), \quad \boldsymbol{H}'_{\mathrm{i}0} = (0, 0, E_0 \cos\theta). \tag{3}$$

For s-polarization, the incident fields change from

$$\boldsymbol{E}_{\mathrm{i}0} = (0, 0, E_0), \quad \boldsymbol{H}_{\mathrm{i}0} = (E_0 \sin\theta, -E_0 \cos\theta, 0) \tag{4}$$

to

$$\boldsymbol{E}'_{\mathrm{i}0} = (0, 0, E_0 \cos\theta), \quad \boldsymbol{H}'_{\mathrm{i}0} = (0, -E_0 \cos\theta, 0), \tag{5}$$

respectively.

Let us estimate the amplitude s_0 of the electron oscillations along the x-axis in the *nonrelativistic* limit. We first find the tangential components E_{t} and H_{t} of the total field at the plasma boundary ($x = 0$). For a highly reflective plasma, the amplitude of the reflected wave is nearly equal to that of the incident wave. For this reason, the total field $\boldsymbol{H}_{\mathrm{t}}$ at the plasma surface is approximately two times as big as the tangential component of the magnetic field of the incident wave. The electric field is given by $\boldsymbol{E}_{\mathrm{t}} = \zeta(\boldsymbol{H}_{\mathrm{t}} \times \boldsymbol{n})$ [39], where $\zeta \cong -\mathrm{i}(\omega_0/\omega_p)$ is the plasma impedance, $\boldsymbol{n}$ is the normal to the plasma surface in x-axis direction, and ω_{p} is the plasma frequency. Correspondingly in the K frame, we have for the tangential components of the field

$$E_y = 2(\omega_0/\omega_p)E_0 \sin\omega_0 t, \quad H_z = 2E_0 \cos\omega_0 t$$

and

$$E_z = 2(\omega_0/\omega_p)E_0 \sin\omega_0 t \cos\theta, \quad H_y = -2E_0 \cos\omega_0 t \cos\theta$$

for the case of p- and s-polarization, respectively. Here we have taken $E \propto \cos\omega_0 t$ for the incident wave. As one would expect, on the reflective surface the electric field strength is low due to the factor $\omega_0/\omega_p \ll 1$.

Changing to K' frame, we find according to (2), (3), (4), (5) [40]

$$E'_y = 2(\omega'_0/\omega_p)(E_0/\cos\theta)\sin\omega'_0 t, \quad H'_z = 2E_0 \cos\omega'_0 t \cos\theta$$

and

$$E'_z = 2(\omega'_0/\omega_p)E_0 \sin\omega'_0 t \cos\theta, \quad H'_y = -2E_0 \cos\omega'_0 t \cos\theta.$$

Now we consider the driving forces for p- and s-polarization at ω'_0 and $2\omega'_0$, respectively. Unlike in the laboratory frame (see Fig. 1a), there is no normal component of the electric field in the moving frame. The equivalent driving force oscillating at the frequency ω'_0 is given by

$$F'_{\mathrm{em}\,\omega_0'} = \frac{e}{c} VH' \cong 2eE_0 \sin\theta\cos\theta\cos\omega'_0 t. \tag{6}$$

For s-polarization, the driving force at $2\omega_0'$ is given by

$$F'_{\mathrm{em}\,2\omega_0'} = -\frac{e}{c} v'H' \cong -\frac{2e^2}{m\omega_p c} E_0^2 \cos^2\theta \cos 2\omega'_0 t. \tag{7}$$

In the nonrelativistic limit with the plasma restoring force $F_p = m\omega_p^2 x$, (1) reduces to the equation of a driven harmonic oscillator, and the oscillation amplitude at the frequency ω is

$$s_0(\omega) = \frac{F_{\mathrm{em}}(\omega)}{m\left(\omega_p^2 - \omega^2\right)}. \tag{8}$$

Substituting (6) and (7) into (8) and taking into account $\omega_p \gg \omega'_0$, we get

$$\frac{s_0}{\lambda} = \frac{1}{\pi}\left(\frac{\omega_0'}{\omega_p}\right)^2 a_0 \sin\theta \propto \frac{n_{\mathrm{cr}}}{n_e} a_0 \tag{9}$$

for p-polarization and

$$\frac{s_0}{\lambda} = \frac{1}{\pi}\left(\frac{\omega_0'}{\omega_p}\right)^3 a_0^2 \cos\theta \propto \left(\frac{n_{\mathrm{cr}}}{n_e}\right)^{3/2} a_0^2 \tag{10}$$

for s-polarization, where $a_0 = eE/(m\omega_0' c)$. The phase shift ψ between the electron oscillations and the driving force is small for $\omega_p \gg \omega_0'$.

As one would expect, the low plasma density is preferable for efficient excitation of the plasma oscillations. For p-polarization, s_0 scales as $(n_{cr}/n_e)a_0$, while for s-polarization, the similarity parameter is $(n_{cr}/n_e)^{3/2}a_0^2$.

2.3 Frequency Spectrum of the Emission from the Plasma Surface

In this section, we deal with the second step of the oscillating mirror model. Assuming that the motion of the plasma boundary is known, the spectrum of the radiation generated by the collective electron oscillations is calculated.

In the K' frame, the fields and velocities depend only on x. The one-dimensional retarded vector potential of the radiated field in Coulomb gauge is

$$\boldsymbol{A}_r'(x,t) = 2\pi \int_{-\infty}^{\infty}\int_{-\infty}^{\infty} \theta\left(t - t_1 - \frac{|x-x_1|}{c}\right)\boldsymbol{j}_\perp'(x_1,t_1)dx_1dt_1, \qquad (11)$$

where $\theta(t)$ is a step function, $\boldsymbol{j}'_\perp$ is an electron current, and the symbols "$'$" and "$_\perp$" indicate the K' frame and transverse (y- and z-) vector components, respectively. The electric and magnetic fields of the emitted electromagnetic wave can be found from (11) as $\boldsymbol{E}_r' = -(1/c)\partial\boldsymbol{A}_r'/\partial t$, $H_{ry}' = -\partial A_{rz}/\partial x$, and $H_{rz}' = \partial A_{ry}/\partial x$ which gives

$$\boldsymbol{E}_r'(x,t) = -\frac{2\pi}{c}\int_{-\infty}^{\infty}\int_{-\infty}^{\infty} \delta\left(t - t_1 - \frac{|x-x_1|}{c}\right)\boldsymbol{j}_\perp'(x_1,t_1)dx_1dt_1, \qquad (12)$$

$H_{ry}' = -E_{rz}'$, and $H_{rz}' = E_{ry}'$.

We are interested in the spectrum $|E_r(\omega)|^2$ of the emitted field. The Lorentz transformation back to the K frame gives $\boldsymbol{E}_r = (-E_{ry}'\tan\theta,\ E_{ry}',\ E_{rz}'/\cos\theta)$, $\boldsymbol{H}_r = (E_{rz}'\tan\theta, -E_{rz}', E_{ry}'/\cos\theta)$. It is clear that $|E_r(\omega)|^2 \propto |E_r'(\omega)|^2$, and we restrict ourselves to calculating $E_r'(\omega)$. The thickness of the layer with nonzero transverse electron current $\boldsymbol{j}'_\perp$ is very small, as it is determined by the skin depth c/ω_p, which is much less than λ. Therefore, the current distribution in the plasma layer is approximated by $\boldsymbol{j}'_\perp(x,t) = \sigma'\delta(x - x_0(t))\boldsymbol{v}'_\perp(t)$. Here σ' and $\boldsymbol{v}'_\perp$ are the charge density and velocity in the plane, respectively, and $x_0(t)$ is the motion of the plane in the x-direction.

For a periodic motion of the plane with period $T = 2\pi/\omega_0'$, the component of the electric field corresponding to the mth harmonic is obtained by performing a Fourier transform of (12). With the expression for $\boldsymbol{j}'_\perp$ given above, we have

$$\boldsymbol{E}'^{m}_{\mathrm{r}}(x) = -\frac{2\pi\sigma'}{c}\frac{1}{T}\int_0^T \left[\boldsymbol{v}'_{\perp}(t)\; e^{imk'(x-x_0(t))}\right] e^{im\omega_0' t}\mathrm{d}t, \tag{13}$$

where $k' = \omega_0'/c$ and $x \gg x_0(t)$.

In (13), two different sources of harmonic emission can be distinguished: (i) the nonlinearity of $\boldsymbol{v}'_{\perp}$ and (ii) the phase modulation introduced by the oscillations along the x-axis. The phase modulation is given by $k'x_0(t)$ in the exponent. Under nonrelativistic conditions, the excursion of the plasma boundary is very small compared with the wavelength, $k'x_0 \ll 1$, and thus the modulation can be neglected. The condition $k'x_0 \ll 1$ corresponds to the normally used approximation of the dipole radiation [36, 41]. In this case, (13) reduces to ordinary reflection from an optical surface. In the relativistic regime, $k'x_0$ is not negligible and the dipole approximation breaks down. Since $k'x_0 \sim 1$ requires $v_x \sim c$, this source of harmonic generation can in fact be regarded as being of relativistic origin.

Below we neglect the nonlinearities in $\boldsymbol{v}'_{\perp}$ and $x_0(t)$ and use simplified expressions $\boldsymbol{v}'_{\perp} = (0, -V + v'_{0y}\cos\omega_0' t, 0)$, $x_0(t) = s_0 \sin\omega_0' t$ for p-polarization and $\boldsymbol{v}'_{\perp} = (0, -V, v'_{0z}\cos\omega_0' t)$, $x_0(t) = s_0\cos 2\omega_0' t$ for s-polarization (see (6) and (7)). We have assumed $E' \propto \sin\omega_0' t$ for the driving field and $\dot{\boldsymbol{v}}'_{\perp} \propto \boldsymbol{E}'$.

By substituting the expressions for $v'_{\perp}$ and $x_0(t)$ into (13) and using the Jacobi expansion $e^{\pm iz\sin\omega t} = \sum_{m=-\infty}^{\infty} J_m(z)e^{\pm im\omega t}$, the spectral distributions of the harmonic intensity can be found. In the case of p-polarization, one obtains

$$\begin{aligned} 2|E'^{m}_{\mathrm{r}y}|^2 &= 8\pi^2\sigma'^2 J_m^2(\chi_m)\sin^2\theta + \\ &\quad + 2\pi^2\sigma'^2\frac{v_{0y}^2}{c^2}\left[J_{m-1}(\chi_m) - J_{m+1}(\chi_m)\right]^2, \end{aligned} \tag{14}$$

where J_m are the Bessel functions of the first kind and mth order ($m = 0, 1, 2, 3...$), and $\chi_m = mk's_0$.

Before proceeding to s-polarization the following points should be noted: (i) A p-polarized driving field produces both *odd and even* harmonics. (ii) For p-polarized laser light the harmonic emission is also p-polarized. (iii) The first term in (14) is *independent* of the transverse velocity. It represents the harmonic emission due to the current associated with the motion $x_0(t)$ of the boundary.

The harmonic distribution for s-polarization is more complicated because in this case the transverse current $\boldsymbol{v}'_{\perp}$ has both a z and a y component. From the term $v'_{\perp,z}$, one obtains

$$2|E'^{m}_{\mathrm{r}z}|^2 = 2\pi^2\sigma'^2\frac{v_{0z}^2}{c^2}\left[J^2_{(m-1)/2}(\chi_m) + J^2_{(m+1)/2}(\chi_m)\right], \tag{15}$$

where m assumes odd integer values, and for the $v'_{\perp,y} = -V$ term,

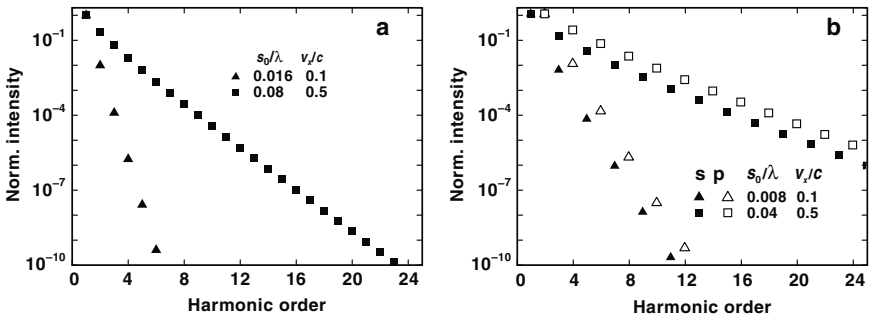

Fig. 2 Harmonic intensity for p-polarized (**a**) and s-polarized (**b**) light. The intensity in (**a**) and for odd harmonics in (**b**) is normalized to $2|E^{\prime 1}_{ry}|^2$. Even harmonics in (**b**) are normalized to $2|E^{\prime 2}_{rz}|^2$

$$2|E^{\prime m}_{ry}|^2 = 8\pi^2\sigma^{\prime 2}J^2_{m/2}(\chi_m)\sin^2\theta, \tag{16}$$

where m is an even integer.

Expression (15) represents s-*polarized odd* harmonics. In addition, we have p-*polarized even* harmonics from (16). Like the emission represented by the first term in (14), the harmonic emission in (16) is also independent of the transverse current, as it is directly caused by the boundary motion. It is quite evident that the harmonic emission due to the normal motion must disappear at normal incidence. Figure 2a and b depicts the harmonic intensity as a function of harmonic order for p-polarization and s-polarization calculated using (14), (15), (16). The efficiency of HOHG increases strongly with s_0/λ or v_x/c (v_x is the velocity of the plasma surface). Comparison of Fig. 2a and b indicates that for the same value of s_0/λ, the high-frequency roll-off of the harmonic spectra for p-polarized light is faster than that for s-polarized light. However, this disadvantage of p-polarization can be compensated by the higher values of s_0/λ for a given driving field (see (9) and (10)).

2.4 The Time Domain Picture: Generation of Attosecond Pulses

Very useful insight into the interaction of light with a moving plasma boundary can be obtained by viewing the process in the time domain. This consideration also stresses the connection between HOHG and the formation of attosecond pulses (see the chapter of Scrinzi and Muller).

Imagine an observer looking at a light wave that is reflected from an oscillating plasma boundary. When the boundary moves toward the observer, the wave form is compressed. Movement in the opposite direction leads to a stretching of the wave form. When the reflecting surface oscillates back and

forth at the frequency of the light, an incident sinusoidal wave experiences an anharmonic distortion upon reflection. For example, under suitable conditions, the mountains of the wave may be so strongly compressed that the sinusoid assumes the form of a train of pulses whose duration is a fraction of an optical cycle. Of course, the frequency spectra of the distorted waves are the harmonic spectra calculated in the forgoing subsection.

The emitted field in the time domain is obtained from (12) by integrating over t_1 and x_1:

$$\boldsymbol{E}'_{\mathrm{r}}(x,t) = \frac{2\pi\sigma'}{c}\frac{\boldsymbol{v}'_{\perp}(t_{\mathrm{r}})}{1-v'_x(t_{\mathrm{r}})/c}, \tag{17}$$

where the retarded time t_{r} follows from the relation $t - t_{\mathrm{r}} = (x - x_0(t_{\mathrm{r}}))/c$.

The actual shape of the reflected wave is critically dependent on the phase difference ψ between $v'_{\perp}$ and v'_x, i.e., the phase difference between the driving field and the oscillating motion of the boundary. For a suitable choice of ψ, the maxima of the sinusoidal incident wave can be compressed into a series of extremely short pulses. This situation is illustrated in Fig. 3. Equation (17) was used to calculate the intensity of the reflected wave as a function of time for different values of s_0/λ and for the oscillation velocities $v'_x(t) = v_0 \sin 2\omega'_0 t$ and $v'_z = v_{0z}\sin(\omega'_0 t + \pi/4)$. The dotted curve represents the undistorted sinusoidal wave. It can be seen that upon reflection this wave assumes the form of a series of short peaks. For the highly relativistic case $s_0/\lambda \sim 0.07$ the compression is quite substantial. The pulse width corresponds to approximately 1% of the fundamental optical cycle. For an optical wavelength of 800 nm, the pulse duration would be 25 as.

Note that the phase difference ψ can be controlled experimentally by using a separate pulse to drive the plasma boundary. A variety of different attosecond wave forms can be generated by changing the phase between the laser pulse to be turned into an attosecond wave and the pulse driving the boundary motion.

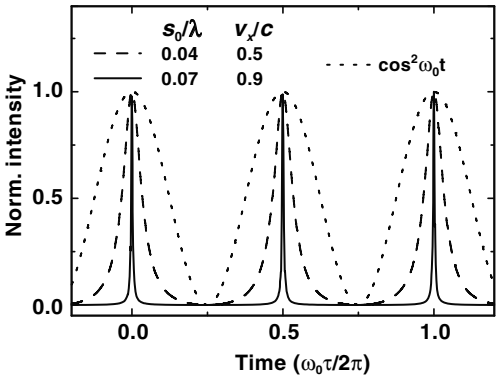

Fig. 3 Train of attosecond pulses generated by the oscillating mirror (*solid* and *dashed lines*). *Dotted curve* represents the undistorted incident wave

2.5 PIC Simulations

We reiterate that the oscillating mirror model discussed above is based on two main assumptions: (i) the details of the electron spatial distribution are neglected and the collective electronic motion is represented by the motion of some characteristic electronic boundary; (ii) the motion of the boundary is considered to be harmonic. Both assumptions are strong simplifications. In this section, we present results of numerical calculations of HOHG using a particle in cell code. These results are quite useful for illustrating the limitations of the described model.

The calculations discussed below were carried out using the fully relativistic PIC code developed by Lichters et al. [16]. The code treats all three velocity components and one spatial dimension (1D3 V code). The plasma was modeled as a 6λ thick slab within a 10λ long simulation box, 3000 cells/λ, and 300 particles per cell corresponding to n_{e0}. The light pulse was assumed to have a $\sin^2$-shape with a total width $\tau = 20T$, where T is the duration of an optical cycle (2.7 fs for an optical cycle of a titanium sapphire laser).

Figure 4 shows examples of the calculated electron density distributions as a function of time for p- and s-polarized incident laser pulses with the normalized amplitudes $a_0 = 0.5$ and 3. The angle of incidence is 45^0. The initial plasma density profile is a step function with an electron density $n_0 = 18.0625 n_c$, where n_c is the critical density.

It can be seen that the plasma boundary shows a periodic density modulation with a fundamental period corresponding to one optical cycle in the case of p-polarization and of half a cycle for s-polarization. This is in agreement with the basic qualitative result of the oscillating mirror model. For p-polarization, the calculated excursion of the critical density surface corresponds to approximately 1% and 5% of the wavelength for $a_0 = 0.5$ and $a_0 = 3$, respectively. This is in reasonable agreement with the predictions of the oscillating mirror model, $s_0/\lambda \cong 0.3\%$ and $s_0/\lambda \cong 2\%$ from formulas (9) and (10).

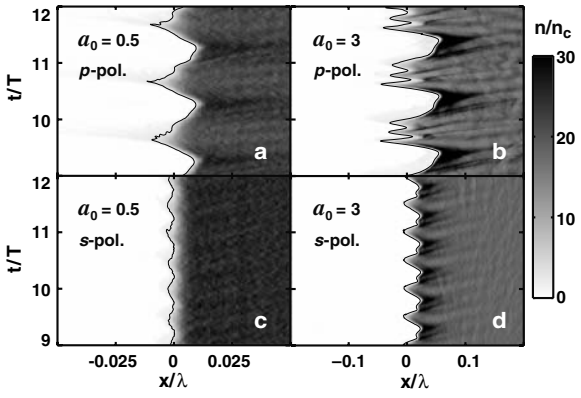

Fig. 4 Electron density distributions for p- and s-polarized incident laser light at different field amplitudes. The initial plasma boundary is located at $x = 0$ with a density $n_{e0} = 18.0625 n_c$. Angle of incidence $\theta = 45^0$. The critical surface $n_e/n_c = 1$ is indicated by a contour line

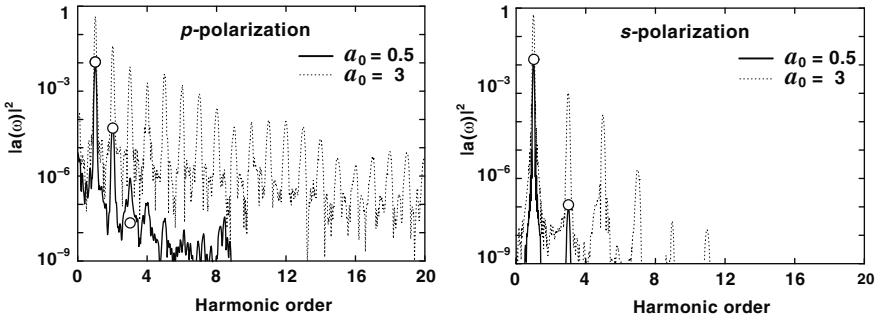

Fig. 5 Harmonic spectra corresponding to the density distributions shown in Fig. 4. *Circles* denote the harmonic amplitudes calculated for $a_0 = 0.5$ using (14) and (14). $a(\omega) \equiv eE'_r(\omega)/m\omega'_0 c$

For s-polarized laser light, appreciable surface excursions are obtained only for strong fields corresponding to relativistic conditions. For $a_0 = 3$, we calculated a surface excursion of approximately 2%. For the same conditions, we obtain 1.3% from (10) of the mirror model.

The harmonic spectra corresponding to the density distributions of Fig. 4 are depicted in Fig. 5. The circles show, for comparison, the harmonic intensities calculated from the oscillating mirror model. There is a good qualitative agreement between the results of the PIC simulations and the simple model.

However, the time-dependent electron density distributions from the PIC simulations clearly show that the actual density modulations are rather complex and not simply sinusoidal. The nonlinearity of the motion significantly enhances the efficiency of harmonic emission. There are two principal reasons for the greater complexity of the density oscillations: First, the plasma restoring force is highly nonlinear and not simply given by $F_p = m\omega_p^2 x$ as assumed in the simple model. Second, relativistic nonlinearities such as the increase of the electron mass must be taken into account for $a_0 > 1$.

In real experiment, the plasma boundary is never step-like. Below we consider a plasma with a boundary that has an exponential decrease of the density toward vacuum. The plasma density $n_{e0} = 49 n_c$ corresponds to the case of a fully ionized polystyrene target interacting with the radiation at the wavelength of 400 nm:

$$n_e = \begin{cases} n_{e0} \exp(x/L) & \text{if } x < 0 \\ n_{e0} & \text{if } x > 0 \,. \end{cases}$$

Figure 6 shows the calculated electron density distributions as a function of time for p-polarized incident laser pulses with a normalized amplitude $a_0 = 0.3$. The angle of incidence is 45^0. According to (9) for $n_{e0} = 45.56 n_c$, we find $s_0/\lambda \cong 0.1\%$. However, the increase in the plasma scale length reduces the influence of the plasma restoring force, making the plasma "softer". It can be seen that for

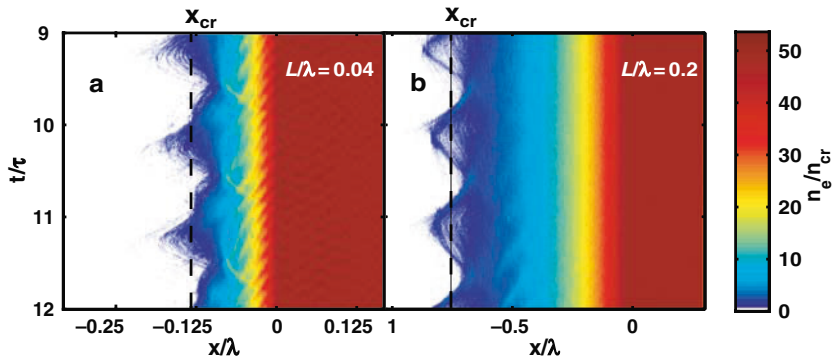

Fig. 6 Electron density distributions for p-polarized incident laser light with $a_0 = 0.5$ and for different plasma scale lengths. The initial plasma boundary is located at $x = 0$ with a density $n_{e0} = 45.56 n_c$. Angle of incidence $\theta = 45°$. The initial position of the critical surface $n_e/n_c = 1$ is indicated by a *dashed line*

$L/\lambda = 0.04$ and $L/\lambda = 0.2$ the amplitude of the plasma oscillations corresponds to about 3% and 6% of the laser wavelength, respectively.

The important parameter is the ratio s_0/L– the oscillation amplitude normalized to the plasma scale length. In the case of $L/\lambda = 0.04$ (Fig. 6a) we have $s_0/L \cong 1$. The electrons are pushed back and forth across the steep plasma–vacuum interface, and their motion is strongly nonlinear. On the other hand, for $L/\lambda = 0.2$ (Fig. 6b) we have $s_0/L \ll 1$, and the oscillations look nearly harmonic.

The harmonic spectra corresponding to the density distributions of Fig. 6 are depicted in Fig. 7. The circles show the spectra calculated from the oscillating mirror model. The normalized amplitudes s_0/λ (3% and 6%) were determined from Fig. 6. For $L/\lambda = 0.2$ the agreement is quite good. However, for

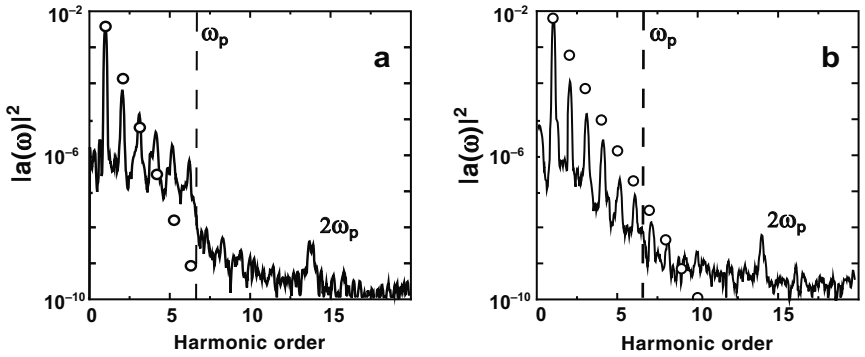

Fig. 7 Harmonic spectra corresponding to the density distributions shown in Fig. 6. *Circles* denote the harmonic amplitudes calculated using (14). The *dashed line* marks the position of the plasma frequency

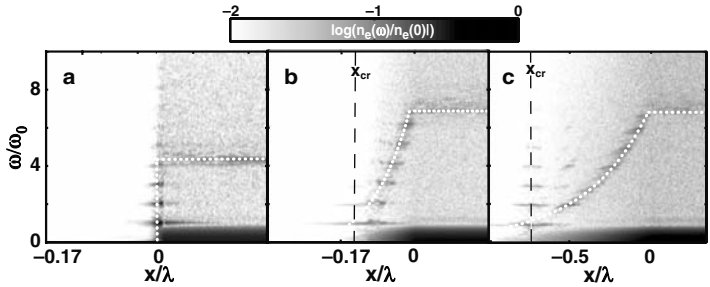

Fig. 8 Spatially resolved spectrum of the electron density. (a), (b), and (c) correspond to the densities shown in Figs. 4a, 6a and b, respectively. The initial position of the critical surface $n_e/n_c = 1$ is indicated by a *dashed line*. *White dotted lines* correspond to $\omega_p(x)$

$L/\lambda = 0.04$, the harmonic efficiency is strongly enhanced due to anharmonicity of the plasma oscillations. This enhancement shows a "cut-off" at the plasma frequency ω_p corresponding to the maximum electron density.

The spatially resolved spectra of the electron density oscillations shown in Fig. 8 provide deeper insight into the process of harmonic generation. The density plots represent the gray scale-coded Fourier transforms $\tilde{n}_e$ of electron density plotted as a function of frequency ω/ω_0 and position x/λ. Results for a step function profile (Fig. 8a, $L = 0$) and for exponential profiles with $L/\lambda = 0.04$ and $L/\lambda = 0.2$ (Fig. 8a and b) are shown. The dotted lines represent the plasma frequency ω_p for the electron density distribution given by (18). In the vicinity of this line the local plasma fluctuations are resonantly enhanced and show up in Fig. 8 as a fuzzy trace.

The horizontal gray streaks at multiples of the fundamental frequency represent the laser-induced localized charge density oscillations. These oscillations combine with the transverse electron velocity $v_\perp$ to give the current density responsible for the generation of harmonics (see (13)). The dark stripes at the bottom of the figures correspond to $\tilde{n}_{e,\omega=0}$, i.e., the stationary density distribution. The gray noisy underground on the right in each plot is the plasma density fluctuations.

For the step-like boundary, all the harmonic sources lie in the same plane $x = 0$ (Fig. 8a), consistent with the moving mirror model. However, the calculations for different values of the scale length indicate that plasma expansion and increase in scale length can lead to situations that cannot be adequately described by this model. For example, for the short scale length $L/\lambda = 0.04$, qualitative and quantitative deviations are quite obvious in Figs. 7a and 8b. First, the electronic motion cannot be represented by the motion of a single characteristic electronic boundary. Instead, the sources of the different harmonic frequencies are located at different positions along the x-axis (see Fig. 8b). Second, the generation of harmonics is resonantly enhanced by the excitation of the local plasma oscillations (Fig. 7a). Third, there is a high-frequency "cut-off" in the harmonic spectra because the local plasma oscillations can be resonantly excited only up the maximum frequency given by ω_p at n_{e0} (see Fig. 8b).

For the longer scale length $L/\lambda = 0.2$, the situation is quite different (Fig 8b). The laser field cannot penetrate much beyond the critical density. The charge density oscillations localized at the critical density are generated, and the harmonics are radiated from this density region. There is no sharp high-frequency "cut-off" in the spectrum. For $s_0/L \ll 1$, the motion of electrons becomes nearly harmonic. The mechanism of harmonic generation is now different. The relativistic retardation effects associated with the large amplitude of the electronic motion are important, and not the anharmonicity. This is further supported by the fact that a very similar harmonic spectrum is achieved in the case of a pure harmonically oscillating mirror with $s_0/\lambda = 0.06$ as shown in Fig. 7b. The relativistic mechanism dominates in this situation, notwithstanding the relatively low value $a_0 = 0.3$.

In summary, we have seen above two different mechanisms of the HOHG. In case of a steep plasma gradient, the HOHG can be achieved due to the nonlinearity of the plasma oscillations (analog to [9, 10]), and is additionally resonantly enhanced by the resonant plasma oscillations. The second one is due to the phase modulation introduced by the oscillating plasma surface (oscillating mirror) and is of the relativistic origin.

3 Experimental Observations of HOHG

3.1 Harmonic Spectra, Divergence, and Conversion Efficiency

Experimentally, the key point in HOHG is the use of femtosecond laser pulses with a very low prepulse level and high-intensity contrast. In this case, a steep plasma gradient can be formed during the interaction of the pulse with the target because there is no time for significant expansion during the pulse. Moreover two-pulse experiments can be performed in which the scale length can be controlled (Section 3.2).

The experimental set-up used in [33] for studying HOHG is shown in Fig. 9. High contrast 45 fs pulses at $\lambda = 800$ nm (Fig. 9a) from a titanium sapphire laser were frequency-doubled in a 0.8 mm thick KDP crystal to produce pump pulses at 400 nm with even higher contrast. An adaptive mirror compensated the residual wave front distortions of both beams and ensured diffraction limited focusing (Fig. 9b). As shown in Fig. 9 the blue beam and the infrared beam were focused onto the target by the same off-axis parabolic mirror. The peak intensity on the target for the 400 nm pulses was as high as 2×10^{19} W/cm^2 ($a_0 \simeq 1.3$).

Using the infrared beam, a plasma could be generated prior to the arrival of the intense blue pulse. By changing the delay time between the two pulses, the plasma scale length could be continuously controlled. The targets (optically polished glass or polystyrene substrates) were raster scanned to provide a fresh surface for each laser pulse.

The spectrum of the light reflected from the target was analyzed with the help of a toroidal grating which imaged the reflected light from the target onto a

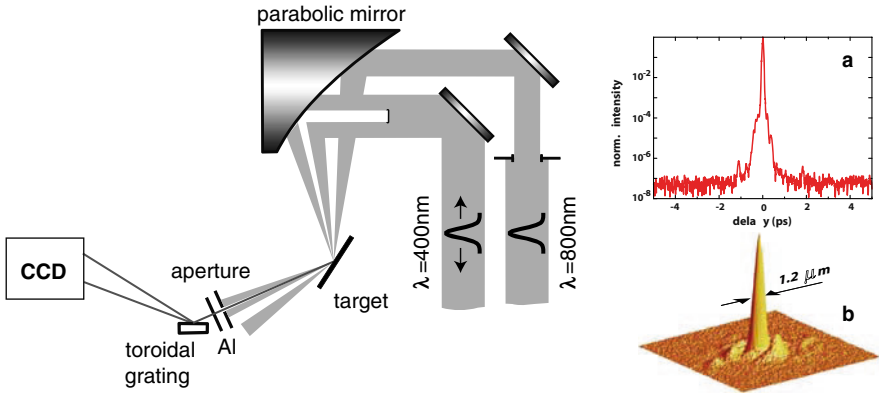

Fig. 9 Experimental schematic for HOHG: (a) third-order autocorrelation function for $\lambda = 800$ nm; (b) intensity distribution in the parabola focal plane for $\lambda = 400$ nm

CCD (charge coupled device) camera. The grating and the CCD chip were protected from the high-power-reflected blue light by a system of apertures and a 170 nm thick aluminum film.

Figure 10 shows the harmonic spectra recorded with pulses at $\lambda_0 = 400$ nm, at $I \simeq 2 \times 10^{18}$ W/cm^2 ($a_0 \simeq 0.5$, Fig. 10a), and $I \simeq 2 \times 10^{19}$ ($a_0 \simeq 1.3$, Fig. 10b). At $a_0 \simeq 0.5$, the harmonic spectra recorded with p-polarization exhibit cut-off at the frequency corresponding to the plasma frequency ω_p of the fully ionized target. This is typical for the resonantly enhanced mechanism described in the previous section. No harmonics could be detected when s-polarized excitation was used.

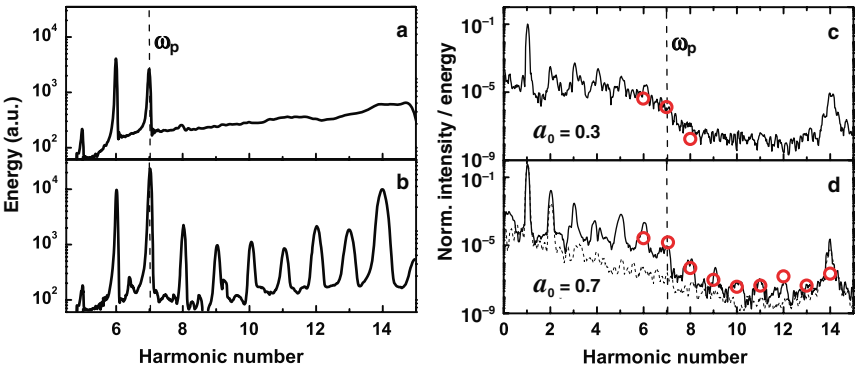

Fig. 10 Experimental and calculated harmonic spectra from polystyrene ($n_{e0}/n_c = 49$) and p-polarized excitation: **(a)** and **(b)** represent single pulse harmonic spectra recorded at 5×10^{18} W/cm^2 and 2×10^{19} W/cm^2, respectively; **(c)** and **(d)** correspond to the normalized spectra calculated for $L/\lambda = 0.02$ (*solid lines*) and $L/\lambda = 0$ (*dashed line*). The open red circles correspond to the experimental energy conversion efficiency calculated from the spectra shown in **(a)** and **(b)**

Two important qualitative changes take place when the intensity is increased to the relativistic level corresponding to $a_0 \simeq 1.3$ (Fig. 10b). First, the spectrum is no longer cut off at ω_p and extends significantly beyond the plasma frequency of the material (as one would expect from the oscillating mirror model). Second, harmonics can be also produced with s-polarized pulses [33]. The extension of the harmonic spectrum beyond ω_p predicted in [21, 16, 18, 19] for high intensity is a clear indication of the relativistic interaction (see also [25, 26]). The harmonic generation by s-polarized light indicates that the relativistic term of the Lorenz force $(1/c)\mathbf{v} \times \mathbf{B}$ comes into play. The harmonic divergence was measured to be within 10° both for $a_0 \simeq 0.3$ and $a_0 \simeq 1.3$. This is somewhat smaller than the divergence of the pump beam ($\sim 15°$).

Figures 10c and d illustrate a very good agreement between the experimental results and the PIC simulations. The filled circles in Fig. 10c represent the experimental data and indicate the transition between the different mechanisms of HOHG upon increasing the pump intensity.

3.2 Influence of the Plasma Scale Length

It is clear that in the experiments some degree of plasma expansion is always present. The actual plasma density profile in HOHG is strongly dependent on the temporal characteristic of the laser pulses. A poor pulse contrast may lead to suppression of the HOHG [19, 20, 21]. On the other hand, Fig. 10d (dashed curve) demonstrates that a certain degree of plasma expansion can be even advantagous. The experimental spectra in Fig. 10c and d agree with the simulated ones only when certain plasma expansion ($L = 2\%$ of the laser wavelength) is assumed.

PIC simulations have demonstrated the very important role of the plasma scale length L (e.g., see Figs. 7 and 8). Figure 11a [33] shows the calculated dependence of the fourth and fifth harmonics on L. It can be seen that on the step-like plasma–vacuum interface, the harmonics are relatively inefficient. Indeed, the high-target electron density $n_{e0} \approx 50 n_c$ prevents according to (9) and (10) efficient excitation of the plasma oscillations ($n_{e0} \approx 100 n_c$ is typical for solid-state targets). Due to plasma "softening" the harmonic efficiency grows with L for $L/\lambda < 0.05$. The resonant mechanism is suppressed around $L/\lambda \sim 0.1$ because it is associated with the steep plasma gradient. As a result, the harmonic efficiency drops and reaches a minimum. With a further increase of L, the relativistic mechanism comes into play and dominates for $L/\lambda > 0.1$, being only weakly dependent on the scale length.

Experimentally the influence of the plasma scale length on HOHG was studied in [29, 33] using the two-pulse technique. In [33] (see Fig. 9), the first pulse (infrared prepulse) generated a plasma on the target surface. The second (main) pulse at the wavelength of 400 nm was used for HOHG. By letting the plasma expand for a certain time before the interaction with the main pulse a

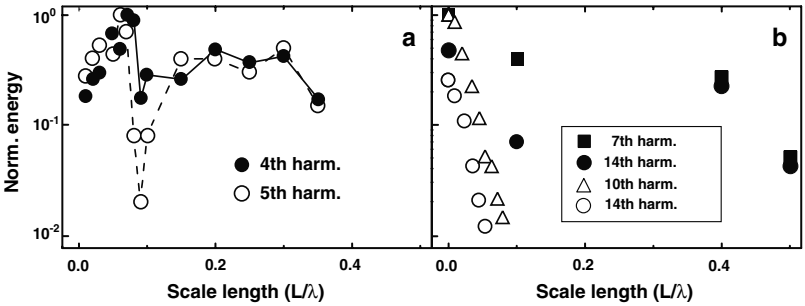

Fig. 11 Calculated dependence of the 4th and 5th harmonic energy on the plasma scale length (**a**), parameters same as in Figs. 6, 7 and 8. Experimental dependence of harmonic energy on the plasma scale length (**b**). *Filled circles* and *squares* correspond to the experimental results at $I = 2 \times 10^{19}$ W/cm^2; *open circles* and *triangles* represent experimental results with $I = 2 \times 10^{17}$ W/cm^2 from [29]

desired plasma scale length could be established. Thus, the influence of the plasma scale length was studied under controlled conditions.

The experimental results qualitatively agree with the predictions of the PIC simulations. In Fig. 11b, data points for harmonic generation with 2×10^{19} W/cm^2 of 400 nm light are compared with earlier experimental results [29] obtained with much lower intensity. It can be seen that for low intensity the harmonic generation decreases very rapidly with scale length. In contrast, for high intensity the dependence on scale length is much weaker, and harmonic generation was observed up to $L/\lambda = 0.5$. Thus, the high-intensity data do in fact show the relatively weak dependence expected for the relativistic mechanism, whereas the drop in the harmonic generation at low intensity is characteristic of the nonrelativistic, resonant mechanism. The predicted slight increase of the energy with the scale length for $L/\lambda < 0.1$ is not observed in the experiments. However, this deviation could be due to certain initial plasma expansion at zero delay time. The decrease of the harmonic energy at $L/\lambda > 0.4$ is accompanied by an increase of the harmonic divergence.

4 Summary

High-order harmonic generation from solid surfaces is an interesting example of relativistic nonlinear plasma physics. The process offers a new means of efficient generation of short wavelength radiation as well as the production of attosecond pulses and attosecond waveforms. The basics of HOHG can be understood from a very simple oscillating mirror model. In general, however, HOHG is determined by the interplay of two different mechanisms: a resonant (nonrelativistic) associated with a steep plasma–vacuum interface and a mechanism which is basically of relativistic origin.

The harmonic efficiency and the transition between mechanisms depend not only on the pump intensity but also on the plasma scale length. Well-collimated harmonics can be observed both below and above the relativistic "threshold". Very high harmonic orders and high conversion efficiencies can be expected when relativistic laser intensities are used. However, for such interactions very high contrast laser pulses are required.

References

1. N. Bloembergen: *Nonlinear Optics* (Benjamin, New York, 1965)
2. Y.R. Shen: *The principles of nonlinear optics* (John Wiley & Sons, New York 1984)
3. Z. Chang, A. Rundquist, H. Wang et al.: Phys. Rev. Lett. **79**, 2967 (1997)
4. Ch. Spielmann, N.H. Burnett, S. Sartania et al.: Science **278**, 661 (1997)
5. P. Sprangle, E. Esarey, and A. Ting: Phys. Rev. A, **41** 4463 (1990)
6. W.B. Mori, C.D. Decker, and W.P. Leemans: IEEE Trans. Plasma Sci. **21**, 110 (1993)
7. S.C. Wilks, W.L. Kruer, and W.B. Mori: IEEE Trans. Plasma Sci. **21**, 120 (1993)
8. P. Gibbon: IEEE J. Quantum Electron. **33**, 1915 (1997)
9. R. L. Carman et al.: Phys. Rev. Lett., **4**6, 29 (1981)
10. R. Bezzerides et al.: Phys. Rev. Lett. **49**, 202 (1982)
11. G. Tsakiris, K. Eidmann, J. Meyer-ter-Vehn, and F. Krausz: New J. Phys. **8**, 19 (2006)
12. G. Mourou, T. Tajima, and S. Bulanov: Rev. Mod. Phys. **78**, 309, (2006)
13. N. Naumova, J. Nees, I. Sokolov, B. Hou, and G. Mourou: Phys. Rev. Lett. **92**, 063902 (2004)
14. S. Gordienko, A. Pukhov, O. Shorokhov, and T. Baeva: Phys. Rev. Lett. **93**, 115002 (2004)
15. S. Gordienko, A. Pukhov, O. Shorokhov, and T. Baeva: Phys. Rev. Lett. **94**, 103903 (2005)
16. R. Lichters, J. Meyer-ter-Vehn, and A. Pukhov: Phys. Plasmas **3**, 3425 (1996)
17. R. Lichters and J. Meyer-ter-Vehn: Inst. Plas. Conf. Ser. **154**, 221 (1997)
18. D. von der Linde and K. Rzízewski: Appl. Phys. B **63**, 499 (1996)
19. D. von der Linde: Appl. Phys. B **68**, 315 (1999)
20. S. Bulanov, N. Naumova, and F. Pegoraro: Phys. Plasmas **1**, 745 (1994)
21. P. Gibbon: Phys. Rev. Lett. **76**, 50 (1996)
22. S-W. Bahk, P. Rousseau, T. Planchon et al.: Appl. Phys. B **80**, 823 (2005)
23. A. Tarasevitch, C. Dietrich, C. Blome et al.: Phys. Rev. E **68**, 026410 (2003)
24. A. Tarasevitch, C. Dietrich, and D. von der Linde: Plasma Mirror Distortions and Parametric Instabilities Induced by High Intensity Femtosecond Pulses on Solid Targets. In: *Superstrong Fields in Plasmas ,Conference Proceedings 611*. ed. by M. Lontano, G. Mourou, O. Svelto, T. Tajima (Am. Inst. of Physics, New York 2002) pp. 294-299
25. P. Norreys, M. Zepf, S. Moustaizis et al.: Phys. Rev. Lett. **76**, 1832 (1996)
26. J. Zhang, M. Zepf, P. Norreys et al.: Phys. Rev. A **54**, 1597 (1996)
27. S. Kohlweyer, G. Tsakiris, C. Wahlstrom et al.: Opt. Commun. **117**, 431 (1995)
28. D. von der Linde, T. Engers, G. Jenke et al.: Phys. Rev. A **52**, R25 (1995)
29. A. Tarasevitch, A. Orisch, D. von der Linde et al.: Phys. Rev. A **62**, 023816 (2000)
30. Ph. Balcou et al.: Applied Physics B **74**, 509 (2002)
31. U. Teubner, G. Pretzler, Th. Schlegel et al.: Phys. Rev. A **67**, 013816 (2003)
32. A. Tarasevitch, K. Lobov, C. Dietrich, and D. von der Linde: Relativistic Surface Harmonics. In: *CLEO/QELS06 Conference Program May 23-25, 2006 Long Beach, CA, USA* p. 169

33. A. Tarasevitch, K. Lobov, C. Wünsche, and D. von der Linde: Phys. Rev. Lett. **98**, 103902 (2007).
34. B. Dromey M. Zepf, A. Gopal et al.: Nature Phys. **2**, 456 (2006).
35. C. Thaury, F. Quéré, J.-P. Geindre et al.: Nature Phys. **3**, 424 (2007)
36. L. Landau and E. Lifshitz: *The classical theory of fields*, 4th edn. (Pergamon press, Oxford 1975)
37. A. Bourdier: Phys. Fluids **26**, 1804 (1983)
38. V. Vshivkov, N. Naumova, F. Pegoraro, and S. Bulanov: Phys. Plasmas **5**, 2727 (1998)
39. L. Landau, E. Lifshitz, and L. Pitaevskii: *Electrodynamics of continuous media*, 2nd edn. (Pergamon Press, Oxford 1984)
40. Strictly speaking the following expression for H'_z on the boundary is valid only outside the plasma. Inside the plasma H'_z is higher by the factor of $\cos^{-2}\theta$. This jump of H'_z takes place because the plasma moves in the K' frame with the velocity $-V$ along the y-axis. However this factor is not important for the qualitative consideration if θ is not too large
41. J. Jackson: *Classical Electrodynamics*, 2nd edn. (J. Wiley & Sons, New York 1975)

Table-Top X-Ray Lasers in Short Laser Pulse and Discharge Driven Plasmas

P.V. Nickles, K.A. Janulewicz, and W. Sandner

1 Introduction

The first proposal for X-ray lasers (XRL) dates back to 1963 [1]. However, the enormous requirements of the pump energy for these short wavelength lasers delayed their experimental realization until 1984 when the first soft X-ray lasers from laser-produced plasmas were demonstrated [2, 3]. The following decade resulted in numerous successful soft X-ray laser experiments and proof-of-principle demonstrations of important applications. However, the large size, complexity and costs of the pump lasers (laser drivers) for these X-ray lasers made a widespread application impossible. The development of the short pulse high-intensity lasers based on the chirped pulse amplification (CPA) technology during the first half of the 1990s helped to make remarkable progress in many laboratories on the way towards compact so-called table-top X-ray lasers. Now, the first table-top X-ray lasers driven by ultrashort high-intensity pulses have been demonstrated and systems with a reasonable averaged coherent output power are expected to be in use soon.

In the present contribution general features of XRLs, including the most important excitation schemes of the table-top systems driven by short optical laser pulses as well as capillary discharges, are described. For additional information we refer to the books by R.C. Elton [4], P. Jaegle [5], A.G. Michette and C.J. Buckley [6] as well as to the review article by J.J. Rocca [7].

1.1 General Properties of X-Ray Lasers

1.1.1 Amplified Spontaneous Emission

Many of the general properties, described in the following sections, are characteristic for most types of XRLs. All these lasers are mirrorless and use the

P.V. Nickles
Max Born Institute, Berlin, Germany; Advanced Photonics Research Institute at the Gwangju Institute of Science and Technology, Gwangju, Republic of Korea, Germany
e-mail: nickles@mbi-berlin.de

T. Brabec (ed.), *Strong Field Laser Physics*,
DOI: 10.1007/978-0-387-34755-4_15,

amplified spontaneous emission (ASE) as the amplifying mechanism – one of the fundamental processes present in nearly all lasers. ASE is a phenomenon in which a group of atoms with a population inversion (active medium) spontaneously emits photons. This emission is subsequently amplified by a similarly excited group of atoms in the stimulated way [8]. If the amplification occurs along a thin cylinder including the inverted medium, for example a plasma column, and is sufficiently high, this can result in an output beam from each end of the cylinder, which can be highly directional, with a reasonable level of coherence. This radiation may become strong enough to extract most of the energy deposited in the inverted medium and put it into intense, directed and coherent beams. Thus, the inverted medium acts as a "mirrorless laser".

1.1.2 Gain Medium

The X-ray laser medium is in most cases a highly ionized plasma. In such a plasma ion energy levels with allowed transitions within the EUV- or X-ray spectral range can be excited. This plasma is created by a fast ionization process usually by either a strong optical pump laser pulse or a fast-pulsed current in a capillary discharge leading to a population inversion between two suited energy levels of ions.

Pump laser intensities in the range between 10^{12} and 10^{18} W/cm^2 are usually used in X-ray lasers to irradiate the target, which is mostly a solid- or gas-like material. This material is ionized and heated by the laser pulse due to inverse Bremsstrahlung absorption (OFI process ionizes and heats the medium directly in the same process – see §2.3) leading to a characteristic distribution of the plasma electron density n_e and temperature T_e. Typical profiles of the electron density and temperature in the laser-produced plasma are given in Fig. 1.

Once the plasma is created the pump laser radiation with the wavelength λ_p propagates with limited losses through subcritical plasma up to the region (surface) of critical electron density n_{ec} given by

$$n_{ec} = \omega_p^2 \varepsilon_0 m_e / e^2 \tag{1}$$

where ε_0 is the electric constant (permittivity of free space), m_e is the electron mass, e is the elementary charge and ω_p is the plasma frequency.

$$\omega_p = (e^2 n_e / \varepsilon_0 m_e)$$

or

$$n_{ec}[\mathrm{cm}^{-3}] = 1.11 \times 10^{21} / \lambda_p^2[\mu\mathrm{m}] \tag{2a}$$

and

$$\omega_p[\mathrm{rd/s}] = 5.64 \times 10^4 (n_e[\mathrm{cm}^{-3}])^{1/2} \tag{2b}$$

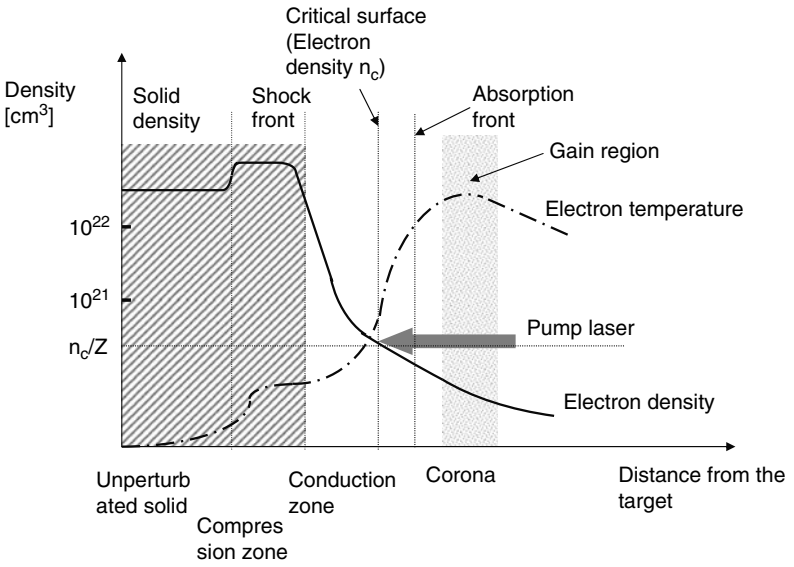

Fig. 1 Typical electron density and temperature distribution in a laser-produced plasma (with the gain region for X-lasing)

The laser pulse is dominantly absorbed near the critical surface due to high density of the medium (plasma) and hence the electrons are mostly heated in this zone (corona zone). The absorbed pump laser energy is then transported by the electron thermal conduction towards the target and into the corona that expands into the vacuum (hydrodynamical expansion). Hence, the region where the X-ray amplification preferentially takes place is the coronal plasma. Examples of the parameters relevant to this process are given below:

Density of a solid target: $\sim 10^{23}$ atoms/cm^3
Critical electron density n_{ec} (pump wavelength $\lambda_p = 1.06\,\mu$m): $\sim 10^{21}$ cm^{-3}
Electron density n_e in the zone of high gain (depending on the atomic number of the target): 10^{19}–10^{21} cm^{-3}
Ion density: 10^{17}–10^{19} cm^{-3}

1.1.3 Emission Wavelength

The wavelength of the lasing transition is given by the difference in the excitation (binding) energy between the two levels involved. In general the wavelength λ of this transition can be calculated using Moseley's rule:

$$1/\lambda = R_\infty (Z - \delta)^2 (1/n_u - 1/n_l) \tag{3}$$

where R_∞ is the Rydberg constant, Z the atomic number, δ the shielding constant (expresses the shielding of nuclear charge by atomic electrons) and

n_u and n_l are the principal quantum numbers of the upper and the lower energetic levels, respectively.

For example, the transition $n_u = 3 \rightarrow n_l = 2$ (Balmer$_\alpha$ transition) of hydrogen-like carbon with $Z = 6$ emits photons with a wavelength of $\lambda = 182.3\,\text{Å}$ or according to the conversion formula

$$\lambda[\text{Å}] = 12.4 \times 10^3 / h\nu[\text{eV}] \tag{4}$$

with an energy of 68 eV.

Usually ions are designated by the number of electrons that have been removed/left, i.e. C^{5+} (CVI) is a hydrogen-like (H-like) carbon ion, which has been produced by removing five electrons from a neutral carbon atom and leaving only one electron bound to the positive nucleus. This carbon ion belongs to the hydrogen-like isoelectronic sequence, i.e. the ions having the same number of bound electrons as a hydrogen atom. In the case of the neon-like (Ne-like) isoelectronic sequence 10 electrons remain bound to the nucleus, i.e. neon-like titanium ($Z = 22$) is a 12-fold ionized (Ti^{12+}) neutral atom. Such isoelectronic scaling to higher Z shifts the emitted wavelength to the X-ray region. In principle all atoms from He ($Z = 2$) up to Uranium ($Z = 92$) can be used as gain medium for an XRL, assuming the required pump energy can be supplied and the plasma is transparent to the X-rays.

Up to date, XRLs with the wavelengths between 3.56 nm (nickel-like Au) and 60.8 nm (neon-like sulphur) have been reported (see Table 1.). In the near future an extension of the emission spectrum to shorter wavelengths seems to be possible (hydrogen-like Na with lasing transition into the ground state 2p→1 s at $\sim$ 1 nm (see Table 4.))

1.1.4 Population Inversion/Gain

The plasma as an active (amplifying) medium, consisting of ions of many different ionization stages, is very unstable in time and has a typical lifetime of several nanoseconds. In order to create a population inversion efficiently (a prerequisite of any gain) a population reservoir should be assigned to a stable ionization stage. Therefore ions with closed outer electronic shells are best suited as an X-ray laser medium. In principle a rich diversity of ions could produce, under special conditions, a reasonable amplification.

The most important closed shell ions following the widely used denomination of ions according to their numbers of the remaining electrons are shown in Table 2. Population inversion can be realized in a system where at least three or four levels are involved.

A simplified case of a three-level scheme is shown in Fig. 2. The upper lasing level is pumped by electrons from the ground state. The population inversion can be produced between the two excited levels above the ground state. The transition from the upper lasing level to the ground level has to be forbidden

Table 1 Operating short pulse pumped transient collisional XRL (selected survey)

Target, z	Ion, transition, J	Wavelength [nm]	Gain [cm^{-1}], *gl* output	Pump scheme*	Pumping	Target configuration	Lit.
Ar, 18	[Ne], 3p–3s, J = 0–1 3d–3p	46.9 45.1	11, *gl*∼10	tr,trv	4 J 600 ps, 7 J 6 ps, ∼1 ns delay	gas puff, 9 mm	[50, 51]
Titan, 22	[Ne], 3p–3s, J = 0–1	32.6	saturation	tr	long/short	slab, 10 mm	[39]
Molybdenum, 42	[Ni], 4d–4p, J = 0–1	18.89	*gl* 16.8 saturation 3–5 μJ	tr	1.2 J–600 ps, 5 J–1 ps, 700 ps delay	flat slab, 0.9 cm, divergence 2–3 mrad	[38]
Palladium, 46	[Ni], 4d–4p, J = 0–1	14.68	41–62 *gl*∼18. saturation,10 μ $B = 1 \times 10^{24}$ phs^{-1} mm^{-2} $mrad^{-2}$	tr,trav	1.2 J–600 ps, 5–7 J–1 ps, 700 ps delay	flat slab, 0.9 cm, divergence 2–3 mrad	[38]
Silver, 47	[Ni], 4d–4p, J = 0–1	13.89	*gl*∼18. saturation	tr, trav		flat slab, 0.9 cm, divergence 2–3 mrad	[26]
Silver, 47	[Ni], 4d–4p, J = 0–1	13.89	*gl*∼18. saturation	tr, trav	1.2 J–600 ps, 5–7 J–1 ps, 700 ps delay	flat slab, 0.9 cm, divergence 2–3 mrad	[42]
Silver, 47	[Ni], 4d–4p, J = 0–1	13.89	*gl*∼15. saturation	tr, trav	3 J, shaped single pulse -	flat slab, 0.6 cm, divergence 5 mrad	[43]
Silver, 47	[Ni], 4d–4p, J = 0–1	13.89 12.	*gl*∼13.6. saturation *gl*∼8	tr, trav	12–14 J, 2 J–4 ps +12 J–4 ps, 1.2 ns delay,	flat slab, 0.5 cm,	[57]
Cadmium, 48	[Ni], 4d–4p, J = 0–1	13.15	near saturation	tr	1.2 J–600 ps, 5 J–1 ps, 700 ps delay	flat slab, 0.9 cm, divergence 2–3 mrad	[42]
Tin, 50	[Ni], 4d–4p, J = 0–1	11,91	*gl*∼10.	tr	1.2 J–600 ps, 5 J–1 ps, 700 ps delay	flat slab, 0.9 cm,	[42]

Table 1 (continued)

Target, z	Ion, transition, J	Wavelength [nm]	Gain [cm^{-1}], *gl* output	Pump scheme*	Pumping	Target configuration	Lit.
Xe, 54	[Ni], 4d–4p, J = 0–1	9.98	g = 17.4 cm^{-1}	T trav	2 J–3 ps and 16 J–3 ps, 1.2 ns delay	Gas puff	[52]
Tungsten (W), 74 predicted	[Ni], 4d–4p, J = 0–1	4.32	g = 220 cm^{-1}, *gl* = 20	tr	1053 nm, 1 ps and 100 ps 2.5 J	1 mm	[58]
Gold 79 shortest realized XRL	[Ni], 4d–4p, J = 0–1	3.46		q-s			[36]
Uran, 92 (shortest coll. XRL)	[Ni], 4d–4p, J = 0–1	2.145		q-s			[59]

* tr and trav denote transient pump scheme and the optional travelling wave arrangement, respectively.

Table 2 XRL-relevant ionic species with a closed outer shell

Ion type	Closed shell $n=$ main quantum number	Number of bound electrons	Fundamental electronic structure
Helium-like	$n=1$	2	$1s^2$
Neon-like	$n=2$	10	$1s^2 2s^2 2p^6$
Nickel-like	$n=3$	28	$1s^2 2s^2 2p^6 3s^2 3p^6 3d^{10}$

(it should be a metastable or long-lived level), while the lower lasing level should be rapidly emptied (see collisional excitation).

The gain, $g(\nu)$, describes the beam amplification in a system without any considerations on the origin of this amplification. As in the case of an optical laser the small signal gain coefficient $g(\nu)$ for an XRL is equal to a product of the stimulated emission cross-section σ and the population inversion density ΔN on the lasing transition [4, 9]:

$$g(\nu) = \sigma \times \Delta N \tag{5}$$

with the population inversion

$$\Delta N = (N_u - N_l f_u / f_l), \tag{6}$$

where $N_{u,l}$ are the upper/lower lasing level population densities and $f_{u,} f_l$ denote the corresponding level degeneracy factors. Hence,

$$g(\nu) = \sigma \times \Delta N \cong A_{ul}\lambda^2 / 8\pi\Delta\nu(N_u - N_l f_u / f_l)[cm^{-1}] \tag{7}$$

where A_{ul} is the Einstein coefficient for spontaneous emission and scales along the isoelectronic sequence as $A_{ul} \propto \lambda^2$.

The gain coefficient depends on the line profile and for the case of a naturally broadened transition with $\Delta\nu \propto A_{ul}$ it follows that

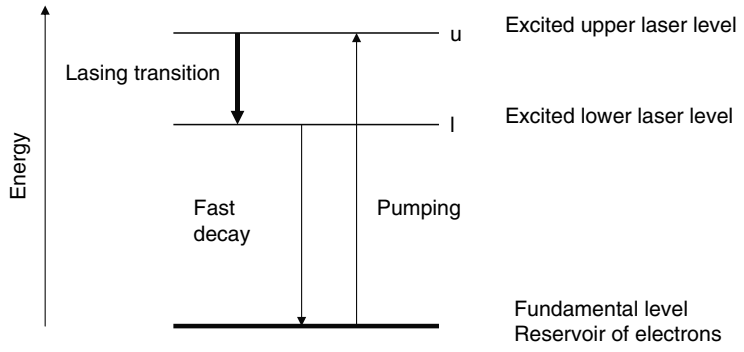

Fig. 2 Principle of a three-level excitation scheme

$$g(\nu) \propto \Delta N \lambda^2 \cong N_u \lambda^2 [cm^{-1}] \tag{8}$$

In general, the gain increases as a function of the plasma electron density n_e. Electron collisions that can thermalize the populations of the lasing levels and under some conditions destroy the population inversion ΔN, determine the upper limit for the gain increase. This limit varies for the different excitation schemes.

1.1.5 Intensity

XRLs operate with a single-pass or a double-pass amplification of the spontaneous emission through the gain medium of length l. In such ASE amplifiers the spectrally integrated intensity of the laser signal increases with plasma length l, as (so-called Linford formula [10])

$$I(\nu) = (E(\nu)/g(\nu))(e^{gl} - 1)^{3/2}(gle^{gl})^{-1/2} \tag{9}$$

where $E(\nu)$ is the medium emissivity. The emissivity is the spectral density of the emitted energy per volume and time unit; if applied within a solid angle Ω it gives

$$E(\nu) = (N_u h\nu\Omega/4\pi)\, A_{ul}(\nu) \tag{10}$$

In experiment, only the intensity integrated over the line emission profile can be observed. Hence the formula (9) has to be integrated over the spectral profile. For a Lorentzian line profile it follows that

$$I(0) = (\pi^{-1/2}/2 \times \Delta\nu E(0)/g(0))(e^{gol} - 1)^{3/2}(g_o le^{gol})^{-1/2} \tag{11}$$

where $\Delta\nu$ is the full linewidth at half-maximum (FWHM), and $g(0)$ and $E(0)$ are the gain and the emissivity at line centre, respectively.

The line intensity is mostly evaluated from XRL spectra, recorded with calibrated spectrometers and detectors like X-CCD cameras or multi-channel plates (MCP) combined with an optical CCD camera (see common arrangement in Fig. 4). A typical spectrum of the emission of a X-ray laser (here of a nickel-like Ag-XRL at 13.9 nm) registered with a flat-field spectrometer is shown in Fig. 3. The lineout of this spectrum, demonstrating clearly how a single emission line of the XRL signal dominates the spectrum of the plasma, is also given in Fig. 3.

1.1.6 Saturation

The most efficient energy extraction from a laser medium (independent of the wavelength range) is reached in an operation regime where gain saturation has

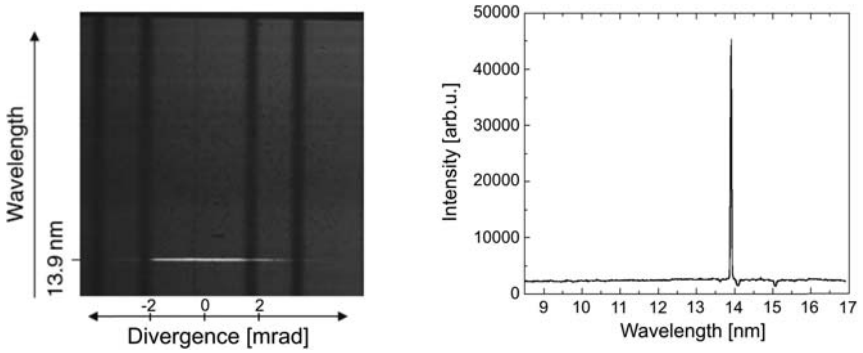

Fig. 3 Emission spectra of a nickel-like Ag X-ray laser at 13.9 nm (4d–4p line, target length 4 mm, pump energy 1.8 J in a single shaped pulse) taken with a flat-field spectrometer. On the left side a CCD camera picture shows the spectrum with the X-ray laser line. The vertical dark lines come from inhomogeneities of the filters used. The signal extension in the abscissa direction allows estimation of the output signal divergence. On the right side is shown the corresponding wavelength scan, demonstrating how the XRL signal dominates the plasma spectrum. The underlying broad, low-level background is due to the incoherent plasma emission

been achieved. Importantly, the saturation effect limits the exponential increase of the intensity with plasma length up to a certain, arbitrarily defined value referred to as saturation intensity I_s. Above this limit the dependence changes to a linear one. The saturation intensity in the form of a formal criterion is defined as the intensity where the actual gain $g(\nu)$ is reduced down to half of its small signal value, g_0. This intensity restriction takes place if the stimulated emission rate becomes comparable with the pumping process. In general, the gain factor at saturation $g(\nu)$ is given by the expression

$$g(\nu) = g_0(\nu)/(1 + I/I_{\text{sat}}) \tag{12}$$

The saturation intensity is found by equating the rate of the stimulated emission to the total exit rate R_{out} of the upper state [10] and integrating over the line profile. In real XRLs the saturation intensity is between 10^8 W/cm^2 for the OFI-XRLs and 10^{11} W/cm^2 for collisionally pumped XRLs. It should be noted that these are not the upper limits of the output but just the starting point at which the energy extraction becomes efficient.

In most lasers an optical feedback provided by an optical cavity (mirrors) helps to reach this saturation intensity by multiple passing of the medium. However, in the X-ray lasers the duration of the gain (usually $<<1$ ns) is much shorter than the time required for the necessary number of round trips in a cavity (for instance for a cavity length of 50 cm the round-trip time is of $\sim$3.3 ns). This short gain lifetime is a result of either the difficulty in maintaining the stringent plasma conditions for a sufficient period necessary for amplification in the quasi-steady-state scheme [11, 12, 13, 14, 15, 16] or a fast self-terminated

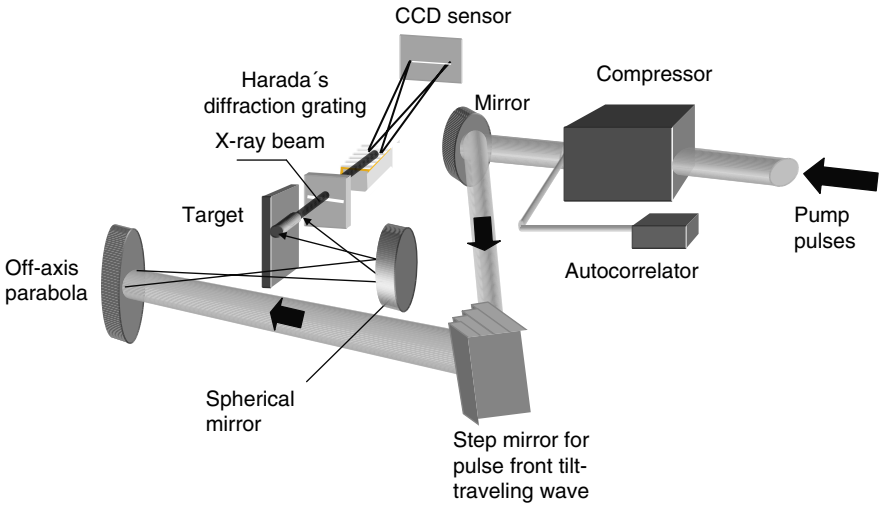

Fig. 4 Typical setup for a transversely laser-pumped single-pass XRL with flat solid target, travelling wave excitation and a coupled X-flat-field spectrometer

nature of the population inversion in transient schemes [17, 18, 19]. Therefore, present day XRLs normally operate with a single-pass or very seldom with double-pass amplification in the medium. A typical experimental setup for a single-pass XRL experiment, used, for example, in the Max Born Institute and other laboratories, is given in Fig. 4.

There is a general rule also valid for XRLs that gain saturation is obtained when the gain–length product $gl \geq 15$ [13, 15, 16, 20, 21]. Figure 5 shows amplification of two 3p–3s lines of a neon-like Ti-XRL with the increasing target length [20, 21]. It is clearly seen that the *gl*-factor becomes saturated at target lengths >6 mm.

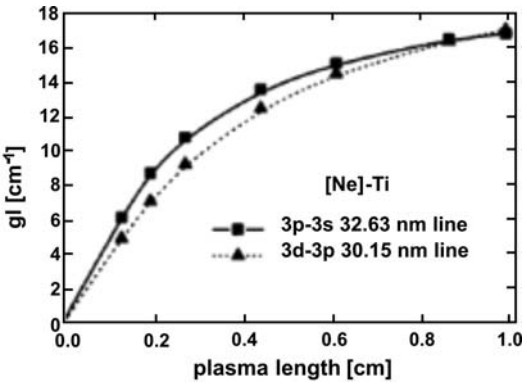

Fig. 5 Gain–length product (*gl*) versus plasma length for two lasing lines of a neon-like Ti–XRL [20, 21]. Both lines show a saturation-like behaviour for plasma lengths $l > 0.6$ cm

1.1.7 Pump Power Requirements for Soft X-Ray Lasers in Plasmas

It follows from (8) that in comparison to the optical range the gain (amplification) in the X-ray range will be dramatically reduced and requires deposition of a significantly higher power density in the active medium to obtain the necessary high gain. The minimum pump power density required to maintain a certain population of the upper level N_u scales with the expected emission wavelength as

$$P = N_u A_{ul} hc/\lambda \propto N_u \lambda^{-3} \tag{13}$$

The actual power density required to obtain a certain gain coefficient depends also on the line profile. Generally, the relation between the pump power required and that being at disposal is one of the fundamental constraints in the realization of an X-ray laser. It limits the volume V of the gain medium and also the gain–length product, which is the important parameter for any real XRL.

From a rough estimate assuming that the upper level decay rate is determined only by radiative transitions and expecting $gl = 10$ the required pump intensity I_p can be estimated from the expression

$$I_p = \text{energy}/(\text{duration} \times \text{area}) \approx 10^{19}/\lambda^4 [\text{Wcm}^{-2}] \tag{14}$$

with λ in [Å].

Equation (14) shows a dramatic increase in the required intensity with decreasing wavelength. For instance, an estimate assuming an efficiency of the energy deposition of 1% and a plasma area of $0.1 \times 10\,\text{mm}^2$ shows according to (14) that for the wavelengths of $\lambda = 100$ Å and $\lambda = 10$ Å, pump intensities of $I_p = 10^{13}$ W/cm^2 and $I_p = 10^{17}$ W/cm^2, respectively, are required. This means that assuming a pump pulse duration of 1 ns one has to supply a pump energy of 10^2 or 10^6 J, respectively.

One of the simplest ways to reduce this enormous amount of the energy needed is applying shorter pump pulses at constant intensity. In the case of a 1 ps pump pulse, the required energies will decrease to 10^{-1} J and 10^3 J, respectively.

1.1.8 Size and Geometrical Output Characteristics

Very high pump power densities and the usual requirement of a small optical thickness in the transverse direction of the elongated plasma column [4] result in gain volumes which are small in comparison to those of longer wavelength plasma lasers in the optical range. Therefore the lasing media have sizes which are typically $2w = 10$–$500\,\mu$m in diameter and $l = 0.1$–50 cm in length, corresponding to an aspect ratio of $2w/l \approx 1{:}1000$.

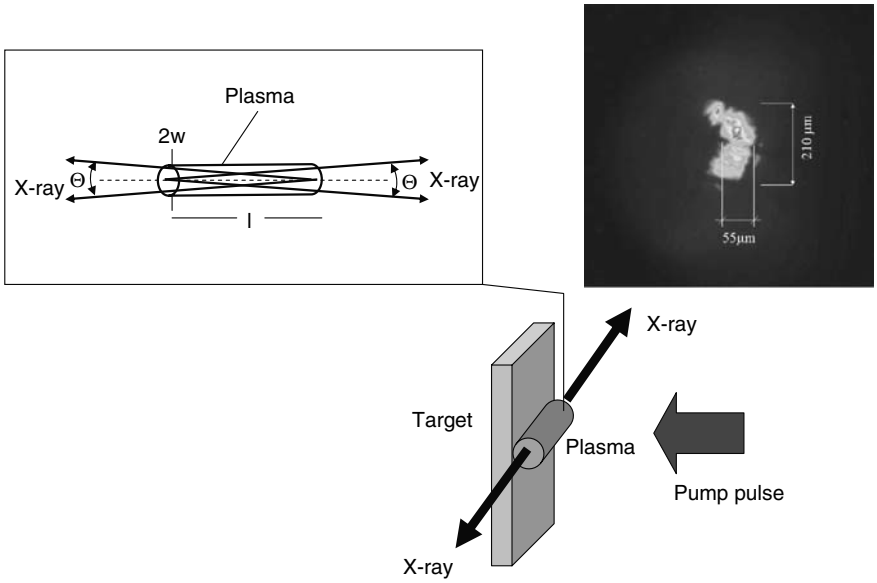

Fig. 6 Output beam of a transversely pumped XRL. Θ – divergence of the XRL beam, $2w$ – diameter of the amplification zone in the plasma, l – length. In the upper right corner it is shown the transverse XRL beam distribution at the output plane (nickel-like Ag-XRL). The dark "hot spot" in the distribution has a diameter of about 25 μm

Generally, it is requested to increase the aspect ratio by lengthening the gain medium in order to operate the XRL in saturation or – also important – to improve the transverse spatial coherence (see coherence). The XRL output signal will create a narrow cone with a divergence determined by the aspect ratio of the gain medium as shown in Fig. 6. For gain medium size with a length of $l = 1$ cm and a diameter of $2w = 50$ μm the beam divergence is equal to

$$\Theta = 2w/l \approx 5\,\text{mrad} \tag{15}$$

A typical near field distribution of the output of the saturated XRL (Ni-like silver at 13.9 nm) is given in Fig. 6. It is visible that the output has no TEM 00-mode distribution as a result of the imperfect homogeneity of the amplifying plasma in the transversely pumped XRL scheme. However, the dominating part of the radiation is contained in a transverse area with a reasonable coherence and an extension of about 50 μm.

If the plasma column is very tight, so that it has a Fresnel number $N_f = w^2/l\lambda \approx 1$, then the emission from the plasma column face could emerge in a single transverse mode. This output beam can have a large degree of spatial coherence (although the total power will not be high, because of the small diameter of the active volume). In the case of a half-cavity arrangement (with only one mirror

M at a distance l_M from the active medium) l in expression (15) must be substituted by $(l+l_M)$ giving a reduction in divergence for the second pass due to the increased length of the optical path.

1.1.9 Efficiency/Output Power/Energy

The currently available efficiency η for conversion of pump energy to X-ray laser output energy is in the range of $\eta = E_X/E_P \sim 10^{-6}$ for collisionally excited XRLs and about 10^{-8} for OFI systems. The XRL peak output power is in the range of several MW, assuming peak pumping power in the TW (terawatt) range. Much effort has been put into increasing the XRL efficiency by optimizing the excitation conditions. The use of only one mirror of the quality currently available can increase the total output by more than a factor of two.

The output energy at saturation is approximately equal to the product of the saturation intensity, the duration of lasing and the cross-section area of the lasing region:

$$E_{out} \cong I_{sat} \times \tau_x \times \text{area}_x \tag{16}$$

1.1.10 Linewidth

The unamplified spectral profile of a plasma emission line is determined in the most general case by spontaneous emission, electron collision, by ion–ion interactions and the radiative transport effects. Amplified lines in the X-ray laser will be narrowed during the amplification process as approximately the square root of the gain–length product in the small signal regime [22]. As the laser with mixed broadening mechanisms saturates, the homogeneous component cancels any noticeable rebroadening effect which is observed for purely inhomogeneously broadened lines. Inhomogeneous or Doppler broadening results typically in a Gaussian-shaped line profile with a width (FWHM) given by the ratio [4, 23]

$$\Delta\lambda_d/\lambda_d \approx 7.7 \times 10^{-15}(kT_i/2Z)^{1/2} \tag{17}$$

where kT_i is in eV, Z is the atomic number.

For a high-temperature transient plasma it is $\Delta\lambda_d/\lambda_d \approx 5 \times 10^{-5}$. For a quasi-stationary neon-like selenium X-ray laser at 20.6 nm a line narrowing with an increase in the gain–length product was measured reaching a minimum value of 0.4×10^{-4} at saturation [24] (see Fig. 7). In the case of a low temperature plasma, as it is expected for optical-field ionization recombination excitation schemes (see OFI laser), further reduction up to $\Delta\lambda_d/\lambda_d \approx 10^{-6}$ seems to be realistic.

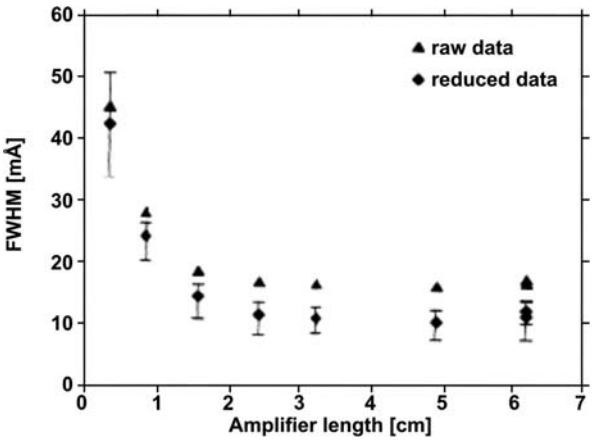

Fig. 7 Measured and modelled linewidths (FWHM) of a 20.6-nm neon-like Se XRL as a function of the amplifier lengths (from [24], Fig. 10)

1.1.11 Pulse Duration

The duration of the XRL pulse strongly depends on the length of the pumping pulse and the level population kinetics of the excitation scheme, i.e. on the gain duration. The latter depends on the temporal behaviour of ions in the ionized plasma, and the gain duration is proportional to Z_{eff}^{-4}, i.e. the gain duration becomes shorter for higher Z-elements [25]. Short pulse pumping with picosecond or femtosecond pulses applied to transient or self-terminating ASE schemes (see transient XRL) as well as to configurations with a travelling excitation wave can result in emission of picosecond or even subpicosecond short wavelength pulses. The shortest-to-date measured XRL pulse duration in a transient Ni-like Ag-XRL pulse at 13.9 nm – was about 2.0 ps [26]. Inner-shell XRLs (§ 2.4.1) should emit even shorter pulses.

1.1.12 Coherence

Spatial Coherence

Spatial coherence in the direction transverse to the axis of an X-ray laser beam defines the length across the wavefront over which the wavefront changes by a wavelength. In other words it is the extent of the undistorted wavefront which can be measured at a plane at a distance L_{d} from the illumination source with a diameter d_{s}:

$$D_{\text{coh}} \approx L_{\text{d}} \lambda_{\text{x}} / d_{\text{s}}. \tag{18}$$

It follows from (18) that an XRL at $\lambda_{\text{x}} = 10\,\text{nm}$ with an output aperture of $d_{\text{s}} = 100\,\mu\text{m}$ illuminates coherently at a distance of $L_{\text{d}} = 1\,\text{m}$ an area with a diameter of $D_{\text{coh}} = 0.1\,\text{mm}$. Such a spatial coherence is of interest for applications requiring a small focal region (microscopy or holography).

The area of coherence is usually smaller than the total illuminated area. The intensity distribution can consist of q small areas of coherence or transverse modes with a correspondingly reduced power. Thus, the transverse coherence in the X-ray beam has dimensions corresponding to $\sim 1/q$ of the beam diameter. The number q decreases with improvement of the plasma homogeneity in the amplification zone. Therefore, the spatial coherence as well as the power in a single transverse mode can be increased by improving the plasma homogeneity, enlarging the gain length or reducing the diameter of the gain region, which is equivalent to a small Fresnel number [27]. Other methods to improve the spatial coherence (or brightness) of an XRL include using either the half-cavity setup or the injection of a seed (for example high harmonics) signal into an X-ray amplifier [28]. In the case of capillary discharge XRLs, refraction at a steep density gradient can also reduce the effective transverse source size, leading to essentially full spatial coherence [19, 29]. This was demonstrated with a plasma column length of 36 cm and an aspect ratio exceeding 1000:1 [29].

Very recently it was shown that a saturated transient X-ray laser in nickel-like Ag with the length of 6 mm and pumped by only one single shaped pulse with the energy lower than 3 J could emit a reasonable coherent output signal [30]. This result is explained by the improved plasma homogeneity caused by the special irradiation conditions.

In practice, the spatial coherence is measured by using diffracting elements like double slits, incoherent slit arrays, knife edges and wires. Young's double-slit interferometer setup and the corresponding fringe modulation are pictured in Fig. 8.

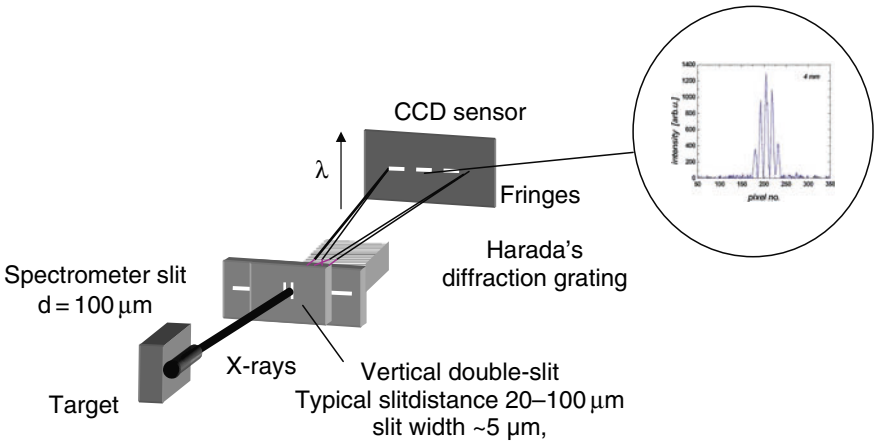

Fig. 8 Double-slit setup for the measurement of the fringe visibility of a X-ray laser (single shaped pulse pumped nickel-like Ag at 13.9 nm with 4 mm target length [141]), which allows the estimation of the spatial coherence of the source from the fringe modulation. The insert shows the fringe modulation for a 20 µm slit distance

The interference patterns are compared to those of an incoherently radiating circular disk. For ideal double-slit interference, in which both slits are equally and uniformly illuminated, the modulus of the complex coherence factor is equal to the fringe visibility, given as

$$|\mu| = (I_{\max} - I_{\min})/(I_{\max} + I_{\min}) \tag{19}$$

where $I_{\max}$ and $I_{\min}$ are the maximum and minimum intensities of the fringe pattern.

From the fringe visibility as a function of slit spacing, the equivalent incoherent source size of the X-ray lasers can be estimated using the following formula:

$$|\mu(\Delta x)| = \frac{2J_1(\pi d_s \Delta x/\lambda L_d)}{\pi d_s \Delta x/\lambda L_d} \tag{20}$$

where Δx is the slit spacing, d_s is the diameter of the source, z the distance from the source to the double slit and J_1 is the Bessel function of the first kind, order 1.

Temporal Coherence

An ASE emitter maintains coherence for a period t_{coh} that is inversely proportional to the spectral linewidth [4]:

With $(\lambda_x/\Delta\lambda_x) \sim 10^4$

$$t_{coh} \approx (\lambda_x/c) \times (\lambda_x/\Delta\lambda_x) \approx (3 \times 10^{-7}) \times \lambda_{x(\text{in cm})}[\text{s}] \tag{21}$$

if $\lambda_x = 10^{-6}$ cm this is equivalent to a temporal coherence of 0.3 ps.

1.1.13 Refraction

Having produced the amplifying medium (plasma), one has to create conditions for propagation of the X-ray beam over long distances with strong amplification, low losses and high directionality. Therefore the plasma should be dense since gain increases with the plasma density n_e. An upper limit on the density is set, as mentioned earlier, by electron collisions which can destroy the population inversion. The other important restriction is often set by density inhomogeneities, because any plasma density gradients, ∇n_e, result in gradients in the refractive index ∇n according to

$$\nabla n = -(1/n)\nabla n_e/2n_e, \tag{22}$$

with the plasma refractive index

$$n = (1 - n_e/n_{ec})^{1/2} \tag{23}$$

n_e is the plasma electron density and n_{ec} the critical density (see (1)).

Typically, in the region of high electron density and high gain the electron density gradient is given by $\nabla(n_e/n_{ec}) \sim 10^{-3} - 10^{-4}\mu m^{-1}$.

Any gradient in the refractive index causes X-ray beam deflection which can bend it out of the gain medium. The problem of refraction is crucial especially for X-ray lasers using slab targets where, due to the pump geometry, the refractive index gradients are directed towards the pump laser beam, i.e. perpendicular to the X-ray beam propagation in the plasma.

Since the favourable high density region in the plasma characterized by high gain has only a narrow spatial extent (about several tens of microns) the X-ray beam suffering refraction is bent out of this region over a distance which can be much shorter than the maximum amplification length l, as seen in Fig. 9 [31, 32, 33]. As a result the effective gain is reduced.

The typical distance over which the X-photon travels in the gain medium before it deflects out of this volume is denoted as the characteristic refraction length l_{ref} and given for a parabolic density profile by

$$l_{ref} = l_{tr}(n_{ec}/n_{oe})1/2 \tag{24}$$

where, the maximum electron density $n_{oe}<n_{ec}$, and l_{tr} is the transverse extension of the high gain region. The corresponding angle of refraction θ_{ref} can be described as

$$\theta_{ref} = (n_{ec}/n_{oe})^{1/2} \tag{25}$$

In the one-dimensional treatment, refraction reduces the gain by a value of $1/l_{ref}$. For large plasma length $l_z > l_{ref}$ the real amplification is then determined by an effective gain coefficient

$$g_{eff} = g - 1/l_{ref}. \tag{26}$$

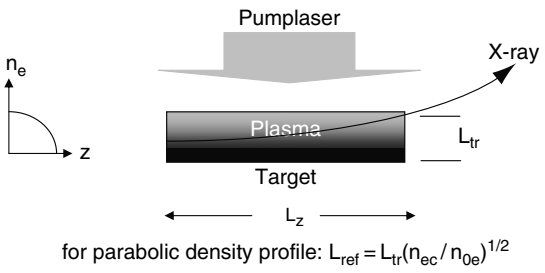

Fig. 9 Refraction of the X-beam in a plasma with density gradient vertical to the amplification direction. n_e – electron density orthogonal to the target surface

In a cylindrical plasma geometry which reflects well the situation in an axially (longitudinally) pumped laser plasma (see OFI) or discharge pumped system (see discharge XRL), the refractive index has a gradient with the same symmetry. Refraction introduces here the loss term of $1/l_{\mathrm{ref}}$ for each direction and the effective gain is [7]

$$g_{\mathrm{eff}} = g - 2/l_{\mathrm{ref}} \tag{27}$$

Several different techniques have been successfully introduced into the experimental practice to reduce the unwanted effect of refraction. They include the reduction of steep density gradients by the use of foil targets and a prepulse technique as well as the use of curved targets. A promising scheme for a future table-top XRL is also a plasma waveguide structure characterized by a density minimum on axis as in the case of capillary discharge schemes [7, 18, 19, 20, 21, 33] (see recombination and OFI-XRL).

1.1.14 General Kinetics of Active Medium: Steady-State – Transient State Approach

Laser medium kinetics is determined by temporal changes in the population of various ionic energy levels in the plasma. In the rate equations describing the changes in the population N_{nZ^*} of the nth electronic level in the ion with the effective charge Z^* different processes in the plasma such as ionization, recombination collisional excitation and de-excitation, as well as a radiative decay [4, 34] have to be included:

$$\mathrm{d}N_{\mathrm{nZ}^*}/dt = \sum\nolimits_i N_{\mathrm{iZ}^*}\Gamma_{\mathrm{in}} - N_{\mathrm{nZ}^*}\sum\nolimits_i \Gamma_{\mathrm{ni}} + R_{\mathrm{nZ}^{*+}} - R_{\mathrm{nZ}^{*-}} \tag{28}$$

The temporal change of the population of the nth level of the Z^*-times charged ions is described by the four terms on the right side of (28): the first term describes the income (increase in the population of the level n in the ion with the charge of Z^*) of electrons from other levels of the same ion and the second one the loss of electrons to those levels. The total rate $\Gamma_{\mathrm{in/ni}}$ in (28) is the sum of specific rates of all processes included in the population changes of a given level n. The third and fourth terms are responsible for the population changes of a given level due to ionization and recombination.

For practical modelling (collisional excitation schemes) one can simplify the (28) by taking into account only collisional ionization and recombination and neglecting the radiative ionization and recombination. A further, often used simplification relies on choosing only the ion species of interest (for example Ne- or Ni-like) and separating the level rate equations from those describing the creation of the given ion species. In this case one can write for these ions the reduced rate equations as follows:

$$\mathrm{d}N_{\mathrm{nZ}^*}/dt = \sum\nolimits_{\mathrm{i}} N_{\mathrm{iZ}^*} S_{\mathrm{in}} - N_{\mathrm{nZ}^*} \sum\nolimits_{i} S_{\mathrm{ni}} \tag{29}$$

where $N_{\mathrm{nZ}*}$ is the population of the nth level of the given ion species, and $S_{\mathrm{in}} = S_{\mathrm{in}}(Z, n_{\mathrm{e}}, T_{\mathrm{e}})$ the total probability of the transition i → n (n→i).

If the ion species concentration ε_Z is the ratio of the number of a given ion species and the number of all ions in a volume unit

$$\varepsilon_{\mathrm{Z}} = \sum\nolimits_{\mathrm{n}} N_{\mathrm{nZ}^*} / \sum\nolimits_{\mathrm{n}} \sum\nolimits_{Z^*} N_{\mathrm{nZ}^*} \tag{30}$$

the dynamics of the ion creation (excitation and recombination of different ion species) can be written as

$$\mathrm{d}\varepsilon_{\mathrm{Z}}/\mathrm{d}t = [\varepsilon_{\mathrm{Z}-1} C^{\mathrm{I}}_{\mathrm{Z}-1} + \varepsilon_{\mathrm{Z}+1} C^{\mathrm{R}}_{\mathrm{Z}+1} - \varepsilon_{\mathrm{Z}}(C^{\mathrm{I}}_{\mathrm{Z}+} C^{\mathrm{R}}_{\mathrm{Z}})] n_{\mathrm{e}} \tag{31}$$

where $C^{\mathrm{I}}{}_{\mathrm{Z}}$ is the ionization rate and $C^{\mathrm{R}}{}_{\mathrm{Z}}$ the recombination rate.

The (30), (31) describe fully the ion system. They must be solved in combination with the hydrodynamics equations for the distributions of n_{e} and T_{e}, which are difficult to solve in a general case. It is therefore useful to distinguish between three different approximations for three different limiting cases [35].

1.1.15 The Steady-State, Quasi-steady-state and Transient Approximation

The transient approach is the most general case and relevant for pumping with short- and high-intensity pulses. Here changes in ε_Z introduce changes in the populations N_{n}:

$$d\varepsilon_Z/dt \neq 0 \,\text{and}\, \mathrm{d}N_{\mathrm{n}}/\mathrm{d}t \neq 0 \tag{32}$$

The electron density n_{e} and temperature T_{e} are still assumed to be constant during lasing.

Which approximation is favourable for a given pump scheme depends on the characteristic times of the processes involved, namely

τ_{hyd}: characteristic time of hydrodynamic changes in the plasma parameters
τ_{i}: characteristic time of ionization
τ_{r}: characteristic time of the relaxation of excited electronic levels.

It is worth noting that all three characteristic times can be considered partially independent. Since both the ionization as well as the excitation result from collisions with free electrons, their characteristic times change with the electron density and temperature. The characteristic time needed for a plasma to get the necessary n_e and T_e, τ_{hyd}, is determined by the pump laser parameters. Hence, slowing down or accelerating plasma heating by choosing duration of

the pump pulse, one can realize different conditions characterized by different relations between, τ_{hyd}, τ_i and τ_r.

The transient approximation is the most relevant approach for short pulse pumping, where neither the populations nor the ionization stages have enough time to equilibrate on a time scale of the hydrodynamic evolution of the plasma. Therefore, not only the above-mentioned kinetic equations but also hydrodynamic equations should be included in the description to determine the temporal dependence of $n_e(t)$ and $T_e(t)$, i.e. to solve the problem fully. Transient approximation means that at t = 0 the electron temperature abruptly increases from T_e = const. 1 to T_e = const. 2. The characteristic time of this change should be very short and after this process one can use the approximation of T_e = const., n_e = const. and $\tau_{hyd} \leq (\tau_i$ and $\tau_r)$, i.e. the rise time of the excitation is comparable to the interatomic relaxation time.

The transient regime is characterized by the highest gain. Simulation predicts values of $g \sim 10^2$–10^3 cm^{-1} and experiments have resulted in g values of several tens of cm^{-1}.

2 Excitation Mechanisms

2.1 Collisional XRLs

The first demonstration of a collisionally excited XRL in a laser-produced plasma dates back to 1985 (Ne-like selenium [2]). At present, X-ray lasers using the collisional excitation mechanism are most frequently used in experiments. This excitation method can be generally described by the equation

$$Z_0^{i+} + \text{electron} \rightarrow Z_u{}^{i+} \tag{33}$$

Here $Z_0{}^{i+}$ represents an i times ionized atom of an element Z in which the transition of interest occurs from the ground state to an excited upper state u. This excitation is accomplished by energetic free electrons in the plasma that collide with the ion $Z_0{}^{i+}$ and populate, beginning at the ground state, usually several levels including the upper lasing level. The condition for efficient excitation of an ion is equality or excess of the free electron energy if compared to the transition energy $\Delta E_{0l,0u}$. Normally, the lower lasing level with a smaller energy gap ΔE_{01} to the ground state is more rapidly populated by an 0–l transition than the upper level by an 0–u transition. Hence, the lower level l must be depopulated more rapidly to achieve a quasi-steady-state (cw) population inversion between the upper u and lower lasing level l. This can be realized if the lower level l is depopulated by a fast radiative decay to the ground state 0 and the upper level is sufficiently long-lived. The high density is favourable as the pump efficiency is proportional to the second power of the electron density ($N_o P_P \propto n_e^2$). Three electron configurations of ions are well suited for this

because they fulfil all these conditions as well as they have the required stability against overionization:

Transition 3p–3s in Ne-like, 4d–4p in Ni-like and 5f–5d in P-like ions.

In reality, the situation is more complex. Taking into account the fine structure of these levels several lasing lines will be allowed for each ion type.

2.1.1 Ne-Like and Ni-Like Schemes

Ne-Like Scheme

In the neon-like scheme (see Fig. 10) lasing is possible on the $1s^2 2s^2 2p^5 3p \rightarrow 1s^2 2s^2 2p^5 3s$ transition. From here on the unchanged core electron configuration will be neglected and only the configurations of the highest valence electron shell (Fig. 10) will be discussed.

According to the fine level structure high population inversion can be obtained for the three transitions: (a) 3p ($J=0$) $\rightarrow$ 3s ($J=1$), (b) 3p ($J=2$) $\rightarrow$ 3s ($J=1$) and (c) 3p ($J=2$)$\rightarrow$ 3s ($J=1$). Here J denotes the total angular momentum of the electron in the j–j coupling. The level description in Fig. 10 includes notation $(j_1, j_2)_J$ with j_1, j_2 being the angular momenta of the core and valence electrons.

The population inversion between these levels is created by a combination of electron collisional excitation from the Ne-like ground state $2p^6$ and dielectronic recombination from the higher lying F-like states followed by radiative–collisional cascades: the "$J=0$–1" population inversion is mostly produced by the collisional excitation, while for the "$J=2$–1" inversion both effects are responsible. The lasing wavelengths of these three main transitions in Ne-like ions with different Z are shown in the Fig. 11 [34]

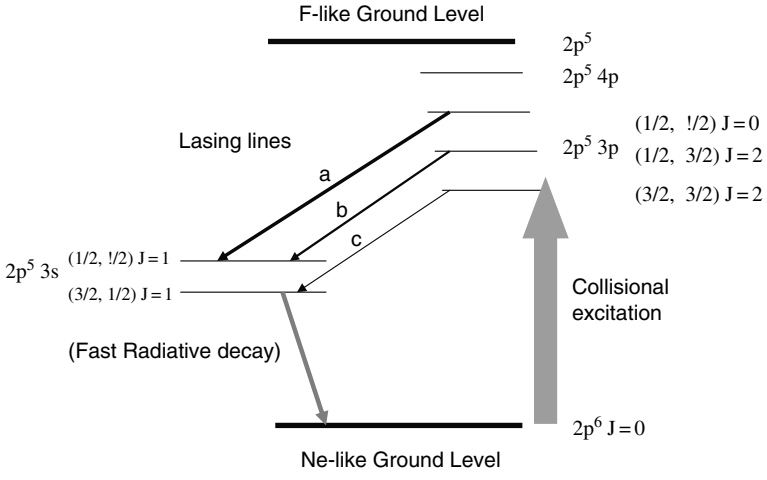

Fig. 10 Simplified X-ray laser excitation scheme on 3p–3 s transitions in Ne-like ions

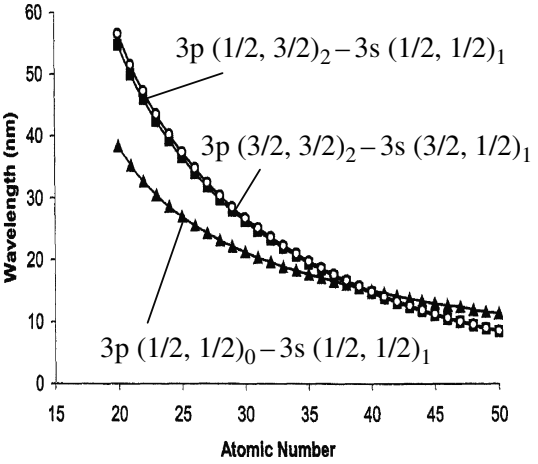

Fig. 11 Wavelength scaling of the Ne-like isoelectronic sequence for the 3p $J=0-3$s $J=1$ transition [34]

Despite the large gain values and gain–length products realized with neon-like X-ray lasers, their scaling to shorter wavelengths is not favourable, since the energy gap between the lasing levels is relatively narrow and ions with higher Z are necessary for shorter wavelengths. This is usually connected with an enormous pump power requirement.

For example, scaling of the necessary pump intensity of a 500-ps pump pulse at 530 nm with the expected X-ray laser wavelength λ_x was empirically determined as [13]

$$I_p[\mathrm{W/cm^2}] \sim 1.2 \times 10^{16}(4.5/\lambda_x[\mathrm{nm}])^{3.5} \tag{34}$$

Approximate scaling of the emitted wavelength with the ion nuclear charge Z^* for neon-like XRLs is given by [4]

$$\lambda_x\ [\mathrm{A}] = 4.6 \times 10^3/z^{*-9} \tag{35}$$

Ni-Like Scheme

The laser transition in a Ni-like ion is a direct analogue of the $2p^5 3p$–$2p^5 3s$ transition in the neon-like ion, but for $n=4$ (see Fig. 12). This transition is denoted as $3d^9 4d$–$3d^9 4p$.

The 4d levels predominantly pumped by collisional excitation from the $3d^{10}$ ground state are long-lived if compared to the characteristic times of the radiative decay to the ground level, while the 4p levels rapidly decay back to the ground state. The quasi-stationary X-ray lasers using this scheme were first demonstrated in 1987 in a laser-produced plasma of Eu at 7.1 nm [36]. The

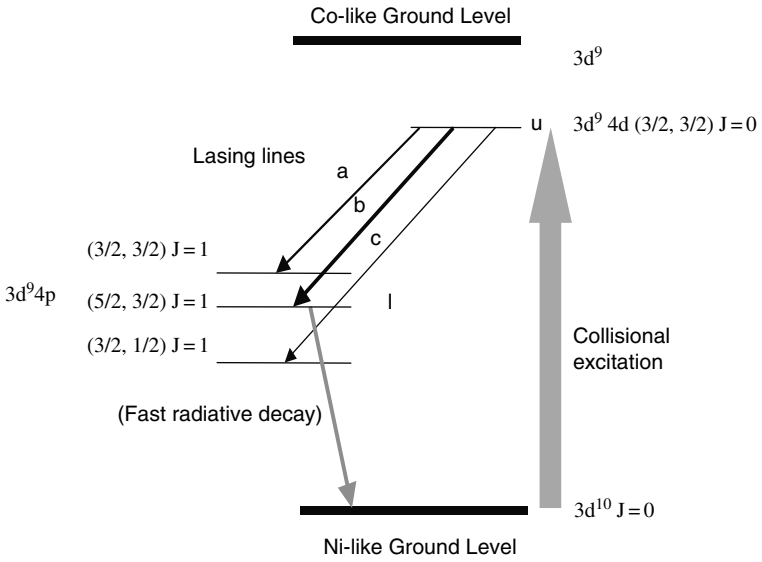

Fig. 12 Simplified X-ray laser excitation scheme on 4d–4p transitions in Ni-like ions. In the case of a transiently pumped XRL the population inversion between the upper and the lower lasing levels is nearly independent of the fast radiative decay from the lower level and only determined by the specific level population kinetics [34]

energy gap between the ground state and the upper lasing levels in Ni-like ions is twice as large as the electron energy, which optimizes the abundance of Ni-like ions. In experiments Ni-like X-ray lasers show significant gain only on the $J = 0$–1 lines while the $J = 2$–1 and $J = 1$–1 transitions have little or no gain [37]. Ni-like ions also show a favourable scaling to shorter wavelengths than Ne-like ones and the spectral range of 4 nm has been reached with high-Z-atoms (Au) in the quasi-stationary scheme. The wavelength scaling along the nickel-like isoelectronic sequence for the $3d^9 4d$–$3d^9 4p$ transitions is shown in Fig. 13 [34]

An empirical scaling law for the necessary pump intensity (again for 500 ps, 530 nm pump pulse) is given as [13]

$$I_p[\mathrm{W/cm^2}] \sim 2.5 \times 10^{14} (4.5/\lambda_x\ [\mathrm{nm}])^{3.5} \tag{36}$$

The required pump intensity for the Ne-like and Ni-like ions differs only by the multiplication factor that is smaller for the Ni-like ions. Therefore Ni-like X-ray lasers can in principle work at shorter wavelengths for the same amount of pumping energy or lower energy at the same wavelength.

Summarizing, the most important requirements that have to be fulfilled for collisionally pumped X-ray lasers are

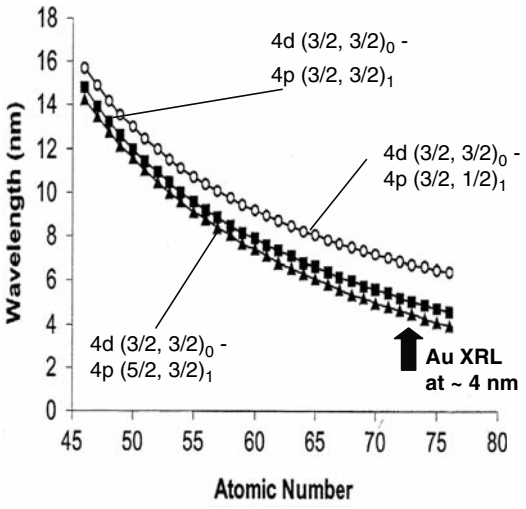

Fig. 13 Wavelength scaling (transition 4p $J=0$ – 4p $J=1$) of collisional XRLs within the Ni-like isoelectronic sequence [34]. The arrow marks the shortest collisional XRL realized (Au-XRL)

- a large abundance of the desired ions (Ne-, Ni- or Pd-like ions [38])
- sufficient electron density, as the collisional pump rate depends on the collisional rate and hence on the electron density
- most probable electron energy should be comparable with the excitation energy from the ground to the upper lasing level
- the decay of the lower lasing level population should be very fast
- the electron density gradient should be as smooth as possible in order to prevent the X-ray beam being refracted out of the gain region.

2.1.2 Realization of Transient Collisionally Pumped X-Ray Lasers

Transient Excitation Scheme

Since 1990 much effort has been put in optimization of the pumping process and reduction of the unwanted refraction effect during the X-ray beam propagation along the plasma. Several irradiation schemes have been successfully established to control the excitation process by irradiating the target with two or several pulses (multi-pulse pumping) delayed relative to each other to separate the most important processes responsible for gain. In all these cases the duration of the pulses was either comparable or equal to at least several tens/hundreds of picoseconds. In spite of the remarkable reduction in the pump laser energy to the level <100 J caused by the new pumping technique, these systems are very far from the class of the compact X-ray lasers.

An important step towards a low-energy-pumped X-ray laser was the proposal to reduce the pump energy by shortening the pump pulse to a ps-level, since the plasma production is dependent on the pump intensity necessary to create the desired ion species. The short pulse pumping method has mainly benefited from the development of the chirped pulse amplification technology

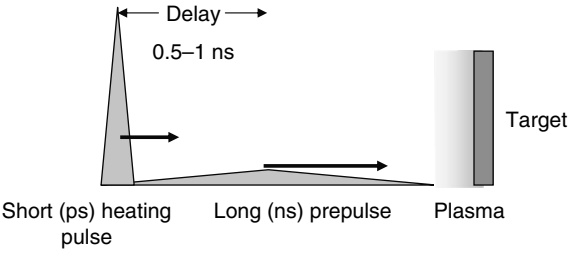

Fig. 14 Transient excitation scheme in two steps: first, a long (ns) pulse creates a homogeneous preplasma; subsequently a short intense ps pulse heats the plasma and creates the transient population inversion

(CPA) in the early 1990s that allowed production of pulses with durations shorter than 1 ps. As a result, the first transient X-ray laser in 3p–3s Ne-like Ti was demonstrated in 1995 [39]. This result originated in an earlier proposal to use ultrashort pumping pulses for collisional XRL schemes [40, 41]. The drastically reduced need of the pump energy in this excitation scheme has shown a new route to table-top XRLs. Nowadays this short pulse excitation scheme dominates the research field of X-ray lasers.

The transient collisional excitation scheme utilizes two laser pulses with a long nanosecond pulse producing a plasma with an abundance of the required Ne-like or Ni-like ions. After a controlled delay to allow for plasma expansion, which is necessary for both efficient pumping and optimum propagation along the plasma column, a short picosecond laser pulse ($\sim$1–2 ps) generates a transient population inversion by fast collisional heating (see Fig. 14).

The short heating time by a very short and intense pumping pulse enables achieving of a high gain within a few picoseconds – before collisional redistribution (relaxation) of the excited state population takes place. That means, the population inversion has a transient character and gains higher than $100\,\mathrm{cm}^{-1}$ are predicted. As a consequence saturation for target lengths of less then 1 cm is possible. After that the system returns to a quasi-steady state with gain values too low for a net amplification. Therefore the pulse duration of a transient XRL pulse is intrinsically short (several ps). The main advantage of this pump scheme is a reduction in the pump energy to the level lower than 10 J which is sufficient to drive the inversion. Transient collisional pumping has been used for Ne- and Ni-like ions where gain values up to $g = 63\,\mathrm{cm}^{-1}$ and saturation were demonstrated using solid slab targets. Moreover, saturated gain with $gl \sim 16$ demonstrated on 4d–4p, $J = 0$–1 transition in Ni-like XRLs with wavelengths between 13.9 and 20.3 nm was accompanied by a further reduction in the necessary pump energy down to $\sim$7 J. The irradiation conditions with travelling wave excitation have been optimized [42, 56].

Very recently, a new modified transient scheme was demonstrated using only one shaped short pumping pulse, in contrast to the common transient schemes with two pulses. The pulse was deliberately shaped to meet the requirements for the creation of a preplasma and following rapid heating phase. This method takes the advantage that the plasma plume created in this way is more symmetric and homogeneous. This gave saturated lasing in Ni-like Ag at 13.9 nm with less than 3 J of pumping energy [43]. One of the specific features of this

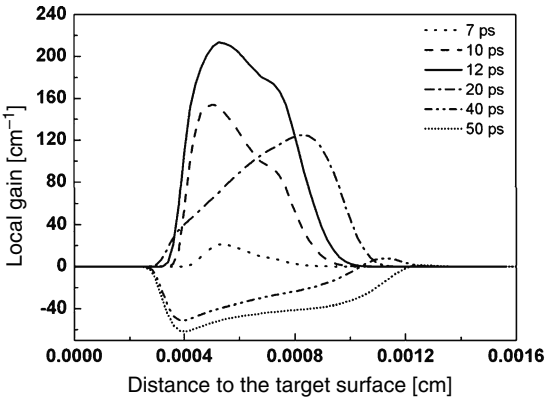

Fig. 15 EHYBRID simulations of the history of the local gain coefficient for a Ni-like Ag-XRL, pumped by a single shaped pulse. Note the long duration of high gain. (The small distance between the gain area and the target surface is caused by specific theoretical difficulties concerning the equation of state treatment that, however, do not have a remarkable influence on the gain calculation)

scheme is the optimum duration of the pump pulse (FWHM) within the gap between 5 and 10 ps. That means, the system can show a moderate transient behaviour. This has also been confirmed by EHYBRID simulations. The temporal dependence of the gain of a Ni-like Ag-XRL at 13.9 nm for the pumping parameters, 20 mJ in the 2 ns background and 2.6 J in the 6 ps main part of the pulse, is shown in Fig. 15. It has been easily seen that the gain is very high even after 20 ps, which is in contrast to the common double pulse pumped transient schemes. The duration of the output pulse is expected to be of the same order of magnitude. This was confirmed by the experiments reported [44, 45]. The pump pulse parameters described are moderate and close to those of commercially available laser systems with higher repetition rate. Therefore, short pulse table-top X-ray lasers of reduced size and high repetition rate are now realistic.

Travelling Wave Pumping

The transient excitation produced by a short pump is accompanied by a short gain duration. Therefore, the finite transit time of X-ray photons as they travel along the plasma column can reduce the effective gain–length product of the X-ray laser. It becomes increasingly important to use a travelling wave pumping scheme in order to increase the effective active medium length that facilitates extraction of the maximum energy from the medium by a short XRL pulse.

In the travelling wave (TW) pump geometry a front of the incident optical beam is tilted in such a way that the pumping beam produces an excitation wave which travels along the target at the same velocity as X-rays propagating through the plasma. A tilt of an additional grating as shown in Fig. 16 is a method frequently applied in practice to achieve the described effect. The grating arrangement is characterized by a tilt angle ϕ:

$$\tan\phi = \lambda_p / D\cos(\theta_0) \tag{37}$$

with λ_p the pump laser wavelength, D the groove spacing of the grating, θ_0 the diffraction angle. In an experiment, one has to select the groove spacing and the

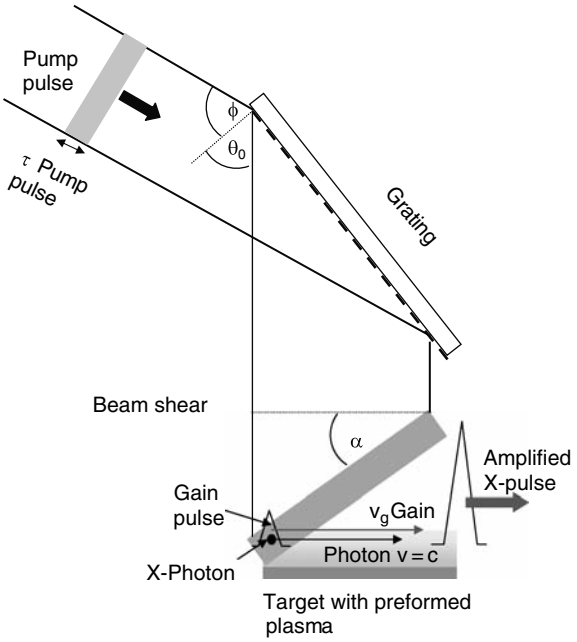

Fig. 16 Travelling wave excitation of a transversely pumped XRL with a tilted grating. The use of a single grating that tilts the wavefront to the necessary angle is a frequently applied method. The grating arrangement is characterized by a tilt angle ϕ: $f = l_L/D \cos(\theta_0)$, λ_p = pump laser wavelength, D = groove spacing of the grating, θ_0 = diffraction angle. Travelling wave velocity $v = c/\tan\alpha$, α– angle between the wavefront and the target surface and l is the target length

angle of incidence θ_1 so that the tilted wavefront synchronizes with the transit time (~33 ps/cm) of X-ray photons in the laser medium.

Travelling wave velocity is given by

$$v = c/\tan\alpha \tag{38}$$

where α is the angle between the wavefront and the target surface and l is the target length.

Other alternative methods of travelling wave excitation are based either on the use of a stepped mirror or prism to divide the beam into separate beamlets with a variable time delay [46, 47] or on a tilt of a diffraction grating in a CPA compressor [48]. Normally, in the latter both gratings should be as parallel as possible to ensure optimum compression of the chirped laser pulse and sometimes an additional grating behind the CPA compressor is used to tilt the front [49].

Gas Puff

Another variant of the prepulse technique is the use of dense gases irradiated with double pulses. An electromagnetic valve is used to produce an elongated homogeneous gas column at high repetition rate. The system can be driven in a transverse or longitudinal pumping arrangement. In the case of a transversely irradiated column of argon high gain was demonstrated on the neon-like,

3p–3s, $J = 0$–1 transition at 46.9 nm [50, 51]. Very recently transient X-ray lasing was demonstrated with a similar setup in nickel-like Xe at 9.9 nm [52].

The gas puff setup is very promising for a highly repetitive X-ray laser supposing the required pump energy can be further reduced.

Fast Discharge Capillary

In comparison to the laser-pumped XRLs the direct excitation of plasma with an electrical discharge has the advantage of generating compact, cheap, simple and very efficient X-ray lasers. Fast capillary discharge plasma as a lasing medium was first proposed in 1988 [53]. The basic capillary scheme is described in [17, 18, 19], and different capillary setups are now under operation [54].

The capillary discharges that have proven to be most efficient among the excitation schemes of soft XRLs have a fast current rise, typically 10–40 ns. The short current rise time minimizes the amount of material that is ablated from the capillary walls before a magnetic field compresses the plasma, detaching it from the walls [17]. The generated plasma of these fast discharges is not stationary but rapidly contracts, heats up and subsequently expands. These discharges with a rapid plasma column compression have several advantages in comparison to efficiently pumped small-scale X-ray lasers [17, 55]:

- high axial uniformity that results from highly uniform initial conditions during very fast compression [17]
- plasma columns with very large length to diameter (aspect) ratio (up to 1000:1) [17]
- reasonable density level with the radial profile showing its minimum on the capillary axis

The radial electron density distribution with its minimum on the capillary axis allows for guiding of the propagating X-ray pulse.

The capillary, typically driven by a very strong pulsed current with the peak up to $\sim$100 kA and a rise time of 11 ns (10–90% current) is dedicated to the excitation of an Ar plasma column with a length of several tens of centimetres. The principle setup is similar to that of a short pulse-excited capillary discharge working in a hybrid scheme (see Fig. 14) described in details in the following chapter of Rousse and Ta Phouc.

In a 40 cm long capillary with a 4 mm diameter saturated lasing in a steady-state regime on the 3p–3s, J = 0–1 transition in neon-like Ar-XRL at 46.9 nm (26.5 eV) has been shown by single and double passing with one Ir mirror at a 4 Hz repetition rate. The output pulse duration was about 0.8 ns. This XRL delivers spatially coherent pulses with an averaged energy of 0.88 mJ ($\cong 2 \times 10^{14}$ photons/pulse), corresponding to an averaged power of 3.5 mW [18, 29]. With a peak spectral brightness of 2×10^{25} this table-top laser belongs to the brightest soft X-ray sources. No other soft X-ray source, independent of its size, is presently capable of producing simultaneously such a high average coherent power and peak spectral brightness. However, in order to shorten the wavelength of the capillary discharge neon-like XRL below the presently

available 46.9 nm one has to apply much higher discharge currents of more than 100 kA in order to excite the suited neon-like ions. This is a serious technological challenge. Shortening of the output pulse duration in this quasi-stationary excitation system up to several tens of picosecond also seems to be impossible.

Hybrid Pumping of Capillary

Both the short laser pulse pumped transient scheme and the quasi-stationary capillary discharge excitation are to some extent complementary and together seem to be very promising candidates for compact and highly efficient XRLs. Capillary discharge is a very compact and cheap source of a preformed homogeneous plasma for transient inversion pumping and it could replace the whole optical laser system delivering the nanosecond pumping pulse (see § on transient pumping). The short, guided in the preformed plasma picosecond pulse can heat it rapidly. Moreover, quasi-travelling wave pumping is inherent for this scheme and guiding in a symmetric plasma pipe reduces the refraction problems strongly present in the conventional laser-pumped transient system. Additionally, the high-intensity short pulse could easily improve the plasma ionization stage by field/multiphoton ionization. The principle scheme of this XRL type is presented in Fig. 17, where also a coupled spectrometer for the XRL signal registration, as used in experiments, is shown.

Such a hybrid laser system was demonstrated for the first time for a neon-like 3p–3s, $J = 0$–1 transition in the form of a sulphur soft X-ray laser at 60.84 nm [44]. The preplasma of the hybrid system created by the discharge has to fulfil two requirements:

- it has to be sufficiently dense to ensure strong energy absorption by the inverse Bremsstrahlung mechanism
- the elongated plasma column should have the specific density profile that ensures an efficient guiding of the pumping pulse and possibly uniform heating over the whole plasma column. The calculated radial density profiles in a sulphur capillary plasma for two diameters of 0.5 and 1 mm are shown in Fig. 18. For the capillary of 1 mm diameter the resulting low electron density on the axis is prevented from strong amplification and no lasing is to be expected

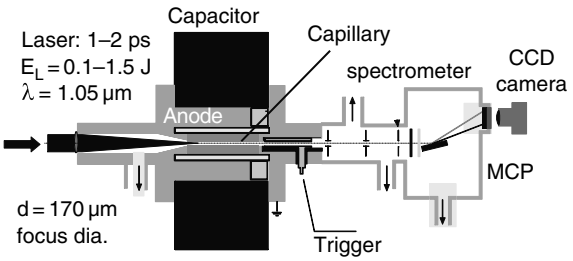

Fig. 17 Scheme of a short pulse pumped hybrid capillary discharge XRL with a coupled soft X-ray flat-field spectrometer [44, 45]

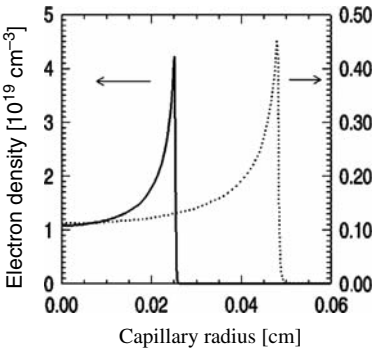

Fig. 18 Density profile in a sulphur capillary plasma for two capillary radii: 0.25 and 0.5 mm. Only the capillary with 0.25 mm has a sufficient electron density suited for gain guiding and lasing [44, 45]

As a consequence, the original capillary design used in [17] had to be modified to make it suitable for IR laser pumping. The maximum gain for a 10-mm long sulphur capillary pumped longitudinally by a 1 ps, 1053 nm pulse with energy lower than 0.5 J was 4.7 cm^{-1}. For a 30 mm capillary a gain–length product of $gl = 6.68$ was obtained. The ratio of gain–length product (gl) to the pumping energy (E_p (J)) was very high and equal to 3.1 J^{-1} (including pumping laser energy as well as the total electrical energy dissipated in the discharge). This value belongs to the highest obtained for collisionally pumped XRLs. Typically this value is between 1 and 2 J^{-1}.

Presently, the work on higher Z-elements used as a capillary material (Ti, Mo, Ag a.o.) to shorten the emission wavelength is in progress. This new type of a transient XRL seems to be a promising scheme for an efficient compact short pulse emitting soft XRL, supposing the durability of the capillary against the current pulse can be improved.

2.2 Recombination XRL

2.2.1 General Features

The recombination laser is conceptually very simple: it consists of four basic processes. The population inversion is produced by electrons from a reservoir of free electrons in a cold plasma that recombine, relax by collisional–radiative cascade and populate the upper lasing level, while the lower level remains less populated. The best efficiency should be obtained if the reservoir is ionized to the next highest (relative to the lasing ion) ionization stage. The process can be described by the relation

$$Z_0^{(i+1)+} + 2\,\text{electrons} \rightarrow Z_n{}^{i+} + \text{electron} \rightarrow Z_u{}^{i+} + \text{electron} \qquad (39)$$

The principle level diagram with the mechanisms involved in creation of the population inversion is shown in Fig. 19.

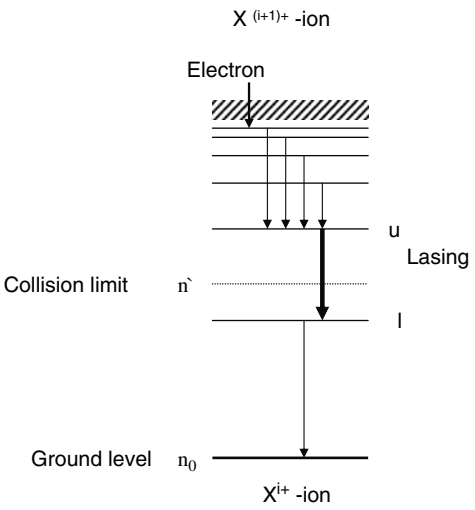

Fig. 19 Simplified energy level scheme for pumping by electron collisional recombination, followed by a cascade. For higher levels than the collision limit level n', collisional excitation dominates over radiative decay. For quantum states lower than n', radiative decay dominates

Required basic plasma parameters to fulfil the conditions for recombination XRLs include low electron temperature (T_e<50 eV) and high density ($n_e \geq 10^{20}$ cm^{-3}). In the specific case of the H-like scheme (other approaches like helium- or lithium-like schemes are direct analogues), the lasing level will be rapidly excited by three-body recombination processes and a subsequent collisional–radiative cascade with rates proportional to n_e^3/T_e^2 [4]). Recombination schemes have the important advantage of more favourable scaling towards shorter wavelengths and an intrinsically higher quantum efficiency [3] than collisional systems. This is due to operation of the recombination schemes on transitions involving a change in the principal quantum number (e.g. $n = 3$–2 or $n = 2$–1; where n is the principal quantum number, and $n = 1$ denotes the ground state). Gain has been observed in many systems, for example, expansion-cooled H-like [60, 61, 62], Li-like and Na-like [63, 64, 65] and radiatively cooled H-like systems (see Table 3).

Recombination X-ray lasers require a short pulse pumping since only in this case a rapid heating close to solid density can be realized that in turn enhances cooling of the plasma during the following expansion phase. The requirement that the expansion rate has to be as rapid as possible but with sufficient time for ionization defines in principle an optimum pulse duration for high gain [66, 67].

Excitation systems working on transitions into the ground state ($n =$ 2–1) require very high intensity and a very short pulse driving laser in order to create significant gain. Lasing to the ground state allows emission of much shorter wavelength, since the shortest wavelengths that can be expected from an electronic transition between two adjacent levels of a given ion require transitions between $n = 2$ and $n = 1$. As the energy of the levels scales as $1/n^2$, the wavelength of a transition decreases with increasing n. For instance, the wavelength of a $n = 2$–1 transition in an ion is five times shorter than that of a $n = 3$–2 transition.

Table 3 Overview of realized recombination XRL (selected survey)

Target, Z	Ion, transition, J	Wavelength [nm]	Gain [cm^{-1}], gl output	Pumping	Target configuration	Lit.
Lithium, 3	Hydrogen-like, n = 2–1	13.5	11 $gl = 5.5$	248 nm, 0.2 J, 20 ns for plasma 1053 nm, $\leq$ 450 mJ,8 ns, 10^{14} W/cm^2	LiF-microcapillary	[72, 73]
Boron, 5	Hydrogen-like, n = 3–2	26.2	14–19, $gl \sim 5$	248 nm, 0.2 J, 20 ns for plasma 1053 nm, $\leq$ 450 mJ, 8 ns, 10^{14} W/cm^2	450 μm-B_2O_3-microcapillary, 3.5 mm	[71]
Carbon, 6	Hydrogen-like, n = 3–2 Balmer-α	18.2	12.5	1053 nm, 2 ps, 20 J, 6×10^{15} W/cm^2	7 μm carbon fibre, 5 mm	[68]
Carbon, 6	Hydrogen-like, n = 3–2 Balmer-α	18.2	$gl \sim 5$	1053 nm, 1.5 ns, $\leq$5 J, 10^{14} W/cm^2 Delay 120 ns	350 μm- microcapillary, 10–15 mm	[70]
Nitrogen, 7	Helium-like, n = 3–2 3^1D–2^1P, 3^1S–2^1P	18.52 18.78	~3	1053 nm, 15 J, 15 ns 4×10^{13} W/cm^2,	7 mm	[74]
Copper, 27	Sodium-like, 5 g–4f	11.1	8.8	1053 nm, 2 ps, 20 J,	7 μm copper coated fibre, 4.6 mm	[67]

In contrast to the transitions to the ground state the systems working on $n = 3$–2 transitions have the advantage that the pumping laser pulse can be relatively long (ns range). This is due to the fact that radiative transition between these levels is about an order of magnitude slower than the transition to the ground level, and the population inversion can exist between them even if the population of the ground level is two to three orders of magnitude higher. This makes it possible in principle to use low power driving lasers (e.g. compact and quite inexpensive commercially available YAG lasers).

2.2.2 Realization of Recombination Pumped X-Ray Lasers

Thin fibre targets have been successfully used to realize a rapid adiabatic cooling that allowed for a high gain with a small plasma length. The first observation of a high gain equal to $g = 12.5\,\mathrm{cm}^{-1}$ on the $n = 3$–2 transition at 18.2 nm in a C^{5+}-recombination XRL driven by a 2 ps, 20 J laser was reported in [68]. Carbon fibres of 0.5 cm length and 7 μm diameter supported at one end have been used as targets. Also lithium-like and sodium-like ions are promising candidates for lasing. They offer higher quantum efficiency than hydrogen-like ions. A recombination sodium-like copper XRL with high gain at 11.1 nm driven by a 2 ps, 20 J laser pulse was reported in [69].

Very promising results on the way to a table-top recombination XRL were obtained in a fast recombining plasma produced in a capillary. In [70] amplification was demonstrated on the $n = 3$–2 transition in hydrogen-like C-ions at 18.2 nm. A preplasma with carbon ions was first created by ablation of the polyethylene microcapillary wall either by a small prepulse or by the front of the single driving pulse, while the main part of the pulse heated the plasma to temperatures at which carbon atoms were totally stripped of electrons. Then the plasma was cooled very rapidly and fast recombination provided an effective gain medium. In a capillary with a 350 μm diameter and a 10–15 mm length a laser pulse of approximately $10^{14}\,\mathrm{W/cm}^2$ irradiated longitudinally, creating a concave transverse electron density profile allowing for good guiding of both the pumping as well as the X-ray pulses. These conditions resulted in amplification on the $n = 3$–2 transition in hydrogen-like C^{5+} ions at 18.2 nm. A more reliable setup in microcapillaries could create the preplasma by a separate laser pulse or high-voltage discharge (see also hybrid discharge XRL). It was demonstrated in [71] that a high gain table-top system with 1 Hz repetition rate on the $n = 3$–2 transition at 26.2 nm in hydrogen-like boron gives a reasonable output. A 350 μm B_2O_3-capillary was irradiated end on first with a 0.2 J KrF-laser pulse followed by a 0.45 J YAG pulse with 400 ns delay. It has been shown that pump pulse propagation is very sensitive to the irradiation conditions.

In general, the most efficient schemes of the recombination XRLs working with the transitions to the ground state have used picosecond and subpicosecond pump pulses, and the optical-field ionization (see § 2.3) as the ionization process. This systems with intrinsic travelling wave operating on $n = 2$–1 transitions show a good scaling to shorter wavelength (see Table 4).

Table 4 Perspectives for short wavelength recombination XRLs-induced by optical-field ionization (pumping pulse duration <250 fs) [72, 73, 97, 98]

Ion	Wavelength [nm]	Radiative transition time for $n=2$–1 [ps]	Required pumping intensity [10^{18} W/cm^2]
Li^{2+} H-like	13.5	26	0.2–0.3
Al^{10+} Li-like	5.2		1
B^{4+} H-like	4.8	3.4	1–2
C^{5+} H-like	3.4	1.6	2–4
N^{6+} H-like	2.5		30
O^{7+} H-like	1.8	0.53	7–10
Na^{10+} H-like	1.0	0.15	20–30

2.3 Optical-Field Ionization Excitation

2.3.1 General Features

Optical-field ionization (OFI) of an atom occurs when the oscillatory electric field of an ultrashort laser pulse becomes comparable to (or larger than) the Coulomb field, attracting the electrons to the nucleus [75]. Under such conditions, optical-field ionization results in multiple-charged ions and plasmas with controllable temperature. The resulting free electron energies can be predicted within the tunnel-ionization model (ADK-approach) [75, 76, 77, 78]. Because of the strong dependence of the ADK-ionization rates (W_{ADK}) on the laser intensity ($W_{ADK} \propto I_L^7$) [79], the ion stage produced by optical-field ionization is controlled by the laser intensity. The energy distribution of the released free electrons is, however, controlled by the polarization of the pumping pulse [99]. Linearly polarized laser pulses produce relatively cold free electrons which are suitable for recombination excitation (see § 2.2) of X-ray lasers [76, 77]. On the other hand, circularly polarized laser pulses produce highly energetic electrons that can be preferentially used in collisional excitation (see § 2.1) [80, 81].

The OFI-X-ray laser pump scheme has the advantage of strongly reduced pump energy, since the oscillatory electric field of the driving laser pulse ionizes the XRL-medium directly. The specific ion stages for X-ray lasing need a threshold laser intensity I_{th} which can be estimated by the formula resulting from the classical barrier suppression model [82, 83, 84]

$$I_{th} = (4 \times 10^9 / Z^{*2}) \times U_I^4 [\mathrm{W/cm^2}] \tag{40}$$

where Z^* is the charge stage of the ion and U_I is the ionization potential in eV of the ion with the charge (Z^*–1). According to (39a) the required intensity to create, for example, He-like C^{4+} is equal to $I_{th} = 4.3 \times 10^{16}$ W/cm^2, which can be produced with a sub-ps pulse of energy far less than 1 J.

These low pump energy requirements ($E_{in} \leq 1$ J) of this XRL scheme allow for higher repetition rates (10 Hz–1 kHz) if the pulses are sufficiently short.

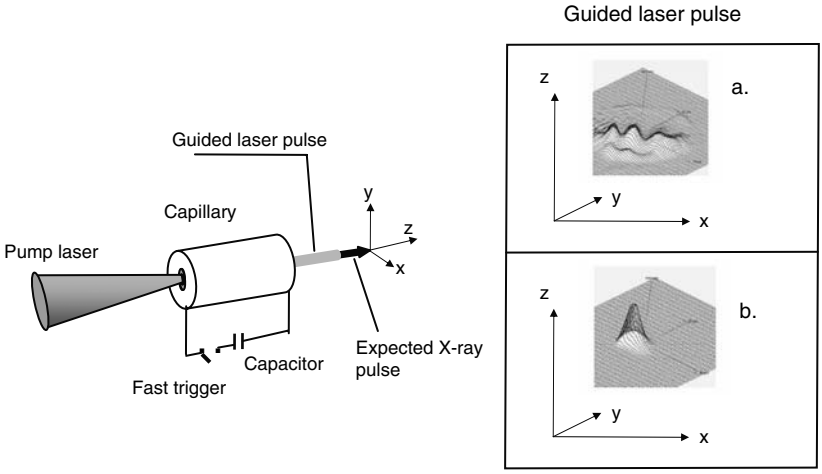

Fig. 20 Guiding of high-intensity fs-laser pulses in low current capillaries: (**a**) without discharge (**b**) with discharge. *Capillary*: plastic, diameter 0.5 mm, length 30 mm. *Laser pulse*: Ti:Sa at 800 nm, 50 fs, $I_{\text{laser}} \sim 10^{17}$ W/cm^2, $2w \sim 40$ μm

A problem for both types of OFI-XRLs is creation in a gas target a sufficiently long excited plasma column with a large gain–length product. A possible solution is the method of self-channelling applied to a tightly focused ultrashort laser pump pulse ensuring propagation over distances much longer than its Rayleigh zone. The interplay between self-focusing and refraction-induced defocusing in the plasma is responsible for the pump beam confinement. Hollow waveguides or discharge-ablated microcapillaries [85] also seem to be promising as guiding structures over the distances longer than 10 mm for both the pump laser pulse as well as the X-ray pulse. Figure 20 shows experimental results [MBI-group and A. Zigler, Jerusalem (2002)] demonstrating how the capillary plasma influences the beam profile of a guided ultrashort laser pulse with an intensity of 10^{17} W/cm^2.

2.3.2 Propagation Issues in OFI-XRL

A crucial problem for longitudinally pumped OFI-XRL is the ionization-induced refraction (see also §.1.1) of the high-intensity short pump laser pulses. As the highest intensity of the laser focused into a gas or plasma is on the axis, this results in the highest degree of ionization, and therefore the largest electron density appears in the same area. The electron density gradient in the radial direction associated with the transverse intensity profile can result in a significant refraction or defocusing of the ionizing pump pulse.

For a XRL one can define a length l_{tr} which a ray travels before its transverse deviation doubles (see refraction §1.1, (24) in a medium with gain spread over the distance l_{ref}

$$l_{\mathrm{ref}} = l_{\mathrm{tr}}(n_{\mathrm{ec}}/n_{\mathrm{oe}})^{1/2} \tag{41}$$

In practice, this means that ionization-induced refraction of the pump beam causes significant reduction in the length of the high-intensity region along the plasma axis which is necessary to create and excite the desired charge state. Therefore a shorter gain–length product will result.

The problem of ionization-induced refraction can be reduced by creating a plasma channel with a density minimum on axis prior to the field ionization [86] by the intense and short laser pulse. This configuration is similar to that of the hybrid collisional system (§ 2.1.2) shown in Fig. 14 but with an ultraintense and femtosecond pumping pulse required here for the OFI-excitation. The plasma channel of a slow capillary discharge has been shown to be essentially fully ionized and with parabolic radial density distribution [87]. At such conditions the spot size of a matched laser pulse propagating through the waveguide can be maintained close to its input value, and the spectral or temporal distortion is minimized. The waveguide also increases the capillary lifetime.

A Gaussian pump laser beam (radial profile $\sim\exp(-r^2/r_1{}^2)$) will be matched and propagated through the plasma channel with a parabolic density distribution in the radial direction ($n_{\mathrm{e}} = n_{\mathrm{o}} + \Delta n_{\mathrm{e}} r^2/r_{\mathrm{ch}}{}^2$,) without significant distortion if the beam spot radius is equal to

$$r_{\mathrm{m}} = [r_{\mathrm{ch}}{}^2/(\pi r_{\mathrm{e}} \Delta n_{\mathrm{e}})]^{1/4]} \tag{42}$$

where $r_{\mathrm{e}} = e^2/mc^2$ is the classical electron radius. For representative parameters $r_{\mathrm{ch}} = 150\,\mu\mathrm{m}$ and $n_0 \cong \Delta n_{\mathrm{e}} = 4 \times 10^{18}\mathrm{cm}^{-3}$ the matched beam radius is of $r_{\mathrm{m}} \sim 30\,\mu\mathrm{m}$. Any mismatch between the input spot size r_{p} of the laser pulse and the matched spot size r_{m} of the waveguide will cause the spot size of the guided laser pulse to oscillate between r_{p} and $r_{\mathrm{m}}{}^2$ with a modulation length along the propagation axis of

$$z_{\mathrm{os}} = \pi^2 r_{\mathrm{m}}{}^2/\lambda_{\mathrm{p}}{}^2 \tag{43}$$

where λ_{p} is the laser pulse wavelength. If the capillary length is an integer multiple of z_{os} the spot sizes at the entrance and exit of the capillary will be the same. If the guiding channel is essentially fully ionized, temporal distortions of the pulse due to ionization should not occur and pulse stretching by group velocity dispersion (GVD) in the plasma is restricted.

Guiding of a short and intense laser pulse over several centimetres in plasma has been primarily caused by an imploding phase of a discharge in capillaries either filled with a gas or with a material ablated from the capillary wall [44, 87, 88, 89]. In the capillary discharge X-ray laser the density distribution obtained by radial hydrodynamic expansion of the plasma ablated from the wall guides the X-ray pulse through the centre of a long plasma column [17, 18, 53] (see § 2.2).

In the case of ultraintense short laser pulses with an intensity $> 10^{18}$ W/cm^2 required to excite some of OFI lasers (H-like C^{5+}, N^{6+}, O^{7+} or Na^{10+}) at wavelengths shorter than 3 nm (see Table 4) the propagation issue becomes more complicated. Here a relativistic charge displacement in the channel can cause transverse density perturbations. However, the studies in [90, 91, 92, 93] have revealed that under certain circumstances the transverse stability can be strongly increased and a robust relativistic self-channelling in underdense plasma is possible, if the incident peak laser power exceeds a critical value P_{cr} with

$$P_{cr} = 1.6198 \times 10^{10}(\omega/\omega_{po})^2[\mathrm{W}] \tag{44}$$

where ω and ω_{po} are the laser frequency and the frequency of the unperturbed plasma, respectively.

Another important parameter is the transmission, T, of the capillary plasma channel. The transmission of such a waveguide can be described by

$$T = T_0 \exp(-\alpha_p l), \tag{45}$$

where T_0 is the coupling efficiency of the laser pulse into the waveguide, and α_p is the propagation loss (absorption) per unit length. In a hydrogen-filled capillary irradiated by a short fs-laser pulse with an intensity of $I_l \sim 10^{17}$ W/cm^2 a transmission T higher than ≥ 0.8 was reached [89]. In principle, gas-filled capillaries should be scalable to lengths of tens of centimetres (except for the relativistic case) that together with the channel diameters of $2r_{ch} = 100$–200 μm could give favourable aspect ratios for X-ray lasers.

For an XRL the capillary must contain a gas (plasma) with the atoms suitable for lasing (Xe, Kr, Li a.o.), and additionally a reasonable transmission must strengthen the requirement of efficient (uniform) pumping along the whole capillary length.

The presence of the ionization effect strongly affects transmission (absorption) of the ultrashort laser beam in a microcapillary. Figure 21 shows the principal scheme of a longitudinally pumped OFI-XRL. As already mentioned above, the electron density profile must have a minimum on axis for guiding of the pump and the X-ray pulses. It is shown schematically that the absorption in the plasma causes the pump intensity to decrease along the plasma and as a consequence also the ion stage. One way to keep a stable ionization balance of the lasing ions over the plasma length is the pump intensity at the optimum value.

2.3.3 OFI with Linearly Polarized Pump Pulse-Recombination Excited XRL

This type of OFI laser also requires (similar to the conventional recombination scheme (§2.2)) a high electron density ($n_e > 10^{20}$ cm^{-3}) and a very low temperature ($T_e < 50$ eV). In the case of linearly polarized driving laser pulse the field ionization remains the electrons with a relatively low energy. The most

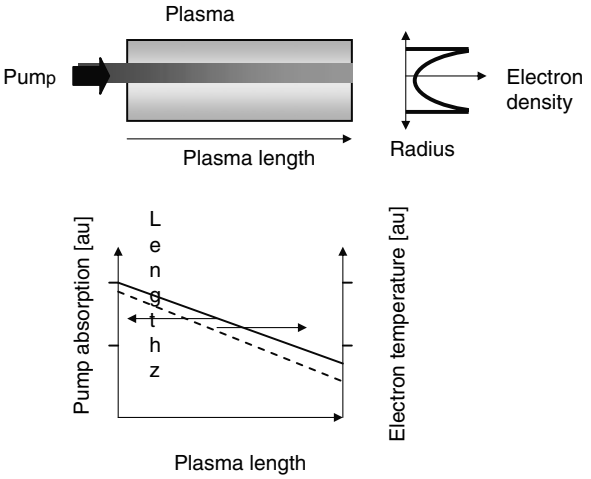

Fig. 21 Setup of a longitudinal pumped OFI-XRL. Electron density profile must have minimum on axis for guiding of the pump and the X-ray pulses. Absorption causes pump intensity to decrease along the plasma. The ionization balance of the lasing ions can be kept stable by choosing the optimum pump intensity

important process here in the creation of a population inversion is three-body electron–ion recombination that strongly depends on electron energy (temperature). The recombination rate is proportional to $T_e^{-9/2}$ [94, 95]. In contrast to the conventional recombination laser (see recombination scheme § 2.2) cooling in the OFI-XRL-plasma is in principle not required, because field ionization produces low-energetic rapidly recombining electrons.

OFI-excitation allows for lasing down to the ground state of the lasant ions. However, nearly complete emptying of the ground state during ionization is required. Fractional population of 10^{-3} or greater remaining in the ground state can significantly reduce the predicted gain [96]. However, since ionization is strongly dependent on the intensity, only a modest increase in intensity above the ionization threshold is required to obtain nearly complete ionization. A disadvantage of lasing into the ground state relies on the slow exit channels out of the ground state resulting in a short duration of population inversion and reduction in the saturation intensity. From another point of view this short lifetime of the population inversion can result in very short XRL output pulses.

One of the drawbacks of the present OFI systems is the low conversion efficiency being about $\eta \sim 10^{-9}$

In Table 4 the possible wavelengths (down to 1 nm) are given for OFI-XRLs using short, linearly polarized pumping pulses [72, 73]. The required pumping intensities of more than 10^{19} W/cm^2 are now available in several laboratories operating CPA-Ti:sapphire lasers or KrF-lasers.

Realization of OFI-Recombination X-Ray Lasers

A reasonable gain at 13.5 nm on the Lyman-α transition of Li^{2+} has been reported in [100, 101]. Material was ablated from a metallic lithium target by a relatively low-intensity long laser pulse. The resulting plasma plume was then

longitudinally irradiated by a high-intensity, short pulse laser which generated Li^{3+}. The same hydrogen-like lithium system was investigated in [102]. Strong lasing with a gain of $g = 11\,cm^{-1}$ on the $n = 2$–1 transition in hydrogen-like Li was also reported in [72, 73] (Table 5).

An important advantage of using microcapillaries for XRLs as compared to gas-filled cells is the fact that they allow for an optimization of the plasma density for maximum gain by adjustment of the delay between the creation of the preplasma and the ultrashort pumping laser. Such systems automatically provide travelling wave gain (see also § 2.1.3) and allow for a very efficient ionization of atoms. In [72, 73] it was realized that an ionization efficiency of the Li-atoms was higher than 70–80% in the microcapillary (at only 50% short pulse laser absorption). However, the problem of the capillary lifetime remains.

2.3.4 OFI with Circularly Polarized Pump Pulse-Collisional XRL

In this approach very intense, circularly polarized pumping pulses produce a highly ionized plasma. The intense circularly polarized femtosecond pump laser pulse ionizes by tunnelling a gaseous target with the ionization rate varying exponentially with laser intensity [76, 77], and produces simultaneously hot electrons with a non-maxwellian distribution that covers a wide range of energy. In contrast to the case of linearly polarized pumping pulses the circularly polarized laser pulse remains the ejected electrons with a kinetic energy that is equal to the quiver energy ε_q (or ponderomotive potential) at the time of ionization:

$$\varepsilon_q = e^2 {E_p}^2 / (4 m_e {\omega_p}^2) \tag{46}$$

where E_p is the average laser field, e is the elementary charge, ω_p is laser frequency and m_e is the electron mass.

The collisional OFI scheme allows for a scaling to shorter wavelength in accordance with the neon- and nickel-like ions of the conventional collisional XRLs (see § 2.1). The required intensity will be very high in order to allow for both the creation of the necessary ion stage and the electron heating. For example an abundance of a nickel-like Xe^{26+}-ions lasing at a wavelength of $\lambda \sim 10\,nm$ would require an intensity of $5 \times 10^{18}\ W/cm^2$ [103, 104].

Realization of OFI-Driven Collisional X-Ray Lasers

After modelling of OFI lasers based on collisional excitation in eight-time-ionized Ne-like Ar at 46.9 nm, and Ni-like Kr at 32.4 nm [103] the first realization was demonstrated in 1995 in Pd-like Xe [104]. This result offered a new route towards table-top, high repetition rate XRLs.

However, it took 5 years to reproduce and improve this original result. Gain saturation on the $5d^1S_0$–$5p^1P_1$ transition at 41.8 nm has been achieved by the

Table 5 Overview of realized OFI-XRL

Target, Z	Ion, transition	Wave-length [nm]	Gain [cm^{-1}], gloutput	Pump scheme*	Pumping configuration	Target configuration	Lit.
Lithium, 3	Li^{2+}, n = 2–1 (Lyman-α)	13.5	20 cm^{-1}	rec	249 nm, 200 mJ, 20 ns for plasma 50 mJ. 0.5 ps,10^{17} W/$cm^2$for OFI, longit. pumped	flat slab 2 mm	[101]
Lithium, 3 (predict.)	Li^{2+}, n = 2–1 (Lyman-α)	13.5	1–10 cm^{-1} at T_e 3–1 eV	rec	<1 ps, 2×10^{17} W/cm^2	gas	[102]
Lithium, 3	Li^{2+}, n = 2–1 (Lyman-α)	13.5	dominant line	rec	1053, 1 J, 12 ns for plasma 248,100 mJ, 0.4 ps, longit.,10^{17} W/cm^2 for OFI	LiF-slab, 2 mm	[107]
Lithium, 3	Li^{2+}, n = 2–1 (Lyman-)	13.5	11 cm^{-1} 5.5	rec.	1053, 100 mJ, 5 ns for plasma 248, 60 mJ, 250 fs, longit., 2×10^{17} W/cm^2 for OFI	LiF-microcapillary, 5 mm, $\Theta = 0.3$ mm	[108]
Carbon, 6	Hydrogen-like, C^{5+} n = 3–2 n = 4–2	18.2 13.5	7.1 cm^{-1} 6.5	rec	1053, 1 J, 12 ns for plasma 248, 100 mJ 0.4 ps, longit.,10^{17} W/cm^2 for OFI	cylindrical fibre 6 mm	[107]
Nitrogen, 7 (predicted)	Lithium-like, N^{4+} N = 2–1	24.8	30 cm^{-1} 6	rec	248,150 mJ, 100 fs, longit., 3×10^{16} W/cm^2 Te$\sim$ 10 eV	gas, 2 mm	[97]
Nitrogen, 7 (predicted)	Hydrogen-like, N^{6+} n = 2–1(Lyman-α) n = 3–2 (Balmer-α)	2.5 13.4[1]	>10 cm^{-1}, (T_e<50 eV, $n_e \sim 10^{20}$ cm^{-3})	rec.	800 nm, 60 fs, 3×10^{19} W/cm^2		[98]
Oxygen, 8	Nitrogen-like, C^{1+} $2p^2 3s\ ^2P–2p^3\ ^2D$ Carbon-like, C^{2+} $2p2\,s\ ^3P–2p^2\ ^3P$	61.7 37.4	$\sim$ 25 cm^1		800 nm, 80 mJ, 150 fs	gas	[109]
Xe, 54	Palladium-like, Xe^{8+}	41.8	13.3 cm^{-1} 11	coll.	800 nm, 30 fs, cir. pol., 3×10^{17} W/cm^2,	gas cell, 12 Torr Xe	[103]

Table 5 (continued)

Target, Z	Ion, transition	Wave-length [nm]	Gain [cm^{-1}], gloutput	Pump scheme*	Pumping configuration	Target configuration	Lit.
	5p–5d						
Xe, 54	Palladium-like, Xe^{8+} 5p–5d	41.8	67 cm^{-1}, 15, 5×10^{9} phot/ pulse saturation	coll.	800 nm, 330 mJ, 35 fs, cir. pol., 3×10^{17} W/cm^2, contrast $\geq 10^6$	gas cell, 15 Torr Xe	[87]
Krypton	Nickel-like, Kr8+ 4d–4p	32.8	78 cm^{-1} 78 saturation?	coll	800 nm, 600 mJ, 35 fs, cir. pol., 5×10^{17} W/cm^2, contrast $\geq 10^6$	gas cell, 20 Torr Xe l = 5.5 mm	[106]

* rec – recombination scheme; coll. – collisional scheme

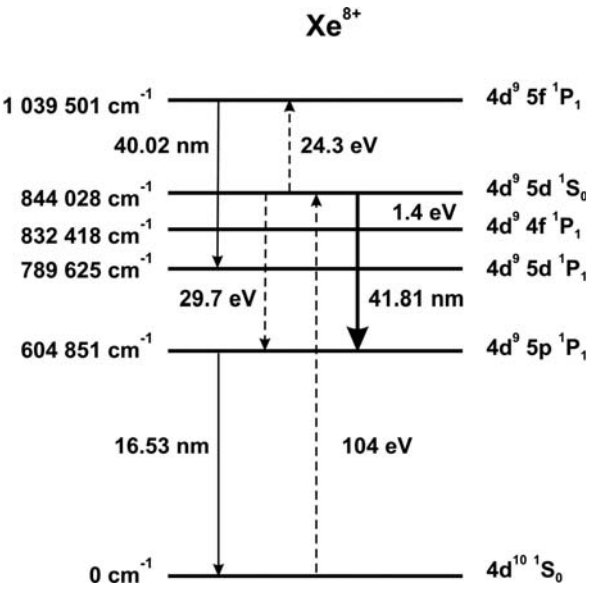

Fig. 22 Simplified energy level system for Xe^{8+}, showing the strong lasing line at 41.81 nm and two other observed weak lines at 16.53 nm and 40.02 nm. The dashed lines indicate the de-excitation channels and the dominant collisional excitation of the upper 5d laser level (from [103] Fig. 1)

focusing of a circularly polarized Ti:Sa laser pulse with an energy of 330 mJ and a 35 fs duration into a gas cell filled with 15 Torr of Xe. [105]. A simplified energy level diagram of Xe^{8+} is shown in Fig. 22. The kinetic energy varies from ~9 eV for the first electron ionized to ~550 eV for the eighth one.

The intensity required to ionize Xe eight times is equal to $\sim 1 \times 10^{16}$ Wcm^{-2} [75]. Because no collisions occur during the short optical pulse (<50 fs), the ions remain very close to room temperature. The laser line is therefore expected to be Stark broadened with the ratio of $\lambda/\Delta\lambda$ being about $\sim 10^6$. However, it is worth noting that the output pulse energy of the system is relatively low and only slightly higher than signals from higher harmonics at comparable wavelengths.

Very recently lasing at 32.4 nm on the 4d–4p transition of nickel-like Kr has been demonstrated by the OFI pump process with an energy of 760 mJ in a circularly polarized 30 fs pulse of a Ti:Sa laser focused on a gas cell filled with 20 Torr of gas lasant. The pump laser intensity was $\geq 1 \times 10^{17}$ W/cm^2, and resulted in a small signal gain coefficient of $g = 78\,\text{cm}^{-1}$ and signal saturation [106]. A comprehensive survey of all realized OFI-XRLs is given in Table 5.

2.4 Inner-Shell-Excitation/Photoionization

Excitation within the inner-shell photoionization scheme (ISPS) was one of the earliest pumping concepts proposed for XRLs [110]. This is a very attractive approach for obtaining lasing wavelengths (<5 nm) with very short output

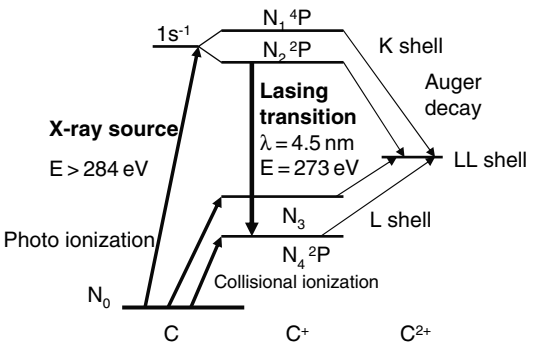

Fig. 23 Energy level diagram for inner-shell photoionization X-ray lasing in carbon at 4.5 nm. A high-energy X-ray photon can preferentially photoionize an inner-shell electron creating a K-shell hole, from which a K–L shell transition can start

pulses (<50 fs). The level scheme of an ISPS laser used here as an example and shown in Fig. 23 is that of carbon [111, 112, 113]. The inner-shell ionization occurs by incoherent X-rays emitted from a second nearby plasma that is produced by a high-intensity ultrashort laser pulse heating a high-Z target, e.g. Au, Ta o.a.

Whereas photons at energy below the inner-shell binding energy of the upper laser level have to be removed by appropriate filtering to avoid pumping of the lower laser level, the remaining hard X-rays preferentially photoionize inner-shell 1 s electrons of the active atoms creating a population inversion and gain on the $(1\,s)^{-1} \rightarrow (2p)^{-1}$ transition of singly ionized carbon. A population inversion by this mechanism is possible because at photon energies just above the threshold for inner-shell photoionization ($h\nu > 273$ eV) the photoionization cross-section of the K-shell is >20 times that of L-shell.

The principal drawback of all up-to-date-analysed ISPS systems is a preferential decay of inner-shell vacancies (K-shell holes) through the Auger process rather than through radiative decay. Additionally, electron collision ionization of the ground state reduces the population inversion by two effects: populating the lower lasing level $(2p)^{-1}$ and reducing the neutral population that feeds the upper laser level. Both effects strongly limit the duration that is allowed for creating a population inversion and also the duration of the pumping high-intensity X-ray photon burst. Therefore the gain is also limited in time.

As depicted in Fig. 23, the lasant material C is pumped by filtered Bremsstrahlung emission of a second target. Filters made of Li, Be or B with a thickness of several microns could be effective in blocking the low-energy X-rays, with only a minimal reduction in intensity of the high-energy X-rays that can expel the inner-shell electrons.

The advantage of the ISPS approach is a very short wavelength of the output (λ between 0.5 and 5 nm with elements positioned in the periodic table between C and Cl is possible) [100, 111, 112, 113, 114, 115] and a large gain during the operation at a very low temperature lower than 1 eV and consequently a small Doppler broadening (expected relative linewidth is $< 10^{-6}$).

In contrast to the OFI scheme (§2.3), which also requires a high-intensity short pulse driving laser (but these are now accessible in several laboratories (see [105, 106])) the requirements of the inner-shell X-ray lasers are significantly higher, because the ionization mechanism is more indirect than that in the above-mentioned OFI scheme or conventional collisional schemes. The required X-ray pump energy for lasing with a gain coefficient of $\sim 10\,cm^{-1}$ at the K_α transition in C^+ at 4.5 nm was estimated to be 1 J [114], disposed during 40 fs FWHM. The gain value as a function of time along with the time-dependent intensity of the optical ultrashort pulse (divided by 100) and the filtered intensity of the X-ray source are visualized in Fig. 24 [114].

The gain value in a ISPI XRL can be increased by further shortening of the X-ray pump pulse. Results of simulations of the gain on the K–L ($1s^{-1}$–$2p^1$) transition in C^+ in dependence on the duration of the incoherent X-ray pump pulse are shown in Fig. 25 (from [114], Fig. 5).

Although the ISPS-X-ray-laser has not been demonstrated up to date, the rapid development of multi-terawatt fs-lasers can change the situation and allows for production of such ultrashort and energetic X-ray pumping pulses.

Also other experimental approaches are possible and it was proposed in [116] to use relativistic channelling of a short laser pulse in a cylindrical target in order to accelerate electrons radially by charge displacement. The channel was surrounded by a high-Z material converter, which in turn generated the high-flux X-ray pulse. The X-ray pulse finally photoionized the outer layers of lasing material in a travelling wave mode.

An excitation mechanism similar to that mentioned above also seems to be possible for Ni-like ions.

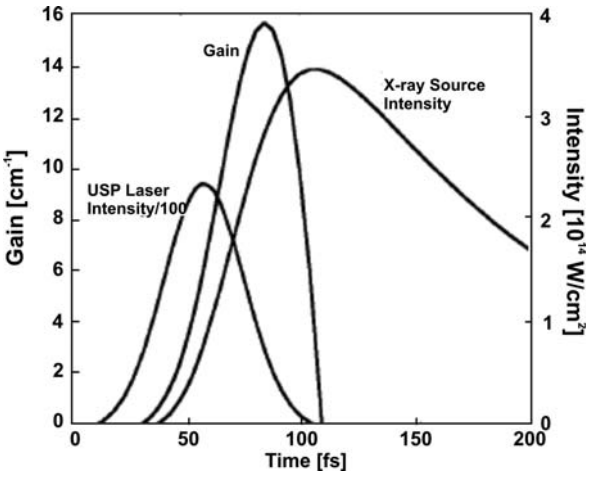

Fig. 24 Gain of the ^2P-K-shell to ^2P L-transition on a C^+-ISPI XRL at 4.5 nm as a function of time along with the time-dependent optical ultrashort pulse laser intensity divided by 100 and the filtered intensity of the X-ray pump source (from [114], Fig. 4)

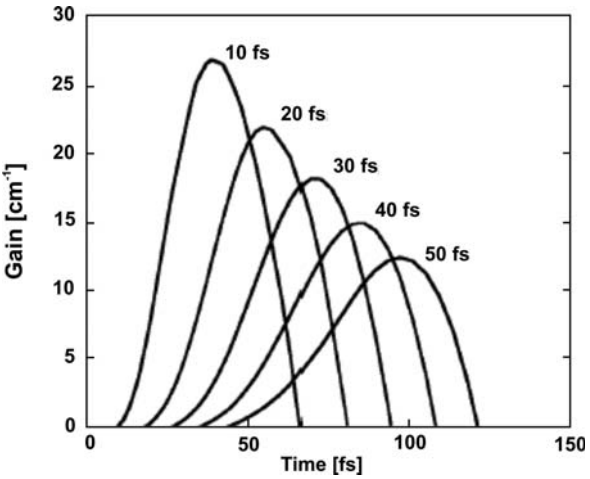

Fig. 25 Calculated gain coefficient for the K–L ($1\,s^{-1}$–$2p^1$) transition of a C^+-ISPI XRL in dependence on the change of the duration of the ultrashort optical pulse from 50 to 10 fs (FWHM) that generates the incoherent X-ray pump pulse. The electron density is kept constant of 1.2×10^{20} cm^{-3} as well as the source energy of 1 J (from [114], Fig. 5)

As the system discussed above is very sensitive to the photoionizing radiation it was proposed in [117] to create an inner-shell population inversion via atomic processes involving electrons. In this case photoionization pumped XRL schemes based on the same transitions would be less sensitive to electron population of the lower level, thus requiring less extreme X-ray pumping. As a result the inversions could live longer as compared to equivalent photo-inner-shell ionization pumped by K_α-transition.

The necessary ultrashort and high-energy (~keV) electron pulses could be created via optical-field ionization. This process could be more efficient than that applying incoherent X-rays of the same energy (Table 6).

Table 6 Predicted ISPS-XRLs

Target, Z	Ion, transition, J	Wavelength [nm]	Gain [cm^{-1}], gl, output	Type	Pumping	Target config.	Lit.
C 6	C^{1+}, 1s–2p	4.5	10	tr	X-pulse, 20 fs, 1 J,	foil	[114, 118]
Neon, 10	Ne^{1+}, 1s–2p	1.46	15 0.4 μJ	tr	X-pulse, 100 fs, 5 J, 10^{17} W/cm^2	foil, 5 μm× 1 cm area	[119]
Neon, 10	Ne^{1+}, 1s–2p	1.46	~10	tr	X-pulse, 50 fs, 3 J,	foil, 10 μm × 1 cm	[111, 112]
Na, 11	Na^+, $2p^5 3s$–$2p^6$	37.2	≤ 20	tr	X-pulse, ≤ 1 ps, 3×10^{13} W/cm2	foil, 100 μm× 1 cm	[120] [121]

2.5 Photoresonant Pumping

Photoresonant XRL schemes are an interesting approach that is described by the relation

$$Z_0{}^{i+} + h\nu \rightarrow Z_u{}^{i+} \tag{48}$$

The level diagram is quite similar to that of electron collisional excitation (§2.1) with the exciting electron replaced by a photon. It follows that this scheme requires one source (plasma) of an intense line at a wavelength well matched to the wavelength of the transition activating laser levels in a second plasma being the lasing material. In principle this could be an advantage since the pumping rate and the specific upper laser level could be controlled by the photon flux and chosen wavelength. Conceptually the separated photon source resembles the pump laser or flash-lamp, common in conventional optical lasers.

However, in practice the requirements of an exact line matching as well as high flux of pumping photons are difficult to fulfil. Although numerous line coincidences have been found (for example, between potential lasing lines in various ions and strong pump lines from H-like, He-like and Li-like ions listed in [4]) it was up to now difficult to realize an efficient photon coupling between both plasmas that could lead to high amplification on the lasing transition.

In the year 1996 another type of photopumping was proposed called self-photopumping of a strong emission line in an optically thick plasma [122]. It predicts a strong lasing on a specific transition for neon-like ions ($3d^1P_1 \rightarrow 3d^1P_1$). The same mechanism allows for lasing in Ni-like ions and gain up to $g \sim 13\,cm^{-1}$ was demonstrated in nickel-like Mo, Nb and Zr ions [123, 124]. The level scheme of the self-photopump excitation of the $4f\ ^1P_1 \rightarrow 4d\ ^1P_1$ Ni-like Mo X-ray laser at 22.6 nm is shown in Fig. 26 [124, Fig. 1]. The self-photopumping rate of the $4f\ ^1P_1$ level from the ground level $3d\ ^1S_0$ is one order of magnitude higher than those for collisional pumping.

However, this new line was never observed to be stronger than the principal, collisionally excited $4d\ ^1S_0 \rightarrow 4p\ ^1P_1$ line. Up to now no real short pulse pumped

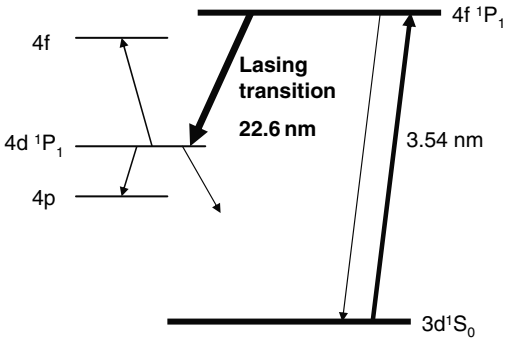

Fig. 26 Energy level diagram for a nickel-like $4f\ ^1P_1$–$4d\ ^1P_1$ Mo-XRL at 22.6 nm. Lasing is caused by the strong photopumping from the $3d^1S_0$ ground level populating the $4f\ ^1P_1$ upper laser level [122]

Table 7 Realized self-photo-pumped Ni-like XRLs at $4f\ ^1P_1 \rightarrow 4d\ ^1P_1$ [122, 34]

Z	Transition	Wavelengths [nm]	Literature
Zr, 40	$4f\ ^1P_1 \rightarrow 4d\ ^1P_1$	27.10	[122]
Nb, 41	$4f\ ^1P_1 \rightarrow 4d\ ^1P_1$	26.64	[122]
Mo, 42	$4f\ ^1P_1 \rightarrow 4d\ ^1P_1$	22.60	[122]
Ag, 47	$4f\ ^1P_1 \rightarrow 4d\ ^1P_1$	16.05	[35]

X-ray laser was realized that uses photo-pumping excitation as the main pump mechanism (Table 7).

2.6 Recent Developments

Longitudinal pump geometry for collisional soft X-ray lasers was proposed in 1998 [125] and this proposal was further improved by applying oblique or grazing incidence irradiation geometries with an incidence angle of 83° [126]. This scheme was the starting point to further development and the first collisionally pumped soft X-ray laser in GRIP (*GR*azing *I*ncidence *P*umping) geometry has been demonstrated in 2004 with a pump energy of 150 mJ at a repetition rate of 10 Hz [127].

2.6.1 Soft X-Ray Lasers in GRIP Geometry

The GRIP arrangement belongs to the double pulse irradiation technique of the short wavelength lasers with transient inversion. The first, long (a few hundreds of picoseconds) pulse creates a plasma column and after an optimized delay a short (a few of picoseconds) pulse irradiates this plasma under grazing incidence angle and rapidly heats it. The GRIP geometry is characterized by a large incidence angle of the heating pulse with a value between 60 and 75 degrees (measured to the normal to the target surface). This angle is optimized to avoid penetration of the pump radiation into the very high-density area in the neighbourhood of the critical surface ($n_{cr} \sim 2 \times 10^{21}$ cm^{-3}). In the traditional lateral irradiation a lot of the delivered energy is deposited there and cannot be used in the amplification process, which occurs in the density range $n_{ampl} \sim 10^{20}$ cm^{-3}. The GRIP offers, by variation of the incidence angle, a control over the area in which the major part of the delivered energy will be deposited. Moreover, in such an irradiation geometry a part of the pump beam is deflected on the plasma density gradient. The deflected part of the beam overlaps the rest of the incident beam (see Fig. 27). This can additionally increase the energy deposited in the active medium.

Three experiments with different pump parameters have been recently conducted [128, 129, 130] but strong irrefragable saturation has been demonstrated only with a total pump energy of 1.2 J [129]. The other two experiments performed at lower pump energies helped to define threshold conditions for

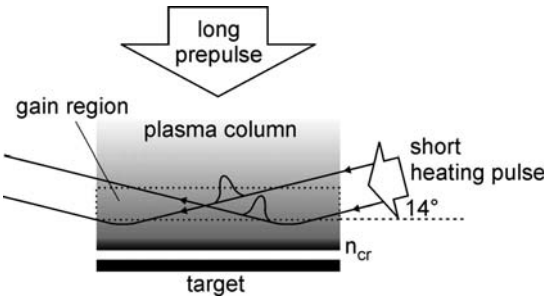

Fig. 27 The principle of the GRIP pump arrangement

lasing and demonstrated dependence of the output signal on the pump pulse intensity. The highest measured output energy was about 1 μJ (close to the theoretical expectation) and this indicates that no dramatic increase in the conversion efficiency, understood as ratio of the output to the input signals can be expected. This is, at the first glance, in apparent contradiction with reduction in the pump energy observed. However, many parameters of the created plasma depend on intensity/fluence of the pumped radiation and conservation of the optimum pump conditions requires reduction in the volume of the created plasma plume, parallel to the energy reduction. This reduction in the volume of active medium, on the other hand, reduces output signal and hinders a significant increase in the conversion efficiency. In fact, this interplay between reduction in the pump energy and decreasing active volume was observed in the progress on X-ray lasers during the last decade. The GRIP arrangement offers a breakthrough in control over the energy deposition. By choice of the incidence angle the pump radiation can sample the plasma areas of specific optimized density. As a result of the reduction in required pump energy, titanium:sapphire laser technology could be, for the first time, used for X-ray lasers pumping and the same a repetitive XRL with an energy in a single pulse of 1 μJ and an average power of 10 μW became the fact.

2.6.2 XMOPA

The limited output energy in the GRIP arrangement, being a consequence of the pump conditions, has enforced search for new solutions enabling output energies sufficiently high to be suitable for applications. One of the feasible solutions is using the X-ray laser active medium as an amplifier seeded by a short wavelength oscillator. This setup follows the known *M*aster *O*scillator-*P*ower *A*mplifier (MOPA) arrangement in the optical range. For such a MOPA in the XUV spectral region (XMOPA) high harmonics (HH) seem to be an ideal candidate as the oscillator since they have in principle controllable, bandwidths/pulse duration, polarization, beam profile and relative high photon numbers. The idea was for the first time tested 10 years ago with gallium as the amplifying medium [131]. The development in OFI lasers

caused a revival of this idea [132]. In the latest experiment radiation at a wavelength of 32.8 nm with the output pulse duration of 500 fs have been reported. The advent of the GRIP-lasers strengthens the interest in XMOPA as such lasers offer repetitively driven active medium with a high saturation parameter and the same high extractable energy. These two techniques (GRIP+XMOPA) combine efficient pump energy deposition and efficient energy extraction. The energy extraction is more efficient, as the amplification process in the amplifier begins at a level significantly higher than the spontaneous noise being the starting point of the amplification process in conventional XRLs. For efficient energy extraction the seeding signal should be significantly higher than the saturation parameter E_S. This is a very challenging task in the XUV spectral range well below 20 nm. The saturation intensity of the laser transitions in collisional soft X-ray lasers is about $10^{10}\,W/cm^2$. As a result, the seed should have a very high photon density over a reasonably big area to fulfil the formulated requirement. This becomes increasingly difficult for decreasing wavelengths, as the efficiency of high harmonics scales with the wavelength as ω^{-5}. Moreover, there is a mismatch between the narrow linewidth of the amplifying medium and a broad bandwidth of the injected harmonic signal. These are severe constraints on the scheme which have to be solved to realize an efficient XMOPA scheme. An output with a very high coherence level, defined polarization of the output radiation and subpicosecond output pulses make XMOPA arrangement a very advantageous, even if difficult, scheme.

3 Applications

The large quasi-steady-state X-ray lasers driven by long ($<$100 ps) and energetic ($>$ 20 J) pumping pulses were used for longer than one decade in selected single shot (one shot each 10–30 min) applications. The output pulses of these lasers delivered energy of several tens of millijoules in a wavelength range between 4 and 30 nm. This situation will certainly not change in the near future, because driving lasers with these parameters and even with a moderate repetition rate are out of the present technological possibilities. However, it is worth noting that there are several projects for high-energy lasers with repetition rates in the Hz-range, which could help to overcome these constraints. In contrast to that a remarkable progress has been made in the last few years in several important aspects of the development of compact and practical soft X-ray lasers. A very compact capillary discharge system has been operated at 46.9 nm (26.5 eV) producing millijoule level pulses of 50–100 ps with a 4 Hz repetition rate and an average power per unit bandwidth that is comparable to values of third generation synchrotron beam line, and a peak coherent power that is several orders of magnitude larger.

Short pulse-driven transient collisional X-ray lasers pumped with short pulses of energy lower than 10 J have been demonstrated in saturation at the wavelength range between 30 and 10 nm. These table-top-like systems have an output energy exceeding 10 microjoules. Saturated OFI lasers operating at repetition rate of 10 Hz and at the wavelengths of 41.8 and 32.4 nm delivered coherent pulses with the energy of several tens of nanojoules.

The knowledge of the XRL radiative properties like pulse energy, duration, source size, beam divergence, bandwidth, as well as spatial coherence or in a common unit their brilliance (brightness) B is highly important for any kind of the application. In Fig. 28 a comparison with different X-ray radiation sources is given.

The average XRL-brilliance is presently far from the potential high value. This is mainly caused by the lack of short pulse pump lasers with the desired average power of ≥ 100 W at pulse energies of several Joules. It is expected that both the optimization of the excitation efficiency of the X-ray lasers as well as the development of pump lasers with higher repetition rate that is in progress will soon lead to further reduction in the size, complexity and costs of XRLs. Therefore a widespread use of these coherent sources in numerous scientific and technological applications is expected in the coming years. Some X-ray lasers have already been used for numerous applications demonstrating their potential as coherent and (partially) short pulse X-ray sources.

Even though a lot of the applications have been performed with quasi-stationary X-ray lasers which are out of the scope of this contribution a short review is given here.

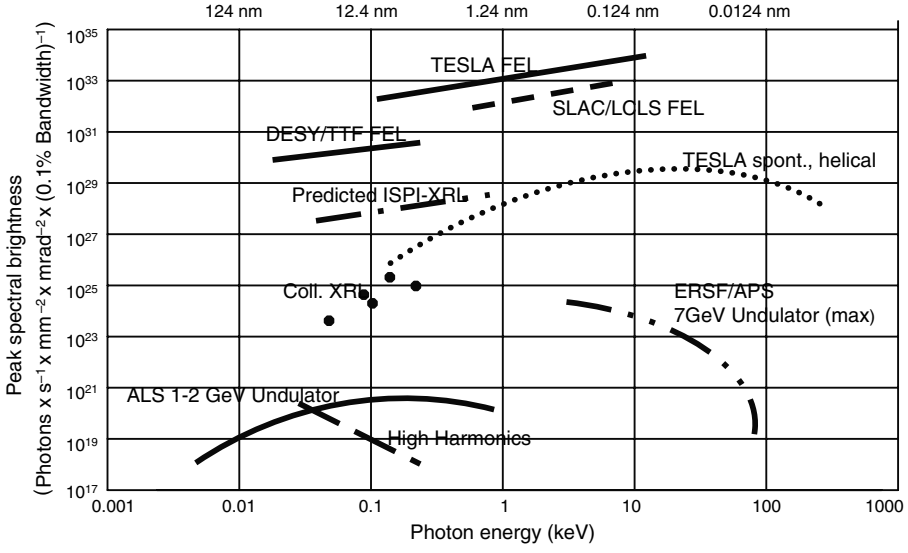

Fig. 28 Peak spectral brightness for free electron lasers (FEL), synchrotrons, high harmonics and XRL-sources (selection)

3.1 Diagnostics with XRL

Owing to their high brightness, X-ray lasers are well suited as a diagnostic tool in interferometry, microscopy, and reflectometry [132, 133, 134, 135]. Imaging biological samples requires short wavelengths near the "water window" covering the range between 2.3 and 4.4 nm. In this wavelength range the contrast between water and carbon-containing substrates (DNA, proteins, etc.) is very high and *in situ* microscopy of wet (living) samples is possible.

Ni-like lasers have been demonstrated [12, 13] in and near the "water window". Wavelengths just longer than the carbon K-edge are also of interest. However, for laboratory use the size and cost of the driving laser for the Ni-like systems must be remarkably reduced. For X-ray holography, the maximum scattering of carbon-containing structures in water is expected to be just above 4.4 nm [14]. It has been shown that for X-ray holography the X-ray dosage received by a cell is minimized for a given image resolution if the illumination wavelength is near to the long wavelength side of the carbon K-edge [14, 136]. This is also a suitable wavelength for imaging of gold-tagged biological specimens [137]. Whereas very interesting biological studies could be conducted using the presently available XRLs at $\lambda = 10$–20 nm, crystallography and semiconductors-related research require compact X-ray sources operating at 1 nm or shorter. Scaling of short pulse-driven recombination XRLs on transition into the ground state could solve this problem and seems to be a promising alternative to the inner-shell laser in this wavelength range.

With the upcoming EUV-lithography at wavelengths of approximately 13 nm, X-ray lasers emitting pulses in this range (i.e. collisional Ni-like Ag-XRL at 13.9 nm) could become an attraction as a source for precision reflectometry, interferometry or other domains of metrology on samples at lithography facilities. Particularly XRLs with high repetition rates could be important here as well as for most pump/probe experiments and for many material science experiments, such as photoelectron spectroscopy. In general, for many pump/probe and time-dependent experiments, a high repetition rate X-ray laser (transient collisional, recombination or OFI-XRL) would be more useful and much less expensive than a synchrotron or a FEL. OFI-XRLs of recombination type could be an interesting tool for time-resolved photoelectron spectroscopy of surfaces. Continuous tunability, which is not obtainable with XRLs, is not required, because the energy of the ejected photoelectrons is measured to determine the binding energy for a given photon energy. The photon energy is known accurately because of the narrow bandwidth ($\Delta\lambda/\lambda = 10^{-4}$–$10^{-6}$) of the XRL. The output energy of the XRL should be of a μJ-level.

Many experiments like photoelectron spectroscopy or nonlinear optics in the soft X-ray range need a high X-ray intensity. Therefore, development of suited focussing optics is necessary and the first adaptive optics for the correction of the wavefront of X-ray laser pulses for the interesting 13 nm range was reported recently [138].

3.2 Interferometry

Short pulse XRLs are required for probing high-density, laser-produced plasmas. Large plasmas (of 3 mm size) with electron peak densities $n_e \geq 4\times10^{21}$ cm^{-3} can be probed only by XUV/X wavelengths, because an optical laser radiation cannot propagate through the plasma at such high densities.

The first XRL-based interferometry of a high-density plasma was reported in 1995 [139, 140] using a Mach–Zehnder-type interferometer working with a 15.5 nm neon-like yttrium laser. However, this method, based on an amplitude division technique, needs plane X-ray beam splitters of very high optical quality (flatness $<\lambda/20$ over the aperture). This requirement can be fulfilled at present only for wavelength between 13 and 15 nm due to the Mo–Si multilayer technology developed for the EUV-lithography. A setup of an XRL Michelson interferometer is shown in Fig. 29.

Another promising method is the wave front division technique by a shaped mirror, first realized with XUV synchrotron radiation [141]. This method is nearly wavelength independent, since the reflection at the mirror is under grazing incidence. X-ray beam division can also be realized by a Fresnel bimirror. This, however, requires a high spatial coherence of the beam to produce interference fringes. A successful experiment was demonstrated in [142] with a Ne-like Zinc-XRL at 21.2 nm [143] using a Fresnel bimirror consisting of two mirrors arranged as a "ridged roof" with a small angle between them. An interferometer of this type was used for an *in situ* investigation of electric field-induced breakdown on one of the surfaces of a Niobium-bimorph mirror [144]. In principle X-ray laser-based XUV interferometry appears to be a powerful tool to investigate any stressed surfaces (with high flatness) and could be of great importance for thin-layer technology and controlling of electronic components.

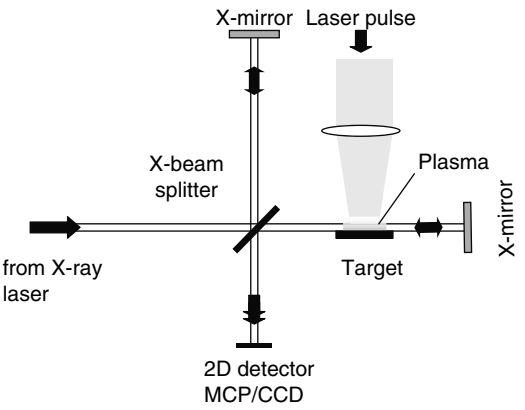

Fig. 29 Setup of Michelson-type interferometer to probe dynamics of a laser pulse-driven plasma. The XRL beam can diagnose regions of higher electron density than that of optical lasers according to n_{ec} [cm^{-3}] $= 1.11\times10^{21}/\lambda^2$ [μm], with λ-XRL wavelength (see also (2))

3.3 Reflectometry

An important application of the XRL would be the determination of XUV optical constants by reflectometry [145]. In this method optical constants at each wavelength can be found by fitting the measured angular dependence of the reflectivity with the Fresnel formula [136]. This method can in principle provide not only optical constants of the bulk material but also information about the surface characteristics (i.e. additional oxide surface layers) of the sample, and could thus be well suited for measurement of the reflectivity of EUV-coatings. Using a high repetition rate table-top capillary discharge Ne-like Ar X-ray laser at 46.9 nm (26.5 eV) with an average power of up to 1 mW [18] optical constants for Si, GaP, InP, GaAs, GaAsP and Ir were determined. The high intensity of a X-ray laser is an advantage for accurate measurements of the reflectivity at near-normal incidence, where the reflectivity of most materials is low.

3.4 Excitation of Nonlinear Processes

X-ray lasers can, owing to their high peak power (brightness), in principle cause efficient excitation processes that cannot be observed with other incoherent X-sources or high harmonics. Multiphoton processes as well as nonlinear laser matter interaction in the soft X-ray range need high intensities, which to date can be delivered in principle only by XRLs (or XUV-free electron lasers). Multiphoton inner-shell spectroscopy, XUV nonlinear optics to generate new short wavelength are in the focus of interest. Also application of such processes to metrology (measurements of ultrashort XUV pulses using correlation techniques) seems to be possible.

An interesting elementary process that needs demonstration is the two-photon ionization of 4d inner-shell electrons in Xe. Among others, intense X-ray laser pulses could also be interesting for the study of the ionization dynamics in clusters. Also macroscopic effects, like the direct pumping of photoionization XRLs or inner-shell XRLs might be realized using bright X-ray lasers as pump source (see § 2.4, 2.5), even though the overall efficiency of this process is expected to be very small.

Study of the excitation of luminescence processes for example in ionic crystals appears as another interesting application aspect. These crystals have a great potential for various practical applications, like scintillation detectors for medical and nuclear applications as also for radiography and crystallography. Studies on UV luminescence of CsI with 58.4 eV photons of a 21.2 nm Zinc-XRL were reported in [145]. Short XRL pulses could allow for "instantaneous" production of the luminescence or for study on nonlinear effects in the luminescence efficiency.

With the advent of new state-of-the-art diffractive optics (i.e. Bragg–Fresnel lenses, which are practically free of geometrical aberrations [146]) or adaptive mirrors it seems to be possible to focus the X-ray laser beam down to several

Table 8 Desired characteristics for X-ray laser application

Application	Average power	Brightness	Short pulse	Coherence
Plasmas				
–Interferometry	–	Yes	Yes	Yes
–Nonlinear optics		Yes	Yes	Yes
–Generation	May be	Yes	Yes /no	Yes
Warm dense matter	Yes	Yes	Yes	–
Biology				
–Microscopy	–	Yes	Yes	–
–Holography	–	Yes	Yes	Yes
–Diffraction	–	Yes	Yes	–
Atomic and molecular interaction				
–Photoionization	Sometimes	Yes	Yes	–
–Multiphoton proc.	–	Yes	Yes	–
Mat. sci.& chemistry				
–Semiconductors	Yes	Yes	Yes	May be
–Photoemission	–	Yes	Yes/no	May be
Industrial				
–EUVL printing	Yes	May be	–	–
–EUV metrology	Yes	–	–	Yes

From table, page XII from proceedings of Workshop on "Applications of X-ray lasers", Jan. 12–14, 1992, San Francisco. CA Ed. by R. London, D. Matthews, and S. Suckewer and table presented by J. Dunn in JD-5 on International X-Ray Laser Conference, May, 2002, Aspen / Colorado.

microns, thus improving the spatial resolution and enlarging the intensity. Therefore, intensities of $\geq 10^{13}$ W/cm^2 should be soon possible in a focal spot of an XRL. At these intensities very dense plasmas could be produced, with the properties different from those produced by optical laser pulses allowing studies on warm dense matter (Table 8).

Acknowledgement We gratefully acknowledge assistance and discussions with Johannes Juemmler, Gerd Priebe and Antonio Lucianetti at the realization of our X-ray laser research. Their work contributed to the results partly reported in this text. Our appreciations go also to the colleagues and friends from the international X-ray laser community, especially to J.J. Rocca, J. Dunn and G.J. Pert, for helpful discussions. We are also very grateful to M.H. Edwards for his help on the manuscript improvement.

Our research activities were partly supported by a DFG-Schwerpunkt-Projekt, the European Network Program as well as the German–Israeli GIF- and GILCULT-projects.

References

1. G.A. Gudzenko, L.A. Shelepin, Zh. Eksp.Teor. Fiz. **45**, 1445 (1963)
2. D.L. Matthews et al., Phys. Rev. Lett. **54**, 110 (1985)
3. S. Suckewer, C.H. Skinner, H. Milchberg et al., Phys. Rev. Lett. **55** 1753 (1985)

4. R. Elton, "X-ray lasers", Academic Press, New York (1990)
5. P. Jaeglé, "Coherent Sources of XUV Radiation: Soft X-Ray Lasers and High-Order Harmonic Generation", Springer Series in Optical Sciences (2006)
6. A.G. Michette and C.J. Buckley Eds. (Iop Publishing, 1993) "X-Ray Science and Technology" (1993)
7. J.J. Rocca, "Table-top soft x-ray-lasers", Rev. Sci. Instrum., **70**, 3799 (1999)
8. A. Siegman, Lasers, University Science Books, Sausalito (1986)
9. R.C. Elton Appl. Opt. **14**, 97 (1975)
10. G.J. Linford. E.R. Peressini, W.R. Sooey, M.L.Spaeth, Appl. Opt. **13**, 379 (1974)
11. R.A. London, Phys. Fluids **31**, 184 (1988)
12. Mac Gowan et al., Phys. Rev. Lett. **65**, 2374 (1990)
13. B.J. Mac Gowan et al., Phys. Fluids B **4**, 2323 (1992), and references cited therein
14. R.A. London, M.D. Rosen, J.E. Trebes, Appl. Opt. **28**, 3397 (1989)
15. A. Carillon et al., Phys. Rev. Lett **68**, 2917 (1992)
16. J.A. Koch et al, Phys. Rev. Lett. **68**, 3291 (1992)
17. J.J Rocca, V. Shlyaptsev, F.G. Tomasel et al., Phys. Rev.Lett. **73**, 2192 (1994)
18. B.R. Benware, C.D. Macchietto, C.H. Moreno, J.J. Rocca, Phys. Rev. Lett. **81,** 5804 (1998)
19. M.C. Marconi, J.L.A. Chilla, C.H. Moreno et al., Phys. Rev. Lett. **79**, 2799 (1997) coherence
20. M.P. Kalachnikov et al., Phys. Rev. A **57**, 4778 (1998)
21. P.J. Warwick et al., J. Opt. Soc. Am. B **15**, 1808 (1998)
22. A. Yariv and R.C.C. Leite, J. Appl. Phys. **34**, 3410 (1963)
23. J.P. Apruzese et al., SPIE Proc. **875**, 2 (1988)
24. J.A. Koch et.al. Phys. Rev. A **50**, 2 1877 (1994)
25. T. Fujimoto, J. Phys. Soc. Jpn **54**, 2905 (1980)
26. A. Klisnick et al., J. Opt. Soc. Am. B **17**, 1093 (2000)
27. M. Born E. Wolf, Principles of Optics, 7th ed, Cambridge University Press, Cambridge (1999)
28. T. Ditmire, M.H.R. Hutchnison, M. Key et al., Phys. Rev. **A 51**, R4337 (1995)
29. Y. Liu et.al. Phys. Rev. A **63**, 033802 (2001)
30. MBI unpublished (2003)
31. R.A. London, Phys. Fluids **31**, 184 (1988)
32. E.E. Fill, Opt. Commun. **67,** 441 (1988)
33. J.A. Chilla, J.J. Rocca, J. Opt. Soc. Am. B **13**, 2841 (1996)
34. J. Kuba, Doctor Thesis, Universite Paris XI, 19 October (2001)
35. Y.V.Afanasyev, V.N. Shlyaptsev, Sov. J. Quantum Electron. **19**, 1606 (1989)
36. B.J. Mac Gowan et al., Phys. Rev. Lett **59**, 2157 (1987)
37. J.H Scofield et al., Physica scripta **46**, 361 (1992)
38. J. Dunn et al., Phys. Rev. Lett. **80**, 2825 (1998)
39. P.V. Nickles, V. Shlyaptsev, M. Kalachnikov et al., Phys. Rev. Lett. **78**, 2748 (1997)
40. V.N. Shlyaptsev et al., Proc. SPIE **2012**, 111 (1993)
41. P.V. Nickles et al., Proc. SPIE **2520**, 373 (1995)
42. J. Dunn, Y. Li, et al., Phys. Rev. Lett. **84**, 4834 (2000)
43. K.A. Janulewicz, A. Lucianetti, G. Priebe, W. Sandner, P.V. Nickles, Phys. Rev.A, **68**, 051802(R) (2003)
44. P.V. Nickles, K.A. Janulewicz, F. Bortolotto et al., Proc. SPIE Conferences, **3776**, Denver (1999)
45. K.A. Janulewicz, J.J. Rocca, F. Bortolotto et al., C.R. Acad. Scien.,1, **Ser IV**, 1083 (2000)
46. J.C. Moreno, J. Nilsen, L.B. Da Silva, Optics Commun. **110**, 585 (1994)
47. E. Fill, Y. Lin, D. Schlögel, J. Steingruber, J. Nilsen, Optics Lett. **20**, 374 (1995)
48. J.-C. Chanteloup, E. Salmon, C. Sauteret, J. Opt. Soc. Am. B **17,** 151 (2000)
49. P.V. Nickles, C. Danson R. Allott et al., Proc. Intern. Conf. "Superstrong Fields in Plasma", Varenna ed. Lontano, CP425 (1997)

50. H. Fiedorowicz, A. Bartnik, M. Szczurek, E. Fill, Y.L. Li, P.X. Lu, G. Pretzler, SPIE Proceedings 2520, 55 (1995)
51. H. Fiedorowicz, A. Bartnik, J. Dunn et al., Optics Lett. **26**, 1403 (2001)
52. P. Lu, T. Kawachi, M. Kishimoto et al., Opt. Lett. **27**, 1911 (2002)
53. 53.J.J. Rocca, D.C. Beetle, M.C. Marconi, Opt. Lett. **13**, 565 (1988)
54. D. Kaganovich, P.V. Sasorov, Y. Ehrlich et al., Appl. Phys. Lett. **71**, 2925 (1997)
55. J.J. Rocca, O.D. Cortazar, B.T. Shapiro et al., Proc. SPIE **2012**, 67 (1993)
56. A.I. Osterheld, V.N. Shlyaptsev, J. Dunn et al., 5 nst. Phys.Conf. Ser. **159**, 353 "X-Ray Lasers", Kyoto (1998)
57. T. Kawachi, M. Kado, M. Tanaka et al., Phys. Rev. A **66**, 033815, (2002)
58. C.D. Decker R.A. London, Phys. Rev. A **57**, 1395 (1998)
59. J.H. Scofield, B.J. MacGowan, Phys.Scr.**45**, 361 (1992)
60. C. Chenais-Popovics, R. Corbett, C.J. Hooker et al., Phys. Rev. Lett. **59**, 2161 (1987)
61. H. Daido, Y. Kato, H. Azuma et al., X-ray lasers 1992, IOP Conf. Series **125**
62. A. Carillon, M.J. Edwards, M. Grange et al., J. Phys. B **23**, 147 (1990)
63. P. Jaegle, G. Jamelot, A. Carillon, A. Klisnick, J.Opt. Soc. Am. B **4**, 563 (1887)
64. J. Steingruber, E. Fill Appl. Phys. B **58**, 29 (1994)
65. J. Steingruber, S. Chen, E. Fill, X-ray lasers 1992, IOP, **125** (1992)
66. J. Zhang, M.H. Key, Appl. Phys. B **58**, 13 (1994)
67. G.J. Pert, in X-Ray Lasers 1994, AIP Press, New York, 1994, p. 49 (1994)
68. J. Zhang, M.H. Key, P.A. Norreys, G.J. Tallents et al., Phys. Rev. Lett. **74**, 1335 (1995)
69. J. Zhang, E. Fill, Y. Li etal., Opt. Lett. 21, 1035 (1996)
70. A. Morozov, L. Polonsky, S. Suckewer, Proc.of 2 nd Int. Symp. "Plasma 95",**2**, 247, Warsaw (1995)
71. D. Korobkin, A. Goltsov, A. Morozov, S. Suckewer, Phys. Rev. Lett. **81**, 1607 (1998)
72. A. Goltsov, D. Korobkin, C.H. Nam, S. Suckewer, Proc.of SPIE (1995)
73. D. Korobkin, C.H. Nam, S. Suckewer, A. Goltsov, Phys. Rev. Lett. **77**, 5206 (1996)
74. T. Ozaki, S. Orimo, H. Kuroda, Opt. Quantum Electron. **28**, 187–200 (1996)
75. M.V. Ammosov, N.B. Delone, V.P. Krainov, Sov. Phys. JETP **64**, 1191 (1986)
76. N.H. Burnett, P.B. Corkum, J. Opt. Soc. Am. B **6**, 1195 (1989)
77. N.H. Burnett, G. D. Enright, J. Quantum Electron. **26**, 1797 (1990)
78. T.E. Glover, T.D. Donnelly, E.A. Lipman et al., Phys. Rev. Lett. **73**, 78 (1994)
79. T. Auguste, P. Monot, L.A. Lompre et al., J. Phys. B **25**, 4181 (1992)
80. P.B. Corkum, N.H. Burnett, OSA Proceed. on Short Wavelength Coherent Radiation, **2**, 225 (1988)
81. B.E. Lemoff, C.P.J. Barty, S.E. Harris, Opt. Lett. **19**, 569 (1994)
82. S. Augst, D. Strickland, D.D. Meyerhofer et al., Phys. Rev. Lett. **63**, 2212 (1989)
83. B.M. Penetrante and J.N. Bardsley, Phys. Rev. **A**, 43, 3100 (1991)
84. E.E. Fill, S. Borgström, J. Larson et al., Phys. Rev. E **51**, 6016 (1995)
85. D. Kaganovich, A. Ting, C.I. Moore, A. Zigler et al., Phys. Rev. E **59**, R4769 (1999)
86. C.G. Durfee III, H.M. Milchberg, Phys. Rev. Lett. **71**, 2409 (1993)
87. P. Sprangle and E. Essarey, Phys.Fluids B **4**, 2241 (1992)
88. Y. Ehrlich, C. Cohen, A. Zigler et al., Phys. Rev. Lett. **77**, 4186 (1995)
89. D.J. Spence et al., J. Phys. B: At. Mol. Opt. Phys. **34**, 4103 (2001)
90. A.B. Borisov, A.V. Borovsky, V.V. Korobkin et al., Phys. Rev. Lett. **68**, 2309 (1992)
91. A.B. Borisov, J.W. Longworth, K. Boyer et al., Proc. Natl. Acad. Sci. USA **95**, 7854
92. P. Monot, T. August, P. Gibbon et al., Phys. Rev. Lett. **74**, 2953 (1995)
93. P. Sprangle, E. Esarey, B. Hafizi, Phys. Rev. Lett. **79**, 1046 (1997)
94. Y. Zeldovich, Y. Raizer, in "Physics of Shock Waves and High-Temperature Hydrodynamic Phenomena", Academic, New York, 1966, pp. 406–413
95. G.J. Pert, J. Phys. B **23**, 619 (1990)
96. D.C. Eder, P. Amendt, S.C. Wilks, Phys. Rev. A **45**, 6761 (1992)

97. D.C. Eder, P. Amendt, L.B. Da Silva et al., Phys. Plasmas **1,** 1744 (1994)
98. S. Hulin, T. Auguste, P.D. Oliveira et al., Phys. Rev. E, **61**, 5693 (2000)
99. W.P. Leemans, C.E. Clayton, W.B. Mori et al., Phys. Rev. A **46**, 1091 (1992)
100. D.C. Eder, P. Amendt, L.B. DaSilva et al., Phys. Plasmas **1**, 1744 (1994)
101. Y. Nagata, K. Midorikawa, S. Kubodera et al., Phys. Rev. Lett.**71**, 3774 (1993)
102. T.D. Donnelly, L. Da Silva, R.W. Lee et al., J. Opt. Soc. Am. B **13**, 185 (1996)
103. B.E. Lemoff, G.Y. Yin, C.L. Gordon III et al., Phys. Rev. Lett. **74**, 1574 (1995)
104. B.E. Lemoff, C.P.J. Barty, S.E. Harris, Opt. Lett. **19**, 569 (1994)
105. S. Sebban, R. Haroutunian, Ph. Balcou, et al., Phys. Rev. Lett. **86**, 3004 (2001)
106. S. Sebban, T. Mocek, D. Ros, et al., Conf. Report, 8. Int.Conf.on X-Ray Lasers, Aspen, Co, 27–31.May (2002)
107. L. Polonsky, C.O. Park, K. Krushelnik, S. Suckewer, Proc.SPIE **2012**, 75 (1993)
108. P. Sprangle, A. Ting, E. Esarey, A. Fisher, J. Appl. Phys. **72**, 5032 (1995)
109. B.N. Chichkov, A. Egbert, H. Eichmann et al., Phys. Rev. A **52**, 1629 (1995)
110. M.A. Duguay, P.M. Rentzepis, Appl. Phys. Lett. **10**, 350 (1967)
111. H.C. Kapteyn, Appl. Opt. **31**, 4931 (1992)
112. M.M Murnane, H.C. Kapteyn, M.D.Rosen, W. Falcone, Science **251**, 531 (1991)
113. R. Li, Z. Xu, Technical Digest, TuB3-1, Conf. on Application of High Field and Short Wavelength Sources IX, Palm Springs, 21–24. October (2001)
114. S.J.Moon D.C. Eder, Phys. Rev A **57**, 1391 (1998)
115. G.L. Strobel, D.C. Eder, R.A. London et al., SPIE Proceed, Conf on Short-Pulse High- Intensity Lasers and Appl., Los Angeles, 1993, SPIE Bellingham, WA, **1860**, 140 (1993)
116. E. Fill, privat communication
117. D. Kim, C. Toth, C. Barty, Phys. Rev. A **59**, R4129 (1999)
118. S.J. Moon, D.C. Eder, G.L. Strobel, Ref. 4, 262 in X-Ray Lasers, edited by D.C. Eder, D.L: Matthews (AIP, NY. 1994)
119. G.L. Strobel, D.C. Eder, P. Amendt, Appl. Phys. B58, **45** (1994)
120. W.T. Silfast, O.R. Wood II, J. Opt. Soc. Am. B **4**, 609 (1987)
121. Y. Li, H. Schillinger, C. Ziener, R. Sauerbrey, Opt. Commun. **144**, 118 (1997)
122. J. Nilsen, Phys. Rev. A **53**, 4539 (1996)
123. J. Dunn, A. L. Osterheld, V. Shlyaptsev et al., X-Ray Lasers, Inst. Phys. Conf. Series **159**, 51 (1999)
124. J. Nilsen, J. Dunn, A. L. Osterheld, Phys. Rev. A **60**, R2677 (1999)
125. R. Li, T. Ozaki, T. Kanai, H. Kuroda, Phys. Rev. E, **57**, 7093 (1998)
126. T. Ozaki, K. Yamamoto, T. Kanai, H. Kuroda, J. Phys. Soc. Jap. **71**, 2963 (2002)
127. R. Keenan, J. Dunn, V.N. Shlyaptsev, R.F. Smith, P. K. Patel, D.F. Price, Proc. SPIE **5197**, 213 (2003)
128. R. Keenan, J. Dunn, P. K. Patel, D.F. Price, R.F. Smith, V.N. Shlyaptsev, Phys. Rev. Lett. **94**, 103901 (2005)
129. B.M. Luther, Y., Wang, M.A. Larotonda, D. Alessi, M. Berill, M.C. Marconi, J.J. Rocca, V.N. Shlyaptsev, Opt. Lett. **30**, 165 (2005)
130. J. Tümmler, K.A. Janulewicz, G. Priebe, P.V. Nickles, Phys. Rev. E, **72**, 037401 (2005)
131. T. Ditmire et al., Phys. Rev. A **51**, R4337 (1995)
132. Ph. Zeitoun et al., Nature **431**, 426 (2004)
133. D. Di Cicco, D. Kim, D. Rosser S. Suckever, Opt. Lett. **17**, 157 (1992)
134. R.E. Burge, M.T. Browne, P. Charalambous et al., Opt. Lett. **18**, 661 (1993)
135. I.A. Artioukov, B.R. Benware, J.J. Rocca et al., IEEE Journ. Select. Topics Quant. Electron. **5**, 1495 (1999)
136. J.C. Solem, C.G. Baldwin, Science **218**, 229 (1982)
137. L.B. Da Silva et al., Science **258**, 269 (1992)
138. P. Zeitoun, privat communication (2001)
139. D.B. Da Silva, T.W. Barbee, R. Cauble et al., Phys. Rev. Lett. **74**, 3991 (1995)

140. D.B. Da Silva, T.W. Barbee, R. Cauble et al., Appl. Opt. **34**, 378 (1995)
141. F. Polack, D. Joyeux, J. Svatos, D. Phalippou, Rev. Sci. Instr. **66**, 2180 (1995)
142. F. Albert, D. Joyeux, P. Jaegle et al., Opt. Commun. **142**, 184 (1997)
143. B. Rus, A. Carillon, P. Dhez, P. Jaegle, G. Jamelot, A. Klisnick, M. Nantel, P. Zeitoun, Phys. Rev. A**55**, 3858 (1997)
144. Ph. Zeitoun, F. Albert, P. Jaegle et al., Nucl. Instrum. Methods A **416**, 189 (1998)
145. G. Jamelot, A. Carillon, P. Jaegle et al., IEEE J. Select. Topics Quant. Electron. **5**, 1486 (1999)
146. Wilhein (private communication) and T.Wilhein, B. Kaulich, J. Susini, Optics Commun. **193**, 19 (2001)

Time-Resolved X-Ray Science: Emergence of X-Ray Beams Using Laser Systems

Antoine Rousse and Kim Ta Phuoc

1 Introduction

Light is a very powerful tool to study matter, and many types of light facilities covering a wide spectral range exist to meet an increasing demand from users coming from many fields of research and industry. From the application point of view, there are strong demands of ultrashort optical pulses. These demands are being met by the European pool of laser facilities. There are also very strong demands for intense beams of X-rays, which are being met by the increasing pool of European accelerator-based sources, like synchrotrons and insertion devices (undulators and wigglers) at electron storage rings.

However, there are also increasing demands from users requesting the combination of the above properties, ultrafast (femtosecond), intense, collimated X-ray pulses ($\sim$10 keV) [1, 2]. In addition, these users frequently request that the ultrafast X-ray pulses can be perfectly synchronized with other optical or X-ray pulses to allow time-resolved pump-probe investigations. Many approaches are being explored and/or planned to meet these demands from the accelerator community. These approaches are all involving very large and costly installations and with different technical difficulties. Producing a high enough X-ray flux within 100 fs for applications, together with a perfect synchronization with an external optical or X-ray pulse, represents significant technical challenges in most of these approaches.

On the other side, intense and ultrafast laser systems can be used to produce secondary radiative sources from laser–matter interaction. Three main types of laser-based X-ray sources, demonstrated now for more than 10 years, currently exist. High harmonic generation [3, 4] and XUV lasers [5] can produce collimated beams but not in the X-ray range ($>$ 1 keV). Characteristic line emission from laser-produced plasmas can be in the X-ray range [6], but not collimated. During the past decade, there has been a race to produce beams of X-rays, with

A. Rousse
Laboratoire d'Optique Appliquèe, ENSTA, CNRS UMR7639, Ecole Polytechnique, Chemin de la Hunière, 91761 Palaiseau, France
e-mail: rousse@enstay.ensta.fr

T. Brabec (ed.), *Strong Field Laser Physics*,
DOI: 10.1007/978-0-387-34755-4_16,

the additional properties of spectral tunability and ultrashort pulse duration. However, none of the above laser-based sources have been able to offer these capabilities. A conceptually new strategy must therefore be used to generate beams of ultrafast X-rays.

By using relativistic laser plasma interaction, we have demonstrated a novel and different approach that meets the users demands for synchronized ultrafast X-ray beams. Recent results obtained at LOA demonstrate how an innovative source of X-ray radiation can be developed from the marriage of laser expertise and synchrotron radiation concepts [7, 8]. It relies on a millimeter scale laser-produced plasma unit that creates, accelerates, and wiggle a relativistic and ultrafast electron beam. This method announced a new class of infrastructure to be developed in the future, combining the specific properties of compact ultrafast lasers and energetic accelerator-based devices; the objective being to produce collimated beams of intense femtosecond X-ray pulses, with duration shorter by orders of magnitude compared with most present-day large-scale instruments.

Fundamentally new X-ray radiation properties would then be provided to the user's community to realize their experiments. In particular, it has been shown that users need a tool to probe the dynamics of matter with ultrafast time resolution [9, 10]. To that purpose, four fundamental technological issues should be fulfilled: 10 keV X-rays in a beam (mrad) to provide enough flux onto the sample; broadband and tunable X-rays for absorption or diffraction studies; femtosecond X-ray bursts to get the time resolution; perfect synchronization between the X-ray probing beam and the onset of the reaction.

The novel laser-based solutions can fulfil all these requirements. In particular, the use of lasers offers the unique power to naturally meet the last issue. The same laser system can be used for both the excitation of a sample and the production of the X-ray beam, ensuring an intrinsic synchronization even on an ultrafast (femtosecond) timescale.

2 Laser-Based X-Ray Beam

2.1 Principle

In laser wakefield accelerators [11], the ponderomotive force of an intense femtosecond laser pulse generates, as it propagates in an underdense plasma, a large amplitude wakefield plasma wave (Fig. 1). This wake can break, trap plasma electrons, and accelerate ultrashort pulse duration electron bunch to high energies (a few hundreds of MeV) on only a millimeter distance scale [12]. A particularly efficient mechanism for wakefield generation occurs in the parameter regime corresponding to ultrashort laser pulses (30 fs), called the forced laser wakefield regime, which has been studied experimentally [13] as

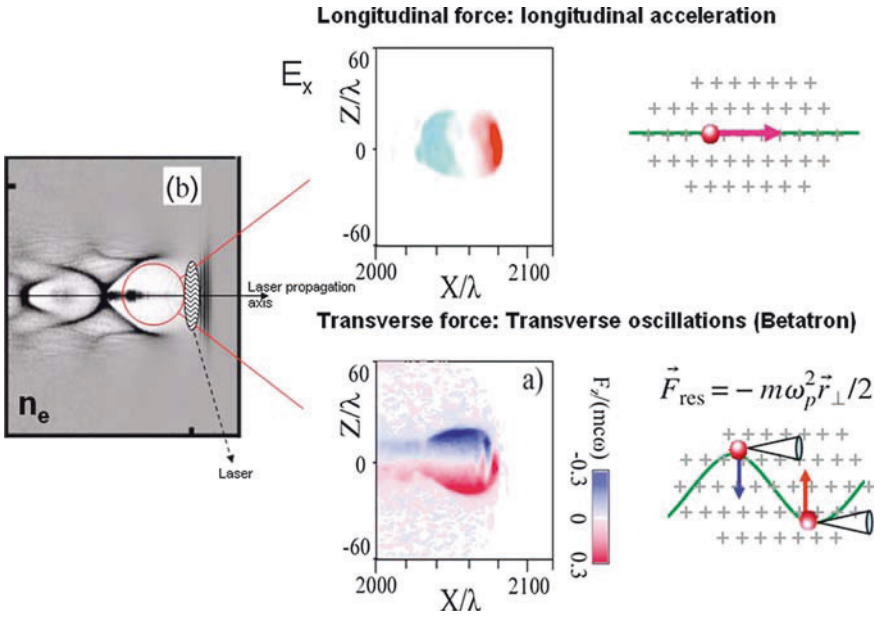

Fig. 1 Principle of the betatron X-ray source. Energetic electrons are accelerated by wakefield in a laser-produced ion channel. They experience the transverse electrostatic field of the channel, make betatron oscillations, and emit collimated beam of synchrotron radiation in the X-ray spectral domain. (**a**) Plot of the transverse force due to the space charge separation calculated from PIC simulation. (**b**) Electronic density plot of the plasma produced by the laser. The ion cavity as well as the accelerated electron beam (encircled in red) can be seen in the wake of the laser propagating in the gas jet

well as with 3D particle-in-cell (PIC) simulations [13, 14]. In this regime, the wake has an electron-density depression right behind the laser pulse, leading to the formation of an ion column [15, 16, 17]. In addition to the longitudinal electrostatic field responsible for the acceleration, this charge displacement also results in a strong radial electrostatic field.

Therefore, as the relativistic electrons propagate through these fields, they can undergo oscillations – called betatron oscillations – at a frequency given by $\omega_b = \omega_p/\sqrt{2\gamma}$. Here ω_p is the plasma frequency and γ the relativistic factor of the electron. As in a conventional synchrotron, this oscillatory relativistic transverse motion produces a collimated X-ray beam [15, 16, 18, 19]. However, because the wavelength of the wiggler can be much shorter in a laser–plasma interaction (micron-scale length) than in a synchrotron based on permanent magnets (centimeter-scale length), the distance required to produce a bright X-ray beam is much shorter (on the scale of millimeters, rather than 10 m); the required energy of the electron beam is also much lower (MeV, instead of GeV).

The oscillatory motion of the relativistic electron in the ion channel is comparable to that of an electron oscillating in an insertion device (undulator or wiggler) of a synchrotron. Here, the ion channel acts as a wiggler – or undulator – with a period λ_b and a strength parameter K given by $K = \gamma k_b r_0$. Consequently, as in a conventional insertion device, synchrotron radiation is emitted by the relativistic electron. The electron trajectory mainly determines the divergence of the produced radiation. It consists of a narrow cone of divergence $\theta = K/\gamma$ directed in the forward direction. The radiation is emitted in regimes that are distinguished by the strength parameter K. For K, the electron motion is near the axis and has a weak amplitude. The ion cavity then acts as an undulator, and the radiation is primarily emitted at the fundamental frequency:

$$\omega_f = \omega_b(2\gamma^2) = (2/\sqrt{2})\omega_p\gamma^{3/2},$$

which corresponds to the betatron frequency Doppler shifted in the laboratory reference frame. For $K > 1$, the amplitude of the electron motion is increased, the plasma then acts as a wiggler, high harmonics are radiated, and broadband radiation is produced. In that case, the spectrum is described by the function $S(\omega/\omega_c)$, characteristic of the synchrotron radiation [20]. In that case, the spectral intensity grows up to a frequency given by

$$w_c = (3/2)\gamma^3 c/R = (3/2)\gamma^3 c r_0 k_b^2,$$

where $R = 1/(r_0 k_b^2)$ is the transverse amplitude of the electron path, and then exponentially decreases. We have calculated the radiation emitted by the electron oscillating in the ion channel by using the trajectories of the oscillating electron (obtained by the numerical integration of the equation of the electron motion in the ion channel) from the general expression of the spectral flux $\frac{d^2I}{d\omega d\Omega}$ emitted in the direction of observation n [20].

We first used a test-particle simulation to calculate the radiation produced by relativistic electrons oscillating in an ion channel. The spectrumof the radiation estimated on the laser axis (in the propagation direction) is presented in Fig. 2 for the sets of parameters ($\gamma = 20$, $r_0 = 0.1$) $K = 0.18$ and ($\gamma = 20$, $r_0 = 3$) $K = 0.94$. For $K = 0.018$ and $\gamma = 20$, the radiation is emitted in the undulator regime at the fundamental frequency: $\omega/\omega_p = 126.5$. For K close to 1, the first few harmonics appear. For larger K, the radiation is emitted in the wiggler regime and has a broadband spectrum. If we consider electrons accelerated in a plasma by wakefield with energies extending up to 200 MeV, Fig. 2 represents the spectrum obtained from more accurate PIC simulations for $K > 1$.

For a more accurate description of the interaction, the acceleration of the electrons, and the radiation they emit, we have used a 3D particle in cell code. In this code, it is supposed that at any given moment of time, the relativistic

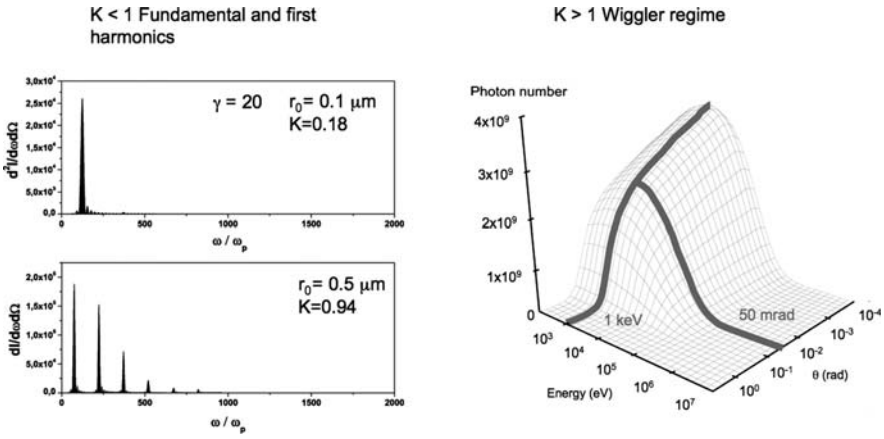

Fig. 2 Spectrum of the expected radiation as a function of the K parameter, the energy of the electrons (γ), and the amplitude of the betatron oscillation (r_0)

electron emits, along its momentum direction, a radiation spectrum defined by the function $S(\omega/\omega_c)$. The trajectories of each electron are described and used to calculate the emission during the interaction. The emitted radiation, exerting a recoil on the electron [16], is included in the equations of the electron motion. In the calculation, the following parameters are used: Gaussian laser pulse with a wavelength $\lambda = 0.820$ nm, a laser pulse duration of 30 fs, a focal spot of 18 μm, and an initial normalized potential vector $a_0 = 1.2$. For these parameters, the laser power exceeds the critical power for relativistic self-focusing. The PIC simulation shows that the laser beam self-focuses, and a_0 is slightly increased in the plasma. As the laser propagates in the plasma, it leaves a large-amplitude plasma wave in which electrons are trapped and accelerated up to about 100 MeV and an ion channel almost free of background electrons. In the channel, the simulation shows that the electrons undergo betatron oscillations with an amplitude of a few microns and produce a beam of keV X-rays. The maximum X-ray emission is observed for an electronic density of $n_e = 1 \times 10^{19}$ cm^{-3}. At this density, the wake amplitude maximizes because the laser pulse duration resonantly fits the relativistically corrected plasma wave period $T_p = 2\pi/\omega_p$.

The X-ray spectrum obtained from the PIC simulation (Fig. 2) is represented as a function of the observation angle, for the optimal plasma density ($n_e = 1 \times 10^{19}$ cm^{-3}), and for a laser propagation distance of 3 mm. It gives the number of X-ray photons emitted within 0.1% of the energy bandwidth per solid angle $2\pi \sin\theta \mathrm{d}\theta$. The energy and the angle θ axes are logarithmically scaled. In this parameter regime, the expected spectrum is a continuum that extends from eV to a few tens of keV, with a maximum of the X-ray emission

located in the energy range of 1 keV, and the divergence of the X-ray beam is about 50 mrad ($\theta = K/\gamma$) full width at half maximum (FWHM).

The average number of photons with mean energy ω_c emitted by one electron is given by [15], $N_\times = 5.6 \times 10^{-3} N_0 K$, where N_0 is the number of betatron oscillations undergone by the electron. For $\gamma = 60$, $n_e = 1 \times 10^{19}$ cm^{-3}, and an amplitude of oscillation $r_0 = 5$ μm (obtained from PIC simulation), an X-ray beam providing 8×10^{-2} photons/electron/betatron oscillation centered at an energy around 1 keV within a full divergence of 300 mrad could be produced. For properly chosen parameters, it is therefore expected to generate an intense beam of keV radiation during the relativistic laser–plasma interaction.

2.2 Experiments

Betatron X-ray emission was observed for the first time at the Laboratoire d'Optique Applique (LOA) using a titanium-doped sapphire (Ti:sapphire) laser operating at 10 Hz with a wavelength 0–820 nm in chirped-pulse amplification mode [21]. The laser delivered energies up to 1 J on target in 30 fs, with a linear horizontal polarization. The laser beam was focused at laser intensities on the order of 3×10^{18} W/cm^2, for which the corresponding normalized vector potential a_0 is 1.2. The X-ray radiation produced in the plasma was measured using a cooled X-ray CCD camera placed directly on the laser axis without any focusing X-ray optic as shown in Fig. 3. For all the measurement, a 25 μm

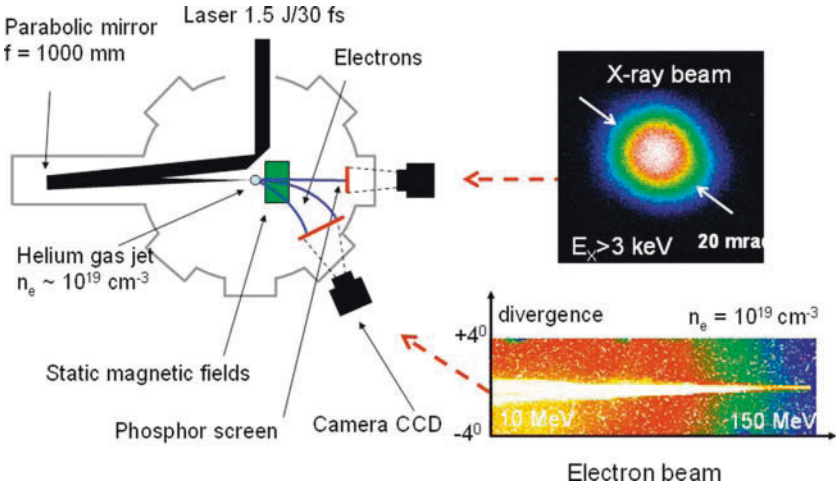

Fig. 3 Experimental setup used for the betatron experiment. Permanent magnets are used simultaneously to deviate off-axis the accelerated electron beam to keep the X-ray detection unperturbed and to provide the spectral distribution in the electron bunch. The figure also shows the CCD picture of the X-ray beam and of the electron spectrum for an electronic density of the gas jet of 10^{19}cm^{-3}

beryllium filter is kept in front of the CCD camera to block any radiation below 0.8 keV. Permanent magnets (1 T along 10 cm) are inserted between the plasma and the X-ray CCD to deviate off-axis the accelerated charged particles. Even if the most energetic electrons are still recorded onto the detector, they are significantly out of the X-ray axis. The spectrum of the radiation was estimated by using an additional set of filters.

As can be seen in Fig. 3, a beam of keV X-ray radiation was observed. The radiation is intense, broadband in the keV spectral range, and confined in the forward direction within a 20 mrad cone (FWHM) for the best shot (Fig. 3). The properties of this X-ray beam are in a good agreement with the synchrotron radiation emitted by the trapped electrons undergoing betatron oscillations in an ion channel as it is described by the numerical simulations (see previous section). The spectral distribution of the radiation was measured from 1 to 10 keV by placing a set of Be, Al, Sn, and Nb filters in front of the detector. The spectral resolution was limited by the bandwidths of the filters. The spectrum decreases exponentially from 1 to 10 keV. The total number of photons (integrated over the bandwidths of the filters and over the divergence of the X-ray beam) is found to be more than 10^8 photons (per shot/solid angle at 0.1% BW).

The most important feature of the observed X-ray emission is its collimation in a low-divergence beam centered onto the laser axis. It strongly depends on the electron density and goes from 20 to 50 mrad (FWHM) as n_e is increased from $n_e = 8 \times 10^{18}$ to $1.1 \times 10^{19}\text{cm}^{-3}$. At larger densities, the X-ray beam divergence is further increased. This feature can be correlated to the K parameter which increases as n_e is increased. It is also strongly linked to the divergence of the electron beam for which similar dependencies are observed. The X-ray beam divergence, averaged over more than ten shots, is found to be 50 ± 20 mrad at FWHM.

Another unique feature of this X-ray beam is its intensity as a function of the electron density of the plasma. It is found to be sharply peaked at $n_e = 1.1 \times 10^{19}$ cm^{-3} as shown in Fig. 4. Below this critical density, the X-ray signal rapidly vanishes mainly because the number of trapped electrons is too low. This is confirmed in the experiment for which no electrons were detected by the spectrometer. At larger densities, the X-ray signal drops down and a plateau is reached. For these experimental conditions, the resulting amplitude of the plasma wave becomes too weak. The pulse must first be modulated and additional laser energy would be needed. As a result, the temperature of the electron beam decreases and its divergence increases.

2.3 Comparison with Other Ultrafast X-Ray Sources

Very large-scale instruments are under consideration in the accelerator community to provide femtosecond X-ray beams. The great potential of ultrafast

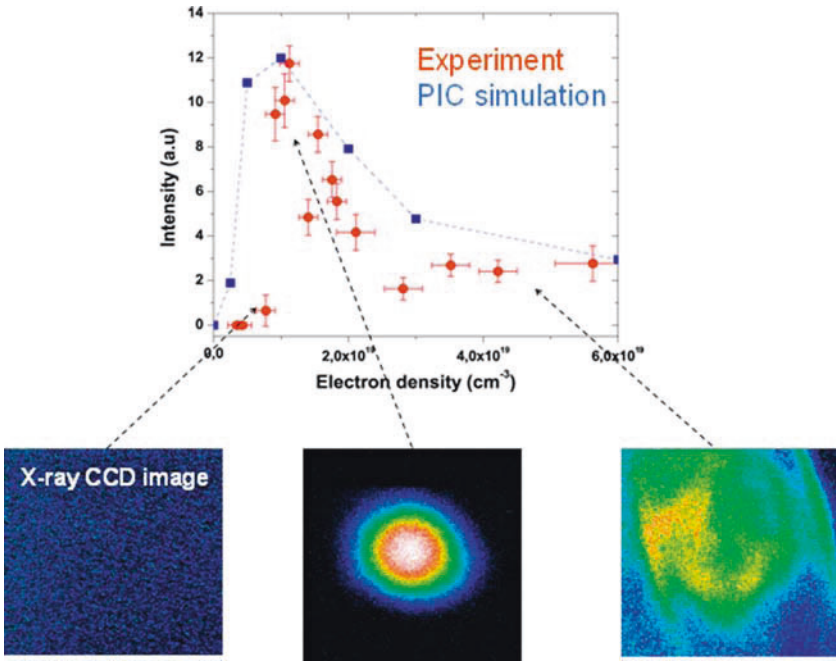

Fig. 4 Betatron X-ray intensity and spatial distribution in the beam as a function of the electronic density of the gas jet. X-ray beam generation is strongly dependent on the electronic density of the plasma. The PIC simulations are represented by the dot–dashed line

X-ray techniques is one of the major arguments to build energy recovery LINAC (ERL, linear accelerator) and free electron lasers (FEL) using the SASE (self-amplified spontaneous emission) scheme. They are based on the production of ultrafast and highly energetic electron beams (few 10 GeVs range). These projects (LCLS at Stanford-USA, TESLA at DESY-Germany) plan to produce femtosecond X-rays in the few 10 keV spectral range with very high brightness. First experiments are presently performed at Stanford (SPPS) with the use of the large-scale LINAC to test the production of ultrafast synchrotron radiation with electron beams compressed in time. This installation will run for a short period of time (2004 - 2006).

In order to overcome the current limitations of the third generation of synchrotrons (few 10 ps X-ray bursts), new experimental techniques aiming to cut a slice of subpicosecond X-rays from a single, several tens of picoseconds synchrotron X-ray pulse recently appeared. In a method developed at the ALS (Berkeley, USA), where the X-ray pulse duration is 30 ps, slicing of a few hundred femtosecond electron bunch is realized within the long electron bunch using a laser.

Finally, smaller scale projects rely on the Compton diffusion of lasers on electron beams generated from moderate LINAC energies (few 10 MeVs) like at LLNL (Livermore, USA) and APS (Chicago, USA).

The following important remarks can be made about these projects: Despite their high flux, X-ray FEL and ERL facilities are not foreseen within the next few years (except at LCLS). Beam time will be in addition very limited. Intermediate (and alternative) solutions should be investigated and explored considering the long-term duration of these projects. LINAC-based facilities (FEL, ERL, SPPS, LLNL, and APS) do not have intrinsic synchronization with the laser used to trigger a reaction in the femtosecond timescale. However, post-synchronization techniques are under investigation (in the frame of the SPPS project) to reach the required time resolution. Slicing projects provide X-ray flux limited to the current charge contained by the electron bunch already setup in the third-generation synchrotron. As a consequence, X-ray flux cannot be scaled up. This technique will benefit from the high-repetition-rate laser systems to increase their average brightness.

Figs. 4 and 5 show the X-ray flux and average brightness of the existing or scheduled femtosecond X-ray sources. The brightness of the betatron X-ray radiation can be estimated from the pulse duration and the size of the X-ray source (20 μm × 20 μm from knife-edge X-ray imaging). The temporal pulse width is fully determined by the temporal profile of the electron bunch, which is close to that of the laser (30 fs). This must nevertheless be proved experimentally. The average brightness is 5×10^6 ph/s/mm^{-2}/$mrad^{-2}$/0.1%BW and the peak spectral brightness is 2×10^{22} ph/s/mm^{-2}/mrad^{-2}/0.1%BW.

As it can be seen in Figs. 4 and 5, the very high collimation of the X-ray beams of such instruments (μrad) leads to a significantly larger brightness. They take advantage of the very high electron energies (10 GeV range) available from these accelerators. This will not be the case for the laser-based X-ray beam (betatron) as electron energies accelerated from plasmas are expected to approach the GeV range within the next 2 years. The SPPS facility using the large LINAC of LCLS is under operation with the possibility to produce few 100 fs X-ray radiation, and make experiments at this time scale if the post-synchronization techniques are successful. It is however interesting to mention that the betatron X-ray flux is approaching what can be produced by SPPS despite its significantly smaller scale environment. SPPS is planned to run up to 2006.

It can be seen from Fig. 5 that the first results on the betatron source have already led to X-ray fluxes exceeding what is provided by the Compton technique or by wigglers and undulator insertion devices using the slicing approach. The betatron X-ray properties expected using a 250 TW laser system is also quoted in the figures (dashed line). The spectral range is significantly shifted to hard X-ray energies, with an increase of the X-ray flux and average brightness of one order of magnitude for the softener energies (Fig. 6).

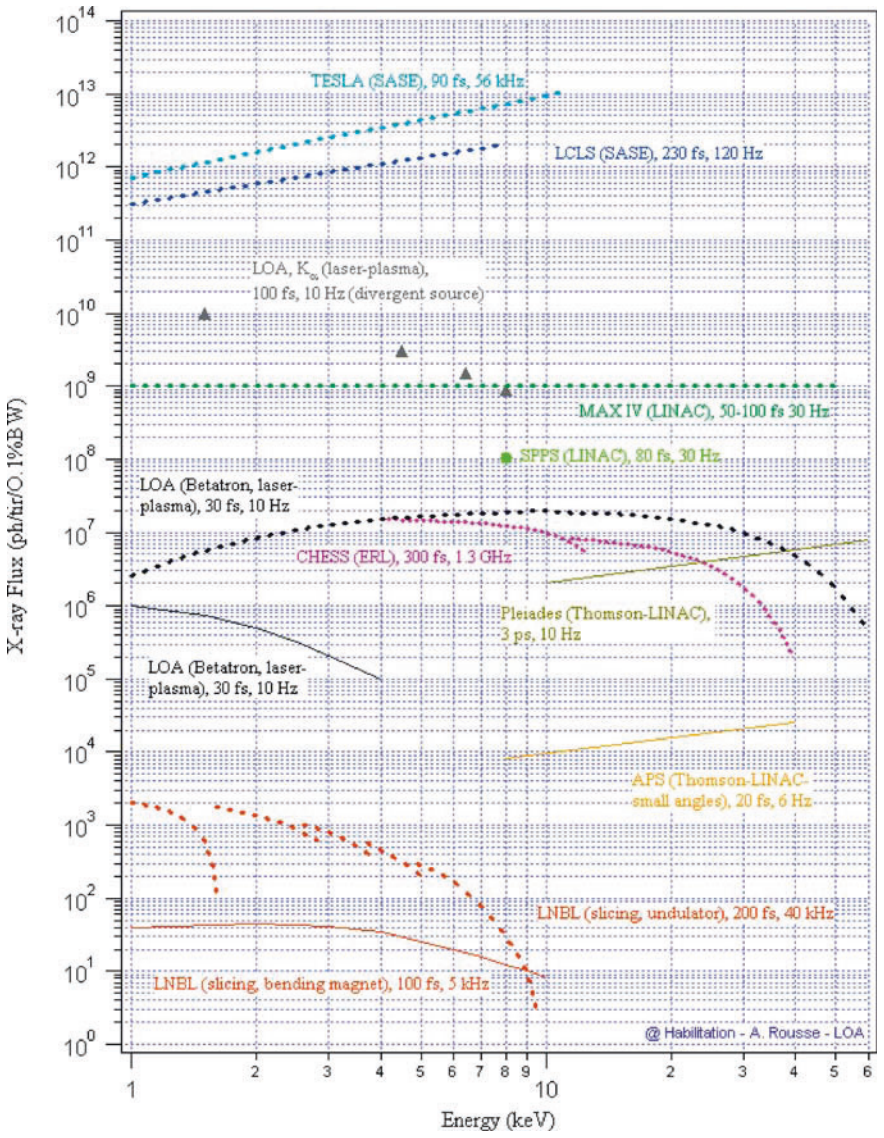

Fig. 5 Comparison of our "PIXEL" projet with the existing and foreseen facilities of ultrafast X-rays: X-ray flux. The *dotted curves* correspond to sources that do not exist. The pulse duration as well as the repetition rate are quoted for each facility. The betatron X-ray properties expected using a 250 TW laser system is represented in *dashed* and *black line*. K_α: laser–plasma source (in operation) LOA (Palaiseau, France); TESLA: Free Electron Laser project (expected in 2015) DESY (Hambourg, Allemagne); LCLS: Free Electron Laser project (2010) SLAC (Stanford, USA); CHESS: Energy Recovery LINAC (not planned) Cornell (USA); SPPS: Ultrafast LINAC with undulator (operate from 2004 to 2006) SLAC (Stanford, USA); Slicing: Slicing of electron beams in third-generation synchrotron (2005) LBNL (Berkeley, USA); Pleiades (LLNL, USA); and APS (Chicago, USA): Compton scattering of a laser onto a LINAC (in operation at LLNL: 3 ps time scale)

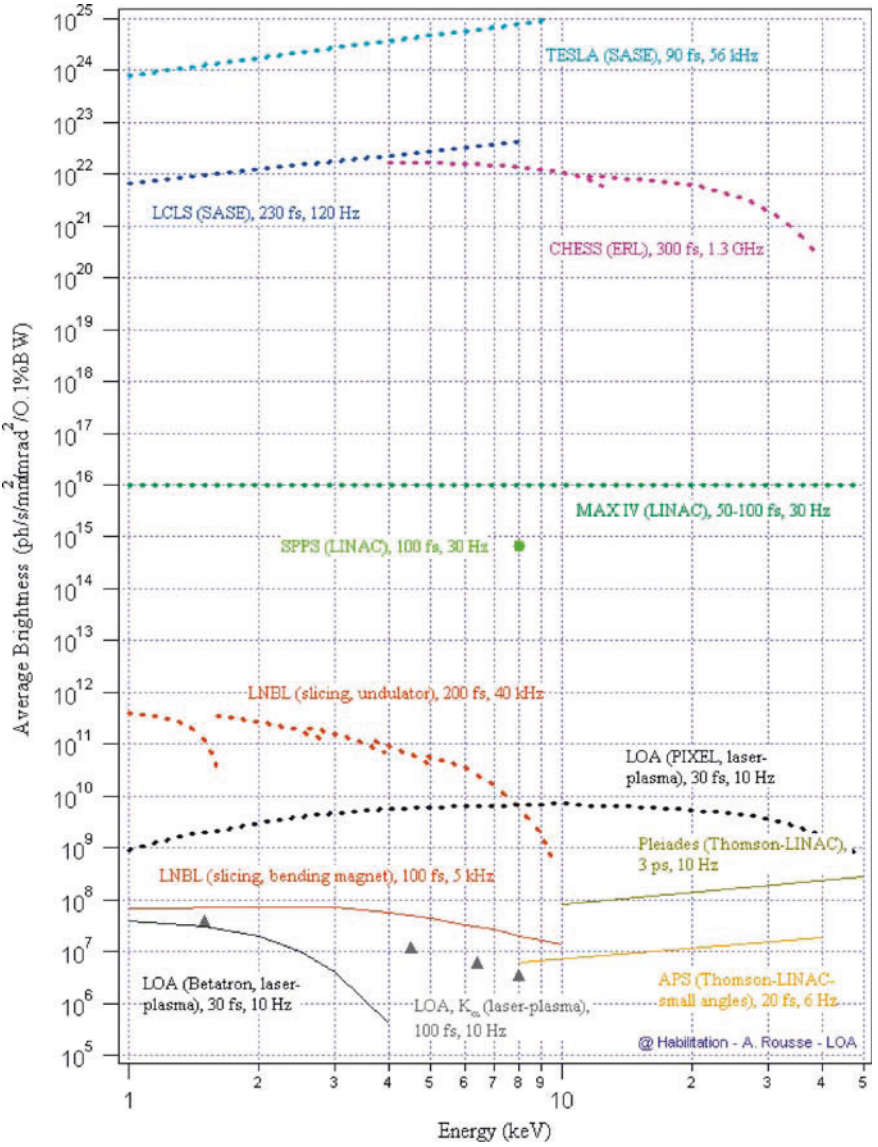

Fig. 6 Comparison of PIXEL with the existing and foreseen facilities of ultrafast: Average brightness

3 Conclusion

X-ray beams can now be produced from laser–plasma interaction using femtosecond and intense laser systems. An increase of the γ factor (1 GeV energies are expected with the present laser systems under construction) of the electron

would result in a significant increase of the X-ray flux, energy, and a further more collimated X-ray beam (below 1 mrad). This opens a new road toward compact and potentially cheap – compared to large scale instruments – femtosecond X-ray tools for the characterization of transient structures in ultrafast X-ray science [22, 23, 24, 25, 26, 27, 28, 29, 30, 31]. It will also have the potential for powerful diagnostics not previously available in plasma physics. For example, it will allow to probe extreme states of matter, with the final goal of addressing astrophysical as well as inertial fusion research issues. Time-resolved absorption spectroscopy and Thomson scattering of high-density plasmas require penetrating radiation like X-rays together with an ultrafast time resolution in order to reveal the properties of the warm, dense, or high-energy matter produced in a laser–plasma experiment. Time-dependent measurements of plasma temperature and density will provide a precious contribution to the understanding of the degeneracy, coupling as well as long- and short-range interactions between charged particles within the plasma.

References

1. http://www-ssrl.slac.stanford.edu/lcls/
2. http://tesla.desy.de/new_pages/TDR_CD/PartV/fel.html
3. Th. Brabec and F. Krausz, Rev. Mod. Phys.: **72**, 545 (2000)
4. A. Tarasevitch et al., Phys. Rev. A: **62**, 023816 (2000)
5. H. Daido, Rep. Prog. Phys.: **65**, 1513 (2002)
6. A. Rousse et al., Phys. Rev. E: **50**, 2200 (1994)
7. K. T a Phuoc et al., Phys. Plasmas: **12**, 023101 (2005)
8. Ch. Bressler et al., Chem. Rev.: **104**, 1781 (2004)
9. A. Rousse et al., Rev. Mod. Phys.: **73**, 17 (2001)
10. Ch. Bressler et al., Chem. Rev.: **104**, 1781 (2004)
11. E. Esarey, et al., IEEE Trans. Plasma. Phys.: **24**, 252 (1996)
12. D. Umstadter, J. Phys. D: **36**, R151 (2003)
13. V. Malka et al., Science: **298**, 1596 (2002).
14. A. Pukhov and J. Meyer ter Vehn, Appl. Phys.: B **74**, 355 (2002)
15. I. Kostyukov, A. Pukhov, and S. Kiselev, Phys. Plasma.: **10**, 4818 (2003).
16. E. Esarey et al., Phys. Rev. E **65**, 056505 (2002)
17. D. H.Whittum, Phys. Fluids B **4**, 730 (1992)
18. S. Wang et al., Phys. Rev. Lett. **88**, 135004-1 (2002)
19. C. Joshi et al., Phys. Plasmas **9**, 1845 (2002)
20. D. Jackson, Classical Electrodynamics (Wiley, New York, 1975)
21. C. Rischel et al., Nature: **390**, 490 (1997)
22. C. Siders et al., Science: **286**, 1340 (1999)
23. Ch. Rose-Petruck et al., Nature: **398**, 310 (1999)
24. A. Rousse et al., Nature: **410**, 65 (2001)
25. K. Sokolowski-Tinten et al., Phys. Rev. Lett.: **87**, 225701 (2001)
26. A. Cavalleri, et al., Phys. Rev. Lett.: **87**, 237401 (2001)
27. Th. Feurer et al., Phys. Rev. E: **65**, 016412 (2002)
28. K. Sokolowski-Tinten et al., Nature: **422**, 287 (2003)
29. A. Lindenberg et al., Science: **308**, 392 (2005)
30. A. Plech et al, Phys.Rev.Lett.: **92**, 125505 (2004)
31. S. A. Rice, Nature: **429**, 255 (2004)

Atomic Multi-photon Interaction with Intense Short-Wavelength Fields

F.H.M. Faisal

1 Introduction

Recent developments in generating intense laser radiation in the laboratory, at wavelengths shorter than the optical, have opened up the possibility of investigating the nature of non-linear laser–atom interaction at hitherto inaccessible intense-field domains (VUV, XUV, X-ray, and possibly beyond). A whole gamut of processes such as multi-photon inner-shell ionization, formation of hollow atom or ions, high-frequency high harmonic generation, multi-photon single-, double-, and multiple ionization, Compton-harmonics generation, coherent radiative electron scattering, population inversion for X-ray amplification, ultra-short pulse generation, stimulated- and inverse-bremsstrahlung, relativistic spin dynamics, laser nuclear reaction, to name only a few, might be possible to investigate in the laboratory in not too distant future. Currently the subject is both experimentally and theoretically at its beginning. Here we briefly introduce and discuss a number of approximate and exact methods that are deemed to be useful for theoretical investigations of intense-field atomic processes at short wavelengths.

2 Parameters Characterizing Intense-Field Dynamics

Intense-field processes are characterized by several dimensionless parameters which help to distinguish different regimes of the dynamics. A critical value of unity of these parameters formally separates two qualitatively distinct neighboring domains. The best known among them are the so-called (a) Keldysh parameter $\gamma = \sqrt{\frac{I_p}{2U_p}} : \gamma \gg 1$, perturbative 'multi-photon' domain and $\gamma \ll 1$ $< n_0\,\gamma$ (n_0 is the minimum photon number for ionization) – for non-perturbative

F.H.M. Faisal
Fakultät für Physik, Universität Bielefeld, D-33615 Bielefeld, Germany
e-mail: ffaisal@physik.uni-bielefeld.de

T. Brabec (ed.), *Strong Field Laser Physics*,
DOI: 10.1007/978-0-387-34755-4_17,

Table 1 Critical intensities in atomic units (1 a.u.= 3×10^{16} W/cm^2), as well as U_p, at selected wavelengths, for the characteristic value of unity of the intense-field parameters, γ, b, and q; the numbers in square brackets refer to exponents

	$\gamma = 1$	$b = 1$	$q = 1$
λ (nm)	1000	1000	1000
I (au)	4.396 [−3]	2.332 [−3]	8.251 [1]
U_p (au)	2.5 [−1]	1.326 [−1]	4.692 [3]
λ (nm)	100	100	100
I (au)	4.396 [−1]	2.332 [0]	8.251 [3]
U_p (au)	2.5 [−1]	1.326 [0]	4.692 [3]
λ (nm)	10	10	10
I (au)	4.396 [1]	2.332 [3]	8.251 [5]
U_p (au)	2.5 [−1]	1.326 [1]	4.692 [3]
λ (nm)	1	1	1
I (au)	4.396 [3]	2.332 [6]	8.251 [7]
U_p(au)	2.5 [−1]	1.326 [2]	4.692 [3]
λ (nm)	0.1	0.1	0.1
I (au)	4.396 [5]	2.332 [9]	8.251 [9]
U_p(au)	2.5 [−1]	1.326 [3]	4.692 [3]

'tunneling' domain, (b) ATI parameter $b = U_p/2\hbar\omega : b > 1$, appearance of above-threshold ionization (ATI) peaks and $b \ll 1$, absence of ATI peaks, and (c) relativistic parameter: $q = eA_0/mc^2 = \varkappa\alpha_0 = \sqrt{(4U_p)/(mc^2)}$, where $\varkappa = \omega/c : q \geq 1$, strongly relativistic domain and $q \ll 1$, non-relativistic domain. In Table 1 we show the critical intensities and the ponderomotive energies at which these parameters take the characteristic value of 1, in different wavelength regimes.

At moderate to low intensities, in the VUV region (say, from 200 to 80 nm) and in the XUV and X-ray regions (say, down to 5 nm, and much shorter wavelengths), one is largely in the perturbative domain. So the lowest (non-vanishing) order perturbation theory (or LOPT) which has been very useful in the early days of multi-photon physics with infrared and optical lasers becomes again useful for the shorter wavelengths. However, at short wavelengths it might be necessary to go beyond the well-known dipole approximation and incorporate systematically possible effects of retardation (or multi-polar effects). For very high intensities, this situation changes again significantly where the relativistic effects, either for the inner-shells of heavier atoms (ions) or for high velocity of the ionized electrons, as well as coupling to the spin degrees of freedom would be necessary to account for. With these possibilities in view, below we briefly discuss a number of approximate and exact theoretical methods for investigating intense-field processes both at moderate and very high intensities. Unless otherwise indicated explicitly, Hartree atomic units [a.u.: $e = \hbar = m_e = 1, c = \alpha^{-1} = 137.036$, $a_b = 1$ (Bohr radius)] are implied in the sequel.

3 Lowest (Non-vanishing) Order Perturbation Theory: LOPT

In the perturbative domain the most useful method for the analysis of multi-photon processes has been the lowest non-vanishing order perturbation theory or LOPT (e.g., [1]).

Typically, an intense laser field is idealized by a sinusoidal vector potential of the form

$$\boldsymbol{A}(\boldsymbol{x}, t) = A_0 \cos(\omega t - \boldsymbol{\varkappa} \cdot \boldsymbol{x}) \tag{1}$$

where is the unit polarization vector, $\boldsymbol{\varkappa}$ is the photon wave vector, $x = \omega/c$ is the wave number, ω is the circular frequency, and $A_0 = c\mathcal{E}_0/\omega$, where $\mathcal{E}_0$ is the maximum electric-field amplitude.

The Schrödinger equation of the system is

$$i\frac{\partial}{\partial t}\Psi(\boldsymbol{x}, t) = \left[\frac{1}{2}\left(\hat{\boldsymbol{p}} - \frac{1}{c}\boldsymbol{A}(\boldsymbol{x}, t)\right)^2 + V\right]\Psi(\boldsymbol{x}, t) \tag{2}$$

where $H_\mathrm{a} = \hat{\boldsymbol{p}}^2/2 + V$ stands for the unperturbed atomic Hamiltonian. Note that, although we have written this equation for a single-electron atom (ion), it has a much greater usefulness if it is formulated as the active part of a many-electron system (the 'single active electron' or SAE approximation) with an effective potential V. The perturbed Hamiltonian contains, besides H_a and a ponderomotive shift term equal to $U_\mathrm{p} = I/4\omega^2$, the first-order perturbation

$$V^{(\pm 1)} = -\frac{\boldsymbol{A}_0 \cdot \hat{\boldsymbol{p}}}{2c}\mathrm{e}^{\pm \mathrm{i}(\omega t - \boldsymbol{\varkappa}\cdot\boldsymbol{x})} \tag{3}$$

and the second-order perturbation

$$V^{(\pm 2)} = \frac{U_\mathrm{p}}{2}\mathrm{e}^{\pm 2\mathrm{i}(\omega t - \boldsymbol{\varkappa}\cdot\boldsymbol{x})} \tag{4}$$

where the $(\pm)$ corresponds to absorption and emission.

According to LOPT, the amplitude for an n-photon transition (due to these perturbations) from an initial (bound) state, $|i\rangle$, to a final (continuum) state $|f\rangle$ can it always be brought to the form

$$A_\mathrm{ion}(\infty) = -2\pi\mathrm{i}\sum_n \delta(E_f + I_\mathrm{p} - n\omega)T^{(n)} \tag{5}$$

where

$$T^{(n)} = \langle f|V_n G_0(E_{n-1})V_{n-1}\cdots G_0(E_2)V_2 G_0(E_1)V_1|i\rangle \tag{6}$$

The corresponding probability of the transition per unit time, i.e., the *rate* is then obtained by (modulo-) squaring the amplitude and dividing by the (usually large) interaction time ($t \gg 2\pi/\omega$),

$$\frac{\mathrm{d}W^{(n)}}{\mathrm{d}\Omega} = 2\pi|T^{(n)}|^2\rho(E_f) \tag{7}$$

where we have used a convenient representation (p. 48 [1]) of the square of the delta function

$$\delta^2(\omega) = \lim_{t\to\infty}\frac{t}{2\pi}\delta(\omega) \tag{8}$$

and integrated over the number of final continuum states using

$$\mathrm{d}\boldsymbol{k}_f = \rho(E_f)\mathrm{d}E_f\,\mathrm{d}\Omega$$

with $\rho(E_f) = k_f/(2\pi)^3$, the density of final states per unit energy per unit volume. The specific transition matrix for a given order photon absorption or emission process, $T^{(\pm n)}$, can be written down most conveniently applying the diagrammatic technique which is described in detail elsewhere (chap. 2 [1]). In the short-wavelength case one may not be able to adopt the dipole approximation:

$$e^{\pm\mathrm{i}\boldsymbol{\varkappa}\cdot\boldsymbol{r}} \approx 1 + o(\varkappa a_b) \quad (\varkappa a_b \ll 1, \text{ dipole or no-retardation approximation}) \tag{9}$$

The usual approach is to handle the retardation effect by an infinite 'multipolar' expansion of the photon plane-waves,

$$e^{\pm\mathrm{i}\boldsymbol{\varkappa}\cdot\boldsymbol{x}} = 4\pi\sum_{l,m}(\pm\mathrm{i})^l j_l(\varkappa r)\,Y_{lm}(\hat{r})\,Y^*_{lm}(\hat{\varkappa}) \tag{10}$$

where $r = |\boldsymbol{x}|, \hat{\varkappa}$, and $\hat{\boldsymbol{r}}$ are unit vectors. Since $j_l(\varkappa r) \approx (\varkappa r)^l$, for $\varkappa r \ll 1$, this expansion is expected to converge rapidly for VUV and XUV radiations but would be slow to converge at hard X-ray and shorter wavelengths.

The general problem of LOPT is the evaluation of the compound matrix elements of the form Eq. (6), where the interaction Hamiltonians V_n (and the propagation energies E_n) can be different but each V_n is restricted to only one of the two types given in Eqs. (3) and (4) above. The Green's functions $G_0(E)$ that appear in the compound matrix elements, Eq. (6), can be expressed formally explicitly in terms of the eigenfunctions and the eigenvalues of the unperturbed atomic Hamiltonian , $H_\mathrm{a}|j\rangle = \epsilon_j|j\rangle$, as

$$G_0(E_n) = \frac{1}{(\epsilon_i + n\omega - H_\mathrm{a})} = \sum_j \int \frac{|j\rangle\langle j|}{E_n - \epsilon_j}$$

with $E_n = \epsilon_i + n\omega$, which contains an integration over the continuum states of the atom; the latter is rather awkward to perform explicitly (nevertheless cf. [2]). Therefore, it is useful whenever possible (for example, for H-like atoms [3,4,1]) to adopt a completely discrete representation using the so-called 'sturmian' radial basis states (and the spherical harmonics, for the angle variables) to represent the Green's function exactly.

4 A Finite-Sum Approximation to Green's Function of Complex Atoms

In general, however, the complete set of eigenfunctions and eigenvalues of a two-or many-electron atom is hardly, if at all, available. It is therefore desirable to have a relatively simple method of estimating the n-photon transition matrix elements. One such method is the so-called finite-sum approximation method which can be shown to give the following approximate expression (p. 86 [1]) for any atomic Green's function, if only a finite number of the eigenfunctions and eigenvalues of the system are known:

$$G_0(E_n) \approx G_p(E_n) + (1 - P)/(E_n - \epsilon^0) \tag{11}$$

where

$$G_p(E_n) = \sum_{j=1,p} \frac{|j\rangle\langle j|}{E_n - \epsilon_j} \tag{12}$$

and $P = \sum_{j=1,p} |j\rangle\langle j|$ is the projection operator for the p discrete states of the target system and ϵ^0 is an average energy parameter of the order of the ionization threshold. One can vary p and estimate the second term in Eq. (11) to test if it becomes small enough compared to the first; in that event Eq. (11) provides a useful approximation which can be employed to estimate the compound matrix elements, Eq. (6), by inserting it in as many places, with the given value of the propagation energy E_n, as necessary. For example, a recent application of the above approximation to the problem of sequential and direct mechanisms of two-photon double ionization of He at VUV/XUV wavelengths at perturbative intensities has shown [5] that the total two-photon double ionization yield (e.g., at $\omega = 2.05$ a.u. and $I = 10^{11}$ W/cm^2) is dominated by the sequential contribution, by a factor of about 300, over that of the 'direct' or non-sequential contribution. Dominance of the sequential process for the double ionization of He can occur already at $\lambda = 248$ nm [6,7,8]. This is in contrast to the well-known dominance of the non-sequential process for double ionization of He atom for intense near-infrared wavelengths (e.g., [9,7,8]).

Unlike in the perturbative regime, theoretical investigation of atomic processes at high intensities is much more demanding. Therefore, at

non-perturbative intensities in the VUV and low XUV domain, where the retardation effect might still be neglected, it is useful to have relatively simple approximate expressions for estimating the ionization rates and their dependence on the field parameters.

5 Coulomb–Volkov Wavefunctions

The long-range Coulomb potential in the presence of an intense field has a significant influence on the final state of the ionization processes. At present no exact solution of the Coulomb–Volkov Schrödinger equation (comparable to the exact plane-wave Volkov solution without the Coulomb potential) is known. We therefore discuss a number of approximate solutions of the Coulomb–Volkov problem, in the asymptotic, adiabatic, and semiclassical approximations. The results are given explicitly in the length gauge; the corresponding expressions in the velocity gauge are obtained simply by multiplying the respective length gauge expressions given below by the 'gauge' factor, $e^{-i(\frac{1}{c}\boldsymbol{A}(t)\cdot\boldsymbol{r})}$. These wavefunctions are applicable not only for long-wavelength fields but also for shorter wavelengths (e.g., from free-electron lasers) for example for inner-shell processes in atoms and molecules and their ions.

5.1 An Asymptotic Coulomb–Volkov Wavefunction

The Coulomb–Volkov Schrödinger equation in a dipole laser field is given by

$$i\frac{\partial}{\partial t}\Phi_{\boldsymbol{p}}(\boldsymbol{r},t)=\left[\frac{\hat{\boldsymbol{p}}^2}{2}-\frac{Z}{r}+\boldsymbol{F}(t)\cdot\boldsymbol{r}\right]\Phi_{\boldsymbol{p}}(\boldsymbol{r},t) \tag{13}$$

where $\hat{\boldsymbol{p}}$ is the momentum operator. We have assumed a general elliptically polarized vector potential

$$\boldsymbol{A}(t)=A_0\left({}_1\cos\frac{\xi}{2}\sin\omega t-{}_2\sin\frac{\xi}{2}\cos\omega t\right) \tag{14}$$

so that the corresponding electric field is given by

$$\boldsymbol{F}(t)=-\frac{1}{c}\dot{\boldsymbol{A}} \tag{15}$$

The ellipticity ξ varies between $[0,\pm\pi/2]$; $\xi=0$ stands for the linear polarization (i.e., $\boldsymbol{A}(t)={}_1A_0\sin\omega t$ and $\boldsymbol{F}(t)=-F_1\cos\omega t, F\equiv\frac{A_0\omega}{c}$); $\xi=\pm\pi/2$, for the left $(+)$ or the right $(-)$ circular polarization.

To include the Coulomb effect in the presence of the laser field, we intend to solve Eq. (13) to order $o(\frac{1}{r^2})$. Let the solution be of the form

$$\Phi_{\boldsymbol{p}}(\boldsymbol{r}, t) = \mathrm{e}^{-\frac{\mathrm{i}}{2}\int^{t} p_{t'}^2 \mathrm{d}t'} \mathrm{e}^{\mathrm{i}\boldsymbol{p}_t \cdot \boldsymbol{r}} \psi(\boldsymbol{r}, t) \tag{16}$$

where $\boldsymbol{p}_t \equiv \boldsymbol{p}(t) = \boldsymbol{p} + \frac{1}{c}\boldsymbol{A}(t)$ (for convenience of writing we shall interchangeably use the notation $\boldsymbol{p}_t$ or $\boldsymbol{p}(t)$, in this section). The function $\psi(\boldsymbol{r}, t)$ is to be determined. Substitution of Eq. (16) in Eq. (13) yields

$$\mathrm{i}\frac{\partial}{\partial t}\psi(\boldsymbol{r}, t) = \left(-\mathrm{i}\boldsymbol{p}_t \cdot \frac{\partial}{\partial r} - \frac{Z}{r} - \frac{1}{2}\frac{\partial^2 \psi(\boldsymbol{r}, t)}{\partial^2 \boldsymbol{r}} / \psi(\boldsymbol{r}, t)\right)\psi(\boldsymbol{r}, t) \tag{17}$$

We neglect the ratio of the second derivative of $\psi(\boldsymbol{r}, t)$ to itself in Eq. (17) (for slowly varying functions and/or order $0(\frac{1}{r^2})$) to obtain a first-order partial differential equation for determining the function $\psi(\boldsymbol{r}, t)$,

$$\mathrm{i}\frac{\partial}{\partial t}\psi(\boldsymbol{r}, t) = \left(-\mathrm{i}\boldsymbol{p}_t \cdot \frac{\partial}{\partial \boldsymbol{r}} - \frac{Z}{r}\right)\psi(\boldsymbol{r}, t) \tag{18}$$

Next, we introduce the coordinate transformations

$$\boldsymbol{r}' = \boldsymbol{r} - \int^{t} \boldsymbol{p}_\tau \mathrm{d}\tau \tag{19}$$

$$t' = t \tag{20}$$

which gives

$$\frac{\partial}{\partial t} + \boldsymbol{p}_t \cdot \frac{\partial}{\partial \boldsymbol{r}} = \frac{\partial}{\partial t'} \tag{21}$$

and simplifies Eq. (18) to

$$\mathrm{i}\frac{\partial}{\partial t'}\psi(\boldsymbol{r}', t') = -\frac{Z}{\left|\boldsymbol{r}' + \int^{t'} \boldsymbol{p}_\tau \mathrm{d}\tau\right|}\psi(\boldsymbol{r}', t') \tag{22}$$

This is readily integrated and the result, expressed in the original variables $(\boldsymbol{r}, t)$, is

$$\psi(\boldsymbol{r}, t) = exp\left(\mathrm{i}\int^{t} \mathrm{d}t' \frac{Z}{\left|\boldsymbol{r} + \int_{t}^{t'} \boldsymbol{p}_\tau \mathrm{d}\tau\right|}\right) \tag{23}$$

Combining Eqs. (16) and (23) we get

$$\Phi_p(\boldsymbol{r},t) = exp\left(-\mathrm{i}\int^t \mathrm{d}t'\left(\frac{p_{t'}^2}{2} - \frac{Z}{\left|\boldsymbol{r} + \int_t^{t'} \boldsymbol{p}_\tau \mathrm{d}\tau\right|}\right)\right)\mathrm{e}^{\mathrm{i}\boldsymbol{p}_t\cdot\boldsymbol{r}} \tag{24}$$

Thus we have arrived at an explicit asymptotic solution of the Coulomb–Volkov Schrödinger equation (13) in terms of a phase integral, which could be used fruitfully, e.g., in numerical works. However, it may not be the most convenient approximation to apply in analytical works. We therefore discuss a number of additional approximate Coulomb–Volkov solutions which can be used more simply.

Perhaps the simplest analytic approximation is obtained in the limit $p_B r >> 1 \hat{\boldsymbol{r}} \parallel \hat{\boldsymbol{p}}$, which we may write as

$$\Phi_{\boldsymbol{p}}^{(-)}(\boldsymbol{r},t) = \mathrm{e}^{-\frac{\mathrm{i}}{2}\int^t p_u^2 \mathrm{d}u}\mathrm{e}^{\mathrm{i}\boldsymbol{p}_t\cdot\boldsymbol{r}+\mathrm{i}\frac{Z}{p_t}\ln(2p_t r)} \tag{25}$$

The accuracy of this rudimentary Coulomb–Volkov wavefunction may be estimated by direct substitution into Eq. (13) and comparison of the rest terms in the Hamiltonian with the initial total energy E_B. It is found to account for the Coulomb interaction asymptotically $\mathrm{o}(1/r^2), \hat{\boldsymbol{r}}\|\hat{\boldsymbol{p}}$, if $F/F_B \ll 1$, $\omega/E_B \ll 1$, and $1 \ll p_B r \leq p_B r_0$, where r_0 is of the order of the outer turning point of the classically forbidden region. In the adiabatic condition this is the most important interaction region where the *combined* effect of the Coulomb potential and the laser field dominates.

5.2 An Adiabatic Coulomb–Volkov Wavefunction

In view of the importance of the adiabatic domain in the intense-field laser atom interaction processes we consider now a more elaborate adiabatic wavefunction which we write as

$$\begin{aligned}\Phi_{\boldsymbol{p}}^{(-)}(\boldsymbol{r},t) = {} & \mathrm{e}^{-\frac{\mathrm{i}}{2}\int^t p_{t'}^2 \mathrm{d}t'}\mathrm{e}^{-\mathrm{i}\eta_t \ln(p_t r_0(t)+\boldsymbol{p}_t\cdot\boldsymbol{r}_0(t))} \\ & \times \mathrm{e}^{\frac{\pi}{2}\eta_t}\Gamma(1+\mathrm{i}\eta_t)\psi_{\boldsymbol{p}_t}^{(-)}(\boldsymbol{r},t), \qquad \eta_t \equiv \frac{Z}{p_t}\end{aligned} \tag{26}$$

with,

$$\psi_{\boldsymbol{p}_t}^{(-)}(\boldsymbol{r}) = \mathrm{e}^{\mathrm{i}\boldsymbol{p}_t\cdot\boldsymbol{r}}F(-\mathrm{i}\eta_t, 1, -\mathrm{i}(p_t r + \boldsymbol{p}_t\cdot\boldsymbol{r})) \tag{27}$$

where $\boldsymbol{r}_0(t)$ is the asymptotic outer turning point in the direction of the motion, $\boldsymbol{r}_0(t) = \frac{\boldsymbol{p}_t E_B}{\boldsymbol{F}(t)\cdot\boldsymbol{p}_t}$. $F(a,c,z)$ is the well-known confluent hypergeometric (or the Kummer) function; the superscript $(-)$ stands for the 'in-going' solution, as

in the case of the unperturbed Coulomb continuum wavefunction [10]. For $1 \ll p_B r \leq p_B r_0(t)$ it simplifies to

$$\Phi_{\boldsymbol{p}}^{(-)}(\boldsymbol{r}, t) = \mathrm{e}^{-\frac{\mathrm{i}}{2}\int^t p_{t'}^2 \mathrm{d}t'} \mathrm{e}^{\mathrm{i}\boldsymbol{p}_t \cdot \boldsymbol{r}} \mathrm{e}^{\mathrm{i}\eta_t \{\ln(p_t r + \boldsymbol{p}_t \cdot \boldsymbol{r}) - \ln(p_t r_0(t) + \boldsymbol{p}_t \cdot \boldsymbol{r}_0(t))\}} \tag{28}$$

In the adiabatic case, the laser field alone dominates at the outer turning point $\boldsymbol{r} = \boldsymbol{r}_0(t)$ and beyond. Accordingly, the boundary condition is chosen to make the Coulomb phase in Eq. (28) to vanish at $\boldsymbol{r} = \boldsymbol{r}_0(t)$. To determine the accuracy of the adiabatic wavefunction, we may directly substitute Eq. (28) in Eq. (13) and note that the Coulomb potential $-Z/r$ is taken into account to $\mathrm{o}(\frac{1}{r^2})$ in all directions. The residual terms compared to the initial total energy E_B are of the order of $\mathrm{o}(\omega/E_B)$ and $\mathrm{o}(F/F_B)$ (in the classically forbidden region $1 < p_B r \leq p_B r_0$) and may be neglected for $\omega/E_B \ll 1$ and $F/F_B \ll 1$. This corresponds to the adiabatic regime of laser interaction below the saturation intensity for ionization. We may note here parenthetically that the adiabatic Coulomb–Volkov wavefunctions given above can be factorized into a time translational part, $\mathrm{e}^{-\mathrm{i}(p^2/2 + U_\mathrm{p})t}$, and a fully periodic part with a period $2\pi/\omega$, which is often useful for analytic simplifications in their applications (see further below). We note finally that they reduce to the well-known plane-wave Volkov solution in the absence of the Coulomb potential. This can be seen directly by putting $Z = 0$ in these wavefunctions.

5.3 A Semiclassical Coulomb–Volkov Wavefunction

In this section we consider a Coulomb–Volkov solution of the semiclassical Schrödinger equation (in the length gauge) in which the dipole interaction potential is replaced by the dipole interaction energy, as obtained from the classical electron trajectory in the field,

$$\mathrm{i}\frac{\partial}{\partial t}\Phi_{\boldsymbol{p}}(\boldsymbol{r}, t) = \left[\frac{\hat{\boldsymbol{p}}^2}{2} - \frac{Z}{r} + \boldsymbol{F}(t) \cdot \boldsymbol{r}(t)\right]\Phi_{\boldsymbol{p}}(\boldsymbol{r}, t) \tag{29}$$

where, the laser field $\boldsymbol{F}(t)$ is defined below Eq. (15), and $\boldsymbol{r}(t)$ is the electron trajectory,

$$\boldsymbol{r}(t) = \boldsymbol{r}_0 + (t - t_0)\boldsymbol{p} + (\boldsymbol{\alpha}(t) - \boldsymbol{\alpha}(t_0)) \tag{30}$$

where $\boldsymbol{\alpha}(t) = \frac{1}{c}\int^t \mathrm{d}t' \boldsymbol{A}(t')$ is the 'quiver radius' and r_0 is the initial position at $t = t_0$. Equation (29) can be readily integrated to obtain the desired semiclassical Coulomb–Volkov wavefunction

$$\boldsymbol{\Phi}_{\boldsymbol{p}}^{(\pm)}(\boldsymbol{r}, t) = \mathrm{e}^{-\frac{\mathrm{i}}{2}p^2 t - \mathrm{i}\phi_c(t)} \mathrm{e}^{(\pi Z/2p)} \Gamma(1 \mp \mathrm{i}Z/p) \mathrm{e}^{\mathrm{i}\boldsymbol{p}\cdot\boldsymbol{r}} F(\pm \mathrm{i}Z/p, 1, \pm\mathrm{i}(pr \mp \boldsymbol{p} \cdot \boldsymbol{r})) \tag{31}$$

where,

$$\begin{aligned}\phi_c(t) &= \int_{t_0}^{t} (\boldsymbol{F}(t')\cdot\boldsymbol{r}(t'))\mathrm{d}t' \\ &= -\frac{1}{c}(\boldsymbol{A}(t)\cdot\boldsymbol{r}(t) - \boldsymbol{A}(t_0)\cdot\boldsymbol{r}(t_0)) \\ &\quad + \frac{1}{c}\int_{t_0}^{t} \mathrm{d}t'\left(\boldsymbol{p} + \frac{1}{c}\boldsymbol{A}(t')\right)\cdot\boldsymbol{A}(t')\end{aligned} \tag{32}$$

In the asymptotic limit $p_B r >> 1$ the semiclassical Coulomb–Volkov wavefunction, Eq. (31), simplifies further to

$$\Phi_p^{(\pm)}(\boldsymbol{r}, t) = \mathrm{e}^{-\frac{\mathrm{i}}{2}p^2 t - \mathrm{i}\phi_c(t)}\mathrm{e}^{\mathrm{i}\boldsymbol{p}\cdot\boldsymbol{r}\mp\mathrm{i}(Z/p)\ln(pr\mp\boldsymbol{p}\cdot\boldsymbol{r})} \tag{33}$$

where the phase function $\phi_c(t)$ is given by Eq. (32).

5.4 Coulomb–Volkov Green's Function

The wavefunctions discussed above may be used to obtain the associated approximate Coulomb–Volkov Green's functions. The latter can be employed directly in the second-order intense-field S-matrix amplitudes for a number of significant physical processes like the non-sequential double ionization (e.g., [11,12]) and high harmonic generation (e.g., [13,14]), as well as in all processes in which the higher-order amplitudes become significant. To this end we first note that the equal-time $(t = t')$ orthogonality relation is satisfied exactly by the Coulomb–Volkov wavefunctions given above. The equal-time completeness relation is satisfied logarithmically, as can be seen by taking the slowly varying logarithmic dependence on $\boldsymbol{r}$ and $\boldsymbol{r}'$ of the phase, at $t = t'$, outside the completeness integral sign. Using then completeness relation, the corresponding Coulomb–Volkov Green's function can be easily derived. For example, we get the adiabatic Coulomb–Volkov Green's function, from the whole set of adiabatic wavefunctions, Eq. (26):

$$\begin{aligned}G^{(c-v)}(\boldsymbol{r}, t; \boldsymbol{r}', t') = -\mathrm{i}\theta(t-t')\int \frac{\mathrm{d}^3 p}{(2\pi)^3}\mathrm{e}^{-\frac{\mathrm{i}}{2}\int_{t'}^{t} p_u^2 \mathrm{d}u} g(\boldsymbol{p}, t) g^*(\boldsymbol{p}, t') \\ \times \psi_{\boldsymbol{p}_t}^{(-)}(\boldsymbol{r}) \times \psi_{\boldsymbol{p}_{t'}}^{(-)*}(\boldsymbol{r}')\end{aligned} \tag{34}$$

where

$$g(\boldsymbol{p}, t) = \mathrm{e}^{\frac{\pi}{2}\eta_t}\Gamma(1 + \mathrm{i}\eta_t)\mathrm{e}^{-\mathrm{i}\eta_t(\ln(p_t r_0(t) + \boldsymbol{p}_t\cdot\boldsymbol{r}_0(t)))}, \qquad \eta_t = \frac{Z}{p_t} \tag{35}$$

is a periodic function of time, and $\psi^{(-)}_{\boldsymbol{p}_{t'}}(\boldsymbol{r}')$ are Coulomb continuum functions defined by Eq. (27).

Or, using the rudimentary wavefunction (25), one gets

$$G^{(c-v)}(\boldsymbol{r},t;\boldsymbol{r}',t') = -\mathrm{i}\theta(t-t')\int \frac{\mathrm{d}^3p}{(2\pi)^3}\mathrm{e}^{-\frac{\mathrm{i}}{2}\int_{t'}^{t}p_\tau^2\mathrm{d}\tau}\mathrm{e}^{\mathrm{i}(\boldsymbol{p}_t\cdot\boldsymbol{r}-\boldsymbol{p}_{t'}\cdot\boldsymbol{r}')} \times \mathrm{e}^{\mathrm{i}\eta_t\ln(2p_tr)-\mathrm{i}\eta_{t'}\ln(2p_{t'}r')} \tag{36}$$

Alternatively, using the wavefunction, Eq. (28), we obtain

$$\begin{aligned} G^{(c-v)}(\boldsymbol{r},t;\boldsymbol{r}',t') = -\mathrm{i}\theta(t-t')\int \frac{\mathrm{d}^3p}{(2\pi)^3}\mathrm{e}^{-\frac{\mathrm{i}}{2}\int_{t'}^{t}p_\tau^2\mathrm{d}\tau} \\ \times \mathrm{e}^{-\mathrm{i}(\eta_t\ln(2p_tr_0(t))-\eta_{t'}\ln(2p_{t'}r_0(t')))}\mathrm{e}^{\mathrm{i}(\boldsymbol{p}_t\cdot\boldsymbol{r}-\boldsymbol{p}_{t'}\cdot\boldsymbol{r}')} \\ \times \mathrm{e}^{\mathrm{i}(\eta_t\ln(p_tr+\boldsymbol{p}_t\cdot\boldsymbol{r})-\eta_{t'}\ln(p_{t'}r'+\boldsymbol{p}_{t'}\cdot\boldsymbol{r}'))} \end{aligned} \tag{37}$$

(And, similarly in the other cases.)

5.5 *Approximate Coulomb–KFR Wavefunctions*

As indicated above, the approximate Coulomb–Volkov wavefunctions satisfy the final continuum state boundary condition. The simplest wavefunction in adiabatic intense-field problems satisfying the initial bound state condition is given by the wavefunction in the well-known KFR approximation [15,16,17], which effectively uses the plane-wave Volkov Green's function. We now easily generalize the plane-wave KFR wavefunction [15,16,17] to include the combined effect of the Coulomb potential and the laser field by using the approximate Coulomb–Volkov Green's functions $G^{(c-v)}$ given above. Thus, we obtain the Coulomb–KFR wavefunctions (that evolve from the initial unperturbed bound state, $\phi_B(\boldsymbol{r},t)$, with binding energy $E_B = \frac{p_B^2}{2}$) in the general form:

$$\Psi(\boldsymbol{r},t) = \phi_B(\boldsymbol{r},t) + \int_{-\infty}^{\infty} G^{(c-v)}(\boldsymbol{r},t;\boldsymbol{r}',t')|\boldsymbol{F}(t')\cdot\boldsymbol{r}'|\phi_B(\boldsymbol{r}',t')>\mathrm{d}t' \tag{38}$$

For example, substituting the Green's function, Eq. (34), in Eq. (38), we get the adiabatic C–KFR wavefunction

$$\begin{aligned} \Psi(r,t) = \Bigg(\phi_B(\boldsymbol{r}) - \mathrm{i}\int \frac{\mathrm{d}^3p}{(2\pi)^3}g(\boldsymbol{p},t)\psi^{(-)}_{\boldsymbol{p}_t}(\boldsymbol{r})\int_{-\infty}^{t}\mathrm{d}t'\mathrm{e}^{-\frac{\mathrm{i}}{2}\int_{t'}^{t}(p_u^2+p_B^2)\mathrm{d}u} \\ \times g^*(\boldsymbol{p},t')\psi^{(-)*}_{\boldsymbol{p}_{t'}}(\boldsymbol{r}')|\boldsymbol{F}(t')\cdot\boldsymbol{r}'|\phi_B(\boldsymbol{r}')\Bigg)\mathrm{e}^{\mathrm{i}E_Bt} \end{aligned} \tag{39}$$

where the time-dependent periodic function $g(\boldsymbol{p}, t)$ is defined by Eq. (35), and $\psi^{(-)}_{\boldsymbol{p}_t}$ is given by Eq. (27). The angle brackets, here and below, stand for the integrations over the coordinates.

Similarly, using the rudimentary Green's function, Eq. (36), we get the simplest C–KFR wavefunction,

$$\Psi(\boldsymbol{r}, t) = \mathrm{e}^{\mathrm{i}E_B t}\left(\phi_B(\boldsymbol{r}) - \mathrm{i}\int \frac{\mathrm{d}^3 p}{(2\pi)^3}\mathrm{e}^{\mathrm{i}\boldsymbol{p}_t\cdot\boldsymbol{r} + \mathrm{i}\frac{Z}{p_t}\ln(2p_t r)} \times \int_{-\infty}^{t} \mathrm{d}t' \mathrm{e}^{-\frac{\mathrm{i}}{2}\int_{t'}^{t}(p_u^2 + p_B^2)\mathrm{d}u} \times < \mathrm{e}^{-\mathrm{i}\boldsymbol{p}_{t'}\cdot\boldsymbol{r}' - \mathrm{i}\frac{Z}{p_{t'}}\ln(2p_{t'}r')} | \boldsymbol{F}(t')\cdot\boldsymbol{r}' | \phi_B(\boldsymbol{r}') > \right) \tag{40}$$

5.6 Signature of Photon Thresholds in the 'Tunnel Regime'

We now briefly consider an example of the usefulness of the Coulomb–KFR wavefunctions just discussed.

The simplest Coulomb–KFR wavefunction, Eq. (40), has been used to analyze [18] a recent (high-resolution) observation of the low-energy parallel-momentum distributions of electrons emitted from ionization of He atoms [19,20], in the well-known tunnel regime of laser parameters (Keldysh $\gamma \equiv \sqrt{\frac{E_B}{2U_\mathrm{p}}} = \frac{\omega p_B}{F} < 0.5$). A set of experimental data from the measurements of Rudenko et al. [20] is shown in Fig. 1. To analyze the data, the bound-free transition amplitude $(S-1)_{B\to\boldsymbol{p}}$ has been obtained in the lowest-order Coulomb–KFR approximation by simply projecting the final Coulomb–Volkov wavefunction, Eq. (25), onto the C–KFR wavefunction (40), to get

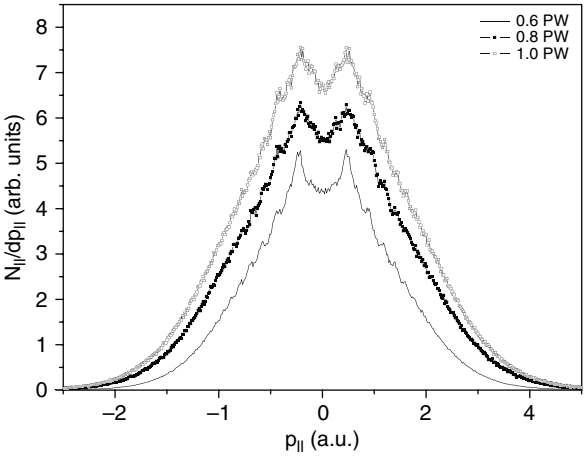

Fig. 1 Experimental distributions of parallel-momentum in the tunnel regime, $\gamma < 0.5$ from ionization of He atoms in intense 25 fs, 795 nm Ti-sapphire laser pulses at three peak intensities: $I = 6 \times 10^{14}$ (*lowest curve*), 8×10^{14} (*middle curve*), and 1×10^{15} W/cm^2 (*upper curve*); the scales of the curves are arbitrary (from [20])

$$(S-1)_{B\to \boldsymbol{p}} = -\mathrm{i}\int_{-\infty}^{\infty} \mathrm{d}t' \mathrm{e}^{\frac{\mathrm{i}}{2}\int^{t'} p_u^2 \mathrm{d}u} \mathrm{e}^{\mathrm{i}E_B t'} \times <\mathrm{e}^{-\mathrm{i}\boldsymbol{p}_{t'}\cdot\boldsymbol{r}' - \mathrm{i}\frac{Z}{p_{t'}}\ln(2p_{t'}r')} |\boldsymbol{F}(t')\cdot\boldsymbol{r}'|\phi_B(\boldsymbol{r}')> \tag{41}$$

(For an evaluation of the above integral see [18].)

A set of theoretical distributions calculated from this amplitude [18] are reproduced in Fig. 2. It can be seen by comparison of Fig. 1 and Fig. 2 that the theory accounts quite well for the high-resolution features of the experimental data [20] including the cusp-like central minimum and the sequence of secondary peak structures that were not expected from field-ionization models in the tunnel regime (Keldysh $\gamma < 0.5$). The main effect of the rudimentary Coulomb correction in the wavefunction (25), on the low-energy parallel-momentum distributions have been found to be, first, a large enhancement of the probability of ionization over that obtained when the Coulomb corrections are omitted (putting $Z = 0$ in the Coulomb–KFR wavefunction). Second, it reduced the interference effect between the sub-waves, generated near the two intensity maxima per laser cycle. This may be thought of as a scattering-like effect (in contrast to a 'rescattering' effect). The cusp-like peaks result from the envelope of the discrete photon absorption thresholds (even in the tunnel regime) that move as the ionization threshold shifts with the field intensity near the peak of the laser pulse (during the passage of the pulse) [18].

5.7 High Harmonic Generation Under Adiabatic Condition

It should be observed that the adiabatic condition that is essentially determined by the requirement $\omega/E_B \ll 1$ can be satisfied not only by near-infrared and optical wavelengths (for the valence shell electrons of the neutral atoms or molecules), but also for the VUV and soft X-ray wavelengths, for the inner-shells of neutral atoms and/or the valence-shells of their (singly or multiply

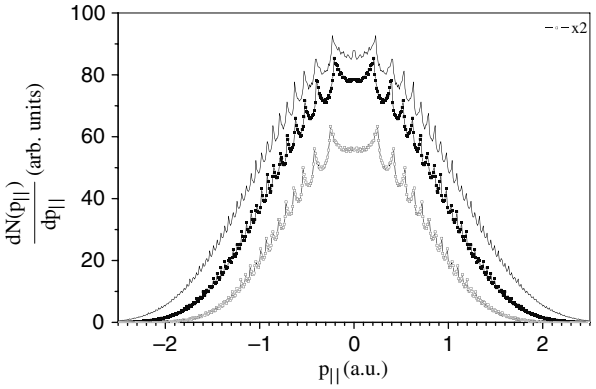

Fig. 2 Theoretical distributions of parallel-momentum in the tunnel regime, $\gamma < 0.5$, from ionization of He atom by intense 25 fs, 795 nm laser pulses at three intensities: $I = 6 \times 10^{14}$ (*empty circles*), 7.9×10^{14} (*solid dots*), and 1×10^{15} W/cm^2 (*continuous curve*) (from [18])

charged) ions. Thus a theory of high harmonic generation (HHG) under adiabatic condition is of interest both for the 'long wavelengths' and for the 'short wavelengths' (e.g., VUV/XUV free-electron laser fields). The HHG spectrum can be calculated from the Fourier transform of the expectation value of the dipole moment in intense field [13] or essentially equivalently from the quantum probability amplitude for the generation of harmonic photons, as given by the intense-field S-matrix theory (e.g., review [14]). HHG can be usefully thought as a three-step event in which the first event leads to the emission of the bound electron into the continuum (qualitatively speaking by 'tunneling'), followed by the propagation in the Volkov continuum and, finally, recombination into the initial state by emission of the harmonic photon.

A popular model for the atomic dipole expectation value is given by the Lewenstein model [13], which is based essentially on the plane-wave KFR approximation. Consequently, as is well known, it does not account for the combined effect of the laser field and the Coulomb potential in the Volkov continuum. This can lead to, among other things, significant underestimates of the strength of HHG signals. Clearly, the Coulomb–KFR wavefunctions discussed above may be used to account approximately for the Coulomb effect in HHG. Thus, for example, using the wavefunction, Eq. (38), in the lowest approximation, the expectation value of the dipole operator projected along any desired direction, $\hat{\boldsymbol{n}}$, can be written as

$$D(t) = \int_{-\infty}^{\infty} \mathrm{d}t' < \phi_B(\boldsymbol{r}, t) | \hat{\boldsymbol{n}} \cdot \boldsymbol{r} | G^{(c-v)}(\boldsymbol{r}, t; \boldsymbol{r}', t') | \boldsymbol{F}(t') \cdot \boldsymbol{r}' | \phi_B(\boldsymbol{r}', t') > + \text{c.c.} \tag{42}$$

More specifically, use of the adiabatic C–KFR wavefunction, Eq. (39), gives

$$\begin{aligned} D(t) = -\mathrm{i} \int \frac{\mathrm{d}^3 p}{(2\pi)^3} \int_{-\infty}^{t} dt' \mathrm{e}^{-\frac{\mathrm{i}}{2}\int_{t'}^{t}(p_u^2 + p_B^2)\mathrm{d}u} \theta(t - t') \\ \times g(\boldsymbol{p}, t) < \phi_B(\boldsymbol{r}) | \hat{\boldsymbol{n}} \cdot \boldsymbol{r} | \psi_{p_t}^{(-)}(\boldsymbol{r}) > \\ \times g^*(\boldsymbol{p}, t) < \psi_{\boldsymbol{p}_{t'}}^{(-)*}(\boldsymbol{r}') | \boldsymbol{F}(t') \cdot \boldsymbol{r}' | \phi_B(\boldsymbol{r}') > \quad + \quad \text{c.c.} \end{aligned} \tag{43}$$

We may next use the stationary phase method (cf. [13]) to carry out the integration over the momentum $\boldsymbol{p}$ and change the variables (t, t') to the variables $(t, \tau \equiv (t - t'))$ and obtain the following expression of the dipole expectation value:

$$\begin{aligned} D(t) = -\mathrm{i} \int_0^{\infty} \mathrm{d}\tau \left(\frac{1}{2\pi\mathrm{i}\tau + \epsilon} \right)^{\frac{3}{2}} \mathrm{e}^{-\frac{\mathrm{i}}{2}\int_{t-\tau}^{t}([p(u)]_{st.}^2 + p_B^2)\mathrm{d}u} \theta(\tau) \\ \times g([\boldsymbol{p}(t)]_{st.}, t) \times d_f([\boldsymbol{p}(t)]_{st.}) \\ \times g^*([\boldsymbol{p}(t - \tau)]_{st.}, t - \tau) \times d_i([\boldsymbol{p}(t - \tau)]_{st.}) \quad + \quad \text{c.c.} \end{aligned} \tag{44}$$

where the the functions g's are defined as in Eq. (35) and the matrix elements d_f and d_i appearing above are

$$d_f([\boldsymbol{p}(t)]_{st.}) = \left\langle \phi_B(\boldsymbol{r})|\hat{\boldsymbol{n}}\cdot\boldsymbol{r}|\psi^{(-)}_{[\boldsymbol{p}(t)]_{st.}}(\boldsymbol{r})\right\rangle \tag{45}$$

and

$$d_i([\boldsymbol{p}(t-\tau)]_{st.}) = \left\langle \psi^{(-)*}_{[\boldsymbol{p}(t-\tau)]_{st.}}(\boldsymbol{r}')|\boldsymbol{F}(t-\tau)\cdot\boldsymbol{r}'|\phi_B(\boldsymbol{r}')\right\rangle \tag{46}$$

The stationary value of $\boldsymbol{p}$ is denoted by $\boldsymbol{p}_{\rm s}(t,\tau)$ and is given by

$$\boldsymbol{p}_{\rm s}(t,\tau) = -\frac{1}{c\tau}\int_{t-\tau}^{\tau}\boldsymbol{A}(u)\mathrm{d}u \tag{47}$$

and the stationary value of the instantaneous momentum at any time u is denoted by

$$[\boldsymbol{p}(u)]_{st.} \equiv \boldsymbol{p}_s(t,\tau) + \frac{1}{c}\boldsymbol{A}(u) \tag{48}$$

(For the sake of simplicity, we do not indicate the τ-dependence inside the notation $[\boldsymbol{p}(u)]_{st.}$, explicitly.)

Given the initial bound state wavefunction, the essentially Coulomb dipole matrix elements, d_i and d_f, can be evaluated more explicitly. For example, assuming an effective hydrogenic ground-state wavefunction of arbitrary charge state $Z_{\rm a} = p_B$, $\phi_B(\boldsymbol{r},t) = B_0\mathrm{e}^{-p_B r}\mathrm{e}^{\mathrm{i}E_B t}$, with $B_0 = \sqrt{\frac{p_B^3}{\pi}}$, we can employ the well-known Nordsiek's method [21], followed by parametric differentiations, to get explicitly:

$$\begin{aligned} d_i([\boldsymbol{p}(t')]) &= \int \mathrm{e}^{-\mathrm{i}[\boldsymbol{p}(t')]\cdot\boldsymbol{r}}F(\mathrm{i}[\eta_{t'}],1,\mathrm{i}[p(t')]r + [\boldsymbol{p}(t')]\cdot\boldsymbol{r})(\boldsymbol{F}(t')\cdot\boldsymbol{r})\mathrm{e}^{-p_B r}\mathrm{d}^3 r \\ &= [16\pi\mathrm{i}(1-\mathrm{i}[\eta(t')])(Z-2p_B)] \\ &\quad\times\frac{\boldsymbol{F}(t')\cdot[\boldsymbol{p}(t')]}{(p_B+\mathrm{i}[p(t')])^{3-\mathrm{i}[\eta(t')]}(p_B-\mathrm{i}|[p(t')])^{3+\mathrm{i}[\eta(t')]}} \end{aligned} \tag{49}$$

where $[\eta(t')] \equiv \frac{Z}{[p(t')]}$. A similar expression holds for $d_f([\boldsymbol{p}(t)]$, which can be obtained from the expression for $d_i([\boldsymbol{p}(t')])$ simply by changing everywhere the argument t' by it t, replacing $\boldsymbol{F}(t')$ by $\hat{\boldsymbol{n}}$, and taking the complex conjugate. $[\mathbf{p}(u)]$s in d_i and d_f in Eq. (44) assume only their stationary values that are quoted above. Clearly, the dipole expectation value $D(t)$ given by Eq. (44) that approximately includes the adiabatic Coulomb effect is a direct extension of the well-known Lewenstein model. Note that the latter model is recovered in the absence of the Coulomb interaction, $Z = 0$, as expected.

We may proceed further to obtain a formula for the Fourier transform of $D(t)$ that is more directly related to the strength of the *nth* harmonic. Thus, going back to Eq. (43), we expand the periodic part of the integrand in it t and t' in Fourier series and carry out the time integrations. Then using a relation discussed below, we may rewrite $D(t)$ in the form

$$D(t) = -\mathrm{i} \sum_{n=-\infty}^{\infty} \mathrm{e}^{\mathrm{i}n\omega t} T^{(n)} + \text{c.c.} \tag{50}$$

where $T^{(n)}$ is the basic *nth* Fourier transform at a harmonic frequency $\Omega = n\omega$. It takes a comparatively simple form:

$$\begin{aligned} T^{(n)}(\Omega = n\omega) = \int \frac{\mathrm{d}^3 p}{(2\pi)^3} \oint \mathrm{d}t \mathrm{e}^{\mathrm{i}n\omega t} \oint \mathrm{d}t' \theta(t-t') \mathrm{e}^{-\frac{\mathrm{i}}{2}\int_{t'}^{t}(p_u^2 + p_B^2)\mathrm{d}u} \\ \times g([\boldsymbol{p}(t)], t) \times d_f([\boldsymbol{p}(t)]) \\ \times g^*([\boldsymbol{p}(t')], t') \times d_i([\boldsymbol{p}(t')]) \end{aligned} \tag{51}$$

where $\oint$ stands for the integration over one cycle. In deriving Eq. (51), we have employed the relation

$$\frac{\omega}{2\pi} \mathrm{i} \sum_{n=-\infty}^{\infty} \frac{\mathrm{e}^{-\mathrm{i}n\omega(t-t')}}{n\omega - (E_B + p^2/2 + U_\mathrm{p}) + \mathrm{i}0} \cong \theta(t-t') \times \mathrm{e}^{-\mathrm{i}(E_B + p^2/2 + U_\mathrm{p})(t-t')} \tag{52}$$

which considerably simplifies the expression by eliminating an otherwise infinite summation with strong cancellations over the intermediate photon numbers. We have derived Eq. (52), by assuming $n\omega \equiv x$(approx. continuous) for $0 \leq \omega \ll E_B + U_\mathrm{p}$, on the left-hand side, and applying the Cauchy residue theorem.

As before, the integration over $\mathrm{d}^3 p$ in Eq. (51) can be performed conveniently by the stationary phase method, with the stationary values as given above. Thus, finally, we get

$$\begin{aligned} T^{(n)}(\Omega = n\omega) = \int_{-\frac{\pi}{\omega}}^{\frac{\pi}{\omega}} \mathrm{d}t \mathrm{e}^{\mathrm{i}n\omega t} \int_{-\frac{\pi}{\omega}}^{\frac{\pi}{\omega}} \mathrm{d}t' \theta(t-t') \left(\frac{1}{2\pi\mathrm{i}(t-t') + \epsilon} \right)^{\frac{3}{2}} \\ \times \mathrm{e}^{-\frac{\mathrm{i}}{2}\int_{t'}^{t}([p(u)]_{st.}^2 + p_B^2)\mathrm{d}u} \\ \times g([\boldsymbol{p}(t)]_{st.}, t) \times d_f([\boldsymbol{p}(t)]_{st.}) \\ \times g^*([\boldsymbol{p}(t')]_{st.}, t') \times d_i([\boldsymbol{p}(t')]_{st.}) \end{aligned} \tag{53}$$

Note that the two time integrations over the cycle may be performed as a *single* quadrature, in view of the presence of the theta function in the integrand.

We may point out explicitly that similar (computationally simple) expressions can be obtained for the related second-order amplitudes for 're-scattering' and non-sequential double ionization, following the same procedure and employing the relation (52) as shown above.

6 Oscillating K–H Frame

At non-perturbative intensities in the VUV and low XUV domain, where the retardation effect might still be neglected, it is useful to have relatively simple approximate expressions for estimating the ionization rates (e.g., from valence shells) and their dependence on the field parameters. To this end it is often useful to go over to an oscillating reference frame, popularly known as the Kramer–Henneberger frame, by a space-translation of the Schrödinger equation of the system in the laboratory frame (e.g., [22,23]):

$$\mathrm{i}\frac{\partial}{\partial t}\Psi(\boldsymbol{r},t) = \left[\frac{\hat{\boldsymbol{p}}^2}{2} - \frac{Z}{|\boldsymbol{r}-\boldsymbol{\alpha}_0(t)|}\right]\Psi(\boldsymbol{r},t) \tag{54}$$

where $\boldsymbol{\alpha}_0(t) = \boldsymbol{\alpha}_0 \sin\omega t$ $\alpha_0 = \frac{eA_0}{mc\omega}$. If one now Fourier transforms the Coulomb potential and expands the time-dependent sinusoidal part in the exponent using the Jacobi–Anger formula $\mathrm{e}^{iz\sin\omega t} = \sum_n J_n(z)\mathrm{e}^{in\omega t}$ one gets the Fourier components of the oscillating potential

$$V_n(\boldsymbol{r},\boldsymbol{\alpha}_0) = -\frac{Z}{2\pi^2}\int \mathrm{d}^3p \frac{J_n(\boldsymbol{p}\cdot\boldsymbol{\alpha}_0)}{p^2}\mathrm{e}^{-\mathrm{i}\boldsymbol{p}\cdot\boldsymbol{r}} \tag{55}$$

For a systematic analytic evaluation of these potentials, for any |n|, we refer to [24]. At a high frequency the terms with $n \neq 0$ would oscillate very rapidly and tend to contribute little compared to the stationary term $V_0(\boldsymbol{r},\boldsymbol{\alpha}_0)$. The corresponding stationary Schrödinger equation,

$$E\,\Phi(\boldsymbol{x},\boldsymbol{\alpha}_0) = \left[\frac{\hat{\boldsymbol{p}}^2}{2} + V_0(\boldsymbol{r},\boldsymbol{\alpha}_0)\right]\Phi(\boldsymbol{r},\boldsymbol{\alpha}_0) \tag{56}$$

then gives the zeroth order wavefunctions for the bound states which provide a basis for the perturbed problem, specially at a high frequency (but not so high as to cause the break-down of the dipole approximation). This so-called high-frequency approximation has been extensively studied by Gavrila and co-workers (see, e.g., review [25]) who obtained much information on the eigenvalues and eigenstates of the stationary equation for H-atom as well as investigated in details the 'adiabatic stabilization' phenomenon for ionization.

Here we assume the zeroth order solutions of the stationary equation (56) and give approximate explicit expressions for the n-photon ionization rates that take account of the Coulombic nature of ionization boundary condition in the presence of the laser field. The ionization amplitude in the first order of the rest potential in K–H frame, $W(\boldsymbol{r},t) \equiv [V(\boldsymbol{r}-\boldsymbol{\alpha}_0(t)) - V(\boldsymbol{r})]$, is obtained by proceeding as in the case of LOPT:

$$A_{\rm ion}(\infty) = -2\pi {\rm i} \sum_n \delta\left(\frac{k^2}{2} + I_{\rm p}(I) - n\omega\right) T^{(n)} \tag{57}$$

where

$$T^{(n)} = \int d^3 r \phi_{\boldsymbol{k}}^{(-)*}(\boldsymbol{r}) V_n(\boldsymbol{r}, \boldsymbol{\alpha}_0) \Phi_0(\boldsymbol{r}, \boldsymbol{\alpha}_0) \tag{58}$$

The final state corresponds to the well-known 'minus' Coulomb wave,

$$\phi_{\boldsymbol{k}}^{(-)}(\boldsymbol{r}) = {\rm e}^{\pi\eta/2}\Gamma(1+{\rm i}\eta)_1{\rm F}_1(-{\rm i}\eta, 1, -{\rm i}(kr + \boldsymbol{k}\cdot\boldsymbol{r})){\rm e}^{{\rm i}\boldsymbol{k}\cdot\boldsymbol{r}} \tag{59}$$

$\eta = \frac{Z}{k}$ and $\Phi_0(\boldsymbol{\rho}, z)$ is the K–H frame initial bound state wavefunction, with the field- dependent binding energy $I_{\rm p}(I)$. We have used the Fourier expansion of the Coulomb potentials, Eq. (55), and carried out a time integration to obtain Eq. (57) (cf. Eq. (5)). Note that the field-shifted ionization potential $I_{\rm p}(I)$ determines the electron momentum in the ionization continuum $k_n = \sqrt{2(n\omega - I_{\rm p}(I))}$.

To evaluate the matrix elements approximately, note first that the zeroth order charge density of the electron (that gives rise to the stationary binding potential $V_0(x,y,z;\boldsymbol{\alpha}_0)$) is (e.g., [22])

$$\rho_0(\boldsymbol{r}) = -\frac{Z}{\pi}\delta(x)\delta(y)\frac{1}{\sqrt{\alpha_0^2 - z^2}} \qquad \text{(linear polarization)} \tag{60}$$

or

$$\rho_0(\boldsymbol{r}) = -\frac{Z}{\pi}\delta(\rho - \alpha_0)\delta(z) \qquad \text{(circular polarization)} \tag{61}$$

It can be seen that the density is highly concentrated (in fact, singular) at two points $\rho = \sqrt{x^2+y^2} = 0$ and $z = \pm\alpha_0$ (for linear polarization) or at one radius $\rho = \alpha_0$ and $z = 0$ (for circular polarization). Since quantum mechanically the charge density is given by the modulo-square of the wavefunction (multiplied by e), one expects that the wavefunction $\Phi_0(\boldsymbol{\rho}, z)$ itself would tend to concentrate near the singular points. One may therefore approximate the

integral over $\boldsymbol{r}$ in $T^{(n)}$ (Eq. 58) by taking the slowly varying part of the integrand (with its value at the critical points) outside the integral sign and carry out the rest of the integrations over $\boldsymbol{r}$ and $\boldsymbol{p}$ exactly. Thus, we get the following results for the ionization matrix elements for linear and circular polarizations:

$$T^{(n)} = -4\pi Z \mathrm{e}^{\pi\eta_n/2}\Gamma(1-\mathrm{i}\eta_n)A_{\mathrm{L}}(\boldsymbol{k},\boldsymbol{\alpha}_0)J_n(k_n\alpha_0\cos\theta_k)/k_n^2 \quad \text{(linear polarization)} \tag{62}$$

where

$$\begin{aligned} A_{\mathrm{L}}(\boldsymbol{k},\boldsymbol{\alpha}_0) = \big[&{}_1\mathrm{F}_1(\mathrm{i}\eta_{\mathrm{n}},1,\mathrm{i}k_{\mathrm{n}}\alpha_0(1+\cos\theta_k))\Phi_0(\rho=0,z=\alpha_0) \\ &+ {}_1\mathrm{F}_1(\mathrm{i}\eta_{\mathrm{n}},1,\mathrm{i}k_{\mathrm{n}}\alpha_0(1-\cos\theta_k))\Phi_0(\rho=0,z=-\alpha_0)\big] \end{aligned} \tag{63}$$

Similarly,

$$T^{(n)} = -4\pi Z \mathrm{e}^{\pi\eta_n/2}\Gamma(1-\mathrm{i}\eta_n)A_{\mathrm{C}}(\boldsymbol{k},\boldsymbol{\alpha}_0)J_n(k_n\alpha_0\sin\theta_k)\mathrm{e}^{\mathrm{i}n\phi_k}/k_n^2 \quad \text{(circular polarization)} \tag{64}$$

where

$$A_{\mathrm{C}}(\boldsymbol{k},\boldsymbol{\alpha}_0) = {}_1\mathrm{F}_1(\mathrm{i}\eta_n,1,\mathrm{i}k_n\alpha_0(1+\sin\theta_k))\Phi_0(\rho=\alpha_0,\mathrm{z}=0) \tag{65}$$

and the 'Sommerfeld number' $\eta_n = Z/k_n$. Note also that the plane-wave Born result obtained earlier for the case of circular polarization (see, e.g., [25]) is reproduced if we put $\eta_n = 0$, $A_C = 1$, in Eq. (64).

The *rate* of ionization, $\frac{\mathrm{d}W}{\mathrm{d}\Omega}$, can now be easily obtained from the standard formula relating the rate with the T-matrix, Eq. (7). Thus, for the case of linear polarization we have

$$\frac{\mathrm{dW_L}}{\mathrm{d}\Omega} = \sum_n \frac{2\pi\eta_n}{1-\mathrm{e}^{-2\pi\eta_n}}|A_{\mathrm{L}}(\boldsymbol{k},\boldsymbol{\alpha}_0)|^2 4Z^2 {J_n}^2(k_n\alpha_0\cos\theta_k)/k_n^3 \tag{66}$$

and for the case of circular polarization

$$\frac{\mathrm{dW_C}}{\mathrm{d}\Omega} = \sum_n \frac{2\pi\eta_n}{1-\mathrm{e}^{-2\pi\eta_n}}|A_{\mathrm{C}}(\boldsymbol{k},\boldsymbol{\alpha}_0)|^2 4Z^2 {J_n}^2(k_n\alpha_0\sin\theta_k)/k_n^3 \tag{67}$$

(A similar expression holds for the general case of elliptic polarization.) The first factor of Eqs. (66) and (67) corresponds to the density of the Coulomb wave at the origin. Note that the second factor arising from the long-range Coulombic nature of the potential in the final state depends on the momentum and quiver radius in an inseparable manner through ${}_1\mathrm{F}_1$ functions which can give rise to field-dependent modulation and/or interference effects. These

approximate expressions could be used conveniently for investigations of non-resonant processes in intense VUV/XUV fields so long as the retardation effect remains negligible. It is worth noting that the intensity-dependent ionization potential $I_p(I)$ decreases with intensity in the 'high-frequency' domain but increases (approximately like U_p) for photon energies smaller than the first excitation energy of the atom, $\omega < \epsilon_1$. In the 'high-frequency' approximation and for small values of α_0, the shifted ionization potential for an s-state of H atom is, for example for linear polarization, $I_p(I) = I_p + \alpha_0{}^2/3n^3$ (e.g., [25]); 'n' here is the principal quantum number. For small α_0 one may also use the unperturbed value of the atomic wavefunction for the initial bound state. For $\alpha_0 \geq 1$ the K–H bound state eigenfunction and the $I_p(I)$ have been given numerically/graphically by Gavrila and co-workers (e.g., [25]).

6.1 A High-Frequency Approximation for High Harmonic Generation

High harmonic generation in high-frequency fields may be investigated most simply semiclassically within a simple 'high-frequency approximation' [18]. According to Larmor's classical electrodynamical formula for the radiation energy $P(t)$ emitted by an electron per unit time (or power) is proportional to the acceleration of the charged particle in the electromagnetic field. We replace the classical acceleration by the expectation value of the acceleration operator with respect to the ground state of the system and write the semiclassical formula for the expectation value of the acceleration of the electron (in the K–H frame) as

$$<\ddot{\boldsymbol{r}}> = \left\langle \phi_B(\boldsymbol{r}, t) \middle| -\nabla\left(\frac{Z}{|\boldsymbol{r} - \alpha(t)|}\right) \middle| \phi_B(\boldsymbol{r}, t) \right\rangle \tag{68}$$

where $\alpha(t) \equiv \alpha_0 \sin\omega t$, with $\alpha_0 = \frac{A_0}{\omega c}$, is the instantaneous quiver radius. Assuming, that the unperturbed ground s-state of the target atom is of the form $|\phi_B(t)> = \sqrt{\frac{p_B^3}{\pi}} e^{-p_B r} e^{iE_B t}$, where $E_B \equiv p_B^2/2$, is the binding energy (or ionization potential). Using Eq. (68), taking the FT of the Coulomb potential and using the Jacobi–Anger formula for the expansion of the exponential of a sine function in terms of the Bessel functions, we can write the acceleration along the incident polarization direction as

$$\begin{aligned} <\cdot\ddot{\boldsymbol{r}}> &= \left(\frac{i8p_B^4}{\pi^2}\right) \sum_{n=-\infty}^{\infty} e^{in\omega t} \int d^3p J_n(\boldsymbol{p}\cdot\boldsymbol{\alpha}_0) \frac{\cdot\,\boldsymbol{p}}{p^2(p^2 + 4p_B^2)^2} \\ &= \sum_{n=0}^{\infty} \frac{1}{2}(T^{(n)} e^{in\omega t} + \text{c.c.}) \end{aligned} \tag{69}$$

Therefore, the component of the *nth* harmonic $T^{(n)}$ is

$$T^{(n)} = c_n \left[\int_0^1 \mathrm{d}x x \int_0^\infty \mathrm{d}p p \frac{J_n(p\alpha_0 x)}{(p^2 + 4p_B^2)^2} \right] \tag{70}$$

$$\begin{aligned} &= c_n \left[\frac{(2p_B)^{n-2} \Gamma(1 + n/2)\Gamma(1 - n/2)}{2^{n+1}\Gamma(n+1)} B_1(n) \right. \\ &\quad \left. + \frac{\Gamma(n/2 - 1)}{2^3 \Gamma(n/2 + 2)} B_2(n) \right] \end{aligned} \tag{71}$$

where

$$\begin{aligned} B_1(n) &= \int_0^1 \mathrm{d}x x (\alpha_0 x)^n {}_1F_2(1 + n/2; n/2, n+1; (p_B \alpha_0 x)^2) \\ B_2(n) &= \int_0^1 \mathrm{d}x x (\alpha_0 x)^2 {}_1F_2(2; n/2 + 2, 2 - n/2; (p_B \alpha_0 x)^2) \end{aligned} \tag{72}$$

Performing the last two integrals (by first expanding in power series and then integrating term by term and re-summing) we get the final result as an algebraic formula:

$$\begin{aligned} T^{(n)} = c_n [& u_n \times {}_2F_3(n/2 + 1, n/2 + 1; n/2 + 2, n/2, n + 1; (p_B \alpha_0)^2) \\ & + v_n \times {}_2F_3(2, 2; 3, n/2 + 2, -n/2 + 2; (p_B \alpha_0)^2)] \end{aligned} \tag{73}$$

where the constants

$$\begin{aligned} c_n &= \left(\frac{32 p_B^4 \mathrm{i}}{\pi} \right) (1 + (-1)^{n+1}) \\ u_n &= \frac{(2p_B \alpha_0)^n \Gamma^2(n/2 + 1)\Gamma(-n/2 + 1)}{(2p_B)^2 2^{n+2} \Gamma(n+1)\Gamma(n/2 + 2)} \\ v_n &= \frac{\Gamma(n/2 - 1)\alpha_0^2}{2^5 \Gamma(n/2 + 2)} \end{aligned} \tag{74}$$

${}_pF_q$ are the generalized hypergeometric functions that are highly convergent series for $p < q$, as is the present case.

Note that the above formula explicitly shows that the $n =$ even harmonics are not generated; this behavior is consistent with the general rule for the harmonic generation in a centro-symmetric system that is initially prepared in a given

parity state (for a general proof cf. [14]). The 'high-frequency approximation' is assumed to apply for $\omega \gg E_B \to I_p(I)$ where $I_p(I)$ is the field-dependent ionization potential (e.g., [25]); the high-frequency harmonic emission strengths are seen to depend on the quiver radius $\alpha_0(\equiv \frac{F}{\omega^2})$ alone (and not separately on F and ω). This is analogous to the dependence of the ionization probability on α_0 only, in the 'high-frequency approximation' [25].

7 Numerical Methods in K–H Frame

For accurate results of the ionization rates one has to take recourse to elaborate numerical methods for solving the time-dependent Schrödinger equation. Here we may point out that for VUV/XUV wavelengths such time-dependent simulations in (3 + 1)-dimensions can be efficiently carried out in the oscillating K–H frame e.g., [26]). Also the stationary Floquet method in general (e.g., chap.8 [1]) and that in the K–H frame has proved to be very useful at VUV/XUV wavelengths (e.g., [27,28,29,30,31]). Floquet equations in the K–H frame can be solved using the coupled-channel methods (also called 'close-coupling' method; (e.g., [32,29]) or its many-electron analog, the 'R-matrix method' (e.g., [33]). Moreover, they can be fruitfully employed to the problems that are rather difficult to simulate in the time domain, such as the radiative scattering involving stimulated bremsstrahlung and inverse-bremsstrahlung processes (e.g., [32,24,33,34,35]). Among other things, accurate numerical analysis both in time domain and within the stationary Floquet methods has confirmed the qualitative predictions of 'high-frequency' approximation for the so-called 'adiabatic stabilization phenomenon', e.g., [25], over certain intensity domains. Adiabatic stabilization implies a *decrease* of the rate of ionization with increasing intensity, at least within a 'window of stabilization' [36]. If the current developments of the sources of intense short-wavelength radiation continue and reach sufficiently high intensities to make $\alpha_0 > 1$, it would be possible to check experimentally this rather counter-intuitive phenomenon with ground-state atoms.

Accurate (3 + 1)-dimensional numerical simulations for the ionization dynamics at high-frequency regime can be carried out conveniently in the K–H frame. As an example of such numerical simulations using the K–H frame Schrödinger equation, Eq. (54), is shown in Fig. 3 [26]. It shows the evolution of ionization of the ground-state hydrogen atom, as a function of the interaction time (50-cycle $\sin^2$-envelope with a rise time of 5.25 cycles) for a high-frequency field ($\omega = 1$ a.u. $= 27.2$ eV) at three different intensities: (a) $I = 4 \times 10^{17}$ W/cm^2, (b) $I = 1.6 \times 10^{18}$ W/cm^2, and (c) $I = 6.4 \times 10^{18}$ W/cm^2. Note that the probability of ionization rises very rapidly at first and exceeds the 50% level within only a few cycles of interaction time. Further evolution depends significantly on the intensity of the field. Thus, after about 10 cycles, a lower intensity pulse is seen to cause more ionization than a higher intensity

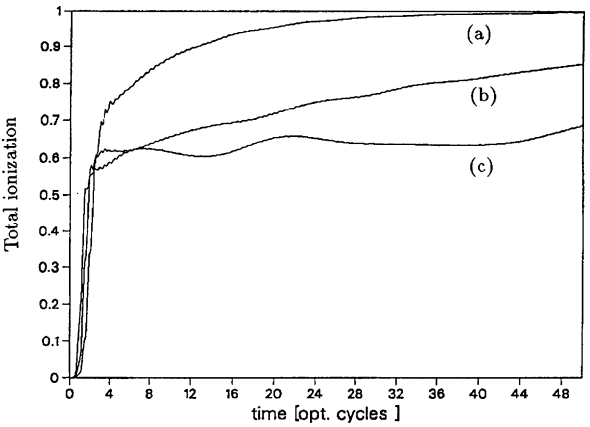

Fig. 3 Evolution of ionization probability for H-Atom in a high-frequency laser field ($\omega = 27.2$ eV) at three intensities: (a) $I = 4 \times 10^{17}$ W/cm^2, (b) $I = 1.6 \times 10^{18}$ W/cm^2, and (c) $I = 6.4 \times 10^{18}$ W/cm^2. Note the *lower* ionization at the higher intensities for interaction times longer than about 10 optical cycles (from [26])

pulse, in all the three cases. This counter-intuitive relative behavior persists right up to the end of the 50-cycle pulse and clearly indicates a 'stabilization'-like behavior in the window of intensities considered.

8 Reduction of the Retardation Problem: A Modified Floquet Expansion

Most non-perturbative numerical integration methods were developed in the past assuming the no-retardation (or dipole) approximation. This, as indicated above, might fail at shorter wavelengths and thereby could seriously compromise the efficiency of the method. With this problem in mind, we introduce below a modified Floquet expansion and the resulting reduced Floquet equations that considerably simplify the problem of retardation, in both the non-relativistic and the relativistic domains of intensity.

We note first that in the presence of the retardation, plane-wave factors involving the photon momentum $\varkappa$ depend periodically on the Lorentz-invariant phase $(\omega t - \boldsymbol{\varkappa} \cdot \boldsymbol{r})$ of the field, which involves both space and time coordinates. However, the atomic potential is not periodic either in the phase of the field or in the space coordinates. Therefore the Floquet theorem, which requires periodicity of the Hamiltonian in the expansion variable, may not be applied directly in the presence of the retardation. We may nevertheless incorporate a *part* of the space dependence along with the periodic time dependence of the full Hamiltonian. This permits the Floquet expansion of the total wavefunction in time, through the Lorentz-invariant phase in Eq. (2) as

$$\Psi(\boldsymbol{x}, t) = \mathrm{e}^{-\mathrm{i}Et} \sum_n \mathrm{e}^{\mathrm{i}n(\omega t - \boldsymbol{\varkappa} \cdot x)} \Psi_n(\boldsymbol{x}) \tag{75}$$

We point out that since the modified expansion ansatz above satisfies the requirement of the Floquet theorem with respect to the periodicity of the Hamiltonian in

time, the Floquet characteristic parameter E still corresponds to the energy of the total (light + atom) quantum system for higher-intensity fields, as shown in the case with no retardation (e.g., chap. 8 [1]). To proceed further, we substitute the above expansion in Eq. (2) and equate the coefficients of the equal powers of the *independent* Fourier components, $e^{in\omega t}$, in time only. One observes that the common factor involving the multiples of the retardation plane-waves, $e^{-in\varkappa\cdot x}$, now cancels out throughout and we get a modified Floquet equation where the retardation plane-waves are fully eliminated:

$$\begin{aligned} E\Psi_n(\boldsymbol{x}) = &\left[(\hat{\boldsymbol{p}}^2 - n\boldsymbol{\varkappa})^2/2 + n\omega + V + U_{\mathrm{p}}\right]\Psi_n(\boldsymbol{x}) \\ &- \frac{\boldsymbol{A}_0\cdot\hat{\boldsymbol{p}}}{2c}[\Psi_{n-1}(\boldsymbol{x}) + \Psi_{n+1}(\boldsymbol{x})] \\ &+ \frac{U_p}{2}[\Psi_{n-2}(\boldsymbol{x}) + \Psi_{n+2}(\boldsymbol{x})] \end{aligned} \tag{76}$$

where we have used the transversality relation $\boldsymbol{\varkappa}\cdot\boldsymbol{A} = 0$ to eliminate an interaction term in the resulting Hamiltonian. A comparison with the usual form of Floquet equations with retardation (e.g., p. 247 [1]) shows the simplicity of the present approach; it removes the need for any multi-polar expansion that would otherwise occur from the usual expansion of the photon plane-waves. In fact now it involves only a *dipole-like* coupling of the momentum operator of the electron with the polarization *and* propagation vectors of the field. Thus, the advantage of the present formulation is that all the methods of treating the Floquet equation which have been developed in the dipole approximation in the past may again be employed to the modified Floquet equations given here, without making the dipole approximation.

9 Relativistic Domain

Relativity can appear in several ways in the strong field problem (see also the chapter of Maquet et al.): (i) if the frequency is so high that the photon energy is comparable to or greater than the rest-mass energy of the electron, $\hbar\omega \approx m_0c^2$; (ii) the atomic electron is very tightly bound by the ion core (as in heavier atoms and their ions) so that the corresponding electron motion becomes relativistic, e.g., the spin–orbit splitting becomes large, e.g., for $Z\alpha \approx \frac{1}{2}$ or more; and (iii) if the field intensity is so high that the energy of the free electron inside the field becomes comparable to or greater than the rest-mass energy of the electron, i.e., $U_{\mathrm{p}} \approx m_0c^2$. In the last case, one should note particularly that even when the initial electron energy is non-relativistic, the intermediate and/or the final energy in the field can be relativistic and hence the dynamics would still require a non-perturbative *relativistic* treatment.

When the effect of electron spin is negligible, intense-field dynamics may be investigated in terms of the Klein–Gordon equation. For example, for a

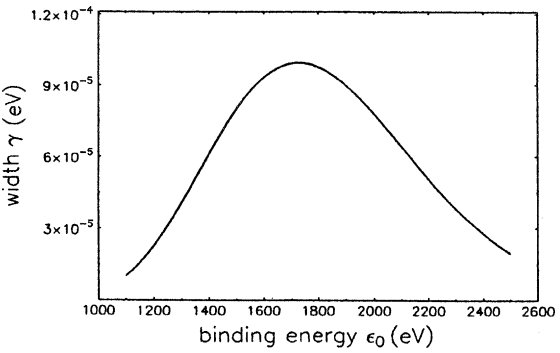

Fig. 4 Variation of the ionization width (rate of ionization) with binding energy of a tightly bound electron in a high-frequency field ($\omega = 100$ eV) at a relativistic intensity $I = 10^{21}$ W/cm^2. Note the increasing ionization with *increasing* binding energy on the left-hand side of the maximum (from [37])

high-frequency field an unexpected phenomenon has been predicted [37] by solving the K–G equation of a model one- electron system exactly in a relativistically intense field [34,35]. One would normally expect that at a given intensity and frequency of the field, ionization of an atom (or ion) would decrease with increasing binding energy of the electron. The anomalous effect consists in an *increase* of ionization with increasing binding energy of the target electron. Figure 4 shows the calculated ionization width γ, i.e., rate of ionization in energy unit ($27.2\,\text{eV} \rightarrow 4.17 \times 10^{16}$ per second) as a function of the binding energy of the electron, ϵ_0. In this case, a tightly bound electron is subjected to a very intense high-frequency laser field ($I = 10^{21}$ W/cm^2 and $\omega = 100$ eV). One sees an anomalous ionization domain, which extends from about 1100 eV to about 1700 eV, where the rate of ionization increases with the binding energy and reaches a maximum. For still higher binding energies the ionization probability behaves normally, i.e., decreases with increasing binding energy. A possible existence of this anomalous effect might be tested experimentally, e.g., by choosing ionic targets with increasing Z and subjecting them to intense laser radiation of not too low frequency.

10 Reduction of Retardation: Reduced Floquet–Dirac Equation

In general, in the relativistic domain of intensity and/or very short wavelengths (X-ray and shorter wavelengths) the Dirac equation forms the fundamental basis (even of quantum field theory) of both perturbative and non-perturbative analyses of electron dynamics. A direct time-dependent simulation of the Dirac equation coupled to the radiation field tends to be extremely arduous or impractical in full $(3+1)$-dimensions. Hence it is desirable in the relativistic domain to look for simplifying indirect approach, specially for reducing the problem posed by the presence of the retardation which cannot be neglected in this regime. It appears therefore to be equally interesting to employ the modified Floquet expansion discussed above also to the Dirac equation

$$\mathrm{i}\frac{\partial}{\partial t}\Psi(\boldsymbol{x},t)=\left[c\hat{\boldsymbol{\alpha}}\cdot\left(\hat{\boldsymbol{p}}-\frac{1}{c}\boldsymbol{A}(\boldsymbol{x},t)\right)+V+\beta c^2\right]\Psi(\boldsymbol{x},t) \tag{77}$$

where $\Psi(\boldsymbol{x},t)$ is the total Dirac bispinor. Taking again the Lorentz-invariant phase $(\omega t-\boldsymbol{\varkappa}\cdot r)$ as the basis for the modified Floquet expansion for the Dirac equation, we expand

$$\Psi(\boldsymbol{x},t)=\mathrm{e}^{-\mathrm{i}Et}\sum_n \mathrm{e}^{\mathrm{i}n(\omega t-\boldsymbol{\varkappa}\cdot\boldsymbol{x})}\Psi_n(\boldsymbol{x}) \tag{78}$$

where $\Psi_n(\boldsymbol{x})$ are now Floquet bispinors, and E is the total energy of the system, for the same reasons as given in the previous section. Proceeding further as in the previous section we arrive at the reduced version of the Dirac–Floquet equation:

$$\begin{aligned}E\Psi_n(\boldsymbol{x})=&\left[c\hat{\boldsymbol{\alpha}}\cdot(\hat{\boldsymbol{p}}-n\boldsymbol{\varkappa})+n\omega+V+\beta c^2\right]\Psi_n(\boldsymbol{x})\\&-\frac{\boldsymbol{A}_0\cdot\hat{\boldsymbol{\alpha}}}{2}\left[\Psi_{n-1}(\boldsymbol{x})+\Psi_{n+1}(\boldsymbol{x})\right]\end{aligned} \tag{79}$$

Clearly, the retardation factors are absent in the equations above and, hence, the usual 'multi-polar' expansion, Eq. (10), is no longer needed. In fact, the reduced Dirac–Floquet equation (79) contains only a *dipole-like* coupling of the Dirac velocity operator $c\hat{\boldsymbol{\alpha}}$ with the propagation and the polarization vectors. Thus, the techniques of solving Floquet equations developed in the Schrödinger case within the dipole approximation may again be employed *mutatis mutandis* to the modified Dirac–Floquet equation as well, and the complex eigenvalues $E=E_{\mathrm{Re}}(I,\tilde{},\omega)-i\Gamma(I,\tilde{},\omega)/2$ can be determined as functions of the field parameters as before (e.g. [28,29,30]). Also in the coordinate space, discrete basis sets like the sturmians (e.g., [38]) can be used with advantage. We may add that the form of the Schrödinger–Floquet and Dirac–Floquet equations, given above, is also suitable for solving them in the momentum space.

11 Super-Intense Fields: Spin Dynamics

For super-intense fields ($q\geq 1$) when a very large number of photons can be exchanged significantly in the transition process, both the time-dependent simulation techniques and the Floquet expansion techniques can be extremely arduous. In the former case the space–time grid, and in the latter case the size of the Floquet matrix, would tend to be too large to be practicable. An alternative *ab initio* approach is a systematic approximation method that is based on a convenient rearrangement of the S-matrix theory in the relativistic regime, analogous to the so-called KFR approach [15,16,17] in the non-relativistic

case. S-matrix amplitude has been formulated within the relativistic strong field approximation (SFA) in the past (e.g., [39]) and more recently within the 'relativistic intense-field many-body S-matrix theory' (RIMST). The latter has been developed originally in the non-relativistic domain [40] and applied fruitfully in analyzing a host of intense-field processes in two *and* many-electron systems, in that domain (e.g., [11,12]).

A characteristic aspect in the relativistic domain is the coupling of the intense field with the spin degrees of freedom. This gives rise to phenomena like stimulated Mott-scattering (e.g., [41]) and other spin-dependent effects in the bound state (e.g., [42]). In connection with ionization in relativistic fields, specific spin information is usually traced out (e.g., [39]) for an unpolarized target atom. However, the rates of spin flips in the ionization process and possibly also spin-asymmetry, even from unpolarized target atoms, could be measured in 'second generation' experiments, e.g., by detecting spin-polarized ionization currents from target atoms prepared with or without spin-selected initial bound states. Analysis of such and related experiments would clearly require a knowledge of the spin dependence of the ionization rates. Such spin-specific ionization rate in intense relativistic fields have been obtained recently [43]. Before concluding this brief discussion of high-field atomic processes at short wavelengths we give explicit analytic expressions of the spin-specific ionization rates for the transition of a Dirac hydrogenic atom (ion) into the spin-specific Dirac–Volkov states. The results are given for the general case of an *elliptically* polarized radiation field, which reduces automatically to the important special cases of linear and circular polarizations for the ellipticity parameter $\xi = 0$ and $\xi = \pi/2$, respectively. These results are derived using the leading term of RIMST (equal to the relativistic SFA approximation). The rate of ionization from the bound spin state $j = \mathrm{u(p)}, \mathrm{d(own)}$ to the continuum spin state $j' = \mathrm{u}, \mathrm{d}$ are (in transverse gauge 'velocity form') as follows.

Elliptic polarization:

$$\frac{dW_{j\to j'}}{d\Omega} = \sum_{n\geq n_0} \left(\frac{A_0}{2c} N_{k_0} N_{1\mathrm{s}} c_0(q)\right)^2 \left|t^{(n)}_{j\to j'}\right|^2 c k_0 \frac{|\boldsymbol{k}|}{(2\pi)^2} \tag{80}$$

The number of absorbed photons n is determined by the energy–momentum conservation relation

$$n\omega = \epsilon_B + \epsilon_{\mathrm{kin}} + \lambda_k \omega \tag{81}$$

where $\epsilon_B = c\left(c - \sqrt{c^2 - k_B^2}\right)$ is the binding energy (ionization potential) and $\epsilon_{\mathrm{kin}} = c\left(\sqrt{c^2 + k^2} - c\right)$ is the kinetic energy. The other parameters are

$$\sqrt{c^2 + \boldsymbol{k}^2} = k_0 = (n - \lambda_k)\varkappa_0 + \sqrt{c^2 - k_B^2}$$

N_{1s} and N_{k_0} are the well-known normalization constants of H-atom ground state and of the free Dirac spinor; we have derived and used here a very useful algebraic form of the Dirac H-atom ground state spinor: $\Psi_{1s} = N_{1s} r^{\gamma'-1} e^{-k_B r}$ $\gamma_{mu} n_{mu} \omega^{(u,d)}$, where $n_{mu} = (1, i\beta' \hat{\mathbf{r}})$, and $\omega^{(u,d)} = [\chi^{(u,d)}, 0]^+; \chi^u = (1,0)^+$, $\chi^d = (0,1)^+$.

$$\boldsymbol{q} = q\hat{\boldsymbol{q}} = \boldsymbol{k} + (\lambda_\kappa - n)\boldsymbol{\varkappa}, \qquad \varkappa_0 = \omega/c\ , \qquad \boldsymbol{\varkappa} = \varkappa_0 \hat{\varkappa}$$

and

$$\varkappa = (\varkappa_0, \boldsymbol{\varkappa})$$

$$c_0(q) = \frac{4\pi}{q} \frac{\Gamma(\gamma'+1)}{\left(k_B^2 + q^2\right)^{\frac{\gamma'+1}{2}}} \sin\left((\gamma'+1)\tan^{-1}\left(\frac{q}{k_B}\right)\right)$$

and

$$g(q) = \beta' \left[\frac{k_B}{q} - \frac{\gamma'+1}{\gamma'} \sqrt{1 + \left(\frac{k_B}{q}\right)^2} \frac{\sin\left(\gamma' \tan^{-1}(q/k_B)\right)}{\sin((\gamma'+1)\tan^{-1}(q/k_B))}\right]$$

where

$$\begin{aligned}
\gamma' &= \sqrt{1 - (Z\alpha)^2} \\
\beta' &= (1 - \gamma')/(Z\alpha) \\
k_B &= Z \\
m_1 &= \sqrt{(k_0 + c)/(2c)} \\
m_2 &= -\sqrt{(k_0 - c)/(2c)} \\
N_{1s} &= (2k_B)^{\gamma' + \frac{1}{2}} \left(\frac{1+\gamma'}{8\pi\Gamma(1+2\gamma')}\right)^{\frac{1}{2}} \\
N_{k_0} &= \sqrt{\frac{c}{k_0}} \\
B_n^0 &= \frac{A_0 \varkappa_0}{4c\varkappa \cdot k} (2J_n + \cos\xi(J_{n+2} + J_{n-2})) \\
\boldsymbol{B}_n &= (\xi) J_{n-1} + {}^*(\xi) J_{n+1} + \hat{\varkappa} B_n^0 \\
\varkappa \cdot k &= \varkappa_0 k_0 - \boldsymbol{\varkappa} \cdot \boldsymbol{k} \\
J_n &= J_n(a_k, b_k, \chi_k) = \sum_m J_{n+2m}(a_k) J_m(b_k) \mathrm{e}^{\mathrm{i}(n+2m)\chi_k}
\end{aligned} \tag{82}$$

are generalized Bessel functions of three arguments with

$$a_k = \frac{A_0\left|(\xi)\cdot\boldsymbol{k}\right|}{c\varkappa\cdot k}$$

$$b_k = \frac{A_0^2}{8c^2\varkappa\cdot k}\cos\xi$$

$$\chi_k = \tan^{-1}[\tan\phi_k\tan(\xi/2)]$$

$$\lambda_k = \frac{A_0^2}{4c^2\varkappa\cdot k}$$

$$(\xi) = [_1\cos(\xi/2) + i_2\sin(\xi/2)],\quad \xi[0,\pi/2]$$

The reduced $t^{(n)}$-matrix elements are explicitly given by

$$\begin{aligned} t^{(n)}_{\mathrm{u}\to\mathrm{u}} &= B_n^{0*}\left(m_1 + m_2 g(q)\left(\hat{\boldsymbol{k}}\cdot\hat{\boldsymbol{q}} + i\left(\hat{\boldsymbol{k}}\times\hat{\boldsymbol{q}}\right)_z\right)\right) \\ &\quad + \boldsymbol{B}_n^*\cdot\left(m_2\hat{\boldsymbol{k}} + m_1 g(q)\hat{\boldsymbol{q}}\right) \\ &\quad - \mathrm{i}\left(\boldsymbol{B}_n^*\times\left(m_2\hat{\boldsymbol{k}} - m_1 g(q)\hat{\boldsymbol{q}}\right)\right)_z \end{aligned} \tag{83}$$

$$\begin{aligned} t^{(n)}_{\mathrm{d}\to\mathrm{u}} &= m_2 g(q) B_n^{0*}\left(\mathrm{i}\left(\hat{\boldsymbol{k}}\times\hat{\boldsymbol{q}}\right)_x - \left(\hat{\boldsymbol{k}}\times\hat{\boldsymbol{q}}\right)_y\right) \\ &\quad - \mathrm{i}\left(\boldsymbol{B}_n^*\times\left(m_2\hat{\boldsymbol{k}} - m_1 g(q)\hat{\boldsymbol{q}}\right)\right)_x \\ &\quad + \left(\boldsymbol{B}_n^*\times\left(m_2\hat{\boldsymbol{k}} - m_1 g(q)\hat{\boldsymbol{q}}\right)\right)_y \end{aligned} \tag{84}$$

$$\begin{aligned} t^{(n)}_{\mathrm{d}\to\mathrm{u}} &= m_2 g(q) B_n^{0*}\left(i\left(\hat{\boldsymbol{k}}\times\hat{\boldsymbol{q}}\right)_x + \left(\hat{\boldsymbol{k}}\times\hat{\boldsymbol{q}}\right)_y\right) \\ &\quad - \mathrm{i}\left(B_n^*\times\left(m_2\hat{\boldsymbol{k}} - m_1 g(q)\hat{\boldsymbol{q}}\right)\right)_x \\ &\quad - \left(B_n^*\times\left(m_2\hat{\boldsymbol{k}} - m_1 g(q)\hat{\boldsymbol{q}}\right)\right)_y \end{aligned} \tag{85}$$

and

$$\begin{aligned} t^{(n)}_{\mathrm{d}\to\mathrm{d}} &= B_n^{0*}\left(m_1 + m_2 g(q)\left(\hat{\boldsymbol{k}}\cdot\hat{\boldsymbol{q}} - \mathrm{i}\left(\hat{\boldsymbol{k}}\times\hat{\boldsymbol{q}}\right)_z\right)\right) \\ &\quad + B_n^*\cdot\left(m_2\hat{\boldsymbol{k}} + m_1 g(q)\hat{\boldsymbol{q}}\right) \\ &\quad + \mathrm{i}\left(B_n^*\times\left(m_2\hat{\boldsymbol{k}} - m_1 g(q)\hat{\boldsymbol{q}}\right)\right)_z \end{aligned} \tag{86}$$

Linear polarization:
The same rate formula (Eqs. (80), (81), (82), (83), (84), (85), (86)) holds, except that, since in this case $\xi = 0$ therefore the generalized Bessel function of three arguments $J_n = J_n(a_k, b_k, \chi_k)$ (Eq. (82)) now simplifies to the generalized Bessel function of two arguments, i.e., $J_n = J_n(a_k, b_k)$; $a_k = a_k(\xi = 0)$, $b_k = b_k(\xi = 0)$ $[\chi_k(\xi = 0) = 0]$.

Circular polarization:
The same rate formula (Eqs. (80), (81), (82), (83), (84), (85), (86)) holds except that, since in this case $\xi = \pi/2$ therefore the generalized Bessel function of three arguments now simplifies to an ordinary Bessel function with a phase, i.e., $J_n = J_n(a_\kappa)\mathrm{e}^{\mathrm{i}n\phi_k}$; $a_k = a_k(\xi = \pi/2)$, $\chi_k = \phi_k$, $[b_k(\xi = \pi/2) = 0]$.

We note that the specific influence of relativity in the rate of ionization arises, first, from the relativistic energy and momentum of both the free and the bound states of the electron *and* the momentum of the photon. They affect the arguments of the Bessel functions in B_ns, the reduced amplitudes $t^{(n)}$s, as well as the 'dressed-momentum' $\boldsymbol{q} = \boldsymbol{k} + (\lambda_{\boldsymbol{k}} - n)\boldsymbol{\varkappa}$. Similarly, the specific influence of the spin arises, first, from the 'weak'-component factor m_2 of the free-electron spinor (which appears in the reduced amplitudes $t^{(n)}$s) and, second, from $g(q)$ in t^ns, which is due to the 'weak' component of the bound electron.

We may note finally that the usual total spin-averaged ionization rate from an unpolarized target atom, if desired, can be easily obtained by simply adding the four spin-specific rates given above and dividing by 2 (for the average with respect to the two degenerate initial spin states):

$$\frac{d\Gamma^{(+)}}{d\Omega_k} = \sum_{n \geq n_0} \left(\frac{A_0}{2c} N_{k_0} N_{1s} c_0(q) \right)^2 c k_0 \frac{\boldsymbol{k}}{(2\pi)^2} \times \frac{1}{2} \sum_{(j,j')=\mathrm{u,d}} \left| t^{(n)}_{j \to j'} \right|^2 \tag{87}$$

12 Spin-Flip and Spin Asymmetry in Ionization

An interesting prediction of the present theory is that a helical photon (e.g., circularly polarized) can flip the helicity of the ionizing electron (at any intensity). Furthermore, the photon can distinguish the sense of the spin flip (with respect to its own sense of helicity) through the *difference* in the rates of 'up → down' vs. 'down → up' spin transitions. It vanishes if only the 'weak' components of the Dirac electron states are neglected. We briefly discuss this effect below.

The specific spin-up and the spin-down electron currents can now be obtained from the matrix elements given above:

$$\frac{dW^{\mathrm{up}}}{d\Omega} = \frac{1}{2} \left(\frac{dW_{\mathrm{u} \to \mathrm{u}}}{d\Omega} + \frac{dW_{\mathrm{d} \to \mathrm{u}}}{d\Omega} \right) \tag{88}$$

$$\frac{dW^{\text{down}}}{d\Omega} = \frac{1}{2}\left(\frac{dW_{\text{d}\to\text{d}}}{d\Omega} + \frac{dW_{\text{u}\to\text{d}}}{d\Omega}\right) \tag{89}$$

It is interesting to ask if there is any asymmetry in the up and down spin electron currents even when the two degenerate initial spin states of the atom are assumed to be occupied statistically ($\frac{1}{2}$:$\frac{1}{2}$, i.e., unpolarized). Any asymmetry in the two currents is best characterized by the initially *unpolarized* target atom (ensemble-averaged) asymmetry parameter $<A>$ defined by

$$<A> = \left(\frac{dW^{up}}{d\Omega} - \frac{dW^{down}}{d\Omega}\right) \Big/ \left(\frac{dW^{up}}{d\Omega} + \frac{dW^{down}}{d\Omega}\right) \tag{90}$$

They have been recently investigated for ionization of H-atom in intense circularly polarized laser fields at low and high frequencies [41].

In Figs. 5 and 6 we show typical results of calculations for the asymmetry parameter $<A>$ in two cases, $I = 10^{16}$ W/cm^2, $\omega = 1.55$ eV (Fig. 5), and $I = 10^{20}$ W/cm^2, $\omega = 20$ eV (Fig. 6). At both intensities $<A>$ is as large as $o(10^{-3})$ in magnitude but negative. And they are well within the current resolution of spin-analyzers in the laboratory [44] to be observed experimentally. This indicates a dominance of the spin-down electron current over the spin-up current at all angles of observation [43]. Remarkably, unlike the asymmetry parameter for Fano effect [45,46], the two curves reveal a strong dependence of $<A>$ on field intensity at all angles. It is also interesting to note that there is no spin–orbit interaction above arising from the derivative of the atomic potential, either in the initial state (ground s-state) or in the final state (Dirac plane-wave Volkov state). At the first sight perhaps even more surprisingly, the asymmetry remains present when the retardation (and hence the laser magnetic field in the laboratory) is neglected ($\boldsymbol{\varkappa} = 0$). So what is the origin of the spin flip as such under the above circumstance? It is a consequence of the Lorentz invariance in

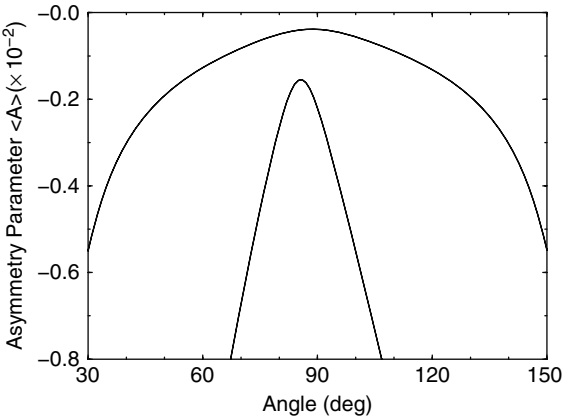

Fig. 5 Intensity-dependent ensemble-averaged asymmetry parameter $<A>$ (see Eq. (90) for definition) vs. electron emission angle; $\omega = 1.55$ eV, $I = 10^{16}$ W/cm^2 (*outer curve*), and $I = 10^{17}$ W/cm^2 (*inner curve*) (from [43])

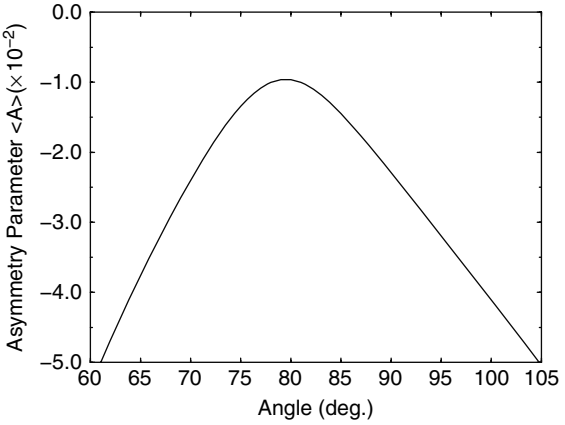

Fig. 6 Ensemble-averaged asymmetry parameter $< A >$ vs. electron emission angle; $\omega = 20$ eV, $I = 10^{20}$ W/cm^2 (from [43])

which the *electric* field in the laboratory (even in the absence of retardation) is Lorentz-transformed, in the moving frame of the emitted electron, into a mixed electric and magnetic field, with a (motional) magnetic field component of order $\boldsymbol{B}' \equiv \boldsymbol{E_0} \times \boldsymbol{p}/c \approx B'$ (a.u.). Thus the finite spin-flip probability is due, even in the absence of retardation effect, to the coupling of the motional magnetic field B' with the magnetic moment ($= -\frac{1}{4c^2}\boldsymbol{\sigma}$ a.u.) of the electron in its own frame of reference [43].

13 Summary

Availability of intense short-wavelength radiation fields opens up the possibility of investigating multi-photon processes in a new regime of high-field physics. In this chapter we have briefly introduced and discussed a number of approximate and exact theoretical methods suitable for application to such processes in intense VUV, XUV, and X-ray wavelengths, or beyond. Particular attention is paid to the basic processes of ionization and high harmonic generation and to approximate solutions of Coulomb–Volkov Schrödinger equation. Theoretical problems posed by the effect of retardation, relativity, and spin degrees of freedom on multi-photon processes, and the ways to reduce them, are discussed. Finally, a recently predicted relativistic effect showing an asymmetry in spin currents during intense-field ionization, and the mechanism behind it, is also discussed.

References

1. F.H.M. Faisal, *Theory of Multi-photon Processes*, Plenum Press, N.Y. (1987)
2. M. Nurhuda, F.H.M. Faisal, and U. Schwengelbeck, Comp. Phys. Commun. **134**, 291 (2001).
3. L. Hostler, J. Math. Phys. (NY) **5**, 1235 (1964).

4. A. Maquet, Phys. Rev. A **15**, 1088 (1977).
5. M.A. Kornberger and P. Lambropoulos, J.Phys. B **32**, L603 (1999).
6. D. Charalambidis, D. Xenakis, C.J.G.J. Uiterwaal, P. Maragakis, Jian Zhang, H. Schröder, O. Faucher, and P. Lambropoulos, J. Phys. B **30**, 1467 (1997).
7. A. Becker and F.H.M. Faisal, Phys. Rev. A **59**, R1742 (1999).
8. A. Becker and F.H.M. Faisal, Phys. Rev. A **59**, R3182 (1999).
9. B. Walker et al., Phys. Rev. Lett. **73**, 1227 (1994),
10. L.D. Landau and E.M. Lifshitz, *Quantum Mechanics*, Pergamon Press, Oxford (1965), p. 522.
11. A. Becker and F.H.M. Faisal, Phys. Rev. Lett. **84** 3546 (2000).
12. A. Becker and F.H.M. Faisal, Phys. Rev. Lett. **89**, 043814 (2002).
13. M. Lewenstein, Ph. Balcou, M. Yu. Ivanov, A. L'Huillier, and P.B. Corkum *Phys. Rev. A* **49** 2117 (1994).
14. A. Becker and F.H.M. Faisal, J. Phys. B. **B 38**, R1-R56 (2005).
15. L.V. Keldysh, Sov. Phys. JETP **20**, 1307 (1965).
16. F.H.M. Faisal, J. Phys. B **6**, L312 (1973).
17. H. Reiss, Phys. Rev. A **22**, 1786 (1980).
18. F.H.M. Faisal and G. Schlegel, J. Phys. **B 38** , L223-L231 (2005). We take this opportunity to correct a number of misprints in this citation: in eqs. (2) and (5), the suffix of $\Phi_{\boldsymbol{p}}$ should read $\Phi_{\boldsymbol{p}}^{(\pm)}$; in eq. (6) a phase factor $e^{iE_B t}$ is to be included; in eq. (7) the powers of $e^{i\pi}$ and p_B are to be exchanged; in eq. (8) d^3p should read $\frac{d^3p}{(2\pi)^3}$; in eq. (11) the '$\times$' sign should appear after the argument of Γ. (The results and conclusions are unaffected.)
19. R. Moshammer, J. Ullrich, B. Feuerstein, D. Fischer, A. Dorn, C.D. Schröter, J.R. Crespo Lopez-Urrutia, C. Hoehr, H. Rottke, C. Trump, M. Wittmann, G. Korn, and W. Sandner, Phys. Rev. Lett. **91**, 113002 (2003).
20. A. Rudenko, K. Zrost, C.D. Schröter, V.L.B. de Jesus, B. Feuerstein, R. Moshammer, and J. Ullrich, J. Phys. B **37** , L407 (2004).
21. A. Nordsiek, Phys. Rev. **93**, 785 (1954).
22. W.C. Henneberger, Phys. Rev. Lett. **21**, 838 (1968).
23. F.H.M. Faisal, J. Phys. B **6**, L89 (1973).
24. L. Dimou and F.H.M. Faisal, Laser Phys. **3**, 440 (1993).
25. M. Gavrila, in *Atoms in Intense Laser Fields*, Ed. M. Gavrila, Acad. Press, N.Y. (1992).
26. F.H.M. Faisal, L. Dimou, H.-J. Stiemke, and M. Nurhuda, J. Nonlinear Opt. Phys. Mater. **4**, 701 (1995).
27. U. Lambrecht, L. Dimou, and F.H.M. Faisal, Phys. Rev. A **57**, 2832 (1998).
28. M.Dörr, R.M. Potvliege, B. Piraux, and R. Shakeshaft, Phys. Rev. A **43**, 3729 (1991).
29. L. Dimou and F.H.M. Faisal, Phys. Rev. A **46**, 4442 (1992); Phys. Rev. A **49**, 4564 (1994).
30. R.M. Potvliege and H.G. Smith, Phys. Rev. A. **48**, R46 (1993).
31. J. Bauer, L. Plucinski, B. Piraux, R. Potvliege, M. Gajda, and J. Krzywinski, J. Phys. B. **34**, 2245 (2001).
32. L. Dimou and F.H.M. Faisal, Phys. Rev. Lett. **59**, 872 (1987).
33. J. Purvis, M. Dörr, M. Terao-Dunseath, C.J. Joachain, P.G. Burke, and C. Noble, Phys. Rev. Lett. **71**, 3943 (1992).
34. F.H.M. Faisal and T. Radozycki, Phys. Rev. A **47**, 4464 (1993).
35. F.H.M. Faisal and T. Radozycki, Phys. Rev. A **48**, 554 (1993).
36. F.H.M. Faisal, in *Multiphoton Processes*, Eds. L. DiMauro, R. Freeman, and K.C. Kulander, AIP, Melville, N.Y. (2000), p.137.
37. T. Radozycki and F.H.M. Faisal, Phys. Rev. A **48**, 2407 (1993).
38. C. Szymanowski, V. Véniard, R. Taïeb, and A. Maquet Phys. Rev. A **56**, 700 (1997).
39. H. Reiss, J. Opt. Soc. Am. B **7**, 574 (1990).
40. F.H.M. Faisal and A. Becker, in *Selected Topics on Electron Physics*, Eds., D.M. Campbell, and H. Kleinpoppen, N.Y., Plenum Press (1996) p. 317.

41. C. Szymanowski, Véniard, R. Taïb, A. Maquet, and C.H. Keitel, Phys. Rev. A **56**, 3846 (1997).
42. M.W. Walser and C.H. Keitel, J. Phys. B. **33**, L221 (2000).
43. F.H.M. Faisal and S. Bhattacharryya, Phys. Rev. Lett. **93**, 053002 (2004).
44. M. Getzlaff, B. Heidemann, J. Bansmann, C. Westphal, and G. Schönhense, Rev. of Sci. Inst. **69**, 3913 (1998).
45. U. Fano, Phys. Rev. **178**, 131 (1969).
46. P. Lambropoulos and M.R. Teague, J.Phys.B. **9**, 587 (1976).
47. K.C. Kulander, K.J. Schafer, and J.L. Krause, Phys. Rev. Lett. **66**, 2601-2604 (1991)
48. J.D. Bjorken and S.D. Drell, *Relativistic Quantum Mechanics*, cGraw-Hill, N.Y. (1964).
49. D.M. Wolkow, Z. Physik, **94**, 250 (1935).

Part IV
Laser–Matter Interaction – Relativistic

Relativistic Laser-Plasma Physics

Alexander Pukhov

This review covers recent progress in laser–matter interaction at intensities I above $I_{\rm rel} = 1.37 \cdot 10^{18}{\rm W/cm}^2$. At these intensities, electrons swing in the laser pulse with relativistic energies. The laser electric field is already much stronger than the atomic fields, and any material is instantaneously ionized creating plasma. The most important applications of relativistic laser-plasma include high-gradient acceleration of charged particles, new sources of short-wavelength, and nuclear radiation. The physics of relativistic laser-plasma is highly nonlinear and kinetic. The best numerical tools applicable here are particle-in-cell (PIC) codes, which exploit the fundamental plasma model as an ensemble of charged particles. The usage of massively parallel processing allows to follow simultaneously up to 10^9 numerical particles. This is enough to simulate directly real laser-plasma experiments even if the full-scale three-dimensional PIC simulations are expensive and parametric studies are difficult. In the ultrarelativistic limit $I \gg I_{\rm rel}$, the Maxwell–Vlasov equations acquire a specific symmetry that leads to a very powerful analytical tool: the relativistic similarity theory. It allows to scale the interaction regimes and gives an important guide in the complex physics of relativistic laser-plasmas

PACS numbers:

1 Introduction

The maximum achievable laser powers were growing fast over the last 10 years and have reached the petawatt (10^{15} W) values in a single shot [1, 2, 3]. This enormous power is comparable to that consumed constantly by the whole mankind on the earth. Of course, these powerful laser pulses last for an extremely short time, from few femtoseconds ($1\,{\rm fs} = 10^{-15}{\rm s}$) to a picosecond

A. Pukhov
Institut für Theoretische Physik I, Heinrich-Heine-Universität Düsseldorf, 40225 Düsseldorf, Germany
e-mail: pukhov@tpl.uni-duesseldorf.de

T. Brabec (ed.), *Strong Field Laser Physics*,
DOI: 10.1007/978-0-387-34755-4_18,

(1 ps= 10^{-12}s). Let us now recall that one cycle of the infrared light emitted by these lasers is about 3 fs (3.3 fs for a light with $\lambda = 1\mu m$). It means that these laser pulses represent just a few cycles of radiation. It is this short-pulse duration that allows for the extremely high powers, while the energy remains in a reasonable range from mJ to some 100 J.

The technology of ultrashort-pulse lasers is known as the chirped pulse amplification (CPA) [4]. Here, an initially short seeding pulse is stretched in time by letting it pass through a dispersive element (stretcher), e.g., a set of diffraction grids. The pulse is decomposed in its spectral components. Each spectral component travels a slightly different way depending on its wavelength, and the pulse is stretched in time. It also gains a spectral "chirp": the pulse frequency changes continuously from its head to the tail. The stretched pulse has a lower power and can be linearly amplified in a conventional way. The amplified pulse pertains the chirp and is compressed back to the original short duration by another dispersive element (compressor) conjugated to the stretcher.

Before the CPA invention, laser pulses could be focused only in the two transverse dimensions by corresponding sets of lenses. The CPA technology has allowed it for the first time to compress laser pulses in the third, longitudinal dimension, and this technological breakthrough has immediately lead to a Jump in the achievable powers and focused intensities. The petawatt shots, where an adaptive mirro has been employed, have resulted in the focal intensity $I = 10^{21} W/cm^2$ [2].

The electric field corresponding to this intensity is 10^{14} V/m. No material can withstand such fields. Atoms are ionized instantaneously and plasma is created. The most promising application of these enormous laser fields is the high-gradient acceleration of charged particles. The conventional accelerators used in high-energy physics have accelerating gradient of some 10 MeV/m. This moderate accelerating field defines the monstrous sizes of the accelerators: the acceleration to 100 GeV energies needs an accelerator of several kilometers length. Would it be possible to exploit the laser fields directly, this accelerating distance could be shortened to few centimeters. Unfortunately, the laser fields are oscillatory and transverse. A particle being accelerated by the laser fields directly slips out of the acceleration phase very fast and the maximum energy gain is limited to a few MeV. Thus, one has to elaborate special accelerating schemes, which can avoid the dephasing problem. In this review, we discuss the laser wake field acceleration (LWFA) schemes [5] and direct laser acceleration (DLA) at the betatron resonance [6].

Recently, a major breakthrough has been achieved in the LWFA studies [7]. Independently, three experimental groups have reported quasi-monoenergetic electron beams with energies in the range 70–170 MeV emerging from short-pulse laser interactions with underdense gas Jets [8, 9, 10]. In all these three experiments, the laser pulse duration was comparable with the plasma period. Previously, quasi-monoenergetic electron beams have been predicted

theoretically in 3D PIC simulations [11], where the so-called bubble regime of LWFA has been identified.

The ion acceleration using lasers is also possible. At the presently available laser intensities, it is never accomplished directly by the laser, but is always mediated by the plasma electrons [12, 13, 14].

Another very important application of the relativistic laser-plasma is for novel sources of short-wavelength and nuclear radiation. The electron motion in the relativistic regime is extremely non-linear. Thus, one expects that the electrons radiate high harmonics [15, 16]. Indeed, it appears that the relativistic laser plasma provides several mechanisms for short-wavelength radiation, both coherent [17, 18, 19, 20, 21, 22, 23, 24, 25] and incoherent [26, 27, 28]. We discuss here shortly the possibilities for synchrotron-like radiation from non-linear plasma waves.

2 Free Electron Motion in Electromagnetic Wave. Relativistic Threshold

It is usually accepted that the transition to the relativistic laser-plasma regime begins at intensities above $I\lambda^2 = 10^{18}\,W\mu m^2/cm^2$. To understand the origin of this threshold, let us consider the simplest configuration, where a free charged particle interacts with a plane electromagnetic wave running in the positive z-direction:

$$\mathbf{a}(\zeta) = \mathbf{a_0}(\zeta)\cos k\zeta, \tag{1}$$

where

$$\mathbf{a} = e\mathbf{A}/mc^2 \tag{2}$$

is the relativistically normalized laser vector potential, $\zeta = z - ct$, $k = 2\pi/\lambda$, and λ is the wavelength. We are working in the Coulomb gauge and set the scalar potential of the electromagnetic wave equal to zero, $\phi(\zeta) = 0$.

Although the exact solution of this problem can be found in literature (see, e.g., [29, 30]), we present here some simple fundamental results.

The wave (1) has two important symmetries, each of them leads to an integral of motion preserved during the charged particle motion. First, the fields (1) do not depend on the transverse coordinates. This results in conservation of the generalized transverse momentum:

$$\mathbf{P}_\perp = \mathbf{p}_\perp + \mathbf{a}mc = \text{const}, \tag{3}$$

where $\mathbf{p}_\perp = m\gamma\mathbf{v}_\perp$ is the kinetic momentum and $\gamma = 1/\sqrt{1-(v/c)^2}$ is the relativistic factor.

Second, the laser pulse is a wave running with a constant phase velocity $v_{\rm ph}$, which in vacuum is $v_{\rm ph} = c$. This symmetry delivers the second integral of motion:

$$W = K - p_z c = \text{const}, \tag{4}$$

where $K = (\gamma - 1)mc^2$ is the particle kinetic energy.

Having the two integrals (3) and (4), we can calculate the particle energy and momenta as a function of the laser amplitude. Let us take a particle that has stayed at rest before the laser pulse overtook it. In this case, both integrals are zeroes and we find

$$p_z = \frac{p_\perp^2}{2mc}; \quad K = \frac{a^2}{2}mc^2. \tag{5}$$

From the expression for the kinetic energy K, we see that a particle quivering in a laser pulse gains energy comparable with its rest energy mc^2, when the normalized laser amplitude becomes close to unity: $a_0 = 1$. When we normalize to the electron mass, this amplitude corresponds to a laser intensity:

$$I_0\lambda^2 = 1.37 \times 10^{18} W\,\mu\text{m}^2/\text{cm}^2. \tag{6}$$

The intensity I_0 is generally considered as the threshold to relativistic laser-plasma interactions, because the bulk of plasma electrons start to oscillate at relativistic velocities. Notice that the relativistic intensity (6) scales as λ^{-2}. This gives 10^{18} W/cm^2 for a glass laser with $\lambda = 1\mu$m and only 10^{16} W/cm^2 for a CO_2 laser with $\lambda = 10$mum.

An exact form of the particle trajectory in a plane wave can also be found analytically, if one introduces the "particle internal times" $s = \omega t/\gamma$. For a plane wave with amplitude a_0 and linear polarization in the X-direction, the trajectory in normalized coordinates ζ, η, τ is

$$\zeta = \frac{kz}{a_0^2} = \frac{1}{8}(2s - \sin 2s), \tag{7}$$

$$\eta = \frac{kx}{a_0} = \cos s, \tag{8}$$

$$\tau = ckt = s + \frac{a_0^2}{8}(2s - \sin 2s). \tag{9}$$

The trajectory (7), (8), (9) is shown in Fig. 1. It is self-similar and does not depend on the laser amplitude in the coordinates (ζ, η, τ). However, when we transform back to the physical coordinates, we find that there is a significant difference in the particle motion at non-relativistic, $a \ll 1$, and relativistic, $a > 1$, amplitudes. Mention that while the particle excursion in the polarization

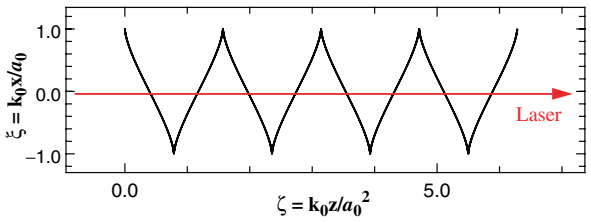

Fig. 1 The self-similar trajectory of an electron in a plane electromagnetic wave

direction scales like the laser amplitude, $\eta \sim a_0$, the longitudinal one scales like the amplitude squared, $\zeta \sim a_0^2$. Thus, at low intensities, particles oscillate mainly in the polarization direction with a small ponderomotive drift in the laser propagation direction. With the transition into relativistic regime, the particle motion becomes predominantly longitudinal. The laser ponderomotive force, $\mathbf{v}_\perp \times \mathbf{B}$, pushes it forward.

As we see from (5), a free electron in a plane electromagnetic wave can get a lot of energy, proportional to the intensity of the wave. At the intensity level of $10^{21}\,\mathrm{W/cm^2}$, one might expect GeV electron energies. Although this value sounds impressive, we must concede that the simple acceleration in vacuum is barely inefficient. From expression (9), we see that the time needed to reach this energy also scales like the laser intensity. Thus, the mean accelerating force $<F>$ acting on a relativistic particle in vacuum saturates at a level $F/mc\omega < 2$. The reason for this unexpected failure is the traitorious behavior of the particle transverse velocity, namely, it rises first at non-relativistic intensities, $v_\perp/c \sim a_0$ for $a_0 \ll 1$, reaches its maximum $v_\perp/c = 2/3$ at $a_0 = 1$, and then goes down inversely proportional to the amplitude, $v_\perp/c \sim 2/a_0$ for large a_0! As a consequence, the $\mathbf{v}_\perp \times \mathbf{B}$ force does not grow anymore, no matter how intense the laser pulse is.

Moreover, the analytic solution (5) is valid for a plane wave only, i.e., for a laser pulse with an infinite power. Only in this particular case the two integrals of motion (3) and (4) hold. This solution is an exception, rather than a rule. Already small deviations from the plane wave geometry break this symmetry and the electron motion in realistic focused laser pulses scales differently.

Let us consider a focused laser pulse. Nearby the focal plane, one has

$$\mathbf{a} = \mathbf{a}(\zeta_\mathrm{g}, \mathbf{r}) \cos k\zeta_\mathrm{ph}, \tag{10}$$

where $\zeta_\mathrm{ph} = z - v_\mathrm{ph} t$, $\zeta_\mathrm{g} = z - v_\mathrm{g} t$, and v_ph and $v_\mathrm{g} < c$ are the phase and the group velocities, respectively. It is important to mention here that a focused electromagnetic wave has not only the transverse components of the vector potential, but also the longitudinal one:

$$\partial_z a_z = -\nabla_\perp \cdot \mathbf{a}_\perp. \tag{11}$$

This follows immediately from the Coulomb gauge condition $\nabla \cdot \mathbf{a} = 0$.

When the focused laser pulse interacts with particles in vacuum, the particles get scattered out from the focal spot. Unfortunately, there is no general exact

analytic solution in this case. However, at low laser intensities $a \ll 1$, the equation of motion can be averaged over the fast laser oscillations and the so-called *relativistic ponderomotive force* (RPF) is introduced [32]:

$$\frac{1}{mc}\frac{\mathrm{d}\overline{\mathbf{p}}}{\mathrm{d}t} = -\nabla\frac{\overline{a^2}}{2}, \tag{12}$$

where $\overline{\mathbf{p}}$ is the electron momentum averaged over the laser period. The RPF concept is a valid description, provided the wave amplitude varies slowly with respect to the wave phase, so that a multiple scale analysis of the particle motion makes sense.

Equation (12) is independent of the laser polarization and works in such a way that electrons are expelled from the regions of high intensity. If one takes a laser pulse focused into a round spot, the electron scattering is radially symmetric, no matter what the laser polarization is.

Quesnel and Mora [31] have performed extensive numerical simulations of laser pulse interaction with electrons in vacuum. They found that it is the small longitudinal component of the vector potential (11) that makes the scattering radially symmetric. Figure 2a taken from [31] shows electron trajectory scattered by a linearly polarized laser pulse focused in a Gaussian spot $a = a_0 \exp(-r^2/\sigma^2 - \zeta^2/(c\tau)^2)$ with $a_0 = 0.3, \sigma = 10\mu\mathrm{m}$, $\tau = 200\,\mathrm{fs}$. Curve 1 gives the scattering including the longitudinal component of the vector potential; it practically coincides with the ponderomotive model. For comparison, curve 2 has been calculated discarding a_z and results in electron confining within the plane of laser polarization.

The RPF concept may remain valid even at higher laser intensities. Equation (12) takes then the form [31, 33]

$$\frac{\mathrm{d}\overline{\mathbf{p}}}{\mathrm{dt}} = -\frac{mc^2}{\overline{\gamma}}\nabla\overline{\gamma}. \tag{13}$$

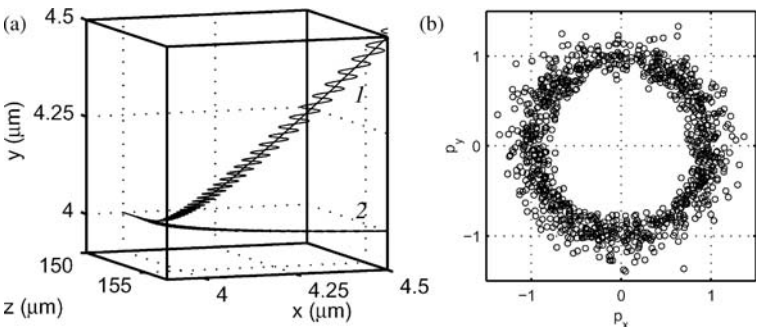

Fig. 2 Scattering of an electron by a focused laser pulse (taken from [31]). (**a**) $a_0 = 0.3$, curve 1 includes the longitudinal field, curve 2 neglects it; (**b**) $a_0 = 3$, final transverse momenta of scattered electrons (see text for further details)

Figure 2b shows final transverse momenta of electrons scattered by a laser pulse with $a_0 = 3, \sigma = 10\mu\text{m}$, and $\tau = 350\,\text{fs}$. Although the laser pulse was linearly polarized, the scattering is nearly symmetric.

Quesnel and Mora [31] have introduced the dimensionless parameter $\alpha = k\sigma/(1 - v_z/c)$, where v_z is the longitudinal velocity of the electron. The scattering is ponderomotive if the parameter $\alpha \ll 1$. In the opposite case, $\alpha > 1$, the electron motion is more complicated and asymmetries due to the polarization appear.

Electrons are the lightest charged particles; they absorb most of the laser energy and reach the relativistic regime first. One may repeat the calculations for ions as well and use in (2) an ion mass instead of the electron one. Taking, e.g., protons, we find that the corresponding relativistic intensity threshold is

$$I_\text{p} = (M_\text{p}/m)^2 I_0 \approx 5 \times 10^{24}\ \text{W}\mu\text{m}^2/\text{cm}^2. \tag{14}$$

The intensity (14) is far beyond the present laser technology. However, the new concepts of optical parametric amplification (OPA-CPA) [34] might make even these fantastic intensities technologically feasible, see in the chapter of Ross.

At the "electron relativistic intensity" I_0 (6), protons oscillate in the laser field with merely some 100 eV energy. Any energetic ions observed in laser–matter interaction experiments till now have been accelerated not directly by the laser field, but by plasma fields induced by the laser-heated electrons [12, 13, 14, 35, 36, 37, 38, 39, 40, 41].

3 Relativistic Similarity

As we have seen above, electron motion at highly relativistic laser amplitudes, $a \gg 1$, may become quite complicated. The simple perturbation theory that uses the laser amplitude a as a small parameter [42] becomes invalid.

Fortunately, the Maxwell–Vlasov system of equations acquires an additional symmetry at the ultra-relativistic laser amplitudes $a_0 = eA_0/mc^2 \gg 1$. Gordienko and Pukhov [43] have shown for the first time that the similarity parameter $S = n_\text{e}/a_0 n_\text{c}$ exists, where n_e is the plasma electron density and $n_\text{c} = m\omega_0^2/4\pi e^2$ is the critical density for a laser with frequency ω_0. The basic ultra-relativistic similarity states that laser-plasma interactions with different a_0 and n_e/n_c are similar if the parameter $S = n_\text{e}/a_0 n_\text{c} = \text{const}$..

Let us consider collisionless laser-plasma dynamics and neglect the ion motion. We also neglect bremsstrahlung and radiation damping. The electron distribution function $f(t, \mathbf{r}, \mathbf{p})$ is described by the Vlasov equation:

$$\left(\partial_t + \mathbf{v}\partial_\mathbf{r} - e(\mathbf{E} + \mathbf{v} \times \mathbf{B}/c)\partial_\mathbf{p}\right) f(t, \mathbf{p}, \mathbf{r}) = 0, \tag{15}$$

where $\mathbf{p} = m\gamma\mathbf{v}$ and self-consistent fields $\mathbf{E}$ and $\mathbf{B}$ satisfy the Maxwell equations [44].

We suppose that the laser pulse vector potential at the time $t = 0$ short before entering the plasma is $\mathbf{A}(t=0) = \mathbf{a}\big((y^2+z^2)/R^2, x/c\tau\big)\cos(k_0 x)$, where $k_0 = \omega_0/c$ is the wavenumber, R is the focal spot radius, and τ is the pulse duration. If one chooses a definite initial laser envelope $\mathbf{a}(\mathbf{r}_\perp, x)$, then the laser-plasma dynamics depends on four dimensionless parameters: the laser amplitude $a_0 = \max|e\mathbf{a}/mc^2|$, the focal spot radius $k_0 R$, the pulse duration $\omega_0\tau$, and the plasma density ratio n_e/n_c.

Now we are going to show that in the ultra-relativistic limit when $a_0 \gg 1$, the number of independent dimensionless parameters reduces to three: $k_0 R$, $\omega_0\tau$, and S, where the similarity parameter S is

$$S = \frac{n_e}{a_0 n_c}. \tag{16}$$

Let us introduce the new dimensionless variables:

$$\begin{gathered} \hat{t} = S^{1/2}\omega_0 t, \quad \hat{\mathbf{r}} = S^{1/2}k_0\mathbf{r}, \quad \hat{\mathbf{p}} = \mathbf{p}/mca_0, \\ \hat{\mathbf{A}} = \frac{e\mathbf{A}}{mc^2 a_0}, \quad \hat{\mathbf{E}} = \frac{S^{-1/2}e\mathbf{E}}{mc\omega_0 a_0}, \quad \hat{\mathbf{B}} = \frac{S^{-1/2}e\mathbf{B}}{mc\omega_0 a_0}, \end{gathered} \tag{17}$$

and the new distribution function $\hat{f}$ is defined as

$$f = \frac{n_e}{(mca_0)^3}\hat{f}(\hat{t}, \hat{\mathbf{p}}, \hat{\mathbf{r}}, a_0, S, \hat{R}, \hat{\tau}), \tag{18}$$

where $\hat{R} = S^{1/2}k_0 R$ and $\hat{\tau} = S^{1/2}\omega_0\tau$.

The normalized distribution function $\hat{f}$ is a universal one describing the interaction of the given laser pulse with a given initial plasma profile. It satisfies the equations

$$\big[\partial_{\hat{t}} + \hat{\mathbf{v}}\partial_{\hat{\mathbf{r}}} - (\hat{\mathbf{E}} + (\hat{\mathbf{v}}\times\hat{\mathbf{B}}))\partial_{\hat{\mathbf{p}}}\big]\hat{f} = 0, \tag{19}$$

$$\begin{gathered} \nabla_{\hat{\mathbf{r}}}\cdot\hat{\mathbf{E}} = 4\pi(1+\hat{\rho}), \nabla_{\hat{\mathbf{r}}}\cdot\hat{\mathbf{B}} = 0, \\ \nabla_{\hat{\mathbf{r}}}\times\hat{\mathbf{B}} = 4\pi\hat{\mathbf{J}} + \partial_{\hat{t}\hat{\mathbf{E}}}, \nabla_{\hat{\mathbf{r}}}\times\hat{\mathbf{E}} = -\partial_{\hat{t}}\hat{\mathbf{B}}, \end{gathered} \tag{20}$$

where $\hat{\mathbf{v}} = \hat{\mathbf{p}}/\sqrt{\hat{\mathbf{p}}^2 + a_0^{-2}}$, $\hat{\rho} = -\int\hat{f}\,\mathrm{d}\hat{\mathbf{p}}$, $\hat{\mathbf{j}} = -\int\hat{\mathbf{v}}\hat{f}\,\mathrm{d}\hat{\mathbf{p}}$, and the initial condition for the vector potential is

$$\hat{\mathbf{A}}(\hat{t}=0) = \hat{\mathbf{a}}((\hat{y}^2+\hat{z}^2)/\hat{R}, \hat{x}/\hat{\tau})\cos(S^{-1/2}\hat{x}), \tag{21}$$

with the slow envelope $\hat{\mathbf{a}}$ such that $\max|\hat{\mathbf{a}}| = 1$.

Equation (19) together with the initial condition (21) still depends on the four dimensionless parameters $\hat{R}$, $\hat{\tau}$, S, and a_0. However, the parameter a_0 appears only in the expression for the electron velocity. In the limit $a_0 \gg 1$, one can write

$$\hat{\mathbf{v}} = \hat{\mathbf{p}}/\sqrt{\hat{\mathbf{p}}^2 + a_0^{-2}} \approx \hat{\mathbf{v}} = \hat{\mathbf{p}}/|\hat{\mathbf{p}}|. \tag{22}$$

Consequently, for the ultra-relativistic amplitude $a_0 \gg 1$, the laser-plasma dynamics does not depend separately on a_0 and n_e/n_c. Rather, they converge into the single similarity parameter S.

The ultra-relativistic similarity means that for different interaction cases with $S = \text{const}$, plasma electrons move along the same trajectories. Number of these electron N_e, their momenta $\mathbf{p}$, and the plasma fields scale as

$$\mathbf{p} \propto a_0; \;\; N_e \propto a_0; \tag{23}$$

$$\phi, \mathbf{A}, \mathbf{E}, \mathbf{B} \propto a_0, \tag{24}$$

for $\omega_0 \tau = \text{const}$, $k_0 R = \text{const}$, and $S = \text{const}$.

The ultra-relativistic similarity is valid for arbitrary S-values. The S parameter appears only in the initial condition (21) so that $S^{-1/2}$ plays the role of the laser frequency. It separates the relativistically overdense plasmas with $S \gg 1$ from the underdense ones with $S \ll 1$.

Let us discuss shortly the applicability area of the similarity theory. The only approximation made is expressed by formula (22). It states that all the electron velocities are equal to the vacuum light velocity c. Is this approximation well grounded in the context of the laser wake field acceleration? We stress that although the electron velocities are always c, their longitudinal components can be arbitrary depending on the particular direction of the 3D electron momentum.

What matters in the LWFA is the electron trapping and dephasing. Both these phenomena are correctly included in our similarity theory. The trapping and dephasing depend on the *longitudinal* component of the electron velocity:

$$v_\parallel = \frac{p_\parallel}{\sqrt{p_\parallel^2 + p_\perp^2 + m^2 c^2}}. \tag{25}$$

When $p_\perp^2 \gg m^2 c^2$, one can neglect the term $m^2 c^2$ under the square root in the denominator of expression (25). According to the similarity theory the transverse electron momentum $p_\perp$ scales as a_0, see (23). Thus, the approximation (22) is valid in the *three-dimensional* geometry if $a_0 \gg 1$.

The similarity in interactions with overdense plasmas has been considered in [17, 18], where the universal harmonics spectra have been derived and their scalability toward very high laser intensities has been discussed. Applied to

underdense plasmas, the similarity theory leads to elegant scalings on the energy and the number of accelerated electrons, as well as the acceleration length [43].

4 Numerical Simulation of Relativistic Laser-Plasma. Particle-in-Cell Method

During the past decades, particle-in-cell (PIC) methods have been proven to be a very reliable and successful method of kinetic plasma simulations [45, 46, 47, 48]. This success of PIC codes relies to a large extent on the very suggestive analogy with the actual plasma. The plasma in reality is an ensemble of many individual particles, electrons and ions, interacting with each other by the self-consistently generated fields. The PIC code is very similar to that, with the difference that the number of numerical particles, or macroparticles we follow in the code, may be significantly smaller. One may think as if one numerical "macroparticle" is a clump, or cloud, of many real particles, which occupy a finite volume in space and all move together with the same velocity. The consequent conclusion is that we have a "numerical plasma" consisting of heavy macroparticles, which have the same charge-to-mass ratio as the real plasma electrons and ions, but substitute many of those. This simplified point of view is straightforward, very intuitive, and not always incorrect.

Historically, the 2D code ZOHAR developed by Langdon and Lasinski [49] and the 3D code TRISTAN developed by O. Buneman [50] were the first multidimensional relativistic electromagnetic PIC codes for plasma simulations. The 2D code ZOHAR appeared to be particularly successful as 2D problems were much easier to handle on computers of that time. Still, the 2D mesh allows to study some multidimensional effects. As an example, we mention here the pioneering simulation of Wilks et al. showing the possibility of channel boring through overdense plasma layer by the laser light pressure [51].

The PIC codes appeared to be so effective for simulations of laser-plasma interactions in relativistic short-pulse regime that research groups at different places have developed their own multidimensional PIC codes. The main progress has been achieved using *parallelization*, when the simulation domain is distributed on a grid of individual processors [52]. Various parallel PIC codes for laser-plasma interactions exist now. We may mention the codes OSIRIS [53] and PEGASUS [54] from the UCLA group, the code Virtual Laser Plasma Laboratory (VLPL) of Pukhov [55], the code REMP written by Esirkepov [56], a 2D PIC code maintained by Adam at Ecole Polytechnique [57], 3D PIC codes written by Ruhl [58], by Sentoku [59], and other codes exist as well. Although it seems that all these codes produce similar results, there was no attempt to gauge all of them against each other and no single 3D PIC "volkscode" for laser-plasma interaction exists in public domain.

All these codes solve the full set of Maxwell equations for the fields and relativistic equations of motion for the particles. To simulate the realistic

experimental parameters, a huge number of numerical particles, on the order of 10^9, must be followed in these codes [55]. This is possible only when massively parallel processing is used. Yet inspite of the huge computational power, the direct PIC simulations of laser-plasma interaction become only possible because of the very short laser pulse duration. The laser pulses consist of only 10–100 optical cycles, and it is this property that allows us to apply the fully electromagnetic PIC code that resolves the laser wavelength. For long laser pulses, one is still forced to use anenvelope approximation.

The direct PIC simulations are able to reproduce experiments. They are very detailed. In fact, they are about as complicated as the experiments themselves. However, the simulations have a significant advantage: we can apply any kind of numerical diagnostics one can imagine. This provides a highly appreciated insight in the non-linear processes of laser-plasma interaction at relativistic intensities.

5 Relativistic Self-Channeling of Light in Plasmas

A relativistically intense laser beam propagating in an underdense plasma modifies the plasma permittivity and the refractive index, which in the weakly non-linear regime can be expressed as

$$n_{\mathrm{rel}}^2 = \epsilon = 1 - \frac{\omega_{\mathrm{p}}^2}{\omega^2}, \tag{26}$$

where $\omega_{\mathrm{p}}^2 = 4\pi ne^2/\gamma m$ is the relativistically corrected plasma frequency. The relativistic mass γm of electrons quivering in the laser pulse increases. In addition, the ponderomotive force of the laser pulse pushes the plasma electrons radially out of the focal spot. Both these effects diminish the local plasma frequency and increase the plasma refractive index (26). The medium then acts as a positive lens. One may show that when the laser power P exceeds the critical value

$$P_{\mathrm{cr}} \approx 17\left(\omega/\omega_{\mathrm{p}}\right)^2 \mathrm{GW}, \tag{27}$$

the laser pulse experiences relativistic self-focusing and channels through the plasma. This has been established both theoretically [60, 61, 62, 63] and experimentally [64, 65].

The power (27) is not too high. Multi-terawatt and petawatt lasers may easily exceed it by a few orders of magnitude. In this case, the laser has enough power to generate not a single, but multiple channels. This effect has been studied in envelope and paraxial approximations [66] and is known as the relativistic filamentation.

The threshold for relativistic self-focusing/filamentation depends on the laser power only. The analytical theory of self-focusing has been developed in the weakly relativistic approximation, $a<1$. When the laser intensity overcomes the relativistic threshold (6), new physical effects appear.

As we have already discussed, trajectories of electrons quivering in the laser pulse, (7), (8), (9), change qualitatively, when the laser amplitude becomes relativistic, $a>1$. At these intensities, the $\mathbf{v}\times\mathbf{B}$ force of the laser pulse drives electrons forward, in the light propagation direction. In plasma, all electrons trapped in the laser channel are driven, and each laser filament carries a strong electron current.

These currents of relativistic electrons pushed forward by the laser pulse magnetize the plasma. The current densities amount to a sizeable fraction f of enc, where n is the background electron density, and generate quasi-static magnetic fields $B_\perp^s=(fen_e)2\pi r$ at distance r from the axis of a current filament. The field $B_\perp^s$ may become as strong as the magnetic field of the light wave itself, which is $B=aB_0$ in units of $B_0=mc\omega/e$. For light of wavelength $\lambda=2\pi c/\omega=1\mu m$, one obtains $B_0=107.1$ MG. In units of B_0, the quasi-static magnetic field has the form

$$B_\perp^s/B_0=(fn_e/n_c)\pi r/\lambda \tag{28}$$

and is of order B_0 when n_e approaches the critical density $n_c=\pi mc^2/(e\lambda)^2$. Notice that the cyclotron frequency ω_c corresponding to $B_\perp^s$ satisfies $\omega_c/\omega=B_\perp^s/B_0$ and may become resonant with the light frequency, affecting the index of refraction.

In this complex situation, a qualitatively new behavior was observed in 2D [67] and 3D PIC simulations [68]. It was found that the quasi-static magnetic field may become strong enough to pinch the relativistic electrons. The co-directed currents flowing in laser filaments magnetically attract each other and may finally coalesce into a narrow single channel [68]. Relativistic electrons carrying these currents modify the plasma refraction index and guide the light. The path of light follows the electron deflection, and the multiple laser filaments also coalesce and form the "super-channel".

A representative case with an incident intensity of 1.24×10^{19} W/cm^2 ($a=3$, $\lambda=1\mu m$) has been chosen in three-dimensional PIC simulations: Fig. 3, [68]. It confirms the formation of a single propagation channel with considerably enhanced concentration of light on the axis. The incident beam first propagates through an unstable filamentory stage and then collapses into a single channel with a width of $1-2\lambda$. We mention that paraxial and envelope approximation as well as hydrodynamic modeling are insufficient to treat the effects discussed here; structures on the scale of a wavelength are involved and non-Maxwellian velocity distributions do demand a kinetic treatment.

A super-channel very similar to the one calculated by the 3D PIC code, [68], has been observed in experiments with the VULCAN laser at Rutherford Appleton Laboratory, where a 10 TW laser pulse interacted with a long-range

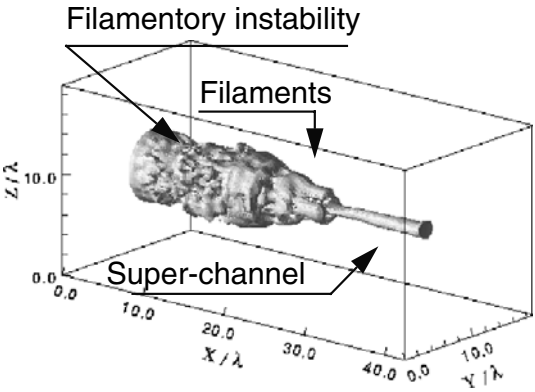

Fig. 3 Perspective view of the self-focusing pulse at time 180 fs. The plotted surface corresponds to $0.67 < I_{max} >$, where the maximum intensity $< I_{max} >$ is taken in each (Y, Z) plane

preformed plasma on a solid body surface [69]. Also the ultra-strong magnetic fields have been detected later using the Faraday rotation technique for a probing laser beam traversing the channel [70]. Although the probing beam has been sent some 18 ps after the main laser, magnetic fields of the order of 5–10 MG were still present in the channel. Indeed, the magnetic fields, once generated, get frozen into the plasma and decay slowly due to collisions or channel expansion.

6 Multiple Filamentation of Wide Laser Pulses

We have seen how multiple laser filaments coalesce into a single super-channel, Fig. 3. Of course, this happens not always. The necessary condition is that the laser pulse is not too wide initially. Indeed, if the laser pulse is much wider than the plasma skin length $d_s = c/\omega_p$, the distance between the individual filaments may be so large that their individual magnetic fields are shielded by the surrounding plasma. These filaments do not feel each other anymore and cannot coalesce. If the laser pulse is relativistically intense, $a_0 >> 1$, then the condition on the laser radius R for the filamentation gets the S-scaling: $k_0 R > S^{-1/2}$.

As an example of the filamentaion, we have simulated a petawatt laser pulse with initially wide focus diameter, 30 μm, and intensity, $I = 10^{20}$ W/cm^2, incident on a plasma with density exponentially growing in the laser propagation direction like $n = n_0 \exp(x/L)$, where the scale length $L = 30$ μm. The laser pulse had a Gaussian temporal profile with the full width at half maximum (FWHM) of 330 fs. The simulation results are shown in Fig. 4.

We see that the strong filamentation starts at the plasma density $n \approx 3 \times 10^{20}$ 1/cc. Later, the tree-like coalescence of the neighboring filaments leads to formation of several larger filaments. The distance between these new filaments is already too large for them to feel each other, and we see no single super-channel formation. The very similar filamentary pattern has been recently observed in 100 TW shots of the GEKKO-XII laser at ILE, University of Osaka [71].

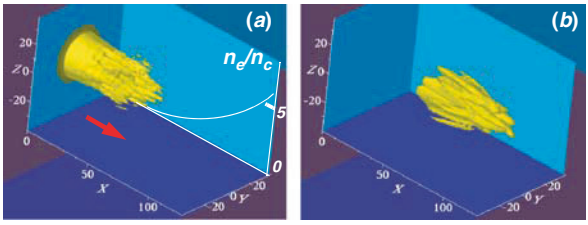

Fig. 4 Multi-filamentation and tree-like filament coalescence of a wide laser pulse of petawatt power. Several super-channels are formed finally, which are screened by plasma and do not interact further

These issues of laser channeling, plasma cavitation along the channel, laser energy conversion into fast electrons, and magnetic field generation are the key issues for fast ignition of fuel targets in the context of inertial confinement fusion [72].

7 Direct Laser Acceleration of Electrons in Plasma Channels

We have seen in the previous section that when a relativistically intense laser pulse channels in sub-critical plasma, it drives strong currents of relativistic electrons [68]. These electrons easily exit the interaction region and are detected experimentally. Both experiments [2, 73, 74, 75, 76] and particle-in-cell (PIC) simulations [68, 77, 78] suggest that this conversion does operate with significant, up to 30–40%, efficiency. These electrons have usually quasi-thermal spectra, which can be characterized by an exponential slope with some effective "temperature".

In [79], the authors have measured angularly resolved and absolutely calibrated spectra of multi-MeV electrons produced by relativistic self-channeling of a laser pulse in a high-density gas Jet. Laser pulses of 200 fs with $P_L = 1.2\,\mathrm{TW}$ were propagating in He plasmas with electron density in the range of $3 \times 10^{19} - 4 \times 10^{20}\ \mathrm{cm}^{-3}$. While varying the plasma density, the highest electron energies were obtained at $n = 2 \times 10^{20}\,\mathrm{cm}^{-3}$. The experimental energy spectrum is marked in Fig. 5 by dots. It follows a Boltzmann-like distribution with an effective temperature of 5 MeV and extends to 12.5 MeV which was the

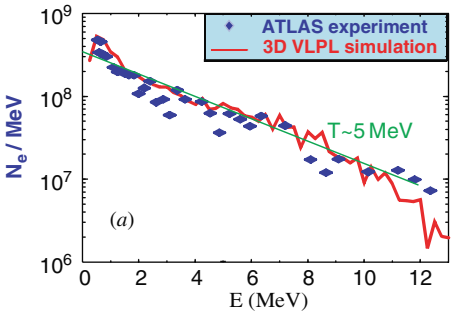

Fig. 5 Electron spectrum measured experimentally, [79], in laser beam direction (*diamonds*) and exponential fit yielding an effective temperature of 5 MeV (*dotted line*); the prediction of 3D PIC simulations is also shown (*solid line*)

spectrometer limit. The solid line in Fig. 5 represents the VLPL results for a simulation. A good agreement between the 3D PIC simulations and the experimental measurements is seen not only in the spectral form but also in the absolute numbers.

The spectral "temperature" depends both on the laser intensity and on the plasma conditions. The tail of these energy spectra reaches far behind the normal ponderomotive energy. A set of 3D PIC simulations for variable laser powers have been reported in [6], where laser pulses relativistically channeled through nearly critical plasmas. The spectra indicate an approximately exponential roll-off at high energies: $n_e(\varepsilon)\tilde{n}_0 \exp(-\varepsilon/T_{\text{eff}})$, with an "effective temperature" T_{eff} growing with the laser intensity. The results of the numerical simulations suggest that T_{eff} grows like the square root of the intensity:

$$T_{\text{eff}} \sim \alpha (I/I_{18})^{1/2}, \tag{29}$$

where the coefficient is $\alpha \approx 1.5$ MeV. Figure 6 illustrates this scaling. Results of 3D PIC simulations and experiments done at MPQ, Garching, are shown here. In the experiment, different laser intensities were achieved by changing the laser pulse duration.

The scaling of the effective temperature T_{eff} with laser intensity like $\propto I^{1/2}$ coincides with the results of 2D PIC simulations [51], in which a laser pulse interacted with a *sharply ramped* plasma–vacuum interface, and the electrons were ponderomotively heated [80]. The proportionality factor α obtained in the 3D simulations of laser channeling is significantly higher than that in [51]. This higher temperature is an indication of the special mechanism of electron acceleration mediated by quasi-static fields existing in laser channels [6].

Ponderomotive expulsion of background plasma electrons out of the channel creates a radial electrostatic field. At the same time, the current of accelerated electrons generates the azimuthal magnetic field. Both these fields depend about linearly on radius and reach their maxima at the channel boundaries, as shown in Fig. 7. The channel works as a potential well. A relativistic electron

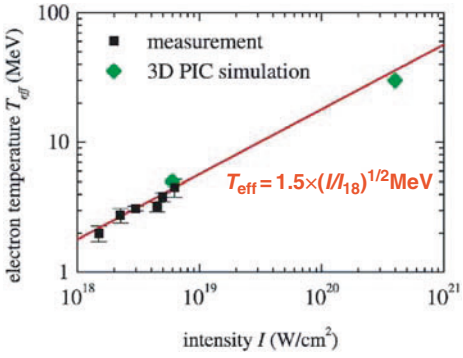

Fig.6 Effective"temperature" of the accelerated electrons for different laser intensities. The best fit gives scaling $T_{\text{eff}} \propto \alpha (I/I_{18})^{1/2}$, with $\alpha \approx 1.5$ MeV

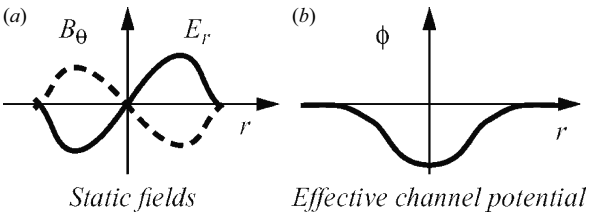

Fig. 7 (**a**) Static electric and magnetic fields in the laser-plasma channel and (**b**) the corresponding effective potential for a relativistic electron

trapped in the channel oscillates radially at the betatron frequency which is roughly $\omega_\beta = \omega_p/2\gamma^{1/2}$ and does not depend on the degree of channel cavitation. These oscillations are along the laser polarization, and thus an efficient energy coupling is possible.

An electron running along the laser propagation with velocity v_z witnesses a strongly downshifted optical frequency. This downshift can be so strong that the transverse betatron oscillations are in resonance with the laser. The resonance condition is

$$\omega_\beta = \left(1 - \frac{v_z}{v_{ph}}\right)\omega_0. \tag{30}$$

It states that when an electron makes one oscillation, the electromagnetic wave, which propagates with a phase velocity v_{ph}, overtakes it exactly by one period, Fig. 8. This is the inverse free electron laser mechanism. The only difference is that instead of the usual spatially periodic wiggler we have the betatron channel frequency.

The resonance condition (30) can be fullfilled for electrons with different energies running at different (small) angles with respect to the channel axis. This effect produces not a monoenergetic spectrum, but rather a Boltzmann-like distributions, see Figs. 5 and 6.

Despite the interaction complexity, the scaling (29) directly follows from the relativistic similarity theory [43]. Let us consider the configuration, where a

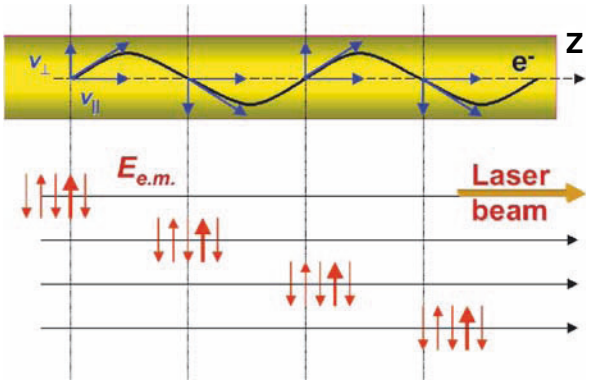

Fig. 8 Resonance between the electromagnetic wave and a co-propagating relativistic electron. The electron makes transverse oscillations in the channel fields along the laser polarization and stays in phase with the electric field of the wave, when the resonance condition (30) is satisfied

relativistically intense laser pulse is incident onto a plasma with an exponential density profile. If the pulse Rayleigh length $Z_R = \pi R^2/\lambda$ is much larger than the characteristic length of the density profile, then the laser will propagate up to a density which scales as the laser amplitude a_0. Consequently, the similarity parameter $S = n_e/a_0 n_c$ is automatically maintained constant and the interaction must be similar. At the same time, the energies and the number of accelerated electrons scale proportional to the laser amplitude a_0.

8 Laser Wake Field Acceleration

In the previous section, we have discussed the direct laser acceleration of electrons. We have seen that this mechanism produces electron spectra of a quasi-thermal form. The future applications for high-energy physics, however, require electron beams of much better quality. They must have low transverse emittance and be monoenergetic. Such beams might be generated by lasers in a plasma employing another mechanism of acceleration: laser wake field acceleration (LWFA) [5, 42].

When a laser pulse propagates through underdense plasmas, it excites a running plasma wave oscillating at the plasma frequency ω_p. The wave trails the laser pulse with the phase velocity set by the laser pulse group velocity $v_{ph}^{wake} = v_g$. It is useful to introduce the relativistic γ-factor related with the pulse group velocity $\gamma_g = 1/\sqrt{1 - v_g^2/c^2}$. The electric field of the plasma wave is longitudinal, i.e., it points in the propagation direction. A relativistic electron can ride on this plasma wave staying in phase with this longitudinal electric field over large distances and be accelerated to high energies.

The laser pulse can excite the plasma wave in different ways. The excitation is most effective, when the laser pulse is shorter than the plasma wavelength, λ_p, and fits completely into the first wave bucket.

The length of the laser pulse is a parameter of particular significance. The pattern of wake field excitation differs significantly for laser pulses longer and shorter than the plasma period. The long laser pulse gets self-modulated with the plasma period, and the resonance between this self-modulation and the plasma frequency leads to effective wake field excitation. The corresponding regime of particle acceleration is called self-modulated laser wake field acceleration (SM-LWFA) [81, 82, 83, 84] in contrast to the short-pulse LWFA described before.

To estimate the maximum energy gain of a relativistic electron in the laser wake field, one introduces the so-called dephasing length L_d. It defines how long the electron remains in the accelerating phase of the wake that makes roughly one half of λ_p. Lorentz transformations then lead to the expression $L_d = 0.5\gamma_g^2\lambda_p$. Consequently, the maximum energy gain $W_{max} = eE_{max}L_d$, where E_{max} is the amplitude of the wake. Here we have supposed that the laser depletion length L_{depl} is longer than the dephasing length: $L_{depl} > L_d$.

To achieve a high quality of the accelerated electron beam, one needs a perfectly synchronized external injector that can produce ultrashort electron bunches, much shorter than the plasma wavelength to occupy a small portion of the accelerating phase, where the electric field is nearly constant. Different schemes have been proposed to accomplish the electron injection by all-optical means involving two or more laser pulses [85, 86, 87].

9 3D Regime of Relativistic LWFA: The Bubble

The properties of laser wake fields can be well described analytically when the laser amplitude is not too high and the plasma wave is regular. However, when the electric field of a planar plasma wave reaches the limit $E_{wb}/E_0 = \sqrt{2(\gamma_p - 1)}$, where $\gamma_p = (1 - v_g^2/c^2)^{-1/2} = \omega_0/\omega_p$, the wave breaks [88]. The wave breaking is manifested in a multi-stream electron motion. The wave amplitude is so high that the oscillation velocity of electrons in the wave becomes comparable with the wave phase velocity. As a consequence, the background plasma electrons can catch the wave, be trapped in the wave potential, and be accelerated. The wave breaking regime is extremely non-linear and needs kinetic description. What happens after the wave is broken, depends on the geometrical dimensionality of the wave breaking region. In the simplest 1D geometry, the breaking happens always in the first half plasma wave. In 2D and 3D geometries, the breaking depends on the strength of plasma wave excitation and other plasma conditions. It has been noticed by the authors of [89, 90, 91, 92] that in the multidimensional relativistic regime the plasma wave fronts are curved. The wave breaks near the axis and for lower values of the electric field than the plane wave limit. Because the breaking region can occupy Just a small portion of the wave around the axis, the large-scale structure of the wave may remain stable. The wave as a whole survives the breaking, and the trapped electrons can be accelerated over large distances and gain energy.

Wave breaking turns out to be of central importance because it leads to abundant self-trapping of electrons in the potential of the wave bucket which are then accelerated in large numbers. This results in high conversion efficiency of laser energy into relativistic beam energy. Trapping of electrons in the plasma waves is a key topic for LWFA. Injection and acceleration of external beams have been demonstrated experimentally [93]. Creation of trapped electrons inside the wave bucket has been proposed, applying supplementary laser pulses [85, 86]. However, copious amounts of accelerated electrons have been observed when driving waves beyond the breaking threshold; this has been shown in SM-LWFA experiments with single TW laser pulses longer than λ_p [94, 95, 96, 97, 98].

When the laser pulse power increases and the pulse duration becomes shorter, electrons can be accelerated in plasmas, where the plasma period is comparable with the pulse duration. In the experiments done at LOA in France,

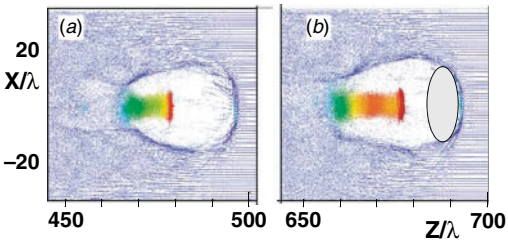

Fig. 9 Solitary laser-plasma cavity produced by 12 J, 33 fs laser pulse. (XY)-cuts of electron density are shown. (**a**) $ct/\lambda = 500$, (**b**) $ct/\lambda = 700$. *Each dot* represents a numerical electron; the *dashed* region schematically shows the laser pulse position

short and relativistically intense laser pulses have propagated through underdense plasma Jets [99]. Electrons with energies up to 200 MeV have been registered, and the energy spectrum has shown some deviations from the Boltzmann-like distribution in the highest energy tail.

A new, highly non-linear regime occurs for laser pulses with large amplitude, $a \gg 1$. The excited wake field takes a particular form of a solitary "bubble" [11]. In this regime, the laser ponderomotive force is high enough to sweep out all electrons out from the first half-plasma wave. As a consequence, an electron cavity, or bubble is formed, Fig. 9, and the wave breaking has washed out all downstream structure. Although the bubble is empty from the cold background electrons, a stem of trapped and accelerated electrons is growing out of the bubble base. Comparing Fig. 9a and b, we see that the cavity stretches and the stem elongates with time. At $ct/\lambda = 700$, the stem contains about 3.5×10^{10} electrons with energy 300 ± 30 MeV. They have an angular spread of $\pm 2^\circ$ and represent a genuine beam of 1.8 J full energy. This amounts to 15% of the incident laser energy.

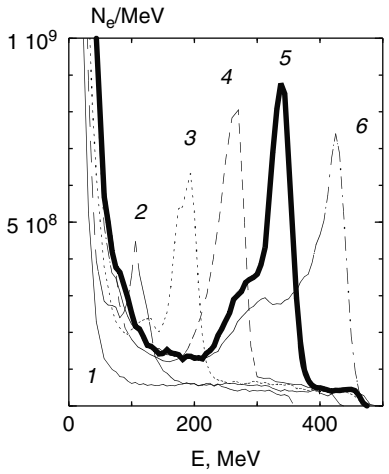

Fig. 10 Spectra of accelerated electrons (from [11]): of the 33 fs, 12 J laser pulse: (1)$ct/\lambda = 350$, (2)$ct/\lambda = 450$, (3)$ct/\lambda = 550$, (4)$ct/\lambda = 650$, (5)$ct/\lambda = 750$, (6)$ct/\lambda = 850$

The growth of the stem and the evolution of its spectrum are continuous. This is shown in Fig. 10. At the time $ct/\lambda = 350$, the high-energy branch of the spectrum corresponding to the stem has the plateau structure. However, the spectrum changes at time $ct/\lambda = 450$ and develops a distinct peak which grows in time. This peak starts to appear when the total charge of the stem becomes equal to the charge expelled from the cavity by the driving laser pulse. Then the cavity elongates, and this has the consequence that the front and the rear sides of the cavity move at different speeds. The formation of the energy peak has been described in detail in [11].

10 Scaling Laws for the Bubble Regime of Electron Acceleration

The relativistic similarity theory of Gordienko and Pukhov [43] allows to write down simple scalings on the electron acceleration in the Bubble regime. The similarity theory [43] tells us that the Bubble regime is stable and scalable.

The optimal radius R of the laser focal spot is

$$k_0 R \approx S^{-1/2}. \tag{31}$$

For the acceleration to be efficient and to generate structured (quasi-monoenergetic) electron energy spectra, the

$$\tau \leq R/c. \tag{32}$$

The characteristic acceleration length L_{acc} scales as

$$L_{\mathrm{acc}} \approx 0.7 \frac{c\tau}{\lambda} Z_{\mathrm{R}}, \tag{33}$$

where $Z_{\mathrm{R}} = \pi R^2/\lambda \approx a_0 \lambda_{\mathrm{p}}^2 / 4\pi\lambda$ is the Rayleigh length.

The scaling for the maximum energy E_{mono} of the quasi-monoenergetic peak in the electron spectrum is

$$E_{\mathrm{mono}} \approx 0.65 mc^2 \sqrt{\frac{\mathcal{P}}{\mathcal{P}_{\mathrm{rel}}}} \frac{c\tau}{\lambda}. \tag{34}$$

Here, $\mathcal{P}$ is the laser pulse power, $\mathcal{P}_{\mathrm{rel}} = m^2 c^5 / e^2 \approx 8.5$ GW is the natural relativistic power unit, and $\lambda = 2\pi c/\omega_0$ is the laser wavelength. The scaling (34) assumes that the laser pulse duration satisfies the condition $c\tau < R$.

The scaling for the number of accelerated electrons N_{mono} in the quasi-monoenergetic peak is

$$N_{\mathrm{mono}} \approx \frac{1.8}{k_0 r_{\mathrm{e}}} \sqrt{\frac{\mathcal{P}}{\mathcal{P}_{\mathrm{rel}}}}, \tag{35}$$

where $r_{\mathrm{e}} = e^2/mc^2$ is the classical electron radius and $k_0 = 2\pi/\lambda$.

It follows from the scalings (34) and (35) that the laser energy conversion efficiency η into the quasi-monoenergetic electrons is a constant. Our 3D PIC simulations suggest that this constant is

$$\eta = \frac{N_{\text{mono}} E_{\text{mono}}}{\mathcal{P}\tau} \approx 20\%. \tag{36}$$

This high-energy efficiency makes the bubble regime of electron acceleration very promising for future applications.

Looking at the scalings (34) and (35), one mentions that the plasma density does not appear explicitly. Rather, everything is defined by the laser pulse parameters: the power $\mathcal{P}$ and the duration τ. This is the consequence of the pulse radius scaling (31) corresponding to the bubble regime.

With a given laser pulse, the bubble regime is achievable only in some density range $n_1 < n_e < n_2$. The lower density limit n_1 is defined by the condition that the laser pulse is still ultra-relativistic, $a_1 > 1$ when focused on the corresponding focal spot $k_0 R_1 = \sqrt{a_1 n_c / n_1}$. The upper density limit is defined by the condition that the corresponding focal spot equals the pulse duration: $\omega_0 \tau = k_0 R_2 = \sqrt{a_2 n_c / n_2}$. This density range can be expressed via the laser parameters:

$$n_1 \approx n_c \frac{\mathcal{P}_{\text{rel}}}{\mathcal{P}}, n_2 \approx n_c \sqrt{\frac{\mathcal{P}}{\mathcal{P}_{\text{rel}}}} \frac{1}{\omega_0 \tau}. \tag{37}$$

The density range (37) exists only when the laser power is large enough:

$$\mathcal{P} > \mathcal{P}_{\text{rel}} (\omega_0 \tau)^2. \tag{38}$$

Condition (38) can be considered as the threshold power needed to reach the bubble regime for a laser pulse with the given duration τ. In practical units, this threshold power is

$$\mathcal{P} > \mathcal{P}_{\text{bubble}} = \left(\frac{\tau[\text{fs}]}{\lambda[\mu m]} \right)^2 \cdot 30 GW. \tag{39}$$

The parametric dependencies in the scalings (34) and (35) follow from the analytical theory while the numerical pre-factors have been obtained from direct 3D particle-in-cell simulations.

11 The Breakthrough Experiments: Quasi-monoenergetic Electron Beams

The conventional accelerators have made a tremendous progress since the very first electrostatic machine was built by Van de Graaff in 1929. Nowadays they deliver particle beams in multi-GeV energy range with excellent parameters.

They are robust, reliable, and efficient. Unfortunately, the accelerating field in the conventional accelerators is limited by 10–100 MeV/m. That is why the multi-GeV accelerators have kilometer lengths and thus are close to the limit of economically Justifiable dimensions. The latest project, the Large Hadron Collider (LHC) currently under construction at CERN in Geneva, attempts to find the Higgs boson, a particle associated with the mechanism through which all other known particles are thought to acquire their masses. But the size and cost of such machines – for the LHC, a 27 km circumference and several billion euros – are fuelling a serious effort to develop new and more compact accelerator technologies.

The concept of laser-plasma electron acceleration has the decisive advantage over conventional accelerators: plasma supports electric fields orders of magnitude higher than the field in radio-frequency cavities of conventional linacs. It is expected that the relativistic laser-plasma will finally lead to a compact high-energy accelerator [7].

But acceleration rate is only one measure of a good accelerator. The number of particles in a beam, and their spread in angle and energy, also matters. Recently, three independent experiments have delivered high-quality electron beams in the energy range 70–170 MeV [8, 9, 10]. In all these three experiments, the laser pulses were very short, in the range 30–40 fs. This was comparable with the plasma period.

The LOA experiment [10] has been simulated with the 3D PIC code VLPL. A comparison of the experimentally measured spectrum and the simulation is

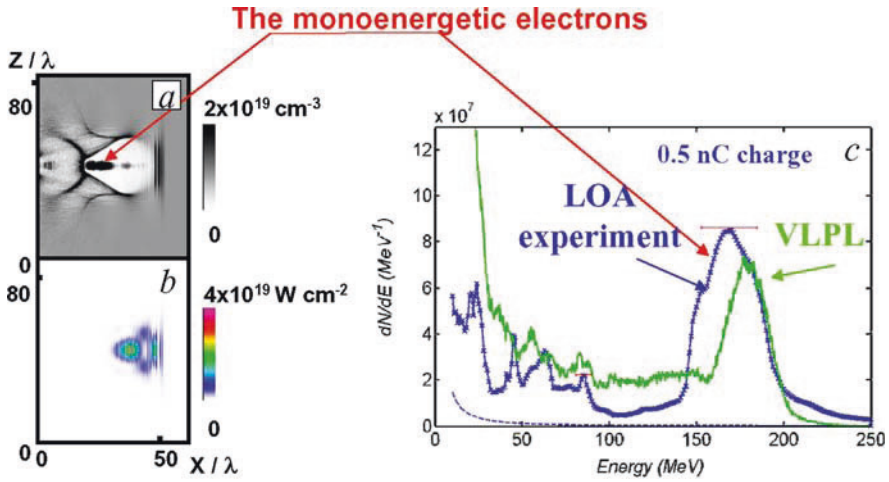

Fig. 11 3D PIC simulations for the LOA experiment [10]. (**a**) On-axis cut of the electron density: the characteristic bubble structure and the trapped electron beam. (**b**) On-axis cut of the laser intensity. The laser pulse is self-focused and compressed. (**c**) Electron spectra measured in the experiment and the simulation

shown in Fig. 11. The electron beam has the energy 170 ± 20 MeV and the charge about 0.5 nC. Looking at the geometry of the laser wake field in the simulation, one can mention that the plasma wave behind the laser pulse starts to remind the characteristic bubble structure. Applying the formula for the threshold laser power needed to form a bubble (38), one obtains that the LOA experiment [10] has been done at the lowest bubble power threshold. One may expect that with upgraded laser power, the stability and quality of the electron beam will be further improved.

12 X-Ray Generation in Strongly Non-linear Plasma Waves

The development of novel high-brightness compact X-ray sources is important for many research, industrial and, medical applications including X-ray microscopy and spectroscopy, holography and nanotechnology, biological imaging, and ultrafast process probing. Synchrotron light sources (SLSs) are the most intense X-ray sources today. In an SLS, the radiation is generated as a result of relativistic electron scattering by a bending magnet, magnetic undulators or wigglers [100], or by high-power laser pulses (Compton scattering) [101, 102, 103, 104]. Recent experiments, which explore the interaction of an intense 28.5 GeV electron beam with plasma at Stanford Linear Accelerator Center (SLAC) [105, 106], have shown that an ion channel can be successfully used as a wiggler to produce the broadband X-ray radiation: the electron beam propagating in plasma blows out the background electrons and generates an ion channel. The ion channel provides an effective wiggler strength, which is higher than that of conventional magnets available now.

A relativistic electron running along the ion channel undergoes betatron oscillations about the channel axis due to the restoring force acting on the electron by the uncompensated ion charge. Relativistic electrons executing betatron oscillations in the ion channel emit short-wavelength EM radiation [44, 107]. Some features of this radiation spectrum have been studied in the recent publications [26, 106]. If the amplitude of the betatron oscillations becomes large, then the electron radiates high harmonics and the radiation spectrum becomes quasi-continuous broadband. It is similar to the synchrotron spectrum.

The synchrotron radiation emitted from an ion channel has been observed in a recent experiment [105], where the ion channel has been produced by the electron beam itself in the blow-out regime [108]. In this regime, the plasma density must be smaller than the beam density, which is limited due to technology reasons. The gain in the radiated power, however, is quadratic in plasma density [27].

The high-power lasers could overcome this limitation. As we have seen in the previous section, the relativistically intense laser pulse can produce a "bubble" free from background electrons. Because of its 3D structure, it

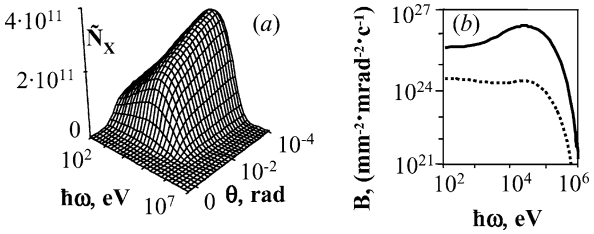

Fig. 12 (a) The synchrotron spectrum from the plasma at $c/\lambda = 4500$; (b) the spectral brilliance, the *dashed line* corresponds to $c/\lambda = 1000$, the *solid line* corresponds to $c/\lambda = 4500$

contains also transverse fields. The accelerated relativistic electrons oscillate in these fields and produce short-wavelength radiation. The bubble can propagate a long distance in plasmas and thus provide a bright source of short-pulsed X-rays.

The synchrotron spectrum emitted from the bubble are presented in Fig. 12 a and b. The surface shown in Fig. 12a gives the number of photons within 0.1% of the bandwidth ($\Delta\hbar\omega = 10^{-3}\hbar\omega$) per solid angle, $2\pi \sin\theta \mathrm{d}\theta$: $\tilde{N}_X = \Delta\omega \mathrm{d}^2 N_X/(2\pi \sin\theta \mathrm{d}\omega \mathrm{d}\theta)$. It is seen that the relativistic bunch radiates highly energetic photons within a very narrow cone. The maximum of the radiation spectrum is located at about 50 keV and the radiation is confined within the angle $\theta \simeq 0.1$ rad. The photon flux (the number of photons per second in 0.1% bandwidth) and the spectral brilliance of the source are shown in Fig. 12b. One can estimate the flux and the brilliance using the following formulas [103]: $\Phi \simeq (\Delta\omega_c/\omega_c) N_X (c/L_b)$ and $B \simeq \Phi/(4\pi^2 \theta_R^2 S_R^2)$, where L_b is the bunch length, $S_R \simeq \pi\left[r_b^2 + c^2 T_{int}^2 \theta_R^2/(4\pi^2)\right]$ is the effective source size of the radiation, r_b is the bunch radius, and T_{int} is the interaction time.

The high ion density in the laser-produced plasma wiggler and the strong transverse plasma fields lead to a much higher power of the X-ray emission and larger photon energies than that in a self-generated ion channel. In terms of the photon energy and the brilliance, the generated radiation is much more intense than the synchrotron radiation sources available today.

The possibility to use the bubble as a source of keV X-rays has been demonstrated experimentally by Rousse et al. [28]. They used a millimeter-scale laser-produced plasma to create, accelerate, and wiggle an ultra-short and relativistic electron bunch. The broadband synchrotron radiation has been observed in the keV spectral range within a narrow 50 mrad cone.

The dense relativistic electrons produced by intense laser pulses can also be used for X-ray generation via Compton scattering. The incident laser pulse can be split into two pulses. The first pulse can be used to produce the bubble and the relativistic bunch, and the second one can collide with the bunch to generate high-energetic photons via direct Compton scattering [101].

13 Conclusions

The physics of strong field laser–matter interaction is a dynamically developing field. In this review, we have tried to digest some of the important physical effects emerging at relativistic laser intensities, as they appear in three-dimensional particle-in-cell simulations. We have seen how the laser pulses filament and self-channel in plasma. The laser channels carry strong currents of relativistic electrons and are surrounded by self-generated quasi-static magnetic fields. We considered different mechanisms of particle acceleration in plasmas leading to directed beams of fast electrons. The electrons are accelerated either directly by the laser field in plasma channels or by the longitudinal electric field of a plasma wave. The accelerating fields acting in laser-plasma are orders of magnitude larger than those in conventional accelerators, and a quasi-monoenergetic beam of 400 MeV electrons is produced over a distance less than a millimeter.

These accelerated electrons wiggle in strong transverse fields of the laser-excited plasma wave and emit X-rays. In terms of the photon energy and the brilliance, the generated radiation is much more intense than the synchrotron radiation sources available today.

These are only a few examples of new physical effects appearing in the highly non-linear regime of relativistic laser–matter interaction.

Acknowledgments This work was supported by Transregio 18 project of DFG (Germany). The simulations have been done on Regatta parallel computer at John von Neumann-Institut for Computing Jülich.

References

1. Mourou G, Barty C, and Perry M D Jan. 1998 *Phys. Today* **22**.
2. Key M H, Cable M D, Cowan T E et al. 1998 *Phys. Plasmas* **5**, 1966.
3. Mourou G A and Umstadter D 2002 *Sci. Am.* **286**, 80.
4. Strickland D and Mourou G 1985 *Opt. Commun.* **56**, 219.
5. Tajima T and Dawson J 1979 *Phys. Rev. Lett.* **43**, 267.
6. Pukhov A et al. 1999 *Phys. Plasmas* **6**, 2847.
7. Katsouleas Th 2004 *Nature* **431**, 515.
8. Mangles S P D et al. 2004 *Nature* **431**, 535.
9. Gedder C G R et al. 2004 *Nature* **431**, 538.
10. Faure J et al. 2004 *Nature* **431**, 541.
11. Pukhov A and Meyer-ter-Vehn J 2002 *Appl. Phys. B* **74**, 355.
12. Denavit J 1979 *Phys. Fluids* **22**, 1384.
13. Wilks S C et al. 2001 *Phys. Plasmas* **8**, 542.
14. Pukhov A 2001 *Phys. Rev. Lett.* **86**.
15. Banerjee S, Valenzuela A R, Shah R C, Maksimchuk A, and Umstadter D 2002 *J. Mod. Opt.* **49**, Sp. Iss. SI 2599.
16. Lau Y Y, He F, Umstadter D P, and Kowalczyk R 2003 *Phys. Plasmas* **10**, 2155.
17. Gordienko S, Pukhov A, Shorokhov O, and Baeva T 2004 *Phys. Rev. Lett.* **93**, 115002.
18. Gordienko S, Pukhov A, Shorokhov O, and Baeva T 2004 *Phys. Rev. Lett.* **94**, 103903.

19. Gibbon P 1996 *Phys. Rev. Lett.* **76**, 50.
20. Wilks S et al. 1993 *IEEE TPS* **21**, 120.
21. Bulanov S et al. 1994 *Plasma Phys.* **1**, 745.
22. Lichters R, Meyer-ter-Vehn J, and Pukhov A 1996 *Plasma Phys.* **3**, 3425.
23. Norreys P et al. 1996 *Phys. Rev. Lett.* **76**, 1832.
24. Kohlweyer S et al. 1995 *Opt. Commun.* **117**, 431.
25. von der Linde D et al. 1995 *Phys. Rev. A* **52**, R25.
26. Esarey E, Shadwick B A, Catravas P, and Leemans W P 2002 *Phys. Rev. E* **65**, 056505.
27. Kiselev S, Pukhov A, and Kostyukov I 2004 *Phys. Rev. Lett.* **93** 135004.
28. Rousse A et al. 2004 *Phys. Rev. Lett.* **93**, 135005.
29. Sarachik E S and Schappert G T 1970 *Phys. Rev. D* **1**, 2738 (1970).
30. Corkum P B, Burnett N H, and Brunel F, in *Atoms in Intense Laser Fields*, ed. Gavrila M, N.Y., Academic Press (1992), p. 109.
31. Quesnel B and Mora P 1998 *Phys. Rev. E* **58**, 3719.
32. Kruer W 1988 *The physics of laser-plasma interactions*, Addison-Wesley.
33. Bauer D, Mulser P, and Steeb W-H 1995 *Phys. Rev. Lett.* **31**, 4622.
34. Ross I N et al. 1997 *Opt. Comm.* **144,** 125.
35. Hatchett S et al. 2000 *Phys. Plasmas* **7**, 2076.
36. Snavely R A et al. 2000 *Phys. Rev. Lett.* **85**, 2945.
37. Clark E L et al. 2000 *Phys. Rev. Lett.* **84**, 670.
38. Krushelnik K et al. 2000 *Phys. Plasmas* **7**, 2055.
39. Roth M et al. 2000 *Phys. Rev. Lett.* **86**, 436.
40. Borghesi M et al. 2002 *Phys. Plasmas* **9**, 2214.
41. Esirkepov T Zh et al. 2002 *Phys. Rev. Lett.* **89**, 175003–1.
42. Esarey E et al. 1996 *IEEE Trans. Plasma Sci.* **24,** 252.
43. Gordienko S and Pukhov A 2005 *Phys. Plasmas* **12**, 043109.
44. J. D. Jackson, *Classical Electrodynamics* (Wiley, N. Y., 1975).
45. Villasenor J and Buneman O 1992 *Comp. Phys. Comm.* **69**, 306.
46. Dawson J 1983 *Reviews Modern Phys.* **55**, 403.
47. Birdsall C K and Langdon A B 1991 *Plasma physics via computer simulations* (Adam Hilger, N.Y.).
48. Hockney R W and Eastwood J W 1981 *Computer Simulation Using Particles* 540 S. (London: McGraw Hill 1981).
49. Langdon A B and Lasinski B 1976 *Meth. Comput. Phys.* **16**, 327.
50. Buneman O 1976 *Comp. Phys. Comm.* **12**, 21.
51. Wilks S C et al. 1992 *Phys. Rev. Lett.* **69**, 1383.
52. Decyk V 1995 *Comp. Phys. Comm.* **87**, 87.
53. Hemker R et al. (unpublished) and Lee S et al. 2000 *Phys. Rev. E* **61**, 7014.
54. Tzeng K C et al. 1996 *Phys. Rev. Lett.* **76**, 3332.
55. Pukhov A 1999 *J. Plasma Phys.* **61**, 425.
56. Esirkepov T Z H 2001 *Comp. Phys. Comm.* **135**, 144.
57. Adam J C et al. 2000 *Phys. Rev. Lett.* **84**, 3598.
58. Ruhl H et al. 2001 *Plasma Phys. Rep.* **27**, 363.
59. Sentoku Y et al. 2002 *Phys. Rev. E* **74**, 046408.
60. Max C E, Arons J, and Langdon A B 1974 *Phys.Rev. Lett.* **33**, 209.
61. Sun G et al. 1987 *Phys. Fluids* **30**, 526.
62. Sprangle P et al. 1983 *IEEE Trans. Plasma Sci.* **PS-15**, 145.
63. Borisov A B et al. 1992 *Phys. Rev. A* **45**, 5830.
64. Borisov A B et al. 1992 *Phys. Rev. Lett.* **68**, 2309.
65. Monot P et al. 1995 *Phys. Rev. Lett.* **74**, 2953.
66. Borisov A B et al. 1995 *Plasma Phys. Contr. Fusion,* **37**, 569.
67. Askar'yan G A et al. 1994 *JETP Lett.* **60**, 251.
68. Pukhov A and Meyer-ter-Vehn J 1996 *Phys. Rev. Lett.* **76**, 3975.

69. Borghesi M et al. 1997 *Phys. Rev. Lett.* **78**, 879.
70. Borghesi M et al. 1998 ,*Phys. Rev. Lett.* **80**, 5137.
71. Tanaka K A et al. 2000 *Phys. Plasmas* **7**, 2014.
72. Tabak M et al. 1994 *Phys. Plasmas* **1**, 1626.
73. Wharton K B et al. 1998 *Phys. Rev. Lett.* **81**, 822.
74. Malka G et al. 1997 *Phys. Rev. Lett.* **78**, 2053.
75. Pretzler G et al. 1998 *Phys. Rev. E* **58**, 1165.
76. Gahn C et al. 1998 *Appl. Phys. Lett.* **73**, 3662.
77. Pukhov A and Meyer-ter-Vehn J 1997 *Phys. Rev. Lett.* **79**, 2686.
78. Pukhov A and Meyer-ter-Vehn A 1998 *Phys. Plasmas* **5**, 1880.
79. Gahn C et al. 2000 *Phys. Rev. Lett.* **83**, 4772.
80. Ruhl H and Mulser P 1998 *Phys. Lett.* **A205**, 388.
81. Sprangle P et al. 1992 *Phys. Rev. Lett.* **69,** 2200.
82. Andreev N E et al. 1992 *JETP. Lett.* **55,** 551.
83. Antonsen T M and Mora P 1992 *Phys. Rev. Lett.* **69,** 2204.
84. Esarey E et al. 1994 *Phys. Rev. Lett.* **72**, 2887.
85. Umstadter D, Kim J K, and Dodd E 1996 *Phys. Rev. Lett.* **76**, 2073.
86. Esarey E, Hubbard R F, Leemans W P, Ting A, and Sprangle P, 1997 *Phys. Rev. Lett.* **79**, 2682.
87. Shvets G, Fisch N J, and Pukhov A 2000 *IEEE Trans. Plasma Sci.* **28**, 1185.
88. Akhieser A I and Polovin R V 1956 *JETP* **3**, 696.
89. Tzeng K-C et al. 1999 *Phys. Plasmas* **6**, 2105.
90. Bulanov S V et al. 1997 *Phys. Rev. Lett.***78**, 4205.
91. Liseikina T V et al. 1999 *Phys. Rev. E* **60**, 5991.
92. Kim J K and Umstadter D 1999 in *Adv. Acc. Conc.: 8th Workshop* AIP Conf. Proc. **472** 404 (AIP Press, N.Y.)
93. Amiranoff F et al. 1998 *Nucl. Instr. and Methods in Phys. Res.* **410A**, 364.
94. Modena et al. 1995 *Nature* **337**, 606.
95. Chen S-Y et al. 1999 *Phys. Plasmas* **6**, 4739.
96. Ting A et al. 1996 *Phys. Rev. Lett.* **77**, 5377.
97. Gordon D et al. 1998 *Phys. Rev. Lett.* **80**, 2133.
98. Santala M et al. 2001 *Phys. Rev. Lett.* **86**, 1227.
99. Malka V, Fritzler S, Lefebvre E, et al. 2002 *Science* **298**, 1596.
100. Kim K J 1989 in *Physics of Particle Accelerators*, edited by Month M and Dienes M, AIP Conf. Proc. No. 184 AIP, N. Y., **I**, p. 565.
101. Leemans W P, Schoenlein R W, Volfbeyn P, Chin A H, Glover T E, Balling P, Zolotorev M, Kim K J, Chattopadhyay S, Shank C V 1997 *IEEE J. Quantum Electron* **33**, 1925.
102. Schoenlein R W et al. 2000 *Appl. Phys. B* **71**, 1.
103. Esarey E, Ride S K, and Sprangle P 1993 *Phys. Rev. E* **48**, 3003.
104. Pogorelsky I V 1998 *Nucl. Instr. Meth.* **A 411**, 172.
105. Wang S et al. 2002 *Phys. Rev. Lett.* **88**, 135004.
106. Joshi C et al. 2002 *Phys. Plas.* **9**, 1845.
107. Schmitz M and Kull H J 2002 *Europhys. Lett.* **58**, 382.
108. Rosenzweig J B, Breizman B, Katsouleas T, and Su J J 1991 *Phys. Rev. A* **44**, R6189.

High-Density Plasma Laser Interaction

Heidi Reinholz and Thomas Bornath

1 Introduction

High-density plasmas are of interest for fundamental research and applications, as e.g., in light sources and fusion, as well as for the understanding of the physics in stellar and planetary systems. In recent years, ultra-short high-intensity laser pulses have become available so that intensities up to 10^{21} W/cm^2 can be reached. New facilities are under construction which produce radiation of frequencies up to the X-ray region with high brilliance. This radiation is used to produce plasmas over a wide range of density, pressure and temperature, as well as subsequently to probe its properties. Dimensionless quantities can be introduced to characterize the properties of the plasma near equilibrium: the degeneracy parameter $\Theta = k_B T/E_F = 2m_e k_B T(3\pi^2 n_e)^{-2/3}\hbar^{-2}$ is the ratio of the electronic temperature to the Fermi energy. For $\Theta < 1$, the plasma has to be treated as a quantum system. The coupling parameter $\Gamma = V_{ei}/k_B T = (4\pi n_e/3)^{1/3} e^2 (4\pi\epsilon_0 k_B T)^{-1}$ characterizes the size of the interaction potential at the mean distance of the electrons with respect to the thermal energy. At high densities or low temperatures ($\Gamma > 1$), the plasma is strongly coupled and correlations and collisions have to be taken into account. Hot and dilute systems are weakly coupled and can be treated perturbatively. Relativistic plasmas, in which a significant part of the electrons reaches a speed close to the speed of light, can also be produced leading to new theoretical and experimental challenges, e.g., about 10% of the electrons in a thermal plasma of $T > 260$ keV have a speed of $0.86c$. Very promising issues are, e.g., the creation of high-energy quasi-monoenergetic electron and ion beams [1] or the investigation of nuclear reactions triggered by laser-accelerated relativistic electron jets [2].

An important question in almost all experiments with interaction of intense laser pulses with matter is the calculation of the energy deposition and the description of the subsequent heating. After the laser field has delivered

H. Reinholz
Institut für Physik, Universität Rostock, 18051 Rostock, Germany
e-mail: heidi.reinholz@uni-rostock.de

T. Brabec (ed.), *Strong Field Laser Physics*,
DOI: 10.1007/978-0-387-34755-4_19,

the energy necessary for a substantial ionization of the system, the electromagnetic field couples to the free charge carriers leading to heating of the system. There are several mechanisms relevant for the absorption of electromagnetic radiation in Coulomb systems. In underdense plasmas, the absorption connected with electron–ion collisions (inverse bremsstrahlung) is the main process. There are experimental hints, however, that also processes like ion acoustic turbulence could play an important role [3]. For overdense plasmas, on the other hand, there are several important collisionless mechanisms depending especially on the density gradients. For gentle density gradients, resonant absorption and parametric instabilities are important [1]. Other mechanisms like $\mathbf{j} \times \mathbf{B}$ heating and Brunel absorption [2] or sheath inverse bremsstrahlung and the anomalous skin effect are dominating for steep density gradients [4].

In the present chapter, we give a survey on some many-particle methods and their application to the interaction of lasers with dense plasmas with focus on the description of bulk properties. In Section 2, we will consider the diagnostics of high-density plasmas using radiation. In this context, weak plasma-radiation interaction is dominating. Using a consistent many-particle description of the dense plasma in connection with optical properties, the determination of plasma properties is possible. In particular, absorption processes, reflectivity and Thomson scattering are discussed as diagnostic tools in Section 3. In the context of plasma creation by intense laser pulses and the subsequent laser-plasma interaction, strong external fields have to be considered. One interesting heating mechanism is nonlinear collisional absorption which is considered in Section 4.

2 Linear Response Theory

The interaction of radiation with charged particle systems is described by the dielectric function $\epsilon(\boldsymbol{k}, \omega)$ from which the optical and transport properties can be derived. We are interested in the refractive index as well as absorption and emission. Considering the optical spectrum, we can restrict ourselves to the long-wavelength limit $k \to 0$. The frequency-dependent dielectric function or correspondingly the dynamical conductivity σ are then related to the dynamical collision frequency ν via a generalized Drude formula [5]:

$$\epsilon(\omega) = 1 - \frac{\sigma(\omega)}{\mathrm{i}\epsilon_0 \omega} = 1 - \frac{\omega_{\mathrm{pl}}^2}{\omega[\omega + \mathrm{i}\nu(\omega)]}. \tag{1}$$

The phenomenological Drude ansatz assumes a static collision frequency which is related to the dc-conductivity via $\sigma_{\mathrm{dc}} = \epsilon_0 \omega_{\mathrm{pl}}^2 / \nu(0)$ where $\omega_{\mathrm{pl}} = \sqrt{e^2 n_{\mathrm{e}} / (\epsilon_0 m_{\mathrm{e}})}$ is the plasma frequency, with n_{e} and m_{e} the electron density and mass, respectively. However, as shown by Reinholz et al. [5], for a description consistent with known limiting cases and generally valid sum rules for the dielectric function, the collision frequency has to be a complex

frequency-dependent quantity. This can be achieved within a generalized linear response theory [5, 6]. The collision frequency is expressed in terms of equilibrium correlation functions which is a representation of the fluctuation dissipation theorem. Calculations of the correlation functions are possible by evaluating analytical expressions derived within perturbation theory. Alternatively, simulation techniques, e.g., molecular dynamics [7, 8, 9], wave packet molecular dynamics [10], quantum molecular dynamics [11] or path integral Monte Carlo (PIMC) techniques [12, 13], are applied.

Within this approach, the well-known Kubo formula $\sigma(\omega) = \beta\Omega\langle J; J\rangle_{\omega+i\eta}$ can be derived which is also known from the solution of kinetic equations [14, 15]. It expresses the dynamical conductivity in terms of the correlation function of the electrical current operator J. Ω is the renormalization volume. This approach is suitable for dynamical properties and the application of molecular dynamics simulations. However, in the static case, divergencies arise [16] if evaluated using perturbation theory. A more consistent perturbative treatment is possible if the collision frequency is expressed in terms of force–force correlation functions:

$$\nu(\omega) = \frac{\beta\,\Omega}{\epsilon_0\omega_{\mathrm{pl}}^2}\,\langle \dot{\boldsymbol{J}}; \dot{\boldsymbol{J}}\rangle_{\omega+i\eta}\ . \tag{2}$$

This can then be related to the conductivity according to Eq. (1). The evaluation of Eq. (2) in Born approximation leads to the expression

$$\nu^{\mathrm{Born}}(\omega) = -\frac{i\epsilon_0 n_i\,\Omega^2}{6\pi^2 e^2\, n_e m_e}\int_0^\infty \mathrm{d}q\, q^6 V_{ei}^2(q) S_i(q)\frac{1}{\omega}[\epsilon_{\mathrm{RPA}}(q,\omega) - \epsilon_{\mathrm{RPA}}(q,0)]. \tag{3}$$

For the electronic part of the dielectric function in random phase approximation (RPA), ϵ_{RPA}, there are analytical expressions available [17]. Only the electronic part contributes while the ionic distribution is taken into account by the ionic static structure factor $S_i(q)$ assuming that the electrons are scattered from ions at fixed positions. $V_{ei}(q)$ is the Coulomb potential. In an attempt to improve this approximation to higher order perturbation theory, several aspects have been discussed and evaluated in the literature, see, e.g., [15] and therein. Considering screening processes, the Lenard–Balescu collision term (LB) is obtained where the bare Coulomb potential is replaced by a dynamically screened one. The behavior at small distances r is determined by strong binary collisions which are accounted for by a higher-order perturbation expansion replacing the interaction potential V_{ei} by a t-matrix (TM). A dynamically screened TM approximation gives a consistent description of collisions combining dynamical screening and strong collisions. It can be approximated by the following so-called Gould–deWitt ansatz:

$$\nu^{\mathrm{GD}}(\omega) \;=\; \nu^{\mathrm{TM}}(\omega) \;-\; \nu^{\mathrm{Born}}(\omega) \;+\; \nu^{\mathrm{LB}}(\omega)\ . \tag{4}$$

For the TM approximation, a static potential such as the Debye potential is taken. To avoid double counting, the collision frequency in Born approximation (3) with respect to the static potential has to be subtracted since the Born approximation is also taken into account in ν^{LB}.

The evaluation of the complex collision frequency for a two-component Coulomb plasma has been performed for a hydrogen plasma at the conditions of the solar core, i.e., $T = 96.15$ Ryd $= 1.52 \cdot 10^7$ K, $n_\mathrm{e} = n_\mathrm{i} = n = 8.9\ a_\mathrm{B}^{-3} = 6.0 \cdot 10^{25}\ \mathrm{cm}^{-3}$ [5]. These parameters are also relevant for laser-induced plasmas [18]. This is a weakly coupled plasma, $\Gamma = 0.069$, which is not strongly degenerate, $\Theta = 2.34$. In Fig. 1, the real part of the dynamical collision frequency is shown in different approximations. The differences between the various results are most pronounced in the static limit. Above the plasma frequency, the correction to the convergent collision term, Eq. (4), decreases with increasing frequency since screening becomes less relevant. The principal high-frequency behavior is the same in all three approximations. The differences between the Born and the TM approximations are most pronounced in the vicinity of the plasma frequency. For a more detailed discussion including the imaginary part of the collision frequency, see Reinholz et al. [5, 15].

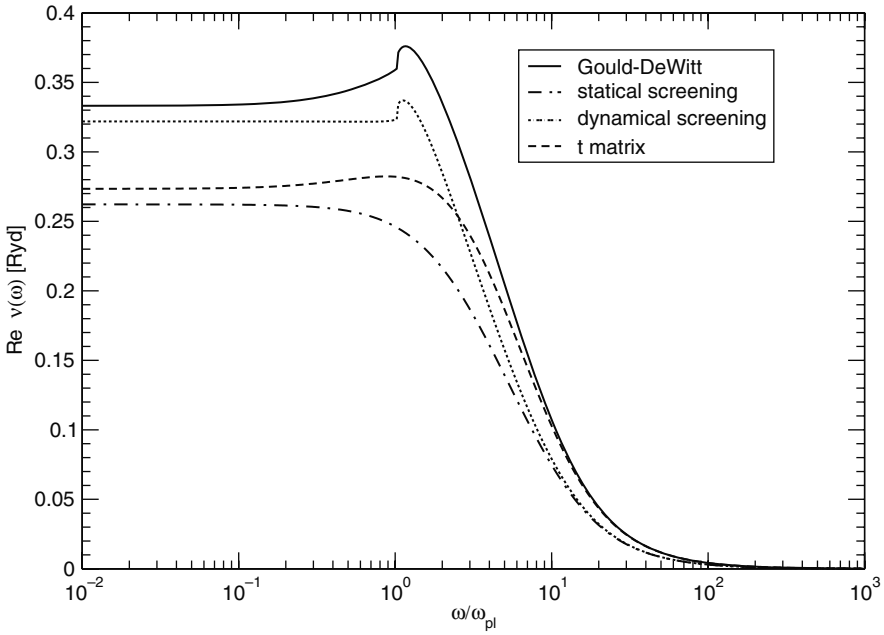

Fig. 1 Real part of the dynamical collision frequency in the Gould–DeWitt approximation as a function of frequency ω for classical electron plasma at solar core conditions [15]. Separate contributions are also given: statically screened Born approximation, dynamically screened Born approximation and ladder approximation

In analogy to the behavior of the collision frequency in the static limit (dc-conductivity) [19], the frequency-dependent conductivity (1) will be rewritten as follows [5, 15]:

$$\sigma(\omega) = \frac{\epsilon_0 \omega_{\mathrm{pl}}^2}{-\mathrm{i}\omega + r(\omega)\nu^{\mathrm{GD}}(\omega)} \tag{5}$$

where $\nu^{\mathrm{GD}}(\omega)$ is determined according to Eq. (4), which is equivalent to the dynamically screened binary collision approximation for the collision frequency. The renormalization factor $r(\omega)$ takes into account corrections due to higher moments of the distribution function, in particular electron–electron correlations which is equivalent to, e.g., the Chapman–Enskog method [20] in solving kinetic equations. In the special case of zero-frequency limit (dc-conductivity), the renormalization factor $r(0)$ gives the correct prefactor known as Spitzer result; details are given in [5].

Analytical expressions have been derived according to the above procedure of perturbation theory and applied to transport coefficients, dielectric function and related quantities [5, 16]. However, these quantum statistical approaches are applicable to small coupling parameters, in the region $\Gamma < 1$, see [15, 21, 22]. Simulations are used to check the range of validity of these approximations for stronger coupling. The following interpolation formula for the static case has been constructed based on correct analytical behavior in limiting cases and simulation data for intermediate regions [23]:

$$\sigma_{\mathrm{dc}}^{\mathrm{ERR}}(\Gamma,\Theta) = a_0 T^{3/2}\left(1+\frac{b_1}{\Theta^{3/2}}\right)\left[D\ln(1+A+B) - C - \frac{b_2}{b_2+\Gamma\Theta}\right]^{-1}, \tag{6}$$

where the temperature T is in K, σ in $(\Omega\mathrm{m})^{-1}$ and the functions

$$A = \Gamma^{-3}\frac{1+a_4/\Gamma^2\Theta}{1+a_2/\Gamma^2\Theta+a_3/\Gamma^4\Theta^2}\left[a_1 + c_1\ln(c_2\Gamma^{3/2}+1)\right]^2,$$

$$B = \frac{b_3(1+c_3\Theta)}{\Gamma\Theta(1+c_3\Theta^{4/5})},$$

$$C = \frac{c_4}{\ln(1+\Gamma^{-1}) + c_5\Gamma^2\Theta},$$

$$D = \frac{\Gamma^3 + a_5(1+a_6\Gamma^{3/2})}{\Gamma^3+a_5}.$$

The set of parameters is presented in Table 1. The validity was checked to be extended to about $\Gamma \leq 2$.

Table 1 Parameters for the interpolation formula (6), σ_{dc}^{ERR}, for the static conductivity

a_0	a_1	a_2	a_3	a_4	a_5	a_6
0.03064	1.1590	0.698	0.4876	0.1748	0.1	0.258
b_1	b_2	b_3	c_1	c_2	c_3	c_4	c_5
1.95	2.88	3.6	1.5	6.2	0.3	0.35	0.1

In Fig. 2, we compare MD data with the evaluation of analytical expressions for the real and imaginary parts of the collision frequency [22]. For the classical MD simulations, quantum effects were taken into account by constructing pseudopotentials using thermodynamic properties. Therefore, the static and low-frequency behavior shows good agreement. In the high-frequency limit, quantum effects for Coulomb systems are not reflected adequately in the classical MD simulations results using the Kelbg pseudopotential.

From MD simulations for the current auto-correlation function, the dc-conductivity $\sigma_{dc} = \epsilon_0 \omega_{pl}^2/\nu(0)$ is obtained. Calculations have been performed for a fixed temperature of $T = 33\,000$ K and varying coupling parameter Γ. Results for the collision frequency and the static conductivity are shown in Fig. 3. Considering the MD simulations for $\Gamma \leq 1$, the systematic behavior agrees very well with the analytical results obtained from the interpolation formula (6) shown for comparison. Discrepancies arise for higher values of Γ. However, the principal behavior of the MD simulations can be reproduced with the interpolation formula. The theoretical description, based on analytical expressions and MD simulations, leads to a good understanding of experimental results which are

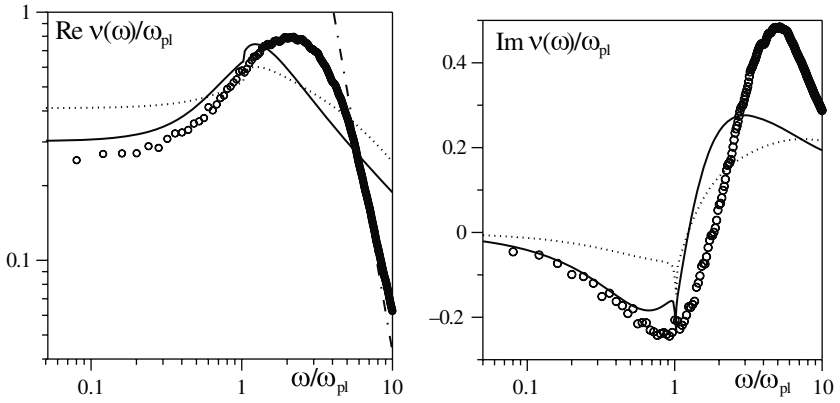

Fig. 2 Comparison between MD data for the Kelbg pseudopotential (○) and the quantum statistical treatment for the Coulomb potential [22]. The Gould–DeWitt scheme, see text, is used. *Full line* – including renormalization factor $r(\omega)$ in Eq. (5), *dotted line* – without renormalization factor. The *dot–dashed line* gives the analytical result for the high-frequency behavior of Re $\nu(\omega)$ for the Born approximation Eq. (3) with Kelbg potential. $\Gamma = 1.28$, $T = 33\,000$ K

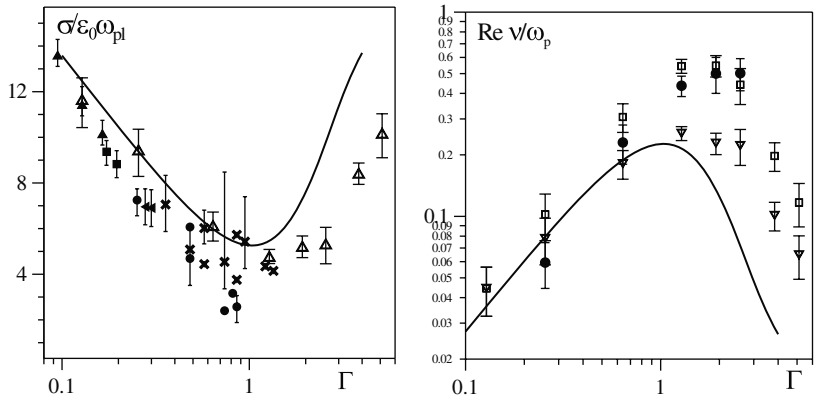

Fig. 3 Static conductivity (*left*) and dynamical conductivity (*right*) in dependence on the coupling parameter Γ [22]. MD results for the Kelbg pseudopotential for $T = 33\,000$ K: $\triangle, \nabla - \omega = 0$, $\square - \omega = \omega_{\rm pl}$ (plasma frequency), $\bullet$ – from collisional damping of the Langmuir waves, *full line* – interpolation formula (6) for $T = 33\,000$ K, experimental data: $\bullet$ – [24], $\times$ – [25], $\blacksquare$ – [26], $\blacktriangle$ – [27], $\blacktriangleleft$ – [28]

shown in the left figure as well. Experimentally, the dc-conductivity is determined for partially ionized plasma. In order to compare with a fully ionized plasma model, we have to separate the contribution of free charge carriers. However, the plasma parameters like temperature and density are not directly accessible. As already seen in Fig. 2, the value for the real part of the collision frequency at $\omega = \omega_{\rm pl}$ and as deduced from the collisional damping is systematically larger in comparison with the static values $\nu(0)$.

3 Applications

The dielectric function is a quantity which is of relevance in various situations where the coupling of a charged particle system with a radiation field is considered. In a first approximation, often the RPA is applied to describe the dielectric response of the Coulomb system. Screening effects are treated on a self-consistent mean field level, but collisions are neglected. It provides closed analytical expressions [17] and can be implemented in an easy way, see textbooks, e.g., [29]. Collective excitations such as plasmons are due to the polarization of free charged particles, leading to self-consistent treatment of screening. Despite the fact that collisions are not considered, the RPA has been proven to be sucessful in describing the plasma response in many applications. Based on the tools developed in the previous section, we will now investigate phenomena that go beyond RPA in the sense that collisions will be relevant. Exemplarily, we discuss bremsstrahlung, reflectivity and Thomson scattering. In each case, there is a very close link to experiments which have

been either done or are intended. This chapter is by no means exhaustive. We hope to inspire the reader, to consider further applications to physical situations where the interaction of charged particle systems with radiation, in particular high-intensity lasers, is relevant.

3.1 Bremsstrahlung

In isotropic plasmas, bremsstrahlung due to collisions between charged particles is the dominant emission process and can be used to infer density and temperature conditions in plasmas [30]. Continuum emission of hot and dense plasmas was measured in a number of experiments, see, e.g., Refs. [31, 32]. On the other hand, inverse bremsstrahlung, the absorption of photons upon collision leading to the attenuation of electromagnetic waves, is a main contribution to radiation loss in plasmas and therefore crucial for modeling radiation transport.

The emission of radiation by a plasma is characterized by the emission coefficient $j(\omega)$, which gives the rate of radiation energy per unit volume, frequency and solid angle. For a system in thermal equilibrium, the emission coefficient at frequency ω is related to the absorption coefficient $\alpha(\omega)$ by Kirchhoff's law [33, 34]:

$$j(\omega) = L_\omega^H(\omega)\,\alpha(\omega), \tag{7}$$

where $L_\omega^H(\omega) = \hbar\omega^3/(4\pi^3c^2)\,[exp(\hbar\omega/k_\mathrm{B}T) - 1]^{-1}$ is the spectral power density of blackbody radiation. The absorption coefficient is related to the dielectric function and the index of refraction $n(\omega)$ via $\epsilon(\omega) = [n(\omega) + \mathrm{i}c\alpha(\omega)/(2\omega)]^2$. An expression for a thermally averaged emission coefficient of a non-relativistic plasma considering free–free transitions without any particle correlations had been given by Kramers [35]. Modifications of bremsstrahlung due to quantum mechanical corrections and particle correlations have been discussed in the literature since Gaunt [36] and are given in terms of a so-called Gaunt factor $g(\omega)$. The first calculation of inverse bremsstrahlung accounting for screening effects was performed by Dawson et al. [37, 38] starting from the Vlasov equation. Their expression is widely used to describe the collisional absorption of intense laser radiation by plasmas [33]. A review on the various attempts and how they can be derived within the linear response theory can be found in Ref. [39]. Nonlinear inverse bremsstrahlung in high-frequency fields will be discussed in Section 4.

Calculating the dielectric function using the generalized Drude-like form (1), the absorption coefficient is a function of the real part of the dynamical collision frequency:

$$\alpha(\omega) = \frac{\omega_\mathrm{pl}^2}{c}\,\frac{Re\,\nu(\omega)}{(\omega^2 + |\nu(\omega)|^2)\,n(\omega)}. \tag{8}$$

Usually, the high-frequency limit $\alpha(\omega) = \omega_{\rm pl}^2 \, Re\nu(\omega)/c\omega^2$ is only considered. However, being interested in frequencies comparable or smaller than the plasma frequency, the full expression (8) should be taken into account [39].

As an example, we apply here Eq. (8) to the absorption coefficient of a hydrogen plasma with density $n_{\rm e} = 6.0 \times 10^{25}\,{\rm cm}^{-3}$ and temperature $T = 1.3\,{\rm keV}$ corresponding to the conditions at the solar center. Since the energy transport in the inner region of the sun is due to radiation, the absorption coefficient is crucial for standard solar models where it enters via the opacities.

The overall frequency dependence of various approximations for the Gaunt factor are shown in Fig. 4. The results are given in units of the Gaunt factor $g_{\rm D}(\omega)$ which is obtained when calculating the absorption coefficient using the collision frequency (3) for a statically screened potential. Besides the results from the Gould–DeWitt approach (4) and its renormalization due to electron–electron correlations, the separate contributions from dynamical screening and strong collisions (T-matrix) are shown. In the high-frequency limit, the dynamical screening and static screening almost coincide. In consequence, the Gould–DeWitt result is dominated by the contribution from strong collisions.

As already noted by Iglesias and Rose [40, 41], the account of dynamical screening is not important for the calculation of Rosseland mean opacities, a spectrally averaged absorption coefficient [34] relevant in optically thick plasmas. The differences are small in the important region around $\hbar\omega/(k_{\rm B}T) = 4$.

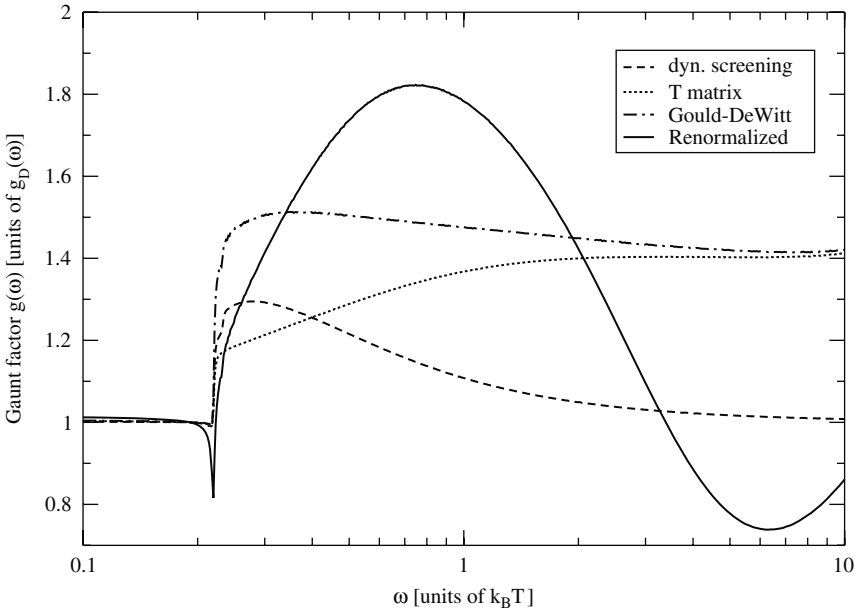

Fig. 4 Frequency dependence of the Gaunt factor [39] for solar core conditions with $n_{\rm e} = 6.0 \times 10^{25}\,{\rm cm}^{-3}$, $T = 1.3\,{\rm keV}$

However, including the renormalization leads to pronounced deviations. Since the maximum of the real part of the renormalization factor is located at $k_B T$, the Gaunt factor is affected even at frequencies large compared to the plasma frequency ω_{pl}. Thus, a recalculation of the Rosseland mean opacities [41] would be interesting. Also, the bremsstrahlung spectrum has contributions from free–free as well as bound–free transitions. Hence, a description of the bremsstrahlung spectrum requires also an appropriate treatment of bound states in a hot and dense plasma. In addition, the transient nature of the expanding laser-induced plasma requires the knowledge of density and temperature profiles as well as ionization degrees, which can be taken, e.g., from a hydrodynamical code. Evidence of its relevance will be given in the discussion of the reflectivity in the next section.

3.2 Reflectivity

Recently, dense plasmas showing the transition from dielectric to metallic behavior were investigated extensively. For the diagnostics of properties in such highly compressed plasmas, optical measurements are most favorable, e.g., the reflectivity is expected to give information on the free charge carrier density.

Reflectivity measurements on Al and Si have been performed by Basko et al. [42, 43]. Whereas the electron density is estimated to change at the shock wave front within a small interval of several nanometers, the change in temperature occurs within a layer of about 0.3 μm. Of high interest are recent experiments in liquid deuterium and water [44, 45] which show a saturation of the reflectivity at values above 50% which is typical for a conducting state. In experiments on shock wave compressed xenon plasmas [46] which have been performed using three different wavelengths $\lambda = 1.064$, 0.694 and 0.532 μm [47, 48], a strong increase of the reflectivity has been observed indicating metallization.

A rigorous treatment for the reflectivity from an arbitrary plasma front requires the Maxwell equations for the electromagnetic field. Considering a planar wave propagating along z-axis and neglecting nonlocal effects for the conductivity, the following Helmholtz equation for the complex amplitude of the electric field E at frequency ω

$$\frac{\mathrm{d}^2 E(z)}{\mathrm{d}z^2} + 4\pi^2 \epsilon(\omega, z) E(z) = 0, \tag{9}$$

where z is the distance in units of the wavelength, has to be solved with appropriate boundary conditions. The dielectric function $\epsilon(\omega, z)$ has to be calculated for given density and temperature profiles $n_e(z)$, $T(z)$.

For normal incidence and assuming a step-like plasma front, the reflectivity can be calculated from the dielectric function using the Fresnel formula

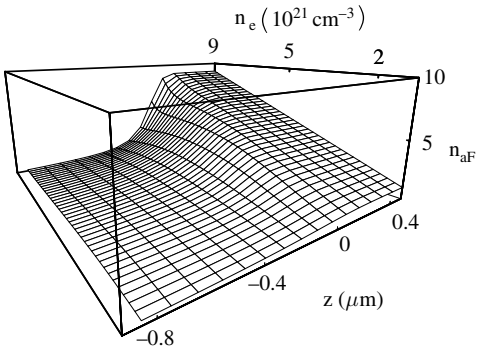

Fig. 5 Profile of the plasma front density $n_{aF}(n_e, z)$ in units of 10^{21} cm^{-3} for different maximum densities n_e in the bulk plasma [49]

$R(\omega) = \left|\sqrt{\epsilon(\omega)} - 1\right|^2 / \left|\sqrt{\epsilon(\omega)} + 1\right|^2$. However, we find that neither analytical expressions for the collision frequency (static or dynamic, local or nonlocal) nor MD simulations as well as the account of neutral components can explain satisfactorily the behavior of the measured reflectivity as long as a step-like plasma front profile is assumed [46]. Instead, a spatial structure of the ionizing shock wave was discussed in [47]. In the region of the shock wave front where the free electron density smoothly increases from zero to its maximum value in the bulk plasma, the reflection of electromagnetic radiation occurs already in the outer region where the density is low. The width of the wave front is determined by relaxation processes in the plasma.

A density profile can be designed by assuming an asymmetric Fermi profile dependence on the position, with the parameters determined using measurements of the reflectivity at two wavelengths [49]. The temperature is assumed to be uniform across the shock front at the plasma temperature. The resulting density profile across the shock front, see Fig. 5, increases at first slowly and becomes steeper toward the plasma region. The density gradient is stronger at higher final plasma densities, i.e., closer to the step-like shock wave front. As Fig. 6 shows, good agreement with the experimental data is obtained. The

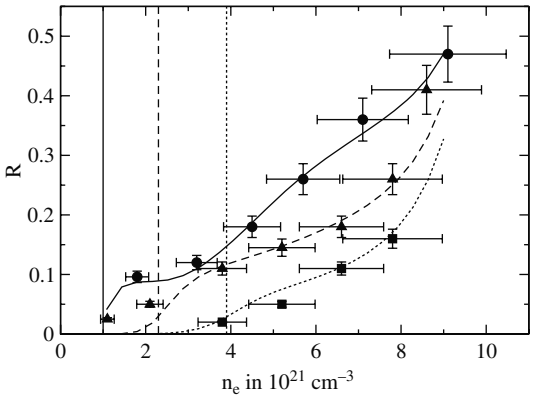

Fig. 6 Reflectivity coefficient R for xenon [49] calculated with plasma front profile n_{aF} (*lines*) in comparison with measurements (*symbols with error bars*) [47, 48, 50] for laser wavelengths 1.06 μm (*solid line*, large ●), 0.694 μm (*dashed line*, ▲); and 0.532 μm (*dotted line*, ■); the corresponding critical densities n_e^{cr} are indicted with *vertical lines*

adjustment of the parameters using measurements at two wavelengths is sufficient to describe the behavior of the reflectivity for the third wavelength and probably other wavelengths as well. The density profile of the free electrons could be modified by including profiles for temperature and the neutral component as well. Further items which should be addressed are the accuracy in determining the composition, in particular the free electron density, and the relevance of the assumption of local equilibrium.

3.3 Thomson Scattering

Dense plasmas are not transparent in the optical region since the frequency of the light becomes less than the plasma frequency ω_{pl}. In this case, X-ray Thomson scattering can be used for the diagnostics of plasma properties [51]. The required intense X-ray sources are obtained using high-power optical lasers in order to pump and probe samples of solid densities [52]. An X-ray free electron laser (FEL) operating in the VUV range from 60 to 5 nm has started operation at DESY, Hamburg. A similar facility is under construction at Stanford Linear Acceleration Center (SLAC). First experiments to measure the averaged ionization state $\bar{Z}$, the electron density and the electron temperature by using incoherent Thomson scattering at a probe wavelength of $\lambda_0 = 263$ nm were performed for high-Z (gold) plasmas [53] with uncertainties of $<20\%$. Spectrally resolved X-ray Thomson scattering at $\lambda = 0.24$ nm was applied to determine plasma parameters for dense Be plasma [54]. Results for Be and C at solid-state-like densities were given recently [55, 56].

The differential scattering cross-section of Thomson scattering is related to the total dynamic structure factor $S(k,\omega)$ of all electrons in the plasma according to

$$\frac{\mathrm{d}^2\sigma}{\mathrm{d}\Omega\,\mathrm{d}\omega} = \left(\frac{\mathrm{d}\sigma}{\mathrm{d}\Omega}\right)_{\mathrm{T}} \frac{k_1}{k_0} S(k,\omega), \tag{10}$$

where $(\mathrm{d}\sigma/\mathrm{d}\Omega)_{\mathrm{T}}$ is the Thomson cross-section [57]. k_0 and k_1 are the wavenumbers of the incident and the scattered light, respectively. The energy and momentum transfer are characterized by $\hbar\omega = \hbar\omega_0 - \hbar\omega_1$ and $\hbar\mathbf{k} = \hbar\mathbf{k}_0 - \hbar\mathbf{k}_1$, respectively. In the limit $\hbar\omega \ll \hbar\omega_0$, the transfer momentum is related to the scattering angle Θ according to $k = 4\pi\sin(\Theta/2)/\lambda_0$. A scattering parameter $\alpha = 1/(k\lambda_{\mathrm{D}})$ is introduced, where the Debye radius $\lambda_{\mathrm{D}} = \sqrt{\epsilon_0 k_{\mathrm{B}} T_{\mathrm{e}}/(n_{\mathrm{e}} e^2)}$ is the screening length in the plasma. Short-range correlations (within the Debye sphere) are relevant for $\alpha \leq 1$ and long-range, collective scattering is dominant for $\alpha \geq 1$ and will be reflected by different cross-section specifics. The dynamic structure factor contains contributions from electrons tight to the ion motion including screening, from free electrons and from inelastic scattering

due to excitations of core electrons. The free electron part of the structure factor

$$S(k,\omega) = \frac{k^2}{\omega}\frac{k_B T}{\omega_{pl}^2 m_e}\,\mathrm{Im}\,\frac{1}{\epsilon_{long}(k,\omega)} \tag{11}$$

is related to the longitudinal dielectric function. Analytical results on the level of the RPA have been applied, see Gregori et al. [55]. Figure 7 illustrates the principal behavior of the structure factor. By changing the temperature, we probe short-range correlations up to collective modes. With decreasing scattering parameter, the plasmon feature, a double peak structure, disappears and a smeared out central peak is observed.

We are interested in conditions where RPA is not sufficient to describe X-ray Thomson scattering and collisions have to be taken into account. For an adequate treatment, the dynamical structure factor is calculated via the Mermin expression [21], which takes into account the collision frequency as an imaginary frequency.

Results indicate that collisions have only a minor influence on the dynamic structure factor in a wide parameter range so that RPA can be applied there. However, we also identified a parameter region (degeneracy parameter $\Theta \approx 1$ and coupling parameter $\Gamma > 1$) where major deviations from the RPA results are found and collisions are important to get reliable results for the plasma parameters, see also Refs. [55, 59, 60].

In Fig. 8, the dynamic structure factor, Eq. (11), obtained from the RPA dielectric function and for the Mermin approximation taking the frequency-dependent collision frequency in the Born approximation, Eq. (3), shows relevant differences. The dynamic structure factor is red-shifted and broadened with increasing scattering angle. With increasing recoil energy, these peaks

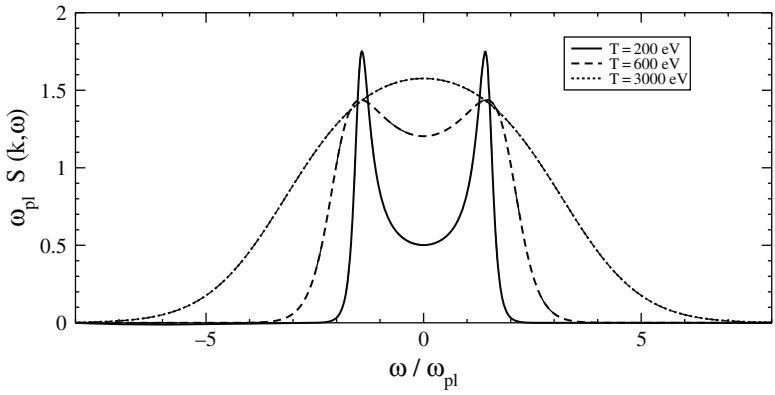

Fig. 7 Dynamic structure factor $S_{ee}(k,\omega)$ from RPA for an electron plasma at $n_e = 10^{19}$ cm^{-3} using radiation of 532 nm [58]

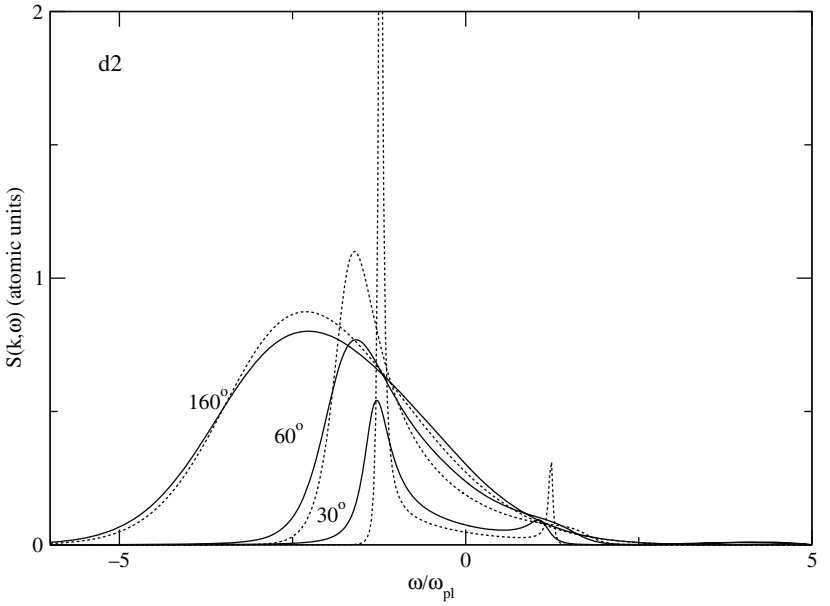

Fig. 8 Angular dependence of the dynamic structure factor [15] for an electron plasma at $n_e = 10^{19}$ cm^{-3} and $T = 2$ eV using radiation of 1 nm [59]. *Dotted lines*: RPA; *solid lines*: Mermin approach with dynamic collision frequency in Born approximation

become asymmetric and the red-shifted peak is more pronounced. Collisions are more important for smaller angles and yield modifications of the RPA results.

The sensitivity of a temperature adjustment via the high-frequency part of the dynamic structure factor with respect to the inclusion of collisions was demonstrated in Ref. [58]. The electron temperature inferred from the RPA structure factor overestimates the electron temperature derived from the Mermin approximation by a factor of about 2 which is important for plasma diagnostics.

Another promising approach to infer plasma parameters is the fact that the double peak structure in the regime $\alpha > 1$ where collective scattering is dominant shows an asymmetry according to the detailed balance:

$$S(k, -\omega) = e^{-\frac{\hbar\omega}{k_B T}} S(k, \omega). \tag{12}$$

If it would be possible to spectrally resolve these side peaks from the ion acoustic and the Rayleigh peak at the probe frequency and measure their intensities, one can directly determine the plasma temperature. The position of the plasmon resonance in a solid density plasma located at values $|\omega_{pl}|$ slightly above the plasma frequency can then be used to determine the free electron density. In the

collective scattering regime of a classical plasma where collisions are not relevant, it is given by the Gross–Bohm dispersion relation [61]:

$$\omega_{\max}^2 \approx \omega_{\mathrm{pl}}^2 + 3k^2 \mathrm{v}_{\mathrm{th}}^2 + \left(\frac{\hbar k^2}{2m_{\mathrm{e}}}\right)^2, \tag{13}$$

with the electron thermal velocity $\mathrm{v}_{\mathrm{th}}^2$. Besides the contribution of free electrons, also those of bound states and of inelastic collisions with weakly bound electrons have to be included in the evaluations when comparing with experimental scattering spectra, see Ref. [55].

4 Nonlinear Collisional Absorption

Due to the impressive progress in laser technology that makes femtosecond lasers pulses of very high intensity available in laboratory experiments, interaction of matter with electromagnetic fields has become a problem of current interest. Under the influence of an external electromagnetic field, e.g., a strong laser field, very interesting effects may be observed. Multiphoton processes [62], creation of higher harmonics, nonlinear absorption [63, 64] and ionization [62, 65, 66, 67] are typical consequences. The theoretical approach to the processes in strong laser fields requires, of course, nonperturbative treatments with respect to the field.

At especially high intensities E_0 of the radiation field, the quiver velocity of the free electrons $\mathrm{v}_0 = eE_0/(m_{\mathrm{e}}\omega)$ can be large compared to the thermal velocity and interesting nonlinear effects have to be expected. One of the important mechanisms of energy deposition is collisional absorption usually described in terms of the electron–ion collision frequency [68, 69, 70, 71, 72].

We consider here a fully ionized plasma. For the investigation of collisional absorption by the dense plasma, it is obvious to start from the balance equation for the energy and the electrical current resulting from a generalized non-Markovian kinetic equation. The energy input into the plasma is given by $\boldsymbol{j} \cdot \boldsymbol{E}$ in accordance with Poynting's theorem.

The balance equation for the electrical current density can be written in the following form [73]:

$$\frac{\mathrm{d}}{\mathrm{d}t}\boldsymbol{j}(t) + \boldsymbol{R}\{\boldsymbol{j}\} + \omega_{\mathrm{pl}}^2 \int_{t_0}^{t} \mathrm{d}\bar{t}\, \boldsymbol{j}(\bar{t}) = \varepsilon_0 \omega_{\mathrm{pl}}^2 \boldsymbol{E}(t), \tag{14}$$

with $\boldsymbol{E}$ being the external electrical field and the third term on the left hand side describes the polarization stemming from the mean field contribution. $\boldsymbol{R}$ describes the friction due to collisions. The friction term is a nonlinear non-Markovian functional of the current which reads (to lowest order in the electron–ion interaction)

$$\boldsymbol{R}\{\boldsymbol{j}\} = \frac{1}{\mathrm{i}} \int \frac{\mathrm{d}^3 q}{(2\pi\hbar)^3}\, \boldsymbol{q} \int_0^{t-t_0} \mathrm{d}\tau\, F(\boldsymbol{q};\tau) \exp\left\{ -\frac{\mathrm{i}}{\hbar} \frac{1}{n_\mathrm{e} e_\mathrm{e}} \boldsymbol{q} \cdot \int_{t-\tau}^{t} \mathrm{d}\bar{t}_1 \boldsymbol{j}(_1) \right\}, \qquad (15)$$

with the abbreviation

$$F(\boldsymbol{q},\tau) = \frac{2\pi}{\hbar} \frac{e_\mathrm{e}}{m_\mathrm{e}} V_\mathrm{ei}^2(q) \Big[\mathcal{S}_\mathrm{ee}(\boldsymbol{q};\tau) \mathcal{L}_\mathrm{ii}^A(\boldsymbol{q};-\tau) + \mathcal{L}_\mathrm{ee}^R(\boldsymbol{q};\tau)\, \mathcal{S}_\mathrm{ii}(\boldsymbol{q};-\tau) \Big], \qquad (16)$$

and the dynamic structure factors $\mathcal{S}$ and density response functions $\mathcal{L}$ of the two subsystems, electrons and ions.

There are two well-known limiting cases: in linear response, the exponential function in Eq. (15) can be expanded and the friction term is linear in the current with the dynamical collision frequency as prefactor, $R(\omega) = \nu(\omega)\, j(\omega)$, cf. Section 2.

For strong fields, on the other hand, the collisions are a small correction to the quiver motion of the particles and one can use in the exponential

$$\boldsymbol{j} \approx \boldsymbol{j}^0 = \sum_\mathrm{a} \frac{e_\mathrm{a}^2 n_\mathrm{a}}{m_\mathrm{a}} \int_{t_0}^{t} \mathrm{d}t' \boldsymbol{E}(t'), \qquad (17)$$

which corresponds to the so-called Silin ansatz. For a harmonic field $\boldsymbol{E} = \boldsymbol{E}_0 \cos\omega t$, this leads to expansions [68, 69, 70] in terms of Bessel functions J_n, and the current $\boldsymbol{j}(t) = \sum_{n=1}^{\infty} \boldsymbol{j}_{n,0} \sin(n\omega t + \phi_n)$ can be calculated as a function of the electrical field. The general case, where Eq. (14) cannot be solved simply for j, was discussed in [73].

The energy absorption rate is given by

$$\nu_\mathrm{E} = \frac{\langle \boldsymbol{j} \cdot \boldsymbol{E} \rangle}{\langle \varepsilon_0 \boldsymbol{E} \cdot \boldsymbol{E} \rangle} = \frac{\omega_\mathrm{pl}^2}{\left[\omega - \frac{\omega_\mathrm{p}^2}{\omega} - \mathrm{Im}\nu(\omega) \right]^2 + [\mathrm{Re}\nu(\omega)]^2} \mathrm{Re}\nu(\omega). \qquad (18)$$

Here the brackets denote cycle-averaged quantities. In the high-frequency limit, we get the familiar expression $\nu_\mathrm{E} = \omega_\mathrm{pl}^2/\omega^2\, \mathrm{Re}\nu(\omega)$, where the energy absorption is determined by the real part of the collision frequency only, cf. the high-frequency limit of Eq. (8). In this expression, the real part sign is often suppressed in the literature.

For a strong harmonic electric field, the cycle-averaged dissipation of energy is given by [74, 75]

$$\langle \boldsymbol{j} \cdot \boldsymbol{E} \rangle = \int \frac{\mathrm{d}^3 q}{(2\pi\hbar)^3} \frac{n_\mathrm{i} V_\mathrm{ei}^2(q)}{V_\mathrm{ee}(q)} \mathcal{S}_\mathrm{ii}(\boldsymbol{q}, T_\mathrm{i}) \sum_{n=-\infty}^{\infty} n\omega\, J_n^2\left(\tfrac{q \cdot v_0}{\hbar\omega}\right) \mathrm{Im}\varepsilon_\mathrm{e}^{-1}(\boldsymbol{q}, -n\omega, T_\mathrm{e}),$$

with ε_e being the dielectric function of the electron component and $\mathcal{S}_\mathrm{ii}$ the static structure factor of the ions. The sum over Bessel functions J_n reflects the non-linear dependence on the field.

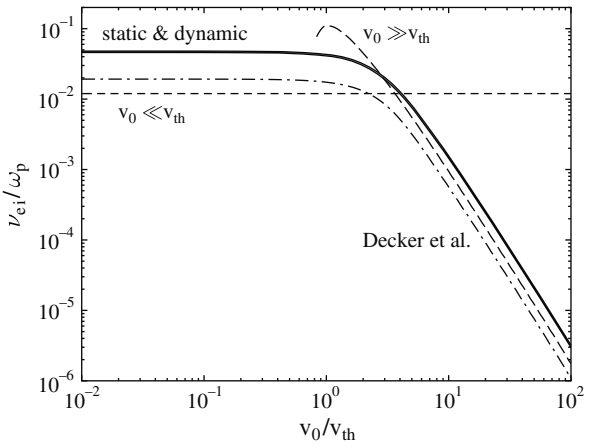

Fig. 9 Electron–ion collision frequency ν_{ei} as a function of the quiver velocity $v_0 = eE/\omega m_e$ for a hydrogen plasma in a laser field ($Z = 1; n_e = 10^{22}\text{cm}^{-3}$; $T = 3 \cdot 10^5\text{K}; \omega/\omega_p = 5$). For comparison, results of Decker et al. (*dash–dotted line*) [63] and of the asymptotic formulae by Silin (*dashed line*) [64] are given

In Fig. 9, the electron–ion collision frequency is shown in dependence of the electrical field strength. With Eq. (19), collisional absorption can be described also for the case of two-temperature plasmas. Molecular dynamics (MD) simulations confirm [75] that mainly the electrons are heated by the laser field whereas the temperature of the ions stays almost constant. The influence of the ion component with temperature T_i is accounted for in Eq. (19) by the static ionic structure factor. The calculations for an ion structure factor in hypernetted chain (HNC) approximation [75] show a considerable influence of structure factor effects on collisional absorption especially for the case T_i. Only for comparatively low electron temperatures is there an enhancement of the collision frequency at all.

In Fig. 10, the collision frequency normalized to the plasma frequency is plotted as a function of the coupling parameter Γ. The solid and dotted lines are results from the approach presented above for an isothermal case with $T_i = T_e$

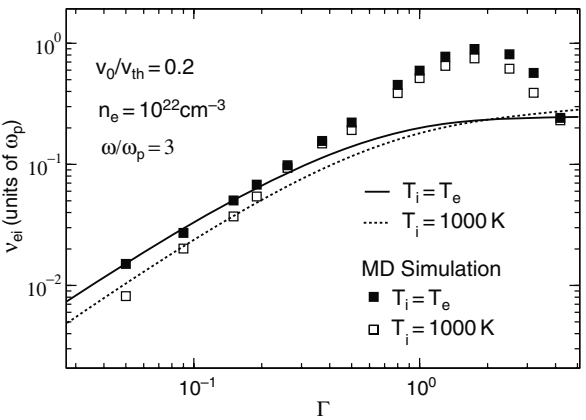

Fig. 10 Electron–ion collision frequency ν_{ei} as a function of the coupling parameter Γ for a hydrogen plasma in a laser field. *Solid line*: quantum statistical approach for an isothermal plasma ($T_i = T_e$). *Dotted line*: same approach but for a two-temperature plasma ($T_i = 1000$ K). The *filled and open squares* denote the corresponding MD simulation data [79]

(this case was also considered in [76] where a comparison is also given with other approaches [77, 78] and for a two-temperature plasma with an ion temperature of 1000 K, respectively). The squares are the corresponding simulation data. The simulation data as well as the analytic calculation show an increase of the collision frequency with increasing coupling. The agreement between the simulation and the quantum statistical results is good in the region of weak and moderate coupling ($\Gamma \leq 0.3$). The lowering of the collision frequency for a two-temperature plasma with cold ions is very well confirmed by MD simulations [75].

In the region of higher coupling, $\Gamma > 0.3$, the deviations between the simulation and the analytic calculations are growing. Both approaches have their limitations in this region. One has to keep in mind that, on one hand, the analytic approach adopts weak coupling with respect to the electron–ion interaction. Enhanced heating rates were also reported in [80] using classical test particle studies. On the other hand, molecular dynamics simulations are valid for arbitrary coupling only in the classical case. Quantum effects were accounted for approximately via an effective quantum potential (Kelbg potential) derived for weakly coupled plasmas only.

The behavior of the collision frequency in an aluminum plasma [79] in dependence on the temperature is shown in Fig. 11 for two different laser wavelengths: 800 nm (a) and 32 nm (b). Field effects are important if the quiver

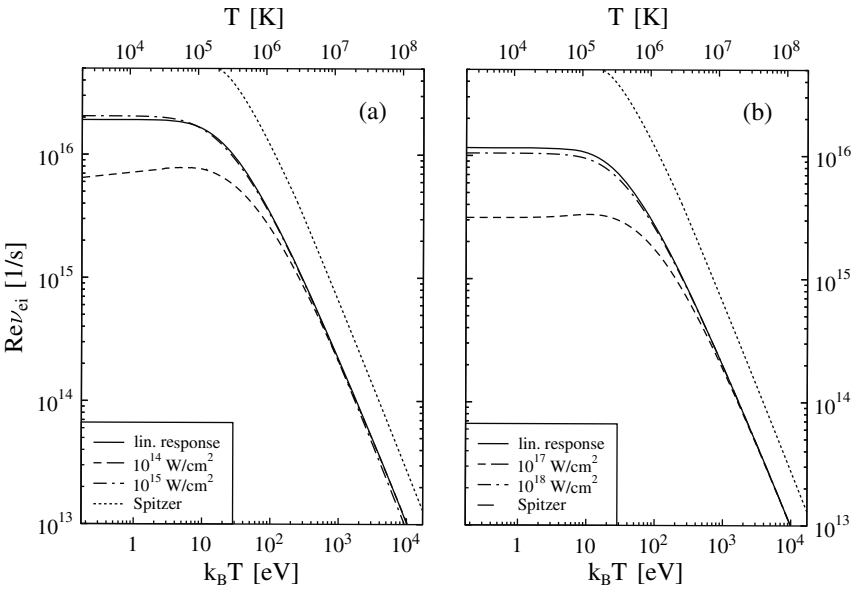

Fig. 11 Real part of the electron–ion collision frequency ν_{ei} vs. electron temperature for aluminum [79], $T_i = T_e$, for two different laser wavelengths: (**a**) $\lambda = 800$ nm, (**b**) $\lambda = 32$ nm and several laser intensities. In addition, the limiting case for high T (Spitzer formula) is shown

velocity is greater than the thermal velocity. Re ν_{ei} can be described therefore by the linear response case up to rather high fields. In the case of the optical laser with $\lambda = 800$ nm, deviations from the weak field behavior occur at $I \gtrsim 10^{14}$ W/cm^2. For the VUV–FEL ($\lambda = 32$ nm), this limit lies even at $I \approx 10^{17}$ W/cm^2 (for comparison: the atomic field strength, i.e., the field of the proton at 1 a_B, corresponds to $I \approx 3.5 \cdot 10^{16}$ W/cm^2). At high temperatures, all curves agree with the weak field result. The deviation from the Spitzer limiting case at high temperatures can be overcome by taking into account higher moments of the distribution function.

Acknowledgments The authors acknowledge support by the Deutsche Forschungsgemeinschaft within Sonderforschungsbereich 652. Many people contributed to this work. The authors wish to thank especially P. Hilse, I. Morozov, R. Redmer, G. Röpke, M. Schlanges and A. Wierling for fruitful collaboration.

References

1. *Physics of Laser Plasma*, Vol. 3 of *Handbook of plasma physics*, edited by A. Rubenchik, and S. Witkowski (North Holland, Amsterdam, 1991).
2. F. Brunel, Phys. Rev. Lett. **59**, 52 (1987).
3. S. H. Glenzer, W. Rozmus, V. Y. Bychenkov, j. D. Moody, J. Albritton, R. L. Berger, A. Brantov, M. E. Foord, B. J. MacGowan, R. K. Kirkwood, H. A. Baldis, and E. A. Williams, Phys. Rev. Lett. **88**, 235002 (2002).
4. T.-Y. B. Yang, W. L. Kruer, R. M. More, and A. B. Langdon, Phys. Plasmas **22**, 3146 (1995).
5. H. Reinholz, R. Redmer, G. Röpke, and A. Wierling, Phys. Rev. E **62**, 5648 (2000).
6. D. Zubarev, V. Morozov, and G. Röpke, *Statistical Mechanics of Nonequlibrium Processes* (Akademie-Verlag, Berlin, 1997), Vol. 2.
7. I. Morozov, G. Norman, and A. Valuev, Doklady Phys. **43**, 608 (1998).
8. I. Morozov, G. Norman, and A. Valuev, Phys. Rev. E **63**, 036405 (2001).
9. I. Morozov, and G. Norman, JETP **100**, 370 (2005).
10. M. Knaup, P.-G. Reinhard, and C. Toepffer, Contrib. Plasma Phys. **41**, 159 (2001).
11. M. P. Desjarlais, Contrib. Plasma Phys. **45**, 300 (2005).
12. B. Militzer, and D. M. Ceperley, Phys. Rev. Lett. **85**, 1890 (2000).
13. V. S. Filinov, M. Bonitz, P. Levashov, V. E. Fortov, W. Ebeling, M. Schlanges, and S. W. Koch, J. Phys. A **36**, 6069 (2003).
14. R. Redmer, Physics Rep. **282**, 35 (1997).
15. H. Reinholz, Annales de Physique **30**, 1 (2005).
16. G. Röpke, Phys. Rev. A **38**, 3001 (1988).
17. N. Arista, and W. Brandt, Phys. Rev. A **29**, 1471 (1984).
18. T. Wilhein, J. Opt. Soc. Am. B **15**, 1235 (1998).
19. G. Röpke, H. Reinholz, R. Redmer, and A. Wierling, J. Phys. IV France **10**, Pr5 (2000).
20. S. Chapman, and T. Cowling, *The Mathematical Theory of Non-Uniform Gases* (University Press, London, 1952).
21. A. Selchow, G. Röpke, A. Wierling, H. Reinholz, T. Pschiwul, and G. Zwicknagel, Phys. Rev. E **64**, 056410 (2001).
22. I. Morozov, H. Reinholz, G. Röpke, A. Wierling, and G. Zwicknagel, Phys. Rev. E **71**, 066408 (2005).
23. A. Esser, R. Redmer, and G. Röpke, Contrib. Plasma Phys. **43**, 33 (2003).

24. V. Sechenov, E. Son, and O. Shchekotov, Sov. Phys.-TVT **15**, 415 (1977).
25. Y. Ivanov, V. Mintsev, V. Fortov, and A. Dremin, Sov. Phys.-TVT **71**, 216 (1976).
26. A. Bakeev, and R. Rovinskii, Sov. Phys.-TVT **8**, 1121 (1970).
27. V. Batenin, and P. Minaev, Sov. Phys.-TVT **92**, 676 (1971).
28. S. Andreev, and T. Gavrilova, Sov. Phys.-TVT **13**, 176 (1975).
29. G. D. Mahan, *Many-Particle Physics*, 2nd ed. (Plenum Press, New York, 1990).
30. H. R. Griem, *Principles of Plasma Spectroscopy* (Cambridge University Press, Cambridge, 1997).
31. A. Mostovych, K. Kearney, J. Stamper, and A. Schmitt, Phys. Rev. Lett. **66**, 612 (1990).
32. M. Lamoureux, P. Waller, P. Charles, and N. Avdonina, Phys. Rev. E **62**, 4091 (2000).
33. W. Kruer, *The Physics of Laser Plasma Interaction* (Addison-Wesley, Redwood City, 1988).
34. S. Atzeni, and J. M. ter Vehn, *The Physics of Inertial Fusion*, Vol. 125 of *International series of monographs on Physics* (Clarendon Press, Oxford, 2004).
35. H. Kramers, Philos. Mag. **46**, 836 (1923).
36. J. Gaunt, Proc. R. Soc. London A **126**, 654 (1930).
37. J. Dawson, and C. Oberman, Phys. Fluids **5**, 517 (1962).
38. T. Johnston, and J. Dawson, Phys. Fluids **16**, 722 (1973).
39. A. Wierling, T. Millat, G. Röpke, R. Redmer, and H. Reinholz, Phys. of Plasmas **8**, 3810 (2001).
40. C. Iglesias, and S. Rose, AstroPhys. J. Lett. **466**, L115 (1996).
41. C. Iglesias, Phys. Lett. A **213**, 313 (1996).
42. M. Basko, T. Löwer, V. Kondrashov, A. Kendl, R. Sigel, and J. M., Phys. Rev. E **56**, 1019 (1997).
43. T. Löwer, V. Kondrashov, M. Basko, A. Kendl, J. M. Meyer-ter-Vehn, R. Sigel, and A. Ng, Phys. Rev. Lett. **80**, 4000 (1998).
44. P. Celliers, G. Collins, L. Da Silva, D. Gold, R. Cauble, R. Wallace, M. Foord, and B. Hammel, Phys. Rev. Lett. **84**, 5564 (2000).
45. R. Cauble, D. Bradley, P. Celliers, G. Collins, and S. Moon, Contr. Plasma Phys. **41**, 239 (2001).
46. H. Reinholz, Y. Zaparoghets, V. Mintsev, . Fortov, I. Morozov, and G. Röpke, Phys. Rev. E **68**, 036403 (2003).
47. V. B. Mintsev, and Y. B. Zaporoghets, Contrib. Plasma Phys. **29**, 493 (1989).
48. Y. Zaporoghets, V. Mintsev, V. Gryaznov, V. Fortov, H. Reinholz, T. Raitza, and G. Röpke, J. Phys. A: Math. Gen. **39**, 4393 (2006).
49. T. Raitza, H. Reinholz, G. Röpke, V. Mintsev, and A. Wierling, J. Phys. A: Math. Gen. **39**, 4393 (2006).
50. Y. B. Zaporoghets, V. B. Mintsev, V. Gryaznov, and V. Fortov, in *Physics of Extreme Matter*, edited by V. Fortov *et al.* (Inst. Probl. Chem. Phys. RAN, Chernogolovka, 2002), p. 188.
51. S. Glenzer, G. Gregori, R. Lee, F. Rogers, S. W. Pollaine, and O. Landen, Phys. Rev. Lett. **90**, 175002 (2003).
52. H. Baldis, J. Dunn, M. Foord, and W. Rozmus, Rev. Sci. Instr. **73**, 4223 (2002).
53. M. Foord, S. Glenzer, R. Thoe, K. Kwong, K. Fournier, B. Wilson, and P. Springer, Phys. Rev. Lett. **85**, 992 (2000).
54. O. Landen, S. Glenzer, M. Edwards, R. Lee, G. Collins, R. Cauble, W. Hsing, and B. Hammel, J. Quant. Spectrosc. Radiat. Transf. **71**, 465 (2001).
55. G. Gregori, S. Glenzer, W. Rozmus, R. Lee, and O. Landen, Phys. Rev. E **67**, 026412 (2003).
56. G. Gregori, S. Glenzer, F. Rogers, S. Pollaine, O. Landen, S. Blancard, G. Faussurier, P. Renaudin, S. Kuhlbrodt, and R. Redmer, Phys. Plasmas **11**, 2754 (2004).
57. J. Chihara, J. Phys. Condens. Matter **12**, 231 (2000).
58. A. Höll, R. Redmer, G. Röpke, and H. Reinholz, Eur. J. Phys. D **29**, 159 (2004).

59. R. Redmer, H. Reinholz, G. Röpke, R. Thiele, and A. Höll, IEEE Trans. Plasma Sci. **33**, 77 (2005).
60. G. Gregori, S. Glenzer, and O. Landen, J. Phys. A: Math. Gen. **36**, 5971 (2003).
61. D. Bohm, and E. P. Gross, Phys. Rev. **75**, 1851 (1949).
62. L. V. Keldysh, Zh. Eksp. Teor. Fiz. **47**, 1945 (1964).
63. C. D. Decker, W. B. Mori, J. M. Dawson, and T. Katsouleas, Phys. Plasmas **1**, 4043 (1994).
64. V. Silin, Zh. Eksp. Teor. Fiz. **47**, 2254 (1964).
65. F. Faisal, J. Phys. B: At. Mol. Opt. Phys. **6**, L 89 (1973).
66. H. R. Reiss, Phys. Rev. A **22**, 1786 (1980).
67. H. R. Reiss, Phys. Rev. A **42**, 1476 (1989).
68. D. Kremp, T. Bornath, M. Bonitz, and M. Schlanges, Phys. Rev. E **60**, 4725 (1999).
69. T. Bornath, M. Schlanges, P. Hilse, and D. Kremp, Phys. Rev. E **64**, 026414 (2001).
70. H.-J. Kull, and J. Plagne, Phys. Plasmas **84**, 5244 (2001).
71. G. Hazak, N. Metzler, M. Klapisch, and J. Gardner, Phys. Plasmas **95**, 345 (2002).
72. D. Kremp, M. Schlanges, and W.-D. Kraeft, *Quantum Statistics of Nonideal Plasmas* (Springer, Berlin, 2005).
73. T. Bornath, and M. Schlanges, J. Phys. A: Math. Gen. **39**, 4699 (2006).
74. T. Bornath, M. Schlanges, P. Hilse, and D. Kremp, J. Phys. A: Math. Gen. **36**, 5941 (2003).
75. P. Hilse, M. Schlanges, T. Bornath, and D. Kremp, Phys. Rev. E **43**, 056408 (2005).
76. M. Schlanges, T. Bornath, P. Hilse, and D. Kremp, Contrib. Plasma Phys. **43**, 360 (2003).
77. R. Cauble, and W. Rozmus, Phys. Fluids **28**, 3387 (1985).
78. S. Pfalzner, and P. Gibbon, Phys. Rev. E **57**, 4698 (1998).
79. D. Semkat, R. Redmer, and T. Bornath, Phys. Rev. E **73**, 066406 (2006).
80. A. Brantov, W. Rozmus, R. Sydrora, C. Capjack, V. Bychenkov, and V. Tikhonchuk, Phys. Plasmas **10**, 3385 (2003).

Relativistic Laser–Atom Physics

Alfred Maquet, Richard Taïeb, and Valérie Véniard

1 Introduction

Relativistic laser–atom physics has emerged recently as a new research area, thanks to the newly opened possibility to submit atoms to ultra-intense pulses of infrared coherent radiation from laser devices. Indeed, recently implemented "table-top" laser sources can deliver radiation pulses with peak intensities so high that a free electron, even initially at rest, can acquire a relativistic velocity [1,2,3]. In fact, the questions related to the dynamics of a free electron embedded within a (constant amplitude-) classical field have been addressed since the early days of relativistic quantum mechanics. In 1935, an exact expression for the wave function had been derived within the framework of the Dirac theory [4]; see also [5] for a recent discussion of the case of an electron submitted to a short laser pulse. In the 1960s, the advent of laser devices has motivated theory studies related to quantum electrodynamics (QED) in strong fields. For a non-exhaustive list of early references, see [6,7,8,9,10]. For many years, these formal results were considered as being only of academic interest. This was because the intensities available at optical frequencies, not only from conventional sources but also from Q-switched and mode-locked lasers, were so low that lowest order perturbative approaches could account for most of the observed effects. Even when strong laser devices were made available, most of the highly non-linear effects observed in laser–atom physics (above-threshold ionization – ATI, high-order harmonic generation, multiple ionization, etc.) could be accounted for within the framework of a non-relativistic approach. In this class of processes, relativity plays only a marginal role and is expected to intervene at intensities beyond the so-called atomic unit of laser intensity

A. Maquet
Université Pierre et Marie Curie, Laboratoire de Chimie Physique—Matière et Rayonnement, 11, rue Pierre et Marie Curie, 75231 Paris Cedex 05, France
e-mail: alfred.maquet@upmc.fr

T. Brabec (ed.), *Strong Field Laser Physics*,
DOI: 10.1007/978-0-387-34755-4_20,

$I_{at} \approx 3.5 \times 10^{+16}$ Wcm^{-2}.[1] This point has been discussed in several review papers including [11,12,13,14].

The state of affairs has significantly changed in the mid-1990s when it has been possible to make to collide a relativistic electron beam (with typical energy 46.6 GeV) from a LINAC with a focused laser (Nd: Yag) radiation. Under such extreme conditions, it has been possible to evidence highly non-linear, essentially relativistic, QED processes, such as non-linear Thomson and Compton scattering and also pair production [15,16,17].

These early QED investigations were primarily concerned with relativistic free electrons colliding with a laser beam. In fact, another class of effects can be observed when focusing the radiation from an ultra-intense laser on atoms. The latter are rapidly stripped of their outer electrons during the rise of the laser pulse. In the pulses delivered by the currently available infrared laser sources, tunneling is the dominant ionization mechanism and the photoelectrons are released with almost zero velocity, within the focal area, i.e., where they can experience the laser field strength at its maximum [18,19,20,21,22,23,24,25,26]. Strong field atomic ionization thus provides a unique source of electrons, initially almost at rest, in the presence of the field. In these conditions, atomic physics effects that govern the initial distribution of the photoelectrons play an essential role in determining the subsequent relativistic dynamics of the electrons within the field. The main objective of this chapter is to report on the key aspects of the physics of laser–atom interactions under these extreme conditions.

In order to clarify the discussion, let us note first that atomic physics is dominated by the Coulomb forces via the electron–electron and electron–nucleus interactions. The relevant energy scales range from the eV for the "optical electrons" in the outer shells to tens of keV for inner shells in high-Z atoms. It is only in the latter case that relativity plays a notable role in the details of the atomic structure. On the other hand, most laser devices used for producing ultra-intense radiation fields are operated in the infrared with photon energies around $\hbar\omega \approx 1$ eV. If atoms are set in the presence of a classical electromagnetic field with time-dependent envelope $f(t)$ and peak field strength $\mathbf{E}_0$ such that $\mathbf{E}(t) = \mathbf{E}_0 f(t)\sin(\omega t)$, the response of the electronic cloud will depend directly on the electron-field coupling energy that is dominated by the electric-dipole term: $H_I(t) = -q\mathbf{E}(t).\mathbf{r}$. A convenient yardstick for apprehending the importance of this coupling, as compared to intra-atomic interactions, is provided by the maximum value of the so-called *ponderomotive energy* $U_p = q^2 {E_0}^2/(4m\omega^2)$, corresponding to the averaged kinetic energy acquired by a free electron set in forced motion within the field. Most laser–atom physics processes which are discussed in this book are observed for U_p values ranging from a few eV up to a few hundreds of eV [27]. In contrast, we shall address here the questions related to the physical processes taking place at

[1] For a constant amplitude field $E(t) = E_0 \sin(\omega t)$, one has $I_L = \frac{1}{2}\sqrt{\frac{\epsilon_0}{\mu_0}}|E_0|^2$.The fictitious intensity associated to the atomic unit of electric field strength $E_{at} = \frac{e}{(4\pi\epsilon_0)a_b^2}$ experienced by an electron on the first Bohr orbit in hydrogen is $I_{at} \approx 3.5 \times 10^{+16}$ W cm^{-2}.

higher intensities, i.e., when the laser field peak strength is well beyond E_{at}, where $E_{\mathrm{at}} \approx 5 \times 10^{11}$ V m^{-1} is the field experienced by an electron on the first Bohr orbit in hydrogen.[2] Then, relativity naturally comes into play because U_{p} becomes comparable to the electron rest-mass energy.[3] We note that another criterion, often used in the literature for delineating the onset of relativistic effects, is the dimensionless parameter $\eta = qE_0/(m\omega c)$ that represents the ratio of the maximum quiver velocity of the particle within the field to the velocity of light. One has $\eta^2 = 4U_{\mathrm{p}}/(mc^2)$ and it is expected that relativistic effects come into play when $\eta^2 \geq 0.1$ that corresponds approximately to a focused intensity around 2×10^{17} W cm^{-2} for a Ti:sapph laser with $\hbar\omega \approx 1.5$ eV.

Regarding the general properties of such intense fields, it turns out that, in applications, they can be considered as being classical, within an excellent approximation. This is because the mode occupation numbers are enormous,[4] and that, consequently, spontaneous emission plays a marginal role as compared to the stimulated exchanges of photons. The question then arises of whether or not it is necessary to use in full the formalism of relativistic quantum mechanics for describing the electronic processes of interest. If the answer is yes, then one has to deal with the challenging task of solving the *time-dependent* Dirac equation on a spatio-temporal grid. We note that the need for a time-dependent treatment originates from the fact that the ultra-intense laser pulses have durations in the femtosecond range [2,3]. This implies that the parameter η, for instance, varies significantly over an attosecond time scale, which is characteristic of the relevant electronic relaxation times in atoms. In spite of the considerable difficulties of the computations, this class of problems has motivated a number of studies on which we shall report. It turns out, however, that most of these processes can be accounted for, to a good approximation, with the help of simpler approaches, e.g., the Klein–Gordon equation when spin effects can be neglected or even purely classical trajectory Monte-Carlo (CTMC) techniques which have revealed themselves to be extremely useful to describe the dynamics of the electrons that are released within the laser beam.

2 Atomic Photoionization in the Relativistic Regime

We turn now to the dominant relativistic effects which have been actually observed in atom–laser interactions. Besides the expected effects of the longitudinal Lorentz force that imparts a momentum transfer in the forward direction, the other major contribution comes from the mass renormalization, or

[2] See note 1.

[3] For a laser field from a Nd:Yag laser with photon energy $\hbar\omega \approx 1.17$ eV and intensity $I = 10^{18}$ W cm^{-2}, the ponderomotive energy $U_{\mathrm{p}} \approx 105$ keV.

[4] For a laser field from a Nd:Yag laser with photon energy $\hbar\omega \approx 1.17$ eV and intensity $I = 10^{18}$ W cm^{-2}, the number N of photons contained in a $V = \lambda^3$ coherence volume (with $\lambda = 1.06$ μm) is $N = \frac{IV}{c\hbar\omega} \approx 2 \times 10^{14}$.

"mass-shift" effect. In a quantum picture, this effect results from the non-linear Compton scattering accompanied by the transfer of momentum from the laser photons to the electron [6,7,8,9,10]. It comes in addition to the standard mass change of a particle with a relativistic drift velocity. In the case of a constant amplitude (plane wave) field, one has

$$m^* = m\sqrt{1 + \frac{2U_\mathrm{p}}{mc^2}}. \tag{1}$$

An interesting point is that the correction term does not contain $\hbar$ and that the classical and quantum approaches lead to the same expression [6,7,8,9,10]. This partially explains the effectiveness of CTMC methods for describing the dynamics of electrons within the field.

The signature of mass renormalization has been first evidenced in the above-mentioned experiments, when colliding a beam of relativistic electrons from a LINAC with an infrared laser [12,15,16,17,14]. A typical illustration, more relevant in the context of laser–atom physics, is provided by the dependence in terms of the field strength of the *polar* angle distribution of the photoelectrons stripped from the outer shells of rare gas atoms submitted to a "long" infrared laser pulse, with peak intensity of the order of $I \approx 10^{18}$ W cm^{-2}. Here, "long" means a few hundreds of femtoseconds [18]. Indeed, as a direct consequence of the forward momentum transfer that accompanies mass renormalization, the polar angle of ejection θ of the photoelectrons with respect to the laser wave vector can be expressed in terms of their ponderomotive energy U_p through the relation

$$\theta = \tan^{-1}\sqrt{\frac{2mc^2}{U_\mathrm{p}}}, \tag{2}$$

which is exact in the limits of both a zero initial velocity and the "long" pulse regime, the latter condition being essential for the photoelectrons to experience the full strength of the ponderomotive forces, when leaving the focal area in their way toward the detector [6,7,8,9,10,28,29]. For classical treatments and analytical expressions valid under more general conditions, namely with arbitrary initial velocities and/or in the presence of external (static) fields, see [30,31,32,33,34]. Very recently, CTMC calculations have confirmed experimental results on the transfer of longitudinal (forward-)momentum, when fast electrons interact with an ultra-strong laser beam [35].

Applications of relativistic dynamics are not limited to describing the dynamics of free electrons within the focal area. It is surmised that it plays also a significant role in the mechanism of multiple ionization of rare gas atoms, when irradiated with such ultra-strong pulses. Ionization stages as high as Xe^{21+} have been observed in pulses with durations of a few tens of fs and with peak intensities up to 10^{18} W cm^{-2} [36,38]. It has been shown that two distinct processes jointly contribute to the double and/or multiple ionization of a given species. The dominant mechanism is sequential, the corresponding yields being globally

reproduced from non-relativistic tunneling ionization probabilities [26,36, 37,38,39,40,41]. We note that relativity affects only slightly the transition rates for the first ionization stages, so long as the charge state of the ionic core $Z < 20$, see [42]. The other mechanism is non-sequential: It originates from the re-collision of an electron which, when freed into the continuum, can be brought back to the ionic core by the oscillating field. In the course of the re-collision, which takes place mostly within a fraction of a laser cycle, the oscillating electron can knock out another (several) electron(s). This process, which is currently the object of much interest also at lower intensities [27], is still observed at intensities close to 10^{17} W cm^{-2}, in xenon [39]. This came somewhat as a surprise since, as already mentioned, at such intensities one would expect that the longitudinal momentum transfer imparted to the re-colliding electron by the laser magnetic field would prevent it from returning to the origin and eject other electrons from the ionic core [36,37]. Very recent experimental results indicate however that non-sequential ionization is suppressed beyond 10^{17} W cm^{-2} in neon [43]. These recent data call for more detailed studies on this point.

It turns out that, as sequential ionization is globally dominant, fair estimates of the total ionization yields for most ionic species can be derived from standard tunneling ionization rates. This has been verified also by comparing with results obtained from the numerical resolution of the time-dependent Schrödinger equation (TDSE) for each ionic species. When available, relativistic treatments based on the Klein–Gordon or Dirac equations for model systems have not evidenced significant departures from the non-relativistic treatment [44]. This can be ascribed to the fact that, so long as the electron remains in the vicinity of the nucleus, its dynamics remains essentially non-relativistic. This holds also in the processes of tunneling or barrier-suppression ionization as the electron is ejected with a low initial velocity. As an illustration of this class of simulations, typical variations in time of the populations of different ionic species for a model Kr atom submitted to an ultra-intense laser pulse are shown in Fig. 1 [44]; see also [45] for simulations based on tunneling ionization rates.

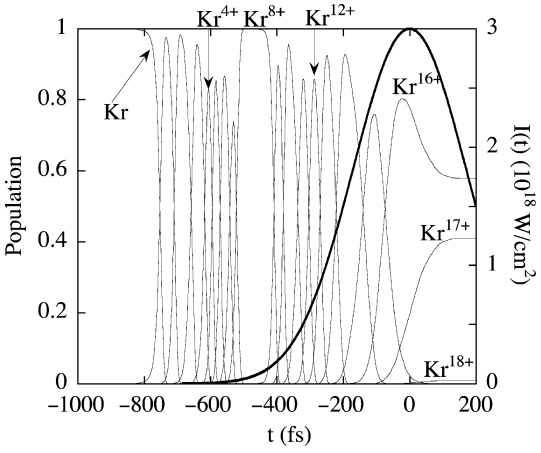

Fig. 1 Time dependence of the populations of different ionic stages for a model Kr atom in the presence of a laser field with peak intensity 3×10^{18} W cm^{-2}; the frequency is $\omega = 0.043$ a.u. The intensity envelope is Gaussian with 400 fs FWHM [23]

An interesting point regarding the population dynamics of the ionized species during the interaction time is related to the dependence of the ionization rates on the value of the magnetic quantum number m, within a given (n, l) sub-shell. In short, the ionization rates are higher for $m = 0$ than for $m = 1$, and so on. The question being whether or not this dependence could play a role in the population dynamics, when a sub-shell is stripped from its electrons [44]. Very recent experimental results, with pulse durations of 40 fs, indicate that, within the field, the m-mixing process is fast enough, so that the ionization rate is the same as the one of a statistical mixture of m-substates and is dominated by the $m = 0$ rate [46].

A common feature of the above atomic processes is that relativity plays only a marginal role on the magnitudes of the total ionization yields, even in the presence of the very strong fields that are currently available. More significant effects are expected regarding the angular distributions of the photoelectrons. Indeed, as soon as the electrons are freed, their motion becomes relativistic, the CTMC calculations providing a convenient tool for describing their trajectories when leaving the focal area. This kind of simulations enables ones to account for the dominant features of the *polar* angle distributions of the photoelectrons recorded in the experiments [18,19,20,21]. However, the question of the *azimuthal* distributions of the photoelectrons, in the plane perpendicular to the propagation direction of the field, is still not settled, as the results reported in the references [18,19,20,21,23] do not agree with each other. For a recent discussion, see [44].

It is expected that mass shift and related effects should also play important roles in other laser-induced processes. Here are a few topics of interest:

(i) *Laser-assisted electron–atom scattering*. During the course of electron–atom collisions taking place in the presence of a strong laser field, the projectile can absorb (or emit, through stimulated emission) photons. In super-intense fields, very large numbers of photons can be exchanged: up to several thousands for "hard" collisions accompanied by large momentum transfers. In the test case of laser-assisted Mott scattering for relativistic electrons [47], one can show that mass-shift effects manifest themselves in the width of the energy span for the scattered electron, see [48,49,50,51]. Note that this comes in addition to spin effects that play also a noticeable role in the Mott scattering of spin-polarized electrons [52,53].

(ii) *Atomic "stabilization"*. Theory and simulations predict that an atom could be "stabilized" in the presence of a super-intense *high-frequency* field. The a priori counter-intuitive prediction is that, under certain conditions, the lifetime of atomic states could increase when the field strength grows [54], see also [55,56] for more recent reviews. Earlier numerical simulations were done in the non-relativistic dipole approximation. Now, the question at stake is whether or not the "stabilization effect" will survive in the relativistic regime, i.e., when taking into account the mass shift and other corrections. We note that the question is no longer academic, in view of the planned development of new powerful sources of radiation in the XUV

and X-ray ranges, either from free-electron Laser (FEL) devices [57,58] or from high harmonic sources [59] or even from X-ray lasers [60]. The implementation of this class of new sources will permit to explore the completely open question of the collective response of electrons pertaining to different atomic shells. For the time being, only a few attempts have been reported which could help to provide quantitative data for a given experimental scheme [61].

Returning to the simpler case of a single-active electron, it is established that the relativistic mass shift tends to reduce the excursion length of the bound electron. This entails a narrowing of the laser-dressed potential well in which it is trapped, thus reinforcing its binding energy [62,63,64]. The question of the signature of such an effect in photoelectron spectra has been discussed in [65]. Broadly speaking, the global influence of the mass shift is to stabilize further the atom. Then, comes the question of the role of retardation which encompasses the forward momentum transfer and the coupling with the magnetic field through the Lorentz force. These processes induce an irreversible drift of the atomic electron, the resulting effect being to hinder stabilization. This has been confirmed in simulations, see, for instance, [66,67,68]. For the time being, it is still not clear to decide to which extent either the mass shift or the retardation effect would dominate the dynamics in the relativistic regime. In the end, even if the range of intensities in which stabilization does occur is reduced, the question of whether or not it is an observable effect is not settled yet; see, for instance, [65].

(iii) *Ionization from highly charged ionic species*. When an atom is submitted to an ultra-strong laser pulse, the first electrons that are ejected do not experience the peak power of the field. In fact, those that are emitted while the field magnitude is maximum originate from highly charged ions (see Fig. 1 for a simulation of the population dynamics in the successive ionization stages). Then, although they have a relatively low initial velocity when released into the continuum, these electrons can be accelerated up to relativistic velocities within the field. More precisely, depending on the time at which ionization takes place during a laser cycle, one can make the electron to "ride" on the laser wave, thus experiencing the field strength at its maximum [69]. Accelerations up to the GeV energy range have been predicted, and the feasibility of implementing this scenario in actual experiments has been confirmed by recent simulations [70,71]. It should be stressed again that this class of scenarios differs from the "collision-like" scheme in the course of which a fast free electron enters a tightly focused laser beam, [72]. Here, the electrons are "born within the field" and they can be prepared so that they experience the phase-dependent field strength.

(iv) *High-order harmonic generation from highly charged ionic species*. The process of high-order harmonic generation from a bound electron driven by an external laser field attracts a lot of interest, as it provides a non-conventional source of coherent XUV radiation delivering pulses with durations in the attosecond range [73, 147]. In the course of the interaction

of atoms with ultra-intense laser pulses, the only species experiencing the peak field strength are highly charged ions. Thus, the question has naturally arisen of the photon emission spectra from this class of ion species in the relativistic regime of intensities. One issue is the possibility of generating sizable amounts of high-frequency photons, notably in the X-ray range. As harmonic generation involves intrinsically a re-collision of the active electron with the ionic core, it is expected that the effect of the relativity-induced drift (through retardation and the Lorentz force) will be to reduce the harmonic generation yield, as compared to the non-relativistic regime. Recent discussions that address these questions include [74,75].

Before leaving the topic of atomic photoionization, we mention that the weakly relativistic regime that prevails at intensities around 10^{16} W cm^{-2} is of much practical interest, in view of the relatively large number of laser facilities that can deliver pulses in this range of intensities. The modifications of the ATI spectra under these conditions have been discussed very recently in [76].

We turn now to the still pending problem of the relative influence of relativistic *quantum* effects on the dynamics of laser–matter interactions in the strong, *time-dependent*, field regime.

3 Numerical Resolution of the Dirac Equation: A Paradigm for Lattice Fermion Field Physics

Pure quantum effects manifest themselves in finer details and, in order to predict where to find their signatures, a first step is to solve numerically the *time-dependent* Dirac equation. It is anticipated that the advent of the new generation of powerful laser sources should help in exploring several intriguing features of relativistic quantum mechanics.

From the theory point of view, the (at first innocuous) problem at stake is to solve the Dirac equation on a lattice, i.e., a spatio-temporal grid. Early attempts were motivated in the context of high-energy ion–atom collision physics, in which atoms can be submitted to a strong, time-varying, external field generated by the passing projectile [77]. There exist strong similarities with the case of the response of an atom to a femtosecond laser pulse [78]. It turns out that this kind of problems provides an illustration of a major difficulty encountered when quantizing a fermion field on a lattice [79]. The difficulty, which has been dubbed "fermion doubling", is that when solving the Dirac equation via a finite difference scheme in a $D+1$ dimension space, the solutions can be associated to 2^D particles instead of one [80,81]. This feature, which is intrinsic to the representation of the derivative operator on a grid, is clearly exemplified in the simple case of a one-dimensional massless field. The Weyl equation reads

$$\mathrm{i}\partial_t \Psi = \mathrm{i}\alpha \partial_z \Psi, \tag{3}$$

with the exact solution

$$\Psi(z,t) \propto \mathrm{e}^{-\mathrm{i}(\omega t \pm kz)} \tag{4}$$

and the dispersion relation $\omega = \alpha k; \alpha = \pm 1$. The discretized version, with step a, of the Weyl equation is

$$\mathrm{i}\partial_t \Psi = \frac{\mathrm{i}\alpha}{2a}[\Psi(z+a) - \Psi(z-a)], \tag{5}$$

which has also an exact solution leading to the modified dispersion relation: $\omega = \alpha \sin(ka)/a$, which entails that, for each Brillouin zone, there are two solutions instead of one as expected for a single particle.

It appears clearly that the original differential equation and its discretized version have different solutions, a direct consequence being that it is difficult to ensure the conservation of the current density on the grid. This difficulty has plagued the early attempts to solve numerically the time-dependent Dirac equation. The problem has been partially solved, via the implementation of sophisticated and rather time-consuming numerical techniques [77]. However, it still represents an obstacle when describing the interaction of an infrared laser pulse with matter in the strong field regime because one has to propagate the solutions over long time sequences as compared to the characteristic relativistic time scale.[5]

Another difficulty encountered when solving numerically the time-dependent Dirac equation comes from the boundary conditions. As one is forced to solve the difference equation in a finite box, one has to take care of spurious reflections of the time-dependent wave function on the walls. Standard mask function techniques, used in similar instances for the Schrödinger equation, do not apply here because the large and small components of the solution cannot vanish simultaneously at a given position in space. This is because each component is globally proportional to the derivative of the other. Again, sophisticated numerical tricks have been devised for curing this disease, including the so-called MIT-bag model and/or imposing periodic boundary conditions, see [82] for a recent account of these problems.

Because of these technical difficulties, most attempts to solve numerically the time-dependent Dirac equation have been limited to simple models in reduced dimension spaces, see [79] and the references regrouped in [83,84,85,86,87]. We turn now to a non-exhaustive list of topics that are associated to highly non-linear phenomena in strong fields, which are currently investigated. As most of them are a matter of discussion for QED in strong fields, see also [88].

---

[5] The relevant time scale in the relativistic domain is the natural unit of time: $t_0 = \frac{\hbar}{mc^2} \approx 1.29 \times 10^{-21}$ s, associated to the inverse of the electon's rest mass energy. In order to describe processes induced by an infrared laser, one has to propagate the solutions over several cycles with durations in the femtosecond range, corresponding to propagation times $\tau \geq 10^7 \times t_0$.

3.1 Spin Effects

As soon as strong lasers became available, the question arose of the relative importance of the coupling of the magnetic component of the field with the electron spin. Up to now, no experimental evidence of such effects has been reported. In the weakly relativistic regime of ionization, the expected influence is very small [76]. This contrasts with the case of the relativistic corrections in atomic structure where the spin–orbit coupling has an important role. Nevertheless, the question has been addressed in several theoretical analysis supported by numerical simulations.

As already mentioned, the signature of the spin coupling appears clearly in the computed energy distribution of the scattered electrons in laser-assisted Mott scattering, which is strongly influenced by the spin–orbit coupling [48,49,50,51]. It turns out, however, that the results derived from a full Dirac treatment differ only slightly from those obtained by using the spinless Klein–Gordon equation. Significant effects are nevertheless observed in the scattering of spin-polarized electrons [52,53]. The same situation prevails when considering the influence of spin on harmonic generation spectra [89], or when evaluating spin-induced forces [90,91]. In fact, significant effects could result from the combined effects of the strong laser and of the static Coulomb field of a high-Z nucleus, the signature being notable changes in the spin–orbit splitting in X-ray emission lines [92].

An outcome of these theory investigations is to indicate that a possibility of observing significant spin effects is to ensure the presence of a strong external field, in addition to the laser. As a first step toward this direction, the Dirac equation has been solved for an electron wavepacket in various relativistic situations in the presence of either an electric or a magnetic or also a time-dependent electromagnetic field, see [93,94]. One notes that the direct influence of relativity on spin variables is a kinematic contraction which, in contrast to the usual Lorentz length contraction along the propagation direction, is relativistically reduced perpendicular to the velocity.

3.2 "Zitterbewegung"

A puzzling consequence of the existence of negative energy states, which are solutions of the Dirac equation, with energies below $-mc^2$, is the elusive *Zitterbewegung* which results from the presence of very high frequency components in the general time-dependent expression for the electron wave function [95,47]. These high-frequency components are associated to virtual transitions between the negative and positive energy states that are solutions of the *single-particle* Dirac equation. A consequence of these highly improbable transitions is that when calculating the expectation values of operators, such as the

Dirac α matrix or the position $\mathbf{r}$, one finds that they oscillate at frequencies of the order of twice the inverse of the natural unit of time [95]:[6]

$$\Omega_{\text{Zitt}} = \frac{2mc^2}{\hbar} \approx 1.55 \times 10^{+21} \text{ Hz}. \tag{6}$$

However, there are very few observable effects resulting from the *Zitterbewegung*, one generally accepted notable exception being the leading contribution to the so-called Darwin term that contributes to the fine structure of atomic energy levels [47]. It is argued that this effect is an artifact resulting from the single-particle Dirac equation treatment, because in a second-quantization formalism, that intrinsically accounts for the existence of positrons, the question is not relevant. However, there is a sustained interest in the question, in the context of strong field atomic physics. One motivation is that, from a practical point of view, these oscillations on such a short time scale represent a nuisance when solving the time-dependent Dirac equation, in the sense that they impose using extremely small time steps.[7] This point has been first addressed in details in [79], where one can find also a discussion of the oscillations found in the expectation values of the spin and position operators. Later, the question has been revisited in different contexts, notably for the more realistic case of Volkov wavepackets that are relevant for describing free electrons embedded within the laser field [96].

One way out of these difficulties in numerical calculations is to implement a second-quantized field theory approach. Recent results obtained within this framework have been reported [97,98,99]. Coming back to relativistic laser–atom calculations with the help of the Dirac equation, it is expected that *stimulated* multiphoton transitions between negative and positive energy states could take place in the presence of the external field. This encompasses pair production and other highly non-linear processes (see below). Assuming that the problem of the numerical stability of the solution of the time-dependent wave equation has been solved, the question remains of finding a signature of *Zitterbewegung* in atomic phenomena. It turns out that, although noticeable effects are predicted in harmonic generation spectra, their magnitudes would remain extremely small [100]. We mention that, besides the strong field physics context, other scenarios are also considered in solid-state physics [101]. In our opinion, the question remains open of evidencing the influence, if any, of *Zitterbewegung* in strong field processes.

3.3 Pair Production

As mentioned in the introduction, γ-ray generation through the non-linear Compton effect has been observed when colliding GeV electrons with a strong

[6] See note 5.

[7] See note 5.

laser field and the subsequent production of $(e^- - e^+)$ pairs resulting in the interaction of the γ and infrared photons have been evidenced [15,16,17]. We note that the non-linear Compton effect and multiphoton pair production are related by the so-called crossing symmetry. This means that the corresponding cross-sections are proportional to each other, to within kinematical and density of states factors. Besides such a sophisticated scheme involving a LINAC, the possibility of generating pairs from the vacuum within an ultra-strong laser field has been envisioned, following Schwinger's early QED calculations [102,103]. Although it has been soon realized that the process could not take place in a plane-wave laser field [104,105], the question has motivated a number of theory studies since the early 1970s [106]. From these calculations, it has been inferred that the critical field intensity (the so-called Schwinger limit), which is required from an IR laser field, is somewhere around the sizable value 10^{+29} W cm^{-2} (see below). As such huge intensities no longer seem to be out of reach [3], there has been a renewed interest in the theory of the process, with the objective to define the conditions for observing pair production from the vacuum. We note that this scenario differs from the ones which involve (laser + high-Z nucleus) configurations that can be realized in plasmas or in laser–ion beam collisions, for recent references, see [107,108,109,110].

In fact, pair production from the interaction of photons in the absence of an external Coulomb potential necessarily implies two fields with different propagation directions, in order to ensure the 4-momentum global conservation in the process. One geometry that has been studied in particular, is the one of a "head-on" collision of two laser beams [111,112]. The case of tightly focused laser beams has been also addressed in [113].

We turn now to a simple approach which helps to delineate the conditions for observing pair production. Although a proper treatment requires, in principle, the use of a second-quantized QED formalism, it turns out that a crude estimate of the corresponding transition probability can be extracted from a discussion of the so-called Klein paradox. Almost every textbook on relativistic quantum mechanics contains a paragraph on the Klein paradox because it illustrates very clearly one of the most intriguing consequence of the existence of the negative energy solutions of the relativistic equations (Dirac or Klein–Gordon) [47]. In short, the paradox is that, within the framework of the Dirac single-particle theory, an incoming electron in the presence of a very high potential step such that $V_0 > 2mc^2$ can tunnel through the barrier and propagate within the step, occupying one of the negative energy states. Though considered for some time as paradoxical, this feature has been linked to the process of pair production. Lucid discussions can be found in recent papers [114,115,116] where it is argued that, following the Feynman-Stückelberg interpretation of this simulation, that part of the wavepacket components associated to negative energy continuum states can be viewed as positrons evolving backward in time. We mention that the question is akin to the one of pair creation in a so-called supercritical field such as the one created by the potential of super-heavy composite nuclei with $Z > 150$; for a recent discussion, see [117].

This picture is confirmed at first, when solving the time-dependent Dirac equation for Gaussian wavepackets with average energy E ingoing onto a repulsive electrostatic potential with strength $V_0 = E + 2mc^2$. Such test-case simulations that have been implemented for different potential steps [79] lead to final states comprising both transmitted and reflected components, in agreement with the Klein paradox picture. When repeated within the framework of a quantum-field theory framework, these calculations resolve part of the paradoxical features mentioned above [97]. However, several issues regarding the questions of electron localization, tunneling, etc., still deserve investigations.

Interestingly, however, in spite of the limitation of the Dirac single-electron picture, it can be exploited for deriving a rough estimate about the possibility of creating pairs from vacuum ("sparking the vacuum") in the presence of a focused ultra-strong laser field. In fact, with the help of the standard semi-classical WKB calculation of the transmission probability through a potential barrier, one can recover the dominant contribution to the pair production probability, as originally derived by Schwinger [102,103]; see also [114,115] for a pedagogical account. More precisely, one obtains

$$|T|^2 \propto \mathrm{e}^{-\pi \frac{\mathcal{E}^3}{\mathcal{E}_0}}, \tag{7}$$

This result indicates that for a laser field with intensity $I \approx 10^{+29}$ W cm^{-2}, the pair production probability would be $|T|^2 \approx e^{-\pi} \approx 0.043$. As already mentioned, although this huge intensity is still beyond the capabilities of the currently operated laser devices, it does not seem to be out of reach in the near future, in view of the recent developments of new laser facilities [3].

3.4 Tunneling Time(s)?

Tunneling remains at the heart of the discussions related to the interplay between classical and quantum physics [118]. Semi-classical (WKB) approaches provide a well-established framework for providing quantitative data regarding tunneling ionization [42]. However, a challenge remains, which reduces ultimately to answering the question, *How much time the tunneling particle spends inside the barrier?* In the context of atomic physics in strong fields, the point is interesting because tunneling is one of the dominant mechanisms governing not only atomic ionization but also high-order harmonic generation and other more complex processes such as double- and multiple ionization. The phase when the electron is released in the continuum strongly influences the dynamics of the strongly coupled system (electron + ionic core + laser field) [27]. Moreover, the question is of interest in view of the recent demonstration of the strong connections existing between classical trajectories

and the Feynman's path integral formalism, for describing delicate features of atomic processes in strong fields [119]. Unfortunately, this apparently innocuous question cannot be answered straightforwardly as explained, for instance, in the review papers [120,121,122,123]. Indeed, there is a controversy regarding the point whether or not one could define univocally a time delay or a dwell time inside a barrier, see, for instance, a recent attempt to unify different approaches in [124].

Nevertheless, in the strong field context, the problem remains of interpreting the data derived from the numerical resolution of the Dirac equation for an incoming wavepacket on a barrier, when solved on a lattice [97,125,126]. We note that this point is also related to the question of the spatio-temporal localization of a particle and to the *zitterbewegung*.

3.5 Cycloatoms

As already mentioned, it is expected that interesting relativistic physics could be observed when atoms are in the presence of both a strong magnetic field and a laser field. It has been predicted that new atomic states, referred to as "Cycloatoms", can be prepared if the cyclotron frequency in the static magnetic field is commensurate with the frequency of the laser [127,128,129,130].

In contrast to a non-relativistic treatment, for which the spatial width of the electronic charge distribution remains comparable to that of the initial state during the entire evolution, a relativistic theory predicts the formation of a ring-shaped charge cloud. The ring rotates around the nucleus with the laser frequency for the case of equal cyclotron and laser frequency. Interestingly, such structures are also found in classical simulations and there is a global agreement between classical and quantum dynamics. However, the Dirac solution displays a second ring-shaped charge cloud which rotates in the direction opposite to that of the electron's [127,128,129,130]. It is tempting to associate this new ring with positrons that could have been generated in this interaction. However, to go beyond these speculations would again require a full theoretical analysis, using the field theoretical framework of the second quantization.

We turn now to two other types of relativistic processes that do not require the numerical resolution of the Dirac equation.

3.6 Two-Photon Bound–Bound Transitions

The advent in the near future of new powerful sources of radiation in the XUV and soft X-ray ranges will open also the possibility of observing multiphoton transitions involving inner shells in high-Z atoms [57,58,59,60]. Although it is well known that relativity plays a determinant role in the fine structure of the atomic levels, it is not so easy to determine to what extent it affects the radiative

transition probabilities. For instance, it has been observed in standard X-ray spectroscopy that *for one-photon transitions*, the non-relativistic dipole approximation leads to correct estimates well beyond its expected range of validity [131]. In order to account for this observation, it has been surmised that there exists a partial cancelation between different higher order corrections beyond the dipole approximation, such as retardation, spin effects and other relativistic effects. An open question is to determine whether or not such cancelations would still hold in the strong field context, i.e., for multiphoton transitions.

Regarding inner-shell multiphoton transitions, it appears that in spite of the remarkable brightness of the currently designed sources in the X-ray range, a perturbative treatment of the processes is adequate. This is because the relevant atomic unit of intensity for hydrogenic systems with charge Z scales like $I_Z = Z^6\ 3.5 \times 10^{16}$ W cm^{-2}. In this context, "exact" computations of two-photon $|\ 1^2S_{1/2}\rangle \rightarrow |\ 2^2S_{1/2}\rangle$ transitions in hydrogenic systems have been reported. The calculations have been performed with the help of a sturmian expansion of the Dirac–Coulomb Green's function [132,133,134].When comparing with less sophisticated computations, it turns out that relativistic corrections become significant already for $Z = 20$, at frequencies $\omega = 2.04$ keV and that they can amount to more than 10% for $Z = 50$, at frequencies $\omega = 12.75$ keV. These results clearly demonstrate that there is a need for more sophisticated calculations, beyond the non-relativistic dipole approximation, in order to determine the multiphoton rates involving inner-shell states in high-Z elements.

For recent analytical calculations performed along similar lines, for the static and dynamic polarizabilities of hydrogenic systems in the relativistic regime, see also [135,136].

3.7 Radiation Reaction

An electron submitted to a super-intense laser field can scatter the radiation through non-linear Thomson or Compton processes, the latter being associated to momentum transfer. Although the theory of these processes is well delineated in the case of *constant amplitude* fields, the question of a proper treatment of their respective influences on the electron's dynamics in time- and space-varying fields remains a challenge for theory, see [137] for a recent discussion of non-linear Thomson scattering. The possibility of generating high-order harmonics [35, 138] and even X-ray pulses [139] from this latter process has been discussed. Moreover, when electrons are born almost at rest from atomic ionization within the field, one expects that they experience huge accelerations and, consequently, they must radiate sizable part of the energy they acquire. The characteristics of the Larmor radiation emitted in such circumstances have been modeled in [140].

Then the question arises of the influence of this damping, or in other words of the "radiation reaction", on the motion of the electron and of the signatures of the effect. It has been surmised that it could induce changes in Compton scattering

profiles or in harmonic generation spectra. A fully quantum (QED) treatment being out of reach, a classical approach, based on the so-called Lorentz–Dirac equation, has been advocated [141]. The difficulty is however that the solutions are plagued by the so-called runaway solutions, the divergence of which being linked to the point-like character of the electron [142]. Nevertheless, clever integration schemes, running backward in time, have been proposed which permit to extract finite quantities from the equation, see the recent discussion in [143]. Then, with the help of a CTMC treatment, it is possible to compare the dynamics of an ensemble of electrons depending on whether the radiation reaction terms are included or not in the equations of motion [144]. The simulations show noticeable, though very small, changes in the emission radiation spectra, already at intensities around $I_L \approx 10^{20}$ W cm^{-2}. An interesting outcome of these studies is to revitalize the topic of Classical Electrodynamics, through the Dirac–Lorentz equation, when applied to strong field physics in a wide range of contexts, including astrophysics [145] and laser–electron interactions [146].

4 Conclusions and Perspectives

In this chapter, we have presented several of the relativistic effects which govern atom–laser interactions in the strong field limit. It appears that at the intensities currently achieved in experiments, the dominant relativistic contributions originate from the mass shift and Lorentz force effects. In a QED perspective, these effects are linked to the non-linear Thomson and Compton scattering processes.

Atomic physics effects come into play when defining the initial state of electrons that can be released into the focal area of strongly focused fields. It is anticipated that in the high-intensity regime, i.e., beyond 10^{20} W cm^{-2}, rather exotic processes could be observed that belong to the realm of QED in strong fields.

In all these instances, interesting results have been derived from simulations based on the numerical resolution of the time-dependent Dirac equation. However, in spite of the remarkable progress registered in the numerical treatment of the latter equation, difficulties still subsist in the interpretation of the results. This is inherent in the single-particle nature of the Dirac equation. Recent progress has been realized toward second-quantized treatments that partially alleviate these difficulties. It is clear that it will be necessary to develop new computational tools in order to perform calculations in the framework of a non-perturbative quantum-field theory for time-dependent laser–atom interactions. It is also of interest to develop classical simulations based on the resolution of the Dirac–Lorentz equation that will bring complementary views on the dynamics of the processes. Then it will be possible to address the fascinating questions related to the prospect of realizing a laser control of fundamental phenomena involving non-linear QED effects.

Acknowledgments Part of our work mentioned here is the result of fruitful collaborations with C.H. Keitel, P.L. Knight and C. Szymanowski. Also, we would like to acknowledge very helpful discussions with R. Grobe and C.J. Joachain.

References

1. M.D. Perry and G. Mourou: Science, **264**, 917 (1994)
2. G.A. Mourou, C.P.J. Barty and M.D. Perry: Phys. Today, **51**, 22 (1998)
3. T. Tajima and G.A. Mourou: Phys. Rev. Special Topics-Accelerators and Beams, **5**, 031301 (2002)
4. D.M. Volkov: Z. Phys. **94**, 250 (1935)
5. J. San Roman, L. Plaja end L. Roso: Phys. Rev. A **64**, 063402 (2001)
6. L.S. Brown and T.W.B. Kibble: Phys. Rev. **133**, A705 (1964)
7. O. von Roos: Phys. Rev. **135**, A43 (1964)
8. Z. Fried and J.H. Eberly: Phys. Rev. **136**, B871 (1964)
9. T.W.B. Kibble: Phys. Rev. **150**, 1060 (1966)
10. E.S. Sarachik and G.T. Schappert: Phys. Rev. D **1**, 2738 (1970)
11. M. Protopapas, C.H. Keitel and P.L. Knight: Rep. Prog. Phys. **60**, 389 (1997)
12. C.J. Joachain, M. Dörr and N. Kylstra: Adv. At. Mol. Opt. Phys. **42**, 225 (2000)
13. Y.I. Salamin, S.X. Hu, K.Z. Hatsagortsyan and C. Keitel: Phys. Rep. **427**, 41 (2006)
14. A. Maquet and R. Grobe: J. Mod. Optics **49** 2001 (2002)
15. C. Bula et al.: Phys. Rev. Lett. **76**, 3116 (1996)
16. D.L. Burke et al.: Phys. Rev. Lett. **79**, 1626 (1997)
17. C. Bamber et al.: Phys. Rev. D **60**, 092004 (1999)
18. C.I. Moore, J.P. Knauer and D. Meyerhofer: Phys. Rev. Lett. **74**, 2439 (1995)
19. D. Meyerhofer et al.: J. Opt. Soc. Am. B, **13**, 113 (1996)
20. S.J. McNaught, J.P. Knauer and D. Meyerhofer: Phys. Rev. Lett. **78**, 626 (1997)
21. S.J. McNaught, J.P. Knauer and D. Meyerhofer: Phys. Rev. A **58**, 1399 (1998)
22. S-Y Chen, A. Maksimchuk and D. Umstadter: Nature **396**, 653 (1998)
23. C.I. Moore et al.: Phys. Rev. Lett. **82**, 1688 (1999)
24. R. Moshammer et al.: Phys. Rev. Lett. **84** 447 (2000)
25. H. Maeda et al.: Phys. Rev. A **62**, 035402 (2000)
26. E.A. Chowdury, C.P.J. Barty and B.C. Walker: Phys. Rev. A **63**, 04712 (2001)
27. M. Lewenstein and P. Salières: this volume.
28. H. Reiss: J. Opt. Soc. Am. B **7**, 574 (1990)
29. P.B. Corkum, N.H. Burnett and F. Brunel: In *Atoms in Intense Laser Fields*, ed. by M. Gavrila, (Academic Press, New York, 1992) pp. 109–37.
30. Y.I. Salamin and F.H.M. Faisal: Phys. Rev. A **55**, 3678 (1997)
31. Y.I. Salamin and F.H.M. Faisal: Phys. Rev. A **58**, 3221 (1998)
32. Y.I. Salamin and F.H.M. Faisal: J. Phys. A **31**, 1319 (1998)
33. F.H.M. Faisal and Y.I. Salamin: Phys. Rev. A **60**, 2505 (1999)
34. Y.I. Salamin and F.H.M. Faisal: Phys. Rev. A **61**, 043801 (2000)
35. S. Banerjee, S. Sepke, R. Shah, A. Valenzuela, A. Maksimchuk and D. Umstadter: Phys. Rev. Lett. **95**, 035004 (2005)
36. M. Dammasch, M. Dörr, U. Eichmann, E. Lenz and W. Sandner: Phys. Rev. A **64**, 061402 (2001)
37. E. Chowdury and B.C. Walker: J. Opt. Soc. Am. B **20**, 109 (2003)
38. K. Yamakawa, Y. Akahane, Y. Fukuda, M. Aoyama, N. Inoue, H. Ueda and T. Utsumi: Phys. Rev. Lett. **92**, 123001 (2004)
39. A. DiChiara, S. Palaniyappan, A.F. Falkowski, E.L. Huskins and B.C. Walker: J. Phys. B **38**, L183 (2005)

40. S. Palaniyappan, A. DiChiara, E. Chowdury, A.F. Falkowski, G. Ongadi, E.L. Huskins and B.C. Walker: Phys. Rev. Lett. **94**, 243003 (2005)
41. V.P. Krainov and A.V. Sofronov: Phys. Rev. A **69**, 015401 (2004)
42. N. Milosevic, V.P. Krainov and T. Brabec: Phys. Rev. Lett. **89**, 193001 (2002) and references therein.
43. S. Palaniyappan, A. DiChiara, E. Chowdury, A.F. Falkowski, G. Ongadi, E.L. Huskins and B.C. Walker: Phys. Rev. Lett. **94**, 243003 (2005)
44. R. Taïeb, V. Véniard and A. Maquet: Phys. Rev. Lett. **87**, 053002 (2001)
45. A.S. Kornev, E.B. Tulenko and B.A. Zon: Phys. Rev. A **68**, 043414 (2003)
46. E. Gubbini, U. Eichmann, M. Kalshnikov and W. Sandner: Phys. Rev. Lett. **94**, 053602 (2005)
47. J.J. Sakurai: *Advanced Quantum Mechanics*, (Addison-Wesley, Reading, MS, 1967)
48. C. Szymanowski, V. Véniard, R. Taïeb, A. Maquet and C.H. Keitel: Phys. Rev. A **56**, 3846 (1997)
49. P. Panek, J.Z. Kamiński and F. Ehlotzky: Can. J. Phys. **77**, 591 (1999)
50. Y. Attaourti and B. Manaut: Phys. Rev. A **68**, 067401 (2003)
51. Y. Attaourti, B. Manaut and S. Taj: Phys. Rev. A **70**, 023404 (2004)
52. C. Szymanowski, R. Taïeb, and A. Maquet: Laser Phys. **8**, 1 (1998)
53. B. Manaut, S. Taj and Y. Attaourti: Phys. Rev. A **71**, 043401 (2005)
54. M. Gavrila: In *shape Atoms in Intense Laser Fields*, ed. by M. Gavrila, (Academic, New York, 1992) p. 435
55. M. Gavrila: J. Phys. B **35**, R147 (2002)
56. A.M. Popov, O.V. Tikhonova and E.A. Volkova: J. Phys. B **36**, R125 (2003)
57. J. Feldhaus and B. Sonntag: this volume.
58. W.B. Colson, E.D. Johnson, M.J. Kelley and H.A. Schwettman, Phys. Today **55**, 35 (2002)
59. T. Brabec and F. Krausz: Rev. Mod. Phys. **72**, 545 (2000)
60. P. Nickles and W. Sandner: this volume.
61. A. Staudt and C.H. Keitel: J. Phys. B **36**, L203 (2003)
62. M. Protopapas, C.H. Keitel and P.L. Knight: J. Phys. B **29**, L591 (1996); see also the ref. [8].
63. N.J. Kylstra, A.M. Ermolaev and C.J. Joachain: J. Phys. B **30**, L449 (1997)
64. A.M. Ermolaev: J. Phys. B **31**, L65 (1998)
65. R. Taïeb, V. Véniard and A. Maquet: Phys. Rev. Lett. **81**, 2882 (1998)
66. N.J. Kylstra, R.A. Worthington, A. Patel, P.L. Knight, J.R. Vazquez de Aldana and L. Roso: Phys. Rev. Lett. **85**, 1835 (2000)
67. J.R. Vazquez de Aldana, N.J. Kylstra, L. Roso, P.L. Knight, A. Patel and R.A. Worthington: Phys. Rev. A **64**, 013411 (2001)
68. L.N. Gaier and C.H. Keitel: Phys. Rev. A **65**, 023406 (2002)
69. S.X. Hu and T. Starace: Phys. Rev. Lett. **88**, 245003 (2002)
70. A. Maltsev and T. Ditmire: Phys. Rev. Lett. **90**, 053002 (2003)
71. I.Y. Dodin and N.J. Fisch: Phys. Rev. E **68**, 056402 (2003)
72. Y.I. Salamin and C.H. Keitel: Phys. Rev. Lett. **88**, 090005 (2002)
73. P. Agostini and L.F. DiMauro: Rep. Prog. Phys. **67**, 813 (2004)
74. S.X. Hu, T. Starace, W. Becker, W. Sandner and D.B. Milosevic: J. Phys. B **35**, 627 (2002)
75. C.C Chirila, C.J. Joachain, N.J. Kylstra and R.M. Potvliege: Phys. Rev. Lett. **93**, 243603 (2004)
76. M. Klaiber, K.Z. Hatsagortsyan and C.H. Keitel: Phys. Rev. A **71**, 033408 (2005)
77. C. Bottcher and M.R. Strayer: Ann. Phys. **175**, 64 (1987)
78. J. Ullrich: this volume.
79. J.W. Braun, Q. Su and R. Grobe: Phys. Rev. A **59**, 604 (1999)
80. L. Susskind: Phys. Rev. D **16**, 3031 (1977)
81. R. Stacey, Phys. Rev. D **26**, 468 (1982)
82. V. Alonso, S. De Vicenzo and L. Mondino: Eur. J. Phys. **18**, 315 (1997)

83. M. Protopapas, C.H. Keitel and P.L. Knight: J. Phys. B **29**, L591 (1996)
84. U.W. Rathe, C.H. Keitel, M. Protopapas and P.L. Knight: J. Phys. B **30**, L531 (1997)
85. N.J. Kylstra, A.M. Ermolaev and C.J. Joachain: J. Phys. B **30**, L449 (1997)
86. R. Taïeb, V. Véniard and A. Maquet: Phys. Rev. Lett. **81**, 2882 (1998)
87. A.M. Ermolaev: J. Phys. B **31**, L65 (1998)
88. A. Melissinos: this volume.
89. M.W. Walser, C. Szymanowski and C.H. Keitel: Europhys. Lett. **48**, 533 (1999)
90. M.W. Walser and C.H. Keitel: J. Phys. B **33**, L221 (2000)
91. J. San Roman, L. Roso and L. Plaja: J. Phys. B **37**, 435 (2004)
92. S.X. Hu and C.H. Keitel: Phys. Rev. Lett. **83**, 4709 (1999)
93. Q. Su, P.J. Peverly, R.E. Wagner, P. Krekora and R. Grobe: Optics Express **8**, 51 (2001)
94. P. Krekora, Q. Su and R. Grobe: J. Phys. B **34**, 2795 (2001)
95. E. Schrödinger: Sitz. Ber. Preuss. Akad. Wiss. Physik-Math. **24**, 418 (1930)
96. J. San Roman, L. Roso and L. Plaja: J. Phys. B **36**, 2253 (2003)
97. P. Krekora, Q. Su and R. Grobe: Phys. Rev. Lett. **92**, 040406 (2004)
98. P. Krekora, Q. Su and R. Grobe: Phys. Rev. Lett. **93**, 043004 (2004)
99. P. Krekora, K. Cooley, Q. Su and R. Grobe: Laser Phys. **15**, 282 (2005)
100. C. Szymanowski, A. Maquet and C.H. Keitel: Laser Phys. **9**, 133 (1999)
101. J. Schliemann, D. Loss and R.M. Westerwelt: Phys. Rev. Lett. **94**, 206801 (2005)
102. J. Schwinger Phys. Rev. **82**, 664 (1951)
103. J. Schwinger Phys. Rev. **93**, 615 (1954)
104. A.M. Perelomov, V.S. Popov and M.V. Terent'ev: Sov. Phys. JETP **23**, 924 (1966)
105. A.M. Perelomov, V.S. Popov and M.V. Terent'ev: Sov. Phys. JETP **24**, 207 (1967)
106. E. Brezin and C. Itzykson: Phys. Rev. D **2**, 1191 (1970)
107. E.P. Liang, S.C. Wilks and M. Tabok: Phys. Rev. Lett. **81**, 4887 (1998)
108. S.S. Bulanov: Phys. Rev. E **69**, 036408 (2004)
109. C. Müller, A.B. Voitkiv and N. Grün: Phys. Rev. A **67**, 063407 (2003)
110. C. Müller, A.B. Voitkiv and N. Grün: Phys. Rev. A **70**, 023412 (2004)
111. H.K. Avetissian, A.K. Avetissian, G.F. Mkrtchian and Kh. V. Sedrakian: Phys. Rev. E **66**, 016502 (2002)
112. A. Di Piazza: Phys. Rev. D **70**, 053013 (2004)
113. N.B. Narozhny, SS. Bulanov, V.D. Mur and V.S. Popov: Phys. Lett. A **330**, 1 (2004)
114. B.R. Holstein: Am. J. Phys. **66**, 507 (1998)
115. B.R. Holstein: Am. J. Phys. **67**, 499 (1999)
116. A. Calogeracos and N. Dombey: Contemp. Phys. **40**, 313 (1999)
117. N. Szpak: Nucl. Instr. Meth. B **205**, 30 (2003)
118. E.J. Heller: J. Phys. Chem. A **103**, 10433 (1999)
119. P. Salières et al.: Science **292**, 902 (2001)
120. E.H. Hauge and J.A. Støvneng: Rev. Mod. Phys. **61**, 917 (1989)
121. R. Landauer and T. Martin: Rev. Mod. Phys. **66**, 217 (1994)
122. M. Büttiker and R. Landauer: Phys. Rev. Lett. **49**, 1739 (1982)
123. J.G. Muga and C.R. Leavens: Phys. Rep. **338**, 353 (2000)
124. N. Yamada: Phys. Rev. Lett. **93**, 170401 (2004)
125. P. Krekora, Q. Su and R. Grobe: Phys. Rev. A **63**, 032107 (2001)
126. P. Krekora, Q. Su and R. Grobe: Phys. Rev. A **64**, 022105 (2001)
127. R.E. Wagner, Q. Su and R. Grobe: Phys. Rev. Lett. **84**, 3282 (2000)
128. P. Krekora, R.E. Wagner, Q. Su and R. Grobe: Phys. Rev. A **63**, 25404 (2001)
129. Q. Su, R.E. Wagner, P.J. Peverly and R. Grobe: In *Frontiers of Laser Physics and Quantum Optics*, ed. by Z. Xu, S. Xie, S.-Y. Zhu and M.O. Scully, (Springer, Berlin, 2000) pp.117–123
130. P.J. Peverly, R.E. Wagner, Q. Su and R. Grobe: Laser Phys. **10**, 303 (2000)
131. A. Ron et al.: Phys. Rev. A **50**, 1312 (1994)

132. A. Maquet, V. Véniard and T.A. Marian: J. Phys. B **31**, 3743 (1998)
133. C. Szymanowski, V. Véniard, R. Taïeb and A. Maquet: Europhys. Lett. **37**, 391 (1997)
134. C. Szymanowski, V. Véniard, R. Taïeb and A. Maquet: Phys. Rev. A **56**, 700 (1997)
135. V. Yakhontov: Phys. Rev. Lett. **91**, 093001 (2003)
136. R. Szmytkowski and K. Mielewczyk: J. Phys. B **37**, 3961 (2004)
137. J. Guo: Phys. Rev. Lett. **93**, 243001 (2004)
138. S. Banerjee, A.R. Valenzuela, R.C. Shah, A. Maksimchuk and D. Umstadter: J. Opt. Soc. Am. B **20**, 182 (2003)
139. W.J. Brown and F.V. Hartemann: Phys. Rev. Spec. Topics-Accel. Beams **7**, 060703 (2004)
140. E.A. Chowdury, I. Ghebregziabiher and B.C. Walker: J. Phys. B **38**, 517 (2005)
141. F.V. Hartemann and A.K. Kerman: Phys. Rev. Lett. **76**, 624 (1996)
142. G.F. Efremov: Sov. Phys. JETP **87**, 899 (1998)
143. J. Koga: Phys. Rev. E **70**, 046502 (2004)
144. C.H. Keitel, C. Szymanowski, P.L. Knight and A. Maquet: J. Phys. B, **31**, L75 (1998)
145. F.V. Hartemann et al.: Astrophys. J. Suppl. Ser. **127**, 347 (2000)
146. F.V. Hartemann, D.J. Gibson and A.K. Kerman: Phys. Rev. E **72**, 026502 (2005)
147. A. Scrinzi, M. Yu. Ivanov, R. Kienberger and D.M. Villeneuve: J. Phys. B: At. Mol. Opt. Phys. **39**, R1 (2006)

Tests of QED with Intense Lasers

Adrian C. Melissinos

1 Introduction

We have seen in the previous chapters that many materials respond nonlinearly to an externally applied electric field. On the other hand, Maxwell's equations for the electromagnetic (em) field in *vacuum* are absolutely linear. This conclusion is not valid any more if we include quantum-mechanical effects, such as the production of particles from the vacuum, in the description of the em field. The particles need not be real but can be virtually produced and reabsorbed (in a time interval Δt) as long as the uncertainty relation $\Delta E \Delta t \simeq \hbar$ holds. Such processes are at the center of all calculations in quantum electrodynamics (QED) and also endow the vacuum with nonlinear properties. That the vacuum would exhibit nonlinear behavior in the presence of em fields was recognized over 70 years ago [1, 2, 3] and since then QED has been developed into a highly accurate theory in perfect agreement with all observations. However, it is only recently that direct experimental evidence was obtained on the nonlinear behavior of the vacuum in the production of e^+e^- pairs in photon–photon collisions.

One expects to observe such nonlinear effects in the presence of strong em fields. Indeed, the interaction of electrons with the intense fields at the focus of short laser pulses has been considered by many authors. Some typical early work is that of refs. [4, 5, 6, 7, 8]. The scattering of visible light from a free electron can be understood classically and leads to the well-known Thomson cross-section. However, in an intense field the motion of the electron can become relativistic and this results in the emission of higher harmonics of the incident light. This nonlinear effect is particularly pronounced in the interaction of intense lasers with atomic electrons. An early observation of harmonic generation in laser free electron scattering was reported in [9]. A more recent and detailed study of nonlinear Thomson scattering of an intense laser from quasi-free electrons is given in [10].

A.C. Melissinos
Department of Physics and Astronomy, University of Rochester, Rochester, NY 14627, USA
e-mail: meliss@pas.rochester.edu

T. Brabec (ed.), *Strong Field Laser Physics*,
DOI: 10.1007/978-0-387-34755-4_21,

A related approach to this problem is to detect the scattered electrons. This has become more practical as the intensity of the available lasers has increased. In the work of ref. [11], electrons with eV energy scattered from a laser field of intensity $\sim 10^{14}$ W/cm^2. When the laser intensity was increased to $\sim 5 \times 10^{17}$ W/cm^2 electrons gained as much as 130 keV of energy [12]. Today, acceleration of electrons to MeV energies by a laser field has been accomplished in many laboratories. For instance at an intensity $\sim 10^{19}$ W/cm^2, 1 MeV electrons have been observed [13].

Whereas the experiments discussed so far rely on the interaction of the electron with the electric field of the laser, strong magnetic fields can also lead to nonlinear interactions. For instance, linearly polarized light propagating through a transverse magnetic field acquires an ellipticity which, in principle, can be detected [14, 15]. The interaction of high-energy electrons with magnetic fields approaching 100 T has also been considered [16]. Finally, the "channeling" of high-energy electrons through crystals leads to observable nonlinear effects due to the high electric fields in the crystal lattice [17, 18, 19].

We will not review this extensive body of work but will describe an experiment where high-energy electrons scatter from an intense laser beam. This results in an *effective* laser intensity as much as ten orders of magnitude higher than the actual intensity in the laboratory frame of reference. At these intensities, the nonlinear effects and in particular the production of e^+e^- pairs from vacuum are unambiguously observed [20, 21, 22].

It is convenient, and customary, to specify the strength of the em field by a dimensionless (and Lorentz invariant) parameter η. This is referred to as the "normalized vector potential" or the "multiphoton parameter", or when multiplied by the electron rest mass as the "ponderomotive potential"

$$\eta = \frac{e}{m} \sqrt{|<A_\mu A^\mu>|} \tag{1}$$

or

$$\eta = \frac{eE_{\text{rms}}}{\omega mc} \tag{2}$$

In the above, e and m are the electron charge and rest mass; ω is the frequency and E_{rms} the rms value of the electric field of the em wave.[1]

By writing $\eta = eE_{\text{rms}}\lambda\!\!\!^{-}/mc^2$ we see that when $\eta = 1$ the energy gained by an electron moving across one wavelength equals its rest-mass energy, mc^2. Thus relativistic effects become important. For motion in the plane transverse to the wave vector the electron acquires an effective mass

[1] The vector potential must be in the Lorentz gauge $\partial_\mu A^\mu = 0$ and $<A^\mu> = 0$, where $<>$ is the time average.

$$\overline{m}^2 = m^2(1+\eta^2) \tag{3}$$

Note that η is a classical parameter (it does not involve $\hbar$) and that as $\eta \to 1$ multiphoton effects become dominant. Of course η can be increased by lowering the frequency of the em wave, and in the limit of a constant field,[2] $\eta \to \infty$.

To describe quantum effects, a second dimensionless (and Lorentz invariant) parameter is appropriate:[3]

$$\Upsilon = \left(\frac{e\hbar}{m^3c^5}\right)\sqrt{<(F_{\mu\nu}p^\nu)^2>} \tag{4}$$

where p^ν is the 4-momentum of an electron moving in the em field described by the tensor $F_{\mu\nu}$ [23]. For an electron at rest, $p^\nu = \{mc; 0, 0, 0\}$ and thus

$$\Upsilon = \frac{e\hbar}{m^2c^3}\ E \tag{5}$$

Since the electron Compton wavelength $\lambda\!\!\!^{-}_{\rm c} = \hbar/mc$, Eq. (5) can be written as $\Upsilon = eE\lambda\!\!\!^{-}_{\rm c}/mc^2$, which shows that when $\Upsilon = 1$, an electron can gain from the external field energy equal to its rest-mass energy in traversing one Compton wavelength. But one Compton wavelength is the distance a virtual electron can traverse (at the speed of light) without violating the uncertainty relation $\Delta E\Delta t \simeq \hbar$; we have $\Delta E = mc^2$ and $\Delta t = \lambda\!\!\!^{-}/c$. Thus a virtual e^+ and e^- can gain enough energy from the electric field to become *real* particles. We therefore expect that when $\Upsilon = 1$ a static[4] electric field will cause the vacuum to break down spontaneously into e^+e^- pairs. The field strength that leads to $\Upsilon = 1$ in Eq. (5) is called the *critical field* (or Schwinger field) and has the value

$$E_{\rm c} = \frac{m^2c^3}{e\hbar} = 1.3 \times 10^{16}\ \text{V/cm} \tag{6}$$

It is interesting to examine if critical electric fields can be generated in the laboratory, by intense laser beams. The (peak) amplitude of the electric field of an em wave of intensity I (W/cm^2) is given by

$$E = \sqrt{2Z_0 I} \qquad (\text{V/cm}) \tag{7}$$

where $Z_0 = \sqrt{\mu_0/\epsilon_0} = 377\ \Omega$ is the impedance of free space. At present, the highest laser intensity in a near diffraction limited spot does not exceed $I = 10^{22}$

---

[2] In this description the effect of a constant field on a charged particle corresponds to the absorption of an infinite number of zero energy photons.

[3] The symbol χ is often used in place of Y.

[4] It can be easily seen that a wave field, or for that matter a static magnetic field, cannot breakdown the vacuum because energy–momentum conservation is not satisfied.

W/cm^2. Thus $E_{\max} \sim 3 \times 10^{12}$ V/cm well below the critical field, E_c, of Eq. (6). Nevertheless it is possible to reach the critical field by exploiting the availability of beams of high-energy electrons.

We first note that Eq. (5) was derived for an electron at rest. If the electron is moving with velocity v (where $\beta = v/c$ and $\gamma = 1/\sqrt{1-\beta^2}$) through a *static* electric field E, we find from the definition of Eq. (4) that

$$\Upsilon = \frac{e\hbar}{m^2c^3}\gamma\beta E = \frac{E^*}{E_c} \tag{8}$$

Here $E^* = \gamma\beta E$ is the electric field[5] seen in the *electron's rest frame*. This can be a large gain since electron beams of GeV energy ($\gamma > 10^3$) are available.

It is instructive to consider the value of the parameters η and Υ for the experiment discussed in section 3. A laser beam of intensity $I = 10^{18}$ W/cm^2 is incident on an electron beam of energy $\mathcal{E} = 46.6$ GeV ($\gamma \sim 0.9 \times 10^5$). Then the electric field in the electron rest frame is $E^* = 2\gamma\sqrt{2Z_0 I} \simeq 0.5 \times 10^{16}$ V/cm or $\Upsilon = 0.38$. On the other hand η does not depend on the electron beam energy, but does depend on the laser wavelength. If we use $\lambda = 527$ nm then $\eta = (eE/mc^2)(\lambda/2\pi) = 0.45$.

Since the laser pulse is focussed to an area $A \simeq 50$ μm^2 and is only 1 ps long, the electron beam must be correspondingly short and focussed to achieve an observable interaction rate. This, coupled with the need for high energy, places difficult demands on the electron beam. The only such beam available was the final focus test beam (FFTB) at the Stanford Linear Accelerator Center (SLAC).

2 Multiphoton Compton Scattering and Multiphoton Pair Production

The scattering of optical photons from free electrons is adequately described by the Thomson differential cross-section

$$\frac{d\sigma}{d\Omega} = \frac{1}{2}\, r_0^2\, (1 + \cos^2\theta) \tag{9}$$

where $r_0 = e^2/(4\pi\epsilon_0 mc^2) = 2.82 \times 10^{-13}$ cm is the classical electron radius. The integral over angles of Eq. (9) gives

$$\sigma_T = \frac{8\pi}{3}\, r_0^2 \tag{10}$$

[5] For a wave field both the $\vec{E}$ and $\vec{B}$ fields transform and contribute equally so that in the electron rest frame (setting $\beta = 1$) we find $|E^*| = |B^*| = 2\gamma|E|$.

When an optical photon is incident on an energetic electron, the photon energy in the electron rest frame is much higher and thus the photon imparts a significant recoil to the electron. In this case we speak of Compton scattering and Eq. (9) is modified.

The kinematics and the cross-section for Compton scattering are derived by considering the scattering of a single energetic photon from the electron. In an intense field, however, several photons may be absorbed from the field with only a single photon being emitted into the final state. We describe this process by

$$e^- + n\omega \rightarrow e^{-\prime} + \gamma \tag{11}$$

The number of photons, n, absorbed from the field can be determined from the kinematics of the scattering. A related process is the scattering of a high-energy γ-ray (photon) from several photons of the field leading to an electron–positron pair in the final state

$$\gamma + n\omega \rightarrow e^+ + e^- \tag{12}$$

Reactions (11) and (12) are related by "crossing symmetry", but experimentally they are quite different! High-energy electrons are directly available in the incident beam, whereas the high-energy photons are produced by the back-scattering process of reaction (11). These high-energy photons must interact within the laser focus to produce the e^+e^- pair. Another important difference is that reaction (11) can proceed for *any value* of n. For reaction (12) to proceed, n must be large enough so that the cm energy exceeds $(2mc^2)$.

In the present experiment where $\hbar\omega = 2.35$ eV the maximum γ-ray energy for $n = 1$ in the process (11) is $E_\gamma = 29$ GeV. We then find for process (12)

$$s = (k_\gamma^\mu + nk_\omega^\mu)^2 = 4n\omega E_\gamma > 4m^2c^4$$

or $n \geq 4$ for the reaction to proceed.

The geometry of the experiment is shown in Fig. 1, where the laser beam crosses the electron beam at an angle $\alpha = 17^\circ$ and the (back)scattered photon angle θ is measured from the electron direction. From here on we shall use units where $\hbar = c = 1$ and where appropriate will make approximations due to the large value of $\gamma = \mathcal{E}/m$ with $\mathcal{E}$ the electron energy. The kinematical variables are defined as

p^μ, p'^μ 4-momentum of the electron before and after scattering. These take the values $(\mathcal{E}, \vec{p}), (\mathcal{E}', \vec{p}')$ in the laboratory frame.

k^μ, k'^μ 4-momentum of a photon before scattering and of the scattered photon. These take the values $(\omega, \vec{k})$ and$(\omega', \vec{k}')$ in the laboratory frame.

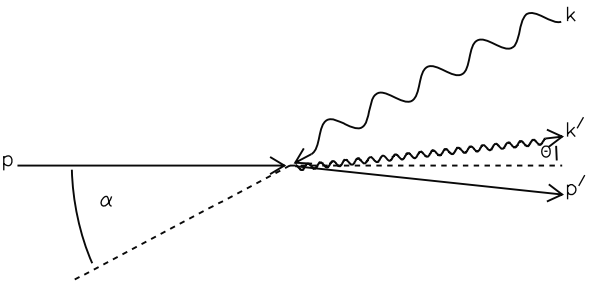

Fig. 1 The geometry for the study of nonlinear Compton scattering

The scattering process is expressed by

$$p^\mu + nk^\mu = p'^\mu + k'^\mu \tag{13}$$

Here n is the number of absorbed photons. The effective mass of the electron[6] in the strong field is taken into account by replacing p^μ by q^μ (and $p'^\mu \to q'^\mu$),

$$q^\mu = p^\mu + \frac{\eta^2 m^2}{2(k\cdot p)}k^\mu \tag{14}$$

The laboratory energy of the scattered photon is given by

$$\omega' = \frac{2n\gamma^2\omega(1+\beta\cos\alpha)}{2\gamma^2(1-\beta\cos\theta)+\left[\frac{2n\omega\gamma}{m}+\frac{\eta^2}{1+\beta\cos\alpha}\right][1+\cos(\theta-\alpha)]} \tag{15}$$

For $\gamma = 1$, $\beta = 0$ and $n = 1, \eta^2 = 0$, Eq. (15) reduces to the familiar condition for Compton scattering

$$\frac{\omega'}{\omega} = \left[1+\frac{\omega}{m}(1+\cos\theta)\right]^{-1}$$

At high incident electron energies the backscattered γ-rays are emitted at angles of order $(1/\gamma)$ and therefore the differential cross-section is most conveniently expressed as a function of the γ-ray energy. By introducing the invariants

$$x = \frac{2p\cdot k}{m^2} \qquad\qquad y = 1 - \frac{p'\cdot k}{p\cdot k} \tag{16}$$

which in the laboratory frame take the values

$$x \simeq \frac{2\omega\mathcal{E}}{m^2}(1+\cos\alpha) \qquad\qquad y \simeq \frac{\omega'}{\mathcal{E}} \tag{17}$$

[6] Note that $q_\mu q^\mu = m^2(1+\eta^2)$ as in Eq. (3).

the Klein–Nishina single photon cross-section [24] can be written in the invariant form

$$\frac{\mathrm{d}\sigma}{\mathrm{d}y} = \frac{2\pi r_0^2}{x}\left[(1-y) + \frac{1}{(1-y)} - \frac{4y}{x(1-y)} + \frac{4y^2}{x^2(1-y^2)}\right] \tag{18}$$

Integration of Eq. (18) yields the total Compton cross-section as a function of collision (cm) energy

$$\sigma_{\mathrm{C}} = \frac{2\pi r_0^2}{x}\left[\left(1 - \frac{4}{x} - \frac{8}{x^2}\right)\ln(1+x) + \frac{1}{2} + \frac{8}{x} - \frac{1}{2(1+x)^2}\right] \tag{19}$$

which reduces to (10) in the limit $x \ll 1$.

The probability for reactions (11) and (12) has been calculated in ref. [7, 8, 25]. The incident wave is treated classically and the modified electron wavefunctions are used to obtain the Born amplitude for the emission (or absorption) of the high-energy γ-ray. For circularly polarized incident photons the results can be expressed in closed form and the differential cross-section is given by

$$\frac{\mathrm{d}\sigma}{\mathrm{d}y} = \sum_{n=1}^{\infty}\frac{\mathrm{d}\sigma_n}{\mathrm{d}y} = \sum_{n=1}^{\infty}\frac{2\pi r_0^2}{u_1} \times$$

$$\times \left\{-\frac{4}{\eta^2}J_n^2(z) + \left(2 + \frac{u^2}{1+u}\right)[J_{n-1}^2(z) + J_{n+1}^2(z) - 2J_n^2(z)]\right\} \tag{20}$$

where the following notation has been introduced

$$u = \frac{k\cdot k'}{k\cdot q'} \qquad u_1 = \frac{2k\cdot q}{\overline{m}^2} \qquad u_n = nu_1$$

and

$$z = \left[2\eta\sqrt{u(u_n - u)}\right] \Big/ \left[u_1\sqrt{1+\eta^2}\right] \tag{21}$$

$J_n(z)$ are ordinary Bessel functions of order n. As $\eta^2 \to 0$ only the $n = 1$ term contributes and Eq. (20) reduces to the Klein–Nishina cross-section [Eq. (18)].

The laboratory energy of the scattered electron can be found from Eq. (15) and has its minimal value when the high-energy γ-ray emerges at $\theta = 0$. This gives rise to a kinematic edge which depends on the number of absorbed photons and the effective mass of the electron

$$\mathcal{E}_{\mathrm{edge}}(n,\eta) = \frac{\mathcal{E}}{1 + nx/(1+\eta^2)} \tag{22}$$

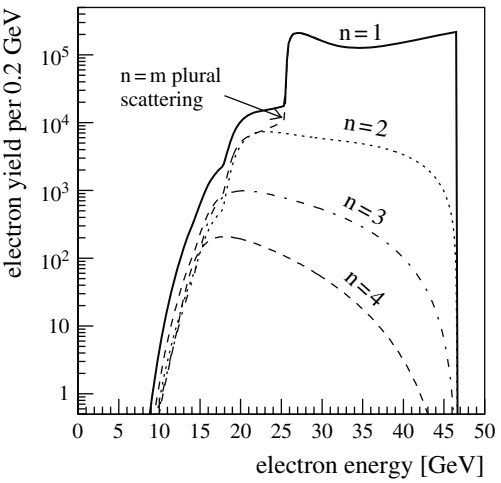

Fig. 2 The calculated rate of scattered electrons for linear, nonlinear and plural Compton scattering for the infrared laser and electron beam parameters given in the text. *The solid line* is the sum of all possible processes. The rates for $n = 2$, 3 and 4 nonlinear Compton scattering are shown separately as well

For green laser light ($\lambda = 527$ nm) and 46.6 GeV electrons the kinematic edges (for $\eta^2 = 0$) are $n = 1$: $\mathcal{E}_e > 17.6$ GeV, $n = 2$: $\mathcal{E}_e > 10.8$ GeV, $n = 3$: $\mathcal{E}_e > 7.8$ GeV, $n = 4$: $\mathcal{E}_e > 6.1$ GeV. By observing electrons with momenta beyond (lower than) the n-photon kinematic edge one identifies events corresponding to the absorption of at least $n + 1$ photons from the laser field. This is shown in Fig. 2 which gives the photon yield for the *infrared laser* $\lambda = 1053$ nm and electron beam parameters used in the experiment.

When observing the recoil electron one must account for the fact that electrons may have scattered *more than once* within the laser focus. This will degrade its energy beyond the corresponding kinematic limit simulating the effects of multiphoton scattering. The effects of such "plural scattering" for the conditions of the experiment have been calculated and are indicated in Fig. 2. This effect is absent when the forward scattered γ-rays are detected.

While this is not obvious from the closed form of Eq. (20) the probability for processes involving the absorption of n photons from the field varies as η^{2n}. In the present experiment $\eta \simeq 0.3$ and the yield of multiphoton effects shown in Fig. 2 obeys this scaling law. However, for a detailed comparison of the data with the theoretical prediction one must account for the variation of η^2 throughout the laser focus. This can only be done by a numerical integration over the laser focus and electron beam parameters, and comparison of the calculated electron momentum spectra with the observed spectra.

Electron–positron production follows reaction (12). A high-energy γ-ray is produced by backscattering and then scatters again, before leaving the laser focus, to produce the pair [26]. The highest energy γ-rays are most effective in producing pairs and this is why green light ($\lambda = 527$ nm) was used by doubling the infrared. Even then, a γ-ray arising from multiphoton scattering would have an energy exceeding that from ordinary ($n = 1$) scattering and thus requires the absorption of a smaller number of photons when it interacts with the field in

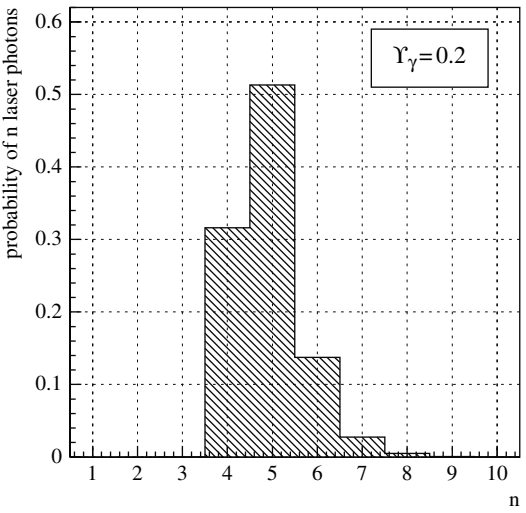

Fig. 3 Calculated probability distribution of the number n of photons absorbed from the laser field in the second step of the two-step pair creation process. Field intensity corresponding to $\Upsilon_\gamma = 0.2$ ($\eta = 0.4$) at the laser focus was used for the simulation

order to produce a pair. The calculated number of photons absorbed from the field is shown in Fig. 3. This is clearly a multiphoton process and for $\eta < 1$, we expect it to vary as η^{2n}.

The calculated rate for e^+e^- production according to reaction (12) is given by an expression analogous to Eq. (20). This must be convoluted with the probability of producing the high- energy γ-ray according to reaction (11). One wonders whether the pair can be produced by a one-step process (i.e., at the same space–time point) such as

$$e^- + n\omega \rightarrow e^{-\prime} + e^+e^- \tag{23}$$

Such processes take place when energetic electrons pass near nuclear targets and are referred to as "tridents". In the present case the probability of reaction (23) is suppressed by a factor $\sim 10^3$ as compared to the two-step process.[7]

For $\eta \gg 1$ the probability for pair production becomes proportional to

$$W \propto e^{-8/3\sqrt{2}\Upsilon_\gamma} \tag{24}$$

where Υ_γ is the dimensionless parameter defined by Eq. (5) but with p^ν replaced by k'^ν, the 4-momentum of the scattered high-energy γ-ray. This form is analogous to the probability per unit volume-unit time for spontaneous pair creation by a strong static field [23]

$$W = \frac{\alpha E^2}{\pi^2} e^{-\pi/\Upsilon} \tag{25}$$

[7] This is due in part to the very high photon density within the laser focus.

We see that the presence of the high-energy electron acts as a catalyst for spontaneous pair creation by the laser field, while also providing the necessary energy–momentum balance. A modification of this result for the case of a wave field is treated in [27].

A standing wave field, for which $E \neq 0$ but $B = 0$, can lead to pair creation without the need for a catalyst, provided $E \gtrsim E_c$. The probability for $\eta \gtrsim 1$ is given by Eq. (25) within a numerical factor of $\pi/2$. In the opposite limit of $\eta \ll 1$ the probability obeys

$$W = \frac{\alpha E^2}{8}\left(\frac{\eta}{\sqrt{2}}\right)^{2n} \tag{26}$$

as expected for a multiphoton process. Here $n = 2mc^2/\hbar\omega$ is the number of photons that must be absorbed from the wave field.

3 Experimental Arrangement

In its simplest form, the experiment consists of scattering an intense laser pulse from a high-energy electron beam. To study multiphoton Compton scattering the scattered electrons which are deflected by a magnetic spectrometer are detected in a silicon–tungsten calorimeter. To study pair production, positrons are identified and detected using the same magnetic spectrometer and a different total absorption calorimeter. The intense flux of forward-going high-energy γ-rays was used mainly to monitor the interaction rate.

As already stated, the experiment was carried out at the FFTB [28] which delivered 5×10^9 electrons per pulse at an energy of 46.6 GeV. The repetition rate was 10 Hz. The experimental layout is shown schematically in Fig. 4. The laser crossed the electron beam at an angle of 17° and was focussed with $f^{\#} \simeq 6$ optics. It was returned to the laser room for diagnostic and monitoring purposes. The magnetic spectrometer consisted of a string of permanent magnets which also directed the beam to the dump. The location of the electron (ECAL) and positron (PCAL) calorimeters is also indicated.

The laser was a 0.5-Hz repetition-rate, tabletop terawatt laser that operated at 1053 nm wavelength (IR), or at 527 nm (green) after efficient ($\sim 45\%$) frequency doubling [29]. It consisted of a mode-locked Nd:YLF oscillator, Nd:glass slab amplifier. The laser system delivered up to 2.4 J in the IR at the interaction point, but typically it was operated only up to 800 mJ of IR and 500 mJ of green. Intensities above 10^{18} W/cm^2 at the laser focus have been produced.

The synchronization of the laser pulse with the electron beam was achieved by using the 119-MHz subharmonic of the accelerator master oscillator frequency to drive the mode locker in the laser oscillator [30]. A Pockels cell was used to select one pulse out of the train and its timing relative to the electron beam was adjusted by changing the phase of the r.f. drive. Fine timing was

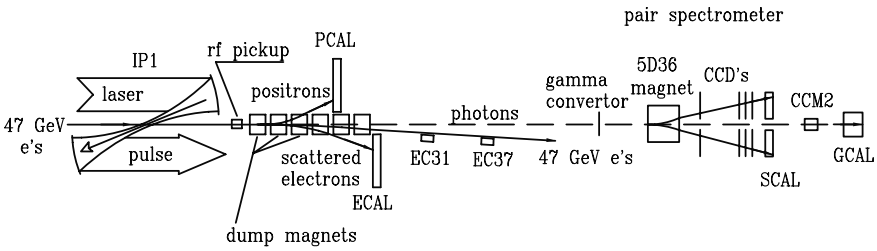

Fig. 4 Schematic of the experimental setup: The laser pulses crossed through the electron beam at the interaction point, IP1. The scattered electrons were deflected by the dump magnets into the electron calorimeter (ECAL). Positrons were deflected into the positron calorimeter (PCAL). The scattered photons were detected in a Čerenkov counter (not shown), or converted to e^+e^- pairs which could be detected by the pair spectrometer

achieved with an optical delay stage by observing the e–laser scattering rate as a function of optical delay. A typical "timing curve" is shown in Fig. 5, with (standard deviation) $\sigma = 4.3\,\text{ps}$; this is the convolution of the pulsewidths of the two beams, $\sigma_e \simeq 3\,\text{ps}$, $\sigma_{\text{laser}} \simeq 0.6\,\text{ps}$, and of the time jitter σ_{j} between their centroids.

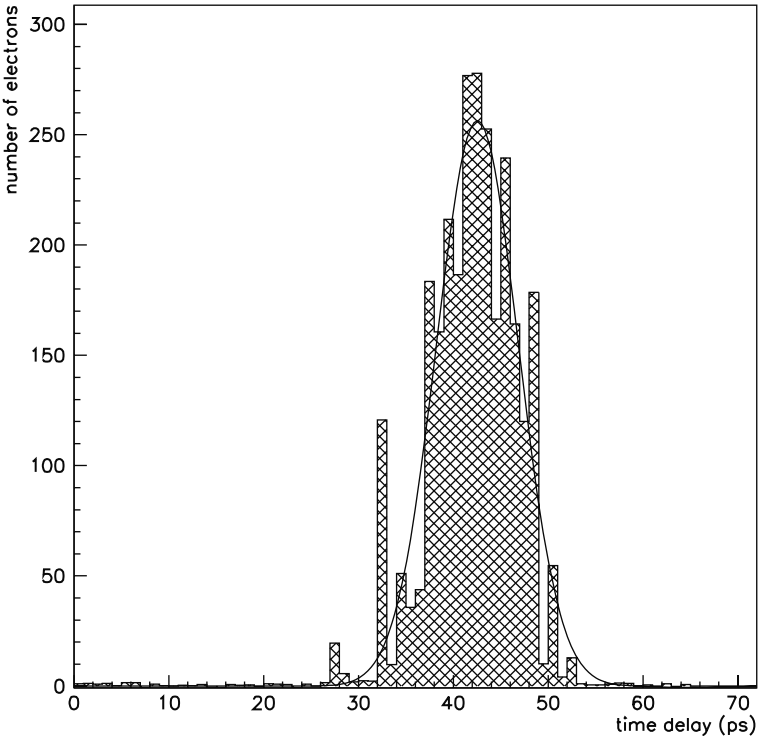

Fig. 5 A "timing curve" showing the number of electrons scattered into the top row of the electron calorimeter as a function of delay of the optical pulse. The standard deviation is $\sigma = 4.3\,\text{ps}$

At the interaction point the electron beam was tuned to a transverse size of $\sigma_x \simeq \sigma_y \simeq 60$ μm; longitudinally, the electron pulse could be adjusted to σ, between 0.5 and 1 mm. The primary spectrometer consisted of six permanent magnets with mean fields of 0.5 T, providing a transverse kick of 816 MeV/c in the vertical plane. Recoil electrons and positrons exited the vacuum chamber through 1/4-inch thick stainless steel windows and were detected by sampling calorimeters.

The calorimeters were made of alternating layers of silicon and tungsten; each layer of tungsten was one radiation length thick, and each silicon layer was 300 μm thick, resulting in a sampling fraction of 1.1%. Each of the layers was divided into 12 rows and 4 columns of $1.6 \times 1.6\,\text{cm}^2$ active area pads, and the longitudinal layers for each tower were ganged into segments. The response (resolution) of the calorimeters to 13 GeV electrons is shown in Fig. 6.

An important aspect of the experiment is the alignment of the electron and laser beams in the transverse plane. Initial alignment was made by lowering a fluorescent flag into the path of the beam and moving the vacuum (IP) box containing the mirrors so that the beam overlapped the image of the HeNe alignment laser. Final adjustment was made by monitoring the forward-photon rate as a function of transverse $(x - y)$ position of the IP box. While the vertical overlap (y) was unambiguous, the overlap in the horizontal plane (x) depended on the relative timing of the two beams, as indicated in Fig. 7(a).

Thus, it was necessary to carry out a raster scan in both the x-position of the box and timing delay. This is shown in Fig. 7(b), where the linear Compton scattering rate observed in one of the monitors is plotted as a function of Δx

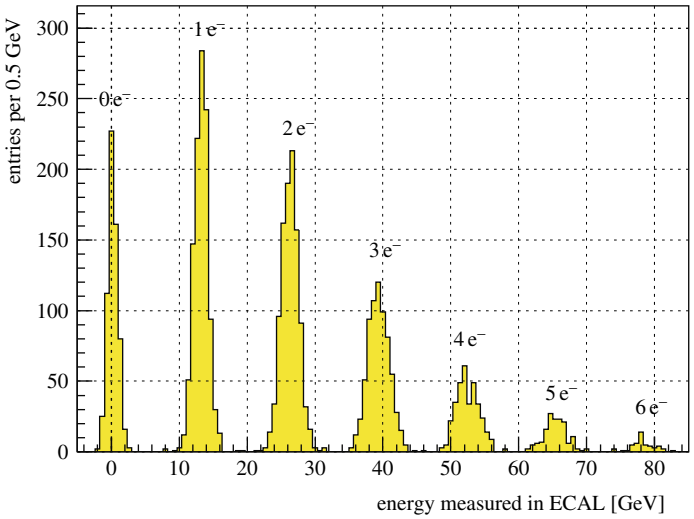

Fig. 6 The response of the ECAL to 13-GeV incident electrons. The peaks due to the simultaneous arrival of up to six electrons are clearly distinguished

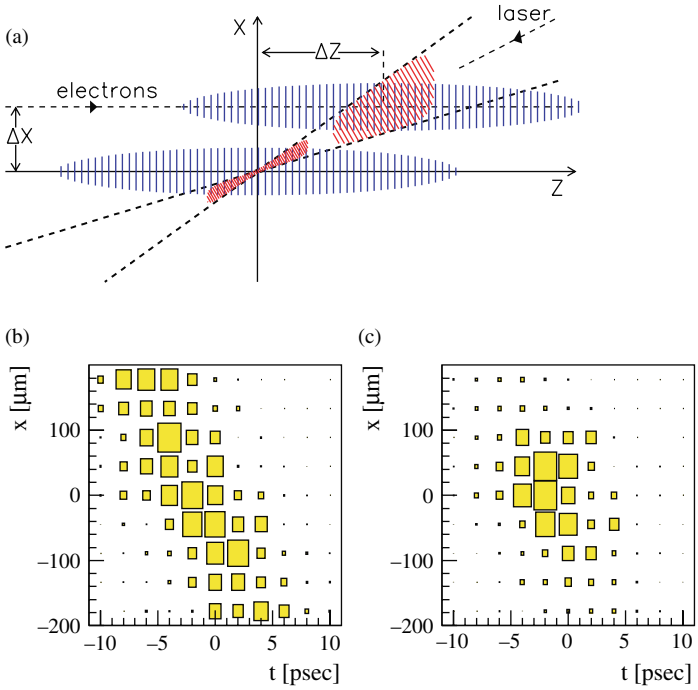

Fig. 7 (**a**) The crossing of the laser pulse and electron beam in the x–t plane; two possible collisions are shown, each giving approximately the same linear Compton scattering rate but drastically different nonlinear Compton rates. (**b**) Linear Compton event rate as a function of transverse beam displacement and relative timing. (**c**) As above, but for the $n = 2$ scattering rate

and Δt. The correlation between the two offsets is clearly evident. In Fig. 7(c), the nonlinear rate, for $n = 2$, is plotted for the same raster scan. A large $n = 2$ signal was obtained only when the electrons crossed through the peak field region of the laser beam, which identifies the optimal space–time alignment of the two beams. These data show that the $n = 2$ yield is of nonlinear origin and depends on the peak intensity of the laser flux.

The laser intensity could be determined from a measurement of the pulse energy U, area A and pulse duration τ. However, for highly nonlinear processes the fluctuations inherent in these measurements were too large. Instead we relied on three monitors which intercepted scattered electrons N_1, N_2, N_3 originating in one-, two- and three-photon Compton scattering. For $\eta^2 < 1$, to a good approximation

$$N_2 = k_2 N_1 \eta^2 \qquad N_3 = k_3 N_1 \eta^4$$

where the factors k_2, k_3 depend on the acceptance and efficiency of the monitors but are the same for all events. They can be obtained from the simulation of the

experiment. By making an overall fit to the data η could be determined for each event with a precision of $\pm$ 11%. This was particularly important for the analysis of the pair production data.

4 Results on Multiphoton Compton Scattering

The spectra of the scattered electrons were measured as a function of the laser intensity for momenta where only multiphoton scattering contributes. This is well beyond the $n = 1$ kinematic edge. The spectra are normalized to the total number of scattered photons N_γ. Thus we present $(1/N_\gamma)(\mathrm{d}N/\mathrm{d}p)$ which should be independent of laser intensity for a linear process. The presentation also has the advantage that to first order fluctuations in timing and/or spatial overlap do not affect the data.

Data are presented for circularly polarized IR ($\lambda = 1053$ nm) and green ($\lambda = 527$ nm), in Figs. 8 and 9. The solid points represent the data whereas the open boxes are the simulation. In general the data extend over three orders of magnitude. The $n = 2$ plateau and the dropoff to $n = 3$ scattering (near the kinematic edge at 17.6 GeV for IR, 10.8 GeV for green) are evident at lower laser intensities. In the green laser data, one can also recognize the $n = 3$ plateau, which extends from 10.8 to 7.8 GeV. A $\pm$ 30% systematic uncertainty in the determination of the laser intensity is not shown and this is the primary cause for the apparent discrepancies between data and simulation.

A simulation that ignores nonlinear Compton scattering, and thereby includes only $n = m$ plural scattering, is shown by the dashed curve. The effect of detector resolution on shifting the position of the inflection between $n = 2$ and $n = 3$ scattering to lower momentum by 0.5–1 GeV/c is especially noticeable in this case. The data at higher laser intensities cannot be accounted for by plural scattering only, and clearly indicate the presence of nonlinear Compton scattering. This is also evident from the measurement of the forward-going photons which is presented in ref. [22].

If the yield $(1/N_\gamma)(\mathrm{d}N/\mathrm{d}p)$ is plotted at fixed momentum as a function of laser intensity, it should follow the approximate form

$$\frac{1}{N_\gamma}\frac{\mathrm{d}N}{\mathrm{d}P} \propto \eta^{2(n-1)} \propto I^{n-1}$$

This is shown for the IR data in Fig. 10. The solid and open circles are the data at momenta dominated by the $n = 2$ Compton process, whereas the triangles and open squares correspond to $n = 3$ and $n = 4$ processes. The bands represent the range predicted by the simulation when the systematic uncertainty is included. A fit to the $n = 2$ data gives the correct exponent $n - 1 = 1.01 \pm 0.13$, but is less reliable for $n = 3$ and $n = 4$. This is because the systematic errors depend on the laser intensity and it is difficult to obtain scatters involving large n at low laser intensity.

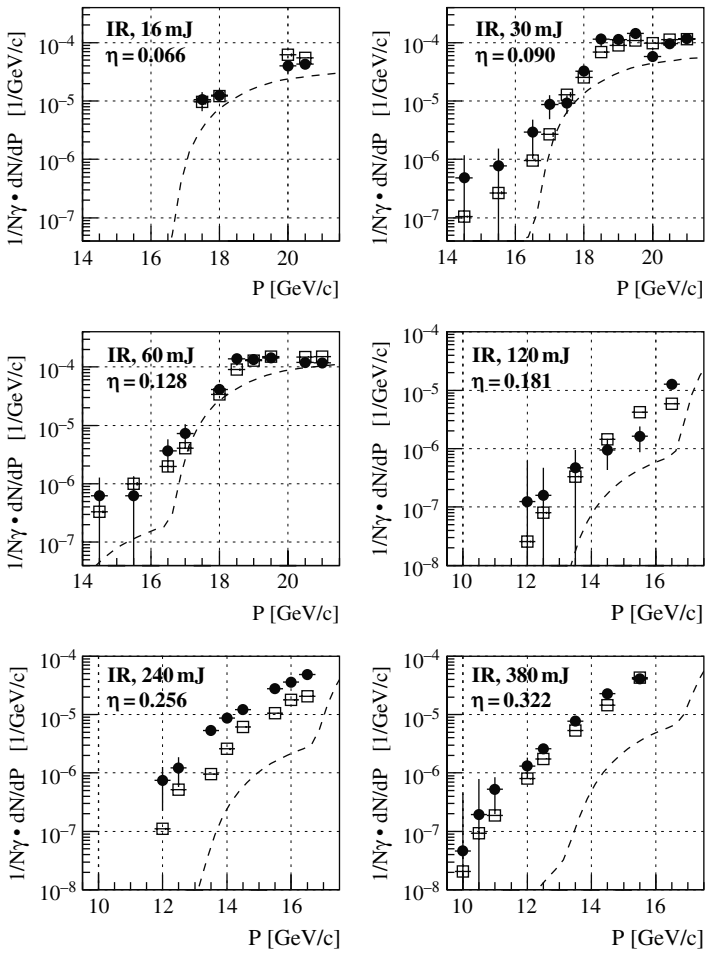

Fig. 8 The yield of nonlinearly scattered electrons, $(1/N_\gamma)(\mathrm{d}N/\mathrm{d}P)$, vs. momentum, P, for six different circularly polarized IR laser energies. The data are *the solid circles* with vertical error bars corresponding to the statistical and reconstruction errors added in quadrature. *The open boxes* are the simulation, with error estimates indicated by the horizontal and vertical lines. The effect of systematic uncertainty in the laser intensity is not shown. *The dashed line* is the simulation of $n = m$ plural scattering without including nonlinear effects

5 Results on e^+e^- Pair Production

As already stated, evidence for the production of an e^+e^- pair was based on the detection of a positron in the PCAL calorimeter. The momentum, p, of the positron is directly related to the location of impact on the calorimeter. The total energy, $\mathcal{E}$, deposited in the calorimeter is also recorded. Thus the ratio $\mathcal{E}/p$ should equal unity for positrons originating from the laser focal area. This was

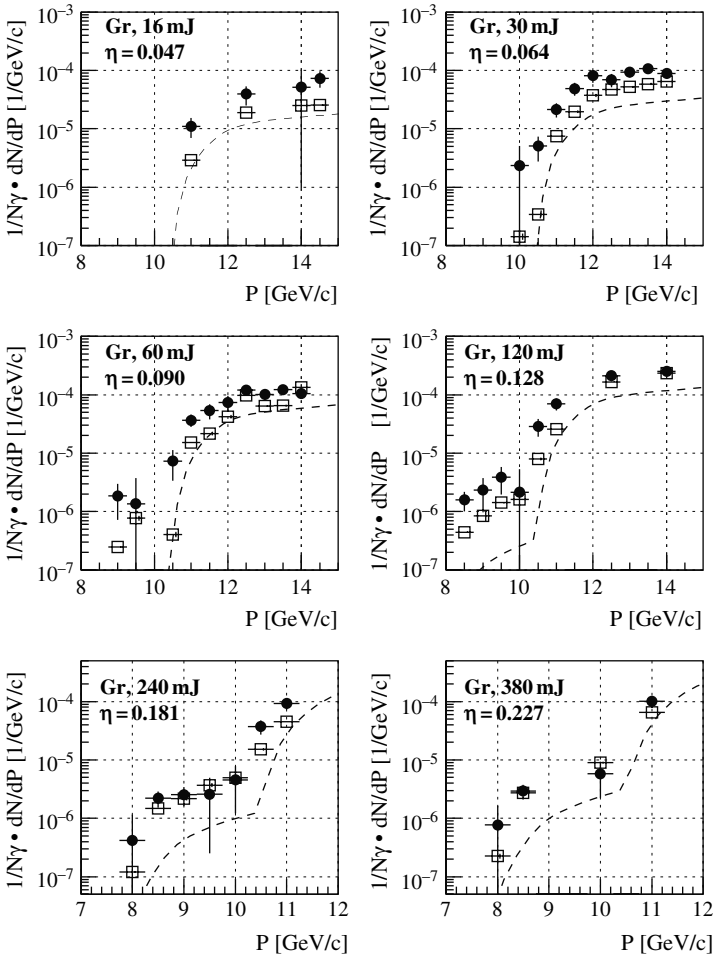

Fig. 9 The yield of nonlinearly scattered electrons, $(1/N_\gamma)(\mathrm{d}N/\mathrm{d}P)$, vs. momentum, P, for six different circularly polarized green laser energies. The data are *the solid circles* with vertical error bars corresponding to the statistical and reconstruction errors added in quadrature. *The open boxes* are the simulation, with error estimates indicated by the horizontal and vertical lines. The effect of systematic uncertainty in the laser intensity is not shown. *The dashed line* is the simulation of $n = m$ plural scattering without including nonlinear effects

tested by placing a thin wire at the focus so that pairs were copiously produced by the Bethe–Heitler process. A plot of $\mathcal{E}/p$ as measured in the calorimeter for $p \sim 21.0\,\mathrm{GeV}$ using this calibration method is shown in Fig. 11. The subsidiary peaks at $\mathcal{E}/p = 2$ and 3 correspond to cases when two or three positrons (at that given momentum) reach the calorimeter in the same pulse.

A total of 175 positrons were identified with the laser on, and data were also taken with the laser off in order to measure the background. The number

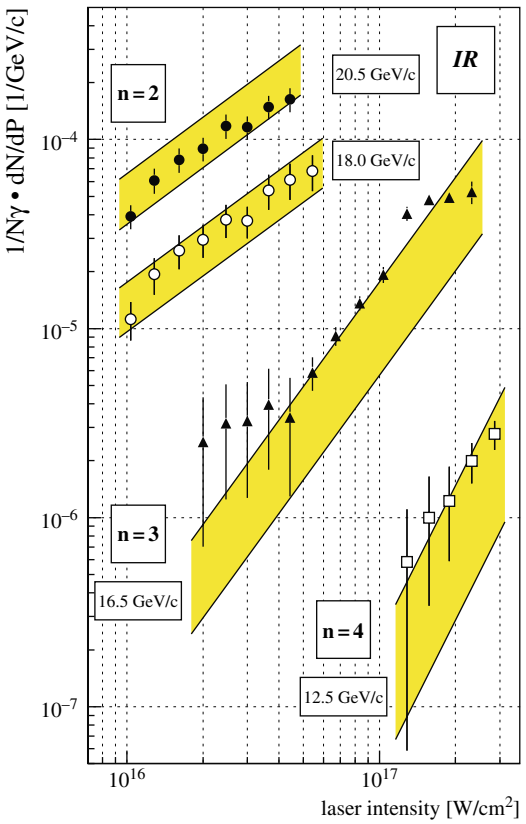

Fig. 10 The scattered electron yield, $(1/N_\gamma)(\mathrm{d}N/\mathrm{d}P)$, vs. IR laser intensity for four representative electron momenta. *The solid* and *open circles* are data for momenta at which the $n=2$ Compton process dominates. *The triangles* and *open squares* are data for momenta at which the $n=3$ and $n=4$ processes dominate, respectively. The simulation for each data set is shown as bands representing the 30% uncertainty in the IR laser intensity. The slopes of the bands are characteristic of the order of the nonlinear process

of positron candidates with the laser "on" and the laser "off" normalized to the same incident flux is shown in Fig. 12(a). The positron momentum spectrum, after subtraction of the background, is given in (b) of the figure. The solid line is the prediction of the simulation.

We can also plot the number of detected positrons as a function of the laser intensity expressed by the parameter $\eta \propto \sqrt{I}$. In Fig. 13 the laser "on" events are shown by the solid circles, while the shaded area gives the background, as deduced from the laser "off" events. A power law fit to the form

$$R_{e^+} \propto \eta^{2n}$$

gives $n = 5.1 \pm 0.2$ and is indicated by the solid line. This is in agreement with the fact that near threshold five photons must be absorbed from the laser field; one photon to create the high-energy γ-ray and at least four photons to create the pair as shown in Fig. 3.

The data are compared with the simulation in Fig. 14. The yield is normalized to the total number of Compton scatters which is directly inferred from

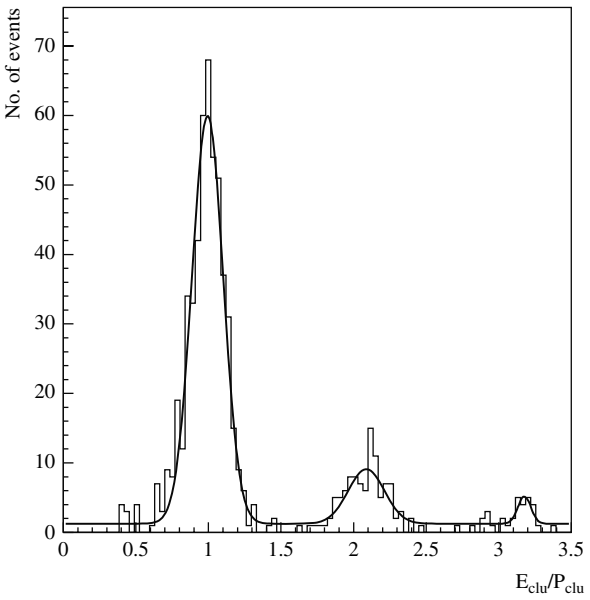

Fig. 11 Distribution of the ratio $E_{\rm clu}/P_{\rm clu}$ for calibration clusters in PCAL row 7, which spans momenta from 20.3 to 21.5 GeV

the monitors while the simulation is shown by the solid line. The prediction of the simulation has *not* been normalized and is in excellent agreement with the data. This would not have been possible without an accurate knowledge of the laser intensity for each event. Therefore for this analysis the laser intensity was determined by the indirect method discussed at the end of section 3.

It is also of interest to consider the positron yield as a function of the parameter Υ defined by Eq. (4), namely $\Upsilon_\gamma = (2k'/m_e c^2)(E/E_{\rm c})$ with k' the γ-ray

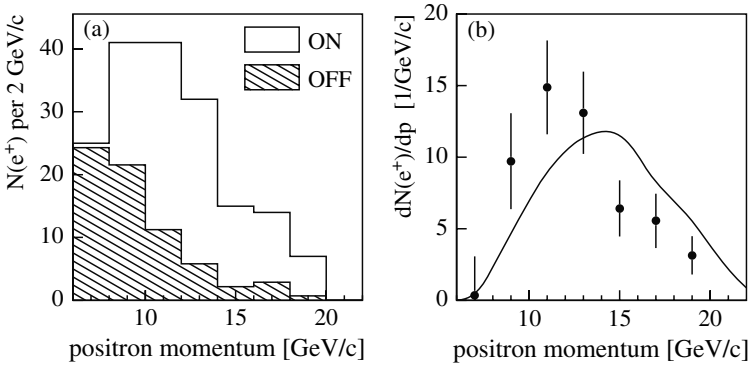

Fig. 12 (**a**) Number of positron candidates vs. momentum for laser-on (ON) and laser-off (OFF) electron pulses. (**b**) Spectrum of signal positrons obtained by subtracting the laser-off from the laser-on distribution. The curve shows the expected momentum spectrum from the model calculation

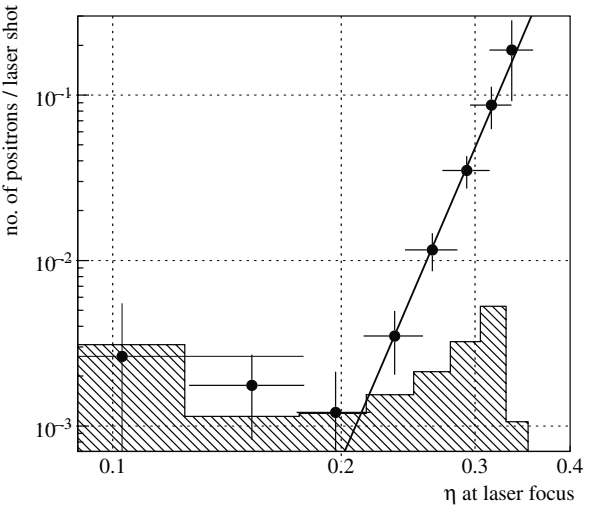

Fig. 13 The dependence of the positron rate per laser shot on the laser field- strength parameter η. *The line* shows a power law fit to the data. The shaded distribution is the 95% confidence limit on the residual background from showers of lost beam particles after subtracting the laser-off positron rate

energy, $k' \sim 29\,\mathrm{GeV}$. We would then expect in the limit $\eta \gtrsim 1$ a dependence such as given by Eqs. (24, 25). This is confirmed by the data which are plotted in Fig. 15 as a function of $1/\Upsilon_\gamma$. A fit to the form

$$R_{e^+} \propto e^{-A/\Upsilon_\gamma}$$

yields $A = 1.27 \pm 0.08 \pm 0.25$, the first error being statistical and the second systematic. This result is to be compared with the asymptotic expectation [see

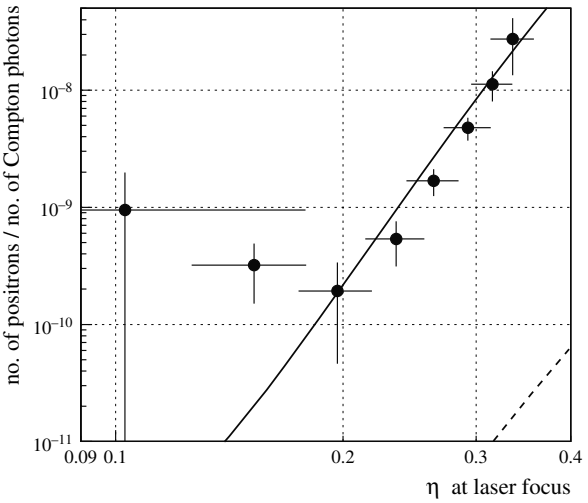

Fig. 14 The dependence of the positron rate on the laser field-strength parameter η when the rate is divided by the number of Compton scatters inferred from the monitors. *The solid line* is the prediction per Compton photon based on the simulation for photon–multiphoton scattering. *The dashed line* represents the simulation for the one-step trident process

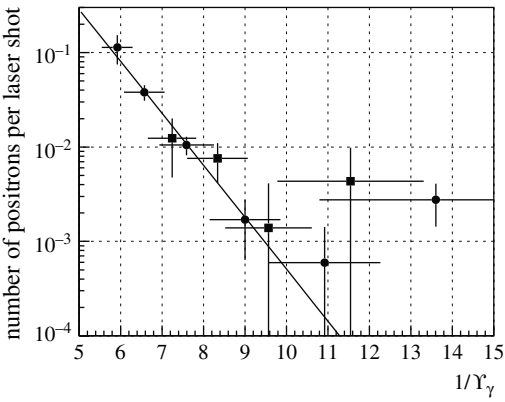

Fig. 15 Number of positrons per laser shot as a function of $1/\Upsilon_\gamma$. *The circles* are the 46.6 GeV data whereas *the squares* are the 49.1 GeV data. *The solid line* is a fit to the data

Eq. (24)] of $8/3\sqrt{2} = 1.89$. However, given the value of η in this experiment the asymptotic value should be reduced to about 1.1 in good agreement with the observed slope. For more details see refs. [22, 27].

Thus the production of positrons observed in this experiment can be interpreted either as photon–multiphoton scattering or as the breakdown of the vacuum by the intense laser field.

6 Discussion

We have seen that when an electron scatters from an intense laser field it can absorb more than one photon while emitting only a single high-energy γ-ray. Furthermore this process depends nonlinearly on the intensity of the field. One can interpret the effect classically by invoking the emission of harmonics of the incident radiation [31], but highly Doppler shifted as a result of the very high energy of the incident electrons. Nevertheless a QED calculation using the modified propagator for the electron in the laser field reproduces the data accurately. It is also of interest that the kinematics of the scattering allows the determination of the number of photons absorbed from the field thus emphasizing the particle properties of the photons in the field.

One expects that the electron will acquire an effective mass for motion in the plane transverse to the laser propagation vector. This would be reflected in the kinematics of the scattered photons but has not been observed as yet. However, the exactly similar effect when electrons radiate as they traverse a magnetic undulator is well established [32].

The production of e^+e^- pairs in the scattering of a high-energy γ-ray from the laser field is a purely quantum-mechanical effect and has no classical interpretation. Technically, it is referred to as arising from "vacuum polarization loops". However, in the experiment that we described pair production

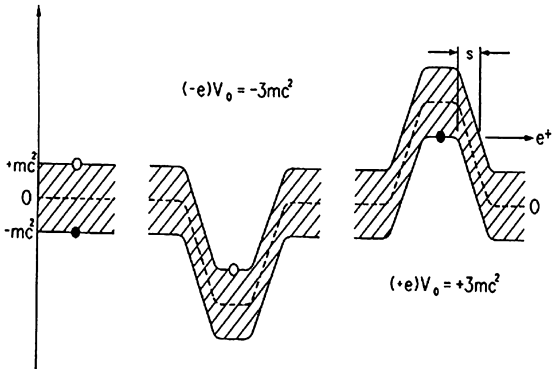

Fig. 16 Illustration of one-dimensional tunneling of a positron from the Dirac sea in the presence of a strong electric field

was possible only by the participation of several photons from the laser field. Thus the effect was nonlinear in the laser intensity exhibiting, for $\eta < 1$, the "perturbative" dependence on the field amplitude $R \propto \eta^{2n}$. Here n is the number of photons participating in the interaction.[8]

Pair production can also be interpreted by a tunneling model. The application of a potential step $V_0 > 2\ mc^2$ will raise the negative energy states of the Dirac sea to an energy $\mathcal{E} > mc^2$. If such a state can tunnel through the potential barrier it will appear as a physical positron. This sequence of events is shown in Fig. 16 where it is evident that the width of the barrier is $s = 2mc^2/eE$ with E the external applied electric field associated with the potential step V_0. Since tunneling is exponential we find for the probability of pair production

$$P \propto e^{-s/\lambda\!\!\!^{-}_c} = e^{-2E_c/E} = e^{-2/\Upsilon}$$

which shows the same dependence on the invariant Υ as Eqs. (24, 25). Achieving critical field without the kinematic boost exploited in the SLAC experiment appears rather difficult. It would require laser intensities of order $I \simeq 10^{30}$ W/cm^2.

The experiments discussed here are among the most stringent and direct tests of "strong QED" but in a region of very low momentum transfers. They are in excellent agreement with the theoretical predictions. Of course, scattering of high-energy particles tests QED in the "perturbative" regime but at high momentum transfer. Again excellent agreement is found between theory and experiment to distances as short as 10^{-16} cm.

---

[8] Positron production has been reported in some recent experiments where intense lasers interact with matter [33]. This is a completely different process whereby an electron is accelerated to high energy by the laser field and then interacts with matter to produce a pair by the Bethe-Heitler process.

Acknowledgment I wish to acknowledge my indebtedness to my colleagues in experiment SLAC-E144, who participated in the research reported here, and to the many others who contributed to its success.

References

1. O. Klein, Zeits f. Phys. *53*, 157 (1929).
2. F. Sauter, Zeits. f. Phys. *69*, 742 (1931).
3. W. Heisenberg and H. Euler, Zeits. f. Phys. *98*, 718 (1936).
4. H.R. Reiss, J. Math. Phys. *3*, 59 (1962).
5. H. R. Reiss Phys. Rev. Lett. *26*, 1072 (1971).
6. L.S. Brown and T.W.B. Kibble, Phys. Rev. *133A*, 705 (1964).
7. A.I. Nikishov and V.I. Ritus, Sov. Phys. JETP *19*, 1191 (1964).
8. A. I. Nikishov and V. I. Ritus, Sov. Phys. JETP *20*, 757 (1965).
9. T.J. Englert and E.A. Rinehart, Phys. Rev. *A28*, 1539 (1983).
10. S.-Y. Chen, A. Maksimchuk and D. Umstadter, Nature *396*, 653 (1998).
11. P.H. Bucksbaum et al., Phys. Rev. Lett. *58*, 349 (1987).
12. C.I. Moore, J.P. Knauer, and D.D. Meyerhofer, Phys. Rev. Lett. *74*, 2439 (1995).
13. G. Malka, E. Lefebvre and J.L. Miquel, Phys. Rev. Lett. *78*, 3314 (1997).
14. V.F. Weisskopf, Mat. Fys. Medd.-K Dan. Vidensk. Selsk. *14*, 6 (1936).
15. R. Cameron et al., Phys. Rev. *D47*, 3707 (1993).
16. T. Erber, Rev. Mod. Phys. *38*, 626 (1966).
17. A. Belkacem et al., Phys. Lett. *B177*, 211 (1986).
18. A. Belkacem et al., Phys. Lett. *B206*, 561 (1988).
19. R. Medenwalt et al., Phys. Lett. *B227*, 483 (1989).
20. C. Bula et al., Phys. Rev. Lett. *76*, 3116 (1996).
21. D.L. Burke et al., Phys. Rev. Lett. *79*, 1626 (1997).
22. C. Bamber et al., Phys. Rev. *D60*, 092004 (1999).
23. J. Schwinger, Phys. Rev. *82*, 664 (1951).
24. O. Klein and Y. Nishina, Zeits. f. Phys. *52*, 853 (1929).
25. N.B. Narozhny et al., Sov. Phys. JETP *20*, 622 (1965).
26. Electron-positron production in photon-photon scattering was first calculated by G. Breit and J.A. Wheeler, Phys. Rev. *46*, 1087 (1934).
27. E. Brezin and C. Itzykson, Phys. Rev. *D2*, 1191 (1970).
28. V. Balakin et al., Phys. Rev. Lett. *74*, 2479 (1995).
29. C. Bamber et al., Laser Physics *7*, 135 (1997).
30. T. Kotseroglou et al., Nucl. Instr. and Meth. *A383*, 309 (1996).
31. See for instance G.A. Schott, *Electromagnetic Radiation*, Cambridge University Press 1912.
32. See for instance K.J. Kim "Characteristics of Synchrotron Radiation" in AIP Conference Proceedings *184* (1989).
33. T.E. Cowan et al., Phys. Rev. Lett. *84*, 903 (2000).

Nuclear Physics with Intense Lasers

Ravi Singhal, Peter Norreys, and Hideaki Habara

1 Introduction

In the past 10 years, multi-terawatt laser systems with subpicosecond pulse lengths have opened up a range of exciting possibilities in the study of laser–matter interactions. For focused laser intensities of 5×10^{19} W cm^{-2}, the electromagnetic fields are of the order of 2×10^{13} V m^{-1} and 10^5 T. The motion of electrons in such high fields is highly relativistic, the quiver energy of the electrons being determined by the product of the laser intensity and the square of the laser wavelength, $I\lambda^2$. For example, for $I = 5\times10^{19}$ W cm^{-2} and $\lambda = 1\,\mu$m, the quiver energy is already several times the electron rest mass. Smaller numbers of electrons of much higher energies of up to 100 MeV are also produced. Bremsstrahlung is produced collaterally by the fast electrons in the target material. Such energies are sufficient to induce nuclear reactions in materials, as the typical energy thresholds may be as low as a few MeV [1].

Rapid progress in the study of the interaction of intense lasers with matter has been fuelled due to the vast possibilities afforded by such measurements. The generation of highly relativistic plasmas with applications in astrophysics and inertial confinement fusion, laser-induced nuclear photophysics, positron emitters for nuclear medicine, high-energy proton beams for cancer therapy, intense neutron sources, treatment of nuclear waste are some of the ideas that have practical applications [2,3]. Theoretical understanding of intense laser–matter interactions and the study of relativistic plasmas is already providing high dividends. Concepts like wakefield acceleration with gradients of about 100 GeV m^{-1} could herald a new era in the design of particle accelerators for high-energy physics research. The production of electron–positron plasmas will open up new fields of research. Lasers under construction will be able to generate exotic particles like pions [2,3].

R. Singhal
Department of Physics & Astronomy, University of Glasgow, Kelvin Building, Room 515a, Glasgow, G12 8QQ, Scotland, UK
e-mail: r.singhal@physics.gla.ac.uk

T. Brabec (ed.), *Strong Field Laser Physics*,
DOI: 10.1007/978-0-387-34755-4_22,

In this chapter, various aspects of the interaction of intense lasers with solid targets will be discussed with particular emphasis on the observation of nuclear effects and their applications in medicine. Most experiments have been carried out at the VULCAN laser facility (which is capable of delivering intensities up to 9×10^{19} W cm^{-2} at 1 ps pulse length to target) at the Rutherford Appleton Laboratory (RAL). The highest peak power experiments to date have been performed at the Lawrence Livermore National Laboratory (LLNL) Nova PetaWatt Laser facility ($>10^{20}$ W cm^{-2} at 450 fs). Single laser shots are employed and the resulting nuclear activation is measured in these experiments. Recently studies of nuclear reactions at shorter pulse lengths produced by Ti–sapphire lasers have also been reported. Ti–sapphire lasers are physically much smaller and their high repetition rates make them ideal candidates for application-based laser-induced nuclear reactions. The peak powers in individual pulses are still modest, but new laser systems are being developed to address this problem (see article by Ian Ross in this volume).

2 Production of High-Energy Electrons and γ-Rays

As a result of the interaction of an intense laser pulse with the surface of a solid target, electrons are first accelerated to high energies. During their travel through the solid target, the electrons radiate bremsstrahlung, the γ-rays being produced predominantly in the forward direction. The energy and angular distributions of the electrons and γ-rays are important parameters in so far as a precise knowledge of these helps to design nuclear activation experiments. The models of electron acceleration mechanisms can also be improved with such data. Cowan et al. [4] have measured energy spectra of electrons at 30° and 90° to the laser direction. Figure 1 shows that for a 1.05 μm wavelength laser pulse of intensity $>10^{20}$ W cm^{-2}, electrons of energy up to 100 MeV are produced. A 2000 times lower energy laser prepulse was focused on the target about 2 ns prior to the main pulse. Cowan et al. performed 2D PIC simulations in the presence of a preformed plasma of scale length ~50 μm created by the prepulse. The predicted electron distribution is in reasonable agreement with the experimentally measured spectrum over most of the energy range responsible for hard bremsstrahlung.

For a range of elements, Ledingham et al. [5] have studied nuclear activation induced by high-energy γ-rays generated in a 1.75 mm thick tantalum target on irradiation by the VULCAN laser pulse of intensity $\sim10^{19}$ W cm^{-2}. The primary reaction is (γ,n) such that the daughter product, being proton rich, is a positron emitter. After the laser shot, the target is removed to a laboratory where the positron activity is measured by coincidence recording of the counter propagating 511 keV annihilation γ-rays. Figure 2 shows the target arrangement and Fig. 3 shows the $3'' \times 3''$ NaI coincidence counting system.

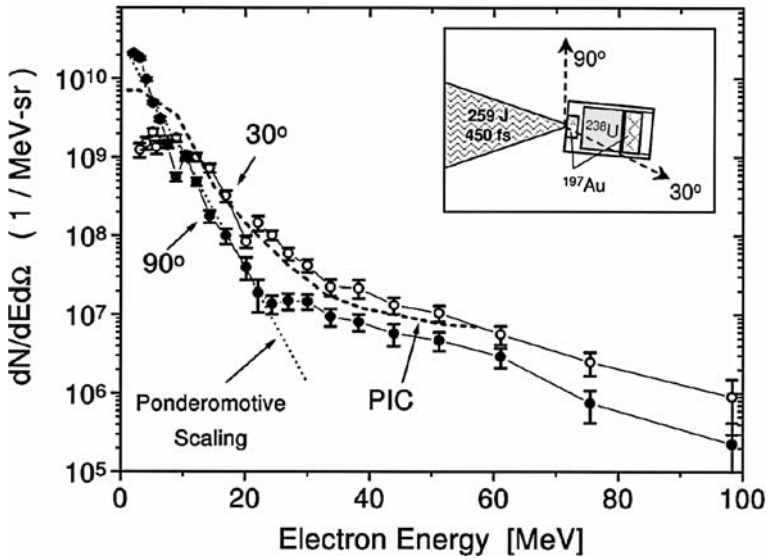

Fig. 1 Measured energy distribution of electrons ejected from the target at 30° (*open circles*) and 90° (*solid squares*) with respect to the incident laser pulse. *The dashed curve* shows the expectation from a ponderomotive potential while *the solid curve* shows the results of a PIC simulation. (Reproduced with permission from the authors)

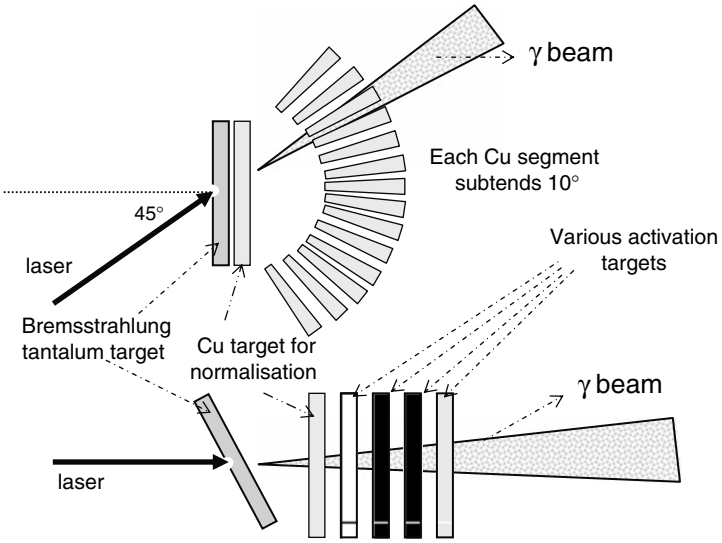

Fig. 2 The *upper* diagram shows the arrangement for measuring the angular distribution of the high-energy γ-rays. The Cu segments are 10 mm long and each subtends an angle of 10°. The *lower* diagram shows the arrangement for irradiating a number of different targets for the determination of electron temperatures in the plasma (see text)

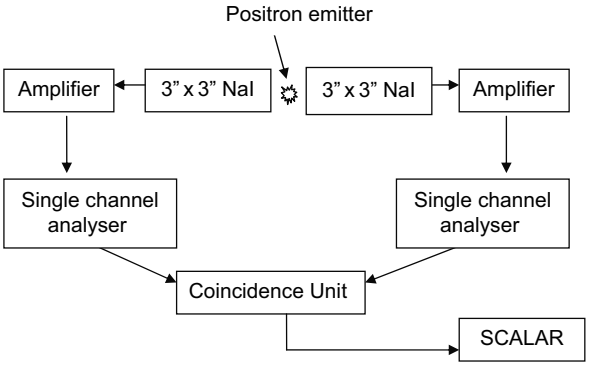

Fig. 3 The coincidence system for measuring positron activity. The counter propagating γ-rays produce a voltage pulse in each NaI detector. The pulses are amplified and only pulses which are in the 511 keV energy window are accepted. If they are in time coincidence then the output is sent to the scalar unit for counting

With laser intensities of about 10^{19} W cm^{-2}, activities up to 3000 Bq were produced. The activity of a sample as a function of time provides a determination of the half-life of the positron-emitting isotope. These half-life measurements agree very well with the known values and provide confirmation of the production of high-energy γ-rays.

Each (γ,n) reaction cross–section has its unique dependence on the γ-ray energy. From the measurements of activities of two target elements having different (γ,n) thresholds, it is possible to estimate the plasma electron temperature. Spencer et al. [6] used ^{12}C (Q-value = 18.7 MeV) and ^{63}Cu (Q-value = 10.9 MeV) targets and the known energy dependence of the (γ,n) cross-sections to compare shot to shot variations of the electron temperature (kT) in the plasma generated by laser intensities of about 10^{19} W cm^{-2} (Fig. 4).

The use of two different targets brings in difficulties of normalisation of γ-flux due to different geometry, etc. This may be circumvented by measuring different orders m of (γ,mn) reactions in a suitable target. For example, the (γ,n) and (γ,3 n) thresholds in ^{181}Ta are at 7.6 and 22.1 MeV, and the positron emitting isotopes ^{180}Ta and ^{178}Ta have half-lives of 8.1 and 2.1 h. For laser

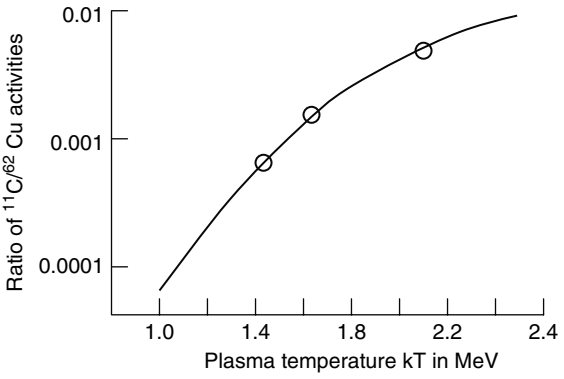

Fig. 4 *Open circles* show results of three different VULCAN shots at about 10^{19} Wcm^{-2}. The continuous line is the result of a calculation with published (γ,n) cross-sections for ^{12}C and ^{63}Cu. A relativistic electron energy distribution has been assumed

intensities of about 10^{20} W cm^{-2}, Spencer [7] measured the X-ray spectra from these daughter products to determine the induced activities and has estimated an electron temperature of 4.5 MeV.

The study of laser-induced (γ,n) reactions results in the production of positron-emitting radionuclides. However, separation of the active nuclides from the sample is not easily possible as the loss of a neutron still leaves the daughter product in the same chemical state. For nuclear medicine applications like positron emission tomography (PET), availability of radionuclides with half-lives of a few minutes to several hours is required. This may be accomplished by utilising high-energy protons that are also produced in the interaction of intense lasers with suitable targets. This is discussed in the following.

3 Production of High-Energy Protons

In the interaction of intense laser pulses with matter, proton emission was first reported in the early 1970s. By the mid-1980s, a sufficiently large database had been assembled to remove systematic uncertainties. A review of the work to that point was summarised by Gitomer et al. [8]. It was shown that the protons arose from hydrocarbon or water contamination layers on the surfaces of the targets and that both the average and maximum ion energy scaled with $I\lambda^2$ on target in the same way as the hot electron temperature that was generated by resonance absorption. Protons were accelerated by electrostatic fields driven by the fast electrons.

Fews et al. [9] and Beg et al. [10] were among the first to measure the generation of multi-MeV protons from the front surface of targets using 1053 nm laser pulses of between 1.0 and 4.0 ps duration with intensities up to $I\lambda^2 = 10^{19}$ W cm^{-2} μm^2. More recently, several measurements of the production of protons from the rear surface of the targets have been reported by Clark et al. [11] and Snavely et al. [12]. The teams observed protons with energies up to 20 and 50 MeV, respectively. An empirical power law relation of proton energy and $I\lambda^2$ has been obtained from the measurements [13]. It is concluded that the production of protons with energies of 200 MeV, required for cancer therapy, needs further increase of laser energy by about a factor of 16. Other application of protons is in the production of positron emitters for PET scanners – currently available energies are adequate but increased proton fluxes are required for commercial viability. These matters are visited later in this section.

Figure 5 shows the experimental arrangement for the production of protons at the VULCAN laser at RAL. Laser intensities up to 10^{20} W cm^{-2} irradiated thin aluminium or CH foil target at 45° incident angle. The target chamber is evacuated to 10^{-5} Torr. In the 'blow-off' direction to the front of the target, protons and ions are produced in a direction perpendicular to the target. Protons are also emitted from the rear of the target – in the 'straight-through' direction. The angle of proton emission in the 'straight-through' direction is

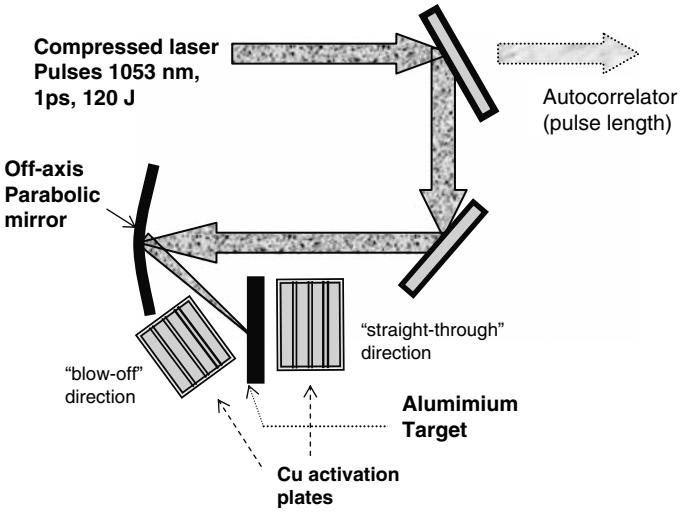

Fig. 5 Schematic experimental lay-out for proton production measurements. The positron activity of $^{63}Cu(p,n)^{63}Zn$ reaction is measured

found to be along the target normal. VULCAN laser prepulse is a long 1 ns laser pulse with an intensity of about 10^{-6} of the main pulse. The prepulse generates a blow-off plasma to the front of the target with which the main laser pulse interacts. The arrival time of the prepulse defines the density scale length L that is a measure of the spatial gradient between the density where energy is absorbed (called the critical density) and the vacuum. Electrons are accelerated into the target in a direction that depends on L. The width of the cone in which fast electrons are emitted has been measured to be about 35° at 10^{19} W cm^{-2} [14] and 20° [12] at somewhat higher laser intensities.

4 Models of Proton and Ion Acceleration

There are a number of mechanisms that can accelerate ions to high energies in ultra-intense laser plasmas, in addition to the electrostatic sheath acceleration away from the front surface of the target. Charge separation occurs at the critical surface over short distances due to the ponderomotive force of the laser pulse, leading to the phenomenon of hole-boring. Here the ponderomotive pressure greatly exceeds the thermal pressure and the plasma is expelled from the focal region [15]. This mechanism is well understood, but is expected to accelerate protons only to the ponderomotive energy of the laser (i.e. up to 4 MeV for intensities of 10^{20} W cm^{-2} on target).

Other theoretical models have also shown that, provided the plasma scale length and the laser pulse duration are sufficiently small, a collisionless

electrostatic shock is launched into the overdense plasma [16,17]. This shock arises from the reflection of the background ions on the electrostatic potential barrier associated with a large amplitude ion acoustic wave that propagates into the target, driven by the intense ponderomotive pressure. The fraction of absorbed laser energy converted to ion kinetic energy is predicted to increase with higher intensities and scales as $\eta_{\mathrm{I}} = 2\left(I_0/\rho c^3\right)^{1/2}$. Here $\rho = n_{\mathrm{i}} M_{\mathrm{i}}$ is the absorber density, n_{i} is the ion density and M_{i} is the ion mass [16].

The most detailed study to date of these complementary processes of hole-boring and collisionless electrostatic shock formation is that reported by Toupin et al. [18], who predict that a highly collimated, multi-MeV ion beam is directed into the target under small scale length and ultra-high-intensity irradiation conditions. They also show that angular distribution of the accelerated ions is strongly dependent on the density scale length L. Some experimental evidence, based on neutron spectroscopy, has been presented that supports this interpretation [19,20,21].

In addition to these collisionless processes, which are well modelled using multi-dimensional particle-in-cell (PIC) tools [22], resistive electric fields are generated inside the target that may also accelerate these multi-MeV ions to still higher energies. This electric field is required to draw the return current from the target so as to maintain charge neutrality. The forward MeV electron beam is generated from electrons drawn out of the skin depth at the critical density surface – but the return current is drawn from the slower drift of background electrons in the solid density plasma. These are strongly affected by collisions, and the resulting electric field can be estimated from the target resistivity [23,24].

Wilks et al. [25] have proposed the target normal sheath acceleration (TNSA) mechanism to explain the proton emission from the rear of the target. This is an extension of earlier models for front surface acceleration. The source of protons is considered to be a thin layer ($\sim$5 nm) of contaminants on the rear target surface, as before. Such hydrocarbon or water-based contaminations are always present and consist of a large number of hydrogen atoms. According to TNSA, at the front surface of the target, the prepulse produces a plasma that expands spherically to a radius of the order of 100 μm before the main pulse arrives. The main laser pulse interacts with this plasma and generates a large number of hot electrons with average temperatures of several MeV. The fast electrons form an energetic electron cloud on the back of the thin target. The proton layer is ionised and accelerated by the electrostatic fields generated in the cloud. The accelerating gradients generated by ultra-short laser pulses may reach values of tens of MeV per μm on the back of the target. Since the protons in the back are in a sharp, flat density gradient, they are accelerated quickly in the first few μm off the target to high energies in the forward direction – normal to the target surface. In the blow-off direction at the front of the target, the scale length is somewhat larger – and consequently the accelerating gradient is much smaller. Therefore, protons on the front of the target are expected to be less

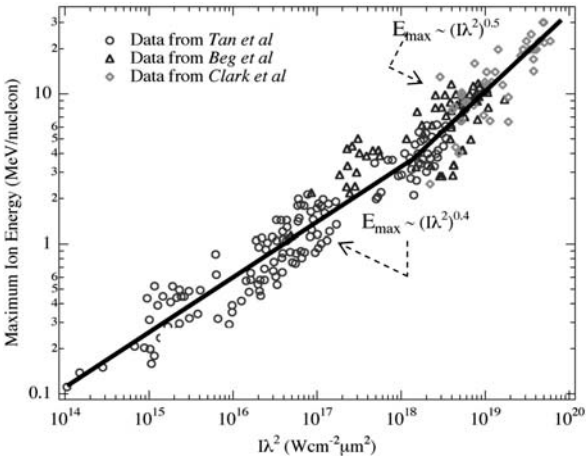

Fig. 6 Maximum ion energy as a function of $I\lambda^2$. (Adapted from [13])

energetic than the ions on the back of the target. Moreover, protons on the front of the target are spread out into 2π steradians.

With the laser pulse intensity of 10^{20} W cm^{-2} Spencer et al. [26] observed the production of 10^{12} protons in the straight-through direction with an energy cut-off at 37 MeV. The maximum proton energy depends on the product $I\lambda^2$. In Fig. 6, this dependence is demonstrated as $(I\lambda^2)^{0.4}$ up to 10^{18} W cm^{-2} μm^2. For higher intensities the maximum proton energy scales as $(I\lambda^2)^{0.5}$. This indicates a transition in the underlying process of hot electron production from classical resonance absorption to ponderomotive $\mathbf{j}\times\mathbf{B}$ acceleration at higher intensities [13,14]. The proton energy does not depend only on $I\lambda^2$; additionally the angle of incidence, pulse length, polarisation of the laser, prepulse characteristics, target properties, etc. also affect the production of protons. The effect of these parameters has not been investigated in sufficient detail and may explain some of the spread in the data in Fig. 6.

An important factor is the efficiency of conversion of the laser energy into proton energy. From the data available, it appears that more of the laser energy is converted into protons as the product $I\lambda^2$ is increased. The absorption into proton energy has been found to increase from 0.5% at $I = 2\times10^{17}$ W cm^{-2} to 12% at 3×10^{20} W cm^{-2}.

The experimental measurements [7] of the differences between front and rear surface proton acceleration are shown in Fig. 7. The rear surface protons are accelerated to higher energy than the front surface protons. The data is consistent with the TNSA model – but is also consistent with protons that are accelerated at the front through collisionless shocks and that then experience the subsequent electric fields generated inside the resistive dense plasma and at the rear surface. The conversion efficiency data is consistent with the Denavit model for collisionless shock formation – but also with the TNSA model. It is clear that it is difficult to accurately model these competing/complementary

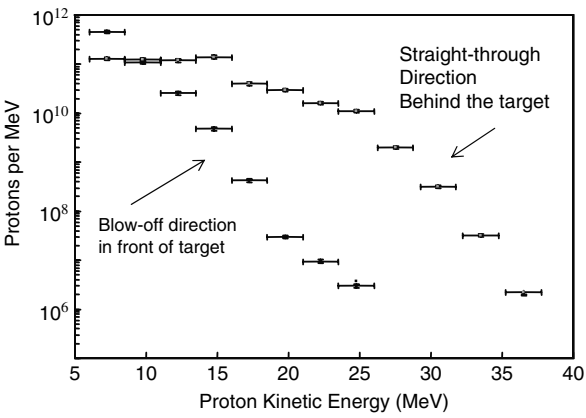

Fig. 7 Proton energy spectra obtained from copper activation stacks in front of and behind the target for laser intensity equal to 10^{20} W cm^{-2} (Adapted from [7])

processes theoretically and to distinguish between them experimentally. The multi-dimensional PIC tools are generally collisionless and computationally expensive for realistic target parameters. The resistive models do a good job modelling the solid density plasma, but fail to handle the laser-plasma interaction processes in the coronal plasma on the front and rear surfaces of the target. Hybrid computer codes that bridge the gap between the two methods and density regimes are under development. Further experiments varying target thickness, material prepulse levels and intensities are needed to distinguish the competing processes.

5 Applications of Laser-Produced Proton Beams

It is clear from the discussion above that current high-intensity lasers can provide proton beams with low divergence, of the order of 20° and up to a maximum energy in the region of 50 MeV. One of applications of the proton beams may be to provide ion sources for accelerators, but the most promising application is in nuclear medicine. With the laser technology advancing rapidly, it is expected that relatively compact laser systems will be able to deliver intensities in the 10^{20-21} W cm^{-2} region. For example, the proton beams can then be used to produce positron-emitting radio-pharmaceuticals for positron emission tomography (PET) scanners. The potential of this is already well researched [27] and is examined in the following.

The important positron emitters for PET scanners are ^{11}C, ^{13}N, ^{15}O and ^{18}F. Their half-lives are 20.34, 9.96, 2.05 and 109.7 min, respectively. Because of the short half-lives, the positron emitters are produced locally. The cross-sections for the production of these isotopes (Fig. 8) peak for proton energies between 5 and 15 MeV, and the current laser intensities are adequate for the efficient production of positron emitters via (p,n) and (p,α) reactions. In these reactions,

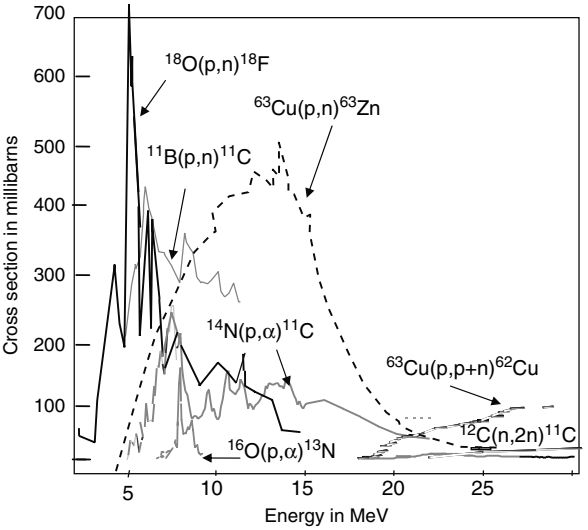

Fig. 8 Experimentally measured cross-section for a range of (p,n) and (p,α) reactions that are suitable for producing positron emitting isotopes for PET scanners. The data are from EXFOR nuclear reactions database

the positron emitters correspond to a different chemical element and may be separated from the target bulk by fast chemistry.

The experiment used a target arrangement similar to that in Fig. 5 for the production of PET isotopes. Targets of boron and silicon nitride were placed in front of the target which were then activated by the 'blow-off' protons produced by a VULCAN laser shot of 10^{20} W cm^{-2}. The targets were removed from the target chamber and the positron activity as a function of time of the sample counted with the coincidence counting system shown in Fig. 3. The measured decay curves are shown in Fig. 9. Definite evidence of the reactions $^{11}B(p,n)^{11}C$ and $^{14}N(p,\alpha)^{11}C$ is obtained from the measured half-life of ^{11}C. An activity of about 2×10^5 Bq for the $^{11}B(p,n)^{11}C$ is inferred from this data.

From the cross-sections for various reactions, it is estimated that a production rate of 10^5 Bq may be achieved for ^{18}F per VULCAN laser shot. These production rates are still some way short of being commercially viable. PET scanners require that positron emitters of initial activity of about 10^9 Bq are produced. This improvement may be achieved through various means. For example, protons at the back of the target are more energetic and are produced in fluxes that are 10–100 times greater. Table-top lasers with 1 J pulse energy operating at 1 kHz would provide a factor of 10^4 improvement if the activity is integrated for 500 s. Yamagiwa and Koga [28] have estimated that with laser pulse intensities of 10^{21} W cm^{-2} it is possible to produce 10^{14} Bq of ^{18}F. This production rate is two orders of magnitude higher than can be generated with present cyclotrons.

A very interesting and potentially extremely important application of laser-produced high-energy protons is in proton oncology. The energy carried by protons may be deposited in the tissue at a desired depth from the surface and

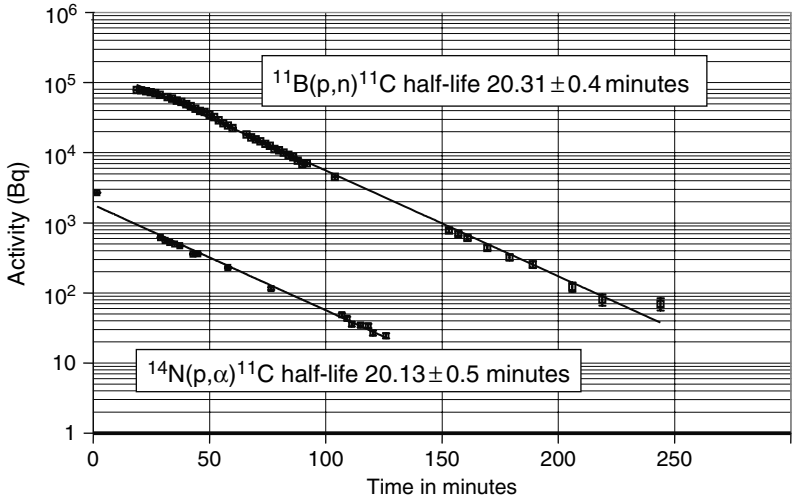

Fig. 9 Production of the isotope ^{11}C via the proton-induced reactions ^{11}B(p,n)^{11}C and ^{14}N(p,α)^{11}C. The samples were boron and silicon nitride. The laser intensity was 10^{20} W cm^{-2} [26]

is very effective in killing tumour cells. The advantages of using high-energy protons is demonstrated in Fig. 10 assembled by the Midwest Proton Radiation Institute, USA. Protons have a unique energy deposition pattern which is very different from that of electrons or electromagnetic radiation. For the latter, energy of the primary beam decreases exponentially with depth and the tissue is more or less uniformly irradiated. This results in unacceptable damage to healthy cells through which the radiation must pass. Protons and other charged

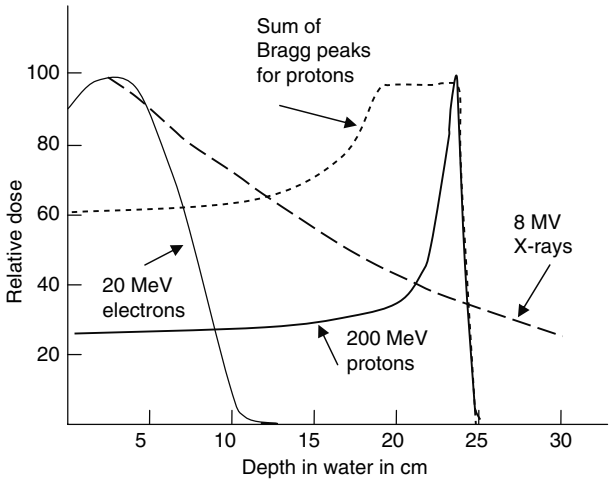

Fig. 10 Energy deposition by various radiation in water (www.iucf.indiana.edu/MPRI/about.htm)

particles like pions and light mass ions are not deflected as they travel in the tissue which is a serious problem with X-rays and electrons. The energy deposition of 200 MeV protons, Fig. 10, shows rather small energy loss until proton energy decreases sufficiently. At this stage, rate of energy loss exhibits a sharp increase, called the Bragg peak, and protons come to rest very quickly. The range of 200 MeV protons in water is 0.24 m. By using a suitable spectrum of proton energies, the volume and depth of the irradiated tissue may be defined. This is also shown in Fig. 10.

Recently, protons accelerated in laser-plasma interactions were applied to investigate nuclear reactions of interest to the traditional fields of nuclear and accelerator science. McKenna et al. [29] have shown that laser-generated protons could potentially be used to investigate residual isotope production in proton-induced nuclear spallation reactions.

Laser-induced production of protons has tremendous promise since the proton beam is highly directional. The present capabilities are the production of about 40 MeV protons at intensities of 3×10^{20} W cm^{-2}. Assuming a 0.5 power dependence of the proton energy on laser intensity, one would require a 16-fold increase in laser intensity to 8×10^{21} W cm^{-2} at 1053 nm wavelength. Such upgrades are being implemented at VULCAN (RAL) and other laboratories.

6 Production of Neutrons

As discussed in this chapter, neutrons may be produced by (γ,n) reactions if the photons have energy greater than the Q-value of the reaction. Such photons are produced in large numbers when intense laser pulses irradiate matter. A solid target of high atomic number, tantalum, is used to produce high-energy photons. For example, using a 10^{19} W cm^{-2} VULCAN pulse, a yield of 10^7 neutrons may be inferred from the measured positron activity of ^{62}Cu. The yield of neutrons is expected to increase with laser intensity and currently 10^{10} neutrons may be produced with (γ,n) reactions.

Another source of neutrons is the D–D fusion reaction d + d $\rightarrow$ ^{3}He (0.82 MeV) + n (2.45 MeV). Deuterons of about 100 keV or greater are required for efficient production of neutrons from the d(d,n)^{3}He reaction. This can be accomplished through several physical processes in which a target containing deuterium, generally a deuterated plastic, is used.

The VULCAN and the NOVA PetaWatt lasers are single shot lasers and tend to be very large in physical size. This makes them impractical for commercial use. Neutrons have many applications such as in damage testing of materials caused by large neutron fluxes, structure studies. For these to be commercially viable, one requires to use table-top Ti-sapphire laser systems that are currently capable of delivering short laser pulses of about 100 fs duration and a few hundred mJ energy at a repetition rate of 10–1000 Hz. Significant improvement in these characteristics is already being reported, and this trend is

expected to continue for the foreseeable future. In the following, the observation of neutrons produced by 10^{18} W cm^{-2} pulses from a table-top laser is described [30]. The underlying physics is highly fascinating and is discussed first.

When a laser pulse is focused in an under-dense plasma (optically transparent), channel formation due to relativistic self-focusing is possible. Relativistic self-focusing leads to an increase of the refractive index due to the relativistic mass increase of the electrons quivering in the focal region. The medium then acts as a convex lens producing an increase in the focal intensity. For intensities greater than 10^{18} W cm^{-2}, electrons are accelerated in the laser direction to multi-MeV energies. The associated very large magnetic fields lead to self-pinching of both the electrons and the laser pulse, resulting in a long narrow channel a few λ across. Pretzler et al. [30] generated a deuterium plasma by using a deuterated polyethylene target and a prepulse. Deuterium ions are accelerated to several hundred keV energies and undergo d(d,n)^{3}He reaction. Neutrons were detected in a NE213 liquid scintillator coupled to a fast photomultiplier tube. From time-of-flight measurements, the neutron energy was determined to be 2.45 MeV. The neutrons are emitted isotropically at an average rate of 140 neutrons per pulse. Extensive PIC code calculations by the authors support the experimental observations.

A promising method of producing fusion neutrons is by the interaction of a laser pulse with a gas jet containing large clusters of deuterium. With a 32 fs pulse at 820 nm wavelength and of intensity 10^{16} W cm^{-2}, Ditmire et al. [31] produced 10^4 neutrons per laser shot with the neutron yield increasing rapidly with laser intensity.

Another source of neutron production is the fission of the actinides. Ledingham et al. [32] and Cowan et al. [4] observed the ^{238}U(γ,f) reaction with the VULCAN 100TeraWatt and the NOVA PetaWatt lasers, respectively. The neutrons are generated as pulses of a few hundred femtoseconds from a region that is a few μm in dimensions. Such sharp time and spatial characteristics provide a unique source for time-resolved neutron physics.

7 Neutron Spectroscopy in Ultra-intense Laser–Matter Interactions

We are planning multi-channel spectroscopy of neutrons generated through nuclear reactions to measure the momentum distribution of accelerated ions inside the target.

One obvious way to measure the ion momentum distribution is the direct observation of ions with track detectors such as a CR-39. The drawback with this method is that the ion motion will be significantly affected by strong electric and/or magnetic fields in the plasma, as we have already discussed. By contrast, neutron spectroscopy has the advantage that neither the target potential nor the

magnetic fields can affect the motion of neutrons generated in the target. Unfortunately, neutron spectra for one direction does not give the dimensional ion momentum needed to fully characterise the ion dynamics. We need to measure the neutron spectra from three different directions to obtain the ion momentum distribution in the target. In this way, we hope to distinguish between the competing processes of hole-boring, collisionless shock formation and the resistive fields inside the dense plasma. This will help quantify the role played by sheath acceleration fields on the total ion energy measured outside the target.

Figure 11a shows an example of neutron spectra in beam-fusion reaction taken from three viewing angles [21]. The 1 μm laser light obliquely irradiated a CD 5 μm target from 40° from target normal for s-polarisation condition at intensity of 10^{19} W cm^{-2}. Figure 11a shows experimental spectra at three observation angles: 90° (solid line), 56° (dashed line) and 38° (dotted line) to the target normal, respectively. To investigate precise momentum distribution of ions, we performed 3D Monte Carlo simulation to compare the calculated spectra with the experimental results. Figure 11b shows the well-fitted calculated spectra at the same view angle with the experiments, which indicates that the ions are accelerated to rear target normal direction. The ion distribution is

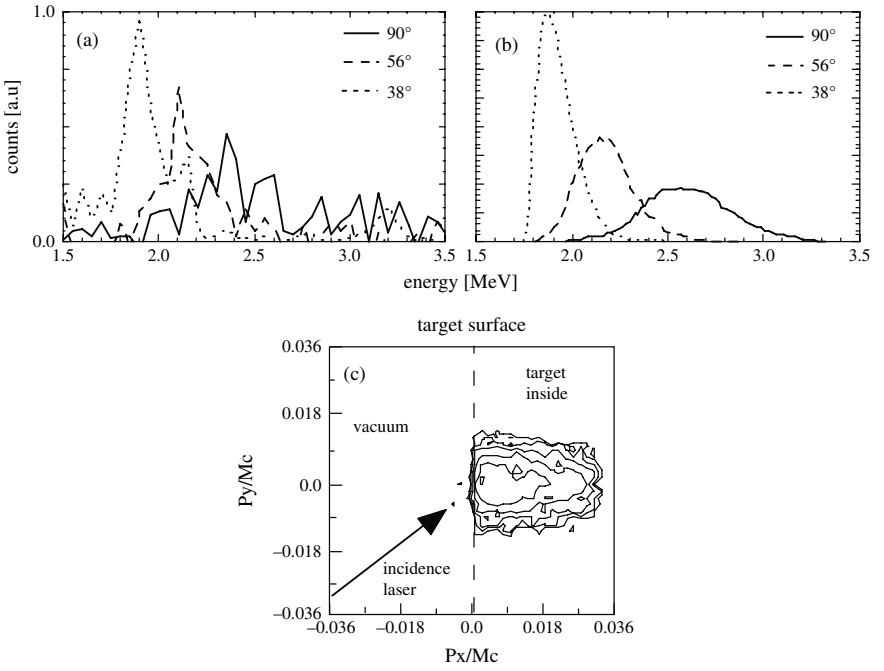

Fig. 11 An example of (**a**) neutron spectra, (**b**) well-fitted calculated spectra and (**c**) the well-fitted ion momentum distribution

shown in Fig.11(c) as a contour plot projected on the x–y plane from 3D distribution. The distributions collimated the target rear direction are given as a momentum ratio of P_x:P_y:$P_z = 2.3{:}1{:}1$. The ion energy to the x-direction corresponding to the rear target normal is 330 keV, whereas the energy to the y- and z-directions is about 70 keV.

The neutron spectrometer detector that we are re-constructing is a multi-channel spectrometer, LaNSA [33], which originally consisted of 960 channels of scintillators/photomultiplier tubes. In order to measure the angular distribution of neutrons, these modules will be divided into three parts, which have 240 channels in each part. The neutron detector consists of a BC505 liquid scintillator and Thorn-EMI9902KB05 photomultiplier. The neutron signals are delivered to a LeCroy Fastbus Time-Digital-Converter (TDC), which records the signal arrival timing, via a discriminator. These timings are collected and then converted into a neutron spectrum through the time-of-flight (TOF) method. The data acquisition of the system is based on PC to control all CAMAC and Fastbus modules. For safety reasons, liquid scintillator leakage will be monitored by fluctuation of high voltage to the scintillators to stop HV supply and other laboratory electronics when there is a leakage.

These three modules are set at target area PetaWatt (TAP) and the 100 TW target area (TAW) at VULCAN laser system in Rutherford Appleton Laboratory. Figure 12 shows an image of neutron detection for one spectrometer in TAP and overview of set-up for PW laser. The distance between the modules and chamber centre at TAP will be about 12 and 5 m.

The energy resolutions of each module are shown in Fig.13 for different neutron energies. Clearly, the shorter the distance between the spectrometer and the focal position, the worse the energy resolution of the neutron spectrum.

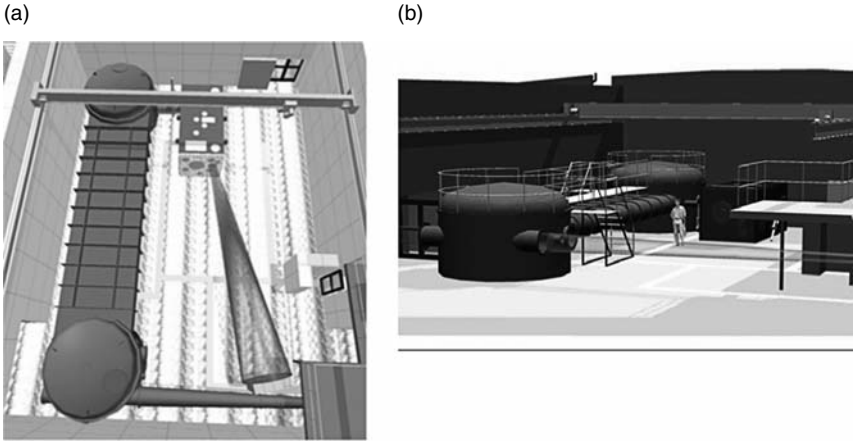

Fig. 12 (**a**) Positioning of one of the neutron spectrometers in the VULCAN PW target area (TAP); (**b**) schematic illustration of the PW compressor chamber and target chamber

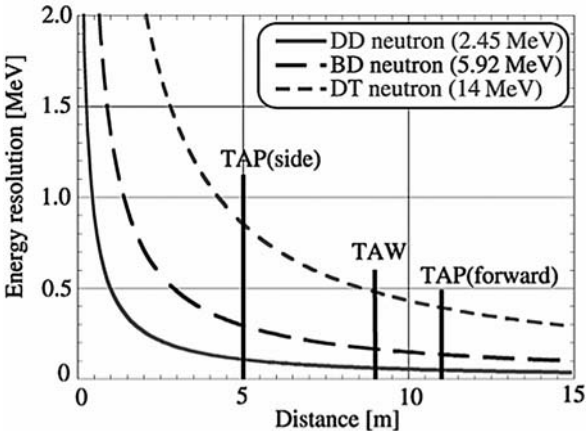

Fig. 13 Energy resolution for different neutron energy as a function of the distance between the spectrometer and laser focal position

For example, at 5 m distance, the module has 300 keV of energy resolution for 2.45 MeV neutrons, and only 800 keV for 14 MeV neutrons. On the other hand, at 12 m distance, the energy resolution is much improved; 100 keV for 2.45 MeV neutron and 350 keV for 14 MeV neutrons. Therefore, when the module at nearer side is set up perpendicularly to the ion acceleration direction adjusting target rotation or incident laser direction, the energy resolution of both modules can remain at a comparably lower level. On the other hand, the dynamic range to be able to detect neutrons can be increased by a factor of 2 by adjusting the sensitivity of the scintillator to neutrons.

Using these neutron spectrometers, we plan to measure the ion acceleration distributions. In the 100 TW target area, it is possible to change plasma density using 6 ns duration, high-energy glass laser pulses, which allows precise measurements of the plasma scale length dependence on the ion acceleration combining the short pulse laser. Furthermore, the laser intensity dependence on the ion acceleration can be obtained in broad range of laser intensities using the upgraded PW laser, which is expected to be 10^{21} W cm^{-2}. The neutron spectroscopy generated by different nuclear fusion reactions will be one of the most interesting measurements. In particular, B-D and Li-D reactions generate higher energy neutrons and have higher energy cross-sections than those of DD reaction which will allow us to measure the high-energy part of the ion distribution simultaneously.

8 Conclusions and Future Outlook

Some of the results of the interaction of intense laser pulses with matter have been discussed. The generation of γ-radiation of energy up to 100 MeV and protons of up to 50 MeV energy has been established. Neutrons are also produced in high fluxes. Production of energetic heavy ions has also been

reported. Laser–matter interaction provides a unique set of projectiles for a host of applications. The very intense, subpicosecond nature of the radiation will afford the study of a new class of experiments, for example, measuring the population of short-lived isomeric states, measurement of photo-nuclear cross-sections on small samples. The heavier ions produced in the laser-plasma interaction may be used as ion sources for heavy-ion accelerators. The production of positron emitters for PET scanners is potentially a very powerful breakthrough and may allow wider availability of PET scanners in hospitals.

The study of nuclear effects has a direct application in the diagnostics of plasma properties. Determination of quantities like plasma electron temperature and testing of PIC simulation codes is facilitated by the measurement of nuclear effects induced in laser–matter interactions.

The availability of high-energy proton and ion beams from laser–matter interactions has potential for managing the fast-ignitor process. The reasons are the same as for the application of protons in cancer therapy. Essentially, in the fast-ignitor context, ions are superior to electrons as they deliver most of their energy just before stopping, and unlike electrons, ions are not easily deflected as they pass through the plasma. We will investigate whether protons can be used directly as the heating source for the fast ignitor through sheath acceleration processes or whether energetic deuteron beams can be used to supplement fast electron heating [9].

Tremendous progress is being made in achieving still higher intensities. Tajima and Mourou [34] have reviewed the progress towards the realisation of exawatt (10^{18} W) and zettawatt (10^{21} W) laser pulses with correspondingly greater focused intensities. They state '. . .could accelerate particles to frontiers of high energy, tera-electron-volt and peta-electron-volt, and would become a tool of fundamental physics encompassing particle physics, gravitational physics, nonlinear field theory, ultrahigh-pressure physics, astrophysics and cosmology'.

Acknowledgments This work was supported by the UK Engineering and Physical Sciences Research Council (EPSRC). The contribution of colleagues at Glasgow, Imperial College, the Queen's University of Belfast and the Rutherford Appleton Laboratory to this research is highly appreciated.

References

1. K. Boyer, T.S. Luk, and C.K. Rhodes, Phys.Rev.Lett. **60**, 557–560 (1988)
2. K.W.D. Ledingham, P. McKenna, and R.P. Singhal, Science **300**, 1107 (2003)
3. R.P. Singhal, K.W.D. Ledingham, and P. McKenna, Recent Res. Dev. Nucl. Phys. **1**, 147 (2004)
4. T.E. Cowan et al., Phys. Rev. Lett. **84**, 903–906 (2000)
5. K.W.D. Ledingham et al., Phys. Rev. Lett. **84**, 899–903 (2000)
6. I. Spencer et al., RAL Report pages 31–32 1998/99
7. I. Spencer, PhD Thesis, University of Glasgow, Scotland, UK (2002)

8. S.J.Gitomer et al., Phys. Fluids **29**, 2679 (1986)
9. A.P. Fews et al., Phys. Rev. Lett. **73**, 1801–1804 (1994)
10. F.N. Beg et al., Phys. Plasmas **4**, 447–457 (1997)
11. E.L. Clark et al., Phys. Rev. Lett. **84**, 670–673 (2000)
12. R.A. Snavely et al., Phys. Rev. Lett. **85**, 2945–2948 (2000)
13. E.L. Clark et al., Phys. Rev. Lett. **85**, 1654 (2000)
14. M.I.K. Santala et al., Phys. Rev. Lett. **84**, 1459–1462 (2000)
15. W.L.Kruer and S.C.Wilks, Plasma Phys. Control. Fusion **34**, 2061 (1992)
16. J. Denavit, Phys. Rev. Lett. **69**, 1383 (1992)
17. S. Miyamoto et al., J. Plasma Fusion Res. **73**, 343 (1997)
18. C. Toupin, E. Lefebvre, and G. Bonnaud, Phys. Plasmas **8**, 1011 (2001)
19. P.A. Norreys, Plasma Phys. Control. Fusion **40**, 175 (1998)
20. L. Disdier, J.-P. Garçonnet, G. Malka, and J.-L. Miquel, Phys. Rev. Lett. **82**, 1454 (1999)
21. H. Habara, PhD Thesis, 'Energetic particle generation in ultra-intense laser-plasma interactions' Osaka University (2000)
22. A. Pukhov, Reports on progress in Physics **66**, 47 (2003)
23. J.R. Davies, A.R. Bell, M.G. Haines, and S.M. Guerin, Phys. Rev. E **56**, 7193 (1997)
24. J.R. Davies, A.R. Bell, and M. Tatarakis, Phys. Rev. E **59**, 6032 (1999)
25. S.C. Wilks et al., Phys. Plasmas **8**, 542–549 (2001)
26. I. Spencer et al., Nucl. Instrum. Methods B **183**, 449–458 (2001)
27. K. Ledingham et al., J. Phys. D **37**, 2341 (2004)
28. M. Yamagiwa and J. Koga, J. Phys. D **32**, 2526–2528 (1999)
29. McKenna et al., Phys. Rev. Lett. **94**, 084801 (2005)
30. G. Pretzler et al., Phys. Rev. E **58**, 1165–1168 (1998)
31. T. Ditmire et al., Nature **398**, 489–492 (1999)
32. K.W.D. Ledingham and P.A. Norreys, Contemp. Phys. **40**, 367–383 (1999)
33. M.D. Cable, S.P. Hatchett, and M.B. Nelson, Rev. Sci. Instrum. **63**, 4823–4827 (1992).
34. T. Tajima and G. Mourou, nslserver.physics.sunysb.edu/icfa/Papers/w1-1.pdf

Part V
Intense Field Physics with Heavy Ions

Ion-Generated, Attosecond Pulses: Interaction with Atoms and Comparison to Femtosecond Laser Fields

Joachim Ullrich and Alexander Voitkiv

1 Introduction

The electromagnetic fields generated by highly charged heavy ions either in a static situation, when the ions are at rest, or in a dynamic scenario, when they move with low up to relativistic velocities, are the strongest and in collisions the shortest fields in time that can be realized in earth-bound laboratories. Three different time-scale regimes of extreme ion-induced fields might be distinguished: First, as illustrated in Fig. 1, the expectation value of the ***static electric field strength*** for a K-shell electron in hydrogen-like uranium is six orders of magnitude higher than in atomic hydrogen, at least a factor of 10^4 larger than any field that can be reached with advanced laser technology and its binding energy approaches its rest mass. Second, in a ***quasi-static situation***, where, for example, two thorium ions collide at moderate velocities, the $1s\sigma$-binding energy of the quasi-molecule forming within about 10^{-19} s at small inter-nuclear distances b even exceeds the electron rest energy 'diving' into the negative energy continuum in 'super-critical' fields and giving rise to such exotic processes like the 'decay of the vacuum' by spontaneous or dynamic pair creation. Third, schematically depicted in Fig. 2, the transient field generated by a fast highly charged ion when passing atoms or molecules at distances of several atomic units, far outside the radius of outer-shell electrons, reaches power densities of up to 10^{23} W/cm^2 in time intervals below attoseconds (as).

Hence, on the one hand, highly charged heavy ions provide an ideal test ground to investigate fundamental questions connected with super-strong fields: In bound states, non-perturbative quantum electrodynamics (QED), few-electron correlation, relativistic effects or properties of nuclei are explored. In time-dependent situations, during collisions, dynamic QED is accessible when pairs are created in close encounters between heavy nuclei and, finally, the behaviour of atoms or molecules being exposed to exawatt/cm^2 power

J. Ullrich
Max-Planck-Institut für Kernphysik, Saupfercheckweg 1, D-69117 Heidelberg, Germany,
e-mail: joachim.ullrich@mpi-hd.mpg.de

T. Brabec (ed.), *Strong Field Laser Physics*,
DOI: 10.1007/978-0-387-34755-4_23,

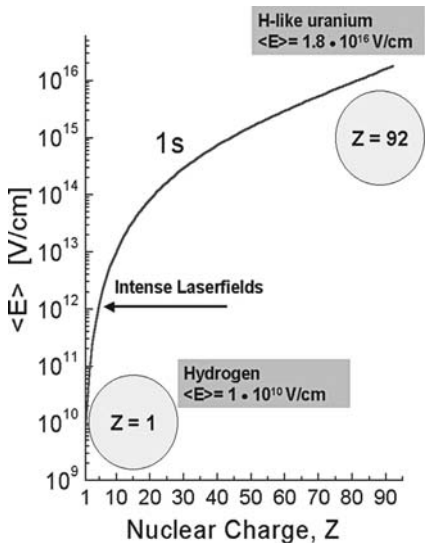

Fig. 1 Expectation value of the electric field strength for a K-shell electron in hydrogen-like systems as a function of the nuclear charge Z (from [1])

densities on attosecond time scales can be investigated in distant collisions with highly charged ions. On the other hand, a variety of applications have emerged, ranging from material analysis or modifications, the generation and heating of (fusion) plasmas, diagnostic methods for terrestrial and astrophysically relevant plasmas and, last not least, cancer tumour therapy using fast highly charged ions, pioneered at the LBNL in Berkeley and successfully applied since few years at the heavy-ion accelerator complex at GSI in Darmstadt.

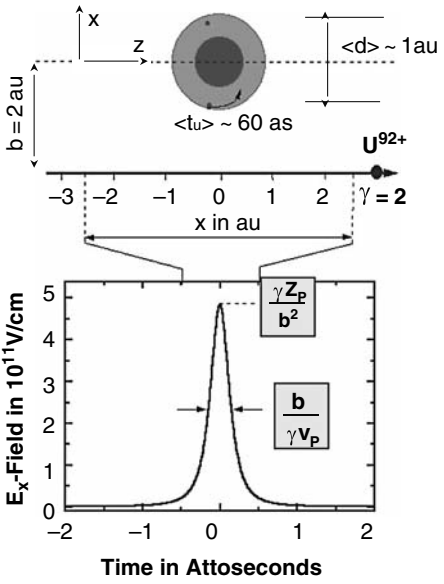

Fig. 2 Transverse (x-) component of the time-dependent electromagnetic field generated by a 1 GeV/u U^{92+} ion ($\gamma = 2.07$; $v_p = 0.87c = 120$ a.u.) at the position of a helium target atom while passing it at an impact parameter of 2 a.u., outside the helium shell radius of about $<d> \sim 1$ a.u. $<t_u>$: classical average revolution time of the electrons in helium

The present contribution will exclusively concentrate on the third scenario, where atoms and molecules are exposed to strong, attosecond 'half-cycle' electromagnetic pulses (Fig. 2). Readers interested in accelerator based atomic physics as well as applications including tumour therapy will find a recent summary in [1]. The basic interaction mechanisms between the field and target atoms will be described in some detail in Section 2. Many-particle momentum spectroscopy techniques for ions and electrons will be shortly outlined in Section 3. In Section 4, a selection of illustrative results will be presented for single and multiple ionization in attosecond as well as femtosecond laser fields. Future developments are addressed in Section 5. Due to the short scope of the contribution and the explosion-like expansion of the field, only the main lines can be sketched and illustrative pictures are developed, sometimes at the expense of a rigorous theoretical treatment which the reader is referred to in literature.

2 Interaction of Ion-Generated Pulses with Atoms

2.1 Introduction

It has been recognized more than 20 years ago from satellites in high-resolution X-ray spectroscopy that a target can be multiply ionized in a collision with a fast highly charged projectile. Subsequently, using efficient time-of-flight methods, total cross-sections for multiple target ionization have been explored in great detail for very different projectile (ionic) charge states Z_p and velocities v_p, ranging from medium charge states and v_p of few percentage of an atomic unit at femtosecond collision times τ to relativistic U^{92+} impact at sub-attosecond time scales (for a review, see [2]). As illustrated in Fig. 3, target ion charge states of up to fully stripped Ar^{18+} or Xe^{32+} have been observed to be produced with

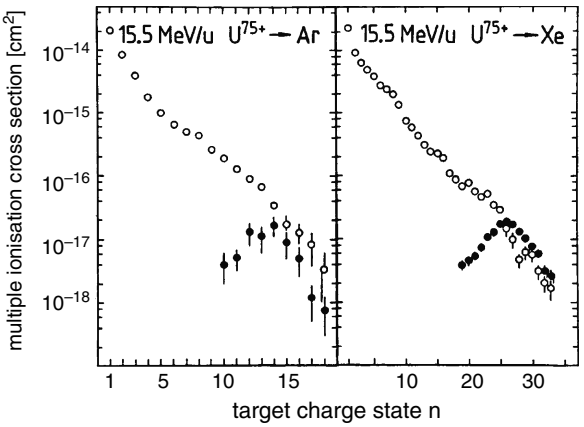

Fig. 3 Cross-sections for the production of highly charged Ar and Xe ions in single collisions with 15.5 MeV/u ($v_p = 25$ a.u.) U^{75+} projectiles

huge cross-sections (10^{-18} cm^2) in collisions with U^{75+} at $v_p = 0.18c$ ($c = 137$ a.u. is the speed of light). Atomic units ($\hbar = e = m_e = 1$) are used throughout unless otherwise stated.

2.2 Ion-Generated Fields and Comparison to Laser Fields

In order to obtain a physical picture on what might happen in such a collision and come to some quantitative comparison with a typical situation in strong-field laser physics, where peak-power densities of a few 10^{16} W/cm^2 are achieved in 25 fs pulses from commercial Ti:Sa lasers, we have calculated the transverse electric field (x-direction) in Fig. 2 for U^{92+} impinging on helium at a (relativistic) velocity of 120 a.u. and an impact parameter of two atomic units, which is typical for double ionization. Here, at a Lorentz factor of $\gamma = 1/\sqrt{1-\beta^2} \simeq 2$, with $\beta = v_p/c$, the longitudinal field component (z-direction) is relativistically suppressed already by a factor of $\gamma^2 \simeq 4$. In any case, it changes sign during the collision, resulting in a net force of zero and, therefore, is not important in many even non-relativistic situations.

Hence, similar as for a light pulse or for single photons, the direction of the electric field and, thus, the effective force mainly occurs transverse to the ion propagation. When the projectile approaches the target, the transverse field strongly rises to a peak value of about $Z_p\gamma/b^2 \sim 50$ a.u. and falls off again with a full width half maximum of $\tau = 0.2$ as, with $\tau \sim b/(\gamma v_p)$. The power density I, the atom is exposed to during this very short time, is close to 10^{20} W/cm^2. Non-relativistic ($\gamma \simeq 1$) fast protons (or electrons) with $Z_p = \pm 1$ at identical impact parameters on the other side will create a field with $I \sim 10^{15}$ W/cm^2. Depending on the impact parameter b and the relativistic factor γ, it is easily seen that power densities between some 10^{13} and 10^{23} W/cm^2 can be realized in ion–atom collisions at typical collision times, i.e. full width half maximum (FWHM) of the electromagnetic pulse, between 1 and 10^{-4} a.u, or, in other words, between a ten attoseconds and a few zeptoseconds in moderate ultrarelativistic encounters of $\gamma = 100$.

Thus, whereas the achievable field strengths, power densities and field direction (transverse to the ion or laser-pulse propagation) are comparable to those obtained with present-day high-power lasers, there are basic differences summarized in Fig. 4. First, time scales are at least a factor of thousand shorter, and hence, typical frequencies involved are much higher. Second, the important transverse part of the field does not change its sign, i.e. it is directed, it depends on **b**, i.e. is different for each single collision, and it is not coherent. Third, there might be a momentum transfer, which (at not too high γ) is mainly in the transverse direction since the longitudinal one, being equal to the minimum momentum transfer, is very small in most cases at large velocities. These differences result in markedly different (many-particle) dynamics when atoms, molecules or clusters are exposed to such pulses.

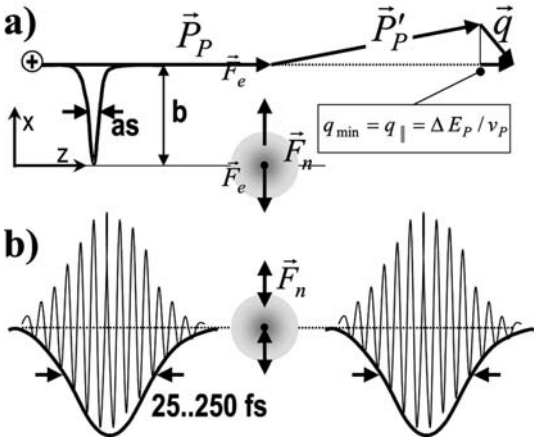

Fig. 4 Schematic illustration for ion (**a**) and laser-pulse (**b**) impact on an atomic target. $\mathbf{P}_p$, $\mathbf{P}'_p$: momentum of incoming and scattered ion, respectively, with momentum transfer $\mathbf{q} = \mathbf{P}_p - \mathbf{P}'_p$ and minimum momentum transfer $q_{min} = q_{\parallel} = \Delta E_p / v_p$ (ΔE_p: projectile energy loss). $\mathbf{F}_n$ and $\mathbf{F}_e$: main forces acting on the nucleus and the electron cloud, respectively

2.3 Single Ionization in As Fields: Connection to Photoionization

2.3.1 Small Perturbations (Single Photon Exchange)

The interaction between charged projectiles and atoms can be regarded as occurring due to an exchange of photons between a projectile and a target. In such an approach, the *n*th term in the perturbation Born series in the projectile–target interaction corresponds to an exchange of *n* photons between a projectile and a target. Many phenomena occurring in collisions of a fast projectile having a relatively low charge Z_p ($Z_p/v_p \ll 1$) can be well understood within the one-photon-exchange approximation. This approximation describes the situation, where an atom makes a transition between initial and final states, which are both eigenstates of the atomic Hamiltonian and are not modified by the field of a projectile. Photons transmitting the interaction between charged projectiles and atomic targets represent the so-called close field which cannot exist without its source (i.e. without a charged particle). In general, such photons are quite different from real ones, which represent radiation fields, and are usually termed as 'virtual' photons. Only ultrarelativistic projectiles can produce virtual photons with properties already very close to those of real photons, and correspondingly, atom ionization by ultrarelativistic projectiles may be fundamentally similar to the photo effect in all essential points (for a detailed discussion of the inter-relation between ionization of light atoms by real and virtual photons see [3] and references therein).

Yet, even virtual photons constituting the electromagnetic field of a fast non-relativistic projectile already have a very important similarity to real photons, namely ionization of light atomic targets by fast charged projectiles occurs mainly in collisions where the amount of energy ΔE_p transferred to the target is substantial on the target scale while the momentum transfer is quite small (on the same scale). In the virtual-photon picture, it means that a virtual photon,

absorption of which results in ionization, transmits a considerable amount of energy but in most cases only a very modest amount of momentum, thus, resembling at this point the action of a real photon in the process of the photo effect. Hence, in fast collisions with small momentum transfers, where the complete non-relativistic transition operator $\sum_j \exp(i\mathbf{q} \cdot \mathbf{r}_j)$ (here $\mathbf{r}_j$ are the coordinates of the j th atomic electron and $\mathbf{q}$ is the total momentum transferred to the atom by the projectile) can be replaced by its dipole approximation, $i \sum_j \mathbf{q} \cdot \mathbf{r}_j$, single and multiple ionization dynamics should reveal some basic signatures inherent in ionization induced by the absorption of a single real 'high-energy' photon with an energy above the single or multiple ionization thresholds, respectively.

Since basically all energy transfers ΔE_p can be realized in a collision, a continuous 'photoelectron' energy spectrum is observed for single ionization, whereas a sharp line at $E_e = E_\gamma - I_P$ (I_P is the ionization potential of the emitted target electron) is observed in the photo effect. In a kinematically complete experiment ΔE_p can be fixed and the results be compared to the photo effect at $E_\gamma = \Delta E_p$ as will be demonstrated for double ionization in Section 4.3. The situation is profoundly different for atom ionization by strong laser fields. In the latter case, the energy of a single laser photon is usually not sufficient to overcome the atom ionization potential and the field has to be such strong that many photons can be absorbed to obtain ionization. One of the consequences of this is that atomic transitions occur in continuum states which are strongly modified by the laser field. This modification is mainly responsible for such interesting phenomena as the above threshold ionization (ATI) and high-harmonic generation (HHG).

In general, all momenta $\mathbf{q}$ up to the maximum momentum transfer are present in ion–atom collisions. This is accounted for by taking the complete non-relativistic transition operator $\sum_j \exp(i\mathbf{q} \cdot \mathbf{r}_j)$. In addition, going to high collision energies, the transition operator has to be modified according to the relativistic theory. Recently, significant modifications in spectra of low-energy electrons emitted along the ion beam axis have been observed in collisions with a moderate value of the Lorentz factor, $\gamma \approx 2$, and their origin was traced back to appear due to relativistic effects [4].

2.3.2 Large Perturbations

In collisions with highly charged projectiles, the field of a projectile cannot be regarded as weak even for high-velocity collisions if the condition $Z_p/v_p \lesssim 1$ is fulfilled. In such a situation, first-order theories in the projectile–target interaction are, as a rule, not applicable even for treating single ionization. Quantitatively, ionization in strong fields of fast highly charged projectiles can be thought of as the 'incoherent' absorption, occurring during a very short effective transition time, of several 'high-energy' virtual photons from the electromagnetic pulse generated by the projectile. Obviously, due to the narrowness of the pulse in time, one obtains a broad distribution in the frequency

domain giving rise to a broad energy spectrum of the emitted 'photoelectrons' for single as well as for multiple atom ionization. As far as this simple virtual-photon picture remains reasonable, fundamental differences to strong-field laser (multiple) ionization emerge: (i) first, due to the completely different time scales involved; (ii) second, a laser field strongly affects the target continuum states whereas they are only relatively weakly influenced by the field of a fast projectile.

If the factor Z_p/v_p substantially exceeds 1, the perturbation Born series and, correspondingly, the virtual-photon picture cease to be well adapted to discuss atom ionization. The most prominent feature in such collisions is that the emitted electrons as well as the recoiling target ion experience a strong force from the (relatively) slowly receding highly charged projectile. Electrons are dragged behind the projectile yielding a pronounced forward shift of the otherwise (nearly) forward–backward symmetric momentum spectra, whereas the recoil ion is pushed backwards with about the same force [5]. Theoretically, the distortion of the initial and final electron states by the projectile field can be taken into account within distorted-wave approaches, of which the continuum-distorted-wave-eikonal-initial-state (CDW-EIS) approximation is mostly frequently used to consider atom ionization [6]. One should add, however, that whereas the emission spectra of low-energy electrons are generally described in very good agreement with the experiment by this theory, major difficulties have been found to arise, when the full three-body dynamics of single ionization is addressed [7].

According to Bohr, when $2Z_p/v_p \gg 1$, the treatment of atom ionization based on the classical Newton equations is expected to receive sound grounds. In such a case, calculations using the classical trajectory Monte Carlo (CTMC) method, which apply the classical description for both heavy (nuclei) and light (electrons) particles, yield good results for both differential and total cross-sections [8].

In the domain of relativistic collision velocities, the distortion of the initial and final target states by a projectile weakens due to the flattening of the projectile field. Still, even for single ionization of atoms occurring in collisions with relativistic highly charged ions, the higher-order effects in the interaction projectile–target interaction turns out to be very important if the full three-body dynamics of the collision is considered [9]. Moreover, such effects become of paramount importance if transitions of two and more electrons occur in the target under the highly charge ion impact.

2.4 Double Ionization

As multiple ionization is concerned, we can realize intensities (see Section 2.2) in ion–atom collisions, where similar processes like 'sequential' or 'non-sequential' ionization might dominate multiple ionization. Double ionization, for example,

either can occur due to an independent interaction (which is one aspect of 'sequential', disregarding the aspect of subsequent times) of the field with both target electrons (*two-step-2*, *TS-2*, in the terminology of collisions) or due to a single interaction of the field with the atom, where the second electron is emitted as a result of the electron–electron correlation.

In ion–atom collisions as for photoionization the latter 'non-sequential' process usually is further subdivided in terms of many-body perturbation-theory diagrams: *Two-step-1* (*TS-1*), a single interaction of the projectile with the target plus a second step, when the emerging first electron interacts with the second one, is distinguished from the *shake-off (SO)* or *ground-state (GS) correlation* contributions (for details and the diagrams, see [10]). Whereas the *TS-2* contribution, which is not present at all in double ionization by single photon absorption, is proportional to the square of the perturbation strength $(Z_p/v_p)^2$, the one-step contributions depends linearly on Z_p/v_p. Accordingly, the ratio of double to single ionization cross-sections σ^{2+}/σ^{+} decreases with decreasing Z_p/v_p until a certain value, the 'high-energy limit', is reached where it stays constant (see Fig. 5).[1] This behaviour has been intensively investigated and verified for a large collection of collision systems and perturbation strengths leading to a profound knowledge of which of the processes, sequential or non-sequential in the 'laser language', *TS-2* or *TS-1*, *SO* and *GO* in the terminology used for charged particle and single photon impact, might dominate if a certain collision system is considered. Furthermore, the ratio observed in the high-energy limit, where the relevant matrix elements attain a certain similarity to those for double ionization by single photons, has been explained in terms of double to single photoionization ratios (see [12] and references

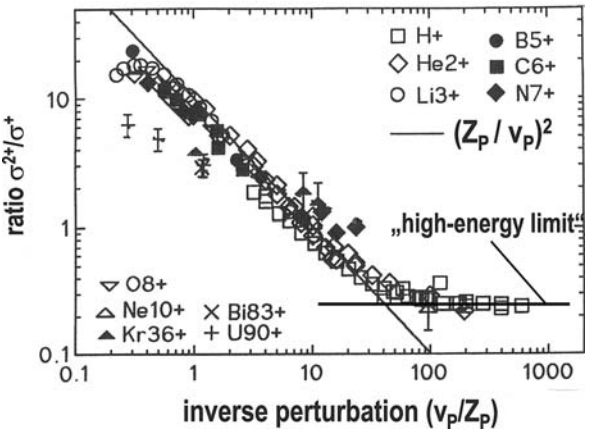

Fig. 5 Ratio of double to single ionization cross-sections σ^{2+}/σ^{+} as a function of v_p/Z_p for various projectile charges Z_p and velocities v_p

[1] One has to note that in collisions at velocities approaching the speed of light, the 'high-energy limit', due to relativistic effects, can be reached at larger values of Z_p/v_p [11] compared to what is suggested by the non-relativistic consideration.

therein). So, for weak perturbations, *TS-2* contributions can be neglected and, as for single ionization, similarities with double ionization by single photon impact can be observed for small momentum transfers, as will be shown in the results. Theoretical approaches which describe the projectile–target interaction in the first order using target states obtained within a coupled-channel approach (CCC: convergent close coupling) are at hand and yield reasonable agreement with experimental data for electron impact even on the level of fully differential cross-sections [13]. Work is in progress to include the *TS-2* in ab initio theories [14]. Doubly differential electron emission spectra have been calculated for double and triple ionization in the non-perturbative regime [15]. The authors of [15] used the CDW-EIS approach for obtaining the single-electron transition probability and constructed multi-electron ionization probabilities by applying a binomial distribution. Very recently a novel approach was proposed in [16] in order to address the full four-body quantum dynamics of collisions between helium (and helium-like ions) and relativistic highly charged ions.

2.5 Summary

To conclude Section 2, we have seen that fast ions generate extremely short electromagnetic half-cycle pulses with a FWHM between 10 and 10^{-3} as and power densities of $10^{13} - 10^{23}$ W/cm^2. Atoms and molecules are efficiently ionized in these fields with large cross-sections, and the simultaneous emission of up to 40 electrons in one single encounter has been observed in uranium on xenon collisions. In a somewhat generalized view, which is quantitatively only substantial in the asymptotic limits, the interaction of the field with the target can be understood by the exchange of one (weak field) or several (strong field) virtual photons causing single or multiple ionization. Due to the short pulse times the virtual-photon frequency distributions are broad, extending up to very high frequencies so that even inner-shell electrons can be 'photoionized' simultaneously with weakly bound outer-shell electrons in strong fields, making multiple ionization to occur with tremendous cross-sections. Thus, during the short collision time, a considerable amount of energy can be very efficiently transferred to the target. In most cases, the energy transfer is accompanied only by a modest momentum transfer so that the many-particle collision dynamics is similar to photoionization. Furthermore, since the projectile recedes very fast after the interaction in swift collisions, it usually does not noticeably interact with the target fragments in the continuum, similar to a single photon which is absorbed and simply does not exist at all in the final channel.

This is very different from the strong-field laser case: First, only low optical frequencies are present in the field and target electrons can only be ionized via multi-photon absorption becoming very inefficient with increasing number of

photons required. Accordingly, direct inner-shell ionization is extremely unlikely and consequently, even at similar power densities, the final degree of ionization is considerably less than in ion collisions (see Fig. 3). Second, since even one optical cycle is on the order of one femtosecond and, thus, much slower than typical revolution times of even outer-shell-bound electrons, the situation is very 'adiabatic'. Electrons can overcome the barrier ('barrier suppression') or tunnel into the laser-modulated continuum (so-called Volkov states in the limit when the residual ion potential can be neglected) and, then, strongly interact with the field, oscillating and receiving considerable quiver as well as drift energies. Thus, in the final state, the optical laser field is much more efficient in transferring energy to the atomic fragments of quivering electrons and ion. Obviously, as correlated dynamics of electrons is concerned, it takes place on the femtosecond time scale, i.e. at some hundreds of atomic units. Correlated bound-state dynamics of atomic ground states, occurring on time scales of one atomic unit and below, i.e. at 10 as for outer-shell electrons, cannot yet be accessed with present short-pulse lasers.

3 Many-Particle Momentum Spectroscopy of Ions and Electrons

Within the last decade, many-particle momentum spectroscopy of ions and electrons has been developed to investigate ionization dynamics in fast heavy ion–atom collisions. These instruments, the so-called Reaction Microscope, turned out to be extremely versatile and can be used for the investigation of multiple ionization or molecular break-up dynamics induced by the impact of ions, single photons, laser pulses, antiparticles or electrons (for details, see two recent reviews on the topic [17, 18]). Only the salient features of these techniques will be summarized here; details can be found in [19]. For the results presented in this contribution, ion beams of 1000 Mev/u U^{92+} and 3.6 Mev/u Au^{53+} were delivered by the SIS and UNILAC facilities at GSI in Darmstadt. Nanosecond, pulsed electron beams are produced in the Heidelberg Max-Planck-Institut für Kernphysik. As outlined in Fig. 6, the given beam was directed on a supersonic,

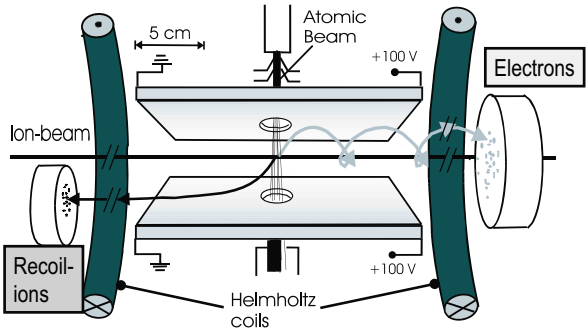

Fig. 6 Schematic drawing of a Reaction Microscope: The electric field along the projectile propagation ($\sim$ 2 V/cm) is generated in between two ceramic plates, covered with resistive layers. The magnetic field (2–100 G) is provided by two 1.5 diameter coils in Helmholtz configuration

internally cold (typically below 1 K) atomic gas jet (density 10^{11} atom/cm^2). Recoiling ions and electrons emitted during the collision are guided by homogeneous electric and magnetic fields to multi-hit, position-sensitive multi-channel plate detectors, mounted in the longitudinal direction, i.e. along the axis of symmetry parallel to the ion beam propagation. From the times of flight (obtained by a coincidence with each projectile or with the trigger for pulsed beams) and the positions of arrival, the initial momenta of the fragments are calculated from the equations of motion for electrons and ions in the well-known electric and magnetic fields.

By varying the strength of the projection fields, both the resolution and the fraction of the fragments in momentum space that are projected can be chosen over a wide range. Typically, all ions of interest with momenta $|\mathbf{P}_R| \leq 5$ a.u. are accepted simultaneously. At the same time, all electrons with transverse energies (transverse to the beam propagation) $E_{e\perp} \leq 100$ eV as well as with longitudinal energies of $E_{e\|} < \infty$ in the forward and $E_{e\|} \leq 15$ eV in the backward directions are detected in a typical experiment. Up to ten hits on the electron detector are accepted for a minimum time between two hits of 15 ns in case that both electrons hit the detector within a distance of less than 1 cm. For all other events, electrons can be detected on the 8 cm diameter detector even if they hit the detector at identical times.

Thus, depending on the collision dynamics and on the exact electric and magnetic fields chosen in the specific experiment, the Reaction Microscope simultaneously monitors between 60% (for 2 keV electron impact) and 80% (for 3.6 Mev/u Au^{53+} and 1000 Mev/u U^{92+}) of the 12-dimensional final-state momentum space for double ionization. Superior momentum resolution of $\Delta|\mathbf{P}_e| = 0.01$ and $\Delta|\mathbf{P}_R| = 0.07$ a.u. has been demonstrated to be achievable, corresponding to an energy resolution of $\Delta E_e = 1.4$ mev for electrons and $\Delta E_R = 9$ μeV for ions close to zero energy in the continuum. Thus, among other advantages, doubly differential electron emission cross-sections are obtained for the first time in a regime that is notoriously difficult to access for conventional electron spectroscopy methods.

With some modifications, the apparatus can be used as well for the investigation of laser-pulse-induced multiple ionization: First, the laser beam traverses the spectrometer in the transverse direction, perpendicular to the supersonic jet, as well as to the extraction directions of electrons and ions. For symmetry reasons, electrons and ions are usually extracted along the light polarization direction, if linear polarized light is used. Second, the rest gas pressure as well as the target density has to be considerably less than that typically used for charged particle or single-photon impact, since the laser pulse ionizes all particles within its focus of about 8 μm diameter. Thus, as correlated emission of electrons and ions from the same atom shall be measured, only one target atom is allowed to be in the focus of the laser pulse and, accordingly, the target is operated at a line density of about 10^8 atoms/cm^2 (usually 10^{11} atoms/cm^2) at a background pressure of 2×10^{-11} Torr (usually 10^{-8} Torr). Third, and finally, the trigger for the time-of-flight measurement can be simply taken from the Q-switch of the

laser. Here, a disadvantage arises in comparison with charged particle or single-photon impact experiments. While in those experiments up to MHz repetition rates of the pulsed beam can be realized, state-of-the-art high-power Ti:Sa lasers operate at repetition rates of typically 1 kHz with an upper limit of 5 kHz for commercial systems. Thus, though using significantly longer measuring times, still much less statistical significance has been obtained and no kinematically complete measurements have been performed for double and multiple ionization up to now in any laser experiment due to that reason (for details, see [20]).

This situation might change substantially in the near future due to usually the rapid progress in the performance of high-power lasers on the one hand but, even more important, due to the advent of *VUV* and soft *X-ray* self-amplified free electron lasers (SASE-FEL) which are expected to work at a repetition rate of 70 kHz, with 1 MHz being envisaged in future schemes (see discussion and references in Section 4.3 and in the chapter of Feldhaus/Sonntag). Results for intense, short-pulse-laser-induced ionization presented in this contribution were obtained at the Max-Born Institut in Berlin using a 25 fs Ti:Sa laser at 1 kHz repetition rate and intensities between 10^{14} and a few times 10^{15} W/cm^2. More recently, plenty of data have been reported using a Ti:Sa laser at 3 kHz at the Max-Planck-Institute für Kerphysik that can be focused to intensities of up to 10^{16} W/cm^2 and compressed to a pulse length between 25 and 6 fs (see, e.g. [21, 22]). For a recent review on differential multiple ionization experiments in intense laser fields using Reaction Microscopes, see [18, 23].

4 Results

Using Reaction Microscopes, multiple ionization dynamics can be explored for all (see above paragraph) momentum and energy transfers in weak fields (exchange of one virtual photon in a simplified picture) as well as in super-strong fields, where many 'high-energy' virtual photons are exchanged 'simultaneously', within less than attoseconds. Both situations have not been accessible up to now, neither in experiments at third-generation light sources, where only one photon is absorbed at a time with well-defined energy, angular-momentum and negligible linear-momentum transfer, nor using femtosecond lasers, where the photon energy is much lower and the time scale larger by at least a factor of thousand.

4.1 Single Ionization Dynamics in Perturbative As Pulses

In Fig. 7, final-state momenta of the electron, the recoiling target ion as well as the momentum change of the scattered projectile ($\Delta \mathbf{P}_p = -\mathbf{q}$) are shown for helium single ionization in collisions with 1000 Mev/u U^{92+} projectiles [24], i.e. at a velocity of 120 a.u. in a situation that has been schematically illustrated in

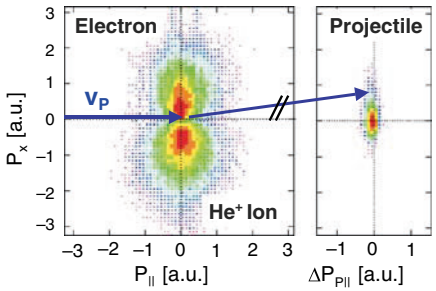

Fig. 7 Two-dimensional final-state momentum distribution for the recoiling He^+ target ion, the electron and the momentum change of the projectile in singly ionizing 1 GeV/u U^{92+} on He collisions (logarithmic z-scale). The projectile initially propagates along the $P_{\|}$ direction, its field mainly acts along the x-axis

Figs. 2 and 4. Exploiting azimuthal symmetry, all momenta are projected onto a plane defined by the incoming projectile momentum vector $\mathbf{P}_p = (0, P_{p\|})$ and the momentum vector $\mathbf{P}_R = (-P_{Rx}, P_{R\|})$ of the recoiling ion. Following the intuitive scenario depicted in Fig. 4, this should be the plane (with respect to the azimuth) containing the projectile-generated electric field. The momentum transfer in the longitudinal direction, calculated from the collision dynamics $q_{\|} = \Delta E_p/v_p$, is very small (≤ 0.06 a.u.) for typical electron energies $E_e < 200$ eV (more than 95% of all events). The FWHM of the $P_{p\|}$-distribution in Fig. 7 is determined by the experimental resolution (mainly of the recoil ion) and it is about 0.2 a.u. in this case. Thus, essentially 'no' momentum is transferred to the target in the longitudinal direction, and even the transverse momentum transfer is found to be small compared to the target fragment momenta. Scattering angles are typically less than 20 nrad.

We therefore trivially rediscover the dynamics for the absorption of a single (virtual) photon of $E_\gamma = \Delta E_p$, where the ejected electron momentum is compensated by the recoiling target momentum alone. In Fig. 8, the applicability of the 'photon picture', i.e. in essence of the dipole approximation, is analysed in some detail by looking on electron spectra as a function of the longitudinal electron momentum $p_{e\|}$ ($p_{e\|} \parallel \mathbf{v_p}$). In examples shown in the figure the transverse electron momentum was restricted to $p_{e\perp} < 3.5$ and $p_{e\perp} < 0.25$ a.u., respectively. A calculation within the dipole approximation [25][2] (dashed line) yields a striking agreement with the experimental data (full circles) in shape as well as in absolute magnitude. Performing a relativistic calculation where the momentum transfer is not assumed to be small (full line) the agreement in general improves, especially for the case $p_{e\|} > p_{e\perp}$, where the dipole approximation fails (for a detailed discussion of relativistic effects, see [4]).

[2] Small non-dipole and post-collision corrections are included as well.

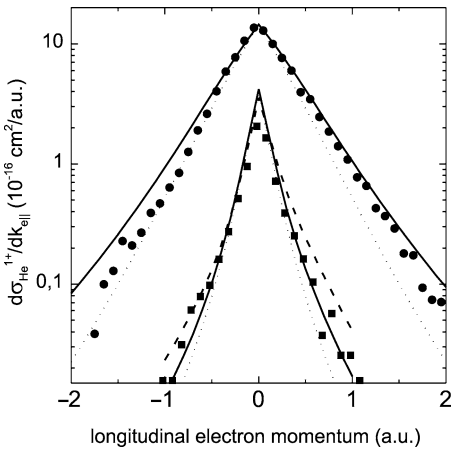

Fig. 8 Longitudinal (along the projectile propagation) momentum distributions for electrons emitted in singly ionizing 1 GeV/u U^{92+} collisions. *Circles and squares*: experiment; *solid and dotted curves*: relativistic first Born and dipole approximations, respectively; *dashed curve*: non-relativistic first Born approximation ($c \to \infty$). *Upper part*: emitted electrons with transverse momentum restricted to $p_{e\perp} < 3.5$; lower part: $p_{e\perp} < 0.25$ a.u.

The analogy to photoionization can be brought forward by Fourier transforming the time-dependent electromagnetic pulse into the frequency domain. Subsequent quantization yields the number of virtual photons per energy interval in the charged particle-induced field. Thus, the cross-section for photo absorption can be deduced from the measured single ionization cross-sections for well-defined energy loss of the projectile as a function of $\hbar\omega = E_\gamma = \Delta E_p$. This is demonstrated in Fig. 9, where the ion-impact 'virtual-photon' results are compared with recommended values for σ_γ, the helium photo cross-sections measured using single real photons from synchrotron radiation sources (full lines).

It has been shown recently (see next section) and directly follows from the photon picture (transferring energy but 'no' momentum) that the shape of the longitudinal electron momentum spectrum strongly reflects the bound-state momentum distribution of the ionized electron. In a (over)simplified picture, the bound state might be seen to be 'imaged' in a 'snapshot' via photoionization by virtual photons of well-known frequency-dependent density distribution by the attosecond pulse.

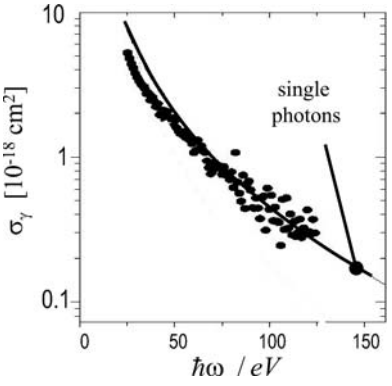

Fig. 9 Cross-section σ_γ for single ionization of helium by absorption of real photons (*full line*: recommended experimental values) and virtual photons generated in 1 GeV/u U^{92+} on He collisions (see text) as a function of the photon energy $E_\gamma = \hbar\omega = \Delta E_p$

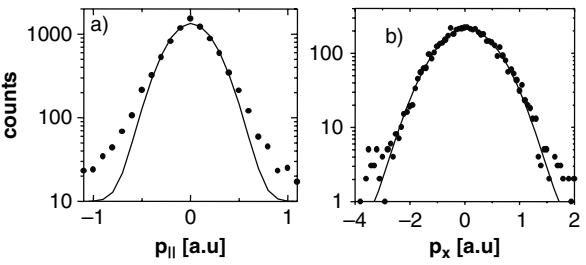

Fig. 10 Longitudinal (**a**) and transverse (**b**) with respect to the photon propagation (see Fig. 4) momentum distributions of Ne^+ ions created in collisions with a 25 fs laser pulse (795 nm) at a power density of about 1 PW/cm^2. *Circles*: experimental data. *Line*: tunnelling theory [26]

In intense laser fields (25 fs, $1{\cdot}10^{15}$ W/cm^2), on the other side, the comparable ion (electron) spectrum transverse to the polarization, i.e. field direction, is determined by the tunnelling probability [26] as illustrated in Fig. 10a (for a Ne target [27], similar results have been obtained for helium [28]). In the polarization direction, transverse to the pulse propagation (Fig. 10b), the ion momentum distribution is still centred around zero, reflecting the oscillating nature of the field. Its shape is determined by the phase dependence of the tunnelling probability defining the final drift momenta the ions receive in the oscillating field. Hence, whereas the magnitude of ion and electron momenta are quite similar for single ionization in both cases, the physical mechanisms producing them and thus the conclusions that might be drawn are considerably different. In simplified words, in ion-induced fields, one mainly sees the short-time bound-state motion of the electron on an attosecond time scale, whereas in laser fields, dynamics on a tenth of a femto-second time scale is explored, since the ion momentum (along the field) is directly proportional to the phase of the field where tunnelling occurred (for recent results in laser fields with very high resolution, see [22, 29]).

4.2 Single Ionization Dynamics in Non-perturbative As Pulses

The visibility of bound-state properties in the longitudinal momentum spectra as well as the influence of the projectile Coulomb potential in the final state has been investigated at lower energies, in a strongly non-perturbative situation, using Ne and Ar targets in collisions with 3.6 Mev/u Au^{53+}, i.e. at $v_p = 12$ a.u. In Fig. 11, experimental longitudinal electron momentum distributions are shown for different cuts in $p_{e\perp}$ for single ionization of argon along with theoretical CDW-EIS predictions (full lines [6, 30]).

Three striking features are observed in the doubly differential cross-sections: First, all electron distributions are shifted into the forward direction (positive momenta), i.e. electron emission into the forward hemisphere is most likely. This has been observed before [5] and has been attributed to the 'post-collision interaction' (PCI) with the highly charged receding projectile that pulls continuum electrons into the forward direction. In Fig. 8, this PCI is not visible

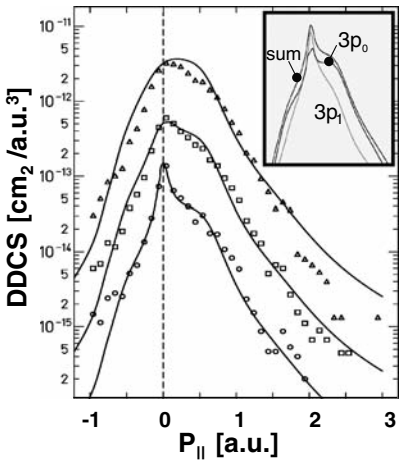

Fig. 11 Double differential cross-section DDCS in singly ionizing 3.6 ($v_p = 12$ a.u.) Mev/u Au^{53+} on Ar collisions as a function of the longitudinal momentum $p_{||}$ of the emitted electrons plotted at fixed electron transverse momenta

since (i) the factor Z_p/v_p was substantially smaller and (ii) the relativistic effects contracted the longitudinal projectile potential making it 'short ranged' and, thus, less effective in the final state. The acceleration of the electron in the final state, after its transition into the continuum during a very short, attosecond time $\tau \sim b/(\gamma v_p)$ within the collision, might be seen in analogy with the oscillation and drift of the unbound charged particles in the laser field, after tunnelling or barrier-suppression ionization had occurred. In the present case, however, this relatively slow varying in time ('femtosecond') component of the projectile field in the final state is (nearly) unidirectional in contrast to the oscillating laser field and hence accelerates ions and electrons along the pulse propagation (projectile velocity) into well-defined but opposite directions. In the laser case, instead, they acquire drift momenta perpendicular to the pulse propagation, along the polarization axes without defining a direction.

Second, structures in the electron longitudinal spectrum at $p_{e||} = \pm 0.5$ a.u. are identified in theory (full line), which are within the error bars of the experimental data. In this first calculation, these enhancements were interpreted to be related to the nodal structure of the $3p_0$ state. Whereas this direct signature of the ground state momentum distribution could not be verified in more recent calculations [31], it was found, however, in agreement with [30] that different subshells lead to pronounced differences in the longitudinal electron momentum distribution and that all substates have to be considered in order to reproduce the experimental spectrum. In summary, strong evidence is provided that the longitudinal electron momentum distributions reflect the properties of the respective bound-state wave functions, independent of the momentum transfer, occurring mainly in the transverse direction. Finally, quantum mechanical CDW-EIS calculations beyond perturbation theory are at hand, which reliably predict the observed features on an absolute scale, taking into account the influence of the slow, 'femtosecond' field component due the final-state interaction with the receding projectile.

4.3 Double Ionization in Perturbative Collisions

Dynamical mechanisms [32] as well as signatures of the correlated initial state [33, 34] have been investigated in spectra projected onto planes transverse and along the pulse propagation direction, respectively, by inspecting partially differential cross-sections for double ionization of He by 100 Mev/u C^{6+} impact ($v_p = 63$ a.u.) in the perturbative regime ($Z_p/v_p = 0.1$). Here, we will elucidate the analogy of charged particle induced to photo double ionization in ultimate detail on the basis of fully differential cross-sections in 2 keV electron on helium collisions at $Z_p/v_p = 0.08$, which might be roughly thought of as corresponding to average intensities of about 1 PW/cm^2. Such data are not yet at hand for ion impact due to limited statistical significance of the above-mentioned results.

At high velocities, where the first Born approximation is valid, electron and proton impacts yield identical results, since within the first-order treatment cross-sections are proportional to Z_p^2. Here, at power densities of the electromagnetic field in the PW regime (depending on the impact parameter b), the electromagnetic pulse induced by a charged particle interacts only once with the target, similar to a single photon, and consequently, double ionization can occur solely due to electron correlation in the target. Thus, strong (in principle up to infinite) enhancement of double (or multiple) ionization cross-sections compared to predictions of any independent electron model does not seem surprising. Leading matrix elements in a many-body perturbation theory are *TS-1*, *GSC* and *SO* which are identical or similar to some of those that have been discussed as 'non-sequential' contributions in double ionization by strong laser pulses [35]. There, in addition, 'collective tunnelling' of two electrons [36] and 'rescattering' [37] have been introduced, the latter being essentially a *TS-1*-like contribution in the presence of a radiation field but at a later time, when the first electron is thrown back on its parent ion by the oscillating field. Both contributions are not present in ion collisions, since the collision time is too short for tunnelling on the one side and recollision does not occur in the half-cycle pulse on the other side. Thus, the situation is considerably simpler for ionization by charged projectiles and, accordingly, ab initio calculations are at hand for a detailed comparison with the experiment.

For illustration, the data are presented in 'coplanar' geometry, where both emitted target electrons (b) and (c) and, as a consequence, the recoiling He^{2+} target ion lie in one plane defined by the vectors of the incoming electron momentum $\mathbf{P}_p$ and the momentum transfer $\mathbf{q}$ (see Fig. 4a for ion impact). Since the effective force induced by this half-cycle electromagnetic pulse acts in this plane along $\mathbf{q}$, not only are most events found in this plane but also a comparison to photo double ionization is straightforward and most illustrative simply replacing $\mathbf{q}$ by the photon polarization direction $\mathbf{e}$.

In Fig. 12, the fivefold differential cross-sections (FDSC), where all kinematical parameters are fixed for a double ionization event, are presented for coplanar geometry in a two-dimensional representation as a function of emission angles ϑ_b

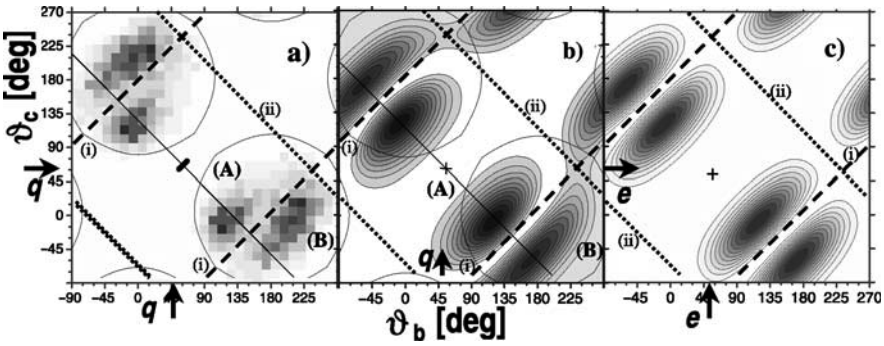

Fig. 12 Fivefold differential cross-section FDCS for helium double ionization by 2 keV electron impact in coplanar geometry as a function of the ejected electron emission angles ϑ_b and ϑ_c relative to the incoming beam direction for $E_b = E_c = 5$ eV. (**a**) Experiment for $E_p = 2$ keV and $q = 0.6$ a.u. The direction of **q** is marked by an *arrow*. *Inside circular full lines*: full acceptance. (**b**) CCC calculations. (**c**) Parameterized experimental photo double ionization data (see text) with the polarization axis **e** oriented along **q** ($\sim 55^0$). *Lines* (i) and (ii): dipole-forbidden correlated angles. *Full lines*: symmetry axis for photo double ionization

and ϑ_c of the ejected electrons for 2 keV electron–helium collisions. The momentum transfer is fixed to $|\mathbf{q}| = 0.6 \pm 0.2$ a.u. and equal energies of both electrons $E_b = E_c = 5 \pm 2.5$ eV are considered. The density plot representation has been chosen to visualize the overall structure of the three-electron continuum containing nodal lines as well as symmetries. In the experiment (Fig. 12a), only events inside the circular solid lines have been detected with full efficiency (see Section 3). Cross-sections for double photoionization (Fig. 12c), obtained by using a phenomenological parameterization [38] of experimental data and orienting **e** along **q** ($\vartheta_\mathbf{e} = \vartheta_\mathbf{q} = 55^0$) for better comparison, exhibit four major structuring elements: First, nodal lines (i and ii) are observed due to dipole selection rules. Second, emission with identical angles $\vartheta_b = \vartheta_c$ (diagonal from lower left to upper right, not indicated in the figure) is forbidden for electrons with $E_b = E_c$. Third, cross-sections are symmetric with respect to an exchange of both electrons, and fourth, reflection symmetry with respect to a plane perpendicular to the electric field (diagonal indicated by the full line) arises since **e** denotes an axes rather than a direction (for a detailed discussion, see [13]).

Obviously, all major structures are rediscovered in the experiment as well as in the CCC predictions [39], which have previously found to be in excellent agreement with double photoionization results. Moreover, deviations from photoionization, observed in the experiment as well as in theory, occur due to deviations from the dipole approximation (peak (A) becomes more intense than (B)). Remaining discrepancies between theory and experiment, the position of peak (B), have been attributed to higher-order projectile–target interactions (for example, *TS-2*; for a recent publication, where second Born contributions are included, see [40]).

In summary, some profound knowledge on double ionization in charged particle-induced attosecond fields has emerged in the recent past on the basis of

kinematically complete experiments and advanced theoretical approaches which treat the interaction between the field and the target in first order (see also [41, 42]). The relationship of charged particle-induced ionization by exchange of a virtual photon to real photo double ionization has been elucidated. Work is in progress to perform experiments for proton and antiproton collisions,[3] the latter at CERN at reversed directions of the pulse, in order to identify interference contributions between first and second order, that manifest themselves in different ratios of double to single ionization for $p, \overline{p}$ – impact. Furthermore, measurements at lower incoming electron energies, where the *TS-2* becomes the dominant contribution, have recently been performed. Here, especially very low energies are of interest, where one proceeds to the double ionization threshold. Such data and theoretical calculations will be of indispensable help for the understanding of 'rescattering' occurring in double or multiple ionization in laser fields, where the electron recollision energies are typically close to threshold up to a few hundreds of eV, at intensities, where 'non-sequential' processes dominate high charge-state production. Furthermore, kinematically complete investigations of (*e,2e*) reactions in the presence of a laser field have become feasible [44] and are urgently required to understand strong-field recollision dynamics: Whereas differential data on non-sequential laser-induced multiple ionization [27, 28] are in excellent agreement with the kinematical boundaries (full lines in Fig. 13a) set by energy and momentum conservation within the recollision model [45], recent data unambiguously demonstrate [46, 47] that the (*e,2e*) recollision dynamics in the presence of the laser field differs dramatically from what would be expected from a field-free situation [48] (e.g. for 2 keV electron impact) illustrated in see Fig. 13b (for more recent theoretical work on two-electron dynamics, see, e.g. [49, 50] and references therein; for experimental work, see [51]).

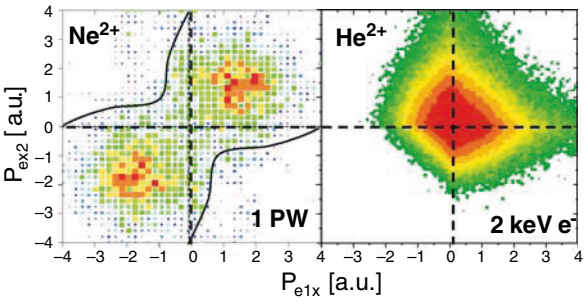

Fig. 13 Correlated two-electron momentum distributions along the force direction **e**, **q** (for (**a**) and (**b**), respectively) for double ionization of Ne by 1 PW/cm^2 laser-pulse impact (**a**) and 2 keV electron impact on He (**b**). *Full line*: kinematical boundaries within the classical recollision model (see text)

[3] Note that even the single ionization dynamics in collisions with protons and antiprotons has profound differences, see, e.g. [43].

4.4 Double Ionization at Strong Perturbation

Assuming that the effective strength of the projectile field is such that target single and double ionization occur mainly due to absorption of one and two virtual photons, respectively, from the pulse generated by the projectile, the simplest way to treat double ionization is to combine the first-order transition probabilities for target electrons with the independent electron model. Using such an approach Moshammer et al. [24] were able to qualitatively describe single differential cross-sections as a function of the energy of one 'typical' electron (integrated over all energies of the second) for double ionization of helium by 1 GeV/u U^{92+} impact. As shown in Fig. 14, shape and absolute magnitude agree reasonably well with the calculation (full line). Since now, in this 'sequential' situation (in the sense of independent interactions with the projectile field), no electron–electron correlation is needed at all to obtain double ionization, one might assume that correlation effects are of minor importance. For a state-of-the-art treatment of the four-body quantum dynamics in double ionization of helium by super-intense fields generated by relativistic ions, see [16].

Nevertheless, as shown in Fig. 15, where the correlated longitudinal (along the beam direction) momenta of two electrons are plotted in a two-dimensional density representation, strong correlation has been observed in recent experiments at lower impact energies [52] for He and Ne double as well as Ne triple ionization.

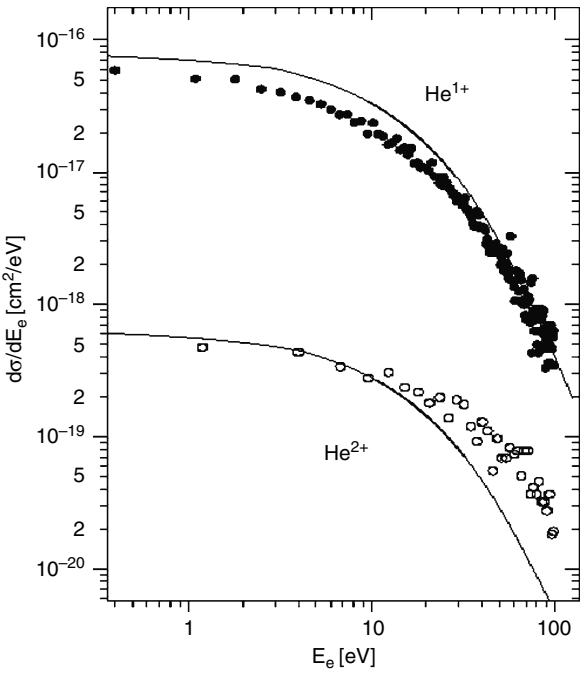

Fig. 14 Cross-section differential in the energy of the emitted electron for single (*upper part*) and double (*lower part*) ionization of He in collisions with 1 GeV/u U^{92+} impact as a function of the electron energy E_e (in the case of double ionization the integration has been performed over the energy distribution of one of the two emitted electrons). *Points*: experiment; *lines*: theoretical estimates based on the dipole approximation

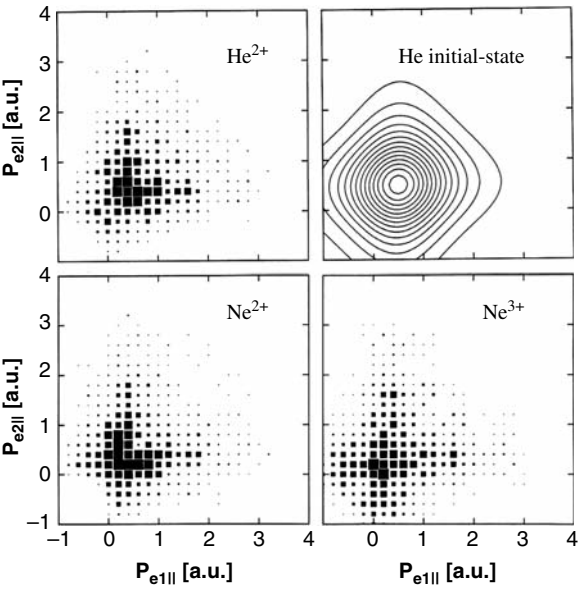

Fig. 15 Correlated two-electron longitudinal momentum distributions in a two-dimensional representation for He^{2+}, Ne^{2+} and Ne^{3+} production in collisions with 3.6 Mev/u Se^{28+} ($v_p = 12$ a.u.). Experiment: different box sizes represent doubly differential cross-sections in 10^{-16} cm^2 on a linear scale. *Upper right frame*: He ground state distribution (see text)

This was partly explained by classical trajectory Monte Carlo calculations (CTMC), where the target electrons move on classical Kepler orbits, with microcanonical distributions, bound with subsequent ionization potentials for many-electron atoms and where Newton's equations are solved during the collision [7]. In order to explain the data, electron correlation had to be included in the initial state by 'dynamical screening', where the effective nuclear charge, seen by either one of the two electrons, dynamically varies as a function of the distance between 'the other' electron and the nucleus. In addition, the final-state interaction between the two electrons has been 'switched' on in the moment, when both electrons are in the continuum, i.e. have positive energies during the collision. Also shown in Fig. 15 is the He ground-state probability distribution of the two electrons in the longitudinal momentum space, shifted by a longitudinal electron sum-momentum of 0.6 a.u. (estimated from the experimental results) to account for the final-state post-collision attraction into the forward direction by the receding projectile. For collisions, where the projectile emerges fast compared to the target fragment velocities, this is a reasonable approximation, since all target fragments experience about the same electric field in the final state. Then, if the result of the collision would be effectively identical to 'sudden switching off', the interaction between the target electrons and the target nucleus and the final-state interaction between the electrons could be neglected; the upper right frame of Fig. 15 would represent the final electron momenta.

It is quite likely that the final-state electron momenta observed in the experiment may indeed closely reflect properties of the initial-state correlated two-electron wave function. It has been even speculated that the (short-time)

correlation of the bound electrons may become visible and then the technique might be an 'attosecond microscope' for the investigation of bound states in atoms, molecules and clusters.

Recently, this idea has been further developed (see, e.g. [53]) by inspecting the so-called correlation function R of the emitted electrons. Here, the probability to find two electrons emitted in the same multiple ionization event with a certain momentum difference is compared to the corresponding probability for two independent electrons emitted in two different collisions. It was demonstrated that the correlation function is sensitive neither on the respective mechanism leading to double ionization (i.e. first-order or *TS-2* interaction with the projectile) nor on the final-state post-collision interaction with the projectile, possibly making R an ideal tool to investigate ground-state properties of the correlated wave function. Recently, this was substantiated by analysing the correlation function R for back-to-back emission of electrons with equal energy. For this particular emission pattern it was found, in qualitative agreement with theory, that not only is the maximum in R sensitive on the mean initial-state separation between the two electrons (see Fig. 16) but, moreover, its shape strongly depends on the correlated initial state used in the calculation.

It is very interesting to note that in first differential experiments on double ionization of He and Ar by femtosecond laser pulses in the 'sequential regime', no [54] or at least very weak [47] correlation has been observed in the two-electron transverse momentum spectra as shown for Ar at 1 PW/cm^2 in Fig. 17 (momentum component transverse to the pulse propagation and parallel to the polarization direction). Here, it becomes obvious that 'sequential' does not only mean that the electrons are removed in independent interactions with the field but, moreover, that the interaction really might be sequential as a function of time, removing the electrons in different, subsequent optical cycles of the field. If that is the case, no correlation at all might be expected, at least as the final state is concerned.

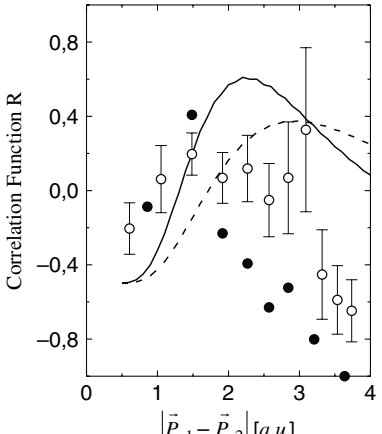

Fig. 16 Correlation function R for double ionization of He (*open circles*) and Ne (*full circles*) in collisions with 3.6 Mev/u Au^{53+} ($v_p = 12$ a.u.) as a function of the electron momentum difference $\Delta p = |\mathbf{p}_{e1} - \mathbf{p}_{e2}|$ for back-to-back emitted electrons. *Solid*, *dashed lines*: calculations for the Ne and He targets, respectively

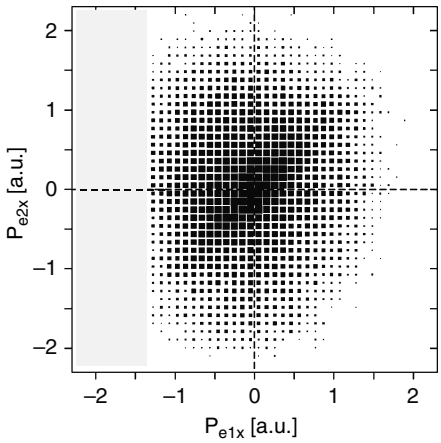

Fig. 17 Correlated two-electron transverse momentum distribution in a two-dimensional density representation for double ionization of Ar by 25 fs, 1 PW/cm^2 laser pulses. Box sizes correspond to the intensity on a linear scale between zero and maximum intensity. Left of $p_{e1x} = -1.4$ a.u.: no experimental acceptance

4.5 Multiple Ionization in Attosecond Fields

Up to now, one kinematically complete pilot experiment on multiple ionization at lower energies has been performed [55], where the final-state interaction cannot be neglected. In Fig. 18, the momentum vectors of triply ionized Ne recoil ions are plotted along with the vector sum-momenta of all three emitted electrons for 3.6 Mev/u Au^{53+} impact together with theoretical results obtained in the nCTMC approach. The collision plane is defined as in Fig. 7. The

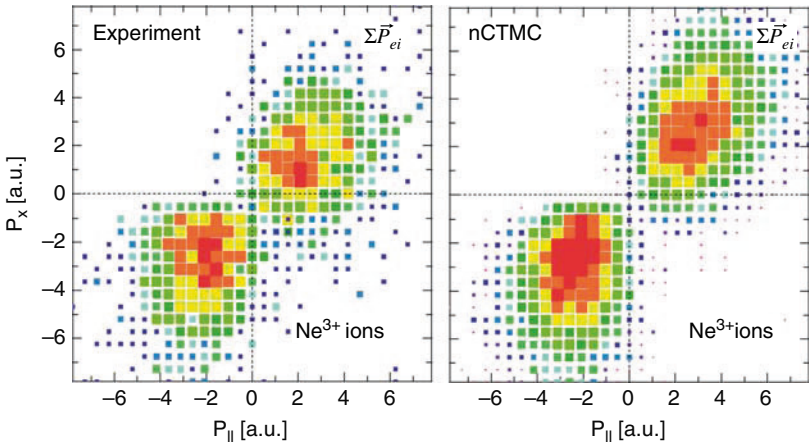

Fig. 18 Two-dimensional final-state momentum distributions for the Ne^{3+} recoil ion and the sum-momentum vector for all three emitted electrons for triple ionization of Ne by 3.6 Mev/u Au^{53+} impact. The collision plane is defined as in Fig. 7. *Left side*: experiment. *Right side*: nCTMC (see text). *Z*-scale is logarithmic

classical calculations are found to be in remarkable agreement with the experimental results, which might be not too surprising since $2Z_p/\upsilon_p \approx 8.8 \gg 1$.

At extreme relativistic velocities, the projectile field will be strongly compressed in the longitudinal direction becoming closely similar to an ideal dipole half-circle pulse that moves at the speed of light. The virtual photons, building the field, more and more resemble transversally polarized real photons and the longitudinal force along the beam direction vanishes, i.e. no post-collision interaction is left.In the present case, at much lower velocities (and high Z_p), we find a strong post-collision effect where the projectile field is dragging each of the electrons behind but at the same time pushing away the Ne^{3+} ions with nearly identical momenta. Thus, following the above ideas, the post-collision effect can be seen as a dissociation of the target fragments in the field of the receding ion, again without any noticeable net-momentum transfer to the fragments. Implying that all the electrons are influenced by the post-collision interaction on the same footing after the collision (strongly supported by the fact that $\mathbf{P}_R \approx -\sum_i \mathbf{P}_{ei}$) independent on their momenta in the instant of ionization, one might separate the influence of the post-collision interaction from the relative motion of the three electrons by choosing the (non-inertial) three-electron centre-of-mass (CM) coordinate frame, where the post-collision effect would be not present at all in the ideal case when the projectile field may be considered in the final state as spatially homogeneous.

We have performed such a transformation and plotted the relative energies of the three electrons in the CM system $\varepsilon_{ei} = E_i^{(CM)} / \sum_j E_j^{(CM)}$ (with $E_i^{(CM)}$ being the CM energy of the ith electron) in a modified Dalitz plot in Fig. 19. This is an equilateral triangle where each triple ionization event is represented by one point inside the triangle, with its distance from each individual side being proportional to the relative energy of the corresponding electron as indicated in the figure. Only events in the inscribed circle are allowed due to momentum

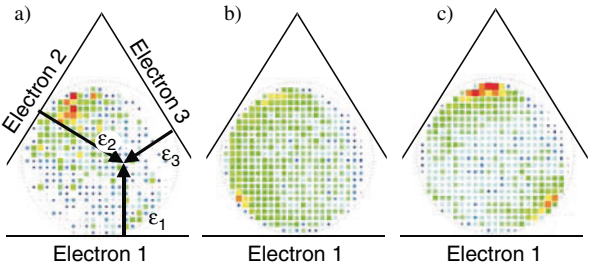

Fig. 19 Dalitz representation (see text) of the energy partitioning of three electrons emitted in triply ionizing 3.6 Mev/u Au^{53+} collisions in the electron centre-of-mass (CM) coordinate system. ε_i: relative energy of the ith electron in the CM system. Electrons are numbered according to their angle with respect to the projectile direction (see text). *Left*: experiment; *middle*: nCTMC without electron–electron interaction; *right*: CTMC with correlated three-electron initial state (see text)

conservation of the three electrons in the CM frame $\sum \mathbf{P}_{ei}^{(\mathrm{CM})} = 0$. Numbering the electrons is achieved by exploiting information on their emission angle: Electron 1 is the one with the smallest angle relative to the projectile propagation direction in each triple ionization event; electron 3 is the one with the largest angle and electron 2 lying in between.

Obviously, the electron energies are not independent of each other, and the many-electron continuum, explored for the first time experimentally, is found to be strongly correlated. There is an increased probability that electrons 1 and 3 have large energies compared to electron 2. Performing nCTMC calculations with the electron–electron interaction not included beyond an effective potential in the initial state, these structures cannot be reproduced (Fig. 19b). This situation is similar to the one described before for double ionization, where qualitative agreement between nCTMC and experiment was only achieved when the electron-electron interaction was explicitly implemented in the final state. Proceeding in the same way for triple ionization did lead to structures in the Dalitz plot but essentially with the role of electrons 2 and 3 exchanged. Introducing in addition a completely correlated, three-electron (p-electrons neglecting the spin) classical initial state, where the individual electrons synchronously move on Kepler ellipses at equal distances relative to each other on the corners of an equilateral triangle in a plane, with the electron–electron interaction 'switched on' during the entire collision (not only in the final state) brought the theoretical results close to the experimental data (Fig. 19c).

Thus, in the light of the results for single ionization by the same projectiles, where the longitudinal electron momentum spectra have been demonstrated to closely reflect features of the Hartree–Fock initial-state wave function (see Fig. 11), it does not seem to be too optimistic to expect that multi-electron momentum distributions might reveal direct information about the correlated many-electron bound-state wave function. Moreover, since the target disintegration occurs within attoseconds, i.e. on a time scale short compared to typical revolution times of ground-state electrons, one might even hope that such experiments will provide direct information on the short-time correlation between the electrons in the initial state.

5 A View into the Future

5.1 Experiments in Storage Rings

Presently, work is in progress to perform such experiments at higher energies, i.e. at 500 Mev/u for projectile charge states between about $30+$ and $92+$ in the experimental storage ring ESR of GSI. To verify whether or not and to what extent the final-state electron momenta mirror the correlated initial state, i.e. whether an 'attosecond-microscope' is realizable, experiments will be performed for ground-state as well as metastable excited helium targets. Due to the

strongly increased luminosity in the storage ring we expect considerable, orders of magnitude, increased event rates, so that fully differential cross-sections should become measurable not only for double but also for triple and quadruple ionization.

As compared to the strong-field laser case, this would correspond to high-power lasers at MHz repetition rates. Different from the attosecond scenario, where one might expect short-time information on correlated ground states of atoms and molecules, one then explores correlated few-electron dynamics on femto- and sub-femtosecond time scales. Here, as demonstrated above, the laser efficiently transfers energy to the system in the final state, once the electrons are set free, whereas the initial (tunnelling or multi-photon) ionization process remains quite ineffective, even if 10^{19} W/cm^2 pulses at MHz repetition rates were at hand.

5.2 *Laser-Assisted Collisions*

An interesting situation arises, and might be realized with the PHELIX laser at GSI, if both, atto- and femtosecond fields act together. The ion-induced pulse efficiently brings a large number of electrons into the continuum, placing them 'simultaneously' with little energy into the oscillating field of the laser, which then accelerates this bunch of electrons very effectively in a coherent way heating them tremendously. Thus, one might envisage that the most effective way to transfer energy to matter might be a concerted action between ion-induced and laser fields.

Unexpectedly strong coupling of an even weak ($F_0 = 0.005$ a.u.), low-frequency ($\omega_L = 0.004$ a.u.) electromagnetic radiation field to matter has been predicted in laser-assisted collisions considering a nearly reversed situation, where target electrons are strongly accelerated in a direct collision with a fast ($v_p \sim 10$ a.u.) proton (the so-called binary encounter electrons; BEE) [56] or a high-energy photon (the laser-assisted Compton effect) [57]. Whereas the laser field considered was by far not strong enough to noticeably disturb the hydrogen target atom ground state alone, strong effects occur during the collision in the high-energy BEE emission, where thousands of laser photons were observed to couple to the system strongly modifying the energy and angular distribution of the BEE. In general, laser-assisted collisions that have been theoretically explored since a while (see [58] for a recent review and other references therein) but were only accessible experimentally for elastic scattering until the advent of Reaction Microscopes combined with intense ns-pulsed *YAG* lasers. Such experiments, first realized with still limited statistical relevance in [44], should in the future help to shed light on the hitherto unexplained 'laser-assisted' (e,ne) dynamics occurring during 'recollision' as leading non-sequential contribution to strong-field multiple ionization.

5.3 VUV- and X-Ray Free Electron Lasers (SASE-FELs)

Novel and exciting strong-field phenomena will arise and can be explored in detail using Reaction Microscopes with the advent of SASE-FELs, presently in the test phase at the TESLA test facility of DESY in Hamburg and proposed as BESSY-FEL in Berlin (see the contribution of Feldhaus/Sonntag in this book). Recently, 50 fs pulses have been demonstrated at power densities reaching 10^{17} W/cm^2 for a photon energy of around 10 eV. Pulses of similar power density with a bandwidth of $\Delta\lambda/\lambda = 10^{-4}$, 50 fs pulse duration and repetition rates between 10 Hz and 70 kHz are envisaged in an energy range of 10 eV to about 300 eV in the second phase, starting in spring 2005. Now, similar to the virtual (quasi-real at ultrarelativistic velocities) photons in the attosecond pulse, individual electrons can be brought into the continuum by separately absorbing a single high-frequency photon from the field which have identical energies, however.

Then, ab initio calculations, solving the time-dependent Schrödinger equation for the two-electron system in three dimensions on a grid [59], which cannot yet be performed for optical laser frequencies due to the limitations set by state-of-the-art massively parallel computing facilities, can be tested in detail. In general, due to the tremendously improved capability to perform ab initio calculations for reduced number of active photons [60], such devices will be of indispensable help to investigate fundamental questions on the interaction of strong electromagnetic radiation fields with matter.

References

1. http://www.nupeec.org/iai.2000
2. C.L. Cocke and R.E. Olson, Phys. Rep. **205**, 155 (1991)
3. A.B. Voitkiv and J. Ullrich, J.Phys. B **34**, 4513 (2001)
4. A.B. Voitkiv, B. Najjari, R. Moshammer, and J. Ullrich, Phys.Rev. A **65** 032707 (2002)
5. R. Moshammer, J. Ullrich, M. Unverzagt, W. Schmidt, J. Jardin, R.E. Olson, R. Mann, R. Dörner, V. Mergel, U. Buck, and H. Schmidt-Böcking, Phys. Rev. Lett. **73** 3371 (1994); W. Schmitt, R. Moshammer, F.S.C. O'Rourke, H. Kollmus, L. Sarkadi, R. Mann, S. Hagmann, R.E. Olson, and J. Ullrich, Phys. Rev. Lett. **81**, 4337 (1998)
6. P. Fainstein, L. Gulyas, F. Martyn, and A. Salin, Phys. Rev. A **53**, 3243 (1996)
7. R. Moshammer, A. Perumal, M. Schulz, H. Kollmus, R. Mann, S. Hagmann, and J. Ullrich, Phys. Rev. Lett. **87**, 223701 (2001); R.E. Olson and J. Fiol, J. Phys. B **34**, L625 (2001); D. Fisher, A.B. Voitkiv, R. Moshammer, and J. Ullrich, Phys. Rev. A **68**, 032709 (2003)
8. R.E. Olson, J. Ullrich, H. Schmidt-Böcking, Phys. Rev. A **39**, 5572 (1989)
9. A.B. Voitkiv, B. Najjari, R. Moshammer, M. Schulz, and J. Ullrich, J. Phys. B **37**, L365 (2004)
10. J. McGuire, *Electron Correlation Dynamics in Atomic Collisions* (Cambridge Monographs on Atomic, Molecular and Chemical Physics) (Cambridge: Cambridge University Press)
11. A.B. Voitkiv, N. Grün, and W. Scheid, Phys.Lett. A **265**, 111 (2000); A.B. Voitkiv, C. Müller, and N. Grün, NIM **B 205** 504 (2000)
12. R. Dörner et al., Phys. Rev. Lett. **76** 2654 (1996)

13. A. Dorn, A. Kheifets, C.D. Schröter, B. Najjari, C. Höhr, R. Moshammer, and J.Ullrich, Phys. Rev. Lett. **86**, 3755 (2001)
14. A. Dorn, A. Kheifets, C.D. Schröter, C. Höhr, Gr. Sakhelashvili, R. Moshammer. J. Lower, and J.Ullrich, Phys. Rev. Lett. **68**, 012715 (2003)
15. T. Kirchner, L. Gulyas, M. Schulz, R. Moshammer, and J. Ullrich, Phys. Rev. A 65 042727 (2002); NIM **B205**, 475 (2003)
16. A.B. Voitkiv and B. Najjari, J.Phys. B **37**, 4831 (2004); A.B. Voitkiv, B. Najjari, and J. Ullrich, J. Phys. B **38**, L107 (2005); A.B. Voitkiv, B. Najjari, and J. Ullrich, JETP **100** 516 (2005)
17. R. Dörner, V. Mergel, O. Jagutzki, L. Spielberger, J. Ullrich, R. Moshammer, and H. Schmidt-Böcking, Phys. Rep. **330**, 95 (2000)
18. J. Ullrich, R. Moshammer, A. Dorn, R. Dörner, L.Ph.H. Schmidt, and H. Schmidt-Böcking, Rep. Progr. Phys. **66**, 1463 (2003)
19. R. Moshammer, M. Unverzagt, W. Schmitt, J. Ullrich, and H. Schmidt-Böcking, Nucl. Instrum. Meth. B **108**, 425 (1996)
20. R. Moshammer, B. Feuerstein, D. Fischer, A. Dorn, C.D. Schröter, J. Deipenwisch, J.R. Crespo Lopez-Urrutia, C. Höhr, P. Neumayer, J. Ullrich, H. Rottke, C. Trump, M. Wittmann, G. Korn, and W. Sander, Optics Express **8**, No7, 358 (2001); V.L.B. de Jesus, A. Rudenko, B. Feuerstein, K. Zrost, C.D. Schröter, R. Moshammer, and J. Ullrich, J. Electron Spectrosc. Related Phenomena **141**, 127 (2004)
21. A. Rudenko, K. Zrost, B. Feuerstein, B.L.B. de Jesus, C.D. Schröter, R. Moshammer, and J. Ullrich, Phys. Rev. Lett. **93**, 253001 (2004)
22. A. Rudenko, K. Zrost, C.D. Schröter, B.L.B. de Jesus, B. Feuerstein, R. Moshammer, and J. Ullrich, J. Phys. B **37**, L407 (2004)
23. R. Dörner, Th. Weber, M. Weckenbrock, A. Staudte, M. Hattass, R. Moshammer, J. Ullrich, H. Schmidt-Böcking, Adv.At.Mol.Phys. ed.: B. Bederson, H. Walther, Adv. At. Mol. Opt. Phys. **48**, 1 (2002)
24. R. Moshammer, W. Schmitt, J. Ullrich, H. Kollmus, A. Cassimi, R. Dörner, O. Jagutzki, R. Mann, R.E. Olson, H.T. Prinz, H. Schmidt-Böcking, and L. Spielberger, Phys. Rev. Lett. **79**, 3621 (1997)
25. A.B. Voitkiv, J. Phys. B **29**, 5433 (1996); A.B. Voitkiv, N. Grün, and W. Scheid, J. Phys. B **32**, 3923 (1999)
26. N.B. Delone and V.P. Krainov, Opt. Soc. Am. B **8**, 1207 (1991)
27. R. Moshammer, B. Feuerstein, W. Schmidt, A. Dorn, C.D. Schröter, J. Ullrich, H. Rottke, C. Trump, M. Wittmann, G. Korn, K. Hoffmann, and W. Sandner, Phys. Rev. Lett. **84**, 447 (2000)
28. Th. Weber, M. Weckenbrock, A. Staudte, L. Spielberger, O. Jagutzki, V. Mergel, G. Urbasch, M. Vollmer, H. Giessen, and R. Dörner, Phys. Rev. Lett. **84**, 443 (2000)
29. A. Rudenko, K. Zrost, T. Ergler, A.B. Voitkiv, B. Najjari, B.L.B. de Jesus, B. Feuerstein, C.D. Schröter, R. Moshammer, and J. Ullrich, J.Phys. B **38**, L191 (2005)
30. R. Moshammer, P.D. Fainstein, M. Schulz, W. Schmitt, H. Kollmus, R. Mann, S. Hagmann, and J. Ullrich, Phys. Rev. Lett. **83**, 4721 (1999)
31. L. Gulyas, T. Kirchner, T. Shirai, and M. Horbatsch, Phys. Rev A **62**, 022702 (2000)
32. B. Bapat, R. Moshammer, S. Keller, W. Schmitt, A. Cassimi, L. Adoui, H. Kollmus, R. Dörner, Th. Weber, K. Khayyat, R. Mann, J.P. Grandin, and J. Ullrich, J. Phys. B **32**, 1859 (1999)
33. B. Bapat, S. Keller, R. Moshammer, R. Mann, and J. Ullrich, J. Phys. B **33**, 1437 (2000)
34. S. Keller, B. Bapat, R. Moshammer, J. Ullrich, and R.M. Dreizler, J. Phys. B **33**, 1447 (2000)
35. D.N. Fittinghoff, P.R. Bolton, B. Chang, and K.D. Kulander, Phys. Rev. Lett. **69**, 2642 (1992)
36. P.B. Corkum, Phys. Rev. Lett. **71**, 1994 (1993)

37. U. Eichmann, M. Dörr, H. Maeda, W. Becker, and W. Sandner, Phys. Rev. Lett. **84**, 3550 (2000)
38. Huetz et al., J. Phys. B **24**, 1917 (1991)
39. A. Kheifets, I. Bray, A. Lahmam-Bennani, A. Duguet, M. Lecas, and L. Avaldi, J. Phys. B **32**, 5047 (1999)
40. A. Dorn, A. Kheifets, C.D. Schröter, C. Höhr, Gr. Sakhelashvili, R. Moshammer, J. Lower, and J. Ullrich, Phys. Rev. Lett. **68**, 012716 (2003)
41. J. Berakdar, Phys. Rev. Lett. **85**, 4036 (2000)
42. A. Dorn, A. Kheifets, C.D. Schröter, C. Höhr, R. Moshammer, and J. Ullrich, Phys. Rev. A **65**, 032709 (2002).
43. A.B. Voitkiv and J. Ullrich, Phys. Rev. A **67**, 062703 (2003)
44. C. Höhr, A. Dorn, B. Najjari, D. Fisher, C.D. Schröter, and J. Ullrich, Phys. Rev. Lett. **94**, 153701 (2005)
45. B. Feuerstein, R. Moshammer, and J. Ullrich, J. Phys. B **33**, L823 (2000)
46. B. Feuerstein, R. Moshammer, D. Fischer, A. Dorn, C.D. Schröter, J. Deipenwisch, J.R. Crespo Lopez-Urrutia, C. Höhr, P. Neumayer, J. Ullrich, H. Rottke, C. Trump, M. Wittmann, G. Korn, K. Hoffmann, and W. Sandner, Phys. Rev. Lett. **87**, 043003 (2001)
47. R. Moshammer, B. Feuerstein, J.R. Crespo Lopez-Urrutia, J. Deipenwisch, A. Dorn, D. Fischer, C. Höhr, P. Neumayer, C.D. Schröter, J. Ullrich, H. Rottke, C. Trump, M. Wittmann, G. Korn, K. Hoffmann, and W. Sandner, Phys. Rev. A **65**, 035401 (2001)
48. S.V. Popruzhenko, Ph.A. Korneev, S.P. Goreslavski, and W. Becker, Phys. Rev. Lett. **89**, 023001 (2001)
49. G. Figuera de Morisson Faria, H. Schomerus, X. Liu, and W. Becker, Phys. Rev. A **69**, 043405 (2004)
50. G. Figuera de Morisson Faria, X. Liu, and W. Becker, Phys. Rev. A **69**, 021402(R) (2004)
51. V.L.B. de Jesus, B. Feuerstein, K. Zrost, D. Fisher, A. Rudenko, F. Afaneh, C.D. Schröter, R. Moshammer, and J. Ullrich, J.Phys. B, **37** L161 (2004)
52. R. Moshammer, J. Ullrich, H. Kollmus, W. Schmitt, M. Unverzagt, O. Jagutzki, V. Mergel, H. Schmidt-Böcking, R. Mann, C.J. Woods, and R.E. Olson, Phys. Rev. Lett. **77**, 1242 (1996)
53. M. Schulz, R. Moshammer, W. Schmitt, H. Kollmus, B. Feuerstein, R. Mann, S. Hagmann, and J. Ullrich, Phys. Rev. Lett. **84**, 863 (2000)
54. T. Weber et al., Nature **405**, 658 (2000)
55. M. Schulz, R. Moshammer, W. Schmitt, H. Kollmus, B. Feuerstein, R. Mann, S. Hagmann, and J. Ullrich, Phys.Rev.Lett. **84** (2000)
56. A.B. Voitkiv and J. Ullrich, J. Phys. B **34**, 1673 (2001); 4383 (2001)
57. A.B. Voitkiv, N. Grün and J. Ullrich, J. Phys. B **36**, 1907 (2003), B **37**, 2641 (2004)
58. F. Ehlotsky, A. Jaron, and J.Z. Kaminski, Phys. Rep. **297**, 63 (1998)
59. D. Dundas, K.T. Taylor, J.S. Parker, and E.S. Smyth, J.Phys. **B 32**, L231 (1999)
60. A. Saenz and P. Lambropoulos, J.Phys. **B 32**, 5629 (1999); R. Hasbani. E. Cormier and H. Bachau, J. Phys. **B 33**, 2101 (2000); S.S. Novikov and A.N. Hopersky, J. Phys. **33**, 2287 (2000)

Index

Springer Series in

OPTICAL SCIENCES

125 **Electromagnetic and Optical Pulse Propagation 1**
Spectral Representations in Temporally Dispersive Media
By K.E. Oughstun, 2007, 74 figs., XX, 456 pages

126 **Quantum Well Infrared Photodetectors**
Physics and Applications
By H. Schneider and H.C. Liu, 2007, 153 figs., XVI, 250 pages

127 **Integrated Ring Resonators**
The Compendium
By D.G. Rabus, 2007, 243 figs., XVI, 258 pages

128 **High Power Diode Lasers**
Technology and Applications
By F. Bachmann, P. Loosen, and R. Poprawe (Eds.), 2007, 543 figs., VI, 548 pages

129 **Laser Ablation and its Applications**
By C.R. Phipps (Ed.), 2007, 300 figs., XX, 586 pages

130 **Concentrator Photovoltaics**
By A. Luque and V. Andreev (Eds.), 2007, 250 figs., XIII, 345 pages

131 **Surface Plasmon Nanophotonics**
By M.L. Brongersma and P.G. Kik (Eds.), 2007, 147 figs., VII, 271 pages

132 **Ultrafast Optics V**
By S. Watanabe and K. Midorikawa (Eds.), 2007, 339 figs., XXXVII, 562 pages. With CD-ROM

133 **Frontiers in Surface Nanophotonics**
Principles and Applications
By D.L. Andrews and Z. Gaburro (Eds.), 2007, 89 figs., X, 176 pages

134 **Strong Field Laser Physics**
By T. Brabec, 2007, 258 figs., XV, 592 pages

135 **Optical Nonlinearities in Chalcogenide Glasses and their Applications**
By A. Zakery and S.R. Elliott, 2007, 92 figs., IX, 199 pages

136 **Optical Measurement Techniques**
Innovations for Industry and the Life Sciences
By K.E. Peiponen, R. Myllylä and A.V. Priezzhev, 2008, approx. 65 figs., IX, 300 pages

137 **Modern Developments in X-Ray and Neutron Optics**
By A. Erko, M. Idir, T. Krist and A.G. Michette, 2008, approx. 150 figs., XV, 400 pages

138 **Optical Micro-Resonators**
Theory, Fabrication, and Applications
By R. Grover, J. Heebner and T. Ibrahim, 2008, approx. 100 figs., XXII, 330 pages

139 **Progress in Nano-Electro-Optics VI**
Nano-Optical Probing, Manipulation, Analysis, and Their Theoretical Bases
By M. Ohtsu (Ed.), 2008, 107 figs., XI, 188 pages